Monitoring the response of head and neck tumour tissue to irradiation using a microfluidic-based approach

Ramsah Cheah

A Dissertation presented for the degree of

Doctor of Philosophy

The University of Hull

Hull York Medical School

June 2016

Abstract

Radiotherapy remains the standard treat74ment for head and neck squamous cell carcinoma (HNSCC), however, resistance remains a real clinical problem despite the improvements and development of new treatment strategies. Patient outcome could potentially be improved if the response to irradiation could be predicted allowing alternative treatments to be implemented. The current project has investigated the ability to maintain HNSCC tissue under pseudo *in vivo*-like conditions using a bespoke microfluidic device. The interrogation of the tissue with irradiation has also been performed with a view to predicting outcome and ultimately personalising medicinal treatment.

Following extensive optimisation of key steps in device establishment, e.g. flow rates, serum concentration, oxygen perfusion, using rat liver and human tumour tissue, a series of HNSCC biopsies were divided and placed into parallel microfluidic devices and pieces of each tumour were subjected to single-dose irradiation (5, 10, 15, and 20Gy). Lactate dehydrogenase (LDH) release was measured in effluent collected every 2hr. In five of the tumours (primary n=3; metastatic lymph node n=2), frozen tissue sections were stained for cytokeratin (CK), M30 (detects cleaved CK-18), γH2AX, Ki-67 and for TUNEL. A CK18-labelling index (CK18-LI) was developed by expressing the percentage of apoptotic area (M30) over the total tumour area (CK+ staining). The positive γH2AX, Ki-67 expression and TUNEL were evaluated as positive nuclei within selected tumour areas.

Single-dose irradiation induced variable, yet higher, CK18-LI compared with non-irradiated controls. In contrast no statistically significant differences in LDH release were observed between irradiated samples and controls. The percentage of Ki-67 expression reduced dose-dependently but not significantly following on-chip irradiation. Variation in expression profiles of these markers was identified between patients when using the same irradiation regimen demonstrating the potential of current microfluidic irradiation experimentation in monitoring patient's radio-therapeutic response. In conclusion, microfluidics offers a potential tool in personalised medicine, capable of predicting a tumours response to irradiation prior to clinical administration although further validation experiments are required. The approach has equal applicability to all solid tumours and multiple types of treatment, i.e. chemo-radiation.

Thesis associated presentations and published abstracts

Cheah R., Srivastava R., Kazmierow H., Patel R., Stafford N., Green V., and Greenman J. 2013. Optimisation of culture conditions for the maintenance of viable tissue samples in a microfluidic device. *Hull York Medical School*. (Poster) 2013 HYMS Postgraduate Research Conference (June 2013, Hull).

Cheah R., Srivastava R., Kazmierow H., Patel R., Stafford N., Green V., and Greenman J. 2013. Optimisation of culture conditions for the maintenance of viable tissue samples in a microfluidic device and the study of tissue response to irradiation. *The National Cancer Research Institute.* (Poster) 2013 NCRI Cancer Conference (November 2013, Liverpool).

Patel R., Green V., Srivastava R., **Cheah R**., Hunter, I. A., and Greenman J. 2013. The use of apoptotic markers to predict rectal cancer response to neo-adjuvant therapy. *The National Cancer Research Institute.* (Poster) 2013 NCRI Cancer Conference (November 2013, Liverpool).

Cheah R., Srivastava R., Stafford N., Green V., and Greenman J. 2014. Investigation of the response of head and neck squamous cell carcinoma (HNSCC) to irradiation using a microfluidic device. *Hull York Medical School (HYMS).* (Poster) 2014 HYMS Postgraduate Research Conference (June 2014, York).

Cheah R., Srivastava R., Stafford N., Green V., and Greenman J. 2014. Analysis of cell death in head and neck squamous cell carcinoma (HNSCC) tissue in response to irradiation during microfluidic culture. *The National Cancer Research Institute.* (Poster) 2014 NCRI Cancer Conference (November 2014, Liverpool).

Cheah R., Srivastava R., Stafford N., Green V., and Greenman J. 2015. Can microfluidic culture be used to determine the response of head and neck squamous cell carcinoma tissue to irradiation using different markers of cell death? *European Association for Cancer Research (EACR)*. (Poster) EACR Conference Series 2015. (February 2015, Essen)

Cheah R., Srivastava R., Stafford N., Green V., and Greenman J. 2015. Exploiting microfluidic culture to determine the radio-sensitivity of head and neck squamous cell carcinoma tissue. *Hull York Medical School (HYMS).* (Poster) 2015 HYMS Postgraduate Research Conference (June 2015, Hull).

Thesis associated journal publication (under reviewed)

Cheah R., Srivastava R., Stafford N., Beavis AW, Green V., and Greenman J. 2015. A microfluidic approach to determine the radio-sensitivity of head and neck squamous cell carcinoma biopsies. *Radiotherapy and Oncology.* Elsevier Publisher. (Under reviewed)

Table of Contents

List of figures **6**
List of tables **12**
Abbreviation **13**
Acknowledgement **18**
Declaration **18**

1. Introduction **19**
1.1. Head and neck cancer 19
1.1.1 Development and progression of HNSCC 20
1.1.2 Incidence and epidemiology of HNSCC 22
1.1.3 Aetiology of HNSCC 24
Tobacco smoking 24
Alcohol consumption 25
Tobacco smoking and alcohol drinking 26
Human Papillomavirus (HPV) Infection 27
1.1.4 TNM staging system 28
1.2. Treatment of HNSCC 30
1.2.1 Surgery 30
1.2.2 Chemotherapy 31
1.2.3 Immunotherapy 32
1.2.4 Radiotherapy 33
1.3. Mechanisms of cell damage by irradiation 38
1.3.1 Cell cycle controls under normal condition 38
1.3.2 Cell death regulation (apoptosis) under normal condition 40
Extrinsic apoptotic pathway- Death receptor pathway 41
Intrinsic apoptotic pathway- Mitochondrial pathway 42
1.3.3 Types of DNA damage and double-strand breaks (DSBs) 46
1.3.4 DNA damage checkpoints and DNA-damage response (DDR) pathway 46
DNA damage checkpoints 46
DNA-damage response (DDR) 49
1.3.5 Predisposition and molecular behaviour of cancer cells 51
1.3.6 Mechanisms of radiotherapy resistance 54
Clinical factors 54
Biological factors 55
1.4. Microfluidics 59
1.4.1 Materials used for the construction of microfluidic devices 60
1.4.2 Benefits and principles of microfluidics 61
Small volumes of samples 62
High surface area to volume (SAV) ratio 62
Particles diffusion transport mechanism 63
Laminar flow 63
Biomimetic microenvironment in microfluidics 65
Maintenance of organ-specific architectural complexity 67
Parallelisation and high-throughput method 68
1.4.3 Drawbacks of microfluidics 69
1.4.4 Applications of microfluidics 70
1.4.5 Microfluidic device used in this study 76
1.5. Aims of the project 78

2. Material and Methods **80**
2.1. Head and neck cancer cell culture 80
2.2. Media Preparation for tissue culture and tissues manipulation 80
2.3. Microfluidics Set-up 81

2.3.1 Cleaning the microfluidic device and checking for blockages 87
2.3.2 Assembly of microfluidics flow system 87
2.3.3 Preparing and using the microfluidics flow system 89
2.4. Microfluidic culture methodologies on HNSCC tissue with and without irradiation/ Irradiation of HNSCC tissue in the microfluidic system ... 91
2.5. Fractionated irradiation methodologies on HNSCC tumours in microfluidics ... 100
2.6. Measurement of cell viability by Lactate Dehydrogenase (LDH) analysis ... 101
2.7. Tissue processing and microtome cryostat sectioning ... 103
2.8. Assessment of morphology and histology of tissue by Haematoxylin and Eosin staining ... 103
2.9. Immunohistochemical (IHC) staining of frozen tissue sections ... 104
2.10. M30 CytoDeath™ ELISA on microfluidic effluent ... 106
2.11. Apoptosis detection on tissue sections using the TUNEL assay ... 108
2.12. Incorporation of fluorescent markers into HNSCC tissue maintained in microfluidic device ... 109
2.12.1 Apoptosis detection following incorporation of CaspACE FITC-VAD-FMK. 110
2.12.2 Incorporation of 2-NBDG to study glucose metabolism 110
2.12.3 Detection of proliferating cells using EdU 110
2.12.4 Incorporation of FITC-dextran to study glucose metabolism 111
2.13. Laser capture microdissection (LCM) ... 112
2.13.1 Sample preparation 112
2.13.2 Laser capture microdissection (LCM) 113
2.14. RNA extraction of laser-microdissected samples ... 114
2.15. Reverse transcription, qualitative PCR and quantitative real-time polymerase chain reaction (qRT-PCR) ... 116
2.15.1 cDNA synthesis 116
2.15.2 Qualitative PCR analysis 116
2.15.3 Quantitative real-time PCR analysis 118
2.16. Statistical analyses ... 119
3. Optimisation of conditions within the microfluidic system ... 121
3.1. Materials and methods of microfluidic device set-up ... 123
3.2. Optimisation of BrdU incorporation and subsequent IHC staining ... 124
3.3. Analysis of rat liver tissue following traditional tissue culture ... 127
3.3.1 LDH cytotoxicity assay 128
3.3.2 Morphological appearance 129
3.4. The interrogation of rat liver tissues in microfluidic perfusion systems ... 130
3.4.1 LDH cytotoxicity assay 130
3.4.2 Morphological appearance 135
3.4.3 BrdU incorporation –Immunohistochemical (IHC) Staining 136
3.5. The use of different serum concentration during rat liver culture in microfluidic device ... 138
3.6. The use of rat serum for microfluidic culture of rat liver tissue ... 140
3.7. The use of HEPES buffer during rat liver culture in microfluidic device ... 142
3.8. The use of medium gassed with a carbogen gas mixture (95% of oxygen and 5% of carbon dioxide) for rat liver in microfluidic device ... 144
3.9. The use of different medium flow rates in the microfluidic device ... 146
3.10. The interrogation of HNSCC tissues in microfluidics for 4-6 days ... 150
3.11. The use of 10% AB serum during HNSCC tissue culture in microfluidics ... 153

3.12. Permeation of FITC-conjugated dextran across tissues in microfluidics 155
3.13. Discussion 158
3.13.1 Determining the optimal experimental conditions for analysis of BrdU incorporation into tissue maintained in a microfluidic device 158
3.13.2 The potential of microfluidics to maintain tissue morphology and proliferation 159
3.13.3 Size dependent marker permeation through tissue in microfluidics 163

4. Measuring the effects of irradiation on HNSCC tissue maintained in a microfluidic device (I) – Cell death and DNA repair 166

4.1. Introduction 166
4.1.1 Cytomorphological alterations 171
4.1.2 Detection of caspase-cleaved substrates- caspase-cleaved CK-18 171
4.1.3 Detection of DNA double-strand breaks using phosphorylated H2AX 172
4.1.4 Detection of caspase activation using caspase inhibitors (CaspACE™ FITC-VAD-FMK) 175
4.1.5 Detection of DNA fragmentation-TUNEL 175
4.1.6 Membrane alterations- Lactate Dehydrogenase (LDH) assay 176
4.1.7 Mitochondrial apoptosis measured using Bcl-2 176
4.2. The expression of caspase-cleaved CK18, γH2AX and Bcl-2 in UMSCC-47 cells following etoposide treatment 178
4.3. Optimisation of the irradiation procedure on tumours maintained in microfluidics 182
4.3.1 Determination of microfluidics termination time for post-irradiation analysis 182
4.3.2 The effects of transport of the tumour tissue for irradiation 185
4.4. The effect of microfluidic culture with and without irradiation on tissue morphology and integrity- H&E staining 186
4.5. Apoptotic labelling index of HNSCC tissues following microfluidic culture with and without irradiation 189
4.5.1 CK18-LI of single-dose irradiated tissues 192
4.5.2 CK18-LI on tissues subjected to fractionated irradiation 197
4.6. The effect of irradiation on the release of caspase-cleaved CK18 into the microfluidic effluent 199
4.7. The effect of irradiation on DNA double-strand breaks in HNSCC tissue maintained in the microfluidic device 201
4.7.1 Percentage of γH2AX expression following single-dose irradiation 204
4.7.2 Percentage of γH2AX expression level following fractioned irradiation 207
4.8. Incorporation of FITC-conjugated caspase inhibitor (CaspACE) as a marker of apoptosis following irradiation 209
4.8.1 Fluorescence detection of CaspACE markers on HSNCC tissues 210
4.9. The effect of irradiation on DNA fragmentation measured using TUNEL assay 213
4.9.1 Fluorescence detection of DNA fragmentation on HNSCC tissues 215
4.10. The effect of irradiation on the release of LDH from HNSCC tissue maintained in a microfluidic device with and without irradiation 218
4.11. The effect of irradiation of apoptotic cell death detection measured using IHC staining of Bcl-2 222
4.11.1 IHC staining of Bcl-2 on HNSCC tissues 222
4.12. Discussion 225
4.12.1 Optimisation of cell death markers staining using ICC on HNSCC cell line 225
4.12.2 Tumour heterogeneity of HNSCC tumour tissue 226
4.12.3 CK18-labelling index as a measure of response to irradiation 227
4.12.4 Measurement of cell death in response to irradiation using soluble markers 228
4.12.5 The detection of DNA-strand breaks by TUNEL in tissues following irradiation in microfluidic device 230

4.12.6 Retention level of γH2AX in predicting tumour sensitivity to irradiation 231
4.12.7 Relationship between single-dose and fractionated irradiation treatments 233

5. Measuring the effects of irradiation on HNSCC tissue maintained in a microfluidic device (II) – Proliferation and metabolism 235

5.1. Introduction 235
5.2. Materials, methods and corresponding results 239
5.2.1 Using BrdU incorporation as a measure of proliferation in response to irradiation 239
Immunocytochemical (ICC) staining of incorporated BrdU in oropharyngeal cells 239
IHC staining of incorporated BrdU in HNSCC tissue maintained in microfluidic device 240
5.2.2 Using Ki-67 detection as a measure of proliferation in response to irradiation 245
ICC staining of Ki-67 on oropharyngeal cells 245
Correlation between cell death and proliferation markers on UMSCC-47 cells treated with etoposide 248
The effect of irradiation on Ki-67 expression in HNSCC tissue maintained in the microfluidic device 250
5.2.3 Using 5-ethynyl-2'-deoxyuridine (EdU) incorporation as a measure of proliferation in response to irradiation 257
5.2.4 Incorporation of 2-NBDG into oropharyngeal cells in cell culture plate and tissues maintained in a microfluidic device 258
5.2.5 Correlation between CK18-LI, TUNEL assay results, expression levels of γH2AX and Ki-67 on the five HNSCC tumours 259
5.2.6 Comparison between *in vitro* results and clinical patients' outcome 265
5.3. Discussion 267
5.3.1 Marker expression in UMSCC-47 cells in response to irradiation 267
5.3.2 BrdU incorporation for measuring proliferation 268
5.3.3 Endogenous Ki-67 antigen expression as a marker of proliferation in response to irradiation 269
5.3.4 The multifaceted responses of HNSCC tissue to irradiation in the microfluidic device 272
5.3.5 Comparison of the microfluidic *in vitro* results and patients' outcome 275

6. Identification of changes in gene expression in response to on-chip irradiation 277

6.1. Introduction 277
6.1.1. Laser Capture Microdissection (LCM) 279
6.1.2. Gene expression in response to irradiation 280
Ataxia telangiectasia mutated (ATM) 280
Apoptotic regulator BAX (Bcl-2-associated X protein) 282
Cyclin dependent kinase inhibitor 1A (CDKN1A; p21) 283
Excision repair cross-complementing group 1 (ERCC1) 284
H2AFX (H2A histone family, member X) 286
X-ray repair complementing defective repair in Chinese hamster cells 1 (XRCC1) ... 286
6.2. Measuring the effects of section fixation, H&E staining and LCM technique on the RNA level and subsequent PCR products 288
6.2.1. Material and methods 288
6.2.2. Standard PCR results on fixed, H&E stained and LCM processed tissue sections 289
6.3. Creation of standard curve of gene expression versus starting RNA/cDNA input using quantitative real-time PCR 290
6.3.1. Material and methods 290
6.3.2. Quantitative RT-PCR results of B2M gene on serially diluted cDNA insert 292
6.4. Quantitative RT-PCR of ATM, BAX, CDKN1A, ERCC1, H2AFX and XRCC1 genes 294

6.4.1. Material and methods 294
6.4.2. Quantitative RT-PCR results of six genes related to radiation response on HNSCC tumours 297
6.5. Discussion 298
6.5.1. Sensitivity of TaqMan gene expression assay on serially diluted cDNA input 298
6.5.2. The presence of RNA on fixed, H&E stained and LCM processed tissue sections 299
6.5.3. LCM and gene expression study on HNSCC tumour response to irradiation under microfluidic-based approach 301
6.5.4. Future work of LCM and qRT-PCR for genomic study 303
7. Final discussion and conclusion 305
7.1. Advantages of microfluidic platform for human tissue maintenance and on-chip irradiation 305
7.2. Limitations of current study 308
7.3. Future perspective 311
7.4. Final conclusions 314
8. References 315
9. Appendix 344
9.1. Patient demographics of HNSCC samples included in current research group 344
9.2. Representative H&E staining on pre-MF tissues 347
9.3. Tris buffered saline (TBS) 348
9.4. TAE buffer 348
9.5. Borate buffer 348
9.6. Mean absorbance values (LDH) of 13 rat liver tissues perfused with medium at different flow rates 349
9.7. Expression data of γH2AX, caspase-cleaved CK18, Ki-67 and Bcl-2 on two HNSCC cell lines 350
9.8. Results of EdU incorporation into HNSCC cells and tissues 351
9.9. Results of 2-NBDG incorporation into HNSCC cells and tissues 353
9.10. Results data of CK18-LI, γH2AX, Ki-67 and TUNEL assay of five HNSCC tumours 360
9.11. Pearson's correlation between tested markers on primary tumours 361
9.12. Quantitative RT-PCR results of six genes related to radiation response on HNSCC tumours 362

List of Figures

Figure 1.1. Diagram showing the cross section of a head and regions implicated in HNSCC. 19
Figure 1.2. The genetic progression model of HNSCC that develops metastasis from normal mucosa. 20
Figure 1.3. The incidence oropharynx cancer, oral cavity cancer, and larynx cancer between 1990 and 2006 23
Figure 1.4. Kaplan-Meier survival curve until overall death between never and ever smokers 25
Figure 1.5. The cell cycle stages and the site of activity of CDK/cyclin complexes in the cell cycle. 39
Figure 1.6. Two types of extrinsic signalling pathways in apoptosis, (A) Fas receptor signalling and (B) tumour necrosis factor (TNF) receptor signalling. 42
Figure 1.7. Intrinsic pathway of apoptosis resulting from cellular stress. 44
Figure 1.8. Representative of the types of DNA damage that can occur following exposure to chemicals and radiation. 46
Figure 1.9. The regulation of cell cycle checkpoints by ATM and ATR following different DNA damage types. 48
Figure 1.10. DNA damage response (DDR) pathway comprises two interconnected pathways, ATM and ATR. 50
Figure 1.11. A schematic diagram showing how a microfluidic device can integrate various laboratory experiments on a single chip that holds tiny amounts of fluids in micrometre channels. 60
Figure 1.12. Laminar flow shows the non-turbulent fluid flow which is the principle flow in microfluidic device. 64
Figure 1.13. Schematic diagram of PARTCELL microfluidic chip. 64
Figure 1.14. Schematic diagram of the tumour microenvironment consisting of tumour cells, non-malignant cells, soluble factors, extracellular matrix, cancer-associated fibroblasts, pericytes and immune cells. 66
Figure 1.15. Pictures and schematics diagrams of microfluidic-based POC tests. 76
Figure 1.16. Schematic diagram of microfluidic flow system used in this study. 77
Figure 2.1. Schematic diagram of microfluidic glass device. 82
Figure 2.2. Outlines of the operational details of photolithography and wet etching method involved for microfluidic glass device fabrication in University of Hull (Tarn, 2008). 84
Figure 2.3. Assembly of microfluidics system. 88
Figure 2.4. Assembly of microfluidics flow system. 89
Figure 2.5. Entire microfluidic system set-up with Harvard syringe pump and the 37ºC incubator. 90
Figure 2.6. Photograph of the Perspex block containing microfluidic device. 92
Figure 2.7. The Perspex block used for irradiation of HNSCC tissue during microfluidic culture. 93
Figure 2.8. Arrangement of the microfluidic system (block and syringe pump) on the couch (table) during irradiation using Linear Clinical Accelerators (LINAC). 93
Figure 2.9. A diagrammatic representation of HNSCC patient tissue recruitment (n=71) and tissue inclusion (n=13) in microfluidic and on-chip irradiation experiments. 96
Figure 2.10. Enzymatic reactions in detecting the presence of LDH. 102
Figure 2.11. Vectorstain ABC immunoperoxidase staining procedure. 105
Figure 2.12. A diagrammatic representation of the steps involved in the M30 CytoDeath™ ELISA. 107
Figure 2.13. Example of linear standard curve created for M30 ELISA analyses. 108

Figure 2.14. Detection of fragmented DNA appeared in apoptosis by terminal deoxynucleotidyl transferase (TdT)-mediated dUTP nick end labelling. 108
Figure 2.15. The mechanism of incorporation of fluorescent (Alexa Fluor 488)-conjugated 5-ethylnyl-2'-deoxyuridine (EdU) into proliferating cells. 111
Figure 2.16. H&E staining and IHC staining by using mouse monoclonal anti-cytokeratin antibody (Dako, Denmark) on serially cut tissue sections of oral cavity floor of mouth tissue which subjected to microfluidics with no irradiation. 113
Figure 2.17. LCM set up. 113
Figure 2.18. LCM software used for selection of target cells on an H&E stained tissue section. 114
Figure 2.19. Gene of GAPDH and the primers used to amplify the target gene sequence (at size of 326 base pair). 117
Figure 3.1. Eukaryotic cell cycle markers presented in different cell cycle phases. 123
Figure 3.2. ICC staining of BrdU on oropharyngeal cells (UMSCC-47) and the corresponding image analysis. 125
Figure 3.3. Representative IHC staining of BrdU on oropharyngeal cells (UMSCC-47) which have been cultured for 24 hours and BrdU addition on culture flask (x400 magnification). 126
Figure 3.4. Photomicrographs of rat liver tissues and lymph neck node tissues that metastasised from oral cavity tumour (TR52) post microfluidic culture, following IHC labelling of BrdU-incorporated cells with different times of BrdU infusion (n=2 on both tissue types). 127
Figure 3.6. Representative of haematoxylin and eosin (H&E) staining on rat liver tissue sections following traditional tissue culture from day 1 to 3 and day 5 to 9 (n=8). 129
Figure 3.7. LDH release from rat liver tissue following 9-day maintenance in microfluidic device. The absorbance values were assessed in duplicate and standardised per mg of tissue biopsy (8.2mg). 130
Figure 3.8. Mean LDH absorbance value of nine rat liver tissues following the maintenance in microfluidic device. 131
Figure 3.9. LDH release from rat liver tissue following 8-day culture in microfluidic device and lysis at the last 6 hours. 132
Figure 3.10. Mean LDH absorbance values from rat liver tissue maintained in microfluidic device and traditional tissue culture. 133
Figure 3.11. Comparison of mean LDH absorbance values from rat liver tissues maintained in same microfluidic system between colleagues' results and current results. 134
Figure 3.12. Representative haematoxylin and eosin (H&E) staining on rat liver tissue sections following microfluidic perfusion from day 1 to 9 (n=9; tissue on day 9 is not shown). 135
Figure 3.13. Representative IHC labelling of BrdU-incorporated cells in rat liver tissues following 1-9 days culture in microfluidic device (n=9; tissue on day 9 is not shown). 137
Figure 3.14. Representative IHC labelling of BrdU incorporating cells in rat liver tissues following in microfluidic flow for 1 days (n=5), 2 days (n=5) and 4 days (n=5). 139
Figure 3.15. Three rat liver tissue subjected to 4, 5 and 6 days of culture in devices with medium containing 10% of rat serum. 141
Figure 3.16. Three rat liver tissue subjected to 4, 5 and 6 days of culture in devices with medium containing 30mM of HEPES buffer at 2µl/min. 143
Figure 3.17. Three rat liver tissue subjected to 4, 5 and 6 days of culture in devices with medium oxygenated with 95% O_2 and 5% of CO_2. 145
Figure 3.18. Mean LDH released from 13 rat liver tissues throughout the 4 days culture in microfluidic device. 147
Figure 3.19. Representative H&E staining of 6 representative rat liver tissues out of 13 tissues following microfluidic perfusion. 148

Figure 3.20. Representative IHC labelling of BrdU incorporating cells in 6 representative rat liver tissues following microfluidic perfusion. 149
Figure 3.21. Three HNSCC tissues (neck node metastasised from floor of mouth primary tumour; TR52) subjected to 4, 5 and 6 days of culture in devices with medium supplemented with 30mM of HEPES and 10% of FBS at flow rate of 2µL/min. 152
Figure 3.22. HNSCC tissues (neck node metastasised from tonsil primary tumour; TR54; n=6) subjected to microfluidics, three of them maintained for respective 4, 5 and 6 days with medium containing 10% of human AB serum and three of them cultured for respective 4, 5 and 6 days with medium containing 10% of FBS. 154
Figure 3.23. Representative images of FITC-conjugated dextran incorporated into HNSCC tumours (TR80 and TR122) following dextran addition for 30 (left) and 120 minutes (right; x400 magnification). 157
Figure 3.23. Phase-contrast photomicrographs with superimposed fluorescence imaging that showed dead hepatocytes. 162
Figure 4.1. Exposure of the CK18-Asp396-NE epitope following the proteolytic cleavage of cytokeratin 18 by caspases and the detection of the epitope by the M30 antibody. 172
Figure 4.2. Cascade of reactions culminating in the γH2AX formation in response to DNA-DSB. 174
Figure 4.3 The catalytic role of lactate dehydrogenase in the conversion of pyruvate to lactate. 176
Figure 4.4. Representative ICC staining of oropharyngeal cells (UMSCC-47; n=3; x400 magnification) with (A) M30 antibody, (B) anti-γH2AX antibody and (C) anti-Bcl-2 antibody. 179
Figure 4.5. ICC staining of UMSCC-47 cells using a (A) mouse matched IgG1 isotype antibody and (B) mouse matched IgG2b isotype antibody as negative control. 180
Figure 4.6. ICC staining of γH2AX, caspase-cleaved cytokeratin using the M30 antibody and anti-apoptotic Bcl-2 on UMSCC-47 oropharyngeal cells treated with no etoposide and with increasing concentrations of etoposide (n=6 on each marker). 181
Figure 4.7. Mean CK18-LI of a laryngeal supraglottic tumour (TR84) following microfluidic culture without irradiation (MF) and with irradiation at increasing single doses. 183
Figure 4.8. Mean percentage of cells positive for γH2AX expression in a laryngeal supraglottic tumour (TR84) following microfluidic culture without irradiation (MF) and with irradiation at increasing single doses. 184
Figure 4.9. Absorbance values of formazan dye indicating the level of LDH release from a floor of mouth oral cavity tumour (TR92) in two parallel microfluidic systems. 186
Figure 4.10. Representative staining on frozen tissue sections of an oral cavity floor of mouth (TR89) which was subjected to different treatments (n=2 on each treatment group). 187
Figure 4.11. Representative staining on frozen tissue sections of lymph node metastasised from an unknown primary tumour (TR73) which was subjected to different treatments (n=2 on each treatment group). 188
Figure 4.12. Flow chart of the HNSCC tissues used for CK18-LI determination and the number of repeats for each treatment in brackets. 190
Figure 4.13. Image to show the tiling of x100 magnification fields throughout the entire cytokeratin stained-HNSCC tissue section. 191
Figure 4.14. Image analysis on IHC staining by using Image-Pro Premier software. 191
Figure 4.15. Representative photomicrographs of IHC staining on the 9 HNSCC tumours (n=3 on lymph node patients (TR73) and n=5 on patients with primary tumour; x400 magnification). 193
Figure 4.16. CK18-LI of pre-microfluidic (Pre-MF) and microfluidic (MF) control tissues. 194

Figure 4.17. Mean CK18-LI of the six primary tumours taken from x100 tiled field (3 oral cavity; 1 oropharyngeal; 1 laryngeal and 1 paranasal sinus) with microfluidics but without irradiation (MF) and irradiation at increasing single doses. 195
Figure 4.18. Mean CK18-LI of the three metastatic lymph node tissues [metastasised from unknown (TR73), laryngeal (TR80) and oropharyngeal (TR59) primary tumours], with microfluidics but without irradiation (MF) and irradiation at single doses. 196
Figure 4.19. Mean percentage of CK18-LI of laryngeal lymph node tumour (TR80), oral cavity floor of mouth I (TR89) and II (TR92) tumours which were subjected to microfluidic culture without irradiation (MF) and different irradiation schedules. 198
Figure 4.20. The concentration of cleaved-CK18 released from HNSCC tissues subjected to different irradiation schedules. 200
Figure 4.21. A flow chart of the nine HNSCC tumours involved in the current microfluidic irradiation study showing which samples were stained for γH2AX. 202
Figure 4.22. Photomicrographs showing the method used to count positive γH2AX staining on all the frozen tissue sections of the five selected HNSCC patients (n=2 for lymph neck node and n=3 for primary tumour). 203
Figure 4.23. Representative IHC staining of γH2AX on an oral cavity floor of mouth tumour II (TR92; n=13). 204
Figure 4.24. Mean percentage of cells positive for DNA-DSBs from five x400 fields of view on two HNSCC lymph neck node tissues following different doses of irradiation. 205
Figure 4.25. Mean percentage of cells positive for γH2AX expression from five x400 fields of view which are positive for DNA-DSBs on three HNSCC primary tumours (oral cavity TR89 and TR92; laryngeal tumour TR84) following different doses of irradiation. 206
Figure 4.26. Mean percentage of cells positive for γH2AX expression on laryngeal lymph node (TR80) tumour and oral cavity floor of mouth I (TR89) and II (TR92) tumours which were subjected to microfluidic culture and different irradiation schedules. 208
Figure 4.27. Representative fluorescence microscopic images of lymph node tissue metastasised from oropharyngeal tonsil TR122 tumour maintained in a microfluidic device 210
Figure 4.28. Representative fluorescence microscopic images of (Left column) lymph node tissue metastasised from an oropharyngeal tonsil tumour (TR54; n=6) and (Right column) a laryngeal supraglottic tumour (TR84; n=3). 211
Figure 4.29. Mean percentage of CaspACE incorporation on (A) the lymph node tissues metastasised from an oropharyngeal tonsil (TR54) tumour and (B) laryngeal supraglottic (TR84) tumour which were subjected to microfluidic culture with and without single-dose irradiation. 212
Figure 4.30. Fluorescent image analysis of TUNEL assay on the five HNSCC tumours (n=5). 214
Figure 4.31. Fluorescent images showing the results of the TUNEL assay on two serially sectioned lymph node tissues (TR73) treated with DNAase. 215
Figure 4.32. Fluorescent images of lymph neck node tissue (TR73) following microfluidic culture with no (0Gy) and with irradiation (5, 10, 15 and 20Gy) and apoptosis analysis using TUNEL. 216
Figure 4.33. Mean percentage of apoptotic cells on the four tumour tissues that subjected to microfluidic culture with and without single-dose irradiation following the TUNEL assay. 217
Figure 4.34. Calculation of mean absorbance values at 4-hour interval from two oral cavity floor of mouth tissues which subjected to parallel microfluidics with no irradiation treatment. 219
Figure 4.35. Mean absorbance values of the tetrazolium product per mg tissue at 4-hour intervals throughout the tissue culture in microfluidic devices with and without irradiation. 221
Figure 4.36. IHC staining of Bcl-2 on HNSCC tissues subjected to microfluidic perfusion. 223

Figure 4.37. IHC staining of Bcl-2 on TR92 and TR84 tissues which were subjected to microfluidics with and without irradiation. 224
Figure 4.38. Flow cytometric analysis on the γH2AX induction of the cells obtained from patients (n=10) throughout 25 hours following 2Gy irradiation. 232
Figure 5.1. Representative ICC staining of oropharyngeal cells (UMSCC-47) following 6 hours of culture with BrdU (10μM) and immunostaining with anti-BrdU antibody (0.01μg/L final concentration, AbD Serotec). 240
Figure 5.2. Representative IHC staining of BrdU (x400 magnification) on lymph neck node metastasised from a laryngeal tumour subjected to microfluidics and 10Gy irradiation. 241
Figure 5.3. Representative staining of BrdU on the microfluidic-cultured tissues of six HNSCC tumours (four primary tumours and two lymph neck node tissues) which were perfused with BrdU for 6 hours. 242
Figure 5.4. Representative IHC staining of BrdU staining (x400 magnification) on two lymph neck nodes (TR73 and TR80) and laryngeal (TR84) tumour which were subjected to microfluidics with different treatments. 243
Figure 5.5. Mean percentage of cells positive for BrdU incorporation on two lymph neck nodes (TR73 and TR80) and a laryngeal (TR84) tumour. 244
Figure 5.6. Representative ICC staining of oropharyngeal cells (UMSCC-47; x400 magnification fields taken and images were cropped to achieved better view on cells) with the Ki-67 antibody (0.46μg/L final concentration). 246
Figure 5.7. ICC staining of Ki-67 on UMSCC-47 oropharyngeal cells treated with no etoposide and with increasing concentrations of etoposide (n=6). 247
Figure 5.8. Scatterplots represents the relationships for the mean expression levels of M30, γH2AX, Ki-67 and Bcl-2 on the oropharyngeal cells (UMSCC-47) that have been subjected to different concentration of etoposide. 249
Figure 5.9. A flow chart of the nine HNSCC tumours involved in the current microfluidics and irradiation study and the analysis methods carried out on each one. 251
Figure 5.10. Representative IHC staining of cytokeratin (CK; x100 magnification) and Ki-67 (x400 magnification) of serially sectioned laryngeal TR84 tumour subjected to microfluidic culture and on-chip 20Gy irradiation. 252
Figure 5.11. Representative IHC staining of Ki-67 on lymph neck node metastasized from an unknown primary tumour (TR73; n=10). 253
Figure 5.12. Mean percentage of cells positive for Ki-67 expression from five x400 fields of view on two HNSCC lymph node tissues (TR73 and TR80) following different doses of irradiation. 254
Figure 5.13. Mean percentage of proliferating cells from five x400 fields of view on three primary HNSCC (TR89, TR92 and TR84) tumours following different doses of irradiation. 255
Figure 5.14. Mean percentage of cells positive for Ki-67 expression on TR80, TR89 and TR92 following (A) fractionated irradiation 5x2Gy and 5x4Gy and (B) single-dose irradiation. 256
Figure 5.15. Representative photomicrographs of staining of CK, m30, γH2AX, TUNEL assay, Ki-67 and BrdU on serial sections of TR73 (n=10; n=2 on each treatment case). 260
Figure 5.16. Evaluation of percentage of cleaved CK18, γH2AX, Ki-67 expressions and TUNEL assay. 261
Figure 5.17. Tumour response of five HNSCC tumours with increasing doses of irradiation in terms of the expression of the caspase-cleaved CK18 (early apoptosis marker; CK18-LI), DNA double-strand breaks (γH2AX), DNA fragmentation assay (TUNEL), and proliferation (Ki-67). 263
Figure 5.18. Scatter plots exemplifying the positive and negative relationships between markers on TR73 and TR80. 264

Figure 5.19. Mechanisms of etoposide in inducing cell cycle alterations. 267
Figure 6.1. H&E staining of a head and neck tumour tissue section. 278
Figure 6.2. Homodimer form of ATM in unstressed cells (top) and the activation of ATM following DNA damage (Bottom). 281
Figure 6.3. The role of ERCC1 and its binding partner XPF in nucleotide excision repair (NER) (shown on the left), double-strand breaks (shown in the middle) and ICL repair (represented on the right). 285
Figure 6.4. Functions of XRCC1 in base excision repair (BER) of small oxidative lesions and a related mechanism for the repair of single-strand breaks (SSB-R), both caused by ionising radiation. 287
Figure 6.5. Gel electrophoresis results of standard PCR on GAPDH gene on the RNA extracts of three different processes. 289
Figure 6.6. Layout of qRT-PCR for detection of the housekeeping gene B2M on a microamp fast 96-well reaction plate using serially diluted cDNA samples (32ng input). 291
Figure 6.7. Layout of the microamp fast 96-well reaction plate used in the qRT-PCR of the B2M gene using serially diluted cDNA samples (2000pg input). 291
Figure 6.8. Standard curve of mean CT versus log RNA input on serially diluted RNA samples extracted from the pre-microfluidic metastatic lymph node sample (TR54). 292
Figure 6.9. Representative of amplification plot of B2M gene expression ΔRn between positive samples (serially diluted sample of 32ng input) and negative control samples that were not reverse transcribed. 293
Figure 6.10. The amount of total RNA (ng) obtained from TR92 and TR80 subjected to different treatments. 297
Figure 7.1. Long-term culture of testis tissue developed by Komeya *et al*. (2015). 312
Figure 7.2. Design diagram of a new microfluidic device developed in-house. 313
Figure 9.1. Representative staining on frozen tissue sections of 5 HNSCC pre-MF tissues which was not subjected to microfluidic system and on-chip irradiation. 347
Figure 9.2. Representative fluorescent microscopy images (x400 magnification) of an oropharyngeal epithelial cell line (UMSCC-47) following 1-hour exposure to EdU and subsequent detection using Click-iT technology. 351
Figure 9.3. Representative fluorescent microscopy (x400 magnification) of EdU on three lymph node tissues 352
Figure 9.4. Representative fluorescent microscopic images (x400 magnification) of an oropharyngeal cell line (UMSCC-47) following 1-hour exposure to PBS containing no 2-NBDG (negative control), 0.01mg/mL and 0.05mg/mL of 2-NBDG. 353
Figure 9.5. Layout of 6 well plates prepared with UMSCC cells on sterile coverslips for the analysis of uptake of the glucose analogue 2-NBDG. 353
Figure 9.6. Representative fluorescent microscopic images (x400 magnification) of an oropharyngeal epithelial cell line (UMSCC-47) following 1-hour exposure to medium only (negative control), 0.05mg/mL of 2-NBDG in: PBS, low-glucose medium and glucose-free medium. 354
Figure 9.7. Representative fluorescent microscopic images (x400 magnification) of oropharyngeal cells (UMSCC-47) following 15, 30 and 60 minutes of exposure to glucose-free medium containing 0.05mg/mL of 2-NBDG and medium only (negative control). 355
Figure 9.8. Representative fluorescent microscopic images (x400 magnification) of oropharyngeal cells (UMSCC-47) which were starved with glucose-free medium for 2 hours and followed by the exposure to medium only (negative control) and medium containing 0.05mg/mL of 2-NBDG for 15, 30 and 60 minutes. 356
Figure 9.9. Representative fluorescent microscopic images (x400 magnification) of second oropharyngeal epithelial cell line (UMSCC-81b) which exposed to medium only

(negative control) and medium containing 0.05mg/mL of 2-NBDG for 30 and 60 minutes. 357
Figure 9.10. Representative fluorescent microscopic images (x400 magnification) of the uptake of 2-NBDG on primary oral cavity SCC (tonsil) tumours following 15, 30, 45, and 60 minutes of incubation with 0.05mg/mL of 2-NBDG. 358
Figure 9.11. Representative fluorescent microscopic images (x400 magnification) of the uptake of 2-NBDG on metastatic lymph neck node from oropharyngeal tumour following 60 minutes of incubation with medium only (negative control) and medium containing 0.05mg/mL of 2-NBDG in two independent sets of microfluidics (A&B). 359
Figure 9.12. Scatter plots exemplifying the Pearson's correlation between markers on the three primary tumour (oral cavity I and II and laryngeal). 361
Figure 9.13. Quantitative RT-PCR analysis of the reference B2M gene and the six irradiation response genes on (A) TR92 and (B) TR80. 362

List of Tables

Table 1.1. TNM clinical classification 29
Table 1.2. The summary of the treatment on different HNSCC sites and stages. 33
Table 1.3. Types of cell death by ionising radiation and the corresponding characteristics. 34
Table 1.4. Summary of different radiation therapies and the corresponding characteristics and advantages. 37
Table 1.5. Summary characteristics of proteins released from mitochondria intermembrane space during apoptosis. 44
Table 1.6. Examples of aberrations in DNA damage response in head and neck cancers 53
Table 1.7. Characteristics of materials used for construction of microfluidic devices. 61
Table 1.8. Comparisons of the basic requirements between conventional and microfluidic cell culture. 62
Table 1.9. Previous studies that performed irradiation treatment on biological sample in microfluidic devices. 72
Table 2.1. Patient demographics of (A) HNSCC primary tumour samples subjected to microfluidic perfusion and single dose irradiations. 97
Table 2.2. Clinical treatment received and the therapy outcome of five HNSCC tumours involved in this study. 99
Table 2.3. Patient demographics of HNSCC tumours (n=2) and metastatic lymph neck node (n=1) subjected to microfluidic culture with and without fractionated irradiations. 100
Table 2.4. Example of LDH data analysis. 102
Table 2.5. Example of M30 ELISA protocol map on plate reader. 106
Table 2.6. Gene expression assays detecting different genes by using TaqMan Fast Advanced Master Mix 119
Table 3.1. The number of rat liver tissues that have been subjected to traditional tissue culture in 96-well plates for different length of culture (day). 127
Table 3.2. LDH release from 15 rat liver tissues following tissue culture in 96-well plates. 128
Table 3.3. Number of rat liver tissues subjected to microfluidic perfusion system with Williams' Medium E containing different concentration of serum (n=15). 138
Table 3.4. Number of rat liver tissues subjected to microfluidic system with different flow rates. 146
Table 3.5. The molecular weight of the nutrients and chemical substances present in culture medium used to perfuse tissue maintained in microfluidics. 155
Table 4.1. Studies of irradiation effects on tumour biopsies from patients presenting with HNSCC, listed according to years of publication. 168

Table 4.2. Details of the primary antibodies used for immunochemical staining following irradiation. 178
Table 4.3. HNSCC samples used to detect apoptotic response in terms of cleaved cytokeratin release, to irradiation in the microfluidic device. 199
Table 4.4. Summary of the number of tissues subjected to microfluidic culture and incubation with 10μM caspACE inhibitor (CaspACETM FITC-VAD-FMK in situ marker). 209
Table 5.1. Proliferation marker studies implemented in determining human tumour response to radiotherapy treatment. 236
Table 5.2. Studies using a panel of biomarkers in studying the prognostic profiles on different tumour types. 272
Table 6.1. Samples of TR54 tumour subjected to different procedures of section fixation, H&E staining and LCM process. 289
Table 6.2. The HNSCC tissues that were subjected to LCM and qRT-PCR for ATM, BAX, CDKN1A, ERCC1, H2AFX and XRCC1 genes. 295
Table 9.1. Patient demographics of HNSCC tumour samples (n=71) which were consented in accordance with Local Research Ethics Committee (LREC-10/H1304/6) and NHS Trust R&D approval (R0987). 344
Table 9.2. Mean LDH absorbance values of 13 rat liver tissues perfused with different flow rates. Mean values of every 24 hours throughout the 4 days in the device were obtained and the standard deviation of the mean was calculated. 349
Table 9.2. Summary of expression data on two cell lines (UMSCC-47 and UMSCC-11) which were subjected to different treatment. 350
Table 9.3. Summary of CK18-LI, mean percentage of cells positive to γH2AX, Ki-67 and TUNEL assay on all individual tissues of the five primary tumours. 360

Abbreviations

μ	Fluid viscosity
μTAS	Micro-total-analysis-systems
2D	Two-dimensional
2-NBDG	2-(N-(7-Nitrobenz-2-oxa-1,3-diazol-4-yl) Amino)-2-Deoxyglucose
3D	Three-dimensional
3DCRT	3D conformal radiotherapy
53BP1	*p*53-binding protein 1
5-FU	5-fluorauracil
AIF	Apoptosis induced factor
ANOVA	Analysis of variance
Apaf-1	Apoptotic protease activating factor 1
APE1	Apurinic/apyrimidinic (AP) endonuclease 1
ASK1	Apoptosis signal-regulating kinase 1
ATM	Ataxia telangiectasia mutated
ATP	Adenosine triphosphate
ATR	ATM and RAD3 related
B2M	β2-microglobulin
Bad	B-cell lymphoma-2 associated agonist of cell death
BAK	B-cell lymphoma-2 homologous antagonist killer
BAX	B-cell lymphoma-2 associated X protein
Bcl-2	B cell lymphoma-2
Bcl-XL	B-cell lymphoma-2 extra-large
BCSS	Breast cancer-specific survival
BER	Base excision repair
BH	B-cell lymphoma-2 homology
Bid	BH3 interacting domain death agonist

Bik	Bcl-2 interacting killer
Bp	Base pairs
BRCA1	Breast cancer 1
BrdU	5-bromo-2'-deoxyuridine
Brti1	BRCT-repeat inhibitor of telomerase reverse transcriptase,
BSA	Bovine serum albumin
CA9	Carbonic anhydrase 9
CAK	CDK activating kinase
CCDN1	Cyclin D1
CD31	Cluster of differentiation 31
CDC	Cell division cycle
CDDP	Cisplatin
CDH	Cadherin
CDK	Cyclin-dependent kinase
CDKN1A	Cyclin-dependent kinase inhibitor 1A
cDNA	Complementary DNA
CHART	Continuous hyperfractionated accelerated radiotherapy
CHK	Checkpoint kinase
Cip	CDK interacting protein
CIS	Carcinoma *in situ*
CK	Cytokeratin
CK18-LI	Cytokeratin 18 labelling index,
c-MET	Crystallographic structure of MET protein
CO_2	Carbon dioxide
COX-2	Cyclooxygenase 2
CRT	Chemo-radiotherapy
CSS	Cause specific survival
C_T	Cycle threshold
CT	Chemotherapy,
CTL	Cytotoxic T cell/lymphocyte,
CXCR4	Chemokine receptor type 4
DAB	3, 3' –diaminobenzidine
DAPI	4',6-diamidino-2-phenylindole
dATP	Deoxyadenosine triphosphate
DDB1	DNA damage-binding protein 1
DDR	DNA-damage response
DED	Death-effector domain
DEDD	Death effector domain containing DNA-binding protein
DEPC	Diethylpyrocarbonate
DFS	Disease-free survival
D_h	Hydraulic diameter
DISC	Death inducing signalling complex
Dmc1	Disrupted meiotic complementary DNA
DMEM	Dulbecco's Modified Eagle's Medium
DMFS	Distant metastasis-free survival
DNA	Deoxyribonucleic acid
DNA-PKcs	DNA-dependent protein kinase, catalytic subunit
dNTPs	Deoxynucleotide triphosphates
DSBs	Double strand breaks
E. coli	*Escherichia coli*
ECM	Extracellular matrix
EDTA	Ethylenediaminetetraacetic acid
EdU	5-ethynyl-2'-deoxyuridine
EGFR	Epidermal growth factor receptor
ELISA	Enzyme-linked immunosorbent assay
Std	Standard

EME1	Essential Meiotic Structure-Specific Endonuclease 1
EndoG	Endonuclease G
ER	Estrogen receptor
ERCC	Excision repair cross-complementation group
ETFE	Ethylene-tetrafluoroethylene
F	Female
FAAP24	Fanconi Anemia Core Complex Associated Protein 24
FADD	Fas-associated death domain-containing protein
FAM	Fluorescein amidite
FANC	Fanconi anemia complementation
FasL	Fas-Ligand
FAT	Focal adhesion targeting
FBS	Foetal bovine serum
FDG	2-[^{18}F] fluoro-2-deoxy-D-glucose
FGF	Fibroblast growth factor
FHIT	Fragile histidine triad gene
FITC	Fluorescein isothiocyanate
FOM	Floor of mouth
GAPDH	Glyceraldehyde-3-phosphate dehydrogenase
GFP	Green fluorescent protein
GLUT	Glucose transporter
H&E	Haematoxylin and eosin
H2AX	H2A histone family, member X
HCl	Hydrochloric acid
HEPES	4-(2-hydroxyethyl)-1-piperazineethanesulfonic acid
hHR23B	Human Rad23 homolog
HIF-1	Hypoxia inducible factor 1
HNSCC	Head and neck squamous cell carcinoma
HPVs	Human papilloma viruses
HR	Homologous recombination
HRP	Horseradish peroxidase
HSCs	Hematopoietic stem cells
HtrA2	High temperature requirement protein A2/
IAP	Inhibitor of apoptosis
ICC	Immunocytochemical
IgG	Immunoglobulin
IGRT	Image-guided radiotherapy
IHC	Immunohistochemical
IL	Interleukin
IMRT	Intensity modulated radiation therapy
IRT	Irradiation
Kip	Kinase inhibitory protein
LCM	Laser capture microdissection
LDH	Lactate dehydrogenase
LI	Labelling index
Lig	Ligase
LINAC	Linear accelerator
LN	Lymph node
LOC	Lab-on-a-chip
LOH	Loss of heterozygosity
LRC	Loco-regional control
LTCC	Low temperature cofired ceramic
M phase	Mitosis phase
M	Male
MAPK	Mitogen-activated protein kinases
MDC1	Mediator of DNA-Damage Checkpoint 1

Mdm2	Mouse double minute 2 homology
MDSC	Myeloid-derived suppressor cell.
MF	Microfluidic
ATM	Ataxia telangiectasia mutated
MMPs	Matrix metalloproteinases.
MOMP	Mitochondrial outer membrane permeabilisation
mPCR	Multiplexed PCR
MRI	Magnetic resonance imaging
MRN	Mre11-Rad50-Nbs1 complex
mRNA	Messenger RNA
MVP	Major vault protein
MVPs	Methylation variable positions
NA	Not applicable
NAD	Nicotinamide adenine dinucleotide
NBS1	Nijmegen Breakage Syndrome 1
NEAA	Non-essential amino acid
NER	Nucleotide excision repair
NF-κB	Nuclear factor kappa-light chain-enhancer of activated B cell
NGS	Next-generation sequencing
NHEJ	Non-homologous end-joining
NHS	National Health Service
NK	Natural killer
NSCLC	Non-small-cell-lung-cancer
NTC	No template control
O_2	Oxygen
OGG1	8-oxoguanine glycosylase
OS	Overall survival
PARP	Poly (ADP-ribose) polymerase
PARTCELL	Partial treatment of cells
PBS	Phosphate buffered saline
PCNA	Proliferating cell nuclear antigen
PDGF	Platelet-derived growth factor
PDMS	Polydimethylsiloxane
PEN	Polyethylene naphthalate
PET	Positron emission tomography
PI3K	Phosphatidylinositol-4,5-bisphosphate 3-kinase
PIKK	Phosphatidylinositol 3-kinase-related kinases
PMM	Permanent magnet microbeam
PNKP	Polynucleotide kinase 3'-phosphatase
POC	Point-of-care
Polβ	DNA polymerase β
PR	Progesterone receptor
Pre-MF	Pre-microfluidic
PT	Primary tumour
PTEN	Phosphatase and tensin homolog
PTFE	Polytetrafluoroethylene
qNPA	Quantitative Nuclease Protection Assay
qRT-PCR	Quantitative real-time polymerase chain reaction
Rad	RADiation sensitive
Rb	Retinoblastoma
Re	Reynolds number
RFS	Recurrence free survival
RIN	RNA integrity number
RIP1	Receptor-interacting protein kinase 1
RNA	Ribonucleic acid
ROS	Reactive oxygen species

RPA	Replication protein A
RR	Radioresistance
R-Ras	Related RAS protein
RS	Radiosensitive
RSSF1A	Ras Association (RalGDS/AF-6) Domain Family Member 1
RT	Radiotherapy
RTK-PI3K	Receptor tyrosine kinases phosphoinositide 3-kinases
RT-PCR	Real-time polymerase chain reaction
SAPKs	Stress-activated protein kinases
SAV	Surface area to volume ratio
SBRT	Stereotactic body radiation therapy
SCC	Squamous cell carcinoma
SDF-1	Stromal cell-derived factor 1
SEM	Standard error of mean
Ser	Serine
Smac/Diablo	Second mitochondria-derived activator of caspases/direct IAP (inhibitor of apoptosis) binding protein with low pI
SOD2	Superoxide dismutase 2
SODD	Suppressor of death domain
Sphk1	Sphingosine kinase-1
SSBs	Single strand breaks
TAE	Tris-acetate-EDTA
TBS	Tris-buffered saline
TdT	Terminal deoxynucleotidyl transferase
TFIIH	Transcription factor II Human
TGF	Transforming growth factor
TGFβ-RII	Transforming growth factor-β type II receptor
TLDs	Thermoluminescent dosimeter
TNF	Tumour necrosis factor
TNF-R1	Tumour necrosis factors receptor 1
TPE	Thermoset polyester
TRADD	Tumour necrosis factor receptor type 1-associated death domain
TRAF2	TNF receptor associated factor 2
TRAIL	Tumour necrosis factor-related apoptosis-inducing ligand
Treg	Regulatory T cell
TUNEL	Terminal deoxynucleotidyl transferase dUTP nick end labelling
UMSCC	University of Michigan Squamous Cell Carcinoma cell lines
UV	Ultraviolet
V	Velocity
VDAC	Voltage-dependent anion channels
VEGF	Vascular endothelial growth factor
WB	Western blotting
WES	Whole-exome sequencing
WST1	Water soluble tetrazolium salts 1
XPA	Xeroderma pigmentosum group A
XPC	Xeroderma pigmentosum group C
XPE	Xeroderma pigmentosum group E
XPF	Xeroderma pigmentosum group F
XPF	Xeroderma pigmentosum group F
XPG	Xeroderma pigmentosum group G
XRCC	X-ray repair complementing defective repair in Chinese hamster cells
YAP-1	Yes-associated protein 1
Z-VAD-FMK	Carbobenzoxy-valyl-alanyl-aspartyl-[O-methyl]-fluoromethylketone)

Acknowledgements

First and foremost, I would like to express my sincere gratitude to my supervisors, Professor J. Greenman and Dr. V. Green for their continuous consideration, encouragement and personal guidance all the way from starting my PhD to the writing of this thesis.

I would like to thank Professor Thomas Carey from University of Michigan for his generosity in providing University of Michigan Squamous Cell Carcinoma cell lines (UMSCC-11b, UMSCC-47, and UMSCC-81b) I have used in this research. I wish to thank Professor N. Stafford, Consultant Head and Neck surgeon, and the rest of the surgical team at Castle Hill Hospital, Hull for providing us with the HNSCC tissue samples. I am also grateful to Professor A. Beavis, the Consultant Medical Physicist and Head of Radiation Physics for the Hull and East Yorkshire Hospital NHS Trust, and Mr. C. Horsfield, Medical Physicist, for their unlimited assistance and support with the radiation treatments. I also wish to thank Mr. R. Srivastava for all the helps during collaboration on this research. I gratefully acknowledge the funding source, the University of Hull, which made my PhD work possible.

Thank you to all my family members for all their love, support and encouragement when I have sometimes been in doubt. Also, I express my deep thanks to my colleagues and friends at the Daisy Research Building who make my life in Hull enjoyable and colourful, making like a big family.

Declaration

I confirm that this work is original and that if any passages or diagrams have been used from academic papers, books, the internet or any other sources these are clearly identified by the use of quotation marks and the references is fully cited. I certify that, other than where indicated, this is my own work and does not breach the regulations of HYMS, the University of Hull or the University of York regarding plagiarism or academic conduct in examinations. I have read the HYMS Code of Practice on Academic Misconduct, and state that this piece of work is my own and does not contain any unacknowledged work from any other sources. I confirm that any patient information obtained to produce this piece of work has been appropriately anonymised.

1. Introduction

1.1. Head and neck cancer

Head and neck cancer is a broad category of various tumour types arising from craniofacial bones, soft tissues, salivary glands, skin and mucosal membranes (Pai and Westra, 2009). This malignancy occurs mainly in the epithelial linings of the nasal cavity, paranasal sinuses, oral cavity, salivary glands, pharynx and larynx (Figure 1.1; Walden and Aygun, 2013; National Cancer Institute, 2013). More than 90% of head and neck malignancies are squamous cell carcinomas which arise in the mucosal surfaces of the head and neck while the remaining malignancies are as lymphomas, adenocarcinomas and sarcomas that arise from lymphocytes, cells lining of glands and the cells of muscles, cartilage, bone or blood vessels (Pai and Westra, 2009; Walden and Aygun, 2013; Schiff, 2016).

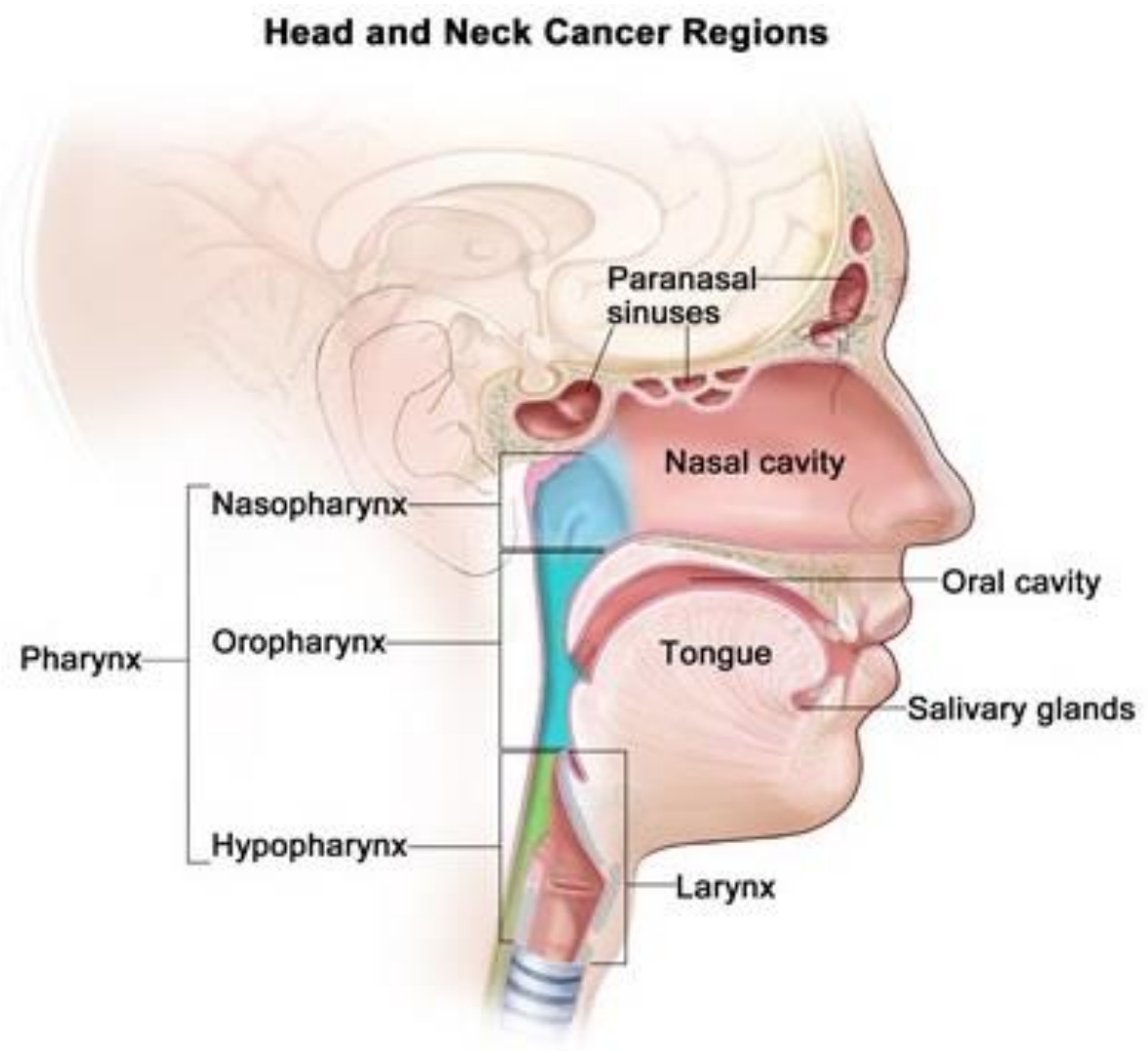


Figure 1.1. Diagram showing the cross section of a head and regions implicated in HNSCC. (National cancer institute, 2013).

1.1.1 Development and progression of HNSCC

The development of head and neck squamous cell carcinoma (HNSCC) involves a multi-step process which begins with genetic alterations that result in the progressive transformation of normal cells to malignant cells (Shaw and Dhanda, 2011). Squamous cell carcinoma (SCC) of the head and neck is considered to be the final stage of this multi-step process developing from normal cells through to hyperplasia, mild dysplasia, moderate dysplasia, severe dysplasia, carcinoma *in situ* (CIS) and finally to invasive carcinoma and metastasis (Figure 1.2; Haddad and Shin 2008; Vermoken and Specenier 2010). Patients with cancer are known to have higher risk for development of second tumour which represents tumour metastasis or *de novo* cancer (Rolston *et al*., 2001). The formation of *de novo* cancer has long latency interval which usually exceeds five years while the recurrent metastatic disease is favoured by short interval to the second cancer formation which have similar histology in the second tumour.

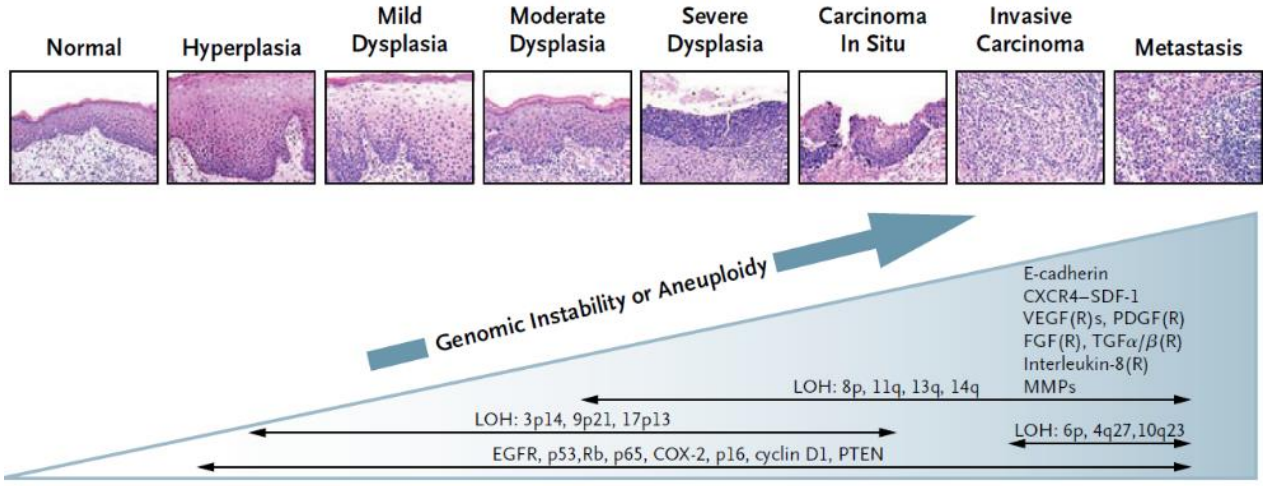


Figure 1.2. The genetic progression model of HNSCC that develops metastasis from normal mucosa.
(Modified from Haddad and Shin 2008)
Abbreviations: LOH: Loss of heterozygosity, EGFR: Epidermal growth factor receptor, Rb: Retinoblastoma, PTEN: Phosphatase and tensin homolog, CXCR4-SDF-1: Chemokine receptor type 4-stromal cell-derived factor 1, VEGF: Vascular endothelial growth factor, PDGF: Platelet-derived growth factor, FGF: Fibroblast growth factor, TGFα: Transforming growth factor alpha, MMPs: Matrix metalloproteinases.

The progression and development of HNSCC is due to the multiple alterations of cellular and molecular pathways in the squamous epithelium (Califano *et al*., 1996; Haddad and Shin 2008; Pai and Westra, 2009). The number of acquired genetic alterations accumulates progressively and increases from squamous hyperplasia via graded dysplasia (mild, moderate and severe dysplasia), to invasive carcinoma and finally metastasised to secondary area (Figure 1.2; Pai and Westra, 2009). The

underlying genetic instabilities which have been identified as genetic alterations in each of the pathological stages of this disease are (Figure 1.2; Haddad and Shin 2008; Pai and Westra, 2009; Vermoken and Specenier 2010):

(1) Amplification, deletion, up-regulation or down-regulation of certain oncogenes or tumour-suppressor genes, including epidermal growth factor receptor (EGFR), *p*53 (Boyle *et al*., 1993; Califano *et al.,* 1996), retinoblastoma (Rb), *p*65, cyclooxygenase 2 (COX-2), *p*16, cyclin D1 and phosphatase and tensin homolog (PTEN) which have been identified as genetic alterations in each of the pathological stages; Vermoken and Specenier 2010; Squarize *et al*., 2013). The mutations and alterations in *p*53 tumour-suppressor gene appear to be an early event in progression while the mutations in *p*16 gene are associated with later stages of tumour progression. The *p*16 gene encodes a protein which inhibits the cyclin-dependent kinases (CDK4 and CDK6) and subsequently prevents the phosphorylation of the Rb protein which, when phosphorylated, would normally promote cell cycle progression from G_1 to S-phase. If *p*16 is lost Rb is free to promote cellular proliferation in an unrestrained manner.

(2) Loss of heterozygosity (LOH) of certain chromosomes (3p14, 9p21, 17p13, 8p, 11q, 13q, 14q, 6p, 4q27 and 10q23).

The loss of chromosome region 9p21, which encodes for the proteins *p*16 and *p*14, is an earliest event associated with transition from normal to benign hyperplasia. It is found in 70-80% of HNSCC (Pai and Westra, 2009; Toner and O'Regan., 2009; Shaw and Dhanda, 2011). The loss of chromosome region 3p is an early genetic event in HNSCC, particularly in about 50% of oral squamous cell carcinomas, and were more often associated with dysplasia (Califano *et al*., 1996; Roz *et al*., 1996; Pai and Westra, 2009; Toner and O'Regan, 2009; Shaw and Dhanda, 2011). The 3p region encodes for tumour suppressor genes such as FHIT (fragile histidine triad gene) and Ras Association (RalGDS/AF-6) Domain Family Member 1 A (RSSF1A) and loss is associated to the progression from hyperplasia to dysplasia. LOH of the chromosome regions 11q or 13q, results in the transition from dysplasia to carcinoma *in situ* (CIS). The 11q13 region contains several genes [cyclin D1, EMS 1, fibroblast growth factor 3 (FGF3) and 4 (FGF4)] that have been previously shown to be amplified and over-expressed in HNSCC (Toner and O'Regan, 2009). A significant rise in the frequency of LOH, which includes 6p, 8p, 8q, and 4q26-28, has been found in later event of

progression from CIS to the invasive stage of HNSCC (Califano *et al*., 1996; Pai and Westra, 2009).

(3) E-cadherin (CDH1), chemokine (C-X-C motif) receptor (CXCR4) and its ligand stromal-cell–derived factor (SDF-1), vascular endothelial growth factor (VEGF), platelet-derived growth factor (PDGF), fibroblast growth factor (FGF), transforming growth factor α and β (TGF-α and TGF-β), interleukin-8, and the respective receptors, along with matrix metalloproteinase (MMP) are the genes involved mainly in metastatic progression of tumour cells (Haddad and Shin 2008). The SDF-1 ligand bind to CXCR4 and direct tumour cells to metastasise from primary sites to other organ sites and such interactions assisted the secretion of angiogenic factors such as VEGF.

1.1.2 Incidence and epidemiology of HNSCC

HNSCC is a common malignancy with approximately 680,000 cases diagnosed and 370,000 death cases estimated worldwide (Ferlay *et al*., 2015). According to data in Cancer Research UK (CRUK, 2016) in UK, the number of newly diagnosed cases of lip, oral cavity, and pharyngeal cancers in 2013 was 7591; 5103 cases are male and 2488 patients are female (CRUK, 2016a) while the mortality rate of this malignant type was 2119 cases (1426 male; 693 female; CRUK, 2016b). In 2013, the number of larynx cancer registrations was 2315 cases (1915 male; 400 female; CRUK, 2016c) while the number of death in 2012 in England was 784 (618 male; 166 female; CRUK, 2016d). In England, the incidence of head and neck cancers rose between 1990 and 2006, especially the incidence of oropharyngeal cancer which has more than doubled in that time (Figure 1.3; Oxford Cancer Intelligence Unit, 2010). This biggest rise was thought to be due to human papilloma virus (HPV), instead of smoking and alcohol consumption, being the main risk factor in young subpopulation. Oral cavity cancer incidence has risen by over 30% between 1990 and 2006 which was most likely due to the immigration of Indian subcontinent and the existence of betel quid chewing as an important risk factor. The number of laryngeal cancers has declined by 20% since 1990 and the falling incidence may indicate a reduction of smoking rates as laryngeal cancer is strongly associated with smoking behaviour (McKean-Cowdin *et al*., 2000; Oxford Cancer Intelligence Unit, 2010).

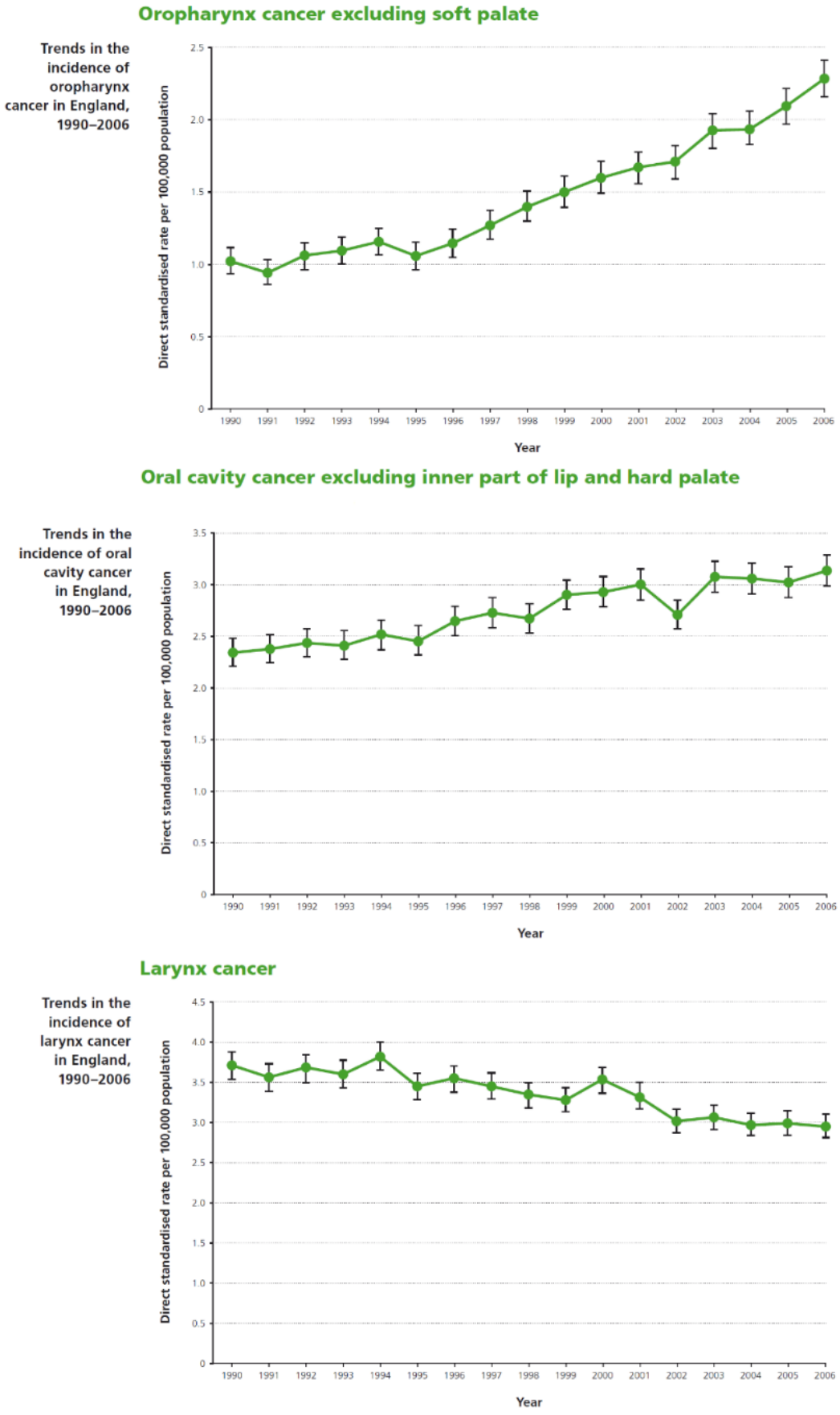


Figure 1.3. The incidence oropharynx cancer, oral cavity cancer, and larynx cancer between 1990 and 2006
(Adapted from Oxford Cancer Intelligence Unit, 2010).

According to the profile of head and neck cancers in England (Oxford Cancer Intelligence Unit, 2010), the trends of 1-year and 5-year relative survival for oral cavity cancer show a significant improvement from 1990 until 2006 with 56% at the most recent period. For oropharyngeal cancer, the trends show an increase of about 13-14% over the same period of time. It has been shown that the 5-year relative survival rates remained unchanged at about 65% since 1990 until 2002. From the latest data available on cancer survival in England, the 5-year survival rate of laryngeal cancer adult patients who were diagnosed between 2008 and 2012 and followed up to the year of 2013 was 66.7% (Office for National Statistics, 2013). A retrospective analysis study proposed by Zhang *et al*., 2013 evaluated the factors that affect the prognosis of 205 patients with laryngeal SCC who received total laryngectomy, partial laryngectomy or laser surgery. The survival rates were shown lower on advanced laryngeal cancer, positive surgical margins and severe comorbidity, indicating that the importance of early diagnosis, early therapies, negative surgical margins and the conditions of comorbidity in improving the cancer prognosis and survival rates.

1.1.3 Aetiology of HNSCC

The aetiological risk factors of HNSCC vary between different subsites leading to biological heterogeneity between subsites (Rothenberg *et al*., 2012). Although historically the majority of HNSCC were associated with tobacco smoking and alcohol consumption, infection with high-risk types of human papilloma viruses (HPVs) has now been recognized as an important risk factor, especially for oropharyngeal squamous cell carcinomas (Leemans *et al*., 2011; Koslabova *et al*., 2013).

Tobacco smoking

Tobacco smoking has for a long time been the single major risk factor for HNSCC and was first recognized as an independent risk factor in cancer of oral cavity in 1957 (Wynder and Bross, 1957). Oral cavity cancer cases were found 3 time higher in current smokers compared with never-smokers whereas pharyngeal cancer patients who are current smokers is 7 times higher than never-smokers (Gandini *et al*., 2008). Laryngeal cancer in particular has been strongly associated with smoking (Pytynia *et al*., 2004; Figure 1.4) and the decline of its incidence since 1990 may reflect the change of smoking habits and the reduction in smoking rates (McKean-Cowdin *et al*., 2000; Oxford Cancer Intelligence Unit, 2010).

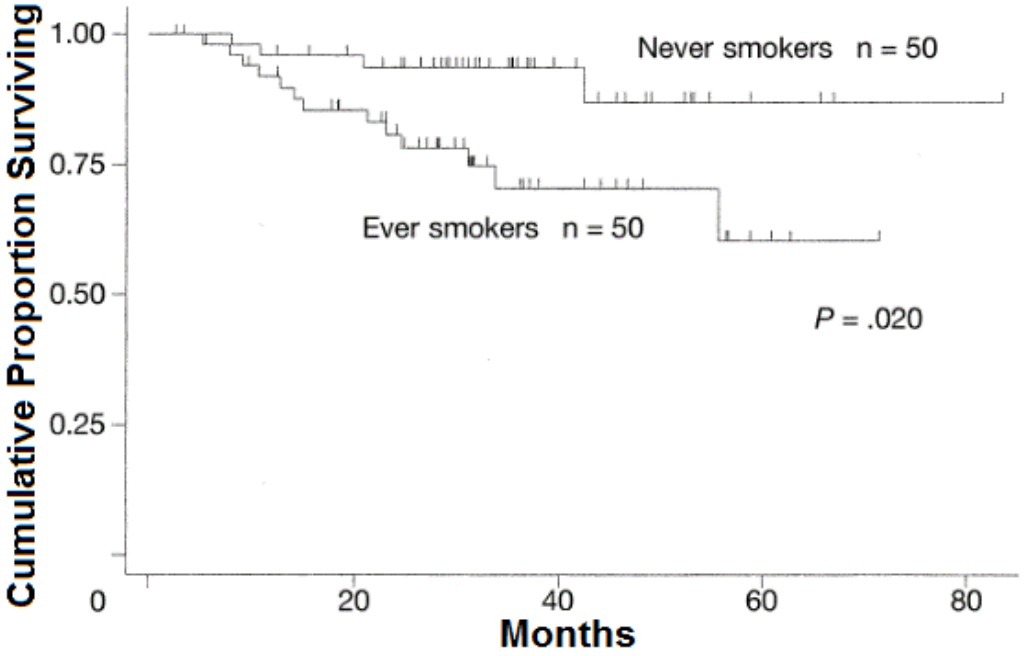


Figure 1.4. Kaplan-Meier survival curve until overall death between never and ever smokers (Pytynia *et al*., 2004).

Tobacco smoke consists of more than 30 different carcinogenic compounds including polycyclic, aromatic hydrocarbons, and tobacco-specific nitrosamines (Maier *et al*., 1992). Many components of tobacco have been confirmed to be carcinogenic such as nitrosamines which emerged as one of the most important groups of carcinogens in tobacco products (Hecht, 2008). In addition to tobacco smoking, tobacco chewing and snuffing have been identified to be carcinogenic risk factors for hypopharyngeal cancer (Sapkota *et al*., 2007).

Alcohol consumption

Alcohol consumption is also an independent risk factor for developing HNSCC. About 30% of oral cavity and pharyngeal cancer diagnosed in 2010 were attributed to alcohol consumption in 2000-2001 whereas 24.6% of the laryngeal cancer diagnosed in 2010 was attributed by alcohol consumption in 2000-2001 (Parkin, 2011). The risk of oral cavity and pharyngeal cancers were found 2.5 times higher in heavy drinkers (more than 4 drinks per day) compared with non- and occasional drinkers (Turati *et al*., 2013).

Alcohol is also a co-carcinogen and is capable of carcinogenesis caused by other factors (Maier *et al.,* 1992; Lubin *et al*., 2009; Saad *et al*., 2015). When the upper digestive tract is exposed to alcohol, it causes direct cell alteration and enhances cellular permeability and sensitivity to chemical carcinogens. Moreover, chronic consumption of alcohol increases the risk of exposure to high concentrations of pro-

carcinogens and carcinogens by significantly decreasing the flow rate of saliva and reducing the clearance over the mucosal surface (Maier *et al.,* 1988; Maier *et al*., 1992). It was recently identified that alcohol induces dysregulation of microRNA-30a and microRNA-934 which plays important action in HNSCC pathogenesis and progression (Saad *et al*., 2015).

Tobacco smoking and alcohol drinking

At least 75% of HNSCC develop as a result of both tobacco smoking and alcohol consumption (Hashibe *et al.,* 2007; Marron *et al*., 2010). Oral cavity and pharyngeal cancer risk is approximately tripled in alcohol drinkers who currently smoke tobacco compared with never drinkers (Hashibe *et al*., 2007; Hashibe and Sturgis, 2013). Among patients who are never users of tobacco, alcohol consumption was associated with an increased risk of head and neck cancer only when the alcohol was consumed at high frequency (>3 drinks/day). The combined effect of tobacco smoking and alcohol drinking has a higher carcinogenic effect than the tobacco smoking or alcohol drinking alone, which acts synergistically rather than inserting additive effect in the HNSCC development (Ragin *et al*., 2007). One of the possible mechanisms to account for the synergistic effect of alcohol and tobacco is thought to be the physical contact between alcohol and the tobacco carcinogens; alcohol might act as a solvent aiding the entry of tobacco carcinogens into the epithelial cells (Flanders *et al*., 1982; Galbiatti *et al*., 2013).

Small population of HNSCC patients, however, are non-smoker and non-drinker which have rarely been studied (Farshadpour *et al*., 2007 and 2011). These subgroups of patients may have specific clinic-pathologic features (gender, age, tumour localization and tumour stage) or additional risk factors (Farshadpour *et al*., 2007). The carcinogenesis is different between the smoking and drinking patients and non-smoking and non-drinking patients and other tumorigenic factors contributing to the latter group may be related to human papillomavirus (HPV) infection. The non-smoking and non-drinking patients group was mainly older female, had mostly tumours of oral cavity and had mostly stage I tumours while the smoking and drinking group mainly had tumours of larynx and had stage II tumours (Farshadpour *et al*., 2011).

Human Papillomavirus (HPV) Infection

The occurrence of HNSCC in certain sites has been slowly decreasing which is attributed by the decrease in the tobacco smoking and alcohol drinking behaviours (Leemans *et al*., 2011). However, the oral cavity tongue and oropharyngeal cancers are becoming more widespread which may be attributed to the increase in oral and oropharyngeal human papillomavirus (HPV) infection. In the study by Farshadpour *et al* (2011), among the non-smoking and non-drinking patients, 78% of them with oropharyngeal SCC were observed to be infected by high-risk HPV, HPV-16. The mode of transmission of HPV in head and neck cancer has not been fully determined, but sexual behaviour is believed to be associated with the increased risk.

Human Papillomaviruses (HPV) are ubiquitous, non-enveloped, oncogenic DNA viruses with more than 120 different types identified (Andrews *et al*., 2009). This virus consists of 9 open-reading frame sequences which are located on only one of the DNA strands (Ragin *et al*., 2007; Andrews *et al*., 2009). Among these sequences, seven of them are early-phase genes (E) while the rest are late-phase genes (L). HPV DNA genomes encode two regulatory proteins (E1 and E2), three oncoproteins (E5, E6 and E7) and two structural capsid proteins (L1 and L2). The HPV-related tumours carcinogenesis is mainly determined by the viral oncogenes E6 and E7 which control the development of the epithelial cells they infect (van Houten *et al.*, 2001; Cognetti, Weber and Lai, 2008; Andrews *et al*., 2009). E6 oncoproteins inactivate the tumour suppressor protein *p*53 preventing cellular apoptosis in response to genetic mutations, whereas the E7 protein causes the degradation of the Rb tumour suppressor protein, resulting in the accumulation of *p*16 and inhibition of cell cycle progression from G_1 to S-phase (van Houten *et al.*, 2001; Andrews, 2007; Gillespie *et al*., 2009). At the beginning of HPV infection, the HPV DNA genome exists in an episomal form with low expression levels of E6 and E7 (Gillespie *et al*., 2009). The DNA then integrates into the host genome where the expression of E6 and E7 increases, transforming epithelial cells into cancer cells (Andrews *et al*., 2009; Gillespie *et al*., 2009).

There are low-risk and high-risk types of HPV. Low-risk HPV such as types 6 and 11 exist as a circular episomal DNA separate from the host cell DNA and induce benign proliferation of the epithelium whereas the genomes of high-risk HPV (types 16 and 18) are usually, but not always, integrated into the host cell DNA (Andrews *et al*., 2009). HPVs are the most common sexually transmitted viruses and the mechanism

of HPV carcinogenesis was first identified in cervical cancer (Dürst *et al*., 1983). More than 90% of cervical cancers are related to HPV infection worldwide and the majority of these involve high-risk HPV types (Types 16 and 18; Walboomers *et al*., 1999). Over the past 15 years, the HPV infection, which is the main cause for cervical cancer, has also been related with HNSCC. In a meta-analysis of HPV infection on HNSCC that obtained from 34 studies published from 1980-2008 and involved 5681 patients, the prevalence of HPV in all HNSCC patients was 21.95% and 41% of oropharyngeal tumours were observed containing the HPV genome (Dayyani *et al*., 2010). The most prevalent HPV genotypes was HPV-16 which achieved 86.69% and HPV-16 accounted for 85% of oropharyngeal, 68% of oral cavity and 69% of laryngeal carcinomas (Kreimer *et al*., 2005; Dayyani *et al*., 2010).

HPV type 16 has been classified by the International Agency for Research on Cancer (IARC) as a carcinogenic agent for oral cavity, oropharyngeal tonsil and pharyngeal cancers while HPV type 18 as a possible cause of oral cavity cancer (Cogliano *et al*., 2010; IARC, 2015). Patients with HPV-16 positive tumours are typically younger (median age 54) compared with HPV-16 negative tumour patients (median age 58), independently associated with sexual behaviour (oral sex and increasing numbers of sexual partners), and were not related with tobacco smoking, alcohol drinking or poor oral hygiene (Gillison *et al*., 2008; Rettig, Kiess and Fakhry, 2015). It has been proposed in a study proposed by Gillison *et al*. (2008) that there are two etiologically distinct pathways for HNSCC pathogenesis, one is mediated by tobacco and alcohol consumptions, and the other is contributed by HPV infection. Therefore, the risk factors for oral HPV incidence, prevalence, clearance and persistence are vital to understand fully how oral HPV infection progresses to malignancy (Rettig, Kiess and Fakhry, 2015).

1.1.4 TNM staging system

Tumour staging is designed according to the TNM staging system which is based on the size of the primary tumour (T), regional lymph node status (N), and the presence or absence of metastases [M; American Joint Committee on Cancer (AJCC), 2016]. The clinical examination that are routinely carried out include a physical examination, chest x-ray, head and neck endoscopy, and head and neck computed tomography scan or magnetic resonance imaging (MRI; Ramos *et al*., 2010), which both offer anatomical information at a high resolution.

The TNM classification enables the physician to assess prognosis and choose the appropriate treatment for each patient (AJCC, 2016). The assessment of the T stage involves the measurement of the primary lesion size, the depth of the invasion and the surrounding structures, this clinical classification system is summarized in Table 1.1 (van der Schroeff and Jong, 2009; AJCC, 2016). Early-stage tumours (I/II) have a higher survival rate compared with later-stage tumours (III/V); unfortunately, too many patients present to their physician with late stage tumours (Brockstein *et al*., 2004; Holliday and Frank, 2014). Even within the early stage tumours there is further segregation since patients with stage I tumours usually have a 90% survival rate, while patients with stage II tumours have about a 70% survival rate, reflecting biological progression of the disease (Argiris *et al*., 2008).

Table 1.1. TNM clinical classification

TNM category	ID	Clinical characteristics
T- Primary Tumour	Tis	Pre-invasive cancer (CIS: carcinoma *in situ*)
	T0	No evidence of primary tumour
	T1	Tumour ≤2 cm
	T2	Tumour - >2 cm and <4 cm
	T3	Tumour - ≥4 cm
	T4	Tumour with extension to bone, muscle, skin, or neck
	Tx	Primary tumour cannot be assessed
N – Regional Lymph Nodes	N0	No evidence of regional lymph node involvement
	N1	Evidence of involvement of ipsilateral regional lymph node - ≤3cm
	N2a	Evidence of involvement of ipsilateral regional lymph node - >3 and ≤6 cm
	N2b	Evidence of involvement of multiple ipsilateral regional lymph nodes - ≤6 cm
	N2c	Evidence of involvement of contralateral or bilateral regional lymph nodes - ≤6 cm
	N3	Any lymph node - >6 cm
	Nx	Regional lymph nodes cannot be assessed
M-Distant Metastases	M0	No evidence of distant metastases
	M1	Evidence of distant metastases
	Mx	Presence of distant metastases cannot be assessed

(van der Schroeff and Jong, 2009; AJCC, 2016)

1.2. Treatment of HNSCC

Over the past five decades, a considerable amount of effort has been put in to improve the treatment of patients with HNSCC. Once the histological diagnosis and clinical staging are established, the treatment options are decided based on the patient parameters (health status, age, other co-existing diseases and the patient's wishes), clinic-pathological features (tumour site and stage), the expected functional and cosmetic results and the anticipated quality of life (Yao *et al*., 2007). Apart from that, other key parameters that should be considered are the potential for recurrences following treatment and its subsequent management. The treatments include surgery, chemotherapy and radiotherapy or a combination of these, and all of them aim to remove the cancer load, prevent subsequent recurrence or metastasis and maintain the quality of patients' life.

1.2.1 Surgery

Following the discovery and development of anaesthesia, antibiotics blood banking and new techniques for reconstruction, complete surgical resection of tumour lesions and the nodal biopsies in the upper aerodigestive tract has rapidly evolved and is used as a first choice of treatment of advanced (stage III-IV tumours) HNSCC (Cognetti, Weber and Lai, 2008). Almost half of the patients (48%) with oral cancer were subjected to surgical resection (CRUK, 2015e). The intraoral mucosa surgery is usually preferred on small oral cavity tumours [T1 and early T2 stages; Head and Neck Network Site Specific Group (NSSG), 2014]. To treat higher volume of T2, T3 and T4 oral cancers, a combination of surgery and radiotherapy is recommended (Head and Neck NSSG, 2014). For the management of laryngeal cancer, surgical treatments consist of minimally invasive transoral laser or robotic surgical resection, open partial laryngectomy, and total laryngectomy (Sheahan, 2014). Total laryngectomy remains the "gold standard" treatment for locally advanced T4 laryngeal cancers and is recommended for patients with T3 laryngeal tumour.

Surgical resection usually includes (Grégoire *et al*., 2010):

1. Reconstruction plus post-operative radiotherapy (RT) or
2. Reconstruction plus post-operative chemo-radiotherapy (CRT) with single-agent platinum (applicable for the patients who were found at surgery to have high-risk features such as extracapsular extension).

Patients who have early stage carcinomas (I-II) can effectively be treated using either conservative surgery or radiotherapy, with both giving similar loco-regional control (Yao *et al*., 2007; Grégoire *et al*., 2010). Although surgery leads to an immediate debulking of the tumour mass, surgical resection often compromises patient quality of life and function, for example, swallowing, speech and breathing can all be affected by the surgery on due to the anatomical locations of these tumours (Pauloski, 2008; Galbiatti *et al*., 2013; Sheahan, 2014), and because of this, organ preservation is now a key endpoint in the treatment of HNSCC (Yao *et al*., 2007). For example, surgical resection is the treatment choice for tumours on oral tongue and oral cavity in which the speech and swallowing can be preserved (Pauloski, 2008; Grégoire *et al*., 2010). The tumours arising from larynx, oropharynx and hypopharynx sites, in contrast, are preferably treated by radiotherapy as these locations are more difficult to access and the resection of these tumour sites commonly leads to severe destruction of the voice and swallowing (Yao *et al*., 2007).

1.2.2 Chemotherapy

In the second half of the 20th century, chemotherapy treatment is focused for functional organ preservation (Cognetti *et al*., 2008). Chemotherapy has the potential to kill tumour cells with organ preservation capabilities and is typically administered before surgical resection or radiotherapy aiming to improve the disease control (Lamont and Vokes, 2001). The chemotherapeutic agents are transported to tumour cells before the vasculature conditions are altered by surgery or radiotherapy. It is hypothesised that the chemotherapy works synergistically with radiotherapy by inhibiting the repair of DNA damage induced by irradiation, synchronising cells in radiosensitive phases and preventing the re-growth between radiotherapy treatments (Lamont and Vokes, 2001; Yao *et al*., 2007).

The chemotherapy drugs that are commonly used for treatment of HNSCC include cisplatin, platinum, 5-fluorauracil (5-FU), taxane docetaxel and paclitaxel (Galbiatti *et al*., 2013). Cisplatin is particularly popular in head and neck cancer either as a single agent or in combination with other anti-cancer drugs (Payne and Miles, 2008). The post-operative concurrent administration of cisplatin with radiotherapy is more effective, in terms of local-regional control and disease-free survival, than that of radiotherapy alone in patients with locally advanced HNSCC (Bernier and Cooper, 2005). The administration of triple sequential drug-based therapy that consisted of

docetaxel, 5-FU and cisplatin followed by concurrent chemo-radiotherapy was shown to be well tolerable with about 66% of locally advanced inoperable head and neck cancer patients achieving complete response (Somani *et al*., 2011). However, there are several limitations of using chemotherapy drugs in terms of safety profile and efficacy. The major drawback is that these are not a targeted therapy and will affect any cells which are rapidly dividing resulting in many damaging side effects (Payne and Miles, 2008). The adverse effects caused by the cytotoxicity induced by the drugs, for example, notably on bone marrow suppression, alopecia, mucositis, nausea and vomiting (Somogyi *et al*., 1996; Naidu *et al*., 2004; Payne and Miles, 2008).

1.2.3 Immunotherapy

The immune system plays an important role in the development of HNSCC with the tumour cells being able to manipulate the immune system in order to promote tumour growth and spread (Economopoulou *et al*., 2016; Fuereder, 2016). Over the last decade, immunotherapy has become a promising strategy for the treatment of head and neck cancer (Economopoulou *et al*., 2016; Fuereder, 2016). The overexpression of epidermal growth factor receptor (EGFR) is frequently observed in HNSCC (Leemans *et al*., 2011; Hansen and Siu, 2013) with ionising radiation reported to increase the expression further. Therefore, the combination of radiotherapy with EGFR targeted therapy, in the form of the Food and Drug Administration (FDA) approved monoclonal antibody Cetuximab, inhibits the EGFR signalling thus sensitising the cells to the effects of ionising radiation (Bonner *et al*., 2006, Vermorken *et al*., 2008; National Cancer Institute, 2013; Yokota, 2014; Economopoulou *et al*., 2016). Several trials have shown that the combination of cetuximab with radiotherapy or chemotherapy resulted in increased overall survival in patients with locoregionally advanced HNSCC (Robert *et al*., 2001; Bonner *et al*., 2006; Vermorken *et al*., 2006). In addition, Pembrolizumab and nivolumab, which are immune checkpoint inhibitors that target the interaction between the programmed death receptor 1/programmed death ligand 1 (PD-1/PDL-1) and PDL-2, have also now been approved for the treatment on HNSCC patients (Gillison, 2016). Other promising targets for immunotherapy include the E6 and E7 proteins expressed in HPV positive tumours; particularly in oropharyngeal cancers (section 1.1.3; Economopoulou *et al., 2016*). Successful treatment with these targeted immunotherapies may lead in the future to the introduction of radiolabelled antibodies

for enhanced killing of the HNSCC cells as is currently the case for the treatment of lymphoma with radioiodine labelled anti-CD20 (rituximab; Calais and Turner, 2012)

1.2.4 Radiotherapy

Due to the lack of antibiotics and the limitations of anaesthesia at the turn of the last century, radiotherapy was used as a primary treatment for the first half of the 20th century (Cognetti, Weber and Lai, 2008). Radiotherapy works by delivering ionizing radiation to target the tumour with minimal effect on the surrounding healthy tissue, and is a standard treatment for patients with HNSCC in order to achieve better life quality with organ preservation (Kamijo *et al.*, 2000; Head and Neck NSSG, 2014). It remains the popular therapy on HNSCC tumours, either in single modality or in combination with surgical treatment and chemotherapy. The summary of the therapeutic options for different tumour sites of head and neck cancer is illustrated in Table 1.2 which is based on the Head and Neck Cancer Treatment Guidelines (Head and Neck NSSG, 2014).

Table 1.2. The summary of the treatment on different HNSCC sites and stages.

HNSCC sites	Stages	Treatment choices
Laryngeal	I	• Single modality of either radiotherapy or surgery
	II	• Laser resection or open partial laryngectomy
	III	• Endoscopic laser resection of tumour • Concomitant chemotherapy with radiotherapy, with surgery at about 3-4 months after treatment
	IV (with no distant metastases)	• Surgery followed by radiotherapy
	IV (with distant metastases)	• Neoadjuvant/concomitant chemotherapy with radiotherapy
Oropharyngeal	I and II	• Single modality surgery or radiotherapy
	III	• Chemoradiotherapy • Surgery and post-operative radiotherapy • Surgery and post-operative chemoradiotherapy
	IV	• Split course radiotherapy, short course radiotherapy and palliative chemotherapy are all considered on an individual basis.
Oral cavity	I	• Laser resection • Radiotherapy if surgery is contraindicated.
	II	• Primary surgery • Radiotherapy
	III	• Primary neck dissection combined with radiotherapy +/- chemotherapy
	IV	• Primary neck dissection combined with radiotherapy +/- chemotherapy

HNSCC tumour sites of laryngeal, oropharyngeal and oral cavity were selected which are representative SCC tumours in UK and mostly used in current study (Head and Neck NSSG, 2014).

Radiotherapy remains one of the most effective techniques in cancer therapy to date. It works via several ways to eradicate the cancer cells that include (1) direct effects of radiation on cellular DNA causing damage and (2) indirect DNA damage caused by free radicals derived from ionization or excitation of water component of the cells (Bucci *et al*., 2006; Baskar *et al*., 2012; Kang *et al*., 2012). The radiotherapy exerts its therapeutic effects by inducing different types of cell death: apoptosis, mitotic catastrophe, necrosis, senescence and autophagy (Table 1.3).

Table 1.3. Types of cell death by ionising radiation and the corresponding characteristics.

Types of cell death	Characteristics
Apoptosis	• Mitochondria play a major role. • The cellular membrane of apoptotic cells remains unbroken. • Morphological features: rounding-up of the cell, retraction of pseudopods, reduction of cellular and nuclear volume (pyknosis), nuclear fragmentation (karyorrhexis) and plasma membrane blebbing. • An important role in the efficacy of radiation therapy on cancer cells.
Necrosis	• Accidental and uncontrolled form of cell death caused by excessive physio-chemical stress. • Morphological features: cytoplasmic swelling, rupture of plasma membrane, disintegration of cytoplasmic organelles, and moderate chromatin condensation. • After radiation, it occurs in cancer tissues but in less frequent mode.
Autophagy	• Morphological features: lack of chromatin condensation, contain massive vacuolization of cytoplasm and double-membrane vacuoles. • Cell digests itself by autophagic/lysosomal compartment.

The features of each cell death modality were summarised and extracted from various studies (Dewey *et al*., 1995; Elmore, 2007; Eriksson and Stigbrand, 2010; Baskar *et al*., 2012; Lauber *et al*., 2012).

Ionising radiation is delivered to the tumour as an external radiation beam (external beam radiotherapy) or less commonly by directly implanting radioactive sources within the tumour [brachytherapy; Scottish Intercollegiate Guidelines Network (SIGN), 2006]. The dose of the radiation has to be balanced with the amount of damage occurring to the surrounding normal tissue and the idea of fractionation is to minimise this, but also to capture proliferating cells which may have been missed in the first rounds of irradiation (Baskar *et al*., 2012). Normal cells replicate relatively slower than the rapidly proliferating cancer cells, allowing more time for these cells to repair damage before replication.

The radiotherapy effects on the tumour depend on the total dose delivered, the size of the fraction and the overall period of treatment. Radiotherapy is commonly fractionated, which means the total dose is delivered over time in smaller doses or fractions. In the UK, 66-70 Gy is considered as a standard treatment in clinical practice

for head and neck cancer and the accepted standard fractionation is 1.8-2 Gy per fraction, five fractions a week in an overall treatment time of 6.5-7 weeks is generally applied (Zackrisson *et al*., 2003; The Royal College of Radiologists, 2006). In order to increase the tumouricidal effect of the radiation, alternative fractionations to the 2 Gy per day, 5 times a week convention have been tried:

(1) Hyper-fractionation: Delivering more than 5 fractions per week resulting in a higher total dose than that of standard fractionation in the same treatment time (SIGN, 2006; Marcu and Bezak, 2009). The reduction of the dose per fraction, in which two to three fractions of irradiation were delivered in daily basis with 1.1 to 1.2Gy dose per fraction, could reduce the risk of late toxicity despite an increased total dose (Baujat *et al*., 2010). The hyperfractionation radiotherapy has been shown to offer the greatest benefits when compared with other altered radiotherapy and conventional radiotherapy schedules based on the 15 randomised trials with 6515 patients (Bourhis *et al*., 2006; Baujat *et al*., 2010). The percentage of survival up to 7 years following hyperfractionated radiotherapy group was observed significantly higher than that of the accelerated radiotherapy and accelerated fractionation with total dose reduction groups (Baujat *et al*., 2010).

(2) Moderate acceleration: Delivering more than 5 fractions per week resulting in a similar total dose to the standard fractionation schedule with a reduction in treatment time by 1-2 weeks (SIGN, 2006). The regime of 6 fractions per week with shorter treatment time has resulted in an improvement of 10% in the 5-year local control (Overgaard *et al*., 2003). In study summarised in Baujat *et al*. (2010), the comparison of different modified radiotherapy based on the 15 trials illustrated that both hyperfractionation and accelerated radiotherapy shared same benefits for local control but had a different effect on survival (hyperfractionation>accelerated).

(3) Marked acceleration plus hyper-fractionation: Delivering more than 5 fractions per week with a reduced total dose and a reduction of treatment time by more than 2 weeks [SIGN, 2006]. Similar local tumour control and fewer late morbidity effects have been demonstrated using this regime (54Gy in 12 days) when compared with conventional radiotherapy (Dische *et al*., 1997). In a phase III randomised trial (GORTEC) proposed by Bourhis *et al*. (2006), the combination of hyperfractionation and accelerated radiotherapy (62-64Gy in 31-32 fractions of

2Gy over 22-23 days) tested on 268 advanced HNSCC tumours showed improved locoregional control at 6 years after treatment but leading to no significant benefits on disease-free survival and overall survival.

(4) Marked acceleration with hypo-fractionation: Delivering less than the conventional number of large-sized fractions. For example, in a study proposed in Das *et al*. (2013), thirty-six patients with inoperable head and neck cancer were subjected to 40Gy in 10 fractions per week and the treatment-related toxicity was assessed (Das *et al*., 2013). Significant pain relief was observed in approximately 88% of the patients at the end of the shortened radiotherapy. Similar symptoms relief was demonstrated in Agarwal *et al*. (2008) study in which the hypofractionated radiotherapy (40Gy in 16 fractions) was delivered to 110 patients with inoperable HNSCC and 57% of the patients had 50-75% of symptomatic relief. This modified radiotherapy regimen was shown to be suitable on inoperable HNSCC tumours.

In order to improve the goal of radiotherapy in delivering as much dose to the tumour whilst protecting normal tissue, a number of technological advances in cancer imaging, high speed computer software and developments in radiation delivery technology have been introduced in recent years (Mehanna *et al*., 2010). The examples of the different radiotherapy treatments are 3D conformal radiotherapy (3DCRT), intensity modulated radiation therapy (IMRT), image-guided radiotherapy (IGRT), stereotactic body radiation therapy (SBRT; Table 1.4).

Table 1.4. Summary of different radiation therapies and the corresponding characteristics and advantages.

Different radiation therapies	Characteristics and advantages	Reference
3D conformal radiotherapy (3DCRT)	• Allows accurate localization of tumour. • Deliver radiation to gross tumour volume with a margin for microscopic tumour extension and further margin uncertainties from organ motion and setup variations.	Baskar *et al*., 2012
Intensity modulated radiation therapy (IMRT)	• Allows the creation of irregular-shaped radiation dose that conform to the 3-dimensional shape of the tumour. • Avoid critical organs.	Baskar *et al*., 2012 Bakiu *et al*., 2013
Image-guided radiotherapy (IGRT)	• Allows the detection of gross positional errors, arise from tighter treatment margin due to organ motion and patient setup variations, by information acquired from pre-radiotherapy imaging. • Allows correction on detected errors.	Baskar *et al*., 2012 The royal Australian and New Zealand College of Radiologists, 2015
Stereotactic body radiation therapy (SBRT)	• Precisely delivers high individual doses of radiation over few treatment fractions. • Able to kill small, well-defined primary and oligometastatic tumours in body.	Baskar *et al*., 2012

Although it is known that tumours from different subsites and tumours of different stage respond differentially to irradiation (SIGN, 2006; Head and Neck NSSG, 2014), and some centres base their treatment accordingly, there is still considerable variation between patients in terms of recurrence and survival (Dubben *et al*., 1998; Begg, 2012). Consequently, the monitoring of the tumours biological response to radiotherapy in individual patients would be highly beneficial providing a more informed, streamlined, approach to treatment.

1.3. Mechanisms of cell damage by irradiation

Under normal conditions, the tissue homeostasis depends on the appropriate relationship among cell proliferation and cell death. The cell mitotic cycle progression is managed by various mechanisms in order to ensure the correct cell division.

1.3.1 Cell cycle controls under normal condition

Cell division comprises two consecutive processes which are categorized by DNA replication and segregation of replicated chromosomes into two separate cells (Vermeulen, Van Bockstaele and Berneman, 2003). There are two stages of cell division: (1) Mitosis (M) phase, which includes nuclear division comprising prophase, metaphase, anaphase and telophase, and (2) interphase, which includes G_1 (preparation for DNA replication or entry to G_0 resting phase), S (DNA synthesis) and G_2 (preparation for mitosis) phases.

Two categories of cell cycle control mechanisms have been recognized: (1) a cascade of protein phosphorylation that monitor a cell's progress from one stage to the next and (2) checkpoints that monitor the cell cycle sequences and delay the progression to the next cycle phase (Collins, Jacks, and Pavletich, 1997). These controls ensure that the DNA is replicated correctly in S-phase and the identical chromosomes are segregated equally during M phase into the resultant daughter cells. A key family of regulator proteins involved in the first type of control are called cyclin-dependent kinases (CDK) which plays a crucial role in the transition from one cell cycle phase to another (Vermeulen, Van Bockstaele and Berneman, 2003; Tanaka *et al*., 2007; Scaife *et al*., 2011). The CDK family is a group of serine/threonine protein kinases, nine of which have been identified to date and five of them (CDK1, CDK2, CDK4, CDK6, and CDK7) being active during the cell cycle (Vermeulen, Van Bockstaele and Berneman, 2003). The activation of CDK is achieved by the phosphorylation on the specific threonine and tyrosine residues and the phosphorylation induces the conformational changes which enables the association with cyclins. CDK perform kinase activity when they are bound with the corresponding cyclins, forming a cyclin-CDK complex. Different CDK proteins appear to function in different stages of the cell cycle as summarised in Figure 1.5. The cell cycle, therefore, is tightly controlled by the regulation of CDK, CDK inhibitors and phosphorylation events all ensuring that the cell division occurs correctly.

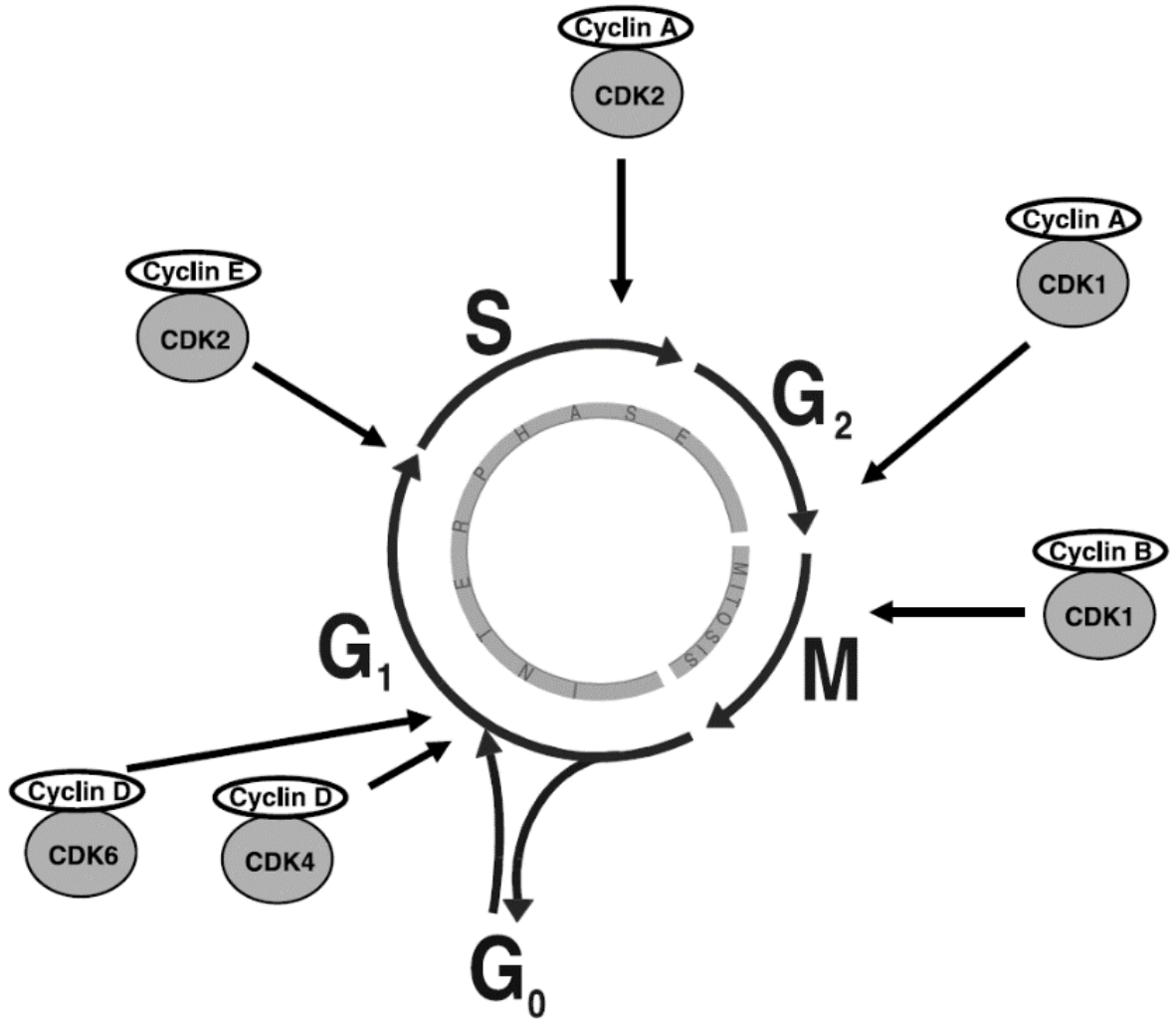


Figure 1.5. The cell cycle stages and the site of activity of CDK/cyclin complexes in the cell cycle.
CDK2, CDK4 and CDK6 involves in G_1 phase, CDK2 in S-phase, and CDK1 in G_2 and M phases (King and Cidlowski, 1998; Vermeulen, Van Bockstaele and Berneman, 2003). CDK7 acts in combination with cyclin H as CDK activating kinase (CAK) in all cell cycle phases (not presented).
Abbreviation: CDK: Cyclin-dependent kinase.

The second type of cell cycle regulation is the surveillance system that interrupts the cell cycle progression when the DNA damage or spindle damage are detected, called cell cycle checkpoints (Paulovick, Toczyski and Hartwell, 1997). The sequence and the timing of the cell cycle events are monitored by the checkpoints that take place at the G_1/S phase boundary, in S-phase, and during the G_2/M phases (King and Cidlowski, 1998; Vermeulen, Van Bockstaele and Berneman, 2003). These checkpoints are responsible for ensuring the events in cell cycle phases are completed before a new phase is started. When the checkpoints are triggered by DNA damage, signals are transduced to affect the activity of critical cell cycle regulators, leading to the delay in cell cycle progression until the danger of mutation has been averted (Collins, Jacks, and Pavletich, 1997; Samuel *et al*., 2002). Upon the repair of the DNA

damage, the cell cycle progression resumes and the alternative way to manage the damaged and unrepaired cells is simply to discard them through programmed cell death, apoptosis, avoiding the risk of creating genetically altered progeny (Samuel *et al*., 2002; Lauber *et al*., 2012).

1.3.2 Cell death regulation (apoptosis) under normal condition

Cell death is highly regulated in order to eliminate unwanted cells without eliciting an inflammatory response (King and Cidlowski, 1998). Apoptosis or programmed cell death is a major cell death mechanisms and is predominantly observed in response to ionizing radiation (Dewey *et al*., 1995; Eriksson and Stigbrand, 2010). It is characterized by rounding-up of the cell, retraction of pseudopods, reduction of cellular volume (pyknosis), condensation of the chromatin, fragmentation of nucleus (karyorhexis), little or no ultrastructural modification of cytoplasmic organelles, plasma membrane blebbing, and maintenance of an intact plasma membrane until the late stages of the process (Table 1.3; Leers *et al*., 1999; Duan *et al*., 2003; Kroemer *et al*., 2005; Lauber *et al*., 2012). The cell membrane loses its asymmetry during apoptosis and glycoconjugates (α-D-mannose and β-D-galactose-specific plasma membrane glycoproteins) and phosphatidylserine which is normally on the cytoplasmic side of the lipid bilayer is exposed on the apoptotic cell surface attracting surrounding macrophages eventually resulting in clearance of the apoptotic cell (Bilyy and Stoika, 2007; de Bruin and Medema, 2008).

The entire apoptosis pathway is tightly regulated and mediated by caspases (Leers *et al*., 1999; Roberg *et al*., 2007; de Bruin and Medema, 2008) which are key components in executing apoptosis and function in protease cascades (Philchenkov, 2004; Blomberg, 2008; Mcllwain *et al*., 2013). Caspases are synthesized as a single-chain inactive zymogen that become activated by proteolytic cleavage. They subsequently activate proteins by either cleaving the negative regulatory domain or inactivating regulatory subunit. Some pro-caspases can also aggregate and auto-activate. This proteolytic cascade, in which one caspase can activate other caspases, amplifies the apoptotic signalling pathway and thus leads to rapid cell death (Mcllwain *et al*., 2013). To date, ten major caspases have been identified and broadly categorized into initiators (caspase-2,-8,-9,-10), effectors or executioners (caspase-3,-6,-7) and inflammatory caspases (caspase-1,-4,-5; Mcllwain *et al*., 2013).

Apoptosis is induced by two main signalling pathways: the extrinsic pathway or death receptor pathway involving extracellular death ligands, such as Fas ligand and TNF-α ligand and the intrinsic mitochondrial pathway involving intracellular stress signals including DNA damage, oxidative stress or oncogene activation (de Bruin and Medema, 2008).

Extrinsic apoptotic pathway- Death receptor pathway

Death receptors located on the plasma membrane are responsible for the extrinsic apoptotic signalling pathway and these receptors are members of the tumour necrosis factor (TNF) receptor superfamily, Fas receptor or TNF-related apoptosis-inducing ligand (TRAIL) receptors (Figure 1.6; Jin and El-Deiry, 2005; Elmore, 2007; Blomberg, 2008). When death ligands such as the Fas-Ligand (FasL) bind to Fas receptors, the death domains of Fas recruit and interact with the death domains of Fas-associated DD-containing protein (FADD). The sequential recruitment of FADD and procaspase-8 leads to the formation of a death inducing signalling complex (DISC) where the interaction between the FADD and caspase-8 occurs and mediates the dimerisation of two caspase-8 molecules. Execution phase of apoptosis is triggered when caspase-8 is activated which subsequently activate the downstream caspase-3, -6 and -7 (Blomberg, 2008).

TRAIL- and TNF-receptor signalling is almost identical to Fas signalling. The function of the TNF-R1 complex is inhibited when it binds with the suppressor of death domain (SODD) while its engagement by TNF- α ligand leads to the release of SODD allowing the binding of the death domain containing proteins like TNF-R1-associated death domain containing protein (TRADD; Jin and El-Deiry, 2005). TRADD recruits TRAF2, RIP1 and FADD which then trigger the activation of several intracellular signalling pathways (Figure 1.6). At first, the TNF-R1, TRAF2, RIP1 complex will induce an anti-apoptotic response by activating the mitogen-activated protein kinases (MAPKs) and the NF-κB-Kinase pathways. An apoptotic response can also be induced via the formation of a cytoplasmic complex containing TRADD, RIP1 and FADD which activates caspase-8 and the downstream effector caspases (as in Fas signalling; Figure 1.6).

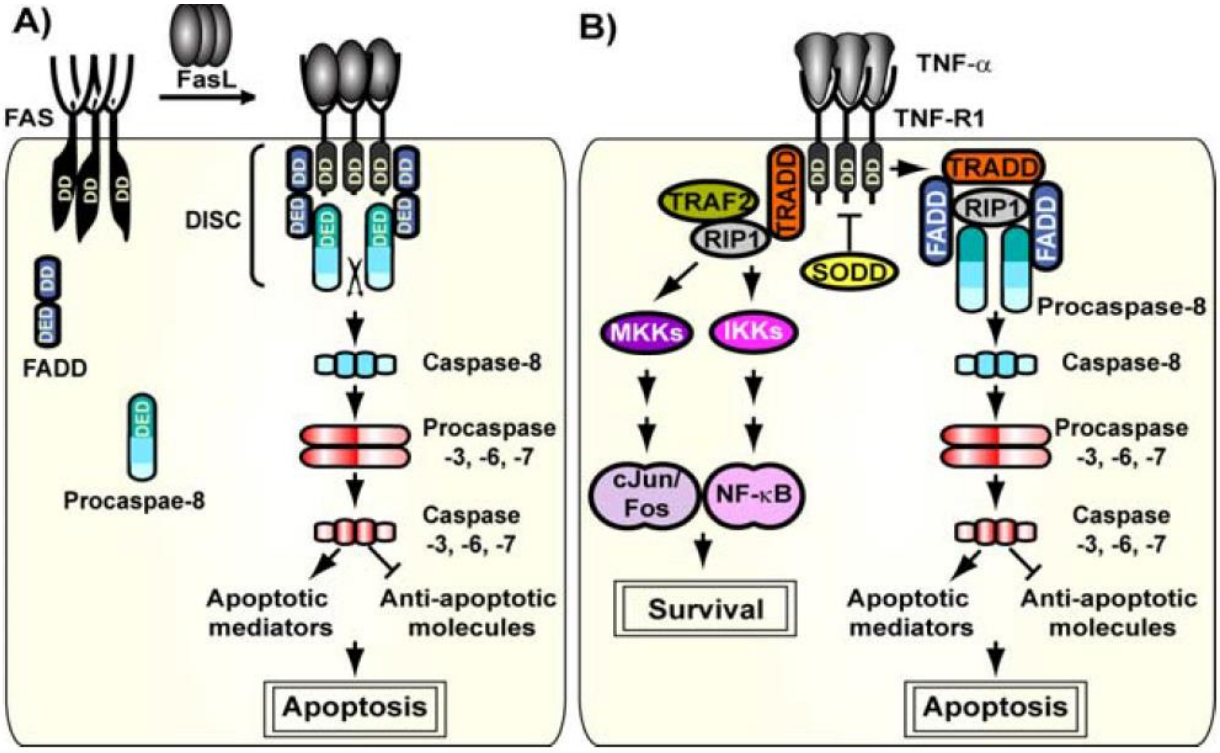


Figure 1.6. Two types of extrinsic signalling pathways in apoptosis, (A) Fas receptor signalling and (B) tumour necrosis factor (TNF) receptor signalling.
(Jin and El-Deiry, 2005; Elmore, 2007; Blomberg, 2008).
Abbreviations: FasL: Fas Ligand, DISC: Death-inducing signalling complex, FADD: Fas-associated protein with death domain, DD: Death domain, DED: Death-effector domain, TNFα: Tumour necrosis factors alpha, TNF-R1: Tumour necrosis factors receptor 1, TRADD: Tumour necrosis factor receptor type 1-associated death domain, TRAF2: TNF receptor associated factor 2, RIP1: Receptor-interacting protein kinase 1, SODD: Suppressor of death domain, NF-κB: Nuclear factor kappa-light chain-enhancer of activated B cell.

Intrinsic apoptotic pathway- Mitochondrial pathway

The intrinsic apoptotic pathway is initiated inside cells at the mitochondria (Figure 1.7; Jin and El-Deiry, 2005; Blomberg, 2008). The key event of the intrinsic pathway is the mitochondrial outer membrane permeabilization (MOMP) which is facilitated by B cell lymphoma (Bcl-2) family members. The Bcl-2 family consists of 20 members in mammals which are categorized into three groups: one group of anti-apoptotic members (Bcl-2, Bcl-XL, Bcl-w and Mcl-1) which promote cell survival and two groups of pro-apoptotic members (Bax, Bak, Bad, Bik and Bid) that induce cell death. All of these members contain the conserved Bcl-2 homology (BH) domains. Apoptosis is induced when pro-apoptotic proteins are activated, for example, dephosphorylation of Bad and cleavage of tBid (Jin and El-Deiry, 2005). The activated pro-apoptotic proteins, that contain Bcl-2 homology domains, lead to conformational changes in Bax and Bak which subsequently trigger the permeabilisation of MOM and the release of cytochrome c into the cytoplasm.

Death signals initiate the disruption and trigger MOMP which then causes cell death via two mechanisms: the release of mitochondrial intramembrane proteins, particularly cytochrome c, and the disruption of essential mitochondrial function (Jin and El-Deiry, 2005; de Bruin and Medema, 2008, Blomberg, 2008). Cytochrome C which was previously known to function within the electron transport chain present in the cytoplasm binds to an adaptor molecule apoptotic protease activating factor (Apaf-1), generating a complex called the apoptosome in the presence of ATP/dATP (Jin and El-Deiry, 2005). The apoptosome recruits and then activates procaspase-9 by oligomerization which subsequently activates the downstream caspase-3, -6 and -7 (Jin and El-Deiry, 2005; de Bruin and Medema, 2008, Blomberg, 2008), eventually executing programmed cell death. The downstream signalling from the initiator caspases are the same for both the intrinsic and extrinsic pathways.

The activation of procaspase-9 and Apaf-1 in response to chemotherapeutic drugs has been studied previously in cisplatin-resistant and cisplatin-sensitive HNSCC (Kuwahara *et al*., 2003). By using direct enzymatic assay, the caspase-9 activity was found to be lower in cisplatin-resistant cells compared with that of cisplatin-sensitive cells following drug treatment, whilst the expression of Apaf-1 was higher in the sensitive cells. This illustrated that both the inhibition of caspase-9 activity and low Apaf-1 expression may contribute to the mechanism of cisplatin resistance in HNSCC. Other proteins which are released from the intermembrane space during the apoptosis include apoptosis induced factor (AIF), endonuclease G (EndoG), second mitochondria-derived activator of caspases/direct IAP binding protein with low PI (Smac/Diablo), and high temperature requirement protein A2 (HtrA2/Omi; summarised in Table 1.5).

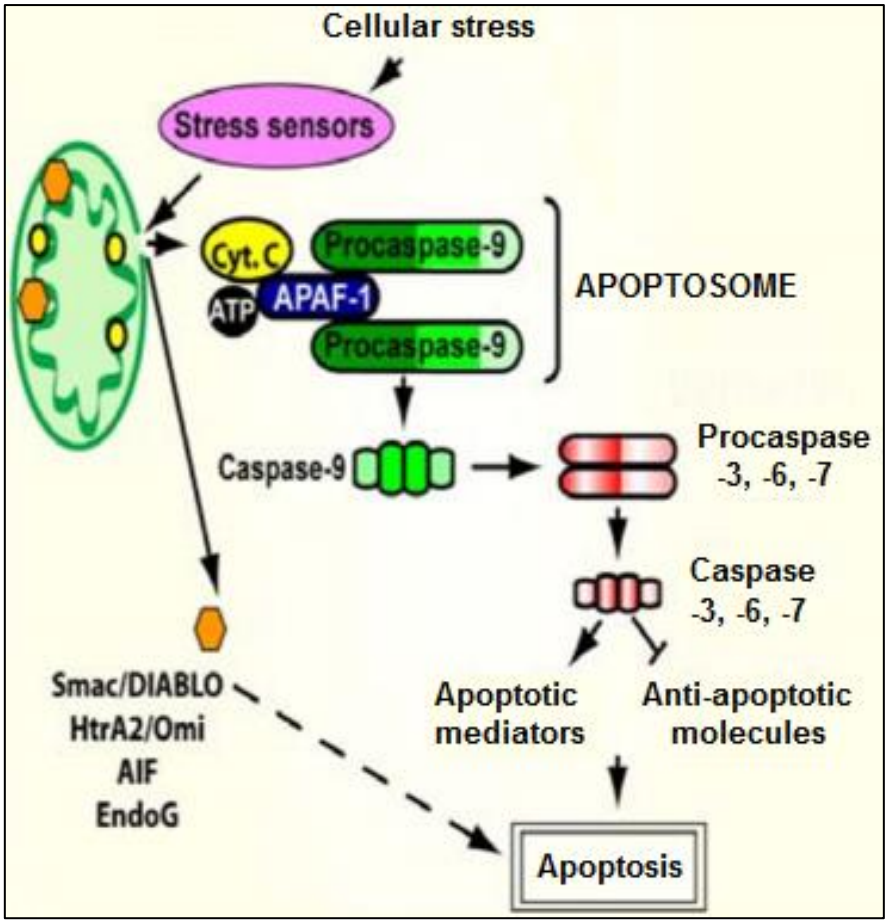


Figure 1.7. Intrinsic pathway of apoptosis resulting from cellular stress.
(Jin and El-Deiry, 2005; Elmore, 2007; Blomberg, 2008).
Abbreviations: HtrA2: high temperature requirement protein A2, Smac/Diablo: second mitochondria-derived activator of caspases/direct IAP (inhibitor of apoptosis) binding protein with low PI, AIF: Apoptosis induced factor, EndoG: Endonuclease G, Cyt. C: Cytochrome C, ATP: Adenosine triphosphate, APAF-1: apoptotic protease activating factor 1.

Table 1.5. Summary characteristics of proteins released from mitochondria intermembrane space during apoptosis.

Proteins	Characteristics in apoptosis
AIF	• Pro-apoptotic protein involved in caspase-independent apoptosis which translocate to nucleus when it is released from mitochondria in response to death stimulus. • Triggers DNA fragmentation and chromatin condensation in nucleus
EndoG	• Released endoG moves to nucleus where it could cause oligonucleosomal DNA fragmentation and eventually to caspase-independent cell death
Smac/ Diablo	• Caspase coactivator • Released along with cytochrome c during apoptosis which functions to neutralize the inhibitory activity of IAPs (which serve as a brake for apoptosis by inhibiting activated caspases) and support cytochrome c-dependent caspase activation
HtrA2/Omi	• Functions as a dual agent which promotes DNA fragmentation under apoptotic conditions and retains the normal mitochondrial functions

(Li *et al*., 2001; Jin and El-Deiry, 2005; Blomberg, 2008; de Bruin and Medema, 2008).
Abbreviations: AIF: Apoptosis- inducing factor, EndoG: endonuclease G, Smac/Diablo: second mitochondria-derived activator of caspases/direct IAP (inhibitor of apoptosis) binding protein with low PI, and HtrA2: high temperature requirement protein A2.

On HNSCC, various studies have researched the key proteins of extrinsic apoptotic pathway to search for potential prognostic markers. It has been shown that the procaspase-8 mutations associated in HNSCC inhibit the activation of extrinsic apoptotic pathway which are likely to represent the markers of resistance to therapeutic regimens on HNSCC patients (Li *et al*., 2014). When the HNSCC cells with procaspase-8 mutation were injected into xenograft mice, the rapid growth was detected on the mutant group compared with that of the wild-type group, suggesting that the enhanced *in vivo* tumour growth was likely to be due to the resistance of tumour cells to death ligands. In addition, the expression of FADD protein, which is a critical apoptotic adaptor molecule that bridges the cell surface death receptors to caspase-8 to form DISC complex during apoptosis, as well as its prognostic impact in primary and metastatic HNSCC were studied in Fan *et al*. (2013). The elevated levels of caspase-8 alone or combination of high levels of FADD or surface death receptor have positive impacts on the survival of patients who have no evidence of lymph node metastasis. This suggested that the FADD and caspase-8 signalling in extrinsic apoptotic pathway possess suppressive function on the cancer metastasis regulation. The role of SMAC in mediating apoptosis induced by various therapeutic agents on HNSCC cells has also been described in Sun *et al*. (2011). In Sun's study, the knockdown of SMAC led to the failure of caspase activation, mitochondrial membrane depolarization and the release of cytochrome c, confirming the roles of SMAC in apoptosis process in HNSCC. Therefore, there are many different markers which take part in both intrinsic and extrinsic pathways available to be used to study programmed cell death in response to anti-cancer therapies.

1.3.3 Types of DNA damage and double-strand breaks (DSBs)

On a daily basis, DNA in the cell suffers a wide variety of lesions from exogenous and endogenous sources, leading to different types of DNA damage (Figure 1.8). Double strand breaks (DSBs) are the most severe form of damage in eukaryotic cells which can be generated by chemical and physical damage caused by ionizing radiation, chemotherapy drugs, and metabolic by products (e.g. reactive oxygen species). In addition, DSB can result from errors during replication and programmed enzymatic activities occurs during meiosis and V(D)J recombination (Lamarche, Orazio and Weitzman, 2011). To respond and combat these lesions, cells consequently developed complex mechanisms to induce DNA repair [DNA-damage response (DDR)].

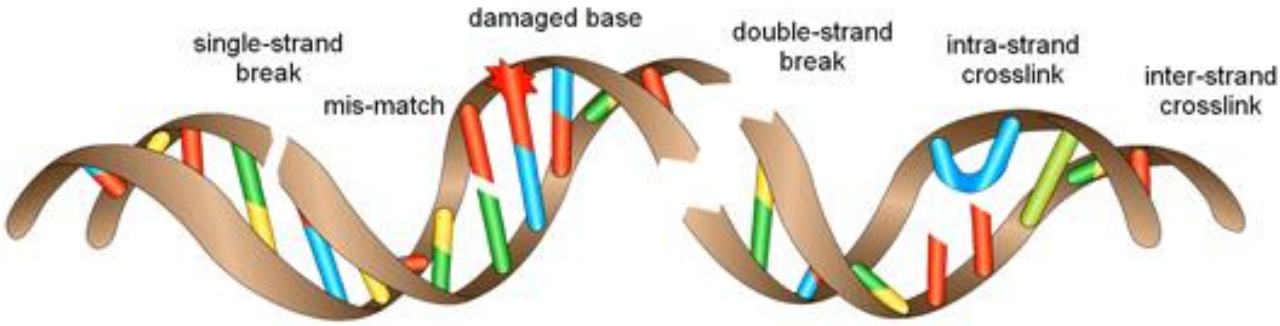


Figure 1.8. Representative of the types of DNA damage that can occur following exposure to chemicals and radiation.
The damages include single-strand breaks (SSBs), DNA mismatches, base loss, double-strand breaks (DSBs), intra-strand crosslink, and inter-strand crosslink (Itzhaki, 2012).

1.3.4 DNA damage checkpoints and DNA-damage response (DDR) pathway

When DNA damage happens on cells, it causes to the activation of DDR pathway which instigates signals that can activate either temporary checkpoints that allow sufficient time for DNA repair by specific DNA repair enzymes (Figure 1.10; Liang *et al*., 2009; Scaife *et al*., 2011) or permanent growth arrest that results in cell death (Shackelford *et al*., 1999; Samuel *et al*., 2002; Pawlik and Keyomarsi, 2004).

DNA damage checkpoints

As described previously in section 1.3.1, the cell cycle progression is interrupted when damage to the genome or spindle, e.g. DSBs, is detected and these surveillance checkpoints take place during G_1/S phase (G_1-S checkpoint), during S-phase, after DNA replication (G_2/M phases; G_2-M checkpoint) and during M phase (King and Cidlowski, 1998; Vermeulen, Van Bockstaele and Berneman, 2003). The continuation of DNA replication is confirmed at the G_1-S checkpoint (Samuel *et al*., 2002;

Vermeulen, Van Bockstaele and Berneman, 2003). DNA damage detected can result in arrest in the G_1 phase which is before the DNA replication. However, unregulated S-phase entry can also cause genetic instability or apoptotic cell death even without DNA damage being detected (Samuel *et al*., 2002).

When DNA damage is detected at the G_1-S checkpoint, the cell cycle arrest is *p*53-dependent because *p*53 is rapidly elevated in response to DNA damage which in turn triggers the transcription of several genes such as p21 (Samuel *et al*., 2002; Vermeulen, Van Bockstaele and Berneman, 2003). The induction of p21 leads to the inhibition of different cyclin/CDK complexes (Cyclin D-CDK4/6 and cyclin A, E-CDK2) and causes cell cycle arrest which avoids the duplication of damaged DNA (Sionov *et al*., 2000). Other genes that are stimulated by *p*53 in this checkpoint are mouse double minute 2 homology (mdm2) and Bax which both contribute to cell cycle arrest at this point. The cell cycle can also be arrested when the damage is detected during G_2, preventing the progression of damage into mitosis (G_2/M phases; G_2-M checkpoint). To prevent the entry into mitosis, CDK1 is maintained in the inhibited form in the cytoplasm during interphase by phosphorylation or the sequestration of the CDK1-cyclin B1 complex by Chk1 and 2 (Samuel *et al*., 2002; Vermeulen, Van Bockstaele and Berneman, 2003).

During the G_1-S checkpoint, ATM phosphorylates and activates *p*53 in response to DSB triggered by ionizing irradiation (Figure 1.9; Shiloh, 2001; Samuel *et al*., 2002; Pawlik and Keyomarsi, 2004; Lopez-Contreras and Fernandez-Capetillo, 2012). The phosphorylation of *p*53 by ATM occurs at serine 15 and serine 20 position which disrupts the binding of *p*53 to mdm2 (a mediator of *p*53 degradation). The modification of *p*53 inhibits the ubiquitous degradation of *p*53 and increases its stability which ultimately activates the gene encoding p21, an inhibitor of the CDK2-cyclin E complex, and inhibits the G_1-S transition (Lopez-Contreras and Fernandez-Capetillo, 2012). ATM also phosphorylates and activates Chk2 in cells following ionizing radiation (Figure 1.9; Pawlik and Keyomarsi, 2004) and its activation is the key regulator of the G_2-M checkpoint where it phosphorylates cell division cycle 25 (cdc25) and inhibits its activity, preventing the cells in from entering mitotic phase (Shiloh, 2001; Pawlik and Keyomarsi, 2004; Lopez-Contreras and Fernandez-Capetillo, 2012).

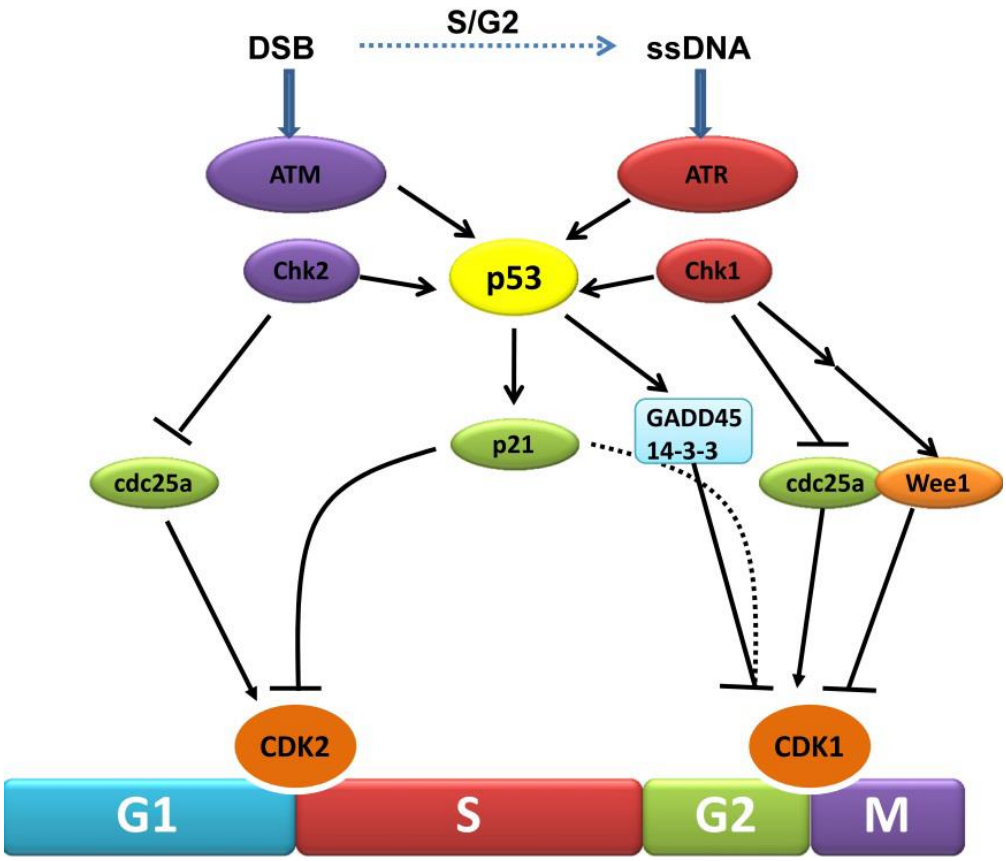


Figure 1.9. The regulation of cell cycle checkpoints by ATM and ATR following different DNA damage types.
ATM and ATR orchestrate a delay of the cell cycle in response to DSBs and ssDNA, respectively. ATM and ATR activate and stabilize *p*53 in response to DNA damage which prevent the G_1-S transition. Cdc25a is degraded, leading to the accumulation of inhibitory phosphorylation on CDK2, allowing establishment of G_1-S checkpoint. In G_2-M checkpoint, the activated ATM and ATR phosphorylate Chk2 and Chk1 respectively which ultimately prevent the activation of cdc2 and the entry of cells to mitotic phase (Lopez-Contreras and Fernandez-Capetillo, 2012).
Abbreviations: ATM: Ataxia telangiectasia mutated, ATR: ATM and RAD3 related, Mdm2: Mouse double minute 2 homolog, CDK: Cyclin-dependent kinase, Cdc: cell division cycle, Chk: Serine/threonine-protein kinase.

The spindle checkpoints arrest the cell growth when the chromosomes are misaligned on the mitotic spindle (King and Cidlowski, 1998; Vermeulen, Van Bockstaele and Berneman, 2003). When the improper alignment of chromosomes is detected in standard cells, the cell cycle will be arrested in metaphase, termed M-phase arrest (Kubiak *et al*., 1993; Vermeulen, Van Bockstaele and Berneman, 2003). The cell cycle progression will be resumed when the DNA damage is successfully repaired. However, the cell cycle arrest mediated by checkpoints may fail for various reasons such as intrinsic error rate in checkpoints, adaptation of signal transduction systems which permits cell cycle progression even though the damage is unrepaired, and checkpoints defects that leads to multiple genetic changes (reviewed by Paulovich *et al*., 1997). When the damage is not repaired prior to DNA replication, different cell death modalities (section 0) are induced in order to prevent the damaged DNA being transmitted to daughter cells (Scaife *et al*., 2011; Lauber *et al*., 2012).

DNA-damage response (DDR)

For DSB repair in healthy cells, there are two principal mechanisms are carried out which are non-homologous end-joining (NHEJ) and homologous recombination (HR). In NHEJ, DSBs are recognized by Ku protein which then binds to the DNA termini, mark the terminus as a node for polymerases, nuclease and ligases. This also activates the DNA-dependent protein kinase, catalytic subunit (DNA-PKcs), which is a serine/threonine protein kinase. This activation of DNA-PKcs leads to the recruitment and activation of the end-processing enzymes, polymerases and DNA ligase IV (Lieber *et al*., 2010). The deleterious lesions can also be eliminated by homologous recombination (HR) which is restricted to S and G_2 phase as it uses sister-chromatid sequences as the template to mediate faithful repair. HR is always initiated by the generation of single stranded DNA and is mediated by recombinases, including Rad51 and disrupted meiotic cDNA (Dmc1), that catalyse the pairing and shuffling of homologous DNA sequences in cells through the pre-synaptic filament on single stranded DNA (San Filippo *et al*., 2008).

The key components that involve in DDR pathway of normal cells are the two phosphatidylinositol-3-related kinases, ATM (ataxia telangiectasia mutated) and ATR (ATM-Rad3-related), which are located at the top of checkpoint signal cascades and are activated by the different DNA damage mechanisms (Figure 1.10; Liang *et al.*, 2009; Smith *et al*., 2010; Lauber *et al*., 2012). ATM is activated by DSBs and functions throughout all cell cycle phases while ATR pathway is induced by agents disrupting with the function of DNA replication forks such as UV light (Liang *et al*., 2009). Both kinases phosphorylate and activate the two respective effector kinases: checkpoint kinase 1 (Chk1) and checkpoint kinase 2 (Chk2) which lead to cell cycle arrest (section 1.3.1; Jackson and Barket, 2009). During the checkpoints, DNA repair occurs in respond to the DNA damage. In addition, the DNA damage elevate the expression level of *p*53 protein which, as well, lead to the temporary cell cycle arrest, DNA damage repair and the cell death (Liu *et al.*, 2001; Jackson and Bartek, 2009; Smith *et al*., 2010; Lauber *et al*., 2012). In response to DNA damage induced by radiotherapy, many molecular proteins participate in DDR pathways and the regulation of checkpoints and, therefore, the regulation of cell cycle and lesion repair of the tumour cells are of interested and important to evaluate the effectiveness of anti-cancer therapies.

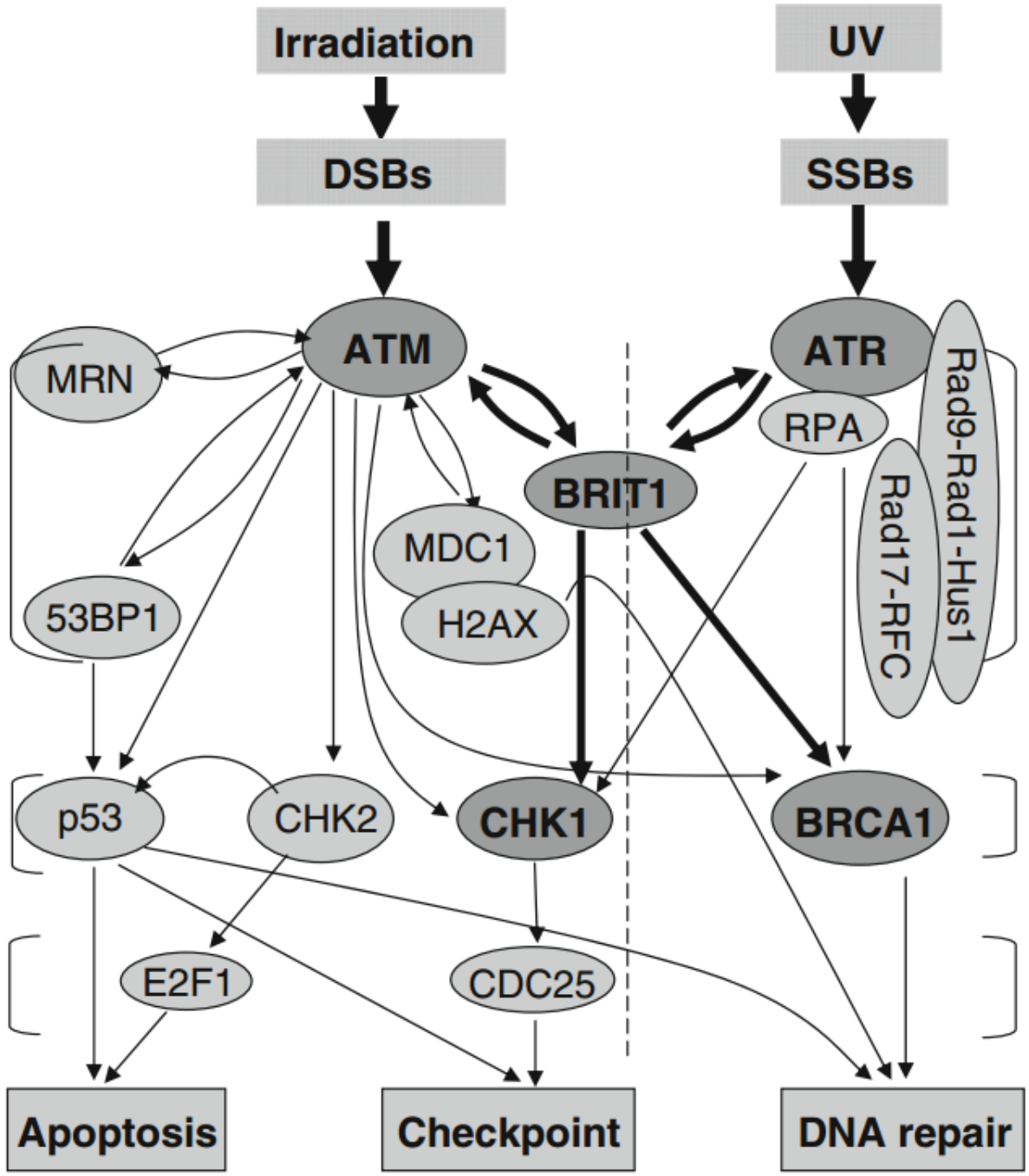


Figure 1.10. DNA damage response (DDR) pathway comprises two interconnected pathways, ATM and ATR.

In response to DNA damage, these two core kinases ATM and ATR are activated and recruit the sensors (MRN complex, 53BP1, and MDC1 in ATM pathway and RPA in ATR pathway), transducers, and effectors proteins and finally regulate the cell cycle checkpoint, DNA repair and apoptosis. The black bold line indicates the pathway that involved BRCT-repeat inhibitor of hTERT (BRIT1) protein which participates in both ATM- and ATR-dependent pathways in modulating checkpoints and DNA repair (Liang *et al*., 2009).

Abbreviations: DSBs: double-strand breaks, SSBs: single-strand breaks, MRN: Mre11-Rad50-Nbs1 complex, 53BP1: *p*53 -binding protein 1, ATM: ataxia telangiectasia mutated, Chk2: checkpoint kinase 2, MDC1: Mediator Of DNA-Damage Checkpoint 1, H2AX: H2A histone family, member X, Chk1: checkpoint kinase 1, CDC25: cell division cycle 25, Brti1: BRCT-repeat inhibitor of hTERT, UV: ultraviolet, ATR: ATM-Rad3-related, RPA: replication protein A, BRCA1: breast cancer 1.

1.3.5 Predisposition and molecular behaviour of cancer cells

The normal control mechanisms in cell involve both tumour suppressor (inhibitory) and proto-oncogene (stimulatory) constituents (Alberts *et al*., 2002). In cancer cells, these proto-oncogenes and tumour suppressor genes are mostly mutated in which many mutations alter the proliferative signal and induce inappropriate cell growth and cell division even when more cells are not needed (Alberts *et al*., 2002). For example, epidermal growth factor receptor (EGFR) is an established oncogene in HNSCC and is overexpressed in 90% of HNSCC (Leemans *et al*., 2011; Hansen and Siu, 2013). Mutation of EGFR in tumour cells may relay signals to trigger the cell cycle progression (Leemans *et al*., 2011; Perri *et al*., 2015); specifically a somatic point mutation of EGFR (EGFRvIII) was found in HNSCC (Sok *et al*., 2006). Overexpression of EGFR on the HNSCC cell surface can be targeted by the FDA approved monoclonal antibody Cetuximab (Bonner *et al*., 2006; Vermorken *et al*., 2008; Cassell and Grandis, 2011; section 1.2.3), which has been shown in combination therapies to improve HNSCC patient survival. However, tumours with EGFRvIII mutation have minimal *in vitro* and *in vivo* response to Cetuximab (Sok *et al*., 2006). In addition, Rb protein is the product of tumour suppressor Rb gene which serves as a brake in restricting the entry of cell into S-phase by binding to gene regulatory proteins required to express genes whose products are needed for cell cycle (Vermeulen, Van Bockstaele and Berneman, 2003). The mutation of *pRb* gene (e.g. deletion and mis-sense mutations) produces truncated and non-functional *p*Rb or complete absence of *p*Rb while the absence or loss of function of *p*Rb results in unrestrained proliferation of cancer cells. Normally, transforming growth factor-β (TGFβ) triggers growth inhibition through TGFβ receptors, however, in HNSCC, TGFβ plays dual roles during carcinogenesis (Papageorgis and Stylianopoulos, 2015). In early stages, it promotes growth inhibition, whereas during late stages, it promotes tumour growth with progressive increase in the levels of secreted TGFβ. A somatic mutation in the gene encoding TGFβ type II receptor (TGFβ-RII) and the subsequent reduction of the protein have been identified in HNSCC which lead to loss of growth inhibition and uncontrollable proliferation (Alberts *et al*., 2002; Fukai *et al*., 2003; Lu *et al*., 2006; Leemans *et al*., 2011). The administration of TGFβ receptor inhibitor (e.g. LY364947) prior to radiotherapy is able to attenuate DDR, increase cell death, delay tumour growth and improve the efficacy of radiotherapy (Bouquet et al., 2011; Papageorgis and Stylianopoulos, 2015). Many drugs have been developed in combination therapies to inhibit TGFβ signaling and

reduce tumour progression in preclinical and clinical trial studies, such as tranilast, AP-12009, SD-208, and pirfenidone (Akhurst and Hata, 2012; Papageorgis and Stylianopoulos, 2015). However, the development of tumour drug resistance is common and has been reported for TGFβ receptor inhibitor LY2109761 (Connolly et al., 2011; Akhurst and Hata, 2012). As a results, the genetic alterations of oncogene and tumour suppressor genes lead to genetic instabilities and become molecular characteristics of cancerous cells that play crucial role in tumour prognosis and targeted therapies in clinical studies.

The defects of DDR pathway, also, commonly predispose to cancer by inducing genomic instability, allowing tumour-cell survival and proliferation (Alberts *et al*., 2002; Jackson and Bartek, 2009; Curtin *et al*., 2012). In terms of activation, the increased autophosphorylation of ATM and ATM-dependent phosphorylation of Chk2 are described in early-stage tumours, suggesting that the DNA damage response acts as a barrier to the malignant progression of tumours (Bartkova *et al*., 2005). The increased expression of ERCC1, APE1, NBS1, RAD50, Chk1, Chk2, CDC25A, CDC25B and CDC25C are also reported in tumours (Curtin *et al*., 2012; Hosoya *et al*., 2014). The inactivation of DDR proteins is also observed in various cancers, including head and neck malignancies. The aberrations in DDR detected in head and neck cancers are summarised in Table 6.1.

Both activation and inactivation of the DDR components detected in head and neck cancers are expected to determine the key properties of DNA damage response machinery in the cancers, particularly in response to anticancer therapies. The efficacy of radiotherapy depends on DNA damage that will be detected and repaired by intrinsic DNA repair pathways described above. The aberrant expression of DDR proteins in HNSCC could be a potential biomarker of resistance or favourable response to therapies that trigger corresponding DNA damage types (Hosoya *et al*., 2014).

Table 1.6. Examples of aberrations in DNA damage response in head and neck cancers

DDR markers	Activation/ inactivation	Aberration types	Clinical correlation	References
ATM	Inactivation	↓expression	The overall 5-year survival is 22% in HNSCC tumours with ATM promoter hypermethylation and 46% in those without ATM promoter hypermethylation.	Ai *et al*., 2004
NBS1	Activation	↑expression	Increased NBS1 expression was found in 45% of advanced HNSCC and this group of patients had a significantly worse 2-year overall survival than patients with lower levels of NBS1 (37.9% vs. 73.2%; Yang *et al*., 2006).	Yang *et al*., 2006; Dzikiewiez-Kraweczyk, 2008
RAD51	Activation	↑expression	Patients with high RAD51 protein levels demonstrated poorer cancer-specific 2-year survival rates than patients with lower RAD51 levels (33.3% vs. 88.9%).	Connell *et al*., 2006.
ERCC1	Activation	↑expression	Survival of tumours with high ERCC1 expression was 2.1 years while patients with low ERCC1 expression group was 2.9 years (Hayes *et al*., 2011).	Takenaka *et al*., 2007; Hayes *et al*., 2011.
APE1	Activation	↑expression	Tumours with high APE1 nuclear expression was significantly associated with poor complete response rate and poorer survival and shorter local relapse-free interval compared with those with low APE1 expression (Koukourakis *et al*., 2001).	Koukourakis *et al*., 2001; Abbotts *et al*., 2010.
FANCF	Inactivation	↓expression	Patients with FANCF methylation had a three times greater chance of an adverse outcome compared to patients without FANCF methylation (Marsit *et al*., 2004).	Marsit *et al*., 2004; Taniguchi *et al*., 2006.

Abbreviation: DDR: DNA damage response, ATM: ataxia telangiectasia mutated, NBS1: Nijmegen Breakage Syndrome 1, ERCC1: excision repair cross-complementation group 1, APE1: apurinic/apyrimidinic endonuclease, FANCF: Fanconi anemia group F protein.

During tumorigenesis, cells undergo mutations that enable the cells to escape the checkpoints (Benada and Macurek, 2015). Many tumour suppressors function and take part in cell cycle checkpoints, including *p*53, ATM, *p*16, CDKN2A and BRCA1, in response to variety of stimuli. The tumour suppressor loss commonly observed in cancers indicates that the checkpoint defects are a common feature of cancer (Samuel *et al*., 2002; Benada and Macurek, 2015). Some cell cycle arrests occur by *p53* when it is activated in response to checkpoints to detect DNA and chromosome damage (Samuel *et al*., 2002; Gabrielli, Brooks and Pavey, 2012). The loss of *p53* would remove the protecting function of the cell cycle arrests and lead to continuous cell cycle progression. The cancer cells deficient in *p*53 pathway are lack of efficient G_1

checkpoint, promoting mitotic entry despite of the presence of DNA damage (Benada and Macurek, 2015).

All of these regulatory mechanisms possessed in tumour cells, consequently, make an ideal target for therapeutic intervention, particularly, in killing cancer cells and minimizing therapeutic resistance. The understanding on how the tumours respond to ionising radiation and alter the cellular pathways in order to escape the therapeutic cell death impacts is of importance specially to improve efficacy of radiotherapy.

1.3.6 Mechanisms of radiotherapy resistance

Recurrence and resistance at the primary tumour site remains the dominant factor of treatment failure in patients with HNSCC (SIGN, 2006). The molecular and cell cycle response to ionizing radiation are varied between different cell types and organs due to the variable intrinsic radiosensitivity of certain human tumour cells (reviewed in Pawlik and Keyomarsi, 2004; Scaife *et al*., 2011), resulting in patients with radiotherapy resistant tumours being subjected to a treatment without therapeutic gain but which contains significant side effects (Scaife *et al*., 2011). Following the recurrence of a tumour due to radiotherapy resistance, patients then have to undergo salvage surgery, which is not as straight forward following radiotherapy as the tumour margins become less apparent (Rukstalis, 2002; British Association of Otorhinolaryngology, 2011).

Despite the effects of radiotherapy in killing cancer cells, a proportion of tumours are resistant to treatment that contributes to the tumour recurrence and relapse. Intrinsic tumour cell radioresistance becomes the significant clinical problem that leads to poor outcome for patients and limits the effectiveness of radiotherapy (Kim *et al*., 2015). To date, there is limited discovery relating to the underlying mechanisms of radiotherapy resistance. However, it is generally accepted that the patient response to radiotherapy and therapy failure is probably because of clinical, both tumour- and patient-related, factors as well as the biological factors with multiple alterations within several different cellular transduction pathways.

Clinical factors

The clinical factors that are thought to affect the tumour response to radiotherapy include the tumour-related factors (tumour site, stage, volume, nodal status and grade) and patient-related factors (patient age, gender, and haemoglobin level (Silva *et al*., 2007). HNSCC consists of heterogeneous group of patients with various tumour

subsites which contribute to the different tumour behaviours, different radiosensitivities as well as the variation in therapeutic outcomes (Dinshaw *et al*., 2006; Silva *et al*., 2007; Scaife *et al*., 2011). The disease stage (TNM classification; 1.1.4) is also an important clinical factor used in HNSCC cancer management (Silva *et al*., 2007; British Association of Otorhinolaryngology, 2011). However, the use of tumour stage in therapeutic decision is based on single dimensional measurement which does not reflect the corresponding tumour volume in which a greater tumour volume is associated with poorer local tumour control and overall survival following fractionated irradiation (Yaromina *et al*., 2007; Werner-Wasik *et al*., 2008). Negative association between the nodal volume and the patient survival outcome is defined in Plataniotis *et al*. (2004) which could be explained the variations of nodal volumes across different subsites (Silva *et al*., 2007). In terms of patient-related factors, Boruk *et al*. (2005) and Silva *et al*. (2007) described that the patient chronological age is not an independent influential factor on the tumour local control and overall survival when the co-morbidity and physiological age is taken into account whereas the gender factor affects to the therapeutic outcome in which women were shown to have better locoregional control and survival compared with men following radiotherapy (Grégoire *et al*., 2010; British Association of Otorhinolaryngology, 2011). The prognostic significance of high haemoglobin level, in terms of locoregional control, disease-specific survival and overall survival, was demonstrated in HNSCC patients treated with radiotherapy in Hoff *et al*. (2011) study and the haemoglobin level may be related to the tumour hypoxia status in causing radioresistance. However, the precise relationship has yet to be confirmed. In summary, the tumour management decisions for patients with HNSCC based on these clinical factors may not sufficient to predict the therapeutic outcomes and, therefore, the development of biological markers are suggested could be used reliably in the clinical practise with clinical information to understand the causes of radiotherapy failure.

Biological factors

Several specific signalling pathways contribute to cellular resistance against radiotherapy and the pathways include adaptive, proliferation, DDR, hypoxic, adhesion, inflammation, developmental and RTK-PI3K/Akt pathways (Silva *et al*., 2007; Willers *et al*., 2013; Kim *et al*., 2015).

In the adaptive pathway, cyclin D1 functions in irradiation-induced adaptive radioresistance in which the increased cyclin D1 protects the cells from apoptotic cell death induced by high-dose radiotherapy by binding to and inhibiting the action of Bax (apoptotic activator; Ahmed *et al*., 2008). This suggested that accumulation and increased cytosolic level of cyclin D1 protein functions in suppressing the mitochondrial apoptosis in irradiation-induced adaptive resistance. Survivin overexpression has also been described in many adaptive responses to cellular stress, showing its role in tumour cell resistance (Khan *et al*., 2010; Grdina *et al*., 2013). Survivin is a member of the inhibitor of apoptosis (IAP) family and acts to prevent caspase activation and inhibit apoptosis. As it is overexpressed in cancer cells and elevated by ionising radiation, it is recognised as an important factor in relation with adverse outcomes of radiotherapy (Grdina *et al*., 2013). However, the mechanism of survivin induction by radiotherapy and radioresistance in cancer cells is not clearly understood.

Tumour proliferation is seen as an important factor in determining radiotherapy outcome (Silva *et al*., 2007). It is evident when the loss of tumour control was observed with increasing radiotherapy overall treatment time which is thought to be due to the tumour cell repopulation (Withers *et al*., 1988; Bourhis *et al*., 2006). Tumour repopulation is an adaptive response to cytotoxic effects of radiation that is likely due to increased tumour proliferation rate, reduction of fraction of cells lost from tumour or re-entry of quiescent cells into growth fraction (Willers *et al*., 2013). The repopulation in tumour cells enable them to compensate for irradiation-induced cell death which leads to survival of tumour cells and local relapse. As a result, the measurement of proliferation may allow the prognosis on HNSCC patients receiving different radiotherapy schedules and various methods have been researched and described to evaluate tumour proliferation, with the immunohistochemical measure of Ki-67 marker becoming increasingly popular.

Tumour cells confer radioresistance by eliciting DNA damage checkpoint and the efficient DNA repair system (DDR), as described earlier, in which the deficiency of DDR pathways may result in radiotherapy resistance. There are many genes involved in, and thus potential biomarkers of, radiation-induced DDR pathways, including KU70, XRCC5, DNA-PK, ATM, RAD51 and XRCC3, which are potential markers for radiotherapy response study (Silva *et al*., 2007; Kim *et al*., 2015). RAD51 is a key

facilitator of the homologous recombination DSB-repair pathway and the overexpression of RAD51 observed in many tumours was shown to relate to increased radioresistance and poor clinical outcomes (Connell *et al*., 2006; Klein, 2008). The overexpression of RAD51 is thought to contribute to inferior tumour control rates by increasing the repair of treatment-induced DNA damage and, alternatively, the poor tumour responsiveness could be also indirectly due to the genetic instability associated with the repair dysregulation (Connell *et al*., 2006). In addition, ATM kinase is one of the activators of DDR and the expression of this kinase may regulate the radiosensitivity (Kim *et al*., 2015). It plays a crucial role in the phosphorylation of histone H2AX as part of the DDR (Shiloh and Ziv, 2013). The downregulation of ATM gene expression, that may cause dysfunctional DNA repair, has been reported to produce poor outcome in laryngeal and pharyngeal cancers, however, the effect of ATM downregulation on HNSCC patient's outcome still remains unclear (Lee *et al*., 2011). The relationship between the deficiency of DDR pathway and tumour radiosensitivity could also be accomplished by measuring the persistence expression of phosphorylated histone H2AX (Taneja *et al*., 2004; Bourton *et al*., 2011). In response to DNA damage induced by radiotherapy, histone H2AX is rapidly phosphorylated by ATM on C-terminal tail on serine 139 (Valdiglesias *et al*., 2013) and the evaluation of phosphorylated H2AX levels allow the monitoring anti-cancer therapy as well as predict tumour sensitivity to DNA damage induced by anti-cancer agents (Podhorecka, Skladanowski and Bozko, 2010).

It is well known that tumour hypoxia is an important factor in affecting HNSCC tumour response to radiotherapy (Kamijo *et al*., 2000; Aebersold *et al*., 2001; Koukourakis *et al*., 2001). Many tumours consist of poorly oxygenated hypoxic regions which are radioresistant and the patients presenting highly hypoxic tumours have reduced therapeutic outcome than those with well-oxygenated tumours (Aebersold *et al*., 2001; Kim *et al*., 2015). Hypoxia inducible factor 1 (HIF-1) is a critical regulator in adaptive responses to hypoxia and has been shown to be involved in hypoxia-related tumour radioresistance (Aebersold *et al*., 2001). The high expression of HIF-1, which indicates low levels of cellular oxygen, in the majority of HNSCC is correlated with poor local failure-free survival, disease-free survival and overall survival (Aebersold *et al*., 2001; Kim *et al*., 2015). It could be because the less-oxygenated region leads to inefficient formation of DNA strand breaks induced by ionising radiation (Kim *et al*., 2015).

Following irradiation, the radiosensitive cells are killed and free up oxygen which will be delivered to previously hypoxic regions to reoxygenate hypoxic cells. The reoxygenation then generated oxidative stress on the cells and activate HIF-1 pathway which may contribute to radioresistance.

Additionally, other pathways involved in mechanisms of radioresistance are the adhesion pathway integrins (Goel *et al*., 2013), the inflammatory pathway [cyclooxygenase-2 (Cox-2; Rosser, Gaar and Porvasnik, 2009) and cytokines such as TNF-α, IL-1α, IL-1β, IL-6 and TGF-β; Kim *et al*., 2015], the developmental pathway (Wnt/β-catenin; Kim *et al*., 2012) and the RTK-PI3K-Akt pathway (EGFR; Rosser, Gaar and Porvasnik, 2009; Hayashi *et al*., 2012; Hansen and Siu, 2013; Perri *et al*., 2015). All of these studies demonstrated the large efforts undertaken in evaluating the causes of radioresistance and showed that the radioresistance acquired in tumours involves extensive and interactive cellular pathways. There are many interactions between pathways described where the activation of certain factor can trigger the activation of downstream pathways, resulting in profound phenotypic effect (Silva *et al*., 2007). As a result, the analysis on more molecular pathways described above would be favourable and beneficial to explore the overall radiosensitivity of HNSCC tumour (Horn *et al*., 2015; Perri *et al*., 2015). In addition, the investigation of the entire tumour tissue biopsy obtained from resected patient, instead of single cell type monitoring using cell culture, is essential to study tumour response against radiotherapy. As a consequence, it is needed to have a platform to carry out the pseudo *in vitro* tissue culture and analysis in accomplishing the current study.

1.4. Microfluidics

Microfluidics is the science and technology of systems manipulating tiny quantities of fluid (10^{-9} to 10^{-18} litres), in micrometre wide micro-fabricated channels (Whitesides, 2006; Nge, Rogers and Woolley, 2013; Lacombe *et al*., 2016). Microfluidics also called lab-on-a-chip (LOC), biochips or micro-total-analysis-systems (μTAS; Lin *et al*., 2010). This technology was developed in the 1990s and offers a promising platform for cell culture and engineering the highly complex and dynamic tumour microenvironments that are controllable, reproducible and optimizable (Lin *et al*., 2010; Liu *et al*., 2014). It has been widely implemented to study cell biology as well as cancer biology for biomedical applications (Li *et al*., 2012; Ma, Xu and Qin, 2013). The miniaturised system in some cases allows several stages of experiments to be integrated onto a single device meaning that protocols which would traditionally require a whole lab can be scaled down onto a small chip the size of a microscope slide (Figure 1.11; Li *et al*., 2012). The sample pre-treatment, reagent transport, mixing, reaction, separation, detection and the product collection can all be performed on a single microfluidic system in which the micropumps, microvalves, microfilters, microreactors and microseparators can be microfabricated and integrated to study tissue behaviour and perform specific assay (Li *et al*., 2012; Nge, Rogers and Woolley, 2013). In this chapter, the materials of microfluidic device that available for biomedical research, the multitude advantages of this technology and its applications in research, particularly on HNSCC assessment, will be described in the following sections.

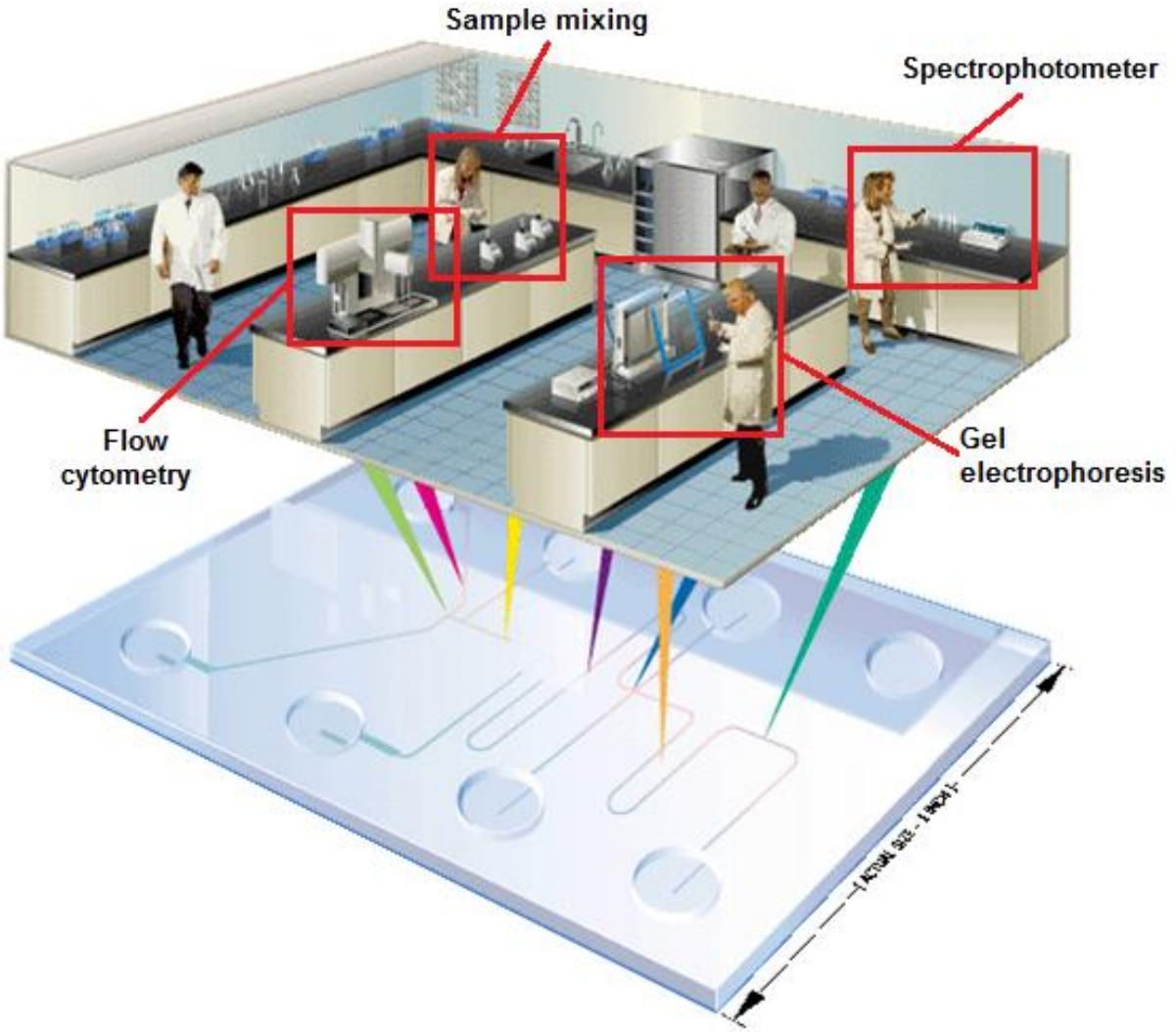


Figure 1.11. A schematic diagram showing how a microfluidic device can integrate various laboratory experiments on a single chip that holds tiny amounts of fluids in micrometre channels.
(Adapted from figure of Sharp Laboratories of Europe, 2014).

1.4.1 Materials used for the construction of microfluidic devices

The materials used for a microfluidic system are important to perform and achieve the required functions and the degree of integration. In addition, the physical characteristics of the chip also needs to be taken into account such as: flexibility, air/gas permeability and optical transparency. There are three main categories of materials which can be used to create microfluidic devices: inorganic, polymeric and paper. Inorganic materials include glass, silicon and ceramics while polymer-based materials are divided into elastomers and thermoplastics (Table 1.7). Each material possesses its own characteristic strengths and weaknesses.

Table 1.7. Characteristics of materials used for construction of microfluidic devices.

Material		Characteristics
Inorganic	Silicon	• First material used in microfluidics. • Transparent to infra-red but not to visible light. Application using fluorescence detection or fluid imaging is difficult. • Has high elasticity and not easily made into active fluidic components, e.g. valves and pumps.
	Glass	• Has low background fluorescence. • Has large, composition-dependent elastic modulus. • Compatible with biological samples. • Has low non-specific adsorption. • Not gas permeable.
	Ceramics	• Has laminar nature. • Has high rates of leaching in acidic and basic solutions. • Low temperature cofired ceramic (LTCC) is patterned laminate sheets, assembled and fired at high temperature. • LTCC can be fabricated into 3-dimensional devices.
Polymeric	Elastomers	• Polydimethylsiloxane (PDMS): most common substrate due to reasonable cost, quick fabrication and ease of operation; low elastic modulus; gas permeable; prone to non-specific adsorption. • Thermoset polyester (TPE): hydrophobic (required surface modification); transparent; high elastic modulus;
	Thermoplastics	• Durable, amenable and transparent. • Non-permeable to small molecules. • Includes: Fluoropolymers, polymethyl-methacrylate, polycarbonate, cyclin-olefin copolymer, polyurethane, zein, and SU-8.
Paper	Paper	• Cellulose-based. • Cheap; readily available. • Can be simply disposed and degraded. • Easy pattern by inkjet or solid wax printing. • White background provides contrast for colour-based detection. • Can be chemically modified.

(Summarised Nge, Rogers and Woolley, 2013).

1.4.2 Benefits and principles of microfluidics

Microfluidics technology offers many significant advantages for the study of complex biological processes and for testing large-scale bioreactors compared with macroscale cell or tissue culture (Kim *et al*., 2007). The major differences of the tools and requirements between the conventional cell/tissue culture and microfluidic-based tissue culture include the temperature monitoring over different amount of medium, the supplement and removal of nutrients, simultaneous sample treatment, cultural automation, maintenance of tissue architecture, and the amount of cells being analysed. The comparisons of the basic requirements of conventional and microfluidic cell culture are summarised in Table 1.8.

.

Table 1.8. Comparisons of the basic requirements between conventional and microfluidic cell culture.

Requirements	Conventional cell culture	Microfluidic cell culture
Temperature control	Large fluid volumes prevent fast changes	Dynamic control due to small fluid volumes
Nutrients supply and removal	Manual and infrequent (2-3days gap)	Continuous in precise flow rates
Simultaneous treatment and imaging	Mostly not feasible; mainly end-point analysis	Feasible and high competence; enhanced cell-based screening assays
Automation of cell culture	Bulky	High capability for automation in cheaper format
Architectural maintenance	2-dimensional monolayer structure; flat morphology	Reserved specific architecture, viability and functionality of organs
Cell numbers analysed	Few thousands (microtiter plate) to tens of millions (large culture flask	Single cell to a few thousands

(Mehling and Tay, 2014; Halldorsson *et al*., 2015).

Small volumes of samples

The small channel dimensions of the microfluidic device require tiny volumes of reagents (10^{-9} to 10^{-18} litres), leading to low costs (Breslauer, Lee and Lee 2006; Nge, Rogers and Woolley, 2013). The ability of microfluidics to manipulate samples at nanoliter volumes and decrease the dosage requirements is crucial in performing high-throughput drug screening, biological and chemical sensing (Breslauer, Lee and Lee 2006). Compared with conventional culture in flasks, dishes and well plates, microfluidics offer the ability in studying small piece of cultured tissue, larger cell populations or even the single-cell level with controllable fluid flow in micro- and nano-meter scale (Mehling and Tay, 2014; Halldorsson *et al*., 2015).

High surface area to volume (SAV) ratio

The small channel sizes in microfluidic devices provide a high surface area to volume ratio (SAV; Walker, Zeringue and Beebe, 2004; Addae-Mensah *et al*., 2010). For example, a 35mm tissue culture dish containing 1mL of culture medium gives a SAV ratio of $11cm^{-1}$ while a microchannel with dimensions of 50µm x 50µm x 3 cm (H x W x L) containing 75nL of medium provides a SAV ratio of $800cm^{-1}$. This large SAV provided in microchannel of microfluidic system improves the mass transport of gases via diffusion to and from the cells and greatly enhances the interaction between chemical substances/molecules and the cells or tissue maintained in microfluidic device (Walker, Zeringue and Beebe, 2004; Addae-Mensah *et al*., 2010; Nge, Rogers, and Woolley, 2013).

Particles diffusion transport mechanism

In macroscale cell culture, large amounts of culture medium are supplied, which is typically stagnant in culture flasks or wells, to ensure the cells/tissues are supplied with essential metabolites. The diffusion in this conventional cell culture is slow while in microfluidics, particles need only travel a small distance resulting in a faster rate of interaction (Lin and Lin, 2015). Diffusion occurs when particles travel from regions of high concentration to low concentrations (Walker, Zeringue and Beebe, 2004) and although it is not the key transport mode in macroscale cell culture systems, which rely on the even distribution of metabolites by stirring, in microfluidics diffusion becomes the main transport mechanism. This transport mechanism in microfluidic flow system potentially maintained the microenvironment of the cells/tissues in a microscale environment as the secreted molecules from the sample do not leave the vicinity of the cell/tissue quickly, which are important for the normal function. The secreted components further facilitate the feedback regulation in producing additional secreted factors, mimicking the cell-cell interaction in natural microenvironment (Walker, Zeringue and Beebe, 2004; Lin and Lin, 2015).

Laminar flow

Given the small dimensions in the microscale and nanoscale, the movement of the fluids in the device is laminar in which the exact timing of the fluid flow is possible allowing the precise chemical and physical control on the microenvironment (Wong *et al*., 2012; Mehling and Tay, 2014). The typical dimensions of channels in a microfluidic device are 50μm width, 15μm height, and 5cm length with a resulting volume of 37.5 nL. The perfusion in this dimension is normally non-turbulent because of the low Reynolds number (Nge, Rogers, and Woolley, 2013). Laminar flow is characterised by a low (<2300) Reynolds number (Re) in which the different layers of fluids flow side by side without turbulent mixing (Takayama *et al*., 2001; Walker, Zeringue and Beebe, 2004). The further illustrations on Reynolds number was revealed in section. Fluid flow with a *Re* of greater than 2300 is usually turbulent which creates mixing of the solutions while a low *Re* flow is usually laminar (Figure 1.12).

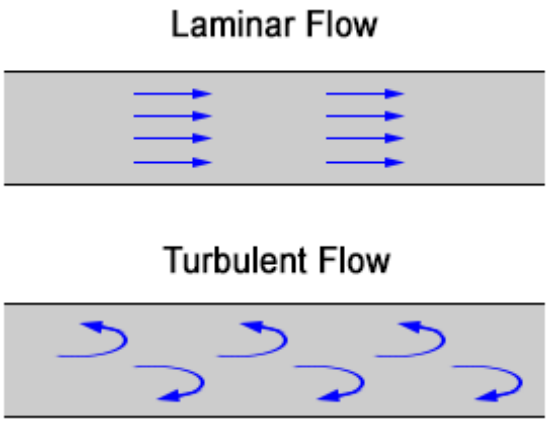


Figure 1.12. Laminar flow shows the non-turbulent fluid flow which is the principle flow in microfluidic device.
Laminar flow is at Reynolds number <2300 and turbulent flow is characterised by Reynolds number >4000.

The laminar flow in microchannels at low Reynolds number conditions generates stable, spatially and temporally controlled gradients for soluble molecule which is difficult to be achieved with conventional methods (Yum *et al*., 2014). This characteristic allows the partial treatment on a single cell and the evaluation on how a cell behaves when it is flowed with two laminar fluid streams (Walker, Zeringue and Beebe, 2004). In a study proposed by Takayama *et al*. (2003), a PARTCELL microfluidic device used multiple laminar fluid streams to deliver different reagents to and remove from defined parts of a cell (Figure 1.13). It allows rapid influx of molecules to one region of a cell and efflux from another portion of a cell to maintain a chemical concentration gradient inside of the cell. In summary, the laminar flow of microfluidic system is able to mimic the *in vivo* tissue microenvironment by maintaining the 3D structure of the multiple cell types within the tissue and tumour.

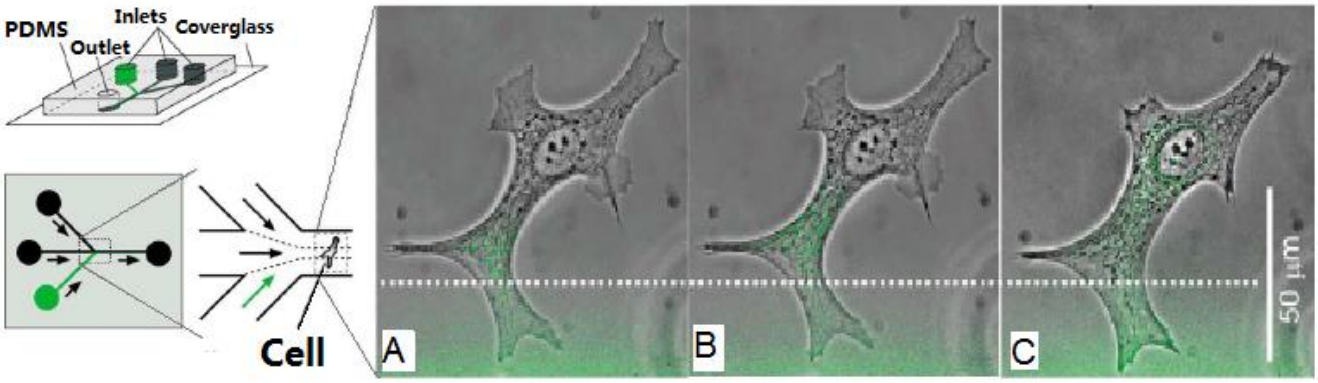


Figure 1.13. Schematic diagram of PARTCELL microfluidic chip.
It generates two partially localized populations (fluorescently labelled and unlabelled) of mitochondria using Mitotracker Green within a single bovine capillary endothelial cell. The overlay of fluorescence was taken when Mitotracker Green solution flowed over the cell for (A) 5 minutes, (B) 11 minutes and (C) 35 minutes (Takayama *et al*., 2003).

Biomimetic microenvironment in microfluidics

The microfluidic technology is able to support the recreation of the micro-scale cell confinement with critical cell-cell interfaces, spatiotemporal chemical gradients and dynamic mechanical microenvironment of cells similar and biomimetic with physiological conditions (Ma, Xu and Qin, 2013; Halldorsson *et al*., 2015). In contrast, the cellular microenvironment in most conventional tissue culture is different to the *in vivo* conditions, largely concentrating on a single cell type, usually epithelial or stromal cells, arranged in monolayers culture (Mehling and Tay, 2014), more recently spheroid culture has provided a more 3D-like structure but still with only one of two cell types involved. In addition, the *in vivo* interactions and communications are not maintained during traditional cell culture in a culture flask as the cells are separated until they grow and become confluent and the large fluid stress will cause the cells to behave differently from the *in vivo* environment (Walker, Zeringue and Beebe, 2004; Meyvantsson and Beebe, 2008).

The biomimetic *in vivo* platform for cell/tissue culture by using microfluidic system, therefore, is crucial in biomedical application, particularly, when studying the complicated interactions in tumour biology as well as radiobiology in the current study. The tumour microenvironment is an important factor involved in cancer initiation, progression, metastasis, angiogenesis, and drug resistance (Fukumura and Jain, 2007; Figure 1.14). It consists of many soluble factors, various non-cancerous cell components, extracellular matrix (ECM), and mechanical signals of cell-to-cell, cell-to-matrix, autocrine, paracrine and hormonal interactions (Ma, Xu and Qin, 2013). These components are tightly regulated and are characterized by high levels of spatio-temporal complexity (El-ali, Sorger and Jensen, 2006; Khademhosseini *et al*., 2006; Ma, Xu and Qin, 2013). In the microfluidic system, the cell-to-cell, cell-to-matrix and cell-to-soluble factor communications are maintained and the heterogeneous mixture of cells present in the tissue is maintained mimicking the closely packed spatio-temporal microenvironment seen *in vivo* (Tanweer *et al.*, 2011; Ma, Xu and Qin, 2013).

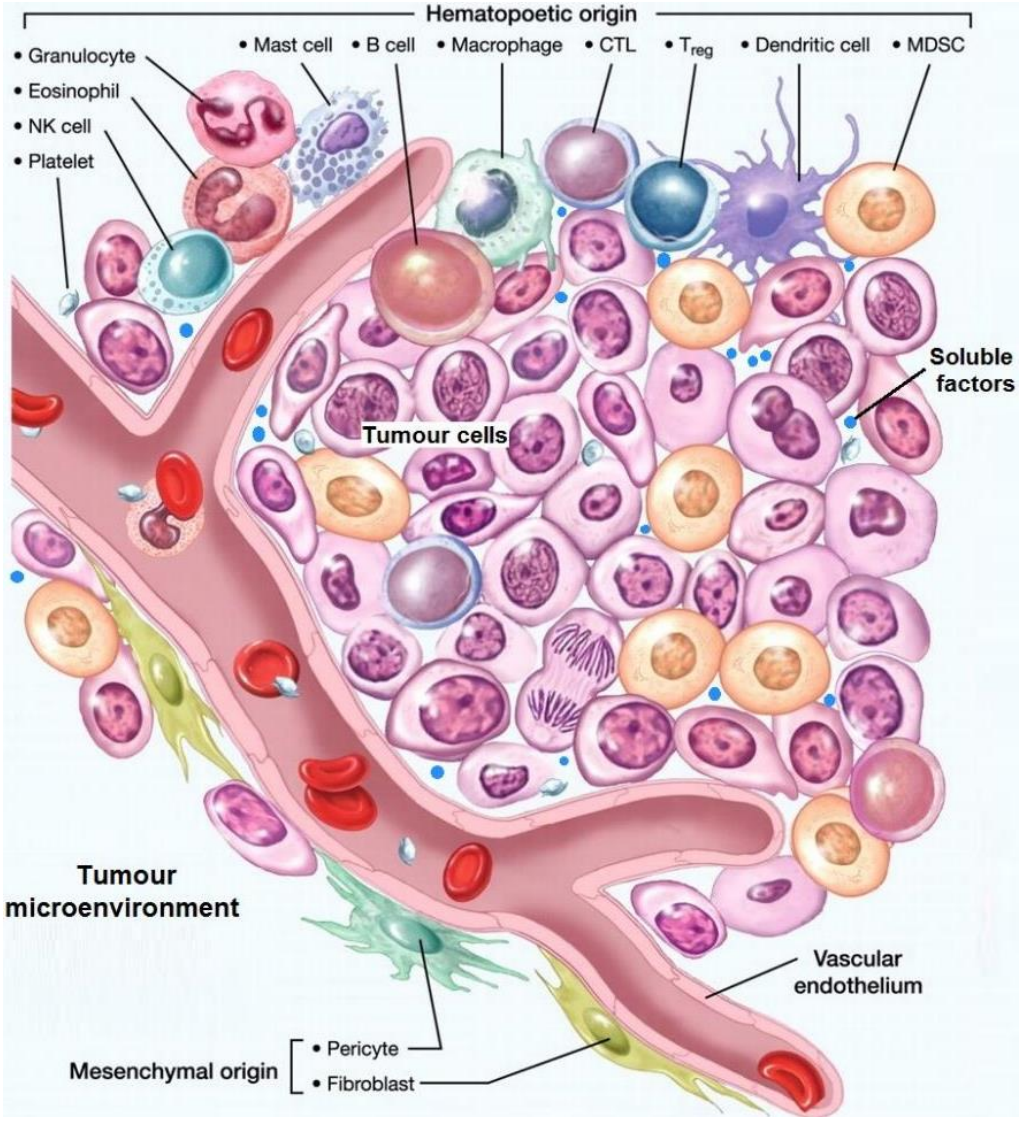


Figure 1.14. Schematic diagram of the tumour microenvironment consisting of tumour cells, non-malignant cells, soluble factors, extracellular matrix, cancer-associated fibroblasts, pericytes and immune cells.
(Adapted from Kerkar and Restifo, 2012).
Abbreviation: NK: natural killer, CTL: cytotoxic T cell/lymphocyte, T_{reg}: regulatory T cell, MDSC: myeloid-derived suppressor cell.

In recent years, microfluidics has been used to test the behaviour of various cell and tissue types *in vitro* and *ex vivo*, whilst retaining *in vivo* conditions (Webster *et al*., 2011; Cheah *et al*., 2012; Hattersley *et al*., 2012; Robertson *et al*., 2014; Komeya *et al*., 2015). For instance, Robertson *et al*. (2014) developed a microfluidic device to culture primary hippocampal neurons in adjacent chambers that were individually fed through inlet and outlet ports. Both chambers were synaptically connected via microchannels through a barrier that prevented exchange of extracellular fluid between the two chambers. They used calcium imaging to measure the electrophysiological communication between neurons in separate chambers in

response to stimulation of neurons in one chamber with stimulants. This study successfully revealed and demonstrated the potential microfluidic system in creating the biomimetic activity of hippocampal neuronal networks and further understand the modulation between the activities of two neuronal networks. Recently, the long-term *ex vivo* maintenance of testis tissues in a simple microfluidic device developed in Komeya *et al*. (2015) has demonstrated the ability of microfluidics in mimicking *in vivo* regional homeostasis. The microfluidic device design contains a porous membrane that separates tissue from flowing culture medium, conceptually reproducing the *in vivo* communication between the microvascular flow and surrounding tissue. The cultured testis tissues in the device successfully maintained the spermatogenesis for up to 6 months and the produced sperm were functional in generating healthy offspring with micro-insemination. Pseudo *in vivo* culture of head and neck tumour tissues has also been demonstrated previously in microfluidic glass device by colleagues (Hattersley *et al*., 2012; Carr *et al*., 2014) in which the viability of the microfluidic tissues was confirmed by measuring the release level of cell death markers [lactate dehydrogenase (LDH) and cytochrome c] and proliferation markers (water soluble tetrazolium salts 1; WST-1).

Maintenance of organ-specific architectural complexity

Microfluidic cell and tissue culture devices can be fabricated that capture the architectural complexity in human organs which could hardly be produced in conventional culture system (Halldorsson *et al*., 2015). The specific architecture, viability and functionality of organs are maintained and can be mimicked in microfluidic devices which have been demonstrated using various tissues. The early examples of organs on chips is a liver model (Lee, Hung and Lee, 2007), in which the physiological microarchitecture of the liver, such as the hepatic structure, sinusoids and the permeable endothelial cell barriers, was reconstructed in the liver-on-a-chip device. In lung-on-a-chip device, the alveolar-capillary interface of the human lung which consists of the channels and closely apposed pulmonary epithelial and endothelial cells was reproduced in the device (Huh *et al*., 2010). Additionally, the cyclic mechanical strain found *in vivo* was uniquely reconstituted in the device, for example, the normal lung breathing movements of the alveolus was also reproduced. In addition, the rat right ventricular and human right atrial tissues have also been tested able to be maintained viable up to 5 and 3.5 hours, respectively, in a microfluidic device

developed in Cheah *et al*. (2012) study in which the effluent levels of LDH and hydrogen peroxide were assessed as the markers of damaged tissue in the device. Based on the heart-on-a-chip implemented in Cheah *et al*. study, human heart tissue can be maintained in microfluidic device which offers a potential platform to investigate heart pathophysiology in cardiac research. There were many other devices have been developed to mimic the organ architecture as well as the corresponding functions, for example, heart-on-a-chip device (Grosberg *et al*., 2011; Marsano *et al*., 2016), kidney-on-a-chip device (Jang *et al*., 2010) and testis tissue (Komeya *et al*., 2015). The ability in mimicking the natural physiological response of an organ with the emerging organ-on-a-chip technology, consequently, may offer a good platform to evaluate real biological responses against various tested conditions and therapies.

Parallelisation and high-throughput method

The ability to perform parallel experiments and the real-time measurement of cellular and tissue dynamics through the delivery of reagents, nutrients, and other stimuli to the samples precisely is a major advantage of the continuous perfusion system in microfluidics (Van Der Meer and Van den Berg, 2012; Ma, Xu and Qin, 2013). In addition, microfluidics allows high-throughput and rapid test on cells/tissue in response to different environments, exposing cells to many different solutions at different concentrations (Sun *et al*., 2011**;** Cho *et al*., 2013; Ostafe *et al*., 2014; Kastner *et al*., 2014; Rotem *et al*., 2015). For example, a high-throughput single-cell labelling droplet-based microfluidic device was developed to encapsulate single cells in drops (Rotem *et al*., 2015). Each cell drop was fused with another droplet that contains many copies of DNA barcode and these barcode label specifically the transcriptome of single cell by hybridising to its RNA transcripts. The use of high-throughput microfluidic device in Rotem *et al*. (2015) study demonstrated the scalability strength of microfluidics as the RNA profiles of 1000 single cells within the same population were obtained in less than two workdays with minor cost. The high-throughput microfluidic system was also presented in Sun *et al*. (2011) to monitor the long-term bacterial growth in response to antibiotics tetracycline and erythromycin in a high-throughput manner. The device contains seven parallel channels and each channel comprises 32 microchambers where the bacterial cells (*Escherichia coli*) were cultured and the real-time analysis of green fluorescent protein (GFP) expression was assessed.

All in all, in realising the wide range of advantages offered by microfluidic technology, many applications in studying different types of biological tissues could be accomplished. The micro-scale device provides a biomimetic platform that enables the current study the biology of human head and neck squamous cell carcinoma tissue and its responses to different treatments. The miniature size of the microfluidic device used in this study, which will be described later, enables the convenient transport from laboratory to radiotherapy suite for tissue on-chip irradiation.

1.4.3 Drawbacks of microfluidics

Although microfluidic culture is cost-effective in terms of the reduction in the use of reagent volume as well as the combination of various biological experiments in single device, the cost of construction of the device and the complexity involved is currently greater than that of the conventional cell culture method, e.g. glass and silicon microdevices vs plastic tissue culture flasks (Valencia *et al*., 2012). It is, however, believed that the cost in producing microfluidic-based devices could be reduced when they are manufactured in large-scale and commercialised synthesis with little to no variations introduced by user handling. Another disadvantage of microfluidics is that the large SAV ratio achieved a large rate of protein adsorption can lead to a significant loss in active protein (Walker, Zeringue and Beebe, 2004). The unwanted cellular attachment in the flow channels or non-specific protein adsorption from the culture medium, therefore, could technically occur because the proteins and hydrophobic components in the medium may attach to the free hydrophobic sites of micro-channel (e.g. PDMS; Halldorsson *et al*., 2015). This may lead to the microfluidic channel blocking which in turn interrupts the fluid flow and pressure built-up in the system. In addition, bubbles accumulation is a frequent problem in microfluidic system and could potentially affect the fluid flow and harm the samples (Zheng *et al*., 2010). Therefore, extra careful operations are essential and several approaches have been researched in solving this problem such as surface layer passivation on microfluidic flow channels, micro-degassing device and hydrophobic degassing plate (He, Tan and Regnier, 1999; Zheng *et al*., 2010).

1.4.4 Applications of microfluidics

Due to the multiple advantages of microfluidic culture, it has been used in many applications of biological research (Nge, Rogers and Woolley, 2013), for example, cell and nucleic acid analysis (Takayama *et al*., 2003; White *et al*., 2011), drug metabolism analysis (Ying-Yan *et al*., 2008; Sung and Shuler, 2009), proteomics and metabolomics analysis (Amenta, Dawoud and Lazar, 2009; Shintu *et al*., 2012) and environmental analysis (Noblitt *et al*., 2009). In the cell and nucleic acid analysis, microfluidic device can be integrated with multiple reverse transcription quantitative PCR (qRT-PCR) reactions that allows the measurement of gene expression from hundreds of single cells in single experiment (White *et al*., 2011). In addition, the culture of cells and organs in microfluidic device was shown possible to mimic the *in vivo* condition where the metabolism of a single/combinations of test drugs can be evaluated. This has included the testing of Tegafur (oral pro-drug of 5-fluorouracil) on colon cancer cells and hepatoma cells (Sung and Shuler, 2009) and topoisomerase II inhibitor-VP-16 drug on human lung cancer cells (Ying-Yan *et al*., 2008).

In realising the advantages of microfluidics in precise sample and reagent control, microfluidics allows the measurement of protein concentrations from tiny volumes and provides precise sample control on small reagent volumes which are usually the limiting factors in these types of study. For example, high resolution mass spectrophotometry has been integrated into a microfluidic device to perform high-throughput proteomic analysis of approximately 40-50 proteins on MCF-7 breast cancer extracts (Armenta, Dawoud and Lazar, 2009). In addition, a single cell can be immobilized in a microfluidic device for metabolomic analysis. The fluorescent labelling and the simultaneous on-chip imaging (1H Nuclear Magnetic Resonance-based metabolomics fooprinting) allowed the study of cellular apoptosis and toxicity towards ammonia, dimethylsulfoxide and paracetamol on hepatocellular carcinoma-derived cells (HepG2/C3A; Shintu *et al*., 2012).

In terms of disease diagnosis and prognosis on human samples, microfluidics technique has also been applied clinically to diagnose infectious diseases such as HIV/AIDS, malaria or tuberculosis (reviewed in Lee *et al*., 2010), to rapidly quantify matrix metalloproteinase-8 in saliva as an oral disease biomarker (Herr *et al*., 2007), to measure platelet functions and diagnose bleeding and thrombotic disorders (Neeves *et al*., 2013). Numerous researchers have also implemented microfluidic

platform to study the effects of anti-cancer therapies on various malignancies, for example using chemotherapy drugs in microfluidic system (Hattersley *et al*., 2012; Krause *et al*., 2015; Liu *et al*., 2015). The works on assessing chemotherapy effects using microfluidic devices, currently, are more developed compared with radiotherapy studies, undoubtedly because of the difficulty in radiation management and manipulating an irradiator (Lacombe, Phillips and Zenhausern, 2016).

There were two studies that have utilised the high-throughput capacity and portable potential of microfluidics to measure the expression of phosphorylated H2AX foci by using a portable microfluidic fluorescence spectrometer device (Pope *et al*., 2011) and assess the gene expression by using microfluidic-integrated quantitative Nuclease Protection Assay (qNPA; Brengues *et al*., 2010) in human lymphoblastoid cells and human whole blood sample, respectively, after X-ray irradiation. Both works have successfully demonstrated the potentials of microfluidic technology for point-of-care application and rapid analysis on the effects of ionising radiation on DNA strand breaks repair and 14 radiation-associated genes expression. The microfluidic techniques used on both studies, however, were designed to develop miniaturised fluorescence analyser (Pope *et al*., 2011) and handheld gene expression detection device (Brengues *et al*., 2010), rather than used as a platform for sample culture and irradiation.

The success of using microfluidic technology in the study of radiobiology has yet to be achieved. By using microfluidic-based approaches, the efforts in developing a platform for administration of ionising radiation on the biological samples have achieved in several studies (Table 1.9). The works included the use of bacteria (Wan and Yeow, 2011; Buonanno *et al*., 2013), isolated DNA (Pješčić *et al*., 2011), bone-marrow-on-a-chip (Torisawa *et al*., 2014), lymphocyte cells (Garty *et al*., 2011), animal liver and human HNSCC tissue sample (Carr *et al*., 2014). The results of these previous studies not only successfully verify the competence of microfluidic devices compared with the traditional cell culture and *in vivo* experiment, but also demonstrated the potential of microfluidics for radiation study.

Table 1.9. Previous studies that performed irradiation treatment on biological sample in microfluidic devices.
The images of the corresponding studies were edited and adapted in order to fit and present in the table.

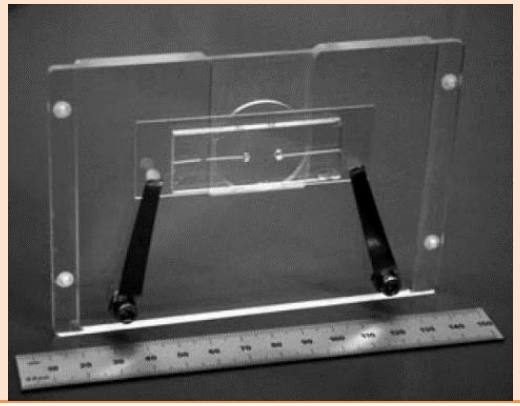
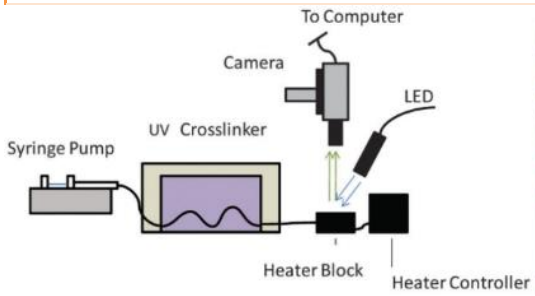
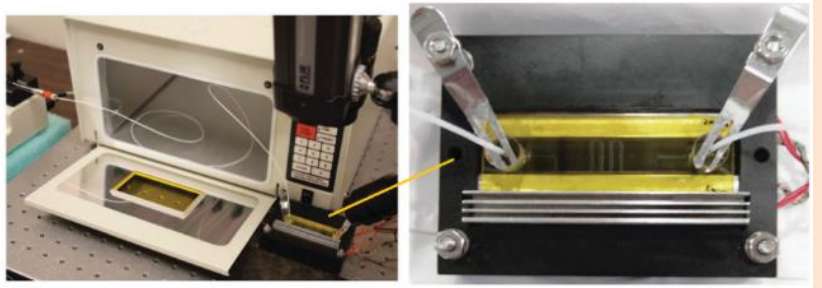
Irradiation application	Biological sample	Microfluidic methods	Findings and description	Reference
Microbeam irradiation	Fluorescent beads serve as models of cells; lymphocyte cells	➢Microfluidic cartridge integrated with permanent magnet microbeam (PMM) is used where the cells can flow through a channel and intersect with the microbeam radiation. ➢The image was captured in real-time by using high-speed camera. 	➢100,000 of cells were able to be irradiated per hour. ➢Able to irradiate non-adherent lymphocyte cells ➢High-throughput manipulation of irradiated cells. ➢Flexible for integrating microbeam into microfluidics to perform cell sorting and encapsulation.	Garty *et al*., 2011
Ultraviolet-C (UV-C) radiation	Isolated DNA	➢DNA sample injected via tubing to microfluidic chip in a UV crosslinker where cumulative radiation was applied. ➢Real-time DNA melting analysis was detected to study radiation damage.  	➢Cumulative damage produced distinct changes in the DNA melting curves, characterized by a shifting and broadening of the melting peaks. ➢Extensive analysis was perform on a subset of 160 melting curves obtained over an 8-minute period on a single microfluidic device.	Pješčić *et al*., 2011

Table 1.9. Previous studies that performed irradiation treatment on biological sample in microfluidic devices.

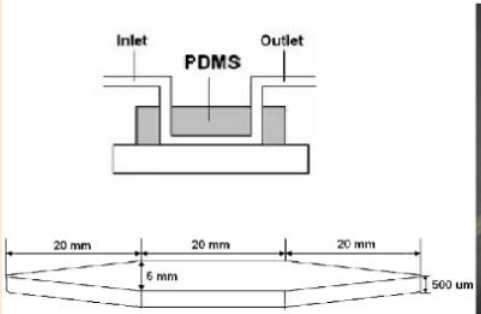
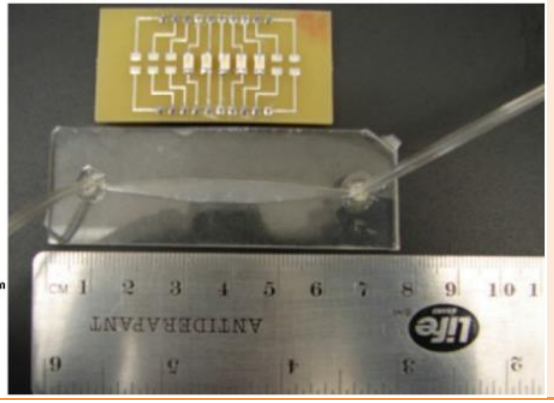
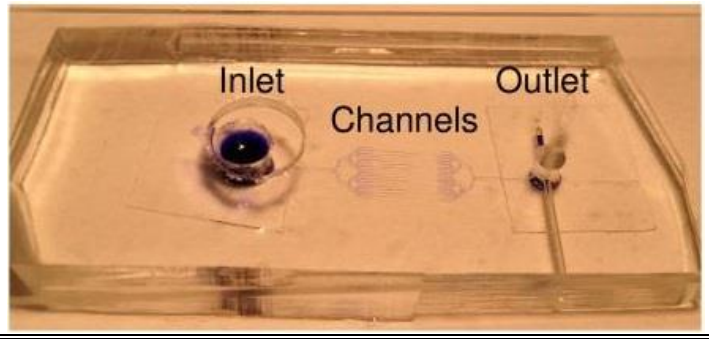
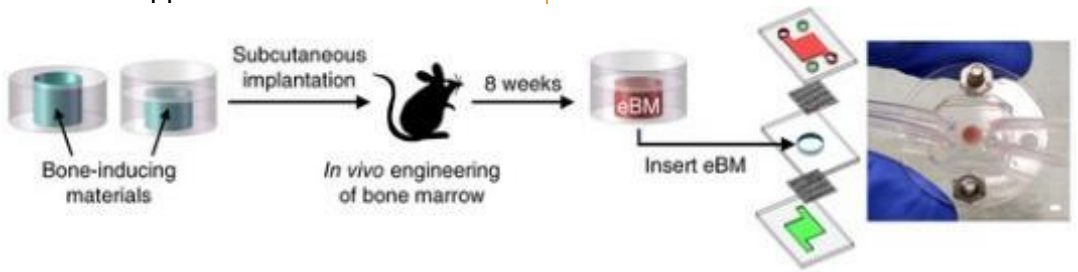
Irradiation application	Biological sample	Microfluidic methods	Findings and description	Reference
UV LED array	gram-negative bacteria (*Escherichia. coli*)	➢*E. coli* was grown in device and treated by titanium dioxide (photocatalysts) and UV LED array to induce cell lysis. ➢Cell viability assessed and recorded by using SYTO9 and propidium iodide markers. 	➢Incorporates titanium dioxide particles (photocatalysts) with a miniaturized UV LED array (excitation light source) to cause cell lysis in microchips. ➢*E. coli* cells can be disrupted in 60 min 	Wan and Yeow, 2011
Microbeam irradiation	*Caenorhabditis elegans*	➢Microfluidic clamp consists of 16 tapered channels with 10-µm-thin bottoms. ➢Analysis: repair of radiation-induced DNA damage (formation of Rad51 foci) 	➢Minimal sample manipulation and reduced use of drugs such as anesthetics. ➢Simultaneous immobilization and imaging for irradiation of several whole living samples on a single device.	Buonanno *et al*., 2013

Table 1.9. Previous studies that performed irradiation treatment on biological sample in microfluidic devices.

Irradiation application	Biological sample	Microfluidic methods	Findings and description	Reference
X-ray irradiation	HNSCC and rat liver	➢Human HNSCC biopsies implanted in microfluidic device and maintained for 24 hours before subjected to irradiation (2Gy, 40Gy and 5x2Gy). ➢Radiation induced cell death was analysed by LDH level, cytochrome c and caspase-3 cleaved cytokeratin-18. 	➢A significant increase of apoptotic index, calculated using the immunostaining of caspase-3- cleaved cytokeratin 18, was observed 72 hours after irradiation compared to the untreated samples. ➢HNSCC biopsies were maintained in viable state; Relationship between radiotherapy dose and cell death was demonstrated.	Carr *et al*., 2014
γ-radiation	Mice bone marrow	➢Live mice, bone-marrow-on-a-chip and stroma-supported cultured marrow were irradiated with 1Gy and 4Gy doses of γ-radiation. ➢The proportions of hematopoietic stem cells (HSCs), hematopoietic progenitors, lymphoid cells and myeloid cells of chip marrow were compared with natural mice marrow and the bone marrow in traditional stroma-supported culture. 	➢Normal *in vivo* cell proportions were retained *in vitro* for at least one week. ➢The cells cultured on stroma (traditional method) were much resistant to radiation and cell proportions of bone-marrow-on-a-chip were similar with that of natural mice marrow.	Torisawa *et al*., 2014

Carr *et al*. (2014) was the previous work performed in the current research group and, to the best of the author's knowledge, it is the only study published in which the response to human HNSCC tissue was investigated by inserting tissue sample into a glass microfluidic device for on-chip X-ray irradiation. A significant higher apoptotic level following on-chip irradiation compared with non-treated samples was demonstrated in Carr *et al.* works by using immunostaining of caspase-cleaved cytokeratin 18. The use of the glass microfluidic device, the irradiation treatment on the chip tissue and the detection of cleaved cytokeratin 18 as a cell death marker have provided a promising platform and set-up to further accomplish the aim of radiotherapy response investigation in the current work.

In addition to the applications described above, the miniaturization of the device and integrated components as well as the small reagent volumes in microfluidic technology have allowed analytical tests to be carried out in a portable format which led to the point-of-care (POC) diagnostics. It is fast, accurate, reproducible, and produced readily interpretable data (El-Ali, Sorger and Jensen, 2006; Nge, Rogers, and Woolley, 2013). There are a number of POC diagnostic applications which have been commercially used including blood glucose measurement, pregnancy testing, drug abuse screening and diagnosis of infectious diseases (streptococcus, influenza and HIV; Figure 1.15). The development of POC devices, therefore, has the potential to be further integrated with analytical processes and greater simplification of their usage to achieve rapid and accurate disease diagnosis and prognosis.

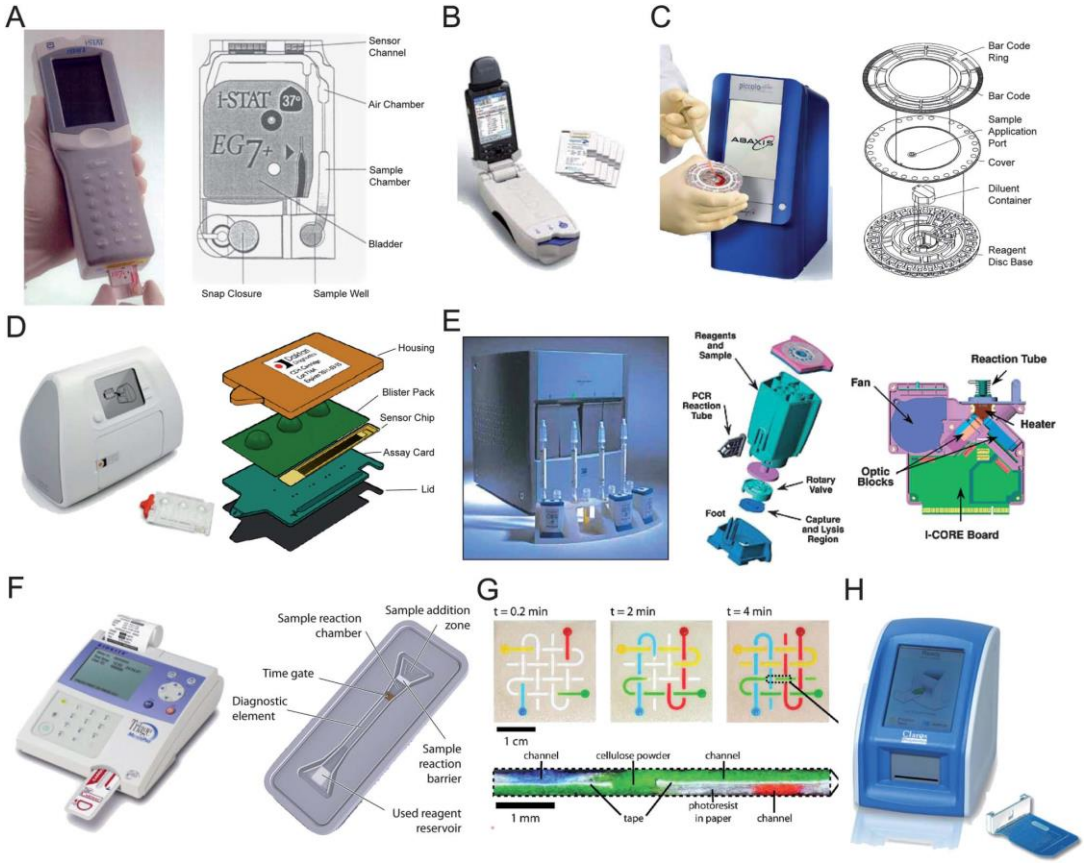


Figure 1.15. Pictures and schematics diagrams of microfluidic-based POC tests.
(A) STAT (Abbott) - Detects blood chemistries, coagulations and cardiac markers. (B) Epocal- Bedside blood analysis using Smart Card technology. (C) Abaxis- Chemistry analyser on metabolites, lipid, electrolytes and gases. (D) Daktari Diagnostics- Read cells for HIV/AIDS detection. (E) Cepheid- Identify nucleic acid for cancer and respiratory infectious disease. (F) Biosite- Detects small molecules and proteins for cardiovascular disease, infectious disease and in toxicology. (G) Diagnostics for All- Simple yet elegant patterned paper diagnostic devices. (H) Claros diagnostics- Whole blood sample quantitative analysis for urological, maladies and infectious diseases.
(Nge, Rogers, and Woolley, 2013).

1.4.5 Microfluidic device used in this study

The microfluidic device used in the current study for HNSCC tissue culture and interrogation is made up of glass materials which is similar with the device implemented in Carr *et al*. (2014) study. Two layers of glass are thermally bonded together with microchannels etched and patterned on the bottom layer while inlet and outlet holes are drilled on upper to correspond with the channels underneath (Figure 1.16). The detailed dimensions and design of the microfluidic glass device and the entire microfluidic system set-up will be described later in more detail in section 2.3. In the microfluidic device, the channels are adapted onto a material which can be inorganic or polymeric, such as PDMS, paper or glass used in current study, and are connected to the fluid source through inlet holes and outlet holes to allow the liquid to flow through. The liquids are continuously flowed through the device using tubing, a

plastic syringe and syringe adapters, pressure controller, or push-syringe pump (Figure 1.16).

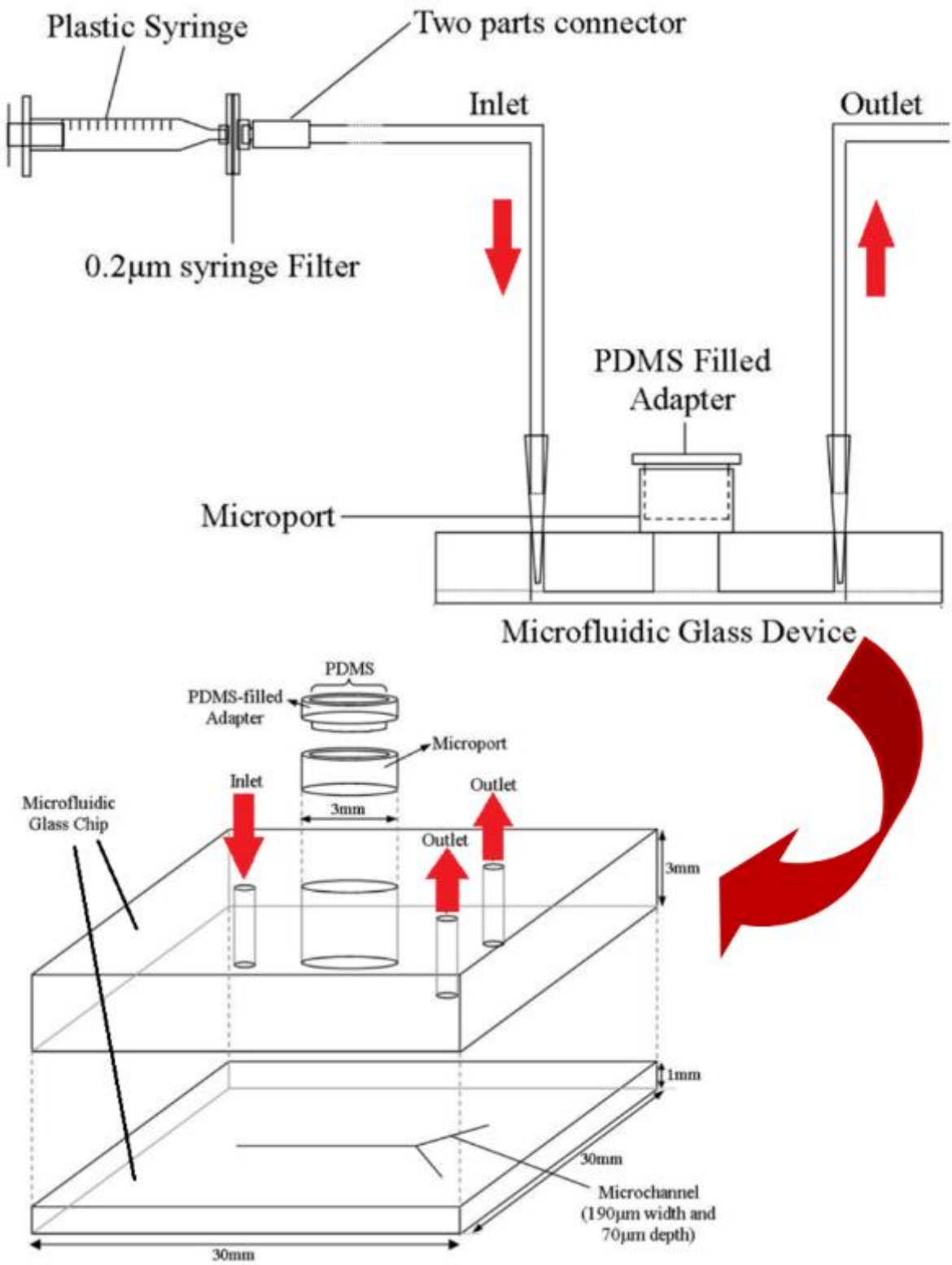


Figure 1.16. Schematic diagram of microfluidic flow system used in this study.
The microfluidic glass device used in the current study is made up of two glass layers: the bottom layer contains channels while the upper later contained inlet and outlet holes.

1.5. Aims of the project

Given the low survival rate of patients with HNSCC treated with radiotherapy and existence of radioresistance, the evaluation of molecular mechanisms of tumour radiosensitivity are of importance to improve the efficiency of radiotherapy. The vision of substantial improvement to therapeutic outcomes, higher cure rates and fewer side effects from the treatment set in NHS could be made if the radiotherapeutic response could be predicted and personalised based on physical and biological characteristics, as alternative treatment strategies could be followed (CRUK, 2015). Although numerous studies have focused on the identification of predictive biomarkers to radioresistance, very few, if any have taken patient tumour pieces and subjected it to research to predict the individualized tumour response and sensitivity to irradiation.

The ultimate aim of this study, in consequence, was to identify molecular biomarkers which could be applied to predict HNSCC patients' responsiveness to radiotherapy before the patients are subjected to treatment. In future, these markers could allow the prescription of optimal, individually-designed treatment plans.

- The tissue maintenance will be firstly optimised and tested in microfluidic device before carrying out the irradiation on HNSCC tissue in the device and downstream analyses (section 3). Both rat liver and human HNSCC tissues will be used to establish an optimised tissue model in microfluidic by measuring the soluble markers released by the tissue (lactate dehydrogenase-LDH). Following the tissue maintenance in the device, the tissue will be cryo-sectioned for haematoxylin and eosin (H&E) staining and immunohistochemical (IHC) staining of 5-bromo-2'-deoxyuridine (BrdU) which detected the incorporated BrdU markers into S-phase cells.
- Once the tissue model has been established for HNSCC tissue, the microfluidic perfusion system will then be used to maintain patients' frozen tissue samples and subjected to irradiation during the microfluidic flow which allow the following analyses of tumour response to irradiation (section 4-6).
- The biological responses of HNSCC tumour to different irradiation regimens will be studied based on the tissue morphology appearance, real-time soluble factors measurement (LDH and cleaved cytokeratin 18), and expression of different cell death markers [cleaved cytokeratin 18, phosphorylated H2AX, B-cell lymphoma 2 (Bcl-2), activated caspase and terminal deoxynucleotidyl transferase dUTP nick

end labelling (TUNEL)], proliferation indicators [BrdU, 5-ethynyl-2'-deoxyuridine (EdU) and Ki-67] and glucose metabolism marker [(2-(N-(7-Nitrobenz-2-oxa-1,3-diazol-4-yl)Amino)-2-Deoxyglucose) 2-NBDG].

- In addition to the assessment on protein expression, the gene expression of the HNSCC pre- and post-irradiation will be evaluated on the frozen tissue sections by using laser capture microdissection (LCM), reverse transcription and quantitative real-time polymerase chain reaction (qRT-PCR). The presence of precious RNA obtained from the tissue section following cryo-microtome sectioning, H&E staining and LCM process will be firstly confirmed and amplified by using standard PCR and gel electrophoresis. Multiple LCM experiments will be carried out and repeated on each tissue to extract RNA sufficient for qRT-PCR reactions and the gene expression of ataxia telangiectasia mutated (ATM), Bcl-2-associated X (BAX), cyclin dependent kinase inhibitor 1A (CDKN1A), excision repair cross-complementing group 1 (ERCC1), H2A histone family, member X (H2AFX), and X-ray repair complementing defective repair in Chinese hamster cells 1 (XRCC1) as well as the β2-microglobulin (B2M) housekeeping gene between the tissues subjected to different microfluidic and irradiation treatments will be measured.

2. Material and Methods

2.1. Head and neck cancer cell culture

Dulbecco's Modified Eagle's Medium (DMEM; PAA, UK) was used to culture head and neck cancer cells and was supplemented with penicillin/streptomycin, L-glutamine, and 10% foetal bovine serum (FBS; Biosera, East Sussex, UK). The epithelial cancer cells used include University of Michigan Squamous Cell Carcinoma cell lines (UMSCC-11b, UMSCC-47, and UMSCC-81b) which were provided by Prof. Thomas Carey (University of Michigan). The cancer cells which were stored in liquid nitrogen were taken out and thawed to room temperature before being re-suspended using the appropriate culture medium. Following centrifugation and re-suspension (1500rpm), cells were transferred to a 25mL-flask (Sarstedt, Leicester, UK) and allowed to grow. When the cells reached sufficient confluence (i.e. 70-80%), the cells were trypsinised and transferred to a larger 75mL-flask. To plate cells onto coverslips and 6-well plate, the medium in the culture flask were rinsed by phosphate buffered saline (PBS) and the cells were detached by incubation with trypsin/EDTA (0.05% w/v of trypsin and 0.02% w/v EDTA in PBS; PAA, UK). After centrifugation and re-suspension, 5 x 10^4 cells were added into a single well of a 6-well plate in laminar flow hood (Airstream ® Class II Biological Safety Cabinet E-series) and allowed to grow until reaching about 70% cell confluence.

2.2. Media Preparation for tissue culture and tissues manipulation

Williams' Medium E (Gibco, Paisley, UK) was used for all rat liver experiments and was supplemented v/v with penicillin/streptomycin (final concentrations penicillin 100U/mL; streptomycin 100µg/mL; PAA, Somerset, UK), 2mM L-glutamine (PAA), 10% FBS (Biosera, UK) and 2.5µg/mL fungizone (Gibco). DMEM (PAA, UK) was used to culture head and neck tissue biopsies which was supplemented with penicillin/streptomycin, L-glutamine, 10% FBS, fungizone as above, along with, and 0.1mM v/v non-essential amino acid (NEAA; PAA). The samples of HNSCC primary tumour and metastatic lymph node tissue were obtained and recruited following written informed consent in accordance with Local Research Ethics Committee (LREC-10/H1304/6) and NHS Trust R&D approval (R0987). The patients involved in the study had undergone resection surgery at Castle Hill Hospital (Hull, UK; within the period of 30.10.2012-08.04.2014) and had no history of previous treatment. The tumour samples were sliced into pieces (about 8mm^3) which were then transferred into

CryoPure tube (Sarstedt, Leicester, UK) and then snap-frozen in liquid nitrogen. The CryoPure tube used is sterile, non-pyrogenic, non-mutagenic and free from cytotoxins. It is engineered with a safe, externally threaded screw cap in minimising contamination. The tissue-contained tubes were snap-frozen in liquid nitrogen and then stored at -80^{o}C. Rat liver tissue from two Wistar rats was used (R1 and R2) and 12 aliquots per animal were generated. The number of rat liver tissues utilized in the current study (chapter 3) are summarised in Section 3.1 and the number of tissues used for each parameter tested was described in the corresponding sections. The liver was taken from rats which had been killed under a Schedule 1 procedure prior to liver extraction. The liver was divided into pieces (each with approximately 1cm^3 in volume) which were stored in CryoPure tube (Sarstedt, UK) in Williams' Medium E (Gibco, Paisley, UK) with 18% (w/v) dimethyl-sulphoxide (DMSO), 10% (w/v) FBS and penicillin/streptomycin 0.1U/ml and 0.1mg/ml. The cryopure tubes were then cooled at 1^{o}C/min in a 'Mr Frosty' container placed in a -80^{o}C freezer for 24 hours prior to storage in liquid nitrogen.

2.3. Microfluidics Set-up

The microfluidic device used throughout the study is a continuous flow device which is designed to maximize liquid flow whilst preventing blockages (Figure 2.1; Tanweer *et al*., 2013). The device is manufactured in house in the Department of Chemistry at The University of Hull. It consists of two layers of thermally bonded glass: bottom (1mm) and top (3mm). The bottom layer of glass houses photolithographic etched channels (190µm wide and 70µm deep) connecting to the inlet (1.5mm), the cylindrical tissue chamber (3mm, 20µL) and two outlet holes (1.5mm) drilled in the top.

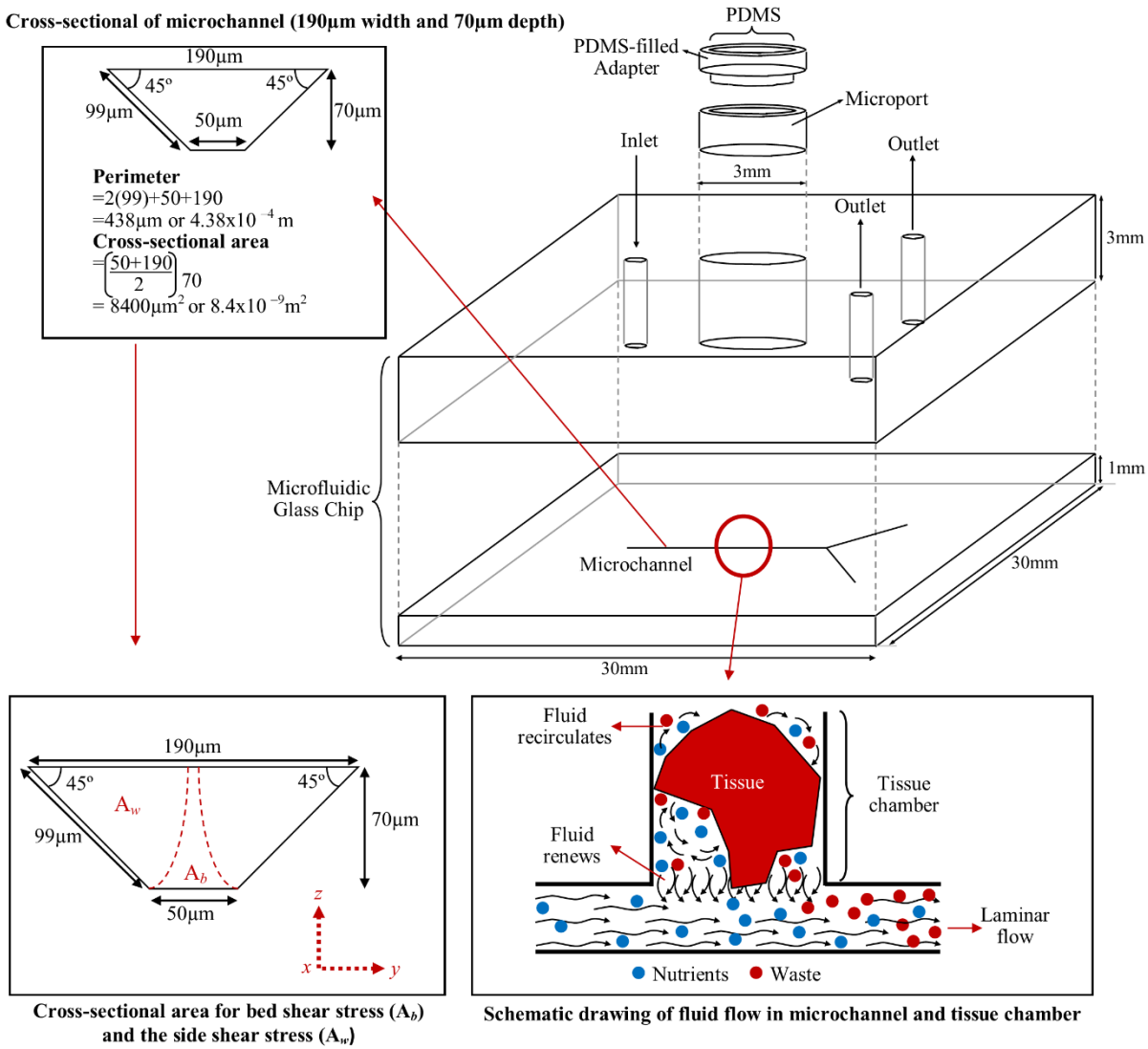


Figure 2.1. Schematic diagram of microfluidic glass device.
Top: Cross-sectional illustration of microchannel and calculations of its perimeter and cross-sectional area. Bottom left: Cross-sectional area for bed shear stress (A_b) and the side shear stress (A_w) (adapted from Javid and Mohammadi, 2012). Bottom right: Schematic drawing of fluid flow in microchannel and tissue chamber (adapted from Astolfi *et al*., 2016)
PDMS: poly-dimethylsiloxane.

Fabrication of microfluidic glass device

The first step in constructing the microfluidic glass device was to draw the channel structure using AutoCAD (computer assisted design) LT software. The drawing was transferred to a mask with the channels left blank on a black background to enable light to penetrate through transposing the channel design on to glass wafers (1mm thick) coated with a chromium layer and a photoresist layer using photolithography (Figure 2.2; Gokhale *et al*., 2005; Tarn, 2008; Hattersley, 2010). The exposed plate was immersed in developer solution for 60 seconds, rinsed under running water and then dried by blowing nitrogen gas (N_2) over it. The plate was then placed into a small

basin containing Chrome Etch MS8 solution for 60 s, or until the pattern was fully exposed onto the glass before being rinsed with deionised water and blown dried again. The glass was then wet etched using hydrofluoric acid (48%), ammonium fluoride (40%), hydrochloric acid (38%) and deionised water. Due to the nature of the etching process, etching occurs both widthways, as well as downwards, creating channels with a cross section that is approximately trapezoidal (Figure 2.1; McCreedy, 2001).

The etched plates were then immersed in acetone until all of the photoresist was removed, rinsed with water and dried with N_2. The chrome layer was removed using a chromium etchant, Chrome Etch MS8, and allowed to dry. By using standard drilling techniques, the access holes were drilled in the 3mm thick top plate using 1.5mm drill bits. The central hole with a diameter of 3mm was drilled into the top plate to provide a chamber for the tissue (Figure 2.1) which is cylindrical with an internal volume of 21µL. The top plate with the drilled holes was then thermally bonded onto the etched bottom plate in a furnace at 590°C for 3 hours. The bonding temperature for the glass wafers was above the transition (or transformation) temperature of 520°C which causes the glass to become rubbery and allows two plates to be bonded together, but below the softening point of 710°C.

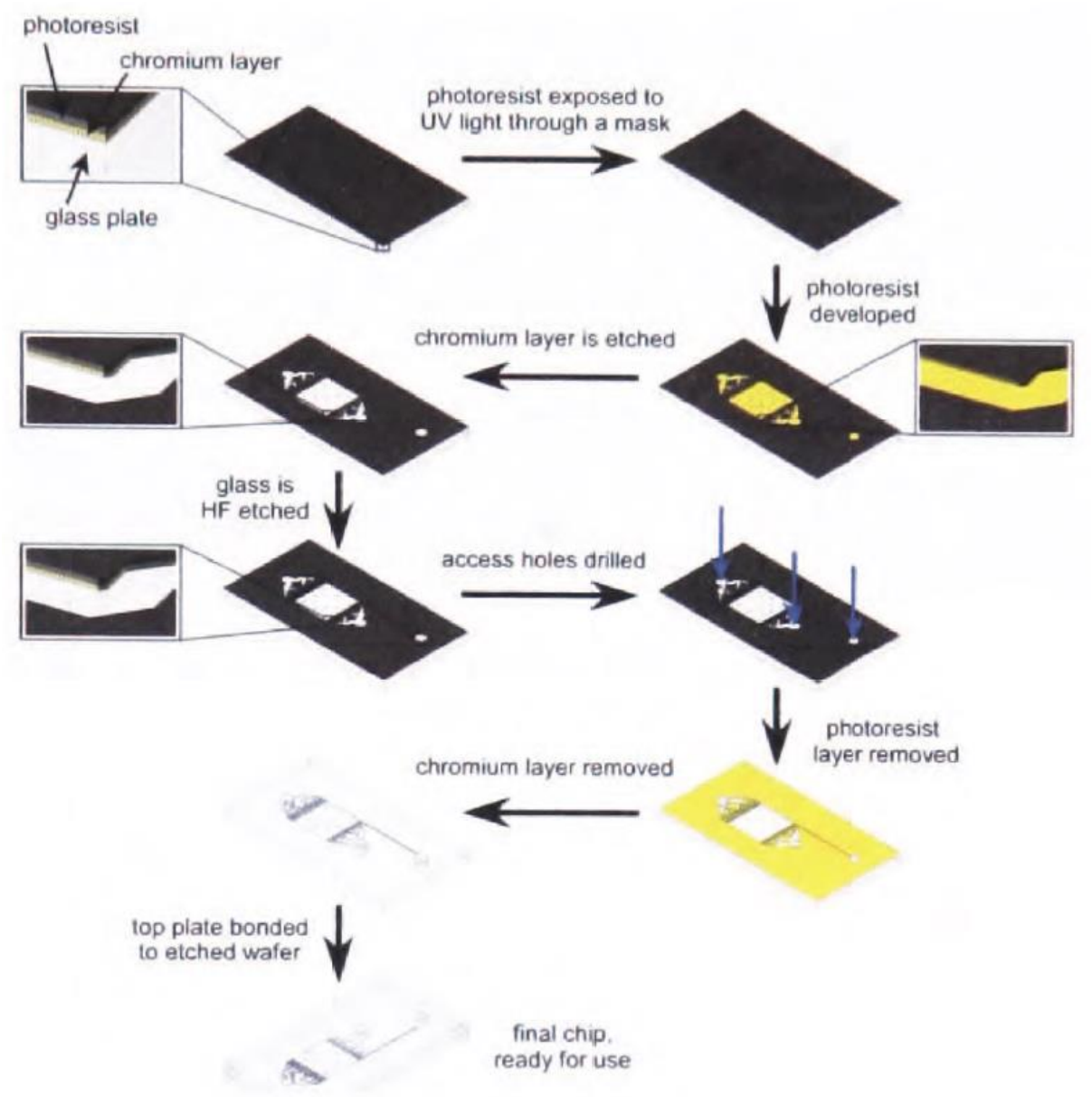


Figure 2.2. Outlines of the operational details of photolithography and wet etching method involved for microfluidic glass device fabrication in University of Hull (Tarn, 2008).

Diffusion property of the current microfluidic device

Diffusion occurs when there is a concentration gradient within a fluid. It is the crucial transport mechanism between capillaries and tissue *in vivo* which can be replicated similarly in a microfluidic platform. The diffusion between the microchannel and the tissue chamber allows the tissue to access nutrients and reagents supplied via culture medium as well as disposing of cellular waste. When the culture medium is perfused into the microchannel, the fluid layer near the channel is renewed rapidly while the liquid within the chamber mostly recirculates (Astolfi *et al*., 2016; Figure 2.1). The nutrients from the channels gradually diffuse into the chamber while the waste products diffuse out from the chamber. According to the microscopic theory of

diffusion, the diffusion of a molecule in a solution can be considered as a phenomenon associated with Brownian motion in which the mean square displacement (x^2) is proportional to the time and the equation is shown below, where D is the molecular diffusion coefficient (m^2/s) and *x* is the mean distance from the starting point that a molecule will have diffused in time, t.:

$$t = \frac{x^2}{2 \cdot D}$$ Equation 1 (Walker, Zeringue and Beebe, 2004)

The diffusion time depends on temperature and the size of the molecule with small molecules diffusing most rapidly. In addition, the diffusion coefficients of particles are different in fluid compared to those inside a solid tissue. For example, an oxygen molecule with a diffusion coefficient, D, of $2.6 \times 10^{-5} cm^2\ s^{-1}$ (Astolfi *et al*., 2016) takes approximately 7min to diffuse through a 0.15cm distance, whereas a larger glucose molecule in water with diffusion coefficient of $9.27 \times 10^{-6}\ cm^2\ s^{-1}$ (Astolfi *et al*., 2016) takes about 20min to diffuse through the same distance. According to a study by Astolfi *et al*, (2016), the diffusion coefficient for the diffusion of oxygen through cancerous tissue is $1.83 \times 10^{-5}\ cm^2/s$ while the diffusion coefficient for the diffusion of a glucose molecule through cancerous tissue is $2.70 \times 10^{-6}\ cm^2/s$ (Astolfi *et al*., 2016). To calculate the diffusion through a cancerous tissue with dimension of about 3mm x 3mm x 3mm, non-polar oxygen will take approximately 10min to travel from edge to centre of the tissue (0.15cm), while glucose will need about 70min to travel the same distance.

In the current study, FITC-conjugated dextran at 4KDa was added to the tissue located in the tissue chamber of the device, allowing the permeation study of the particles through the tissue (section 2.12.4). The diffusion coefficient of FITC-dextran was not determined experimentally in the current study and the diffusion calculation of the dextran marker into the solid tumour is complex and difficult due to the heterogeneous matrix and microenvironment compartments that contain cell membranes and non-uniform extracellular spaces. However, it has been reported that the diffusion coefficient of dextran in cells (e.g. cytoplasm) was much lower than that in aqueous medium (Arrio-Dupont *et al*., 1996). The diffusion rate of dextran in collagen hydrogels, which are in widespread use as scaffolds for 3D cell culture, is dependent on both the size of dextran and the temperature (Antoine, Vlachos and Rylander, 2015). The higher the Stokes-Einstein Radius R_e of the dextrans, the smaller the diffusion

coefficient resulting in slower diffusion (Audus and Raub, 1993). Similarly, the temperature and the diffusion rate are negatively correlated (Antoine, Vlachos and Rylander, 2015).

Reynolds number of fluid flow in the microfluidic device

The Reynolds number is a non-dimensional parameter (Equation 2) that defines the tendency of a flowing liquid to develop turbulence where ρ is the fluid density, μ is the fluid viscosity, D_h is the hydraulic diameter, and V is the velocity. The low Reynolds number (Re) lower than 2300 is characterised as laminar flow (Takayama *et al*., 2001; Walker, Zeringue and Beebe, 2004).

$$Re = \frac{\rho V D_h}{\mu} \qquad \text{Equation 2 (Walker, Zeringue and Beebe, 2004)}$$

The Reynolds number was calculated (Equation 2) using a combination of constant values from the literature and calculated values (fluid flow velocity and hydraulic diameter). In the current microfluidic device, the fluid density (ρ) of culture medium (DMEM with supplements) used to perfuse tissue samples in the device was 990 kg/m^3 (Bacabac *et al*., 2005) while the fluid viscosity (μ), was 0.00078 Ns/m^2 (Bacabac *et al*., 2005; Wang, Lu and Schwartz, 2012). For the calculation of the hydraulic diameter of the microchannel, the cross-sectional area and the wetted perimeter of the trapezoidal shaped microchannel were included (Figure 2.1; Equation 3), giving 7.67x10^{-5}m.

$$d_h = 4\frac{Cross\text{-}sectional\ Area}{Wetted\ perimeter} \qquad \text{Equation 3}$$

The velocity of the fluid flow using a flow rate of 2μL/min was 3.96 x 10^{-3} m/s. Finally, the Reynolds number within the microchannels of the current microfluidic device was calculated as 0.386, which defines the flow pattern in the device as laminar flow.

Shear stress in the current microfluidic device

Shear stress is felt by an entity when a tangential force is applied to its surface (Walker, Zeringue and Beebe, 2004). In liquids, the shear stress present throughout a channel can be represented mathematically using Newton's law of viscosity:

$$T = -\mu\left(\frac{dv}{dx}\right) \qquad \text{Equation 4 (Walker, Zeringue and Beebe, 2004)}$$

Where T is the shear stress, μ is the viscosity, v is the velocity, and x is the position within the channel. The distribution of the wall shear stress around the wetted perimeter in open channels depends on the cross-sectional microchannel shape, the

longitudinal variation in platform geometry and the boundary surface roughness (Javid and Mohammadi, 2012). A mathematical model has been developed to calculate the shear stress in trapezoidal microchannel (Javid and Mohammadi, 2012). The flow direction is defined as axis x while the cross-sectional plane, y-z is shown in Figure 2.1 and the shear stress on a trapezoidal shape microchannel is made up of the cross-sectional area for bed shear stress (A_b) and the side shear stress (A_w; Figure 2.1). In addition, the gravitational, secondary flows (shear stress on y-z and z-x planes) and the interfacial shear stress have to be included into the calculation. Unfortunately, the calculation of the shear properties was limited due to the lack of certain informative values, for example the secondary currents velocities, shear stress on y-x planes and y-z planes and the integration path (red dotted lines shown in Figure 2.1).

2.3.1 Cleaning the microfluidic device and checking for blockages

Before microfluidics system was set up the device, tubing and connectors were washed through with 70% v/v ethanol and sterile water and checked for blockages. If the channels of the microfluidics device were found blocked during the washes, the device was immersed in concentrated hydrochloric acid (HCl; 11.6-12.0M) for one to two days. If the device was still blocked, they were sent to furnace in the Department of Chemistry. The devices were then cleaned with ethanol and sterile water.

2.3.2 Assembly of microfluidics flow system

A microport (Upchurch Scientific, Washington, USA) was glued on the circular tissue chamber of the top glass layer using Araldite (B&Q) and held in place with a bulldog clip whilst drying for 24 hours at room temperature or about 3 hours in 37ºC incubator (Figure 2.3 A and B). The tissue chamber was sealed using a poly-dimethylsiloxane (PDMS; Dow Corning, Midland, UK)-filled adapter with polytetrafluoroethylene (PTFE) tape (B&Q) wrapped around the thread to provide an improved seal (Figure 2.3 C and D). The PDMS was prepared by mixing PDMS monomer and curing agent in a 10:1 ratio before pouring carefully into the adapter which was then placed at room temperature for overnight to set. The PDMS is highly gas permeable and allows diffusion of carbon dioxide (CO_2) and oxygen into the medium inside the microfluidic channels, with the permeability coefficients of 3800 Barrer [10^{-10}cm^3(STP) ·cm/cm^2·s·cm Hg; measured as a function of transmembrane pressure difference] for CO_2 gas and 800 Barrer for oxygen gas (Merkel *et al*., 2000; Halldorsson *et al*., 2015). This provides the culture with oxygen and removes CO_2 released from cellular

respiration and maintaining the pH in culture medium (Saito *et al*., 2006, Whitesides, 2006; Halldorsson *et al*., 2015).

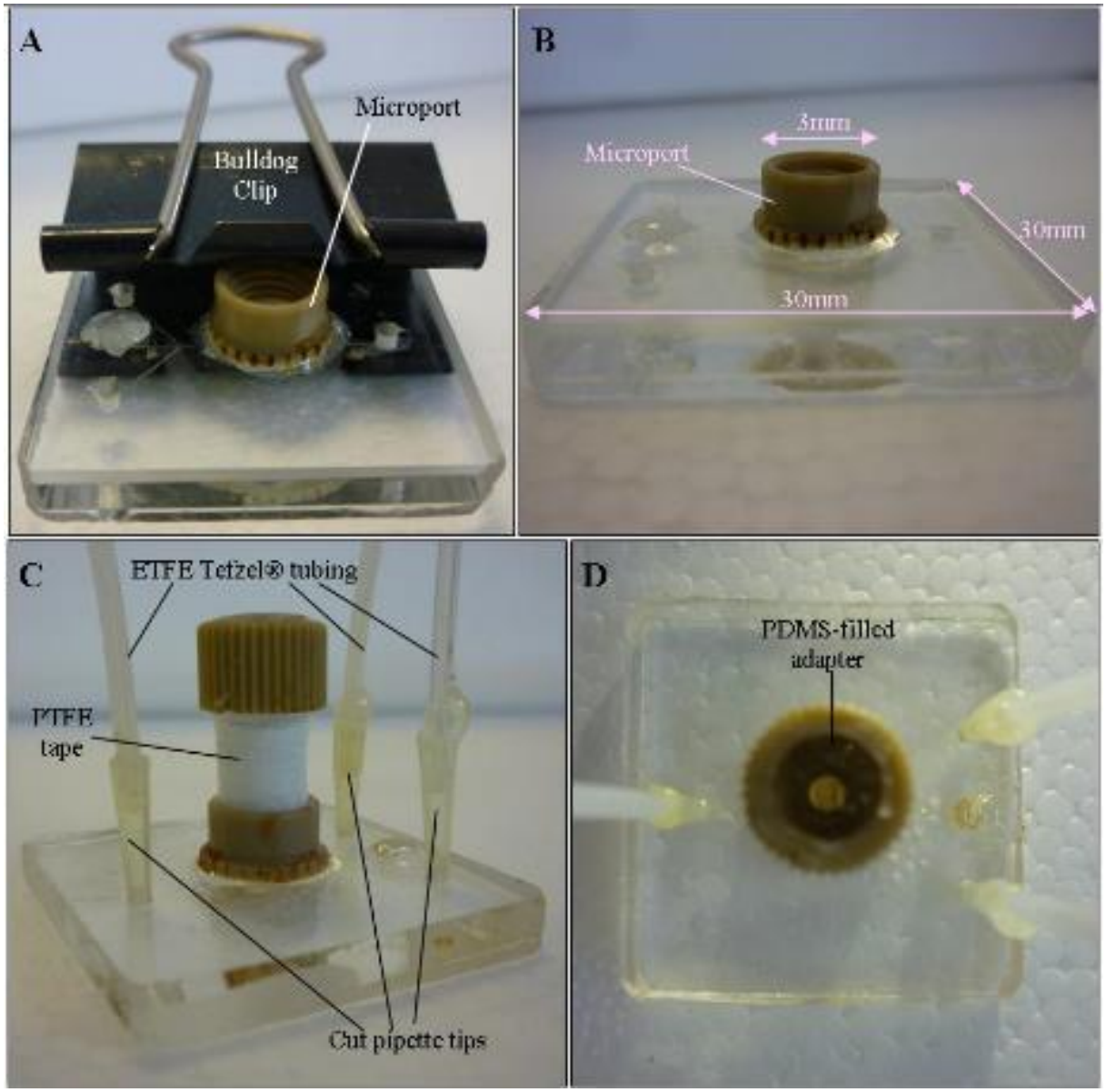


Figure 2.3. Assembly of microfluidics system.
(A) Assembly of microfluidic glass device and tissue chamber microport by using Araldite glue. (B) Dimension of microfluidic device. (C) Set up of microfluidic with inlet and outlet tubes. (D) Bird-eye view of microfluidic set-up.

Liquid was supplied to and removed from the device via 0.5mm (internal diameter) x 1.58mm (external diameter) ethylene-tetrafluoroethylene (ETFE), Tefzel ® tubing (Kinesis, Cambridgeshire, UK). The tubing was attached to the inlet and outlet holes of the device via adapted yellow pipettes tips glued onto the ends (Figure 2.3). The inlet tubing was about 35cm in length to provide sufficient time (flow rate of 2µl/min allowed approximately 34 minutes for medium to reach tissue chamber of the device) for the medium to be heated to 37°C before reaching the tissue in the microfluidic device. Two-part connector (Mengel Engineering, Denmark; Figure 2.4) was attached to another end of the inlet tubing which enabled the connection between the syringe filter (0.2µm; Millipore, UK) and inlet tubing. The assembly of the entire microfluidic flow system is shown in Figure 2.4.

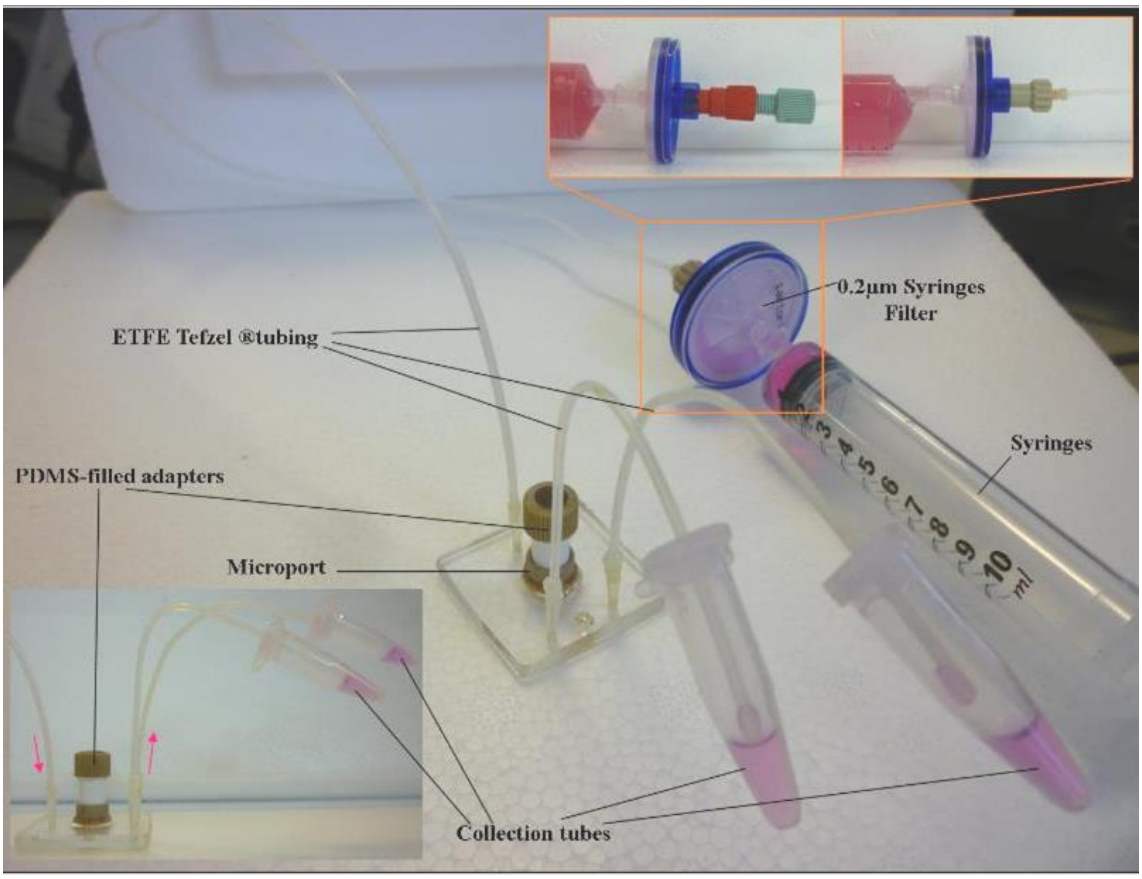


Figure 2.4. Assembly of microfluidics flow system.

2.3.3 Preparing and using the microfluidics flow system

The syringe was connected to a Harvard PhD 2000 syringe pump (Harvard, Kent, UK) and the microfluidics device was placed in a 37ºC egg incubator (Novital, Italy) shown in Figure 2.5. The inlet tubing of the system was attached to the syringe with an inline filter (0.2µm; Millipore, UK) which functions to prevent bacterial contamination and minimize the entry of gas bubbles into the perfusion system.



Figure 2.5. Entire microfluidic system set-up with Harvard syringe pump and the 37ºC incubator.

After the assembly of microfluidic flow system, the system was perfused with 70% (v/v) ethanol/water at a perfuse rate of 10mL/hour for 15 minutes and then rinsed with sterile distilled water for another 15 minutes. Subsequently, the device was primed with sterile medium for 30 minutes at a flow rate of 20µL/minute. During the priming process, the microfluidic device was continually checked for leakages or blockages. The temperature of the incubator was measured by using a digital thermometer and adjusted to human body temperature (36-37 ºC).

The tissue-contained cryopure tube was taken out from freezer and placed in a class II laminar flow hood to allow to thaw at room temperature. After thawing, the tissue biopsy was taken out from the tube and rinsed in PBS containing 2.5µg/mL v/v fungizone (Gibco). Then, on a sterile petri dish, the biopsy was cut into sections each weighing approximately 5-10mg using minimal cuts with a pair of scalpels. The weights of each tissue sample were recorded and PDMS-filled adapter of the primed microfluidic devices was opened inside hood. A single piece of tissue was placed into the medium filled tissue chamber of the device carefully using sterile tweezers to minimize any further tissue damage. The tissue chamber was sealed with the PDMS-filled adapter, taking care not to trap air bubbles inside, placed back in the 37ºC incubator and the entire system was perfused with medium at a flow rate of 2µL/min. Following microfluidic set-up, the flow of the medium was regularly checked, ensuring that there were no leakages or bubbles trapped within the channel and chamber. Microcentrifuge tubes (0.5mL; Sarstedt) were attached to each of the outlet tubes to collect the effluent flowing from the device. Effluent was collected every two hours and

stored at 4ºC for LDH analysis or -80ºC for soluble factor analysis. At the end of experiment, microfluidics perfusion was terminated. The tissue was removed from the tissue chamber of device using clean tweezers or a pipette tip, embedded on a cork tile covered with OCT (optimal cutting temperature compound) embedding medium and frozen in liquid nitrogen-cooled 2-methyl-butane solution (Sigma-aldrich, UK). The frozen tissue was then stored in -80°C freezer.

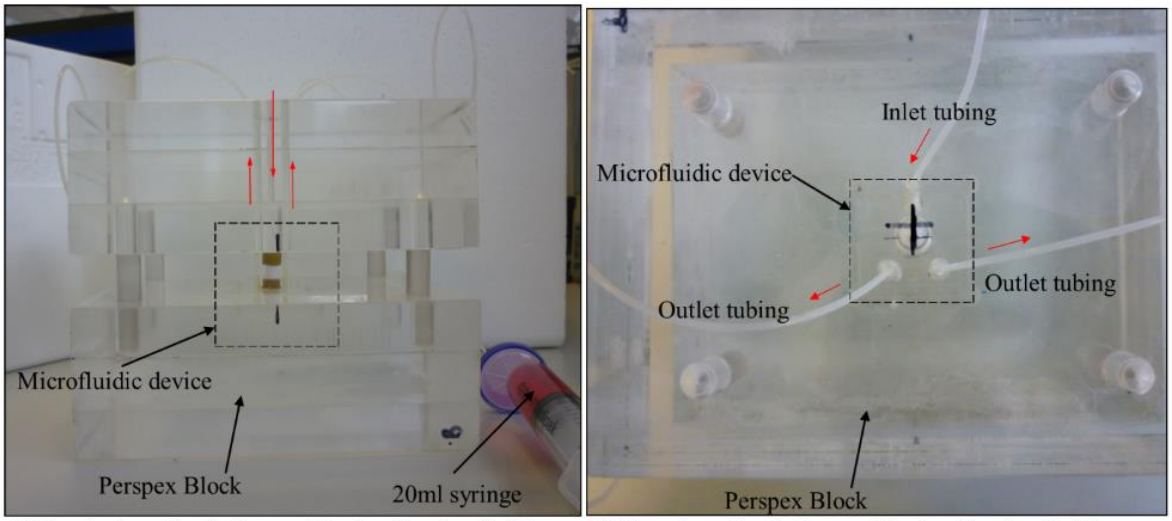
2.4. Microfluidic culture methodologies on HNSCC tissue with and without irradiation/ Irradiation of HNSCC tissue in the microfluidic system

In order to compare the effects of irradiation on HNSCC tissue with that of non-irradiated tissue, at least two parallel microfluidic systems were set up approximately 24 hours before irradiation was delivered by following the procedure as described in section 2.2. One of the microfluidic devices was treated as a control which received no irradiation treatment whilst the other device was subjected to irradiation doses appropriate for the individual experiments. Approximately 4 hours before irradiation, one of the microfluidic devices containing the test tissue was placed in a Perspex block.

The Perspex block was synthesized by the medical physics department at Castle Hill Hospital and consisted of two parts: an upper part which has holes to allow the inlet and outlet tubing to be inserted and a lower part with indent in which the microfluidic device sits (Figure 2.6). It was made by welding separate blocks together using Tensol. The indent and the edges were indexed and cut using a milling machine while the holes on the blocks were indexed and drilled. The size and dimension of the Perspex block was calculated and determined by the radiation physicists (Figure 2.7). The usage of Perspex block enables the doses of irradiation to be focused more accurately on tissue sample. The doses of irradiation and settings of the LINAC machines were calculated and calibrated by the physicists in the radiation physics department at Castle Hill Hospital. To ensure an accurate delivery of a specified dose of irradiation to the tissue biopsy in the microfluidic system and create a model associates the tissues around the tumour *in vivo*, the whole device was placed in a Perspex block manufactured specifically for this purpose.

To determine whether the irradiation dose was delivered to target point without producing a scatter dose to other parallel tissue samples on the couch, the dose received on the surface and at the centre of the block was measured by the radiation physicists using a thermoluminescent dosimeter (TLDs). Two TLDs were used, one of them was placed in the block in the direct field (8x8 field; centre of the Perspex block where the tissue sample was placed) and the other TLD was taped to the surface of the block outside of the direct field. The delivery of 530 monitor units (equal to 5Gy) to the centre of the block from equal weighted and parallel opposed fields was used to measure the charge received on the surface of the block. This was determined to be equal to approximately 0.0026% of the prescribed dose. Therefore, the scatter dose to the surrounding surfaces, e.g. other Perspex block containing tissue samples on the couch, was negligible.

Before the device was taken for irradiation, the entire set up, which includes the incubator containing the Perspex block and microfluidic device, the syringe pump and power supply (Riello Ups Ltd, Wrexham, UK) were transferred to a trolley and pulled to the radiotherapy department with care so as to cause minimal disruption to the tissue in the device. Once in the radiotherapy department, the Perspex block containing the microfluidic device and syringe pump were taken out from the trolley and placed on the couch where patients usually lie for the administration of irradiation (Figure 2.8). It was ensured that there was no interruption to the flow during the transportation and irradiation.



A) Front view of radiotherapy block with microfluidic device

B) Top view of radiotherapy block with microfluidic device

Figure 2.6. Photograph of the Perspex block containing microfluidic device.
A) Front/side view and B) top view of Perspex block. Special holes were in the top of the Perspex block to allow the inlet and outlet tubing to be fed through.

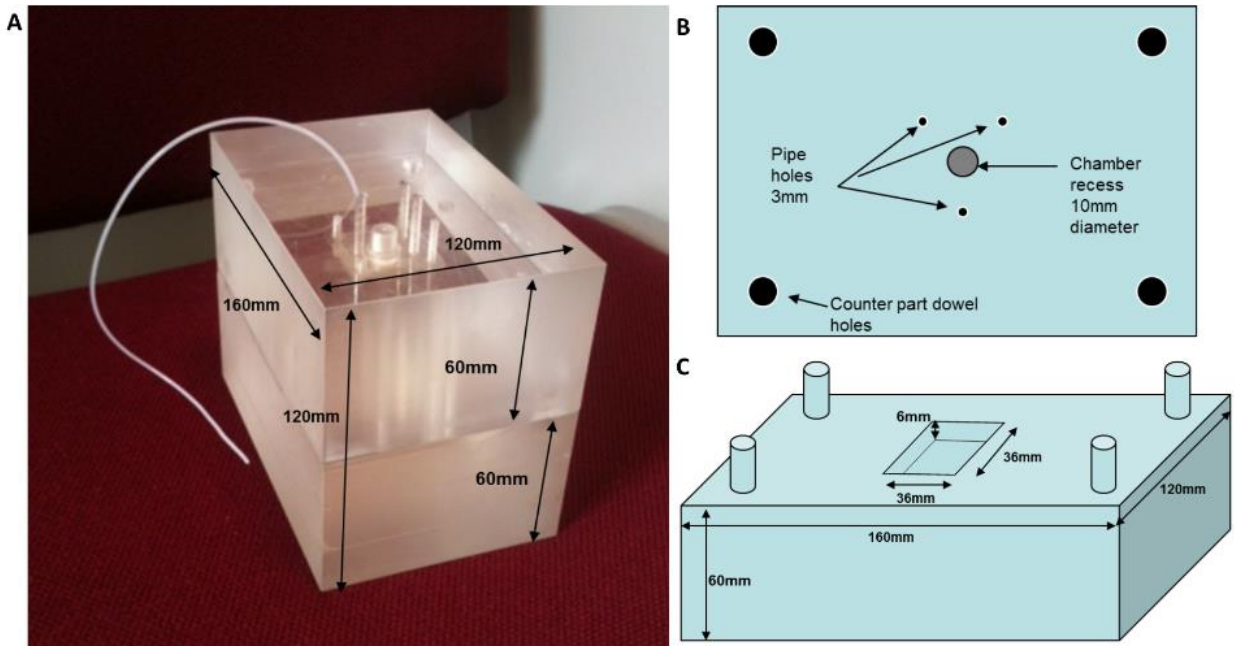


Figure 2.7. The Perspex block used for irradiation of HNSCC tissue during microfluidic culture. (A) Photograph of the Perspex block which was designed in two halves to accommodate the microfluidic chip and the associated tubing. (B and C) Schematic to show the dimensions used in the construction of the block. The upper irradiation block contained 3x3mm holes for inlet and outlet tubing, a 10mm recess for to accommodate the tissue chamber and PDMS bung, along with four dowel holes (B). (C) The bottom irradiation block consisted of a 6x36x36mm recess where the glass microfluidic device was placed and four dowels to lock the top and bottom sections together.

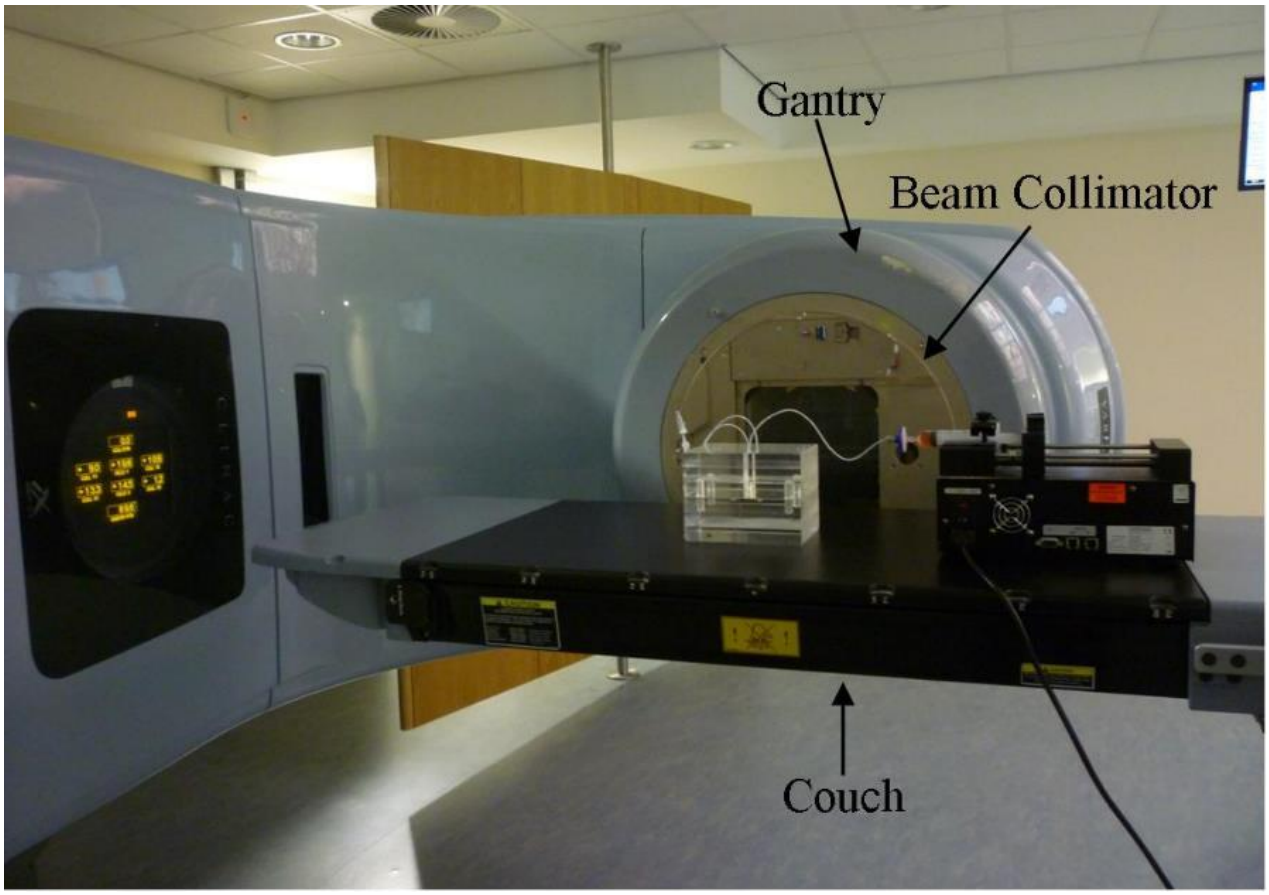


Figure 2.8. Arrangement of the microfluidic system (block and syringe pump) on the couch (table) during irradiation using Linear Clinical Accelerators (LINAC).

The devices used for irradiation within the radiotherapy department (Figure 2.8) are Linear Accelerators which generate X-rays by accelerating electrons to relativistic speeds and colliding them with a tungsten “target” (Pope, 1999). This process yields a very high-energy x-ray beam when the electrons are decelerated rapidly through a bremsstrahlung (braking radiation) process in close proximity to the tungsten nucleus. In the current study, a nominal energy of 6 MegaVolts (MV) was used because this energy is suitable for shallower depths (1.5cm of depth of maximum dose) and was thought to be the most appropriate for this experiment (Gazda and Coia, 2007)

The x-ray beam field was focused by magnets in the treatment head, shaped by collimation, and transmitted in a specific dose to the centre of the block from both sides (angle of 90° and 270°). During irradiation of the tissue biopsy in the microfluidic device, access to the radiotherapy area was prohibited and the irradiation dose delivery was monitored and controlled by medical physicians in the control area. Following irradiation, the entire microfluidic set up was transferred back to the trolley and was transported back to the Daisy research laboratory.

There were, in total, 71 tissue and blood samples obtained from newly presenting HNSCC patients for current head and neck research group, which consists of 22 lymph node samples (8 oropharyngeal primary, 8 unknwon primary, 2 laryngeal primary, 1 oral cavity primary, 1 paranasal sinus primary, 1 nasal cavity primary and 1 parotid primary), 43 primary tumours (15 laryngeal, 13 oropharyngeal, 13 oral cavity and 2 paranasal sinus tumour) and 5 not known tumours. The samples were obtained during resection surgery at Castle Hill Hospital (Ear, Nose and Throat Department) following written informed consent. Seventeen of the samples were blood samples only which were used for other researches while one of the patient had received other therapies previously. The fresly resected tissues were placed in transport culture medium (DMEM supplemented with penicillin/streptomycin, L-glutamine, 10% FBS, fungizone as above) and transported to Daisy Research laboratory in Castle Hill Hospital as quick as possible (within 10 minutes). Under sterile condition in laminar flow cabinet, the samples were sliced into small biopsies on petri dish using minimal cuts (criss-cross) with a pair of scalpels. Each tissue piece was transferred into cryopure tube (Sarstedt, UK) and then snap-frozen in liquid nitrogen (section 2.2). The details of the patient tissues recruited for current head and neck cancer research group were summarised in appendix Section Table 9.1.

In current PhD research study, six primary HNSCC tumours and seven lymph neck nodes metastasised from different primary tumours (snap-frozen and stored at -80ºC; Table 2.1) were subjected to microfluidic flow system, according to procedure described im section 2.3. The schematic diagram of the entire processes is illustrated in Figure 2.9. For irradiation experiment, the tumour specimens maintained in the device weret then exposed to single-dose irradiation in the Radiation Physics Department of the same hospital (0Gy, 5Gy, 10Gy, 15Gy and 20Gy; section 2.4; Figure 2.9). In total, 178 microfluidic experiments (the sum of the number of microfluidic and single-dose irradiated tissues in Table 2.1) to investigate the effects of irradiation on the tissue. In each experiment tissue biopsies were maintained in parallel microfluidic devices and where possible each were subjected to four single-dose irradiations (5, 10, 15, 20Gy; Figure 2.9). In all experiments, at least one microfluidic device was set up to act as a non-irradiated control for the comparison with irradiated HNSCC and the number of repeats for each case (0Gy/MF, 5Gy, 10Gy, 15Gy and 20Gy) is illustrated in Table 2.1.

The radiation physics department at Castle Hill Hospital has six linear accelerator (LINAC) machines which were mainly used for patient treatment, and physicists' projects. Therefore, the experiments in the current project needed prior planning and booking onto the irradiator at least one week prior to experiments. The irradiation was usually scheduled outside of normal patient treatment hours (after 5pm during the weekday). However, the fractionated irradiation experiments were carried out additionally in the morning (10 or 11am) to fit in with patient treatment and machine servicing times. Due to the limitations of the amount of tissue and of the availability of the Perspex block, all four doses of irradiation were not able to be performed on every tissue (Table 2.1). In addition, technical problems during microfluidic culture including device leakages and channel blockage meant that not all doses could always be applied. Once the irradiation was complete different analyses including the assessment of the morphological integrity of the tissue, IHC staining of apoptotic/DSB repair markers and measurement of markers of cell death in the effluent collected were applied.

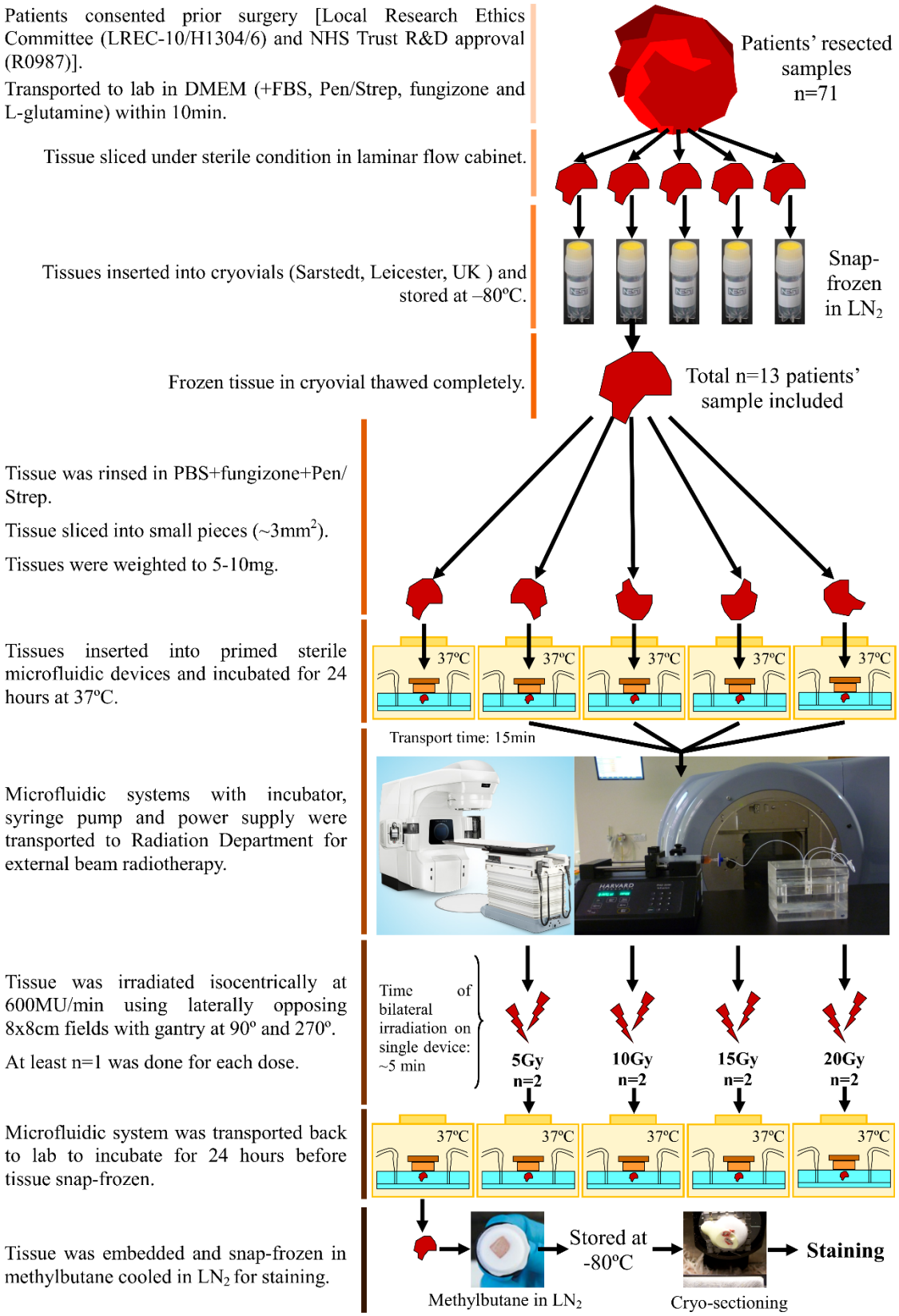


Figure 2.9. A diagrammatic representation of HNSCC patient tissue recruitment (n=71) and tissue inclusion (n=13) in microfluidic and on-chip irradiation experiments.
A frozen tissue sample (with weight between 5-10mg) obtained from each patient was divided and subjected to parallel microfluidic perfusion runs; at least one piece of tissue was not irradiated while the others were transported for irradiation to the Radiation Physics Department, Castle Hill Hospital, Hull. The entire microfluidics and irradiation runs were repeated using the tumour biopsies from the same patient to achieve n=2 for each irradiation dose.

Table 2.1. Patient demographics of (A) HNSCC primary tumour samples subjected to microfluidic perfusion and single dose irradiations.

	HNSCC tissue	Tumour site	Tumour stage	Gender; age	No. of Pre-MF †	No. of MF	No. of irradiated tissues; doses received (Gy)	Cryo-tube used	Analytical methods						
									LDH	CK18-LI	γH2AX	Ki-67	TUNEL	BrdU	Others
(A) Primary HNSCC tumour	Oral Cavity	FOM (TR62)	T4N0M0	59; M	1	1	1; 20	3	√					√	
					2	2	3; 5, 10 and 15								
		Tongue (TR71)	T2N2bM0	61; M	1	2	2; 10 and 20	3	√	√				√	
					1	1	2; 5 and 15								
		FOM (TR89)	T3N0M0	49; M	1	2	4; 5, 10, 15 and 20	4	√	√	√	√			
					1	2	4; 5, 10, 15 and 20								
		FOM (TR92)	T2N0	64; M	2	2	4; 5, 10, 15 and 20	6	√	√	√	√	√		
					1	2	3; 10, 15 and 20								
					1	1	1; 5								
	Oro-pharyngeal	Tonsil (TR77)	T2N2a	64; M	1	2	2; 15 and 20	4	√	√				√	
					2	2	2; 5 and 10								
					2	2	2; 15 and 20								
					1	2	2; 5 and 10								
	Laryngeal	Supraglottic (TR84)	T2N0M0	68; F	1	2	2; 15 and 20	6	√	√	√	√	√	√	
					2	2	2; 15 and 20								
					2	2	2; 5 and 10								
					1	1	1; 10								
					1	2	2; 5 and 20								
						2	1; 20	1							Cas
	Paranasal sinus	Maxillary sinus (TR66)	T4N2b	82; F	1	2	2; 15 and 20	6	√	√				√	
					2	2	2; 5 and 10								
					1	2	4; 5, 10, 15 and 20								

Table 2.2. Patient demographics of (B) metastatic lymph neck node tissues subjected to microfluidic perfusion and single dose irradiations.

	HNSCC tissue	Tumour site	Tumour Stage	Gender; age	No. of Pre-MF †	No. of MF	No. of irradiated tissues; doses received (Gy)	Cryo-tube	Analytical methods						
									LDH	CK18-LI	γH2AX	Ki-67	TUNEL	BrdU	Others
(B) Metastatic Lymph Neck Node	From oropharyngeal	Base of tongue (TR72)	NA	NA	1	1	3; 10, 15 and 20	7	√					√	
					1	2	2; 5 and 20								
					2	2	3; 5, 10 and 15								
		Tonsil (TR54)	NA	46; M	2	2	2; 15 and 20	5	√					√	
					1	2	3; 5, 10 and 20								
					2	2	3; 5, 10 and 15								
						3	3; 20Gy	2							Cas
		Tonsil (TR59)	T4N2b	68; M	2	2	4; 5, 10, 15 and 20	6	√	√					
					2	2	4; 5, 10, 15 and 20								
					2	2	2; 10								
						1		1							EdU
		Tonsil (TR122)	NA	32; M		2		1							Cas
						1		1							EdU
						4		2							2-NBDG
	From laryngeal	Larynx (TR80)	T4N2bM0	58; M	1	2	4; 5, 10, 15 and 20	7	√	√	√	√	√	√	
					2	2	2; 15 and 20								
					2	2	2; 5 and 10								
						1		1							EdU
	From oral cavity	FOM (TR52)	T1/T2N2c	59; M	1	1	1; 20	6	√						
					1	1	1; 20								
					1	2	1; 15								
					1	1	1; 20								
					1	1	2; 5 and 10								
	From unknown primary	Unknown primary (TR73)	N2aM0	61; M	1	1	1; 20	7	√	√	√	√	√	√	
					1	2	1; 20								
					1	2	2; 10 and 15								
					1	1	1; 5								
					1	1	4; 5, 10, 15 and 20								
					1	2	4; 5, 10, 15 and 20								

† Pre-MF (Pre-microfluidics) is tissue not subjected to microfluidic perfusion or irradiation treatment. MF (microfluidics) is tissue subject to microfluidic perfusion with no irradiation treatment. The tissues were embedded in OCT (optimal cutting temperature compound) embedding matrix and snap-frozen at the beginning of the experiment.
Abbreviation: Pre-MF: pre-microfluidic, MF: microfluidic, FOM: floor of mouth, LDH: lactate dehydrogenase, CK18-LI: cytokeratin 18 labelling index, M: male, F: female, NA: not applicable, Cas: CasPACE.

Following microfluidic and on-chip irradiation experiments, five tumour samples were subjected to the expression analysis based on the cleaved-CK18 (section 4.5), phorphorylated H2AX (section 4.7), TUNEL (section 4.9) and Ki-67 (section 5.2.2). The expression results were further described in the corresponding chapters. The corresponding treatment outcomes of these five tumour samples (two lymph nodes and three primary tumours) were recruited from NHS ENT secretaries and Lorenzo system with the assistants of few ENT doctors (Table 2.2).

Table 2.2. Clinical treatment received and the therapy outcome of five HNSCC tumours involved in this study.

HNSCC subsites	Sample date	Tumour stage	Therapy received and date †	Treatment outcome (Updated on June 2016)
TR73	09.04.13	N2aM0	Surgery and CRT	No local or regional recurrence
TR80	11.06.13	T4N2bM0	Surgery and CRT	No record available
TR89	15.08.13	T3N0M0	Surgery	Passed away due to alcoholic liver disease
TR92	29.08.13	T2N0	Surgery	No evidence of recurrence
TR84	02.07.13	T2N0M0	Surgery and Radiotherapy	No evidence of loco-regional recurrence

† The therapy details administered on these patients, including the doses and the chemotherapy drugs, were not available.
CRT: chemo-radiotherapy

2.5. Fractionated irradiation methodologies on HNSCC tumours in microfluidics

In order to see if there was a difference between single and fractionated doses of irradiation, three HNSCC tumours, including one lymph neck node (metastasised from laryngeal tumour; TR80) and two oral cavity floor of mouth tumours (TR89 and TR92), were subjected to fractionated irradiation treatment whilst being maintained in the microfluidic device (5 x 2Gy or 5 x 4Gy; Table 2.3). In total, eleven tissues were subjected to microfluidic culture and irradiation (section 2.3 and 2.4).

Control tissues (maintained in the device with no irradiation) were placed and remained in the incubator in the laboratory. After the first irradiation treatment, 2Gy and 4Gy on respective tissues, the microfluidics were transported back to the laboratory and further maintained for at least 6 hours before the next irradiation treatment. The five fractions of irradiation were continued and carried out in the morning (between 8.30-11.30am) and evening times (between 5.00-6.00pm) for 3 days. The tissues were maintained for a further 24 hours after the final irradiation treatment. The tissues were then snap-frozen and serially sectioned (section 2.7) before IHC staining of CK (section 4.5), M30 (section 4.5) and γH2AX (section 4.6).

Table 2.3. Patient demographics of HNSCC tumours (n=2) and metastatic lymph neck node (n=1) subjected to microfluidic culture with and without fractionated irradiations.

HNSCC tissue	Tumour site	Tumour stage	Age; Gender	Treatments	Number of samples	Number of cryo-tubes used
Oral Cavity	FOM (TR89)	T3N0M0	49; M	MF Control	2	1
				5 x 2Gy	1	
				5 x 4Gy	1	
	FOM (TR92)	T2N0	64; M	MF Control	1	1
				5 x 2Gy	1	
				5 x 4Gy	1	
Lymph node	Metastasised from laryngeal tumours (TR80)	T2N2a	64; M	MF Control	2	1
				5 x 2Gy	1	
				5 x 4Gy	1	

MF: microfluidic, FOM: floor of mouth, M: male, F: female.

2.6. Measurement of cell viability by Lactate Dehydrogenase (LDH) analysis

Cell death of tissue biopsies were measured using a colorimetric cytotoxicity assay (Cytotoxicity Detection Kit Plus, LDH, Roche, Hertfordshire, UK), determining the amount of LDH released from the tumour tissue in the microfluidic device. LDH is a stable cytoplasmic enzyme in almost all cell types, and it is rapidly released from the cell when the cell membrane is damaged, allowing cell death to be measured. The analyses were performed according to the protocols provided by the manufacturer and 50µL of effluent media (which were collected in every two hours) were transferred in duplicate into a 96-well-plate and the labels of the effluent media on the plate were recorded. After that, reaction mixture was prepared by the addition of the catalyst (Diaphorase/nicotinamide adenine dinucleotide, NAD+ mixture) with the dye solution (tetrazolium and sodium lactate). The 50µL reaction mixture was mixed with the effluent media in each well for the reaction. The plate was then placed in a 37˚C incubator for 30 minutes where the catalytic reaction takes place.

The principle of the assay is based on the cleavage of a tetrazolium salt when LDH is present in the effluent. The catalyst and dye mixed solution contain all the necessary components that allows two coupled enzymatic reactions occur in detecting the LDH present in effluent sample (Figure 2.10; Roche Diagnostics GmbH, 2011). First, any LDH present catalyses the oxidation of lactate to pyruvate while the NAD+ is reduced to form NADH + H^+. The reduced form of NADH is then recycled and oxidized to NAD+ by donating hydrogen ions for the second reaction. In the presence of diaphorase catalyst, tetrazolium salt is reduced to formazan salt by accepting the hydrogen ions. The generated formazan salt is responsible for the colour development during the incubation.

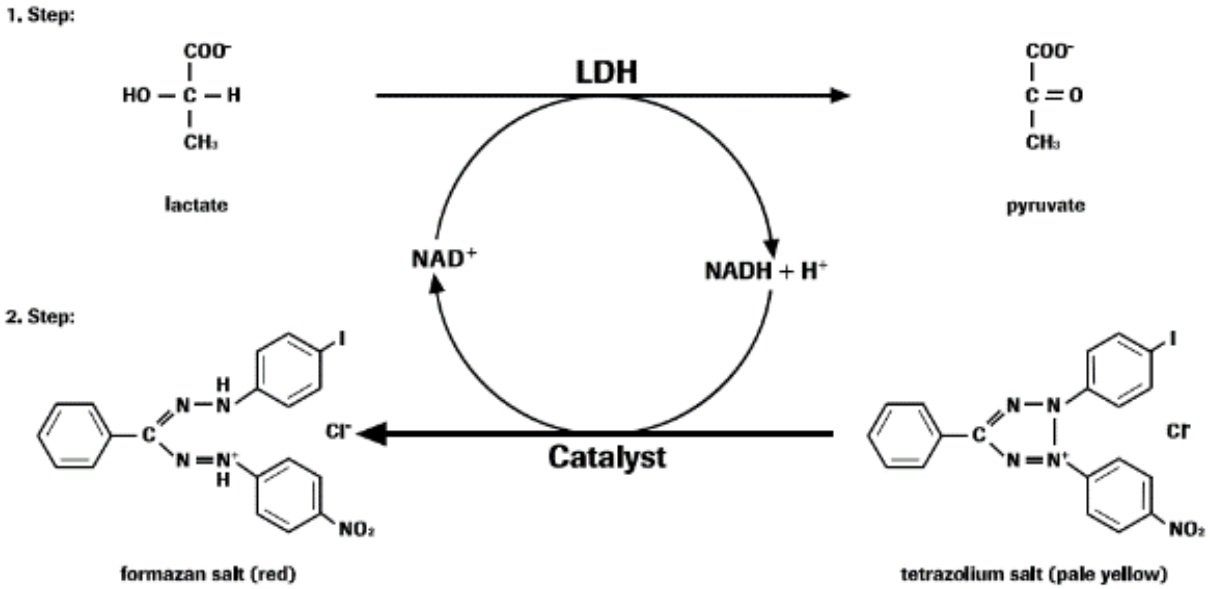


Figure 2.10. Enzymatic reactions in detecting the presence of LDH.
(Roche Diagnostics GmbH, 2011).

After the 30-minute incubation, the reaction was terminated by adding 25µL of stop solution (1M of hydrochloric acid). The absorbance of water soluble formazan dye produced was measured at 490nm with an ELISA plate reader (BioTek, USA). The mean values of the duplicated samples were calculated as shown in table 2.1. The medium which was not subjected to microfluidic flow was added into the 96-well-plate in duplicate and the mean value of the "medium only" was measured. To obtain the amount of LDH released from 1mg of tissue, the mean absorbance value obtained from duplicated samples was deducted with the mean absorbance value of medium only and then normalized by the weight of tissue (mg). An example of LDH analysis and the quantification were summarized in Table below (Table 2.4).

Table 2.4. Example of LDH data analysis.

Weight (mg)	Time	Hour	Reading 1	Reading 2	Average reading	Average reading-media absorbance	Absorbance
7.1	1400-1600	2	3.708	3.86	3.784	2.8	0.3944
	0900	67	1.165	1.191	1.178	0.194	0.0273
	1100	69	1.021	1.043	1.032	0.048	0.0068
	1300	71	1.024	0.954	0.989	0.005	0.0007
	1500	73	3.015	2.833	2.924	1.94	0.2732
	1700	75	3.323	3.203	3.263	2.279	0.3210
	0900	91	3.565	3.528	3.5465	2.5625	0.3609
	1100	93	3.697	3.688	3.6925	2.7085	0.3815
	1300	95	3.46	3.418	3.439	2.455	0.3458
	1400	96	3.128	2.097	3.128	2.144	0.3020

2.7. Tissue processing and microtome cryostat sectioning

Frozen tissue was transferred from -80°C freezer to -20°C microtome cryostat approximately 5 minutes before it was sectioned, allowing the tissue to be cut at -20°C. The frozen tissue was then cut in 8µm thick sections using a microtome cryostat (Leica CM 1100; Leica Microsystems, Nussloch, Germany) and arranged onto poly-L-Lysine-coated microscope slides (Knittel Glass, Germany). Following 30 minutes of tissue sections drying, the slides were processed for staining or stored in -20°C.

2.8. Assessment of morphology and histology of tissue by Haematoxylin and Eosin staining

Haematoxylin and eosin (H&E) staining was carried out in order to study the morphological appearance and cell architecture following perfusion in the microfluidics device. H&E staining is the most commonly and widely used tissue staining procedure for routine pathology and animal histology which uses haematoxylin for nuclear staining whereas eosin for cytoplasmic staining (Merck Millipore, 2016). Haematoxylin is a dark purplish dye which stains the chromatin (nuclear material) within the nucleus, giving purplish-blue colour. Eosinophilic structures such as most cytoplasmic proteins are stained by eosin which is an acidic and orangish-pink to red dye, giving pinkish-red counterstain.

The frozen sections on poly-L-Lysine coated slides were fixed in cooled 100% methanol for 10 minutes before H&E staining (Grounds, 2010). The slides were then washed with running tap water for about 2 minutes and placed in filtered Harris Haematoxylin (Sigma-aldrich, UK) for 5 minutes. After that, slides were washed with running tap water for two minutes, placed in eosin (dissolved in 95% of ethanol/water; Sigma-aldrich, UK) for two minutes, and washed with running tap water for one minute. Following haematoxylin and eosin staining, the tissue sections were dehydrated in serial graded alcohol and histoclear in the following order: 70%, 95%, 100% dehydrating ethanol and three times of dehydrating histoclear (National Diagnostics, Hessle, UK), each for 2 minutes. Next, the dehydrated slides were mounted with histological mounting agent (National Diagnostics, UK) covered with coverslips (Fisherbrand, Loughborough, UK) and ready to be viewed under light microscope. In the current study, it was important to photograph all the stained images using the same settings. This included brightness, the exposure time, colour intensity, capture enhance gain (set to 1) and the bit depth (24 bit colour). To photograph the staining

image at x100 magnification field, 3-10ms of exposure time was used while 100-150ms of exposure time was used for x400 magnification field. In addition, the same colour setting was used; 1.10-1.20 for red, 1.40-1.50 for blue and 1.0 for green, which were established by Nikon E800 microscope specialist. The variation of the colour intensities on observed different tissues was most likely to be due to the slight differences in the thickness of the cryostat-sectioned tissue.

The morphology of the frozen/thawed tissue, which was not subjected to microfluidic analysis or any treatment (pre-microfluidic; pre-MF), was assessed using H&E staining. The representative staining of the pre-MF tissues is shown in the appendix (section 9.2/Figure 9.1) which showed more nuclei and better cellular integrity compared with the corresponding microfluidic-cultured tissues. Therefore, the irradiated tissues were compared like-for-like with the non-irradiated tissues, which were maintained in the device for same time length.

2.9. Immunohistochemical (IHC) staining of frozen tissue sections

IHC staining is a method that detects the presence and location of proteins of interest in tissue sections using antibodies which specifically detect the protein (AbD Serotec, 2016). Tissue was sectioned as described in section 2.7 and the sections were then fixed in cooled 100% methanol for 20 minutes and rinsed with tris-buffered saline (TBS; section 9.3) for 5 minutes. Endogenous peroxidase activity of the tissue was then quenched by placing the sections in 3% (v/v) hydrogen peroxide (Sigma-Aldrich, UK; 30% diluted in methanol) for 15 minutes before being rinsed for 2 minutes under running tap water. The slides were then attached to Sequenza immunostaining coverplate (ThermoFisher Scientific, UK) and clipped in their racks. Sequenza Immunostaining racks provides a cost-effective IHC system with several advantages such as consistent high quality staining, considerable time saving, substantial reagent saving (use only 100µl of reagents), and protects tissue specimens from drying (Thermo Scientific, 2015).

Non-specific binding sites on the tissue sections were then blocked with normal horse serum (Vector Laboratories, Burlingame, CA) for 20 minutes which is identical to the host-animal of secondary antibody. Avidin and Biotin binding sites were then blocked by adding both an avidin and a biotin solution (Vector, Avidin Biotin blocking kit) separately for 15 minutes each with three washes of TBS in between. The tissue sections were then incubated with 100µL of the appropriate dilution of primary antibody

for one hour at room temperature. At the same time, a negative control section was incubated with a matched isotype control antibody to detect any non-specific binding of the secondary antibody and subsequent detection reagents. This antibody has no specific interaction but has the same isotype as the primary antibody. The sections were rinsed three times in TBS and incubated with biotinylated secondary antibody (horse anti-mouse; Vector laboratories; Figure 2.11) and normal horse serum for 30 minutes. During the incubation, the streptavidin complex was prepared by adding exactly two drops of reagent A and two drops of reagent B (Vectorstain Elite Kit) to 5mL of TBS, and this was allowed to sit for 30 minutes.

Following at least three washes with TBS, the horseradish peroxidase-conjugated streptavidin complex was added to each section (Vector laboratories) for a further 30 minutes at room temperature. After that, the slides were disassembled from the Sequenza rack and the sections were dried and then the sample was isolated with a wax pen before 100µL 3, 3' –diamobenzidine (DAB; Sigma-Aldrich, UK) was added to all tissue sections and incubated for 5 minutes, or until sufficient brown colour had developed. Following approximately 2 minutes of washing under running tap water, the tissue sections were counterstained in filtered Harris haematoxylin for 20 seconds, rinsed in running tap water and dehydrated in a serial graded alcohol and Histoclear II, as shown in the dehydrating procedures in section 2.8. Harris haematoxylin was used as a counterstain which gives good contrast of nuclei without cytoplasmic staining (McGinley *et al*., 2000). Finally, the slide was mounted using Histomount (National Diagnostics, UK) and covered with glass coverslips (Fisherbrand, UK), as described in section 2.8.

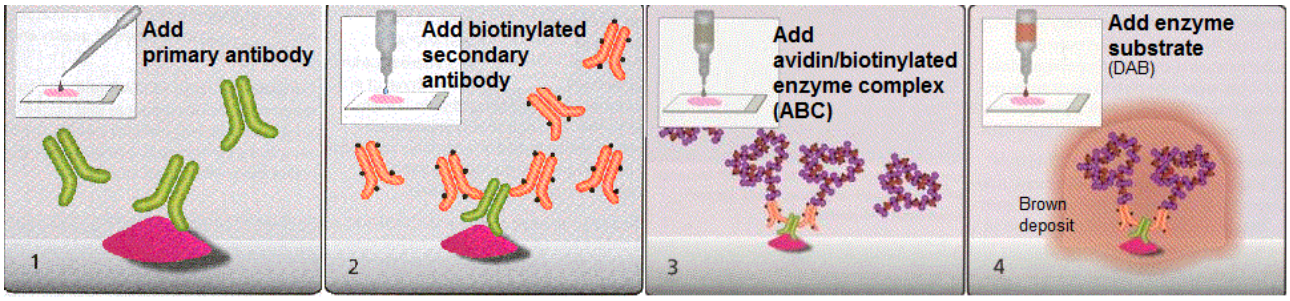


Figure 2.11. Vectorstain ABC immunoperoxidase staining procedure.
(Adapted from Meiring *et al*., 2011).
Abbreviation: DAB: 3, 3' –diamobenzidine.

2.10. M30 CytoDeath^{TM} ELISA on microfluidic effluent.

The M30 CytoDeath^{TM} ELISA is a solid-phase sandwich enzyme immunoassay (Figure 2.12). It quantitatively measures the level of apoptosis occurring, within the tissue biopsy being maintained in the microfluidic device, by determining the concentration of cleaved cytokeratin in the effluent. The M30 CytoDeath^{TM} ELISA kit (PEVIVA, Tewkesbury, UK) is based on a 96-well plate format and was operated according to manufacturer's instructions (PEVIVA, 2011). The detection limit of the M30 CytoDeath^{TM} ELISA kit was 60U/L which is calculated as the zero standard plus three standard deviations.

Effluent medium collected from microfluidic culture was stored at -80°C, and was brought to room temperature prior to M30 ELISA analysis. Each effluent was vortexed to ensure thorough mixing and samples were added in duplicate (25µL/well) to corresponding wells of a 96-well plate (Table 2.5), alongside a set of standards [0 U/L (Zero), 250 U/L (Low), 1 000 U/L (Medium) and 3 000 U/L (High)] and a medium only blank. The wells of the 96 well plate were pre-coated with a mouse monoclonal anti-cytokeratin antibody (M6) that binds specifically to a distinct epitope on CK18 (Cummings *et al*., 2006). Immediately following the addition of samples and standards, 75µl of M30 Cytodeath^{TM} horseradish peroxidase (HRP) conjugate, provided in the kit, was added into each well; this reagent is a second anti-CK18 antibody (Figure 2.12).

Table 2.5. Example of M30 ELISA protocol map on plate reader.

Blank	Blank	T	T	T	T	T	T	T	T	T	T
Std 62.5U/l	Std 62.5U/l	T	T	T	T	T	T	T	T	T	T
Std 125 U/l	Std 125 U/l	T	T	T	T	T	T	T	T	T	T
Std 250 U/l	Std 250 U/l	T	T	T	T	T	T	T	T	T	T
Std 500 U/l	Std 500 U/l	T	T	T	T	T	T	T	T	T	T
Std 1000 U/l	Std 1000 U/l	T	T	T	T	T	T	T	T	T	T
Std 1500 U/l	Std 1500 U/l	T	T	T	T	T	T	T	T	T	T
Std 3000 U/l	Std 3000 U/l	T	T	T	T	T	T	T	T	T	T

Std: known concentration standard, T: test sample.

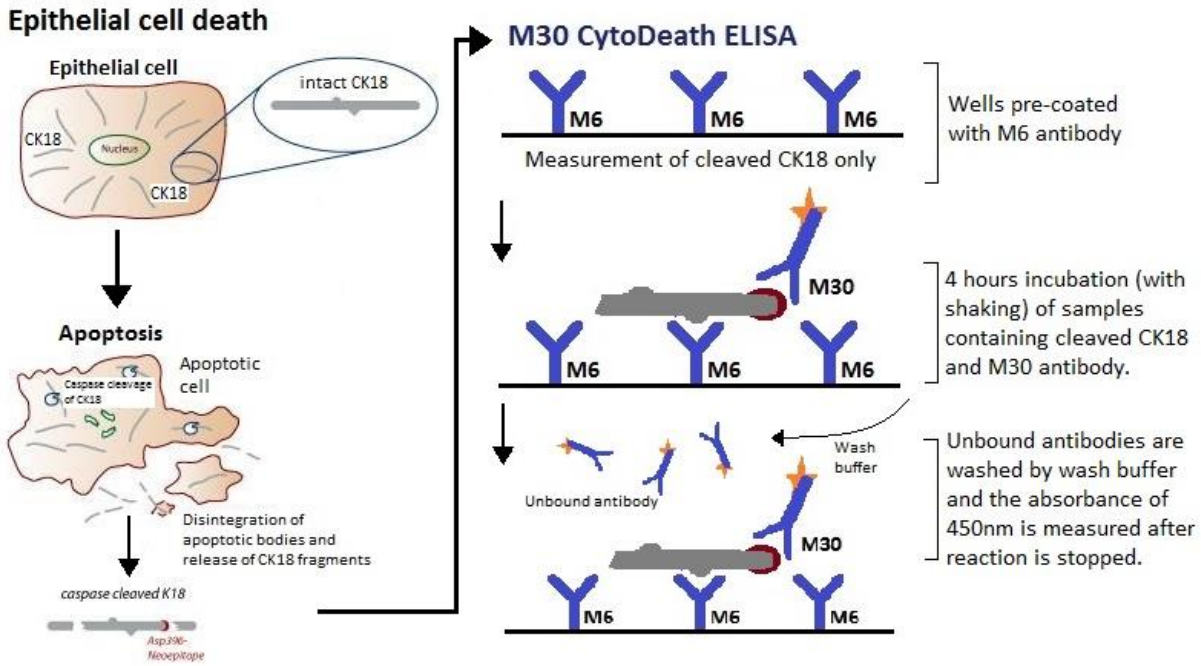


Figure 2.12. **A diagrammatic representation of the steps involved in the M30 CytoDeath™ ELISA.** (modified from PEVIVA, 2011).

The plate was covered and incubated on a shaker at 600rpm for 4 hours at room temperature to allow the mobilisation of antibodies of the conjugated reagents in the well. After the incubation, excess unbound conjugate was removed by washing each well five times with wash solution (400µL; provided in the kit) using a plate washer. Colour development was achieved by adding 200µL of 3, 3', 5, 5'-tetramethyl-benzidine (TMB; provided in the kit) solution to each well for 20 minutes in the dark and the reaction was stopped by adding 50µL of 1.0M sulphuric acid. The plate was shaken for 5-10 seconds prior to determining the absorbance at 450nm in a microplate reader (Multiskan FC microplate photometer, ThermoFisher Scientific, UK). The average absorbance value from duplicate values of each sample and standard was obtained and the average absorbance value of the medium only blank was deducted from each reading. A linear standard curve of the known concentrations of M30 antigen standards versus absorbance was plotted (Figure 2.13) and unknown concentrations determined using the equation of the curve.

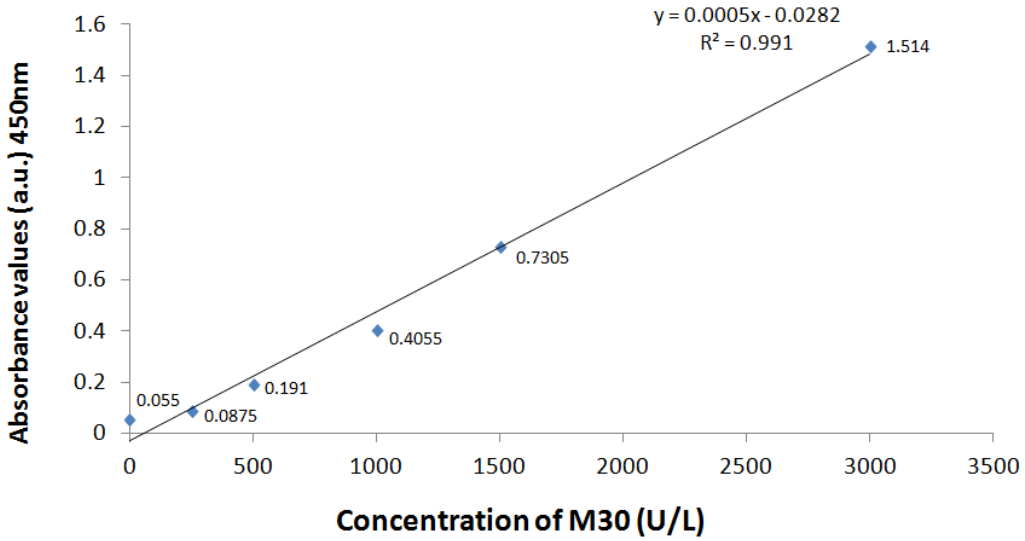


Figure 2.13. **Example of linear standard curve created for M30 ELISA analyses.**
The graph shows the standard curve of absorbance values (a.u.) in 450nm versus concentration of M30 in U/L. The absorbance values of eight standards with known concentration (zero, 62.5, 125, 250, 500, 1000, 1500 and 3000 U/L) were measured in duplicate.

2.11. Apoptosis detection on tissue sections using the TUNEL assay

The terminal deoxynucleotidyl transferase (TdT) - mediated dUTP nick end labelling (TUNEL) assay is a method used to detect apoptosis based on the labelling of DNA strand breaks (Loo, 2002). During apoptosis, the cleavage of genomic DNA may yield double stranded or single stranded breaks (called 'nicks'). The strand breaks can be identified by labelling the free 3'-OH terminal ends with modified nucleotides in an enzymatic reaction (Loo, 2002; Figure 2.14).

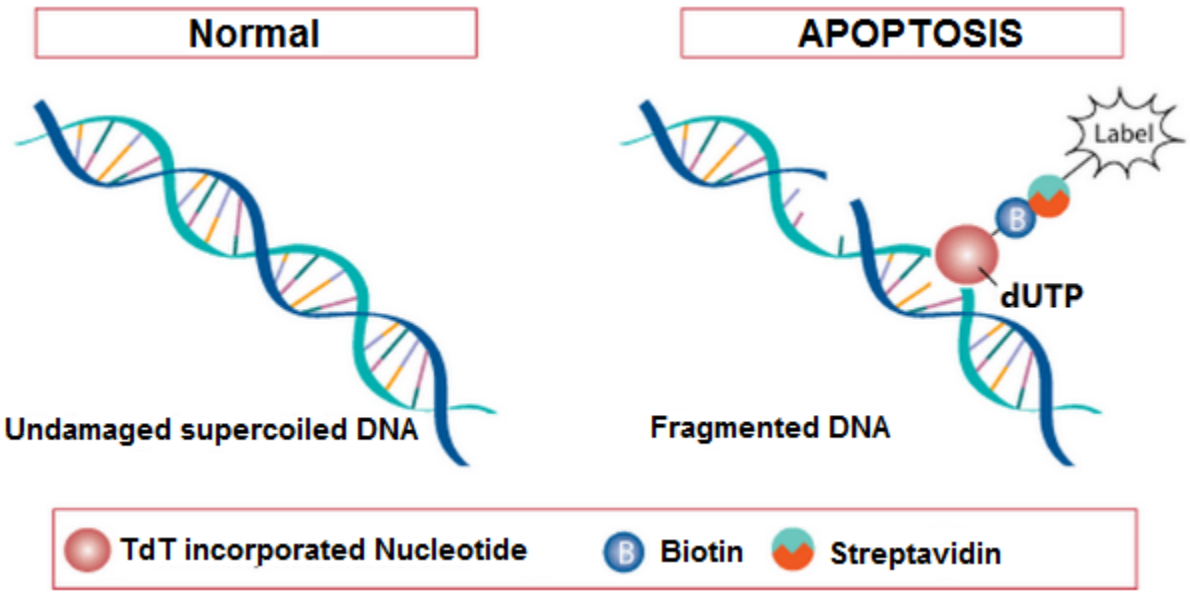


Figure 2.14. Detection of fragmented DNA appeared in apoptosis by terminal deoxynucleotidyl transferase (TdT)-mediated dUTP nick end labelling.
(modified from R&D systems a biotechne brand, 2015). Fluorescein-12- 2'-deoxyuridine 5'-triphosphate (dUTP) at 3'-OH DNA ends by using TdT enzyme which forms a polymeric tail that can be visualized by fluorescence microscope.

Frozen tissue sections (at thickness of 8µm; section 2.7) were fixed in 4% paraformaldehyde in phosphate buffered saline (PBS) pH 7.4 for 20 minutes at room temperature (general TUNEL protocol described from Loo, 2002). Following the fixation, the sections were washed with PBS for 30minutes, followed by 2 minutes of permeabilisation on ice in permeabilisation solution (0.1% of Triton-x100 and 0.1% of sodium citrate). The slides were then rinsed twice in PBS and 100 µl of TdT enzyme and dUTP conjugate [conjugated to fluorescein isothiocyanate (FITC)] were added to the tissue sections according to the manufacturer's specifications (Roche, UK) and incubated in a humidified box at 37˚C for one hour in the dark to prevent photo-bleaching of the fluorescent markers. Tissue sections that were not subjected to microfluidic perfusion or irradiation were used for both positive and negative controls. Positive controls were pretreated with 3000U/L DNase (Roche, UK) for 10 minutes at room temperature which induces DNA strand degradation while negative controls were incubated without the TdT enzyme.

The slides were rinsed three times in PBS following the one-hour enzyme incubation and finally mounted with a coverslip (Fisherbrand, UK) using Vectashield® hardest mounting medium containing 4',6-diamidino-2-phenylindole (DAPI; Vector Laboratories Inc, Peterbrough, UK) which counterstained nuclei in the tissue sections. Specimens were then examined and photographed on a fluorescence microscope. Both DAPI and FITC filters were captured on all magnification fields and the exposure time for DAPI filter was set to 250ms while FITC filter was adjusted to 1000ms exposure time (ZEN 2012; blue edition). The contrast and brightness of the captured images were adjusted by using ZEN 2012 software in order to reduce the background staining with minimal impact on the positive staining. The DAPI and FITC staining on each field were counted and measured by Image-Pro Premier software (Media Cybernetics).

2.12. Incorporation of fluorescent markers into HNSCC tissue maintained in microfluidic device

The incorporation of caspase inhibitor (CaspACE FITC-VAD-FMK), 2-NBDG (2-(*N*-(7-Nitrobenz-2-oxa-1,3-diazol-4-yl)Amino)-2-Deoxyglucose), EdU (5-ethylnyl-2'-deoxyuridine), and FITC-dextran (fluorescein isothiocyanate-dextran) markers into HNSCC tissue were investigated as measures of apoptosis, metabolism and proliferation. Tissues were cultured in microfluidic devices (section 2.2) and perfused

with medium containing each marker for a fixed time period. Tissues were then sectioned (8µm; section 2.7) in the dark before being fixed in 4% w/v paraformaldehyde for 20 minutes. The sections were washed three times in PBS, mounted in hardest mounting medium containing DAPI and viewed using a fluorescent microscope (Nikon E800). The entire procedure was carried out in the dark to prevent photo-bleaching on the fluorescent markers.

2.12.1 Apoptosis detection following incorporation of CaspACE FITC-VAD-FMK.

Caspase inhibitor (CaspACE FITC-VAD-FMK), is a fluorescent apoptosis marker [fluorescent analogue of the pan caspase inhibitor Z-VAD-FMK (carbobenzoxy-valyl-alanyl-aspartyl-[O-methyl]-fluoromethylketone)] which irreversibly binds to activated caspases in the tissue biopsy allowing the total number of apoptotic cells to be identified using fluorescent microscopy (Promega, 2013).

The apoptosis inducer, etoposide (10µM; Sigma-aldrich, UK) was added to at least one of the tissues on the microfluidic device in order to induce maximum apoptosis to act as a positive control for the uptake of CaspACE marker into the tissue, CaspACE FITC-VAD-FMK (10µM) was added to all devices for the final two hours of microfluidic culture before snap freezing in embedding medium in the dark.

2.12.2 Incorporation of 2-NBDG to study glucose metabolism

The incorporation of 2-NBDG (2-(*N*-(7-Nitrobenz-2-oxa-1,3-diazol-4-yl)Amino)-2-Deoxyglucose) into oropharyngeal cells (UMSCC-47) and HNSCC tissues was investigated. 2-NBDG is a fluorescent glucose analogue which was used to monitor glucose uptake in living cells, allowing the study of cell viability (Cayman Chemical, 2015). Tissue biopsies were cultured in the device for a minimum of 24 hours and medium containing 0.05mg/mL of 2-NBDG was added for 1 hour in the dark prior to snap freezing (section 2.3).

2.12.3 Detection of proliferating cells using EdU

The incorporation of the thymidine analogue EdU (5-ethylnyl-2'-deoxyuridine) into the DNA of replicating cells is based on the same principle as that of BrdU (5-bromo-2'-deoxyuridine; section 3.2 and 5.1.1.1; BioSpotlight, 2008). It directly measures *de novo* DNA synthesis and cells undergoing s-phase of the cell cycle by a 'click' reaction between ethynyl moiety in EdU and the small azide-modified fluorescent dye which is catalysed by copper (I) catalyst (Figure 2.15).

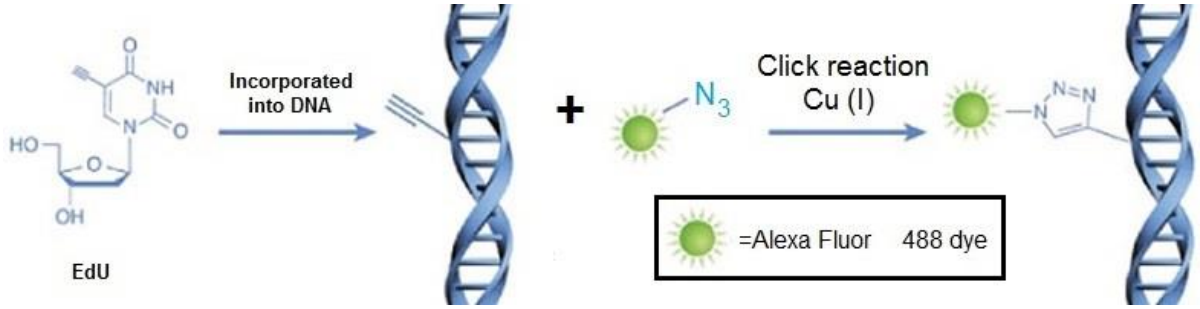


Figure 2.15. The mechanism of incorporation of fluorescent (Alexa Fluor 488)-conjugated 5-ethylnyl-2'-deoxyuridine (EdU) into proliferating cells.
The cells that undergoing s-phase cell cycle were detected by using the 'click chemistry' reaction (BioSpotlight, 2008).

The test samples were incubated with 10µM of EdU and the incorporated EdU in the replicating cells was then detected by using the manufacturer's protocol (Click-iT ® EdU Alexa Fluor ® 488 Imaging Kit; C10337; ThermoFisher Scientific, UK). Following cells and tissues fixation by using 4% w/v of paraformaldehyde dissolved in PBS for 20 minutes, the samples were then incubated with a reaction cocktail that contained Click-iT Alexa Fluor 488 azide for 30 minutes at room temperature in the dark. The samples were then washed three times with PBS and mounted on a glass slide. Nuclei with incorporated EdU marker were viewed and captured using a fluorescent microscope (Nikon E800) within two days to avoid photo-bleaching of the fluorescence markers.

2.12.4 Incorporation of FITC-dextran to study glucose metabolism

FITC-conjugated dextran (4kDa) was added to HNSCC tissues maintained in the microfluidic device in order to investigate the permeation ability of the marker into the tissue. The size of 4kDa was chosen as this was bigger than the largest molecule among others that were added into the culture medium, which is fungizone with 1339.84g/mol. Dextran is a polymer of anhydroglucose and contains about 95% of alpha-D-linkages. The remaining linkages contribute to the branching of dextran. Lower molecular weight dextrans (2-10kDa) have less branching and have the properties of an expandable coil, allowing cell permeability research. Dalton is the mass of individual atomic entities while g/mol is the mass of one more of the entities in which the conversion of Daltons to g/mol is multiply by one. To determine the ability of markers with different size to perfuse into entire tissue, FITC-dextran at size of 4,000 Da was much higher than the MW of other markers (2-NBDG has 342.26g/mol; EdU has 252.23g/mol and BrdU has 307.1g/mol) and was selected as the most suitable size of the marker. FITC-dextran (1mg/mL) in glucose free medium was used to

perfuse tissue for either 30 minutes or 2 hours, following perfusion with complete DMEM for 24 hours and a 'starvation' period of up to 2 hours in glucose free medium.

2.13. Laser capture microdissection (LCM)

2.13.1 Sample preparation

Frozen tissue (-80°) was cryosectioned (section 2.7) at 8µm thickness using a new microtome blade each time to prevent cross-contamination between different tissues. Arcturus ® polyethylene naphthalate (PEN) membrane glass slides (LifeTechnologies, Germany) were used to capture the sections as recommended (Carl Zeiss MicroImaging GmbH, 2008). The membrane facilitates the laser cutting process in which the membrane will be cut together with the tissue, serving as a stabilizing 'backbone' during lifting process (Datta *et al*., 2015). The slide was pre-cooled to -20ºC in the cryotome and the reverse side of the slide was touched with a gloved finger to only warm the specific region to accommodate the tissue (Carl Zeiss MicroImaging GmbH, 2008). The sectioned tissue was transferred to the slide from the blade by touching the warmed area of the slide onto the tissue. The sections were air dried at -20ºC for 2-3 minutes prior to H&E staining (section 2.8) modified using a protocol provided by Carl Zeiss microscopy to maximize RNA yield.

Briefly, sections were dehydrated in ice-cold 70% ethanol for 1 minute and dipped into RNase-free water 5-6 times to remove OCT embedding medium. The slides were then placed in filtered Harris Haematoxylin (Sigma-aldrich, UK) for 1 minute and rinsed in diethylpyrocarbonate (DEPC)-treated water (Fisher BioReagents, New Jersey, US) before transfer into 1% w/v eosin (Eosin Y in distilled water; Sigma-aldrich, UK) for 10 seconds followed by dehydration in serially graded alcohols (70%, 95% and 100%), for 30 seconds each. The dehydrated sections were allowed to air-dry for 20-30 seconds before being subjected to LCM. All the reagents were prepared using DEPC treated water and the work bench surface, all glassware, plastic surfaces, pipettes and pipette tip boxes were wiped with RNaseZAP to remove RNases (Life Technologies). In addition, all the plastic wares used, including collection tubes, were pre-soaked in 0.1% DEPC water overnight at room temperature before being autoclaved and dried at 50-80°C to remove RNases. On the serial sections of the corresponding tissue, IHC staining by using monoclonal mouse anti-human cytokeratin (CK) antibody (1.16mg/mL; Clone MNF116, Dako, Produktionsvej, Denmark) was carried out in order to ease the identification on the location of tumour cells on the H&E stained tissue

section. The IHC staining was performed according to section 2.9 and the staining was photographed at x100 magnification fields and tiled to obtain the full section view, e.g. Figure 2.16.

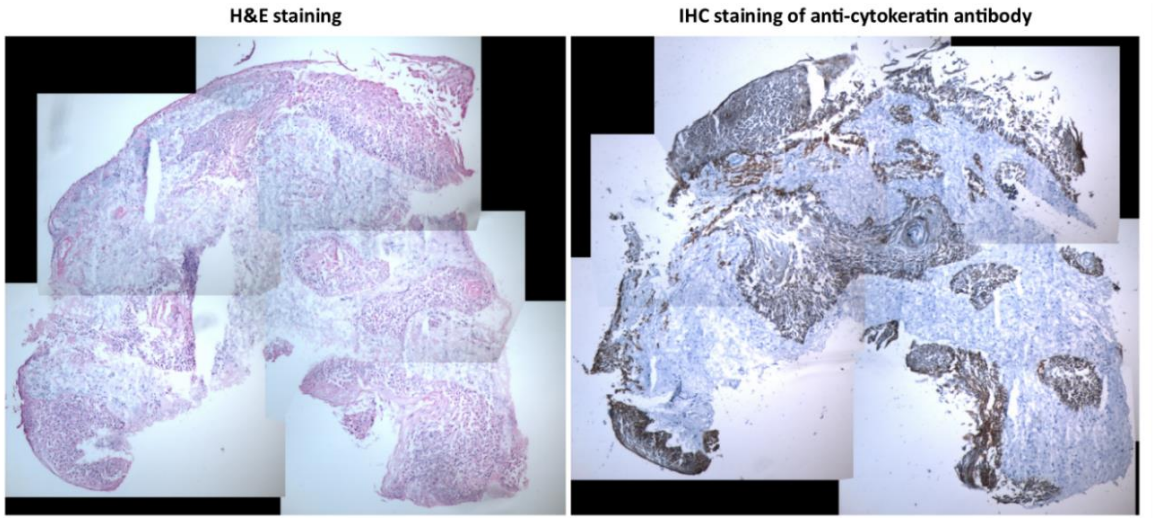


Figure 2.16. H&E staining and IHC staining by using mouse monoclonal anti-cytokeratin antibody (Dako, Denmark) on serially cut tissue sections of oral cavity floor of mouth tissue which subjected to microfluidics with no irradiation.
The staining was photographed at x100 magnification and tiled to make full section view.

2.13.2 Laser capture microdissection (LCM)

The air-dried sections were immediately placed on the LCM microscope (Zeiss, Axiovert 200) platform (Figure 2.17.A) and 50µL of lysis buffer (RLT buffer supplied in RNeasy Micro Kit containing 1% of β-Mercaptoethanol) was added into the DEPC treated collection tube cap. The collection tube containing buffer was clipped on the microscope (Figure 2.17.B) and placed upside down so that the lid was just above the target tissue section (Figure 2.17.C).

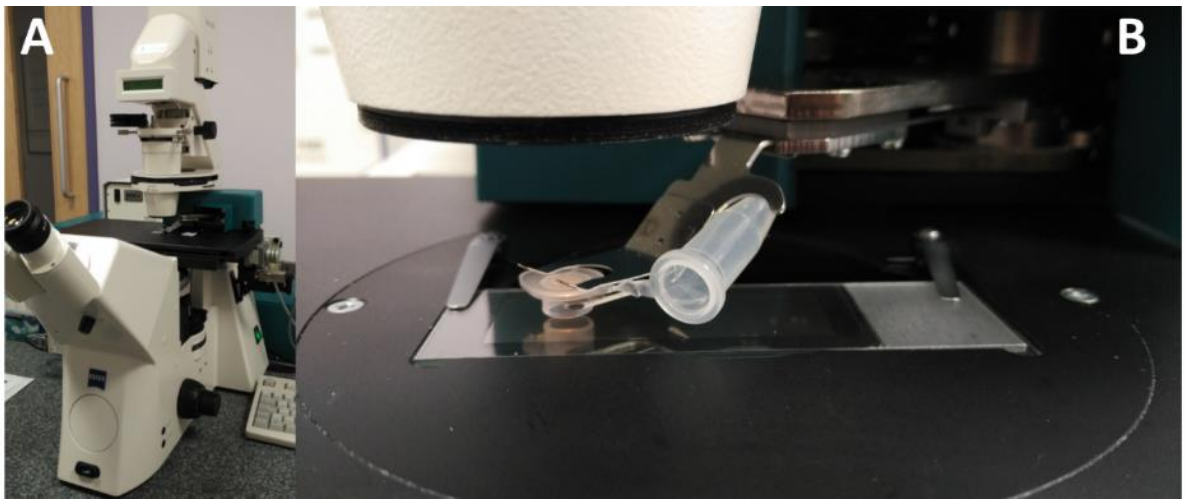


Figure 2.17. LCM set up.
(A) LCM microscope (Zeiss Axiovert 200). (B) Collection tube held in place with lid, containing lysis buffer, held directly above the target tissue section. Arcturus ® polyethylene naphthalate (PEN) membrane glass slide was used and placed on LCM microscope platform with two clips fixing the slide position.

PALM Software (PALM ® Microbeam) was used to select the target cell area for microdissection at x50 and x400 magnification. The selected cell area was laser cut and catapulted into the lysis buffer held in the microfuge cap using the pre-set laser energy (80-95) and laser focus (62-73; Figure 2.18). The highly denaturing lysis buffer functioned to inactivate the RNases and other proteins, preventing RNA degradation as well as the downregulation or upregulation of transcripts (Qiagen, 2014). The entire microdissection of tissue sections on one glass slide was carried out as quickly as possible, about 1 hour, to preserve the RNA integrity. It has also been demonstrated that the total time required to carry out LCM protocol for downstream applications (such as DNA genotyping, RNA transcript profiling and cDNA library generation) is typically 1 to 1.5 hour (Espina *et al*., 2006). When collection was complete, the tube was removed from the holder and an additional 300µL of lysis buffer was added to the tube, vigorously mixed and incubated upside down for a further 30 minutes prior to RNA extraction.

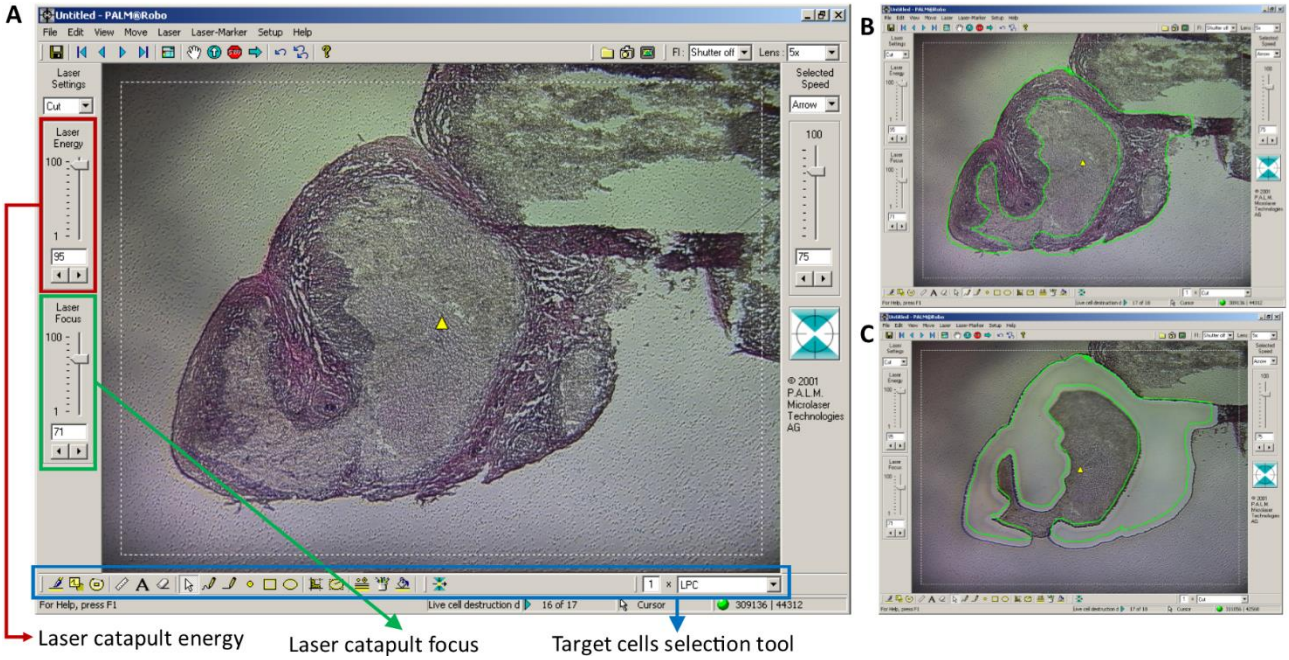


Figure 2.18. LCM software used for selection of target cells on an H&E stained tissue section. (A) The area of interest was identified using x50 magnification, (B) the target area (tumour) was selected and (C) the selected area was laser cut and catapulted into lysis buffer.

2.14. RNA extraction of laser-microdissected samples

RNA extraction from the cells in the microdissected from tissue sections was achieved using the RNeasy Micro Kit (Qiagen, Hilden, Germany). The lysate obtained from microdissection was centrifuged for 5 minutes at 10620xg in a microfuge and an equal volume of 70% of ethanol was added to the lysate. The mixture was triturated and

transferred to an RNeasy MinElute spin column fitted in a supplied 1.5mL collection tube. The sample was then centrifuged for 15s at over >8000 x g and the flow-through was discarded. A mixture of 10µL of DNase I stock solution and 70µL buffer RDD (supplied) was added to the spin column membrane and incubated at room temperature for 15 minutes. The buffer RDD is designed for on-column DNase digestion of 15 minutes and it is well-suited for efficient DNase digestion in solution. Buffer RW1 (350µL) was added to the spin column and centrifuged again (15s at over 8000xg), which contained guanidine salt and ethanol that used to wash membrane-bound RNA, remove biomolecules (carbohydrates, proteins and fatty acid). The flow-through and the collection tube was discarded and the spin column was transferred to a new 2mL collection tube before 500µL of RPE buffer was added to the spin column. This buffer serves as mild washing buffer, removing traces of salts which are still remained on the column. Centrifugation was repeated and flow through discarded again before the addition of 500µL of 80% ethanol to the spin column. The spin column was again transferred to a new 2mL of collection tube and centrifuged at full speed in a microfuge for 5 minutes to dry the membrane. The flow through was discarded and the column placed in a new 1.5mL collection tube and 14µL of RNase-free water was added directly to the centre of the spin column membrane. To elute the RNA the column was centrifuged for 1 minute at full speed (14800rpm; 16160xg) in a microfuge. The 1.2µL of RNA elute was aliquoted to 0.5µL microcentrifuge tube for the quantification of RNA level before the RNA elute was stored at -80°C. To measure the amount of RNA, the undiluted RNA elute (1.2µL) was inserted onto a cleaned nanodrop lite spectrophotometer (LT2654; ThermoFisher Scientific, UK). All nucleotides, RNA, single-strand DNA, and double-strand DNA absorb wavelength of 260nm which contribute to the total absorbance of the eluted sample (Thermo Scientific, 2008). The ratio of absorbance at 260nm and 280nm, therefore, was used to assess the purity of DNA and RNA on the nucleic acid samples. On each of the sample, the concentration of RNA, A260/A280 ratio and A280 were recorded. The A260/A280 ratio around 2 is accepted to be ‘pure’ for RNA. Lower ratio may indicate the existence of protein, phenol or other contaminants which absorb strongly at 280nm.

2.15. Reverse transcription, qualitative PCR and quantitative real-time polymerase chain reaction (qRT-PCR)

2.15.1 cDNA synthesis

Complementary DNA (cDNA) was synthesised by using the iScript advanced cDNA synthesis kit (Bio-Rad laboratories, California, USA). Each extracted RNA sample (15µL) was mixed with 4µL of reaction mix containing deoxynucleotide triphosphates (dNTPs), oligo (dT) and random primers and 1µL of reverse transcriptase. The RNA samples were reverse transcribed by incubating the mixture at 42ºC for 30 minutes. The reverse transcription was then inactivated at 85ºC for 5 minutes and the cDNA stored at -20ºC for subsequent polymerase chain reactions (PCR; either qualitative PCR or quantitative RT-PCR).

2.15.2 Qualitative PCR analysis

Qualitative PCR is widely carried out to amplify small amounts of genetic material which involves denaturation, annealing and extension steps. For successful PCR reactions, good primer design is essential to achieve high amplification yield. The target amplicon length near to 500 base pairs (bp), 18-22 bp optimal length of PCR primer and 40-60% of GC content of the primer were taken in careful consideration when choosing and designing suitable primer pairs for Homo sapiens glyceraldehyde-3-phosphate dehydrogenase (GAPDH) gene using NCBI website (Figure 2.19; Dieffenbach, Lowe and Dveksler, 1993).

The reactions were carried out in 50µL reaction mixture containing 1µL of forward GAPDH primer (0.133µM) and 1µL of reverse GAPDH primer (0.125µM; Sigma-Aldrich, UK; Figure 2.19), 25µL of BioMix buffer solution (a complete ready to use 2x reaction mix with ultra-stable DNA polymerase; Bioline, London, UK), 23µL of nuclease-free water and 1µL of prepared cDNA. The thermocycler program (Techne Genius, Duxford Cambridge, UK) was set up to do an initial denaturation of 4 minutes at 95ºC followed by 35 cycles of denaturation at 95ºC for 30 seconds, primer annealing at 55ºC for 30 seconds and primer extension at 72ºC for 30 seconds. This was followed by a final extension for 10 minutes at 72ºC. The PCR products were visualized by using agarose gel electrophoresis.

Agarose gel was prepared and made by mixing 2.25g of agarose (Melford, Suffolk, UK) and 150mL of Tris-acetate-EDTA (TAE) buffer (section 9.4). The mixture was

heated in microwave for about 5 minutes with the lid off the bottle and swirled at every minutes to avoid the overflow of the heated solution. When the agarose was fully dissolved, the solution was cooled by swirling the bottle under running cold water. Midori Green (5µL; Midori Green Advance DNA stain, GeneFlow, Lichfield, UK), which is a nucleic acid stain to detect nucleic acid in agarose gel, was added into the agarose mixture before they were poured into the gel rig where comb was inserted. The hardened gel was placed in the buffer tank and covered with 1x TAE buffer (section 9.4). On a clean parafilm sheet, 3µl of 5x DNA loading buffer blue (Bioline, UK) was mixed with 12µl of PCR reaction mixture before the entire 15µL of mixture was loaded into each well. Alongside the PCR products, 5µl of molecular weight marker, HyperLadder ™ 1Kb (Bioline, UK) which gives 14 regularly spaced bands from 200bp to 10,037bp, was loaded into the first well. The gel electrophoresis (Bio-Rad Power PAC 300) was carried out at 280mV for approximately 30 minutes until the dye front had migrated and the different-sized DNA bands could be visualised. The bands on the gel were viewed and observed under UV illumination using the gel doc system (UVP Laboratory products, EPI Chem II Darkroom) and Image Acquisition and Analysis Software (Labworks 4.6, Media Cybernetics). The exposure time was set in the range 2ms to 8ms and the PCR amplification products on the gel were captured for semi-quantitative measurement.

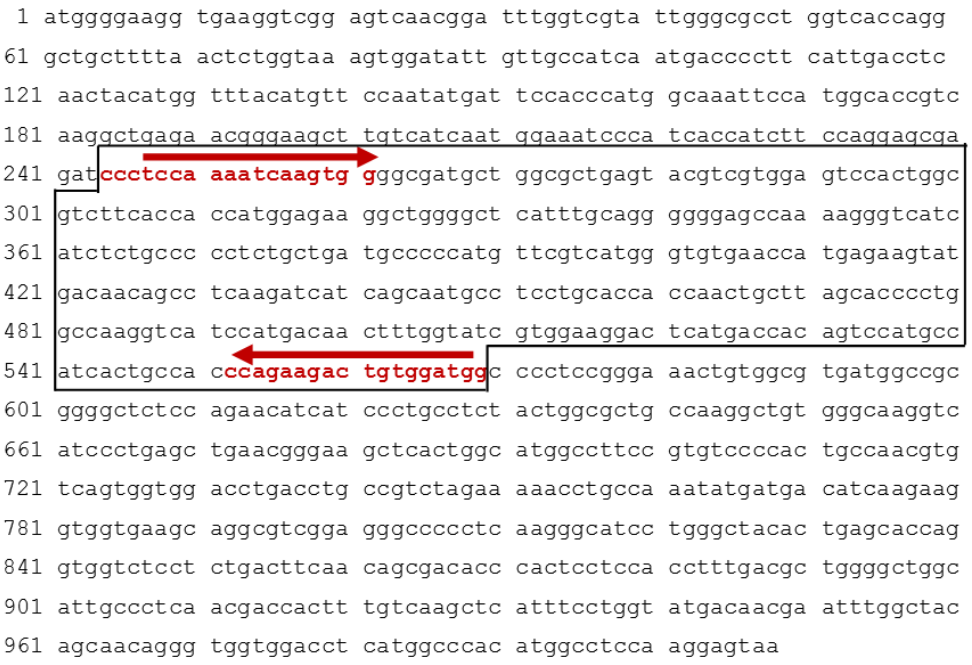


Figure 2.19. Gene of GAPDH and the primers used to amplify the target gene sequence (at size of 326 base pair).
Forward primer: GGGAGGTTTTAGTTCACC-3' (contains 50% of GC contents), Reverse primer 5'-CCATCCACAGTCTTCTGG-3' (contains 55.5% of GC contents)

2.15.3 Quantitative real-time PCR analysis

Quantitative real-time-PCR reactions were carried out using TaqMan Fast Advanced Master Mix (Applied Biosystems, California, USA) using StepOnePlus system on fast mode. Due to the different amount of RNA extracted on each sample and the synthesis of corresponding cDNA (assuming the synthesis of cDNA from RNA is in 100% efficiency), the amount of RNA or cDNA input was standardised to the same concentration by diluting the sample in nuclease-free water. The reactions were performed by adding 9µL prepared cDNA (prepared and standardised using nuclease-free water) to each well of a 96-well PCR plate, followed by 11µl of reaction mix (10µL 2X TaqMan fast advanced master mix, 1µL (20X) TaqMan gene expression assay and 1µL (20X) of gene expression assay (Table 2.6). The procedure of the qRT-PCR was carried out according to manufacturer's protocol (Applied Biosystems by Life technologies, 2011). Microamp fast 96-well reaction plate (Applied Biosystems, California, USA) was used for Applied Biosystems ® Fast PCR systems which reduces the PCR reaction time from 2 hours to approximately 30 minutes. The design of this plate, which has consistent well-to-well thickness, increases the thermal contact with the Applied Biosystems ® Thermal Cycler (Applied Biosystems, USA), providing maximum thermal conductivity for precise thermal cycling, reproducible and sensitive results in short period of time (ThermoFisher Scientific, 2015).

The expression of individual gene was tested on each sample in triplicates. Optical adhesive covers (Applied Biosystems, USA) were used to carefully cover each well and the reaction was mixed and centrifuged in a PCR plate spinner (Labnet International, New Jersey, US) prior to RT-PCR reactions. The thermocycler program of the StepOnePlus ™ Real-Time PCR system (Applied Biosystems, USA) was set up to perform a polymerase activation at 95ºC for 20 seconds followed by 40 cycles of denaturation at 95ºC for 1 second and primer annealing and extension at 60ºC for 20 seconds. The expression data of the target genes and sample names on each well, including the corresponding gene reporters (VIC and FAM), the cycle threshold (C_T) values and the record of amplification failure, were recorded and saved from the PCR system.

Table 2.6. Gene expression assays detecting different genes by using TaqMan Fast Advanced Master Mix

Name of target gene		UniGene	Amplicon length
Cyclin-dependent kinase inhibitor 1A (CDKN1A, p21)	CDKN1A	Hs370771	66
Target gene sequence: GACAGATTTCTACCACTCCAAACGCCGGCTGATCTTCTCCAAGAGGAAGCCCTAATCCGCCCACAG			
BCL2-associated X protein	BAX	Hs624291	62
Target gene sequence: GCCCTGTGCACCAAGGTGCCGGAACTGATCAGAACCATCATGGGCTGGACATTGGACTTCCT			
Ataxia telangiectasia mutated	ATM	Hs.367437	74
Target gene sequence: AAGAAAGAAGTTGAGAAATTTAAGCGCCTGATTCGAGATCCTGAAACAATTAAACATCTAGATCGGCATTCAGA			
Excision repair cross-complementing rodent repair deficiency, complementation group 1	ERCC1	Hs435981	55
Target gene sequence: CCTCCGCTACCACAACCTGCACCCAGACTACATCCATGGGCGGCTGCAGAGCCTG			
X-ray repair complementing defective repair in Chinese hamster cells 1	XRCC1	Hs98493	75
Target gene sequence: TCCCCCTTTGGCTTGAGTTTTGTACGGTTTCATAGCCCCCCAGACAAAGATGAGGCAGAGGCCCCGTCCCAGAAG			
H2A histone family, member X	H2AFX	Hs477879	48
Target gene sequence: AGCCGCTTCAGACTGCGGGGCAAGCGGGCCGCGGCTCCCTTCCCCTCC			
Beta-2-microglobulin (House-keeping gene)	B2M	Hs534255	81
Target gene sequence: GGAGGTTTGAAGATGCCGCATTTGGATTGGATGAATTCCAAATTCTGCTTGCTTGCTTTTTAATATTGATATGCTTATACA			

(Applied Biosystems, California, USA). The primer sequences targeted for each gene expression assay were confidential from manufacturer. The commercialised Taqman gene expression assays purchased for current qRT-PCR experiments were validated by the manufacture.

2.16. Statistical analyses

The majority of the optimisation experiments (both rat liver tissues and HNSCC tumour samples; Chapter 3) were described qualitatively, due to the low number of repeats for each individual parameter (e.g. different serum concentration, addition of rat serum, addition of HEPES buffer, culture medium gassed with carbogen gas mixture and addition of human AB serum; n=1 for each case).

The effect of etoposide on HNSCC cell lines was studied based on the cleaved cytokeratin 18 (CK18), phosphorylated H2AX (γH2AX), Bcl-2 and Ki-67 and expression levels were compared between the non-treated cells and the etoposide-treated cells using the Student's paired *t*-test. One-way analysis of variance (ANOVA) followed by Tukey post-Hoc multiple analyses was used to compare the CK-18 labelling index (section 4.5), percentage of cells positive to γH2AX (section 4.7), TUNEL (section 4.9), BrdU (section 5.2.1), Ki-67 (section 5.2.2) between the non-irradiated tissues and tissue samples from five patients treated with four different doses of irradiation. The expression levels of CK18-LI, γH2AX and Ki-67 between the two post-treatment time-points (6 hours vs 24 hours; section 4.3.1) and between fractionated dose irradiations (0Gy, 5x2Gy and 5x4Gy; section 4.5.2, 4.7.2 and 5.2.2) were not subjected to statistical analysis due to the limited number of repeats (n=1 on 6 hours post-treatment and fractionated-dose irradiation groups). The low number of repeats was due to the limited availability of the LINAC machine in a morning due to the busy treatment schedules for NHS patients.

3. Optimisation of conditions within the microfluidic system

Traditional *in vitro* tissue culture has widely been used to study the biological behaviour of head and neck cancer tissue in the response to different types of treatments (chemotherapeutic agents or ionizing radiation). These conventional methods, however, lack the complexity of the *in vivo* microenvironment often culturing single cell types which lack the biomimetic environment under these *in vitro* conditions (Cheah *et al*., 2010; Hattersley *et al*., 2012; Ma, Xu and Qin, 2013). This macroscale approach often requires large volumes of reagents (millilitres) throughout the experiment and does not allow for the real time monitoring of tissue behaviour (Chung *et al*., 2007). In addition, traditional cell culture methods typically involve the culture of cells in medium which is immobile in culture flasks or wells, with the medium only being replaced every few days, raising the risk of waste product accumulation and nutrient depletion (Hattersley *et al*., 2008), relying on the excess amounts of nutrients in the medium to feed the cells over a number of days (Halldorsson *et al*., 2015).

In order to address the limitations of traditional cell culture and develop a more *in vivo*-like model, different microfluidic devices were developed, in which small pieces of tissue which maintain their three-dimensional tissue architecture can be cultured under the continuous flow of medium [ovarian follicles (Desai *et al*., 2010); vascular study (Stroock *et al*., 2010; Zheng *et al*., 2012; Baranski *et al*., 2013); human lung organ (Huh *et al*., 2010)]. The continuous flow of the microfluidic system maintains the tissue by constantly supplying nutrients to and removing waste products from the tissue (section 1.4.2 and Table 1.8) and maintains the tissue so that all cells of the tumour microenvironment are kept in close proximity to each other allowing for cell-cell contact and local secretory pathways to be maintained. This technology allows the design of microchannel network with inherent comparable dimensions to the size of cells and blood vessels, and controllable laminar fluidic flow with ultralow volumes at microscale, mimicking the complex tumour microenvironment (Ma, Xu and Qin, 2013). Experiments were performed in order to compare traditional culture of tissue with that in the microfluidic device prior to its use for on-chip irradiation.

One such device is that developed by the Hull microreactor group, however, before HNSCC biopsies could be used in the microfluidic perfusion system, culture conditions were optimised. Rat liver was chosen to perform these optimisation experiments

because of its homogenous nature and uniform availability compared with the more diverse HNSCC tissue biopsies which were obtained from different head and neck cancer patients and were limited in number and size for optimisation experiments.

Various response parameters were investigated to evaluate the tissue behaviour under different conditions in microfluidic cultures, including the release of lactate dehydrogenase (LDH) enzyme as a measure of total cell death, morphological assessment based on haematoxylin and eosin staining (H&E staining) and 5-bromo-2'-deoxyuridine (BrdU) incorporation as a cellular proliferation indicator. The release of lactate dehydrogenase (LDH) into the effluent medium throughout the microfluidic flow enables the time-course measurement of the cell/tissue damage (Hattersley *et al*., 2008; Hattersley *et al*., 2012; Carr *et al*., 2014). H&E staining is widely used in medical diagnosis and pathological investigation on suspected cancer which allowing the study of morphological changes under different conditions and treatments (Onul *et al*., 2012).

Many cell cycle markers have been identified and are currently being used to study cellular proliferation, such as [3H]-thymidine, BrdU, 5-ethynyl-2'-deoxyuridine (EdU), and Ki-67 (Hassan *et al*., 2002; Millipore, 2010). Some markers are designed to incorporate into the DNA at different phases of the cell cycle (Figure 3.1; Millipore, 2010), for example, [3H]-thymidine, BrdU and EdU all incorporate into cells during the S-phase of the cells cycle (Figure 3.1; Millipore, 2010).

The traditional method to detect proliferating cells by using [3H]-thymidine incorporation is slow (autoradiography detection often lasts several months) and labour intensive and has limitations in the disposal and handling of radioactive materials, therefore the detection of incorporated BrdU using IHC was implemented (Salic and Mitchison, 2007; Hong and Ghosh, 2008; Millipore, 2010). In the 1950s, BrdU was introduced as a marker to target rapidly dividing cancer cells (Levkoff *et al*., 2008). It is a synthetic nucleoside analogue of thymidine that incorporates into the DNA of replicating cells during the S-phase of the cell cycle (Figure 3.1; Sakai *et al*., 2002; Hong and Ghosh, 2008; Millipore, 2010; Vega-avilla *et al*., 2011). The following detection of incorporated BrdU by using IHC staining allows the identification of proliferating cells in response to different parameters under microfluidic culture. Different parameters including length of culture in the device, flow rate of medium perfusion, oxygen tension, and different constituents of the culture medium (serum

concentrations and presence of [4-(2-hydroxyethyl)-1-piperazineethanesulfonic acid] HEPES buffer) were tested in order to develop optimal conditions to maintain HNSCC tissues in the microfluidic device.

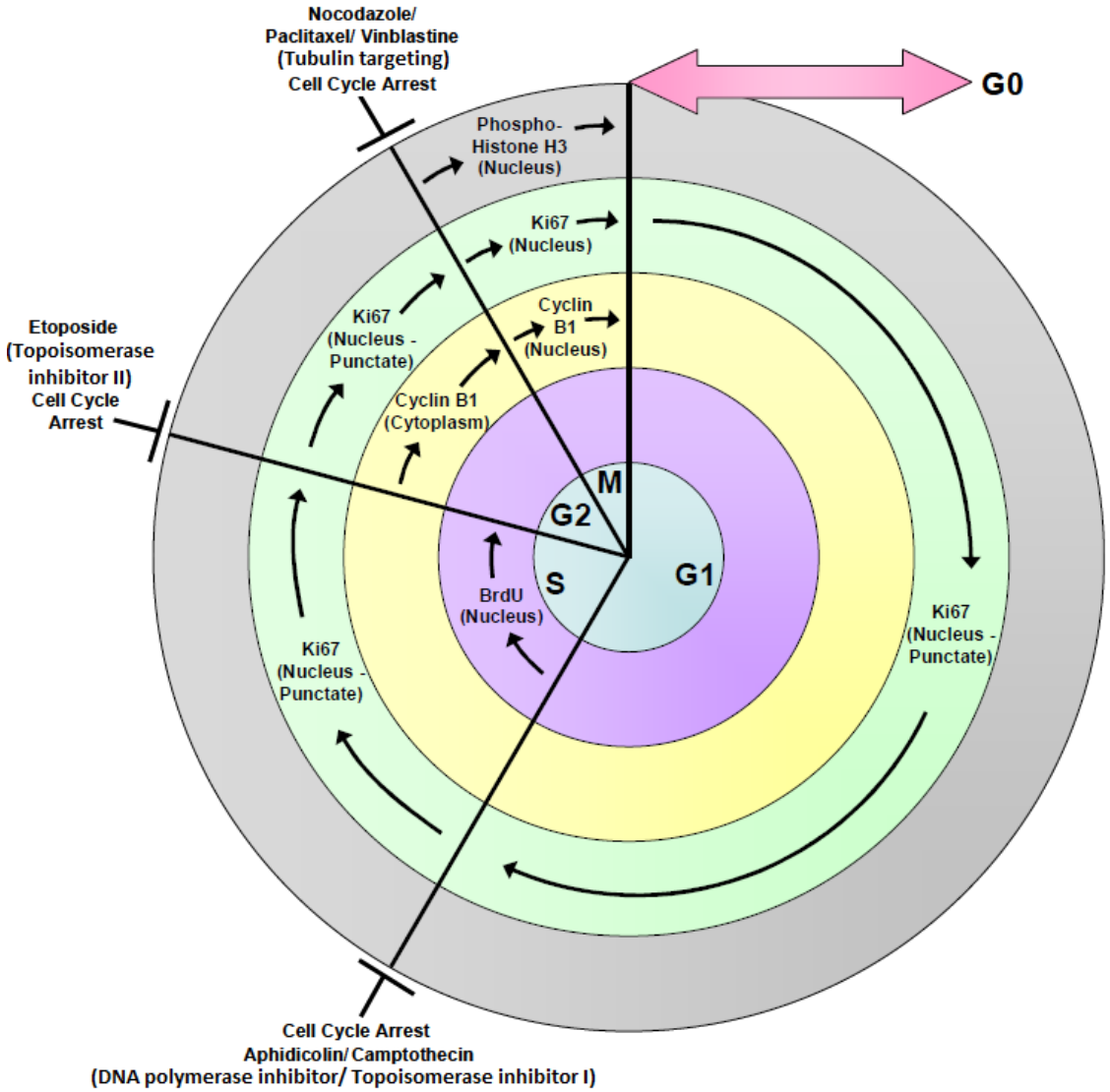


Figure 3.1. Eukaryotic cell cycle markers presented in different cell cycle phases.
Both EdU and [3H]-thymidine are also the markers presented in S-phase. The effects of drugs on different stages of cell cycle arrest were illustrated. G_0 and the left right arrow (pink) indicate the resting cell cycle phase in which no markers were detected at this phase (Millipore, 2010).
Abbreviations: BrdU: 5-bromo-2'-deoxyuridine.

3.1. Materials and methods of microfluidic device set-up

In this chapter, the optimisation of the microfluidic culture conditions was carried out by using frozen rat liver tissues before interrogating the human tumour tissues into the device. In total, 78 rat liver tissues were utilised: 32 tissues (R1) were subjected to traditional tissue culture (section 3.3) and 46 tissues were subjected to 46 microfluidic devices: 9 R1 tissues in section 3.4, 15 R2 tissues in section 3.5, 3 R2 tissues in

section 3.6, 3 R2 tissues in section 3.7, 3 R2 tissues in section 3.8, and 13 R2 tissues in section 3.9. Microfluidics set-up for tissue culture was carried out according to procedures described in section 2.3. Throughout the microfluidic flow, the effluent medium was collected from the outlet tubes every two hours throughout the day; but overnight and during the weekend in which the effluent was collected in 1.5mL microcentrifuge tubes and in a 15mL tube respectively. The effluent medium was aliquoted and stored at 4ºC for no longer than 7 days before being subjected to the LDH cytotoxicity assay according to manufacturer's protocol (LDH Cytotoxicity Detection Kit Plus; section 2.6). Following microfluidic perfusion, tissue was taken out, snap-frozen in OCT embedding medium and sectioned (section 2.7) before being stained with H&E for morphological assessment (section 2.8). The BrdU incorporation method was first optimised and the maintenance of tissue under traditional culture versus microfluidic device were compared.

3.2. Optimisation of BrdU incorporation and subsequent IHC staining

The BrdU pulse of 1 hour and 6 hours was tested initially on oropharyngeal cells (UMSCC-47) for comparative purposes. These two time points were selected based on various BrdU-proliferation studies, which have used different lengths of time for pulsing the cells with BrdU, depending on the proliferation status (Gasparri *et al*., 2004; Crane *et al*., 2011). The shorter BrdU-pulse time is required for actively proliferating cells, while a longer BrdU-pulse time (>4hours) is optimal for less actively proliferating cells (e.g. normal human dermal fibroblasts; Gasparri *et al*., 2004). It was unknown how actively the cells in the tumour biopsy would be proliferating, therefore, 1 hour and 6 hours BrdU pulse times were investigated.

Cells ($5x10^4$) were seeded respectively on four coverslips in 6-well-plate according to the culture methods described in section 2.1. Prior to cell fixation, two of the coverslips were incubated with 10µM of BrdU (BD Bioscience, Plymouth, UK) for 1 hour and another two were incubated with BrdU for 6 hours. Following the incubation, the cells were subjected to DNA denaturation (using 2M hydrochloric acid; HCl), neutralisation (using borate buffer; section 9.5) and immunocytochemical (ICC) staining by using anti-BrdU antibodies (0.01mg/mL; AbD Serotec, UK). The entire ICC staining was performed in the wells of 6-well-plate except the primary antibody incubation in which the primary antibody was pipetted on a clean sheet of parafilm and the coverslips were placed upside down on to the antibody droplet for one-hour antibody incubation.

Matched isotype control (IgG1; AbD Serotec, UK) at the same concentration with the primary antibody was added to two additional coverslips (1 hour and 6 hours) to serve as a negative control for the primary antibody. The stained and mounted coverslips were viewed and captured under microscope (Nikon E800). The total nucleus number and the positive stained nucleus over x400 magnification field were counted manually by using the Point or Multi-point function of ImageJ 1.48v (Java 1.6.0_20 64-bit). The percentage of each field was expressed by multiplying the ratio of positive nucleus over total nucleus number by 100 and the mean percentage of the BrdU incorporation over four x400 magnification fields was calculated (Figure 3.2). On each field, approximately 100-200 total cells were counted.

When all the UMSCC-47 cells were cultured in cell culture flask, the incorporation of BrdU into the S-phase cells was time dependent and was highest following 6 hours of BrdU pulse (65.9±3.4%), followed 1 hour of BrdU pulse which reached 36.7±4.2% (Figure 3.2). The useful feature of BrdU incorporation is its long-term retention in divided cells and the passage of incorporated BrdU to daughter cells (Kee *et al*., 2002). The high percentage of cells positive for BrdU incorporation after 6 hours of BrdU pulse-time could be due to the continuous cell division as the longer the time of BrdU incubation, the more cells enter S-phase.

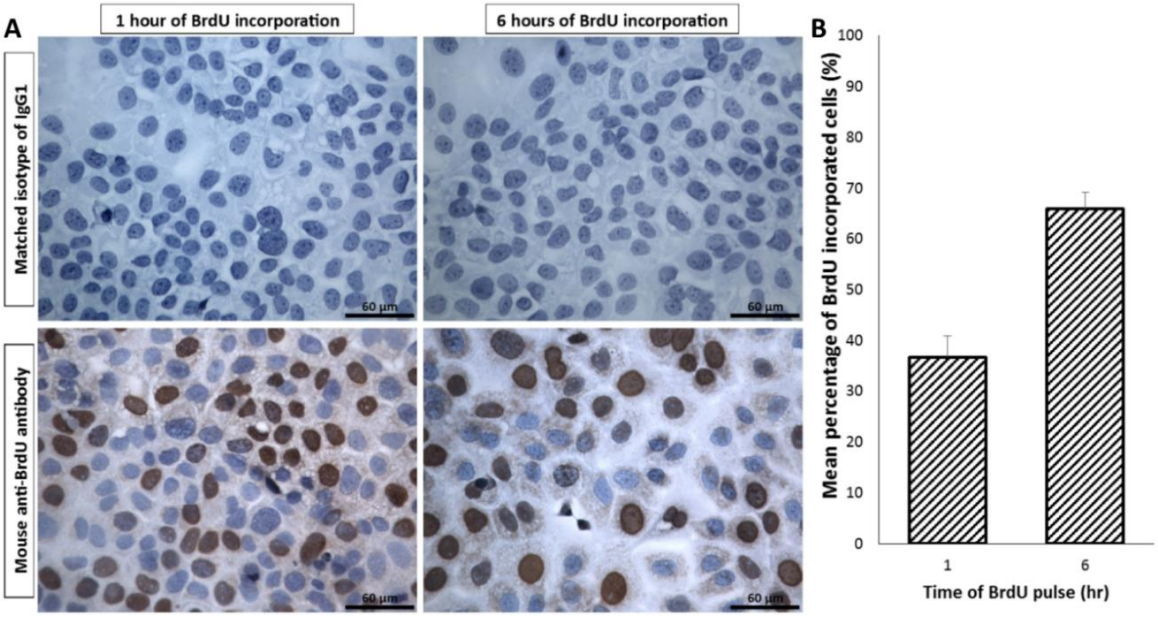


Figure 3.2. ICC staining of BrdU on oropharyngeal cells (UMSCC-47) and the corresponding image analysis.

(A) Representative ICC staining of BrdU on the cells cultured in total 48 hours in culture flask and 1 and 6 hours with BrdU before fixation (x400 magnification). Negative controls were included using matched isotype IgG1 antibody (Top row). Brown indicates the positive incorporation of BrdU into the cells in S-phase. (B) The mean percentage of cells positive to BrdU staining and the corresponding standard error of mean were calculated from four x400 magnification fields; percentage of positive staining over total nucleus number was obtained on each field.

Cells in the late mitosis (anaphase and telophase) were evident at x400 magnification (Figure 3.3.A), but these were negative for BrdU incorporation. The S-phase nuclei with incorporated BrdU were stained brown and two types of incorporation patterns were observed; complete brown staining and brown foci staining within the nucleus both of which were classed as positive (Figure 3.3.B).

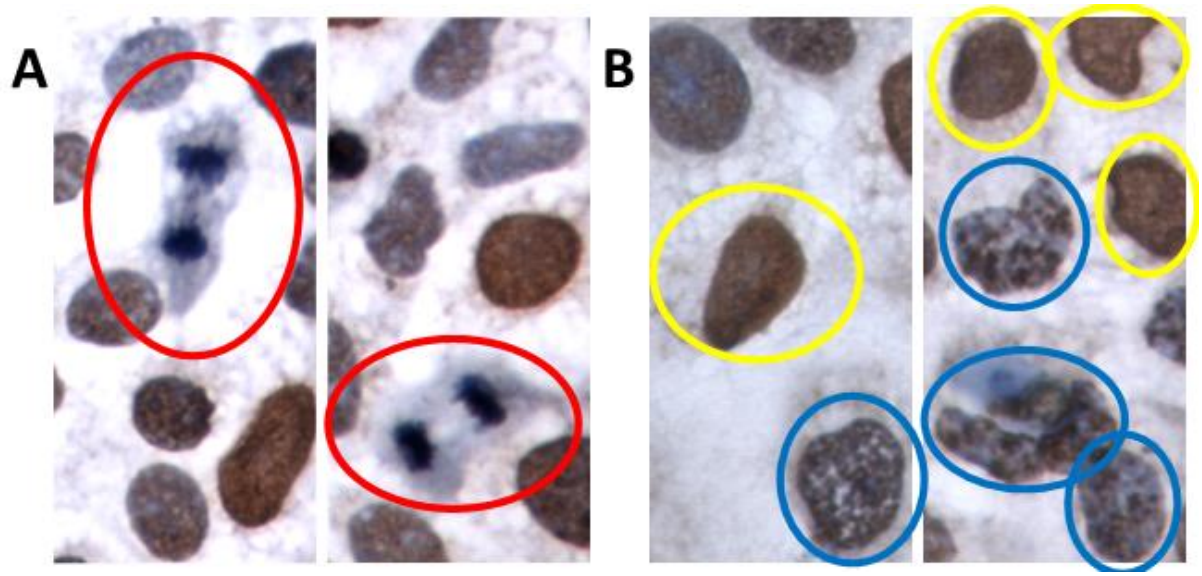


Figure 3.3. Representative IHC staining of BrdU on oropharyngeal cells (UMSCC-47) with 24-hour culture and BrdU addition on culture flask (x400 magnification).
(A) The cells in late mitosis phase, either anaphase or telophase, were observed in haematoxylin blue counterstaining (red circle) and stained negative under IHC staining for BrdU. (B) Two types of positive BrdU staining in the nucleus of UMSCC-47 cells: complete brown staining (yellow circle) and brown foci staining (blue circle).

Four parallel microfluidic perfusion systems were set up. Two of the devices used to culture two rat liver tissues and another two devices used to culture two TR52 lymph node tissues (a tissue from 1 cryopure tube was used). They were cultured in the devices for 24 hours and the culture medium containing 10 µM of BrdU was added into the devices for 1 and 6 hours. The tissues were snap-frozen, sectioned and subjected to IHC staining of BrdU. The additional serial tissue section of 6 hours with BrdU was subjected to IHC staining with matched isotype antibody as a negative control. The staining of the sections was photographed on a Nikon E800 microscope at x400 magnification. Following IHC staining with anti-BrdU, photomicrographs of the four tissues were taken and staining results showed that the tissue perfused with 1 hour of BrdU pulse has a lower number of positive brown nuclei compared with the cells perfused with BrdU for 6 hours (Figure 3.4). This was in agreement with the BrdU staining results on UMSCC-47 cells. From these results, a 6-hour pulse of BrdU was used in the following microfluidic experiments to evaluate the level of proliferating cells using tissue biopsy.

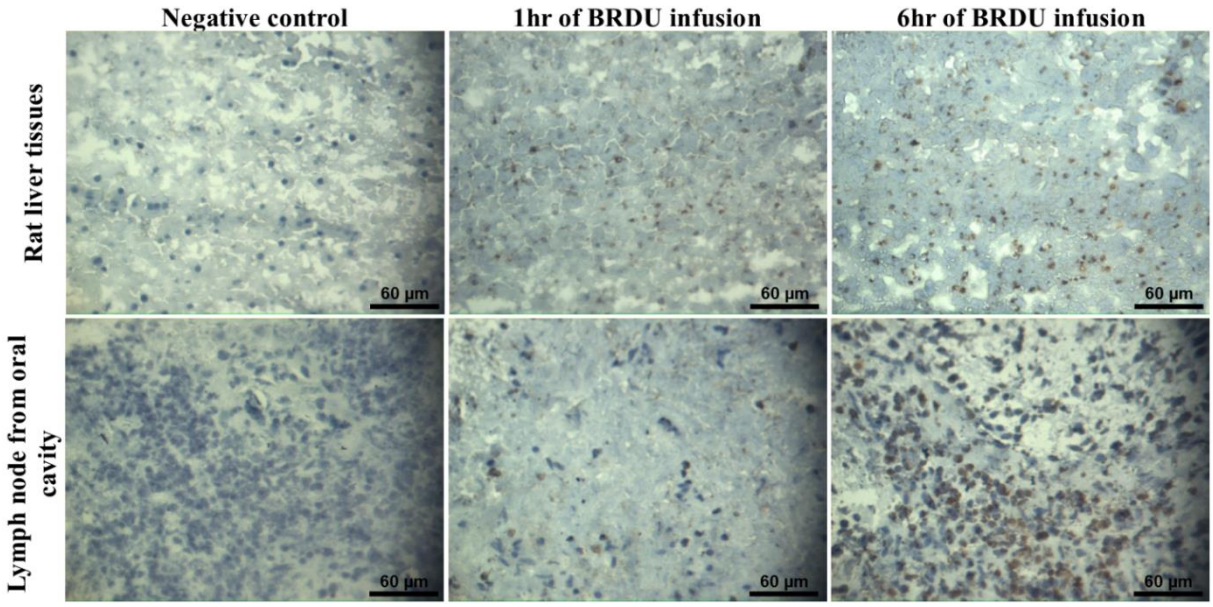


Figure 3.4. Photomicrographs of rat liver tissues and lymph neck node tissues that metastasised from oral cavity tumour (TR52) post microfluidic culture, following IHC labelling of BrdU-incorporated cells with different times of BrdU infusion (n=2 on both tissue types).
Mouse anti-BrdU (1:50) was used to detect incorporated BrdU and an isotype control antibody (IgG1, κ) was used as a negative control. The negative control was carried out on the section of tissue with 6 hours of BrdU perfusion. Proliferating cells were identified by brown nuclei and counterstained with haematoxylin (Blue). The two rows of x400 magnification fields represent two fields taken on a single tissue section.

3.3. Analysis of rat liver tissue following traditional tissue culture

Overall 32 rat liver (R1) tissues pieces were subjected to the traditional flask tissue culture and these tissues were frozen down on different days of the culture in the 96-well plates. However, 17 pieces showed 'cloudiness' in the medium which was likely due to the bacteria contamination of the tissues. These tissues were discarded by immersing them in virkon. Culture medium of the remaining 15 rat liver tissues remained clear for the variable times of culture. Table 3.1 summarized the number of tissues and different times of culture in the flask.

Table 3.1. The number of rat liver tissues cultured in 96-well plates for different length of culture (day).

Time (day)	Number of tissues
1	2
2	2
3	2
4	1
5	1
6	1
7	2
8	2
9	2
Total	15

3.3.1 LDH cytotoxicity assay

The medium was collected on a daily basis and subsequently subjected to LDH cytotoxicity assay. The absorbance of the LDH released was summarized in Table 3.2. Based on the LDH results, the average of LDH absorbance values at the first 5 days is more than 0.30 and the level reduced to less than 0.20. The cell death occurs at the first 5 days in the culture flask but decreased afterwards. The decreased of cell death by the end could possibly be due to that the tissues have died completely.

Table 3.2. LDH release from 15 rat liver tissues following tissue culture in 96-well plates.

Tissues/End time (day)	1	2	3	4	5	6	7	8	9
1	0.60								
2	0.45								
3	0.60	0.63							
4	0.39	0.46							
5		0.31	0.42						
6	0.35	0.34	0.36						
7	0.54			0.33					
8	0.52	0.49			0.46				
9	0.65	0.66			0.65	0.44			
10	0.43	0.42			0.42	0.28	0.21		
11	0.33	0.35	0.30			0.32	0.26		
12	0.40	0.37	0.37			0.37	0.16	0.11	
13	0.34	0.33			0.35	0.26	0.18	0.14	
14	0.26	0.34			0.32	0.24	0.25	0.14	0.12
15	0.44	0.47	0.44			0.41	0.13	0.11	0.07
Mean LDH Absorbance	0.45	0.43	0.38	0.33	0.44	0.33	0.20	0.12	0.09
SEM	0.03	0.03	0.02		0.06	0.03	0.02	0.01	0.02

The absorbance values were assessed in duplicate at 492nm wavelength and standardised per mg of tissue biopsy according to the analysis method described in section 2.5 and Table 2.1. The average of LDH absorbance values at each day from different tissues and the standard error of mean (SEM) were obtained. n (1 day) = 14, n (2 days) = 12, n (3 days) = 5, n (4 days) = 1, n (5 days) = 5, n (6 days) = 7, n (7 days) = 6, n (8 days) = 4, n (9 days) = 2.

3.3.2 Morphological appearance

Each tissue was snap-frozen after they were respectively maintained for 1 to 9 days in flask. H&E staining was carried out on tissue sections of 8 rat liver tissues with different time length in traditional tissue culture (1-3 days and 5-9 days). The morphological appearance of each tissue was viewed under the microscope and photographed (Figure 3.5). Based on the staining, the morphology started to deteriorate on day 3 of tissue culture. The cells appeared to be loosen with gaps in between cells on the tissues visible from the 3 days and onwards. Apart from that, the visibility of nucleus is reduced on the tissues cultured for 3 days compared with that of the 2-day culture. It is suggested that the nucleus could not be observed on the tissues maintained longer than 3 days in the 96-well plate.

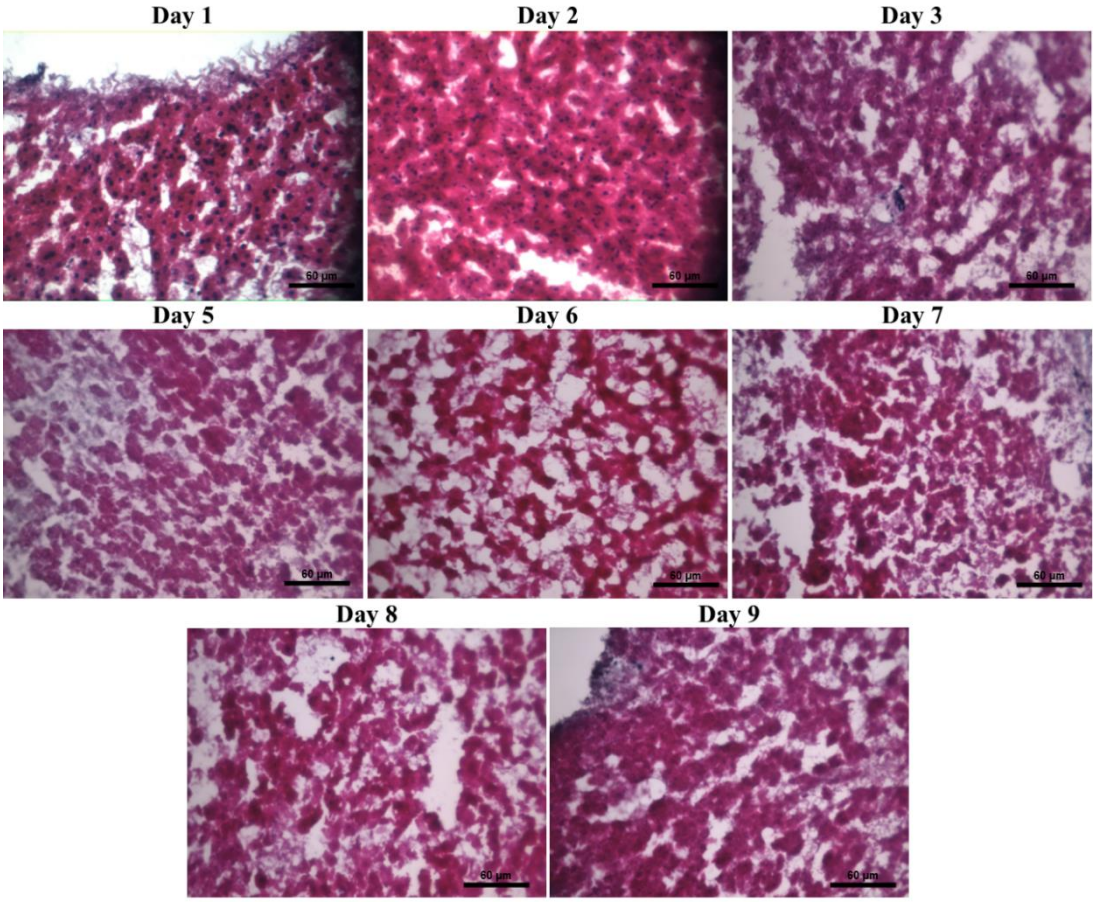


Figure 3.5. Representative of haematoxylin and eosin (H&E) staining on rat liver tissue sections following traditional tissue culture from day 1 to 3 and day 5 to 9 (n=8).
Red represents eosin stained cytoplasm and blue is haematoxylin stained nuclei. Magnification of x400 field was photographed and shown. Due to thicker tissue section, the colour intensity of day 2 tissue was higher compared with others.

Based on both the measurement of LDH release and the morphology H&E staining, it is suggested that the rat liver tissues could be maintained up to 2 days in the traditional tissue culture using 96-well plate.

3.4. The interrogation of rat liver tissues in microfluidic perfusion systems

Nine rat liver (R1) tissue biopsies were maintained in parallel in nine microfluidic devices according to protocol described in section 2.3. Each microfluidic perfusion system was flowed and terminated on each day between 1 and 9 days. Medium containing 10µM of BrdU was added 6 hours before the flow was terminated and the tissue was snap-frozen. During the time the tissue was maintained in the microfluidic device, the effluent medium was collected every two hours which will make up to 240 µl of medium for one collection when using a flow rate of 2µL/min. The tissues were sectioned and subjected to H&E staining and IHC staining using anti-BrdU antibody. The images of all stained sections (1-9 days in microfluidics) at x400 magnification were photographed.

3.4.1 LDH cytotoxicity assay

Based on the LDH cytotoxicity assays on the collected medium from one rat liver tissue which was maintained for 9 days in the microfluidic device, the LDH released from the tissue reduced from the initial peak at the beginning of the experiment (Figure 3.6). The highest amount of LDH released was at 18 hours in the device with about 0.30a.u. absorbance value. The reduction of the LDH released following the peak value could be due to the cellular damage at the tissue surface when the tissue biopsies were harvested and handled such as tissue slicing during the tissue preparation at the beginning.

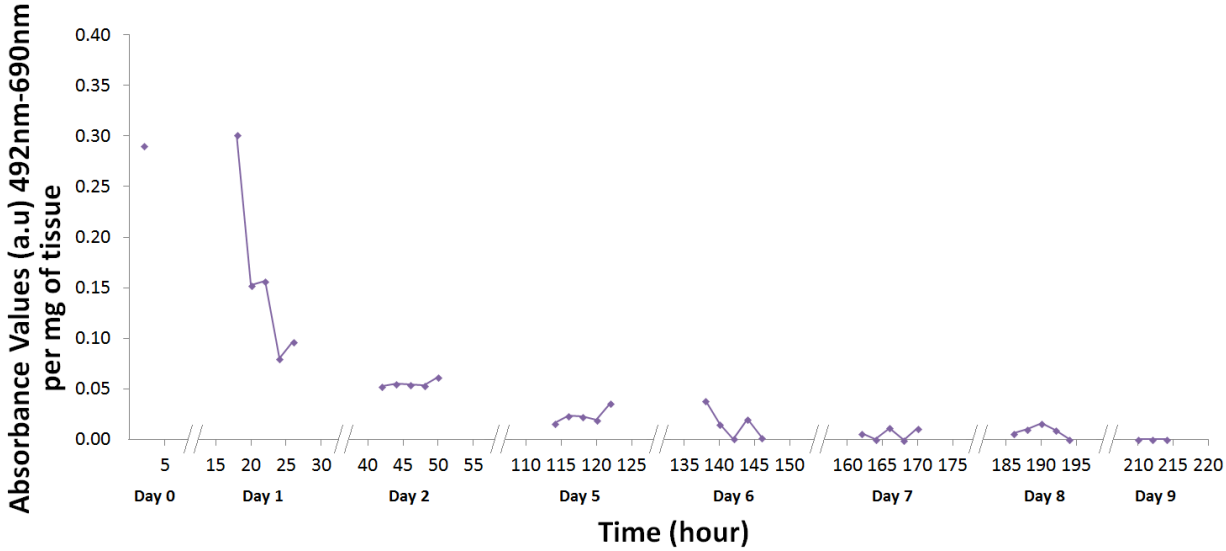


Figure 3.6. LDH release from rat liver tissue following 9-day maintenance in microfluidic device. The absorbance values were assessed in duplicate and standardised per mg of tissue biopsy (8.2mg).

The similar pattern of the reduction of LDH released at the beginning of the experiment was observed on another eight rat liver tissues perfused in microfluidic device (Figure 3.7). In each rat liver tissue (n=8; day 1-3 and day 5-9), the average LDH collected on each day was obtained and the mean of daily LDH level from the nine rat liver tissues was calculated and the results is presented in Figure 3.7. The amount of LDH released measured from other rat liver tissues remained at the constant and relatively low value following the reduction from the initial peak.

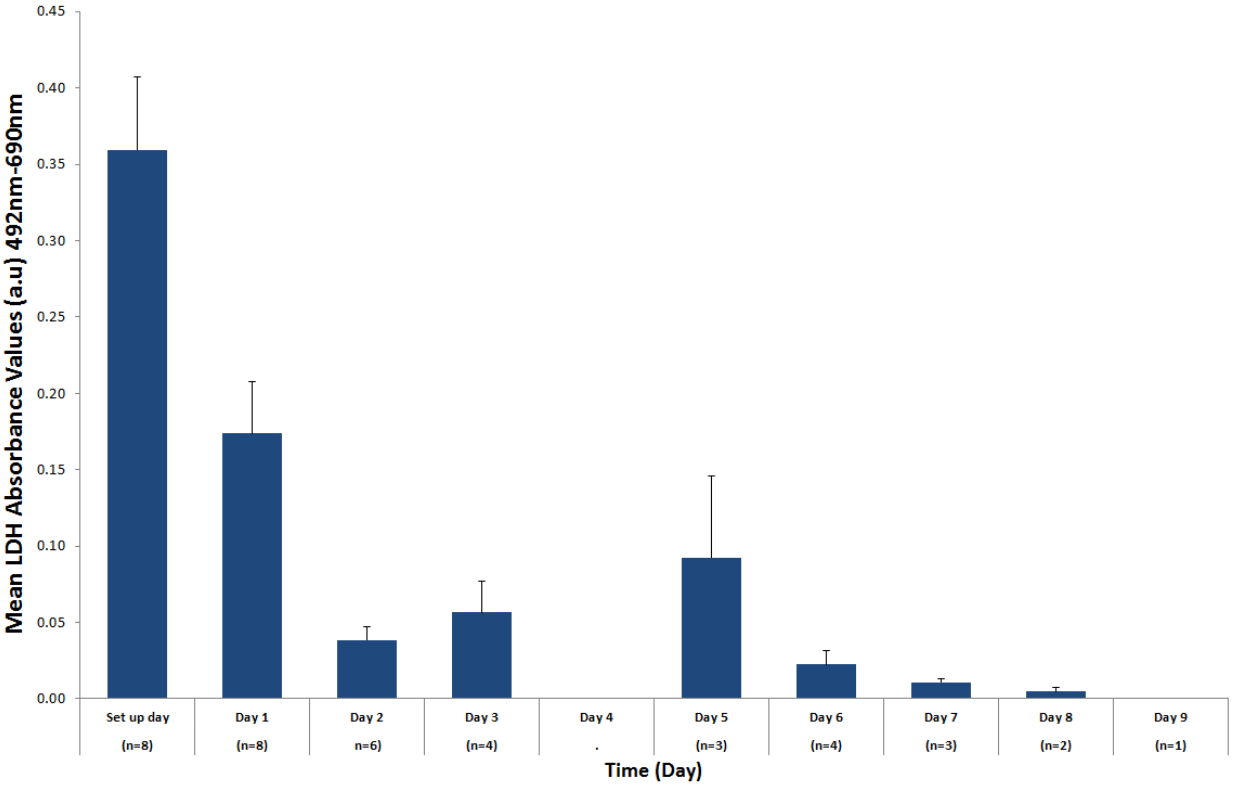


Figure 3.7. Mean LDH absorbance value of nine rat liver tissues following the maintenance in microfluidic device.
The absorbance values were assessed in duplicate and standardised per mg of tissue biopsy. Data are expressed as Mean+SEM.

The results presented in Figure 3.6 and Figure 3.7 showed that the LDH released from the rat liver tissue remains in the low level throughout the 9 days in the microfluidic system. The low level of LDH released could represent two possibilities: either the tissue (i) remains intact (non-apoptotic or non-necrotic) or (ii) has died following the first peak of high LDH released. In order to determine the presence of intact cells in rat liver tissue throughout the microfluidic flow, 10% lysis buffer (Roche, UK) was added into the medium at 6 hours before microfluidic flow system was stopped. At 6 hours before the tissue was frozen, the normal medium in the syringe was replaced with medium containing 10% of lysis buffer in the laminar flow hood. The lysis buffer functions to lyse the tissue and achieve the maximum LDH released.

During the 6-hour treatment with lysis buffer, the LDH level released to the effluent medium increased and peak at more than 0.40a.u. (Figure 3.8). The sharp increment of LDH released from the tissue after addition of lysis buffer suggested that the tissue cells remained intact throughout the flow and before the lysis treatment.

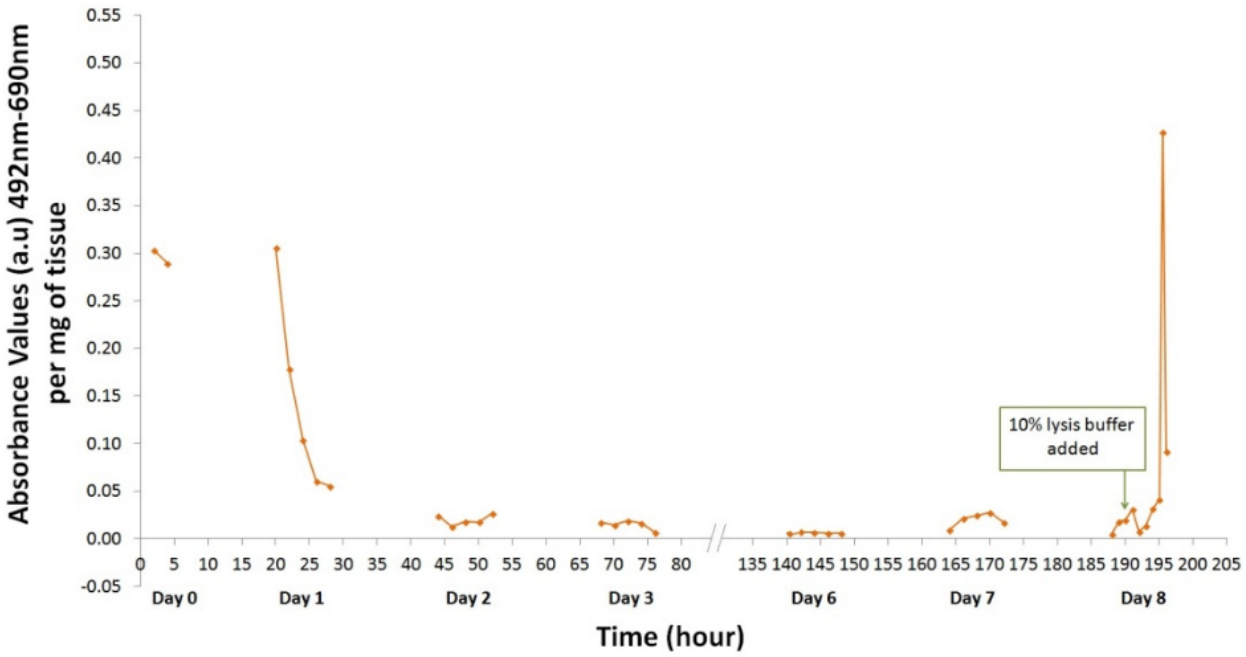


Figure 3.8. LDH release from rat liver tissue following 8-day culture in microfluidic device and lysis at the last 6 hours.
The absorbance values were assessed in duplicate and standardised per mg of tissue biopsy (6.9mg).

LDH release from the rat liver tissue separately cultured in traditional method and in microfluidic device was investigated. Figure 3.9 shows that throughout the 9-day of perfusion, LDH release from the microfluidic device was lower, indicating that culturing in microfluidic platform is superior to the conventional mean, inducing less damage to the tissue sample.

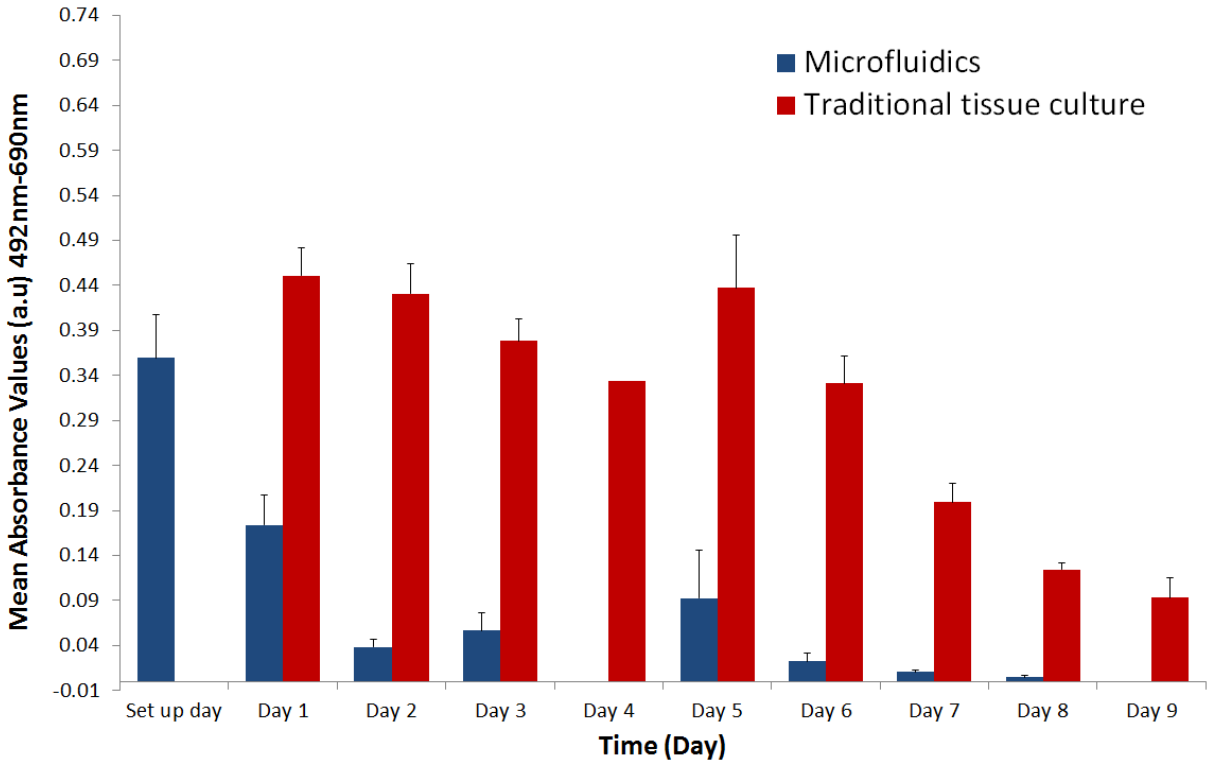


Figure 3.9. Mean LDH absorbance values from rat liver tissue maintained in microfluidic device and traditional tissue culture.
The absorbance values were assessed in duplicate and standardised per mg of tissue biopsy. Mean+SEM.

In addition, the similar microfluidics were carried out by a colleague in the same research group to maintain rat liver tissues for up to 9 days and the release of LDH from the tissues was analysed by the same way described in section 2.6. Based on the mean of daily LDH level, the absorbance values between present results and colleague's results were compared and observed similar except the tissues maintained up to day 4 (Figure 3.10). On the colleague's results, the low LDH release was detected following the initial high LDH release due to tissue manipulation. In overall, the tissues were maintained with low cell death throughout the microfluidic flow.

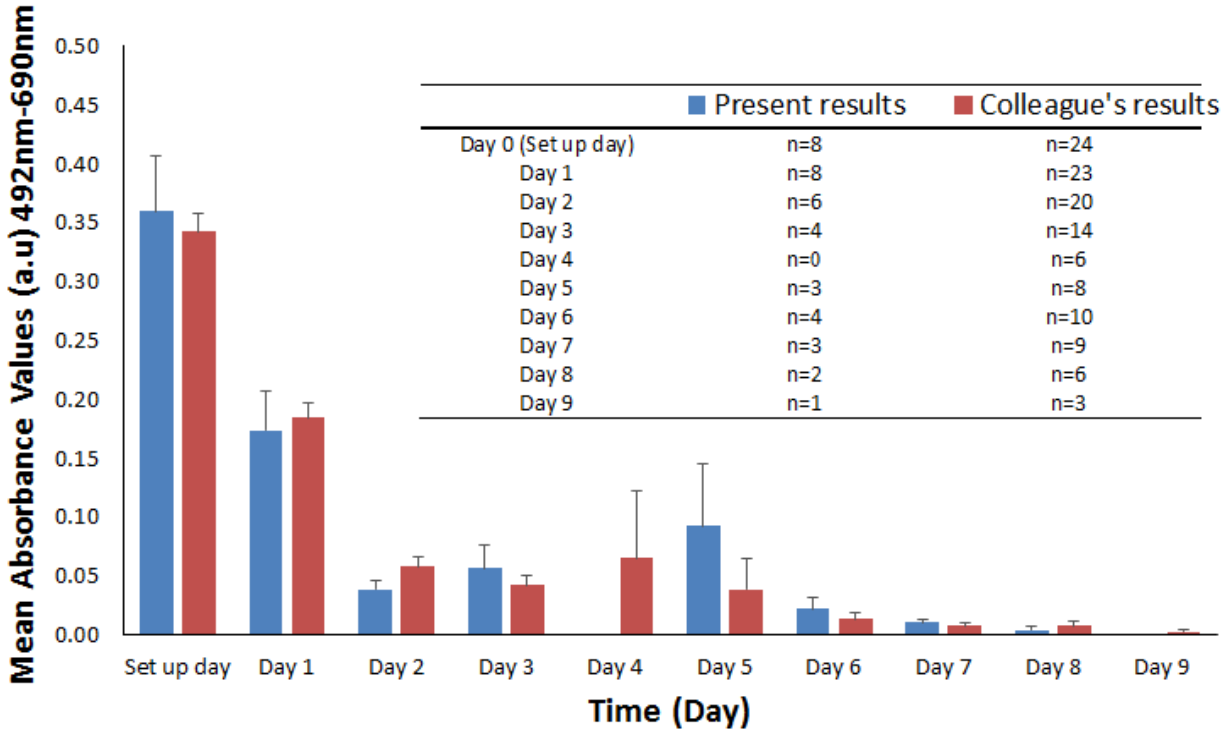


Figure 3.10. Comparison of mean LDH absorbance values from rat liver tissues maintained in same microfluidic system between colleagues' results and current results.
The absorbance values were assessed in duplicate and standardised per mg of tissue biopsy. Mean+SEM

3.4.2 Morphological appearance

Based on the H&E staining (Figure 3.11), there is no obvious difference observed in the morphological appearance for the first 4 days in microfluidic system. During the first four days, the nucleus was observable and clear. However, on the tissue maintained for 4 days in the device, the morphology of the tissues started to decrease. The number of nucleus is less and the gap between cells in the tissue was large compared with that of the 3 days. The rat liver tissues which were maintained longer than 4 days in the device showed poor morphology with no nucleus and larger gaps between cells. Therefore, it is suggested that the rat liver tissues can be maintained in the device up to 3 days following the microfluidic set up according to the H&E staining.

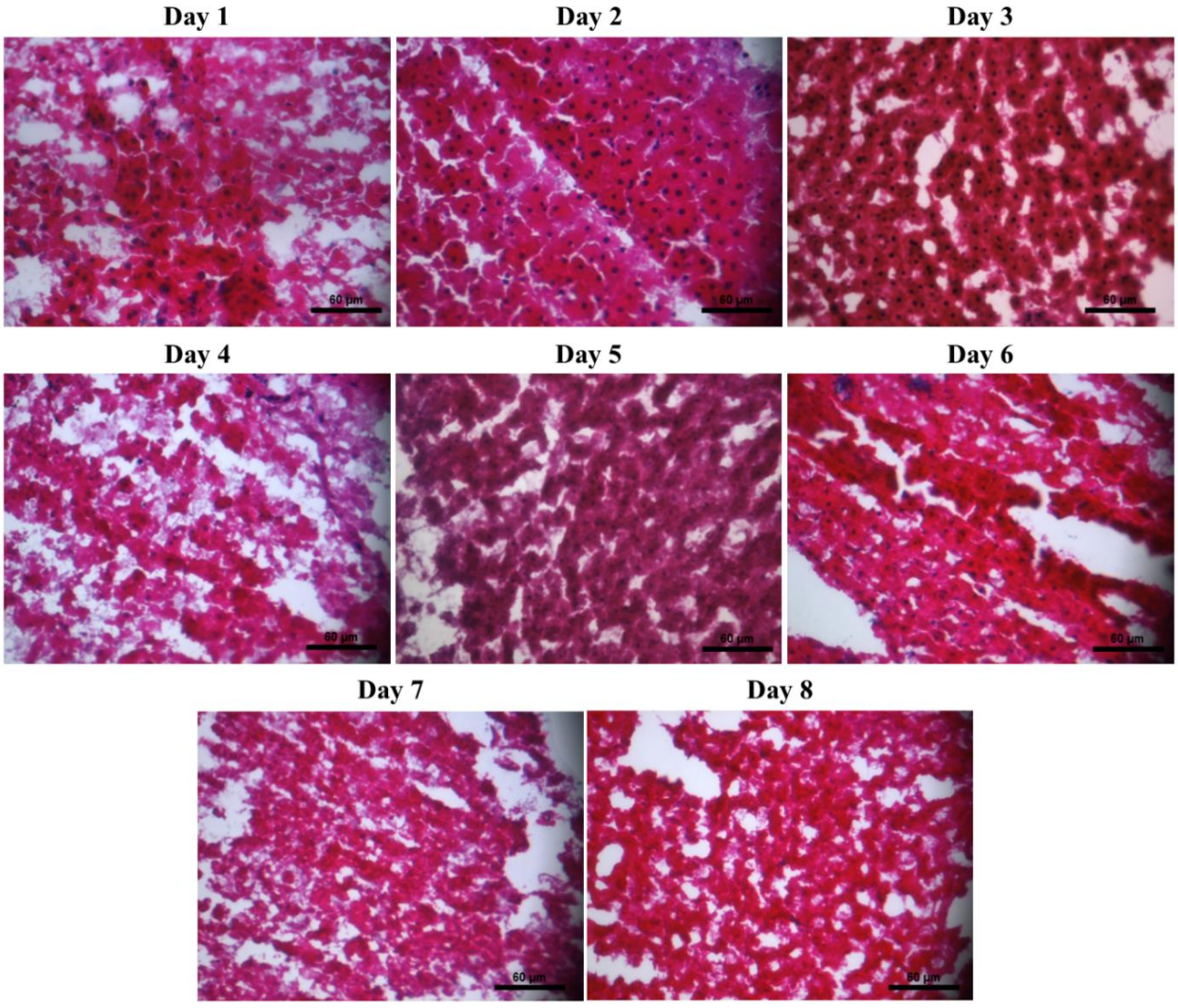


Figure 3.11. Representative haematoxylin and eosin (H&E) staining on rat liver tissue sections following microfluidic perfusion from day 1 to 9 (n=9; tissue on day 9 is not shown).
Red represents eosin stained cytoplasm and blue is haematoxylin stained nuclei. Magnification of x400 field was photographed and shown.

3.4.3 BrdU incorporation –Immunohistochemical (IHC) Staining

In the IHC staining of BrdU (Figure 3.12), positive brown nuclear staining was observed on tissues cultured up to day 4 except the tissue on day 3. No positive BrdU nuclei were evident in rat liver tissue that was maintained for five days in the device. Hence, it is suggested that the tissues were still undergoing proliferation up to 4 days in the device based on the detection of S-phase cells.

Both morphological appearance and the S-phase cells detection results suggested that the tissue can be maintained in microfluidics for up to four days. However, the LDH cytotoxicity assays showed very low level of cell death throughout the 9 days of tissue culture in microfluidics. The addition of the 10% lysis buffer to the microfluidic perfusion system and the following high release of LDH (Figure 3.8) suggested that there are intact cells. The cell membrane might stay uninterrupted throughout the microfluidic flow, resulting the low amount of LDH released detected. In overall, based on the above analyses and results, the morphology and proliferation of tissue could be maintained in the device for up to 4 days.

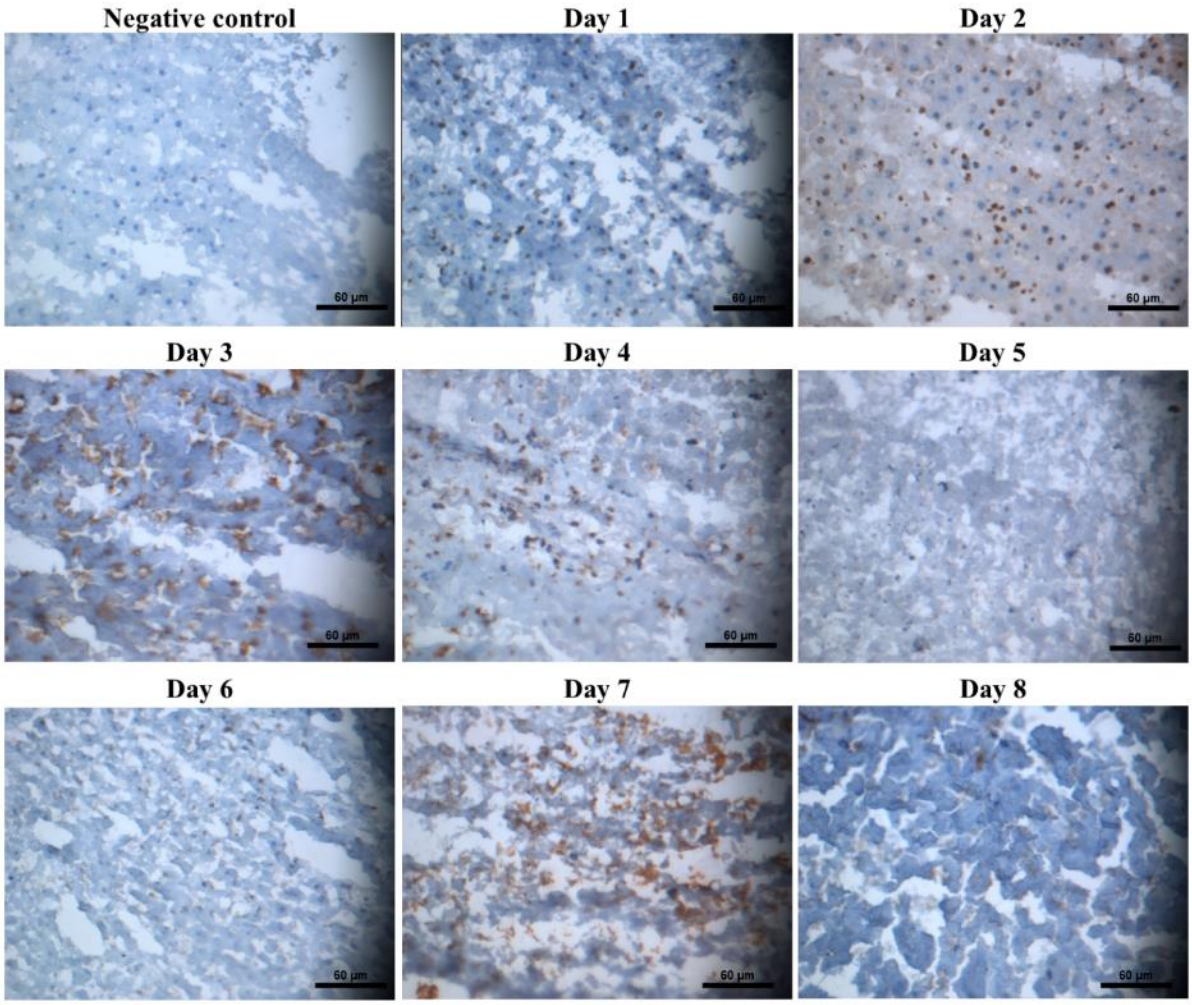


Figure 3.12. Representative IHC labelling of BrdU-incorporated cells in rat liver tissues following 1-9 days culture in microfluidic device (n=9; tissue on day 9 is not shown).
Mouse anti-BrdU (1:50) was added to the positive sections and a negative control antibody that had the same isotype as the primary antibody (IgG1, κ) was used as a negative control. Proliferating cells were identified by brown nuclear staining and counterstained with light blue haematoxylin (x400 Magnification).

3.5. The use of different serum concentration during rat liver culture in microfluidic device

Since the tissue size was relatively small, the changes in the release of soluble factors into the effluent medium could be subtle, and might be masked by the serum contents in the medium. Therefore, to avoid the problem, the medium with different serum parameters (no serum media, 0.1% bovine serum albumin [BSA], 1% FBS, 5% FBS and 10%FBS) was supplemented to 15 rat liver (R2) tissues in the microfluidic device in order to determine the effect of medium with low serum concentration on the tissues in the microfluidic.

The rat liver tissues (with weight 5-10mg) were subjected to 15 parallel microfluidic devices. Table 3.3 showed the number of rat liver tissues used in the optimisation of different serum concentration. The devices were flowed with medium containing different concentration of serum (Table 3.3). Medium containing 1%, 5% and 10% (v/v) of serum was prepared by adding FBS into Williams' Medium E according to the stated concentration while the medium containing 0.1% of serum was made up by adding 0.1% of bovine serum albumin (BSA; Sigma-aldrich, UK) instead of using FBS to the medium. After the tissues were maintained in the microfluidic device, each tissue was frozen at a specific time (24, 48, and 96 hours) as stated in Table 3.3. In the last 6 hours before the tissues were frozen, each tissues were perfused with medium containing 10μM of BrdU. The proliferation levels of each treatment were investigated by IHC staining using anti-BrdU antibody (Figure 3.13).

Table 3.3. Number of rat liver tissues subjected to microfluidic perfusion system with Williams' Medium E containing different concentration of serum (n=15).

Different serum concentrations	Number of rat liver tissues		
	1 day in microfluidics	2 days in microfluidics	4 days in microfluidics
Serum free	1	1	1
0.1% BSA (w/v)	1	1	1
1% FBS (v/v)	1	1	1
5% FBS (v/v)	1	1	1
10% FBS (v/v)	1	1	1
Total	15 rat liver tissues		

Based on the IHC staining (Figure 3.13), the tissues perfused with medium containing the five different serum concentrations have high BrdU-positive staining during the first 24 hours in the device (BrdU staining of 0.1% BSA and 1% FBS are not presented). However, only the tissues cultured with 5% (v/v) and 10% (v/v) FBS-media showed replicating cells following 48 hours in the device. When the tissues were maintained in microfluidic system for 4 days, there was no positive BrdU staining shown on rat liver tissue perfused with medium containing 5% (v/v) FBS. The medium containing 10% (v/v) FBS is the lowest serum concentration that could maintain the proliferation of tissue cells for up to 4 days in the device.

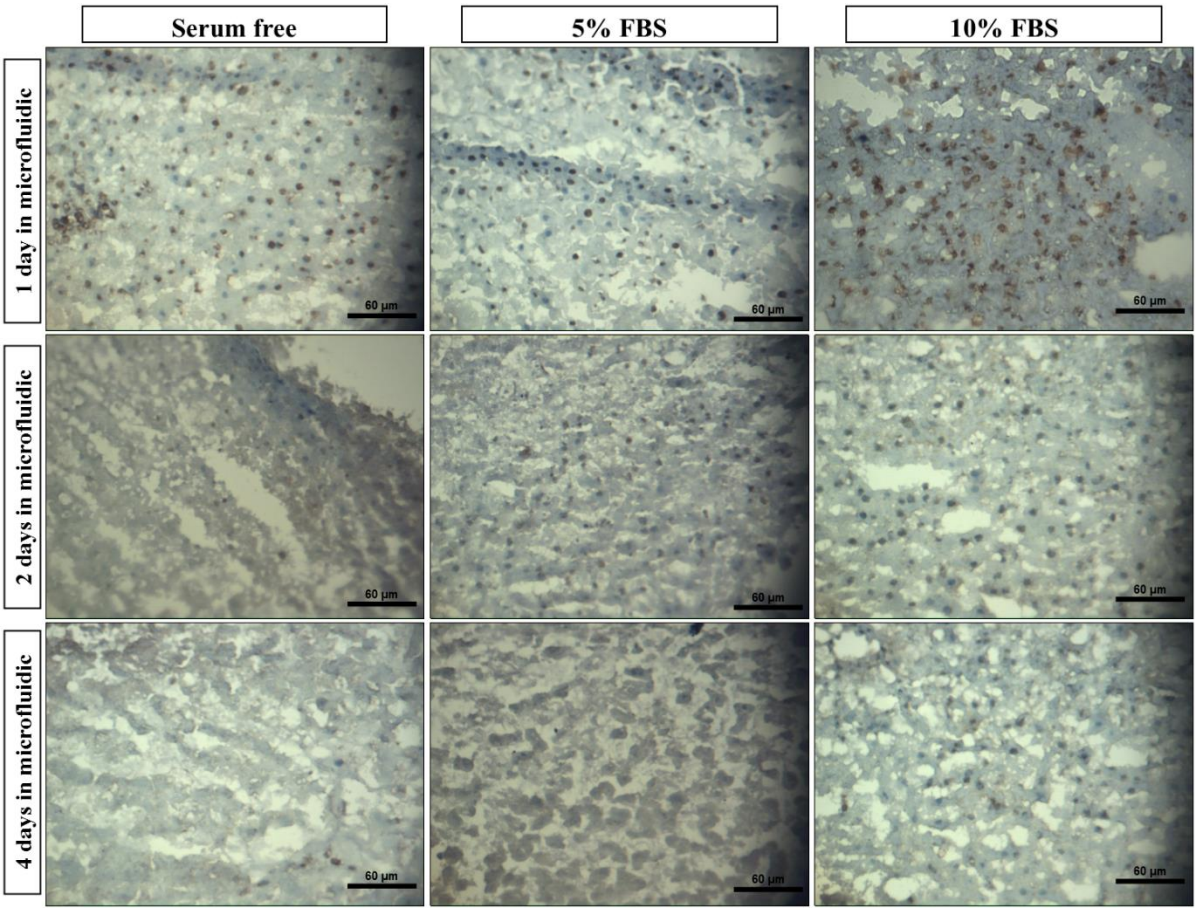


Figure 3.13. Representative IHC labelling of BrdU incorporating cells in rat liver tissues following in microfluidic flow for 1 days (n=5), 2 days (n=5) and 4 days (n=5).
Medium containing different serum concentrations [serum free, 5% and 10% (v/v) of FBS] was respectively used to perfuse each tissue while the staining images of tissues perfused with 0.1% (w/v) bovine serum albumin (BSA), 1% (v/v) of FBS were not presented. A mouse anti-BrdU (1:50) monoclonal antibody was added to all sections. Proliferating cells are identified by brown nuclear staining and counterstained with light haematoxylin (x400 Magnification).

3.6. The use of rat serum for microfluidic culture of rat liver tissue

The serum used in the Williams' Medium E for rat liver tissue culture was FBS. Rat serum (Sera Laboratories International, West Sussex, UK) was hypothesised to be more suitable for rat liver tissue culture (Rutzky, Taylor and Pumper, 1971). Therefore, medium containing 10% of rat serum instead of FBS was used to culture three rat liver (R2) tissues in three parallel microfluidic devices for 4, 5 and 6 days, respectively. Similarly, the amount of LDH released from each tissue was measured, the H&E staining and IHC staining of BrdU incorporation were photographed.

The LDH absorbance values obtained from the three rat liver maintained in the devices and the daily mean LDH absorbance values of obtained from these tissues are illustrated in Figure 3.14.A and B. At the first 5 hours of the tissue culture, the amount of LDH released from these tissues was high at about 0.35a.u. (Figure 3.14.A). Following the initial high release of LDH, the LDH absorbance values and the mean LDH level remained at low level. Although the LDH level was low which showed less cell death occurred, the morphology and the proliferation status presented, however, suggested that the tissues have died in the device (Figure 3.14.C). Therefore, medium supplemented with rat serum does not appear to assist the maintenance of tissue culture in the device.

Following 6-hour perfusion with BrdU-contained medium, the tissues were frozen and sectioned. Tissue sections were then subjected to morphological study using H&E staining (Figure 3.14.C) and proliferative study using BrdU IHC staining (Figure 3.14.D). Based on the results of H&E staining, the morphology of the rat liver tissues was disrupted and no nuclear staining was seen on the tissue sections maintained for 4, 5 and 6 days in the device. The BrdU IHC staining showed no positive BrdU staining and much general background staining. These results showed that the addition of rat serum could not maintain the rat liver tissue in the device, of morphology and proliferation study as effectively as 10% (v/v) FBS.

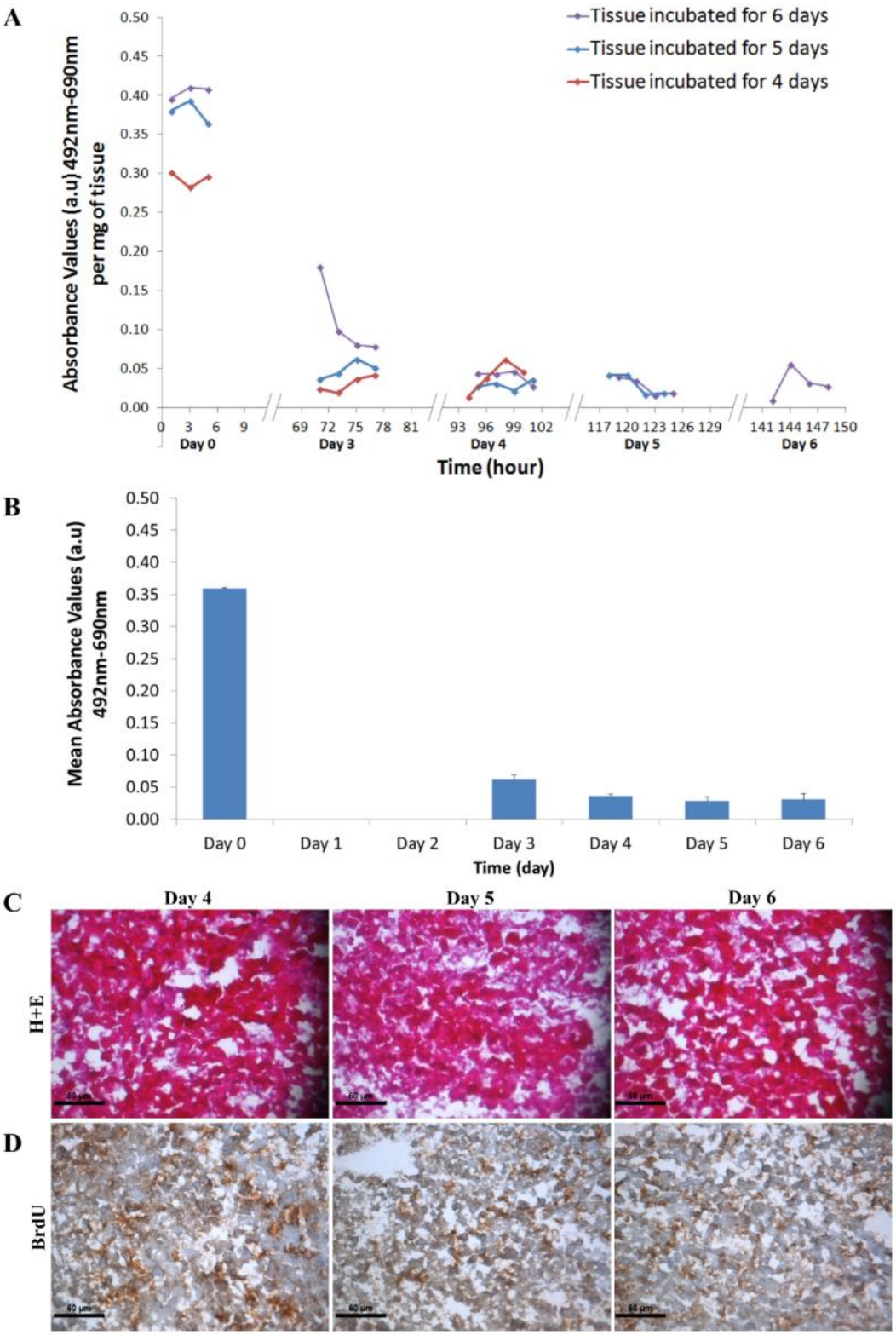


Figure 3.14. Three rat liver tissue subjected to 4, 5 and 6 days of culture in devices with medium containing 10% of rat serum.

(A) LDH release from the three tissues measured at every two hours. The absorbance values were assessed in duplicate and standardised per mg of tissue biopsy (Day 4: 8.7mg; Day 5: 7.4mg; Day 6: 7.7mg). (B) Mean LDH released obtained on daily basis from the three tissues. Mean+SEM. n (Day 0, 3 and 4) = 3, n (Day 5) = 1, n (Day 6) =1. (C) Representative H&E staining of the three tissues (x400 magnification). Red represents eosin stained cytoplasm and blue is haematoxylin stained nuclei. (D) Representative IHC labelling of BrdU on rat liver tissues following microfluidic flow. A mouse anti-BrdU (1:50) antibody was added to all sections. Proliferating cells are identified by brown nuclear staining and counterstained with light haematoxylin (x400 magnification).

3.7. The use of HEPES buffer during rat liver culture in microfluidic device

HEPES [4-(2-hydroxyethyl)-1-piperazineethanesulfonic acid] is a zwitterionic organic chemical buffering agent which has widely been used as a tissue culture buffer. It is an effective buffer, providing supplemental buffering to culture medium at pH 7.2 through 7.6. The addition of HEPES to the culture medium gives extra buffering capacity to maintain physiological pH when the tissue culture was manipulated outside of CO_2 incubator for prolonged periods (Halldorsson *et al*., 2015). As a result, in order to improve the tissue culture in microfluidic device, HEPES was added into the culture medium.

Three rat liver (R2) tissues were subjected to three parallel microfluidic devices cultured with medium containing 30mM of HEPES (PAA, Somerset, UK). The three tissues were respectively maintained in the devices for 4, 5 and 6 days and 10μM of BrdU was added into perfusion for 6 hours before the tissues were frozen. The amount of LDH released from the tissues is presented in Figure 3.15.A and the daily mean LDH absorbance values of the three rat liver tissues is illustrated in Figure 3.15.B. After the initial high level of LDH released at the beginning of experiment, the LDH level remained at low levels (below 0.25a.u.).

Based on the H&E staining (Figure 3.15.C), the morphology of rat liver tissue deteriorated when it was maintained for 6 days in the device. The two rat liver tissues that were cultured for 4 and 5 days showed good morphology with clear nuclear staining. The visibility of nuclei reduced markedly on the rat liver tissue that was maintained for 6 days in the device compared with earlier time points. Similar results were observed in BrdU IHC staining presented in Figure 3.15.D. The morphology of the rat liver tissues for 4 and 5 days in the device was maintained but not for the one cultured for 6 days. Proliferative cells were observed in tissues maintained up to day 5 as positive brown nuclei staining were clearly been seen. When all the analyses were combined, the rat liver tissue could be maintained for up to day 5 in the device. This suggested that the addition of HEPES into the culture medium improved the tissue culture in the microfluidic platform. Hence, the culture medium used for the tissue culture in following experiments was added with 30mM of HEPES buffer.

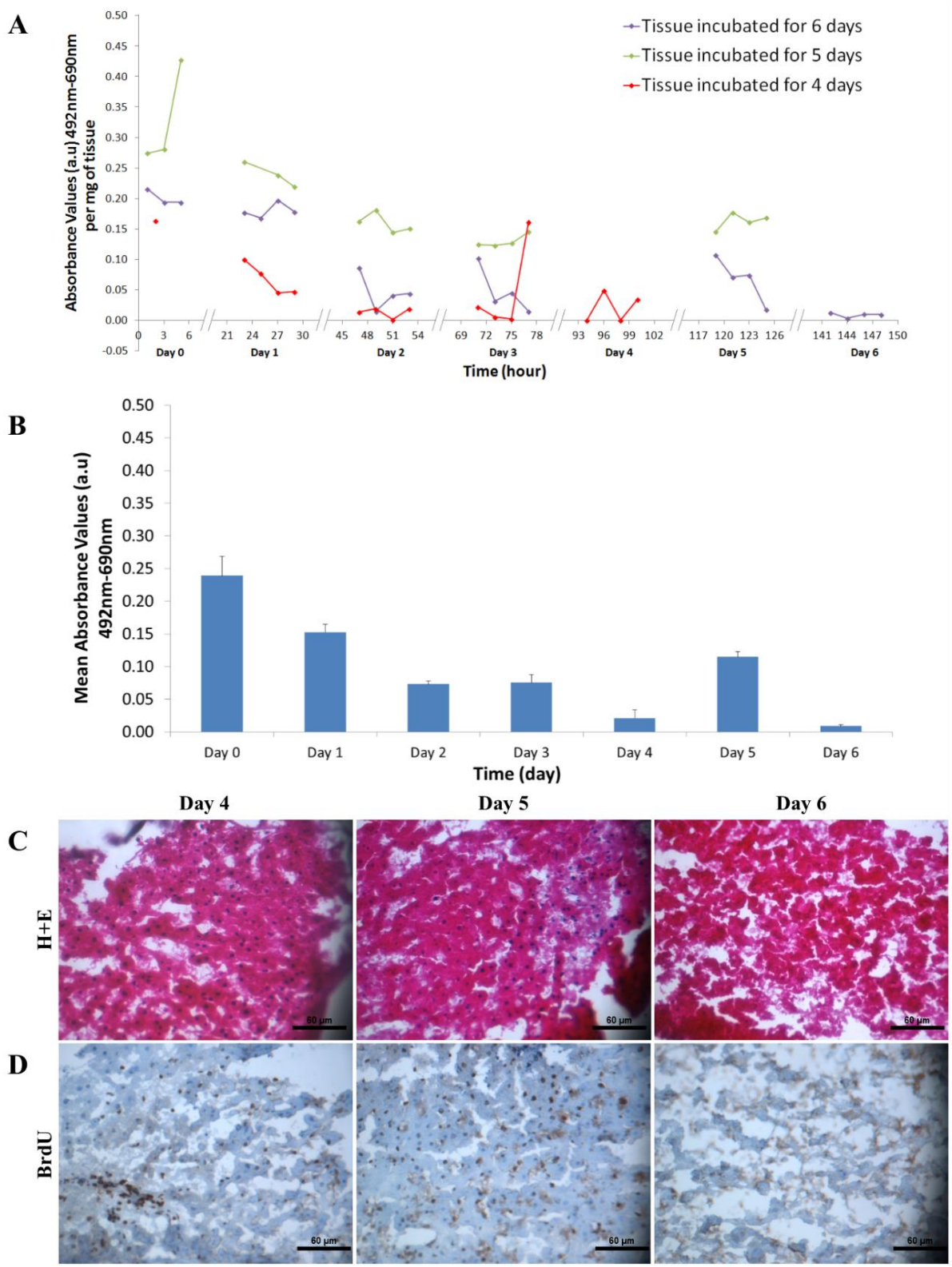


Figure 3.15. Three rat liver tissue subjected to 4, 5 and 6 days of culture in devices with medium containing 30mM of HEPES buffer at 2µl/min.

(A) LDH release from the three tissues measured at every two hours. The absorbance values were assessed in duplicate and standardised per mg of tissue biopsy (Day 4: 8.6mg; Day 5: 5.7mg; Day 6: 6.9mg). (B) Mean LDH released obtained on daily basis from the three tissues. Mean+SEM. n (Day 0-4) = 3, n (Day 5) = 1, n (Day 6) =1. (C) Representative H&E staining of the three tissues (x400 magnification). Red represents eosin stained cytoplasm and blue is haematoxylin stained nuclei. (D) Representative IHC labelling of BrdU on rat liver tissues following microfluidic flow. A mouse anti-BrdU (1:50) antibody was added to all sections. Proliferating cells are identified by brown nuclear staining and counterstained with light haematoxylin (x400 magnification).

3.8. The use of medium gassed with a carbogen gas mixture (95% of oxygen and 5% of carbon dioxide) for rat liver in microfluidic device

Normal tissue contains oxygen level ranging from about 3% to 7.4% while the oxygen levels of most tumours ranging are lower, ranging from 0.3-4.2% (McKeown, 2014). The supplement of oxygen into the culture medium for tissue culture in the microfluidic device is thought to be able to improve the viability of tissue. Therefore, three rat liver (R2) tissues with similar weight (5-10mg) were subjected to three parallel microfluidic devices and maintained for 4, 5 and 6 days with medium containing carbogen gas mixture (95% of oxygen and 5% of carbon dioxide). In a sterile laminar flow hood, the culture medium was oxygenated by gassing with a carbogen gas mixture (95% O_2/ 5% CO_2; BOC, UK; Pakola and Grunwald, 1993; Stubbs *et al*., 1998; Fluckey, Ploug and Galbo, 1999; McKeown, 2014) into the medium-filled glass bottle which was covered by parafilm for 10 minutes. After that, the oxygenated medium was used to culture the three rat liver tissues for 4, 5 and 6 days. LDH cytotoxicity assay was carried out on the effluent medium collected, the morphology appearance and the proliferative status were investigated as stated previously.

The amount of LDH released from tissue which was subjected to culture with high oxygen medium for different time periods is presented in Figure 3.16.A and the daily mean LDH absorbance values of these tissues is illustrated in Figure 3.16.B. At the beginning of the experiment, the amount of LDH released from all tissues was high presumably due to the set up and the tissue processing as seen previously. Following the initial high LDH released, the amount of LDH released from the three tissues was remained in low level (below 0.15a.u. in individual LDH levels and less than 0.06a.u. in the mean LDH values of the three tissues).

The morphology appearance and the proliferative status were investigated as stated previously and the results are shown in Figure 3.16.C and Figure 3.16.D, respectively. The three rat liver tissues showed deteriorated morphology with no nucleus detected (haematoxylin blue staining). There was no brown positive staining observed in three tissues, showing that the tissues maintained for 4 days or more have no replicating cells. In summary, the medium contained high percentage of oxygen (consists of 95% of oxygen and 5% of carbon dioxide) showed no positive or additive effects on the maintenance of HNSCC tissues in microfluidics.

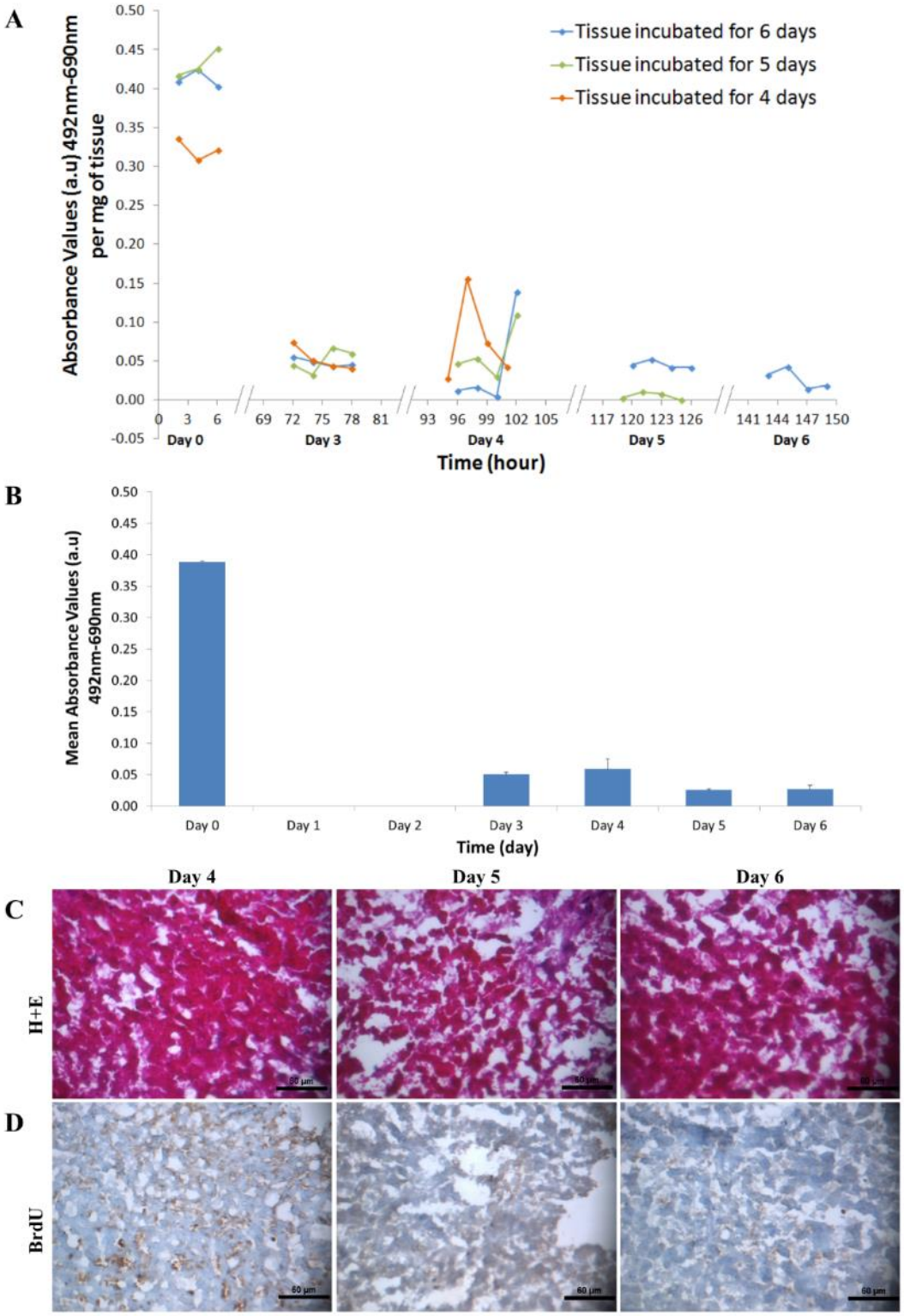


Figure 3.16. Three rat liver tissue subjected to 4, 5 and 6 days of culture in devices with medium oxygenated with 95% O_2 and 5% of CO_2.

(A) LDH release from the three tissues measured at every two hours. The absorbance values were assessed in duplicate and standardised per mg of tissue biopsy (Day 4: 7.1mg; Day 5: 5.2mg; Day 6: 5.7mg). (B) Mean LDH released obtained on daily basis from the three tissues. Mean+SEM. n (Day 0, 3 and 4) = 3, n (Day 5) = 1, n (Day 6) = 1. (C) Representative H&E staining of the three tissues (x400 magnification). Red represents eosin stained cytoplasm and blue is haematoxylin stained nuclei. (D) Representative IHC labelling of BrdU on rat liver tissues following microfluidic flow. A mouse anti-BrdU (1:50) monoclonal antibody was added to all sections. Proliferating cells are identified by brown nuclear staining and counterstained with light haematoxylin (x400 magnification).

3.9. The use of different medium flow rates in the microfluidic device

The supplement of nutrients to and the removal of waste products from the tissues in the microfluidic device are carried out by the continuous pump of medium. Therefore, the perfusion rate of medium perfused throughout the microfluidic system is an important parameter for the viability of the tissues. Thirteen rat liver (R2) tissues were subjected in 13 parallel microfluidic devices and perfused with medium at different flow rates (2, 5, 7 10, 12 and 15µL/min) according to the table listed below (Table 3.4). The microfluidic was carried out (according to section 2.3) but with different flow rates throughout the perfusion. The effluent medium was collected for LDH cytotoxicity assay while each tissue was subjected to H&E staining and BrdU proliferation study.

Table 3.4. Number of rat liver tissues subjected to microfluidic system with different flow rates.

Different serum concentrations	Number of rat liver tissues
	96hrs in microfluidics
2µL/min	4
5µL/min	3
7µL/min	2
10µL/min	2
12µL/min	1
15µL/min	1
Total	13 rat liver tissues

The daily mean LDH values of the rat liver tissues which were subjected to microfluidics at the same flow rates were obtained and summarised in section 9.6/Table 9.2. The mean LDH absorbance values for every 24 hours were illustrated in Figure 3.17. Based on the results, the mean LDH absorbance values for all tissues were highest at the beginning of the experiment. The mean values for each flow rate started to decrease on the following days. The absorbance values were remained less than 0.2a.u. after 1 day of incubation and reduced to below 0.05a.u. after 2 days in the device.

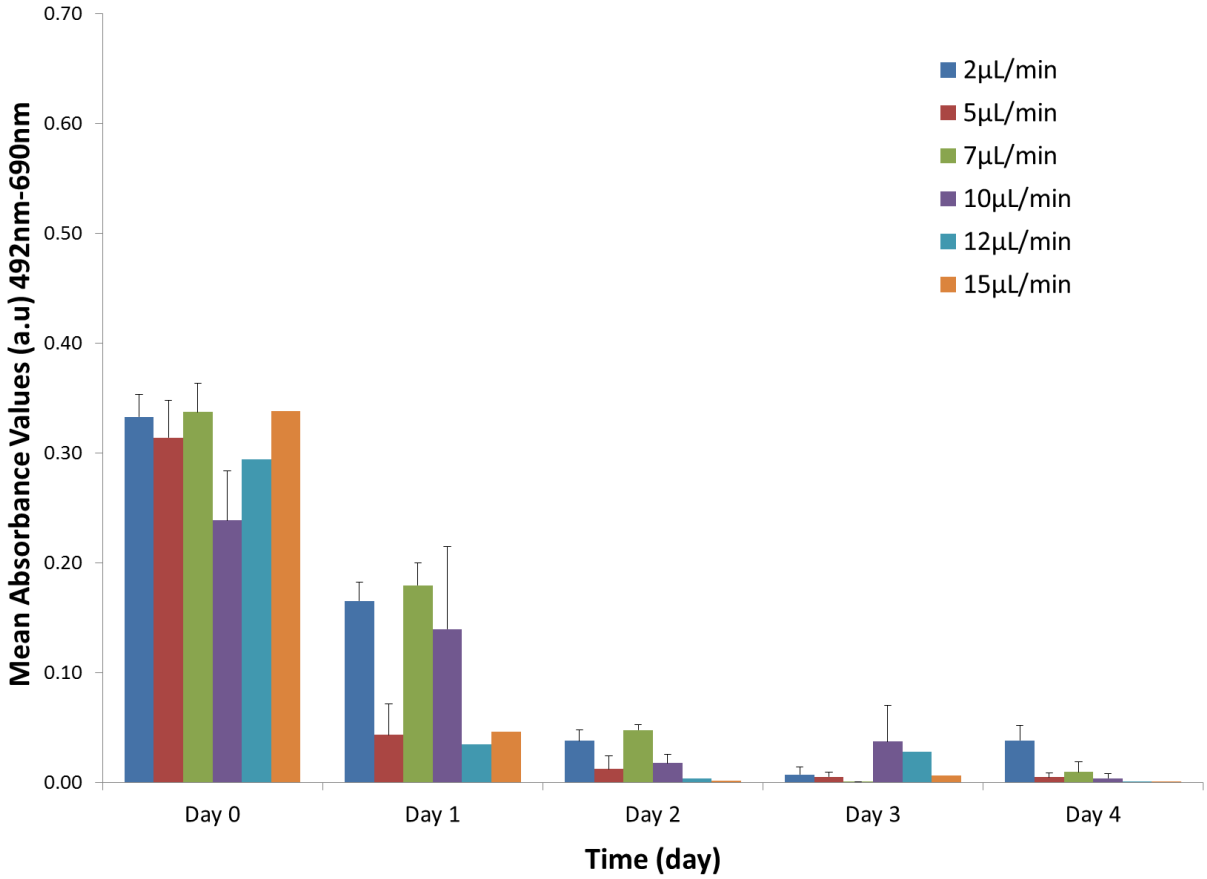


Figure 3.17. Mean LDH released from 13 rat liver tissues throughout the 4 days culture in microfluidic device.

Medium was perfused at different flow rate (2, 5, 7, 10, 12, and 15 µL/min). The absorbance values were assessed in duplicate and standardised per mg of tissue biopsy. Mean+SEM. n (2 µL/min) = 4, n (5 µL/min) =3, n (7 µL/min) =2, n (10 µL/min) =2, n (12 µL/min) = 1, n (15 µL/min) = 1 (Results data was summarised in section 9.6/Table 9.2).

H&E staining was carried out on all tissues with different flow rates (Figure 3.18). The rat liver tissues that were perfused at flow rates of 2, 7 and 12µL/min showed clear and observable nucleus staining. Although the number and the visibility of the nucleus are clear and obvious on the tissue at flow rate of 12µL/min, the gap between the cells on the tissue section was large and the tissue was looser. The tissues with other different flow rates demonstrated poor morphology and fewer nuclei was observed. The flow rates of 2 and 7µL/min showed better and optimal in maintaining the morphology of rat liver tissues in the device.

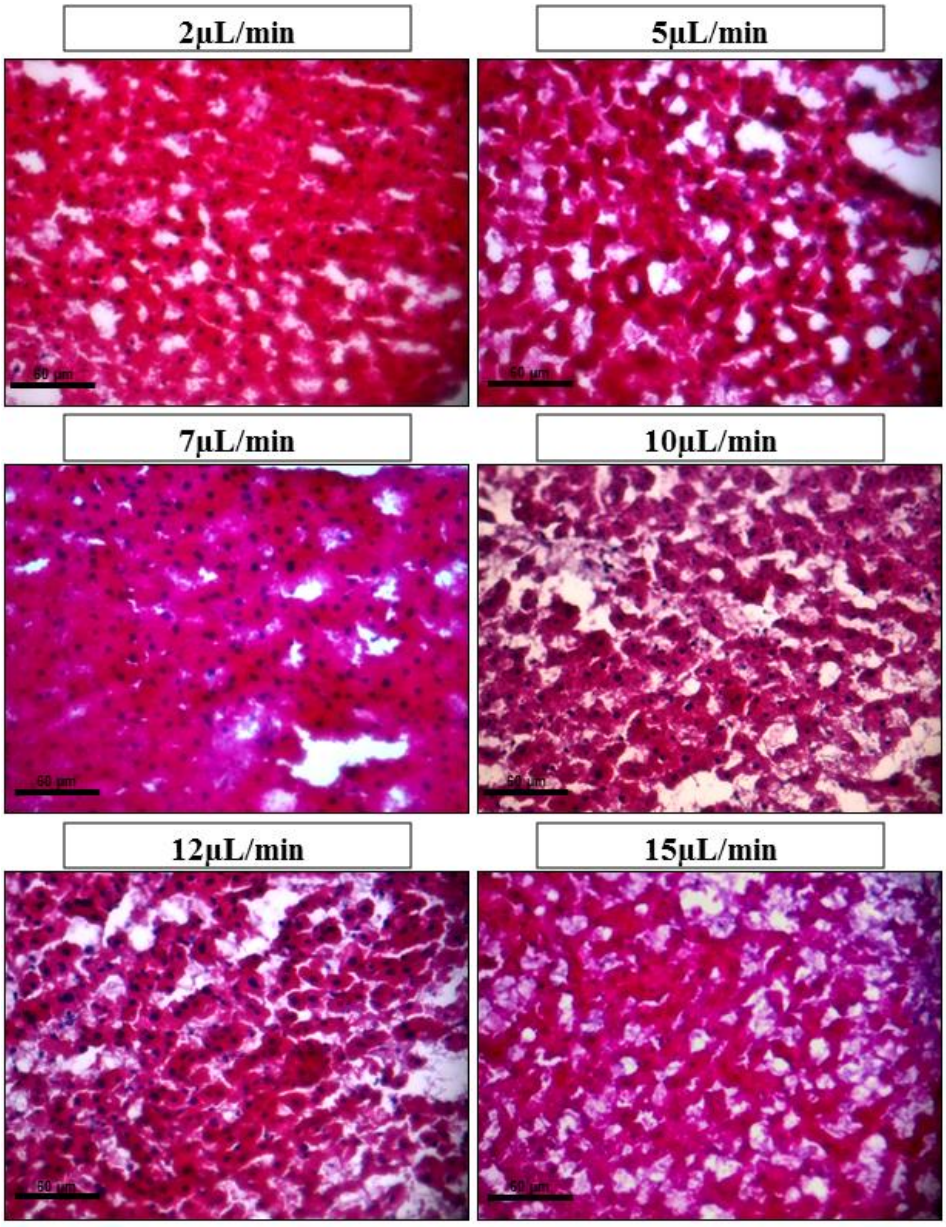


Figure 3.18. Representative H&E staining of 6 representative rat liver tissues out of 13 tissues following microfluidic perfusion.
Six different flow rates: n (2 µL/min) = 4, n (5 µL/min) =3, n (7 µL/min) =2, n (10 µL/min) =2, n (12 µL/min) = 1, n (15 µL/min) = 1. Red represents eosin stained cytoplasm and blue is haematoxylin stained nuclei (x400 magnification).

IHC staining using anti-BrdU antibody as a primary antibody was carried out on all tissues with different flow rates (Figure 3.19). Based on the staining results, the results were found similar with that of the H&E staining. The rat liver tissues that were perfused at flow rates of 2, 7 and 12µL/min showed positive brown staining, suggesting that these tissues were still replicating on day 4.

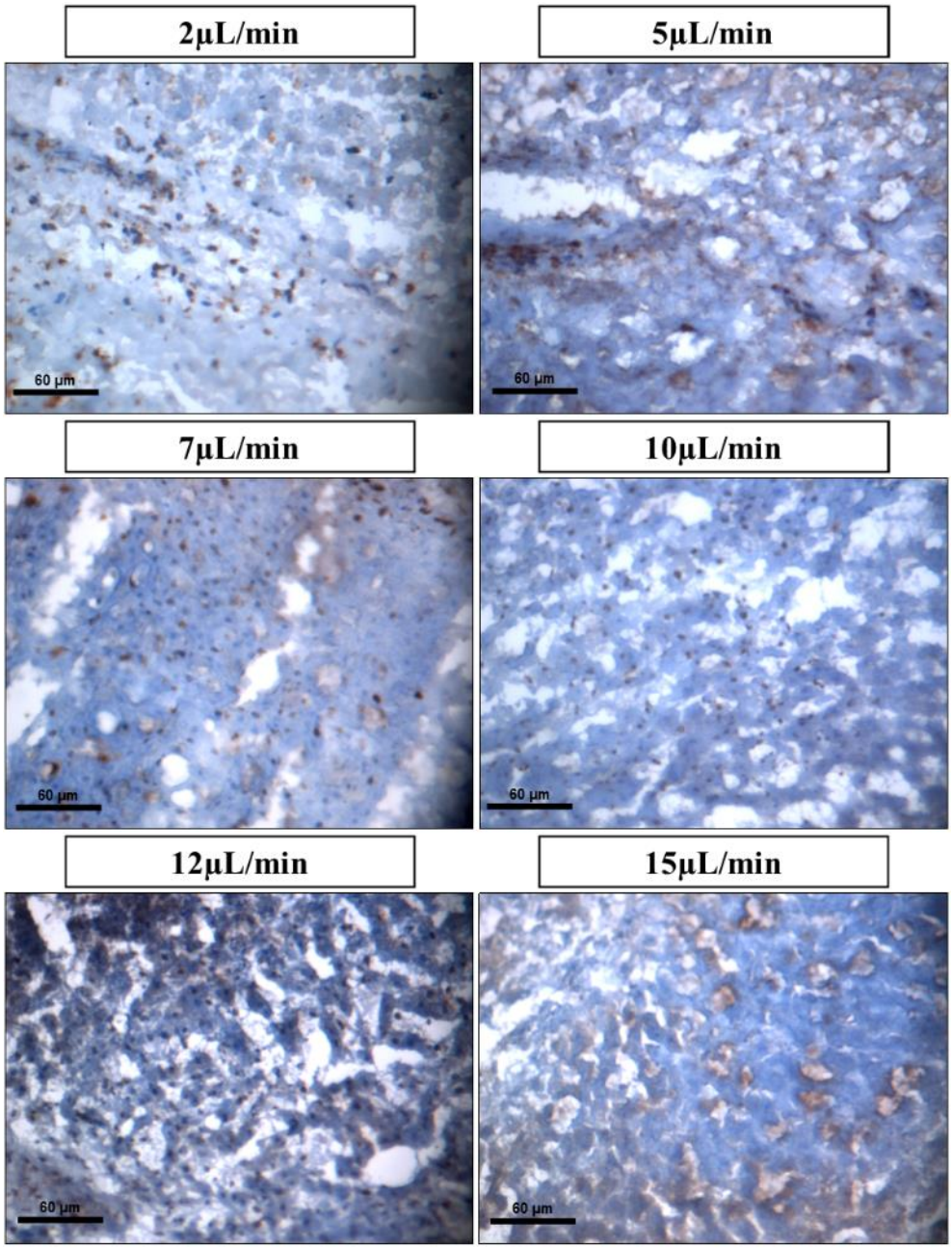


Figure 3.19. Representative IHC labelling of BrdU incorporating cells in 6 representative rat liver tissues following microfluidic perfusion.
Six different flow rates: n (2 µL/min) = 4, n (5 µL/min) =3, n (7 µL/min) =2, n (10 µL/min) =2, n (12 µL/min) = 1, n (15 µL/min) = 1. Mouse anti-BrdU (1:50) was added in positive control sections and negative control antibody that has same isotype as primary antibody (IgG1, κ) was used in negative control. Proliferating cells are identified by brown nuclear staining and counterstained with light haematoxylin (x400 magnification).

In conclusion, according to the analyses performed in determining the best flow rates for the tissue culture using microfluidic device, the flow rates of 2µL/min and 7µL/min were found optimal in perfusing the rat liver tissues without inducing high release of LDH, affecting the morphology and inhibiting the proliferative status of the tissue. As a result, these two flow rates were then applied to the culture of head and neck cancer tissues at the microfluidic platform.

3.10. The interrogation of HNSCC tissues in microfluidics for 4-6 days

Once optimised on rat liver tissue, the same parameters were tried using frozen head and neck tumour (HNSCC) tissue and adjusted accordingly to maintain the ideal culture. Three HNSCC tissues (neck node metastasis from floor of mouth primary tumour; TR52; 1 cryopure tube) with similar weight (between 5-10mg) were sliced and subjected to three parallel microfluidic devices. The culture medium used throughout the flow system was at the flow rate of 2µL/min and was Dulbecco's Modified Eagle's Medium (DMEM; PAA) which was supplemented with penicillin/streptomycin, L-glutamine, 10% FBS, fungizone, 1% non-essential amino acid (NEAA; PAA) and 30mM of HEPES buffer. The three HNSCC tissues were then taken out from the device and frozen at 4, 5 and 6 days of microfluidic flow, respectively. At 6 hours prior the tissue freezing, 10µM of BrdU was added into the perfusion system to allow the study of proliferation status on each tissue. Effluent medium was collected at every two hours for LDH cytotoxicity assay while the tissues were sectioned and subjected to H&E staining and BrdU IHC staining.

The absorbance values of the formazan dyes at every 2-hour time point are shown in Figure 3.20.A and B. At the first five hours after the tissues inserted into the device, the amount of LDH released was high due to the frozen tissue thawing and the manipulation of the tissue biopsy prior to being placed into the device. Following the initial high level of LDH release, the levels dropped to very low level which was near to zero absorbance value. This could come to an explanation that the tissues were maintained with low LDH release, retained morphology and proliferation in the device throughout the 6 days of culture. This was further validated by the increased LDH release on tissue following addition of 10% lysis buffer (Figure 3.20.A).

The morphology H&E staining of the HNSCC tissues was carried out on the frozen tissue sections (Figure 3.20.C). Based on the photographs of the HNSCC tissue sections at magnification of x400, the morphology was good in the three HNSCC

tissues following respective 4, 5 and 6 days in the devices. The haematoxylin staining of nucleus was seen clearly in the tissue that was cultured for 6 days, although the number of nucleus was less than that cultured for 4 and 5 days. According to the BrdU staining results (Figure 3.20.D), BrdU-incorporated cells were detected on the tissue maintained for up to 6 days in the device. This result was similar with the morphological H&E staining and the LDH cytotoxicity assay, suggesting that the lymph neck node tissue (TR52) could be maintained in the microfluidic device for up to 6 days.

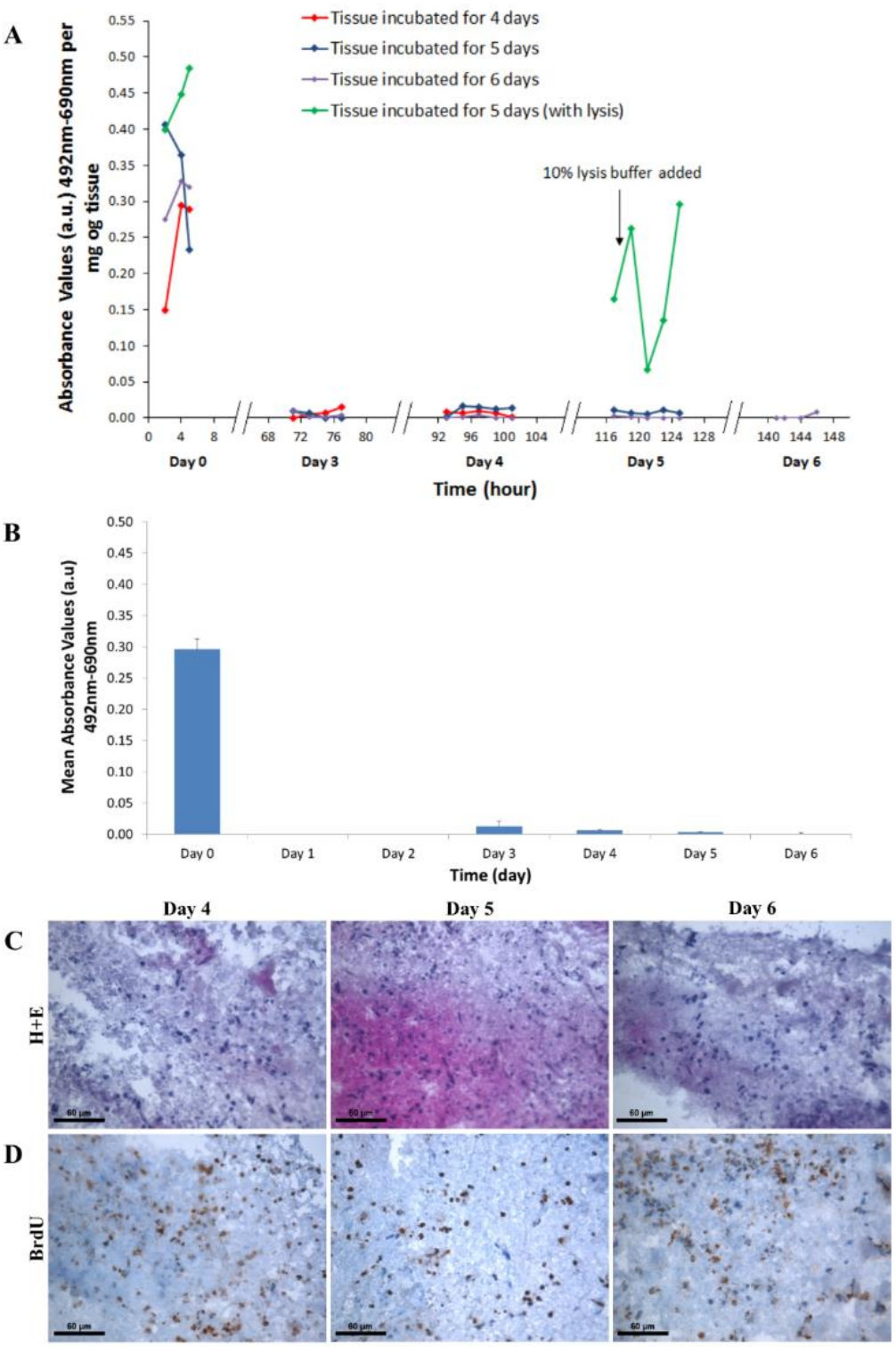


Figure 3.20. Three HNSCC tissues (neck node metastasised from floor of mouth primary tumour; TR52) subjected to 4, 5 and 6 days of culture in devices with medium supplemented with 30mM of HEPES and 10% of FBS at flow rate of 2µL/min.

(A) LDH release from the three tissues measured at every two hours. The absorbance values were assessed in duplicate and standardised per mg of tissue biopsy (Day 4: 7.5mg; Day 5: 5.4mg; Day 6: 9.1mg). Additional tissue maintained for 5 days and 10% lysis buffer was added about 6 hours before tissue freezing. (B) Mean LDH released obtained on daily basis from the three tissues. Mean+SEM. (C) Representative H&E staining of the three tissues (x400 magnification). Red represents eosin stained cytoplasm and blue is haematoxylin stained nuclei. (D) Representative IHC labelling of BrdU on rat liver tissues following microfluidic flow. A mouse anti-BrdU (1:50) monoclonal antibody was added to all sections. Proliferating cells are identified by brown nuclear staining and counterstained with haematoxylin (x400 magnification).

3.11. The use of 10% AB serum during HNSCC tissue culture in microfluidics

Since human tissue was subjected to the tissue culture in microfluidic system, the medium consists of 10% (v/v) of AB human serum (ThermoFisher Scientific) instead of FBS is believed able to improve the maintenance of head and neck cancer tissue in microfluidics. Therefore, three tissues of a lymph node which metastasised from an oropharyngeal cancer (tonsil; TR54; 1 cryopure tube used) were subjected to microfluidics for respective 4, 5 and 6 days. Similar analyses were carried out: LDH assay, H&E staining and IHC staining of BrdU. In order to compare between the medium containing FBS and AB-human serum, another three tissues were perfused with medium containing 10% FBS for respective 4, 5 and 6 days and the same analyses were carried out.

The amount of LDH released from the three tissues is presented in Figure 3.21.A. At the first five hours of the culture, the amount of LDH released from the tissues was high due to the cellular damage on the tissue surface that was created by tissue handling at the beginning. The amount of LDH released was then reduced significantly to very low level (below 0.10a.u.). There was no difference in the LDH released from the tissues maintained in the medium containing the two different serums. However, there was no additional tissue subjecting to lysis carried out. According to the H&E tissue staining (Figure 3.21.D for AB serum and Figure 3.21.C for FBS), the tissue that cultured in the FBS-contained medium on day 5 showed good morphology with better maintenance of the nuclear structure compared with the tissue that was perfused with AB serum-contained medium. On day 6, the tissue cultured with AB serum-contained medium has clear nuclear staining whereas the morphology of the tissue cultured with FBS-contained medium showed considerably fewer nuclei.

The proliferating cells were highly detected on the tissue that was cultured with AB serum-contained medium on day 5 (Figure 3.21.E). The positive brown nucleus staining was found less on the tissue on day 6 compared with that on day 5. The results were found similar with the H&E staining. In summary, the use of 10% human AB serum instead of 10% FBS in the culture medium does not add cultural benefits to prolong the morphological and proliferative maintenance of the tumour in microfluidics.

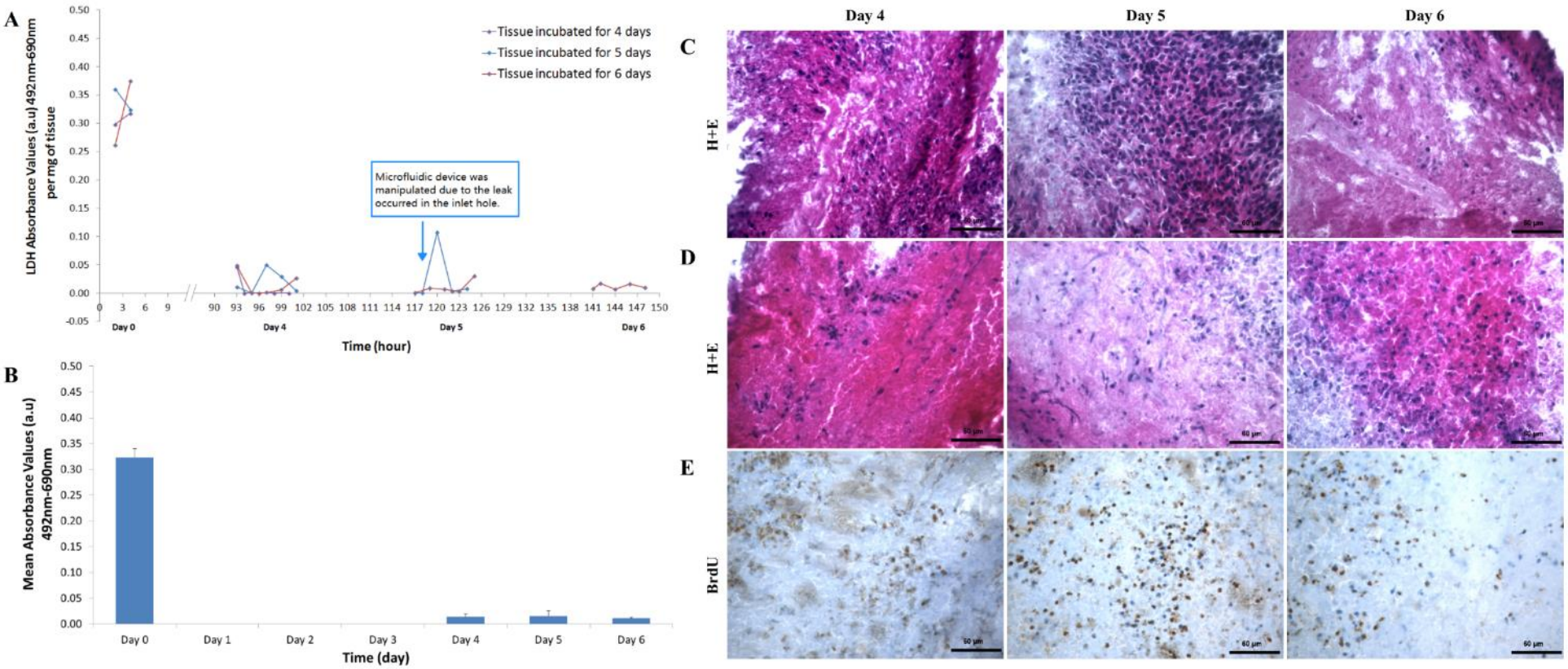


Figure 3.21. HNSCC tissues (neck node metastasised from tonsil primary tumour; TR54; n=6) subjected to microfluidics, three of them maintained for respective 4, 5 and 6 days with medium containing 10% of human AB serum and three of them cultured for respective 4, 5 and 6 days with medium containing 10% of FBS.

(A) LDH release from the three tissues at every two hours throughout microfluidic flow with human AB serum medium. The absorbance values were assessed in duplicate and standardised per mg of tissue biopsy (Day 4: 7.0mg; Day 5: 7.1mg; Day 6: 6.9mg). (B) Mean LDH released obtained on daily basis from the three tissues. Mean+SEM. Representative H&E staining of (C) three tissues perfused with FBS medium and (D) three tissues perfused with human AB serum medium (x400 magnification). Red represents eosin stained cytoplasm and blue is haematoxylin stained nuclei. (E) IHC staining of BrdU on tissues perfused with human AB serum medium (x400 Magnification). Proliferating cells are identified by brown nuclear staining and counterstained with haematoxylin.

3.12. Permeation of FITC-conjugated dextran across tissues in microfluidics

The diffusion ability of nutrients in medium through the tissue in microfluidics are unknown for the current microfluidic set up. It was, therefore, essential to evaluate the permeation pattern of molecules present in the medium across the tissue biopsy in order to understand whether factors such as BrdU, EdU, fluorescein isothiocyanate (FITC)-conjugated caspase inhibitor (CaspACE), and FITC-conjugated 2-NBDG could potentially reach the centre of the tissue. The molecular weights of each nutrients and the biological markers added into culture medium are summarised in Table 3.5. One Dalton (Da) represents one atomic mass unit which is a unit of mass defined as 1/12 weight of carbon-12 atom in ground state, indicating that the conversion of 1 Dalton to g/mol is by one. Therefore, direct conversion and comparison on both molecular weight units could be done and the permeation of molecules of different molecular weights into tissue was compared in microfluidics based on the incorporation of FITC-dextran (4kDa) molecules throughout the tissue.

Table 3.5. The molecular weight of the nutrients and chemical substances present in culture medium used to perfuse tissue maintained in microfluidics.

Nutrients and chemical substances perfused	Molecular weight (g/mol or Da)
Penicillin	334.39 g/mol
Streptomycin	581.57 g/mol
HEPES	238.30 g/mol
Fungizone	1339.84 g/mol
L-glutamine	146.14 g/mol
Non-essential amino acids (NEAA)	75-147 g/mol
BrdU	307.1 g/mol
EdU	252.23 g/mol
2-NBDG	342.26 g/mol
FITC-conjugated dextran	4,000Da

The permeation of FITC-conjugated dextran at 4kDa molecular weight was tested on a lymph neck nodes metastasised from a laryngeal tumour (TR80; 1 cryopure tube) and an oropharyngeal tonsil tumour (TR122; 1 cryopure tube) respectively. The reason the dextran at 4,000 Dalton was used because this size is larger than the molecular sizes of the nutrients and other incorporation markers (2-NBDG, BrdU and EdU) used in this project (Table 3.5). The incorporation of FITC-conjugated dextran at 1mg/mL

into the tissue between 30 minutes and 2 hours of perfusion was compared and the location of the dextran was captured at x400 magnification following tissue freezing and slicing (Figure 3.22). The procedure of dextran incorporation in microfluidics was repeated twice on both neck nodes to validate the reproducibility of the permeation.

The lymph node tissue (from oropharyngeal tumour), which was maintained in parallel microfluidic device in the absence of dextran for the same period of time, showed no green positive fluorescence, confirming the negative control and no auto-fluorescence in the FITC channel. Following addition of both lymph node tissues with FITC-labelled dextran (4kDa) for 30 and 120 minutes in the device, green fluorescent staining was observed across the sections at both time points (Figure 3.22). This suggested that the FITC-dextran marker (4kDa) could permeate across the tumour tissue at size of $3mm^3$ (5-10mg) in the device and the nutrients or markers at 4kDa size or smaller size could perfuse and permeate through the tissue in the device.

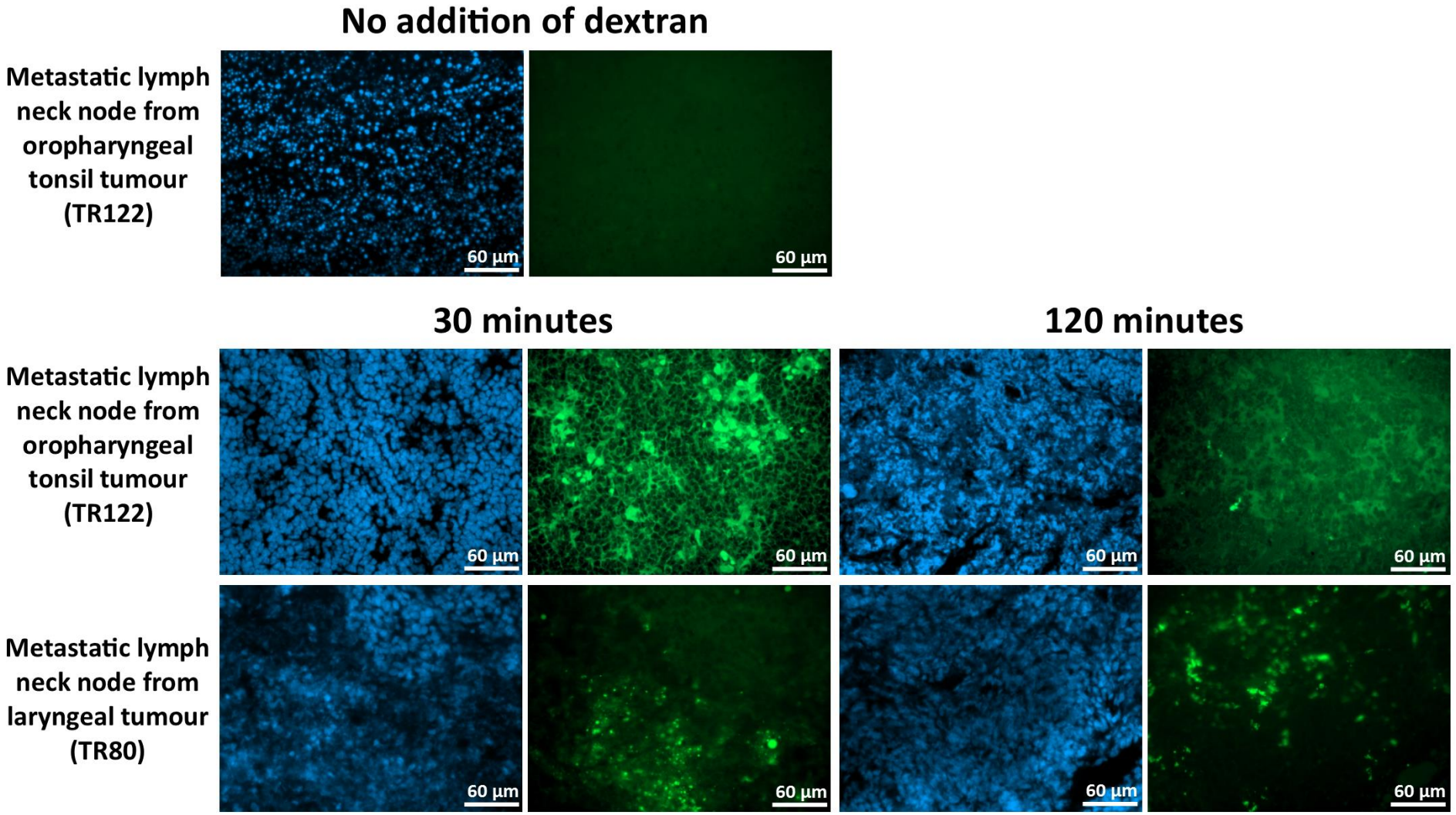


Figure 3.22. Representative images of FITC-conjugated dextran incorporated into HNSCC tumours (TR80 and TR122) following dextran addition for 30 (left) and 120 minutes (right; x400 magnification).
Negative control for the incorporation was tested on the metastatic lymph neck node from oropharyngeal tonsil tumour which was maintained in microfluidics for same period of time with no addition of dextran.

3.13. Discussion

The aim of this chapter was to evaluate various parameters to determine the optimal microfluidic culture conditions for HNSCC tumour tissue prior to irradiation experiments. In addition, to ensure that the nutrients and markers present in the culture medium could reach the tissue in microfluidic device, the size-dependent permeation of the nutrients and markers across tissue was determined.

3.13.1 Determining the optimal experimental conditions for analysis of BrdU incorporation into tissue maintained in a microfluidic device

Cell proliferation and cell cycle distribution are important indicators of the cellular response to anti-cancer therapeutics. In order to assess the changes in the percentage of cells undergoing proliferation following irradiation, the optimal time of tissue perfusion with the thymidine analogue BrdU in the microfluidic device had to be determined. This is the first attempt of incorporating BrdU into biopsies, and published cell line experiments were used as a starting point. Time courses for the BrdU addition to cell lines have been carried out in the Jurkat human T-cell line using BD Pharmingen ™ FITC BrdU flow kit (Crane *et al*., 2011). The cells were fixed and stained using the flow kit after 3, 6, 9 and 24 hours post BrdU-pulse and the bivariate contour plots of 7-AAD vs BrdU FITC were accomplished. Based on the results obtained, the 3 hours of BrdU incubation resulted in 43% of the BrdU labelled cells being in S-phase. These cells were then transitioned to late S and G_2 phase at 6 hours and 38% of BrdU-labelled G_1 cells were observed at 24 hours. The amount of BrdU S-phase signal weakened and was then diluted over the next 24 hours indicating the turnover of the label with cell division, emphasising the importance of the BrdU-pulse time point to detect specific proliferating populations.

The pulse time of BrdU with cells varies depending on the experimental system and different cell/tissue types. For example, the effective length of time for pulsing an actively proliferating cell line (e.g. IL-2-dependent cytotoxic T-cell line, CTLL-2 cells) with BrdU has been found to be 30-45 minutes whereas a less actively proliferating cell culture such as normal human dermal fibroblasts require a 4 hours BrdU pulse for optimal staining (Gasparri *et al*., 2004).

It was envisaged that longer time periods of BrdU incorporation would be required compared to the 2D cultures mentioned previously, therefore, 1 and 6 hours of BrdU-pulse on both oropharyngeal cells (UMSCC-47) on coverslips and tissue biopsies (rat

liver and HNSCC tissues) in the microfluidic device were evaluated (section 3.2). The oropharyngeal cancer cells showed 36.7+4.2% of BrdU-labelled signals even at 1-hour BrdU pulse time. This agreed with the positive BrdU staining on the lymph node tissue which was similarly perfused with 1 hour of BrdU in microfluidics but less staining was observed on the rat liver tissue (Figure 3.4). The observed difference of the proliferation levels between the HNSCC tissue (TR52) and rat liver tissue at 1 hour BrdU pulse time could be explained that the cancerous cells proliferate more than the normal rat liver cells (Cooper, 2000). In microfluidics, the 6 hours of BrdU perfusion on both rat liver tissue and HNSCC tissue showed more suitable for detecting proliferating cells compared with that of 1-hour, perhaps, due to the limited time allowed for diffusion.

3.13.2 The potential of microfluidics to maintain tissue morphology and proliferation

To validate the ability of microfluidic device in maintaining the *in vivo* cancer microenvironment, the frozen rat liver tissue and HNSCC tissues were placed in the microfluidic system and the tissue behaviour was examined based on the release of LDH, morphology H&E staining and BrdU proliferation markers. When the LDH released by the tissue was measured in the effluent medium, the LDH level was high at the beginning of the experiment which reproducibly indicated a large amount of initial cell death thought to be associated with tissue manipulation (Van Midwoud *et al*., 2010). The LDH levels then rapidly decreased to minimal detectable levels, suggesting the low cell death of the tissue in the device. The initial release and the subsequent stabilisation was detected in both rat liver tissues and HNSCC tumours and has also commonly been observed by other colleagues in the research group (Hattersley *et al*., 2008; Hattersley *et al*., 2012; Carr *et al*., 2014) which also measured the absorbance values of formazan dye formed to achieved the LDH relative comparison.

Van Midwoud *et al* (2010) also assessed the leakage of enzymes (including LDH) as the percentage of the total LDH present in three rat slices during the perfusion in biochips and determine the cell death level of liver slices maintained in devices. The results obtained in this study was in agreement with our results which showed an initial high percentage of LDH leakage/release (during the first hour; ~9%) was reduced to a low level, less than 0.5% of the slice content per hour. One might argue that the

tissue may simply have all died within the first few hours after being placed in the device and this is why the LDH levels reduce down to minimal throughout the remainder of the experiment. Therefore, the lysis reagent was added to the perfusion system and it showed, in most of the tissues in this chapter, that the further increase of LDH levels was observed following lysis treatment. The increase of LDH release induced by lysis suggested that the LDH was retained in the tissue in the device throughout the period and the cells within the tissue are not all dead throughout the microfluidic flow. This agrees with the results obtained in Van Midwoud *et al*. (2010), in which the LDH content on the effluent medium collected throughout the microfluidic flow was assessed. Following microfluidic culture, the tissue slices were homogenized, centrifuged and the LDH content on the supernatant was then measured which was used to evaluate the LDH leakage as a percentage of the total LDH present in the tissue slice. After 24 hours, more than 95% of the LDH that was present after the first hour was retained in the tissue slices (Van Midwoud *et al*., 2010), indicating that the cells are not damaged by the microfluidic flow.

Based on current LDH study, the LDH release level remained low up to 9 days in the device whereas the H&E staining showed the morphology of HNSCC tissue can be maintained up to 6 days in microfluidics (Figure 3.10 and Figure 3.20). Although different results were obtained among similar microfluidics studies, in which the rat liver tissues could be maintained in device up to 15 days (Carr *et al*., 2014) and the primary HNSCC tissue could be maintained in microfluidics up to 7 days (Hattersley *et al*., 2012), both studies, however, utilised LDH cytotoxicity assay but not assessed the tissue morphology and proliferation following the tissue culture in microfluidic device.

Therefore, in addition to LDH assay, H&E and BrdU incorporation staining were also used in the current study. In contrast to the LDH results which demonstrated very little cell death in the rat liver tissue for up to 9 days in the devices, both H&E staining and IHC of BrdU showed that the morphology and the proliferation of the tissue respectively deteriorated after three days cultured in the device. However, by altering the constituents of the medium flowing over the tissue and the rate of flow, the maximum time the tissue can be maintained in the device was increased to 5 or 6 days. The changes made included the addition of HEPES buffer to stabilise the pH of the medium in the device and flow rate of 2µL/min to perfuse the tissue.

Under *in vitro* tissue culture condition without vascular blood supply, nutrient delivery to cells throughout the tissue in tissue chamber is important to maintain the cellular activity and viability. The higher medium flow rate is thought to be beneficial in delivering nutrients and oxygen to the cells. However, the cellular functions (e.g. hepatocyte functions, albumin and urea synthesis rates) in the device could be diminished by the increased shear stress created by the higher flow rate (5-21 dyn/cm^2; Tilles *et al*., 2001). Different flow rates of culture medium perfusing a tissue biopsy in a microfluidic device and cellular viability, therefore, were tested and evaluated in current microfluidic system and in other studies (Tilles *et al*., 2001; Cartmell *et al*., 2003; Cullen *et al*., 2007).

In the study proposed by Tilles *et al*. (2001), the daily albumin and urea synthesis rates were compared between the tissues perfused with higher flow rates (3460, 3820 and 4180µL/min) and those at lower flow rate (60µL/min). They found that the synthesis rates ar the higher flow rates were significantly lower on day 3 of culture in the device compared with that on day 0. It has also been shown in a study by Cartmell *et al.* (2003) that the highest flow rate (1000µL/min) caused nearly complete cell death when assessed by confocal microscope (calcein and ethidium homodimer fluorescent cell stains that labels viable and dead cells respectively) throughout the tissue after 7 days of microfluidic culture. In addition, the functionality of the rat liver tissue culture maintained in the same in-house microfluidic glass device with same medium flow rate has been assessed previously by a colleague using the ELISA assays to detect the albumin and urea production (Hattersley *et al*., 2008). Hattersley *et al*. (2008) showed that the fluidic properties and geometric size of the device are able to maintain the tissue functions based on the continuous production of albumin and urea. Therefore, culture medium perfused at flow rate of 2µL/min to maintain tissue in microfluidics was implemented to study the tissue response to irradiation.

Insufficient oxygen delivery to the culture tissue in microfluidic device could result in decreased viability and function (Tilles *et al*., 2001). In a microscale device implemented in Tilles *et al*. (2001), the hepatocyte cells at the entrance (15mm from inlet) were exposed to progressively lower oxygen tensions which caused the reduced viability (>98% of viable cells detected at entrance, 48% at middle position and no viable cell was detected at exit positions; Figure 3.23). The integrated membrane oxygenator in the device assisted the efficient oxygen delivery to all cells via diffusion

and most cells were observed viable consistently at all locations within the bioreactor (85%, 82% and 87% at entrance, middle and exit positions).

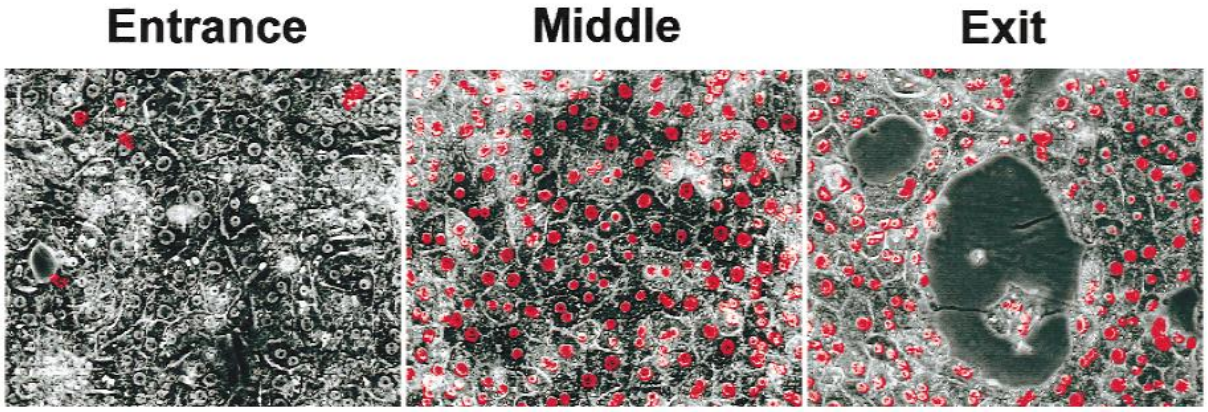


Figure 3.23. Phase-contrast photomicrographs with superimposed fluorescence imaging that showed dead hepatocytes.
The indication of dead hepatocytes at the entrance, middle and exit positions after 8 hours of continuous perfusion in the microfluidic device was presented in red. Flow rate of 0.1 mL/min was implemented (Image adapted from Tilles *et al*., 2001)

In our study, although there was no oxygen bioreactor integrated in the microfluidic device, the oxygenated culture medium was used, aiming to improve the oxygen supplement to tissue inside the microfluidic chamber. The uses of culture medium gassed with carbogen gas mixture (95% O_2 and 5% CO_2) on the rat liver tissues in our microfluidic devices showed no benefits to the tissue morphological and proliferative maintenance. It is unclear that whether the high oxygen level on the medium in syringe can be maintained throughout the microfluidic set up from inlet till the outlet tube. Therefore, accurate and continuous measurement of the oxygen level in culture medium at different parts of the microfluidic system is necessary to identify the beneficial effects of high oxygen level on the tissue culture. The poor tissue morphology following perfusion of oxygenated medium may be because of the inefficient oxygenation methods to increase the oxygen level in medium or due to the toxicity created by high oxygen level on medium perfusing the tissue, affecting the cellular behaviour (Rueckert and Mueller, 1960; Gregory, Goscin and Fridovich, 1974; Baez and Shiloach, 2014). Therefore, in the current microfluidics, the high oxygen level in culture medium might be toxic to the tissue which could exert cytotoxic effects and DNA damage by reactive oxygen species (ROS; Dennog *et al*., 1999; Lo, Sinkala and Eddington, 2010).

The 10% (v/v) of FBS in culture medium on rat liver tissues in microfluidics showed better morphology and proliferation maintenance than the use of 10% (v/v) of rat

serum in medium. It was known for more than 25 years that the higher FBS concentration allowed faster growth on hybridoma cells (CRL-8018 cell line; Kunas and Papoutsakis, 1989, 167.4G5.3 cell line; Ozturk and Palsson, 1991). The effects of the serum concentration in culture medium on the cell growth based on cell viability and metabolism by glucose consumption and lactate production rates have been studied in HeLa S3 culture by El-Ensahsy *et al*. (2009). They showed that increasing serum (FBS) concentration from 5% to 15% in the culture medium induced 30% increase on the total viable cell number while the further increase of the concentration caused significant reduction in number of living cells. Combining these with the results obtained in this chapter, the culture medium containing 10% of FBS was used to culture HNSCC tissue in microfluidic system.

Similar with current microfluidic study, human AB serum which was identified as alternatives to FBS for long-term culture was implemented and compared with foetal calf serum in a study proposed by Kocaoemer *et al*. (2007). The use of human AB serum has been shown to have significantly higher proliferative effects on adipose tissue-derived mesenchymal stem cells with 1320-1400-fold expansion compared with that incubated with foetal calf serum which achieved 254-fold expansion. Contradictory results were observed between our microfluidics and human AB serum study and the mesenchymal stem cells study on Kocaoemer *et al*. (2007). In current study, human AB serum showed no cultural benefits to maintain HNSCC tissue in microfluidics based on H&E staining, LDH cell death assay and BrdU proliferation expression (Figure 3.21). However, only one repeat (n=1 for each day; 4, 5, and 6) was carried out in microfluidic device with medium containing human AB serum. With the optimum parameters in place, it was demonstrated that microfluidic culture has the potential to maintain tissue for a sufficient period of time to enable tissue response to radiation to be determined.

3.13.3 Size dependent marker permeation through tissue in microfluidics

FITC-conjugated dextran comes in different molecular weights dependent on the number of glucose molecules present and can range from 4kDa to 2000kDa (Sigma, UK). It is possible to label dextran fluorescently allowing the tracking of the molecule, making it an ideal candidate to measure the capability of specific sized substances to penetrate tissue. FITC-conjugated dextran at 4kDa was implemented as fluorescent probe to study permeability of epithelial tissues such as intestinal (Moeser *et al*., 2012)

and renal (Ikari *et al*., 2011) *in vivo* while the FITC-conjugated dextran at 2000kDa was used to determine the vascular permeability (Debefve *et al*., 2011) and the integrity of the blood brain barrier (Prabhakarpandian *et al.,* 2013). In this chapter, therefore, a specific size of FITC-conjugated dextran (4kDa) was added to the tissue biopsy that maintained in microfluidic device, aiming to determine whether all the nutrients or markers presented in culture medium can supply to all cells, particularly the cells located at the middle of the tissue.

The integration of the FITC-dextran diffusion method with the microfluidic approach to evaluate the vascular and epithelial permeability was evaluated by various studies (Hallow *et al*., 2008; Jeon *et al*., 2013; Lee *et al*., 2014; Prabhakarpandian *et al.,* 2013; Park *et al*., 2014). Lee *et al*. (2014) used FITC-dextrans at different molecular weights (4kDa, 20kDa, 70kDa) to measure the permeability of the endothelial barrier and they showed clearly that the permeability coefficient decreased with increasing molecular weight (7.33×10^{-6} cm/s for 4 kDa to 1.55×10^{-6} cm/s for 70 kDa). An *in vitro* model to investigate tumour cell extravasation through an endothelial monolayer also implemented by Jeon *et al* (2013) in which the integrity of the endothelial monolayer was monitored by the fluorescence imaging of FITC-dextran (70kDa) distribution. The real-time tracking of FITC-dextran in a microfluidic synthetic microvasculature model of the blood-brain barrier (SyM-BBB) has also successfully been established (Prabhakarpandian *et al.,* 2013). The tight junction between the cerebral endothelial cells formed a diffusion barrier for the permeation of the fluorescence marker and the permeation experiment on the tissue cultured in the device enable the investigation on the device capability in maintaining pseudo *in vivo* tissue characteristic. Therefore, the rat brain endothelial cells cultured in SyM-BBB microfluidic device were perfused with the dextran marker (3-5kDa) and the distribution and the permeation of FITC-dextran marker was imaged at regular time points. They showed that the device exhibited significantly low permeation levels even after 60 minutes of incubation which suggested that the formation of tight junction between the endothelial cells in the device.

The ability of biological markers and culture nutrients to perfuse the head and neck cancer tissue maintained in the microfluidic device was predicted using FITC-dextran (4kDa) as a guide in the current study. Fluorescent images were captured of the dextran-perfused and control tissues which were harvested at same time point and

showed that the dextran at this molecular size was able to perfuse across the tissue to the centre. This suggested that the nutrients in culture medium and the cellular markers with a molecular weight smaller than 4kDa could enter the 5-10mg of tissue in microfluidic device (Table 3.5). Although liquid nitrogen was used to snap freeze both the rat liver and the human tumour samples to minimise the formation of ice crystals, some damage is inevitable which may skew the diffusion/permeation of the FITC-dextran markers from the medium through the centre of the tissue, giving the false-positive results, however all tissues were treated the same to minimise discrepancies. Furthermore, the additional viability test used to evaluate the survival of cells inside tissues, for example, LDH staining on cryosections, calcein AM/ethidium homodimer-1 staining and trypan blue assay (Gantenbein-Ritter *et al*., 2008).

In conclusion, optimal conditions for the maintenance of tissue in the hull microfluidic device for up to 6 days were established in which the morphology and proliferation were maintained with low LDH release throughout the microfluidic flow. In summary, the addition of 30mM HEPES buffer in WME culture medium at flow rate of 2µL/min was observed to be optimal to culture rat liver tissue in microfluidics based on the LDH release measurement, H&E staining and BrdU incorporation detection. The medium containing low serum concentration (serum free-5% of FBS), 10% of rat serum and high percentage of oxygen (consists of 95% of oxygen and 5% of carbon dioxide) showed no positive and additive effects on the maintenance of HNSCC tissues in microfluidics. This provides a platform for the study of the response of the tissue to irradiation or other therapeutic treatments to be carried out as described in subsequent chapters.

4. Measuring the effects of irradiation on HNSCC tissue maintained in a microfluidic device (I) – Cell death and DNA repair

4.1. Introduction

The resistance of HNSCC patients to radiotherapy and the recurrence of the tumour following radiotherapeutic treatment remains a serious barrier to successful treatment outcome of these patients. The 5-year survival rate remains low, for example, laryngeal patients diagnosed between 2008 and 2012 achieved only a 66.7% 5-year survival in 2013 (section 1.1.2; Siegel, Miller and Jemal, 2015). Patients, who are radioresistant and relapse after radiotherapy treatment, are then subjected to salvage surgery which proves to be more difficult due to the disrupted planes of tumour margins following irradiation (Temam *et al*., 2005). The salvage surgery for 136 HNSCC patients who had relapsed following accelerated radiotherapy, in the Temam *et al* (2005) study, resulted in limited survival benefit based on the investigation of local recurrence, cervical node recurrence and distant metastasis. In addition, salvage surgery can potentially affect vital functions including speaking, swallowing, and breathing, resulting in a poorer quality of life for the patient and greater morbidity (Yao *et al*., 2007). The increased cost to the NHS when first line treatment is unsuccessful is substantial meaning that identifying radio-resistant malignancies in patients would be beneficial to both patient and the NHS creating a more personalized therapy.

The ionising radiation affects the tumour cells by inducing different kinds of cell death modalities (Kroemer *et al*., 2009), altering the DNA damage repair pathway (Scully and Xie, 2013), as well as the tumour microenvironment (Ma, Xu and Qian, 2013; Barker *et al*., 2015). Therefore, many researches have concentrated on many and diverse areas such as the tumour microenvironment (Barker *et al*., 2015), the identification of types of cell death (Kroemer *et al*., 2009), the genes and pathways that are used to repair DNA damage (Mah, El-Osta and Karagiannis, 2010; Scully and Xie, 2013), and the signalling pathways used in activating cell cycle arrest (Yang *et al*., 2015), cellular metabolic pathways (Koukourakis *et al*., 2000; Zhong *et al*., 2013), and cell membrane damage (Bhosle *et al*., 2002; Mishra, 2004). To understand and predict the radio-sensitivity on HNSCC tumour, many studies have used surgically removed tumour biopsies from HNSCC patients to identify markers of the altered processes involved in irradiation resistance (Table 4.1). The markers implemented in

the following chapters were selected based on the literatures review and a mixture of cell death, proliferation and DNA damage response markers were selected which have also been used previously by other studies (illustrated in each relevant chapters and sections).

Table 4.1. Studies of irradiation effects on tumour biopsies from patients presenting with HNSCC, listed according to years of publication.

Reference	Number	Patient samples	Treatment	Markers	Results findings
Gallo *et al*., 1996a	35 (23 laryngeal, 6 oral cavity, 3 oropharyngeal)	Specimens collected pre- and post-RT from patients who failed primary RT	Daily dose (1.8-2Gy), >60 to 72Gy	*p53* (DNA isolation and PCR)	*p53* gene mutation in both pre- and post-IRT samples correlated with increased survival.
Gallo *et al*., 1996b	71 (67M, 4F)	Specimens collected pre- and post-RT from patients who failed primary RT	Daily dose (1.8-2Gy), > 52 to 70Gy.	Bcl-2 (IHC)	Patients with oral cavity cancers who experienced a radiation failure had high Bcl-2 protein expression.
Koukourakis *et al*., 2000	94	Patients with primary HNSCC were treated with conventionally fractionated RT combined with CT.	Daily dose (2Gy), giving total dose 70Gy	Thymidine phosphorylase (TP; IHC)	Low TP expression was associated with a high rate of complete response after CRT. High TP expression is associated with resistance to RT and CT, and with poorer survival following CRT.
Condon *et al*., 2002	21 (8 RR; 13 RS)	Patients with stage T1 or T2 laryngeal squamous cell carcinoma.	Total dose 60±2Gy in 25 fractions	*p53*, ATM, *p16*, p21, Ki-67, Bcl-2 and BAX (IHC)	Overexpression of Bcl-2 significantly correlated with radioresistance.
Hassan *et al*., 2002	80 (59M, 21F)	Patients were histologically proven advanced SCC of oral cavity, oropharynx, larynx and hypopharynx.	Daily dose 1.8Gy, giving total dose 57.6Gy	Cyclin-B1 (IHC)	Overexpressed cyclin-B1 tumours had significantly associated with high rate of recurrence and metastasis.

Ataman *et al*., 2004	309	Patients with HNSCC in oropharyngeal, hypopharyngeal, laryngeal and oral cavity sites	CHART 54Gy (in 36 fractions over 12 days) versus conventional radiotherapy 66Gy (in 33 fractions over 6.5 weeks)	Bcl-2, *p*53, CD31, cyclin D1, Ki-67 (IHC)	Bcl-2-positivity increased the time to T- and N-failures. High cyclin D1 score decreased the time to N-failures. Low Ki-67 decreased the time to M-failures. High CD31 score associated with a significantly longer time to T-failure.
Nix *et al*., 2004	54 RR 54 RS	Patients diagnosed with laryngeal carcinoma and pre-treatment laryngeal biopsy obtained	55Gy in 20 fractions or 60Gy in 25 fractions	ERCC1 and XRCC1 (IHC)	'Normal' expression of both XRCC1 and ERCC1 (uniformly stained) was significantly associated with radioresistance.
Kumar *et al*., 2008	50 (38M, 12F)	Pre-treatment biopsies obtained from patients with stage III and IV oropharyngeal tumours	CRT with CDDP or carboplatin and fluorouracil.	EGFR, *p*16, Bcl-xL, *p*53 (IHC)	Low EGFR and high p16 expression was significantly associated with better OS and DFS
Giotakis *et al*., 2010	27	Patients with parotid carcinoma	RT (64.8Gy). CT (5-FU and CDDP)	Caspase 8, cytochrome *c*, Bax (IHC)	Caspase-8-negative patients had significantly increased disease-free survival. Bax-negative tumours had improved 4-year DFS.
Rahimi *et al*., 2012	106	Patients with oropharyngeal squamous cell carcinoma.	66-70Gy	EGFR, *p*16, HIF-1α, p21, cyclin-D1, MVP, cyclophilin B, and CA9 (IHC)	*p*16 positive staining significantly correlated with higher LRC and longer DFS

Abbreviation**:** M: male; F: female; RR: radioresistance, RS: radiosensitive, IRT: irradiation, CT: chemotherapy, CRT: chemoradiotherapy, RT: radiotherapy, CHART: continuous hyperfractionated accelerated radiotherapy, DFS: disease-free survival, LRC: locoregional control, IHC: immunohistochemistry, CDDP: cisplatin, 5-FU: 5-fluorouracil, WB: western blotting, RT-PCR: real-time polymerase chain reaction, VEGF: vascular endothelial growth factor, YAP-1: yes-associated protein 1, c-MET: crystallographic structure of MET protein, CD31: cluster of differentiation 31, ATM: ataxia telangiectasia mutated , BAX: B-cell lymphoma-2 associated X protein, EGFR: epidermal growth factor receptor, Bcl-XL: B-cell lymphoma-2 extra-large, ERCC1: excision repair cross-complementation group 1, XRCC1: X-ray repair complementing defective repair in Chinese hamster cells 1, HIF-1α: hypoxia inducible factor 1 alpha subunit , MVP: major vault protein, CA9: carbonic anhydrase 9.

To date very few studies have used microfluidic technology to study HNSCC tissue response to irradiation prior to any clinical therapies. A study performed by the Hull microfluidics group employed the microfluidic device to maintain HNSCC tissue obtained from patients with T1-T3 laryngeal or oropharyngeal SCC and N1-N2 metastatic cervical lymph nodes (Carr *et al*., 2014). The response of the tissues to single irradiation doses (between 2Gy and 40Gy) and a fractionated schedule (5 x 2Gy) was determined using IHC staining of the caspase-3-cleaved CK18. The current study has expanded upon the work carried out by Carr *et al* (2014) by using a greater number of patients, a wider range of irradiation doses and different analytical methods of the tissue.

In the UK, the standard clinical irradiation schedule for HNSCC patients is 66-70Gy, given in fractions of 1.8-2Gy, five times a week for an overall treatment time of 6.5-7 weeks (section 0; The Royal College of Radiologists, 2006). Therefore, it was important in the current study to try and mimic this schedule. Fractionation of the irradiation dose allows time for repair of sublethal damage to normal tissue, allows the redistribution of cells within the cell cycle, because those in s-phase tend to be least radiosensitive, limits the accelerated cell repopulation that can compensate for cell killing induced by irradiation, and permits the tissue reoxygenation between dose fractions which increases tumour sensitivity to radiation (Muriel, 2002; Pawlik and Keyomarsi, 2004; Pajonk *et al*., 2010).

To mimic the fractionated schedule administered to patients exactly was impractical when culturing biopsies in the microfluidic devices due to the limitation of the length of time the HNSCC tissue could be maintained in a morphological intact state within the device. Therefore, alternative irradiation treatments for the tissue were devised in which two fractions of irradiation were administered in each day, five fractions for two and a half days.

Following irradiation, the effects on cell death were evaluated by various assays on both effluent medium and on tissue. Programmed cell death (apoptosis) takes place through a complex signalling cascade (extrinsic pathway, intrinsic pathway and execution pathway; section 1.1) that is tightly regulated at multiple points. As a consequence of these pathways, there are many methods to evaluate apoptosis, some of which detect early apoptotic events and other assays detect later events (Leers *et al*., 1999; Schutte *et al*., 2004; Sundquist *et al*., 2006). The assays used in

the current study to detect cell death between irradiated and non-irradiated tissues are described below.

4.1.1 Cytomorphological alterations

Without the development of stains and staining procedures, the cellular materials and the subcellular structures which appear transparent cannot be viewed. The most common stains routinely in histopathology laboratories are haematoxylin and eosin (H&E) which allows the visualization of cell structures such as cytoplasm, nucleus, organelles and extracellular components. H&E staining allows the identification of the underlying tissue morphology giving pathologists the ability to diagnose disease based on the structure and organization of cells. Haematoxylin is a basic dye that binds the negatively charged phosphate groups of nuclear DNA, giving a dark purplish stain in the nucleus, while eosin is an acidic dye which binds to positively charged arginine, histidine and lysine side chains of cellular proteins, giving a pinkish red stain in the cytoplasm (Horobin, 2010, Merck Millipore, 2016). In this chapter, the morphological changes which appear on non-irradiated control and following irradiation treatment in microfluidic device can be assessed by light microscopy.

4.1.2 Detection of caspase-cleaved substrates- caspase-cleaved CK-18

Cytokeratin (CKs) 18 is expressed by most types of carcinomas, including those of the breast, prostate, lung, colon and ovary (Kadyrov *et al*., 2001; Kramer *et al*., 2004). CKs are expressed at high levels in epithelial cells and the expression is usually increased after oncogenic transformation to the stage where the CKs are released from tumour cells. The released form in serum serves as a useful circulating marker for determining the clinical progression in patient with epithelial malignancies (Kramer *et al*., 2004; Cummings *et al*., 2008; Ulukaya *et al*., 2011).

During apoptosis, CK18 is cleaved by caspases within the region that links the two major α helical domains shared by all intermediate filament proteins (Caulin *et al*., 1997; Leers *et al*., 1999). In the early phase of apoptosis, CK18 is retained in a filamentous network and then cleaved at Asp 238 and Asp396 sites (Caulin *et al*., 1997; Leers *et al*., 1999; Kramer *et al*., 2004). The cleavage at Asp396 liberates a neo-epitope which is specifically recognized by the M30 monoclonal antibody, termed CK18-Asp396-NE (Figure 4.1). The M30 epitope (CK18-Asp396-NE) is then lost when the cells become necrotic during the end phase of apoptosis.

Caspases are the proteases mediating the cleavage of CK18 (Leers *et al*., 1999). At least 14 protein members of the caspase family have been identified to date and one distinctive feature of these proteases is the requirement of an aspartate adjacent to the cleavage site (Caulin *et al*., 1997; Riedl and Shi, 2004). The specific proteolytic cleavage of CK18 by caspase 3, 6, 7 and 9 takes place before the disruption of membrane asymmetry and DNA strand-breaks producing a smaller CK18 fragment containing an aspartic acid residue at position 396 (CK18-Asp396-NE; Figure 4.1; Leers *et al*., 1999; Schutte *et al*., 2004).

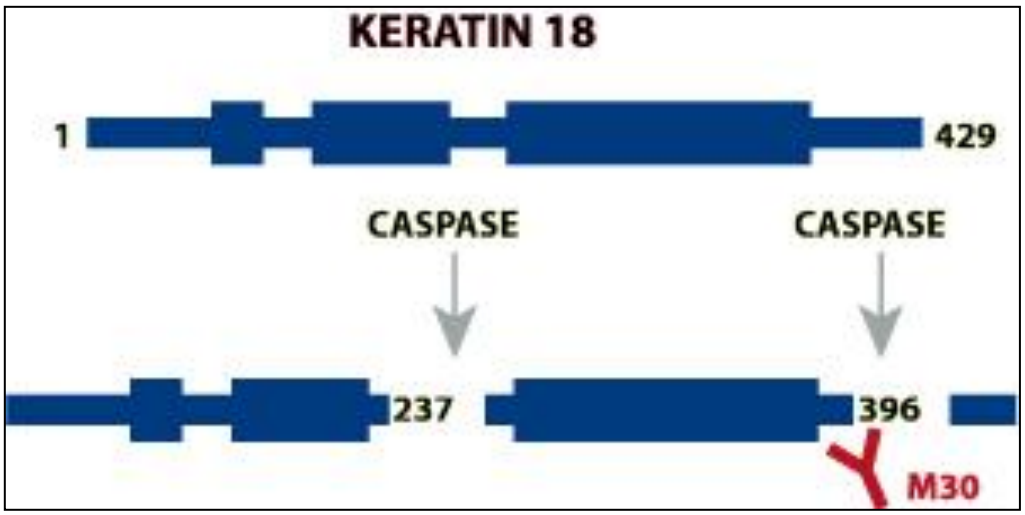


Figure 4.1. Exposure of the CK18-Asp396-NE epitope following the proteolytic cleavage of cytokeratin 18 by caspases and the detection of the epitope by the M30 antibody.
(Leers *et al*., 1999).

Using the same antibody, the soluble form of the caspase-cleaved CK18 released from cells can be measured using ELISAs (Kramer *et al*., 2004; Dive *et al*., 2010). The released levels of cleaved CK18 (M30) into the effluent medium collected from microfluidics was measured using M30 ELISA method. This method offers the advantages of continuous study on the tumour apoptotic response to irradiation at any time point.

4.1.3 Detection of DNA double-strand breaks using phosphorylated H2AX

DNA double strand breaks (DSBs) may arise directly by the action of exogenous agents including ionising radiation, chemical exposure or chromosome breakage produced during the development of the adaptive immune system (Chapman, Taylor and Boulton, 2012; Scully and Xie, 2013). The induced DNA DSBs are then detected and repaired by the cellular repair mechanisms, for example, sister chromatid recombination, error-free repair pathway of homologous recombination, or non-homologous end-joining (NHEJ). Those breaks which cannot be repaired may lead to

chromosome rearrangements, chromosomal deletions, other potentially damaging mutations or cell death (Chapman, Taylor and Boulton, 2012; Scully and Xie, 2013).

H2AX is the H2A core histone variant and constitutes about 10% of the nucleosomal H2A in human cell nucleus (Fernandez-Capetillo *et al*., 2004). It contributes to the nucleosome-formation thus maintaining the structure of DNA. In response to ionizing radiation, radiomimetic chemicals or oxidative stress which provoke the DNA strand breaks, H2AX is phosphorylated on serine 139 of its C terminal tail (Fernandez-Capetillo *et al*., 2004; Scully and Xie, 2013). The H2AX Ser139 phorphorylation site is a canonical target of the nuclear DNA damage phosphoiniositide-3-kinase-related protein kinases (PIKKs), ataxia teleangiectasia mutated (ATM), ATM and Rad3-related (ATR) and DNA-protein kinase catalytic subunit (PKcs; Podhorecka *et al*., 2010; Scully and Xie, 2013; Valdiglesias *et al*., 2013; Figure 4.2). ATM kinase is a major physiological mediator of H2AX phosphorylation in response to DSB formation. When DSBs are generated, the damaged DNA is recognised by a tri-protein complex called MRN complex (MRE11-RAD50-NBS1) which subsequently recruits ATM to the site of damage (Valdiglesias *et al*., 2013). ATM immediately phosphorylates the histone protein H2AX on the C-terminal tail on serine 139 and the ATM is activated by its auto-phosphorylation at Serine-1981 which leads to the dissociation of the inactive ATM dimers into single protein molecules with increased kinase activity. The activated ATM initiate phosphorylation of the respective substrates such as BRCA1, 53BP1m and MDC1 as well as the checkpoint proteins, Chk1 and Chk2, which act to cease the cell cycle progression and activate proteins involved in DNA repair such as H2AX (Valdiglesias *et al*., 2013).

In addition, H2AX can also be phosphorylated by ATR and DNA-dependent protein kinases (DNA-PK). ATR phosphorylates H2AX in response to single-stranded DNA breaks and during replication stress, for example replication fork arrest, whereas the phosphorylation of H2AX triggered by DNA-PK occurs in cells under hypertonic conditions and during apoptotic DNA fragmentation (Wang, *et al*., 2005; Podhorecka *et al*., 2010). With the involvement of phosphatidylinositol 3-kinase-related kinases (PIKK) kinases, ATM, ATR and DNA-PK, the DNA damage induced by ionising radiation triggers the phosphorylation of H2AX which serves as a marker of DNA damage and DNA damage repair (Podhorecka *et al*., 2010).

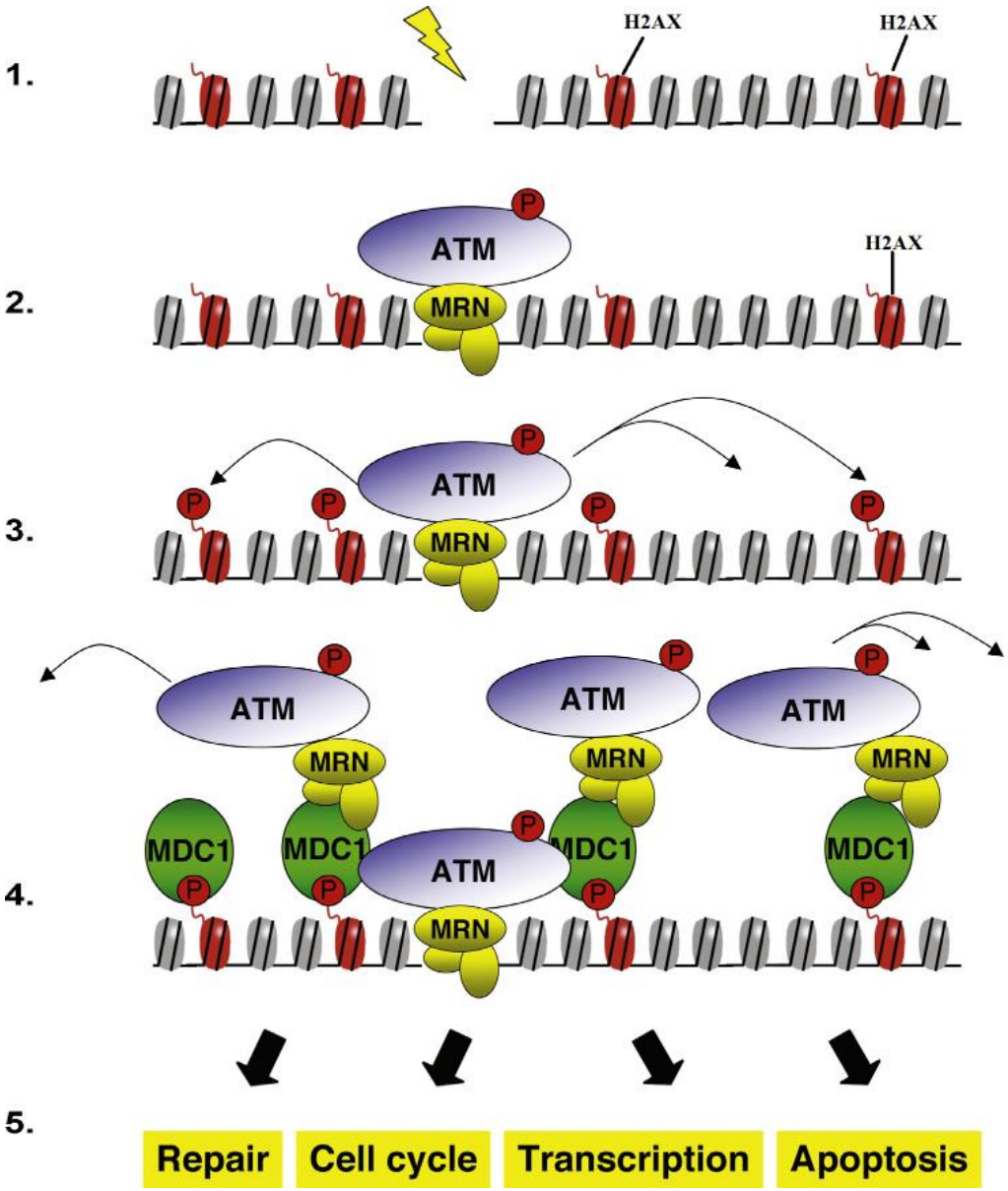


Figure 4.2. Cascade of reactions culminating in the γH2AX formation in response to DNA-DSB. (1) Induction of DSB by ionizing radiation, radiomimetic chemicals or oxidative stress. (2) The broken DNA strands are detected by the MRN complex which recruits ATM to the damage site. ATM is activated by its auto-phosphorylation on Serine-1981 site. (3) ATM phosphorylates the H2AX histone on its C-terminal tail on serine 139, called γH2AX. (4) The phosphorylated H2AX acts as a docking site for the recruitment of the DDR-mediator MDC1 on the chromatin flanking the DSB, amplifying the signalling cascade. (5) The signal is then channelled to downstream effector kinases that mediate the cellular events including the DNA damage checkpoint, repair of DNA lesions and transcriptional responses. The phosphorylation of H2AX is represented by the red oval (Valdiglesias *et al*., 2013).

The phosphorylated form of H2AX is called γH2AX and forms a nuclear domain called a DNA damage focus. The number of foci formed per cell nucleus reflects the number of induced DSBs (Scully and Xie, 2013; Valdiglesias *et al*., 2013). The accumulation of γH2AX occurs within seconds after the induction of DSBs and this accumulation serves as a docking site where the DNA damage response factors described above

are recruited to chromatin, flanking the DSBs (Sedelnikova *et al*., 2002; Scully and Xie, 2013; Valdiglesias *et al*., 2013).

These events serve as an amplifier, intensifying the DNA damage responses (DDR) signalling cascade. The DDR signal is channelled to the downstream effector kinases which mediate cellular events, including activation of the DNA damage checkpoints, repair of the DNA lesion and transcriptional responses (Figure 4.2; Valdiglesias *et al*., 2013). The accumulation of γH2AX spreads over a region spanning millions of bases surrounding the lesion, thus allowing microscopic detection of the protein (Fernandez-Capetillo *et al*., 2004). The most important application of γH2AX measurements is to quantify the retained level of DSBs following radiotherapy or chemotherapy as a marker of treatment efficacy (Banath, MacPhail, and Olive, 2004; Olive and Banath, 2009; Taneja *et al*., 2004), and the assessment of the efficiency of DNA repair is aimed and thought to be able to predict the possible tumour sensitivity to DNA damaging anticancer treatment; (Podhorecka, Skladanowski and Bozko, 2011; Unger, witte and David, 2015).

4.1.4 Detection of caspase activation using caspase inhibitors (CaspACE™ FITC-VAD-FMK)

Mechanisms of cell death involve the cleavage of zymogens to generate of specific proteases called caspases (Figure 1.7 and Figure 1.8). All caspases are cysteine proteases and act to cleave their substrates immediately after an aspartate residue and form part of the apoptotic cascade. Caspase activation and thus the apoptotic potential can be identified using the addition of caspase inhibitors, CaspACE™ FITC-VAD-FMK (fluoroisothiocyanate-valyl-alanyl-aspartyl- fluoromethylketone). CaspACE™ FITC-VAD-FMK *in situ* marker is a fluorescent, cell-permeable, derivative of VAD-FMK that binds with varying affinities to most caspases.

4.1.5 Detection of DNA fragmentation-TUNEL

The TUNEL assay is the most widely used method to detect apoptotic cells and DNA degradation during the late stage of programmed cell death in tissues. This method relies on the template-independent identification of blunt ends of double-stranded DNA breaks by the enzyme terminal deoxynucleotidyl transferase to add fluorescent nucleotides (dUTP) to the 3'-hydroxyl end of the damaged DNA (TdT; Kyrylkova *et al*., 2012). Cells with DNA strand breaks can then be visualised using fluorescence

microscopy. The sensitivity and the ease of the technique have led to its current wide acceptance and use (Kelly *et al*., 2003).

4.1.6 Membrane alterations- Lactate Dehydrogenase (LDH) assay

Lactate dehydrogenase (LDH) is a cytoplasmic enzyme which is constitutively expressed in most mammalian cells (Hudder, Nathanson and Deutscher 2003). In the cytosol of all cells, it functions as a hydrogen transfer enzyme and is involved in the glycolysis pathway. During anaerobic conditions, LDH acts as a catalyst in the conversion of the final product of glycolysis, pyruvate, to lactate and, at the same time, it causes the reduction of nicotinamide adenine dinucleotide (NADH) to NAD+ (Figure 4.3). When the cell membrane is damaged following cell death, LDH is released from both apoptotic and necrotic cells allowing its widespread use in the assessment of plasma membrane integrity and overall cell death (Kroemer *et al*., 2009; Hattersley *et al*., 2012). A number of previous studies have successfully used the LDH assay to detect the LDH released into the effluent from tumour biopsies maintained in a microfluidic device (Hattersley *et al*., 2008; Cheah *et al*. 2010; Hattersley *et al*., 2012).

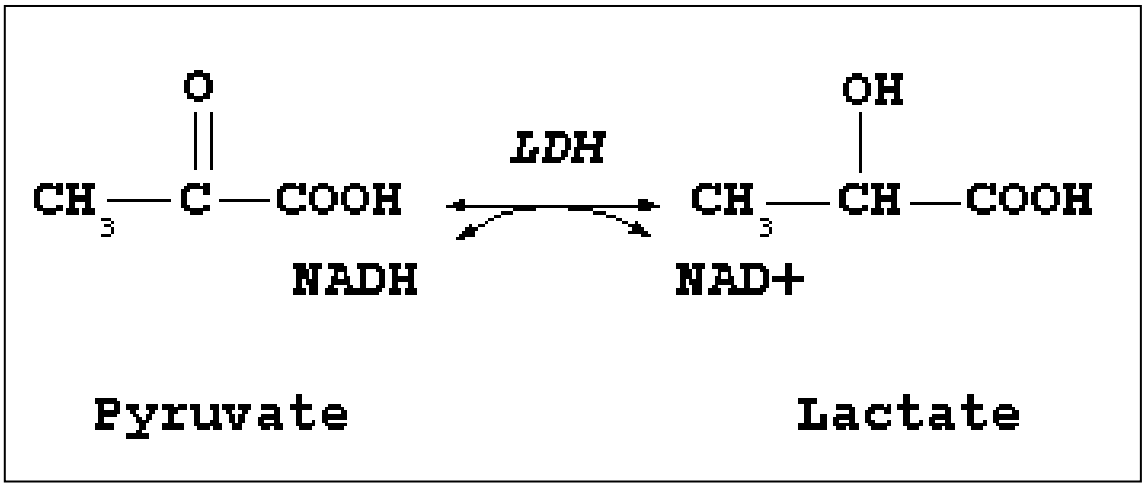


Figure 4.3 The catalytic role of lactate dehydrogenase in the conversion of pyruvate to lactate.

4.1.7 Mitochondrial apoptosis measured using Bcl-2

Apoptosis is regulated in part by the Bcl-2 gene, which promotes cell survival (Lu *et al*., 1994). The Bcl-2 gene encodes a 26kDa pro-survival/anti-apoptotic Bcl-2 protein which prevents the cells from entering apoptosis by inhibiting the pro-apoptotic members of the same family thus preserving mitochondrial membrane integrity (Bose *et al*., 2012). However, the entire mechanism by which Bcl-2 regulates apoptosis is yet to be fully determined. The location of Bcl-2 on the intermembrane space of mitochondria, which was found in 20th century, suggested that its role is related to the

function of mitochondria (Hockenbery *et al*., 1990; Lu *et al*., 1994; Yang *et al*., 1997). It has been reviewed that this protein primarily performs its pro-survival effects by binding to the pro-apoptotic proteins, Bcl-2-Associated-X-protein (BAX) and Bcl-2 homologous antagonist killer (BAK), diminishing their ability to release cytochrome c from the mitochondria (Abdullah and Chow, 2013). As mitochondrial membrane depolarization and the release of cytochrome c are early events of apoptosis, the overexpression of Bcl-2 prevents the membrane depolarization along with the subsequent release of cytochrome c, therefore inhibiting apoptosis. The overexpression of Bcl-2, usually measured using immunohistochemistry or immunoblotting, was reported in many tumour types and correlates with radioresistance, poor survival and poor clinical outcome (Gallo *et al*., 1999; Adams and Cory, 2007; Nichols *et al*., 2010; Kelly and Strasser, 2011; Wong *et al*., 2012; Abdullah and Chow, 2013; Zerp *et al*., 2015). In this study, therefore, it is interesting to evaluate and compare the expression levels of Bcl-2 proteins between the non-irradiated and irradiated HNSCC tissues.

By using all the analytical methods described above, the different cell death mechanisms of HNSCC tumours in response to different irradiation doses were evaluated. In this chapter, it is also aimed to determine the feasibility of using microfluidic technology to evaluate the response of tumour tissues to irradiation.

4.2. The expression of caspase-cleaved CK18, γH2AX and Bcl-2 in UMSCC-47 cells following etoposide treatment

The immunocytochemical (ICC) detection of cleaved-CK18, γH2AX, and Bcl-2 was done on oropharyngeal cells (UMSCC 47) treated with the apoptosis inducer, etoposide. In total, to evaluate the expression of M30, γH2AX, and Bcl-2 on oropharyngeal cells following no treatment and treatment with different concentration etoposide, 18 coverslips (three 6 well plate) were cultured with cells. Oropharyngeal cells ($5x10^4$) were plated into each well of a 6 well plate containing sterile square glass coverslips (section 2.1), four of the coverslips were treated with different concentrations of etoposide (2.5µM, 5µM, 10µM and 20µM), one coverslip was incubated with medium only and another coverslip was subjected to 20µM of etoposide to serve as a negative staining control. Following etoposide treatment for 24 hours, the medium was removed and the cells were rinsed with PBS before ICC detection.

Washing steps were carried out in the wells of the 6 well plate and during the primary antibody incubation, 100µL of the primary antibody (Table 4.2) was pipetted on to a clean sheet of parafilm and the coverslip with adherent cells was taken out from the well with tweezers and placed cell-side down onto the antibody droplet and incubated at room temperature for 1 hour. Matched isotype controls at the same concentration as the primary antibody were added to the 20µM etoposide treated coverslip to act as a negative control.

Table 4.2. Details of the primary antibodies used for immunochemical staining following irradiation.

Primary antibody		Concentration	Matched isotype
Mouse monoclonal	M30 (PEVIVA, UK)	500mg/mL	IgG2b (AbD Serotec, UK)
	Anti-phosphorylated H2AX (Ser139; BioLegend, UK)	5µg/µL	IgG2b
	Anti-Bcl-2 (AbD Serotec, UK)	10µg/µL	IgG1 (AbD Serotec)

Following ICC staining with the M30 primary antibody on the oropharyngeal cells, cytoplasmic positive brown staining was observed (Figure 4.4.A). The brown nuclear staining of γH2AX and Bcl-2 was detected on oropharyngeal cells, indicating the presence of DNA double strand breaks (DSBs; Figure 4.4.B) and apoptotic cells (Figure 4.4.C), respectively. The IHC staining of both matched isotype negative control

(IgG1) and matched isotype negative control (IgG2b) at the same concentration with the corresponding primary antibodies on oropharyngeal cells showed negative staining and no non-specific staining of the isotype antibody (Figure 4.5).

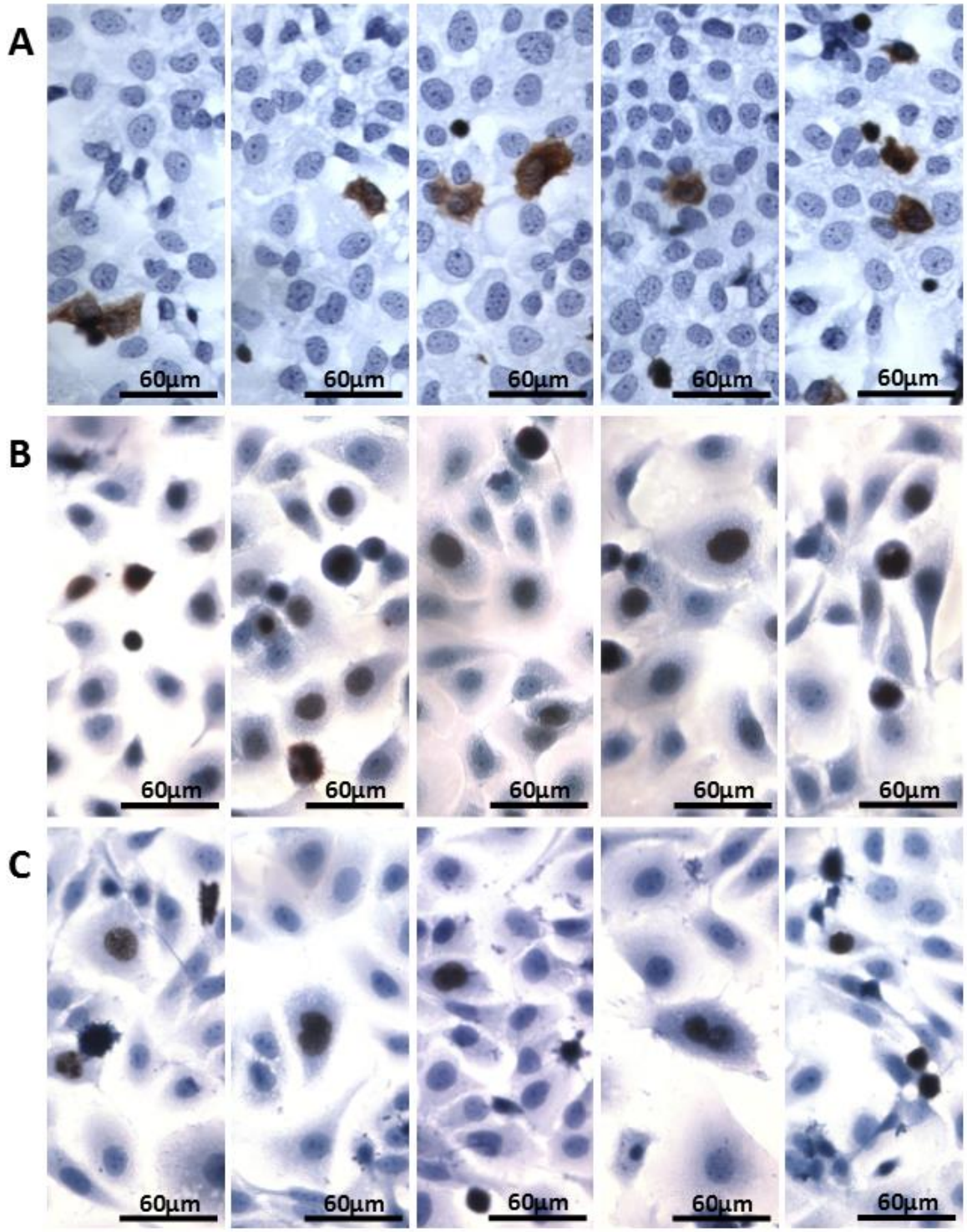


Figure 4.4. Representative ICC staining of oropharyngeal cells (UMSCC-47; n=3; x400 magnification) with (A) M30 antibody, (B) anti-γH2AX antibody and (C) anti-Bcl-2 antibody.
Brown cytoplasmic (A) and brown nuclear staining (B and C) represent cells that positive to expression and blue is the haematoxylin counterstain.

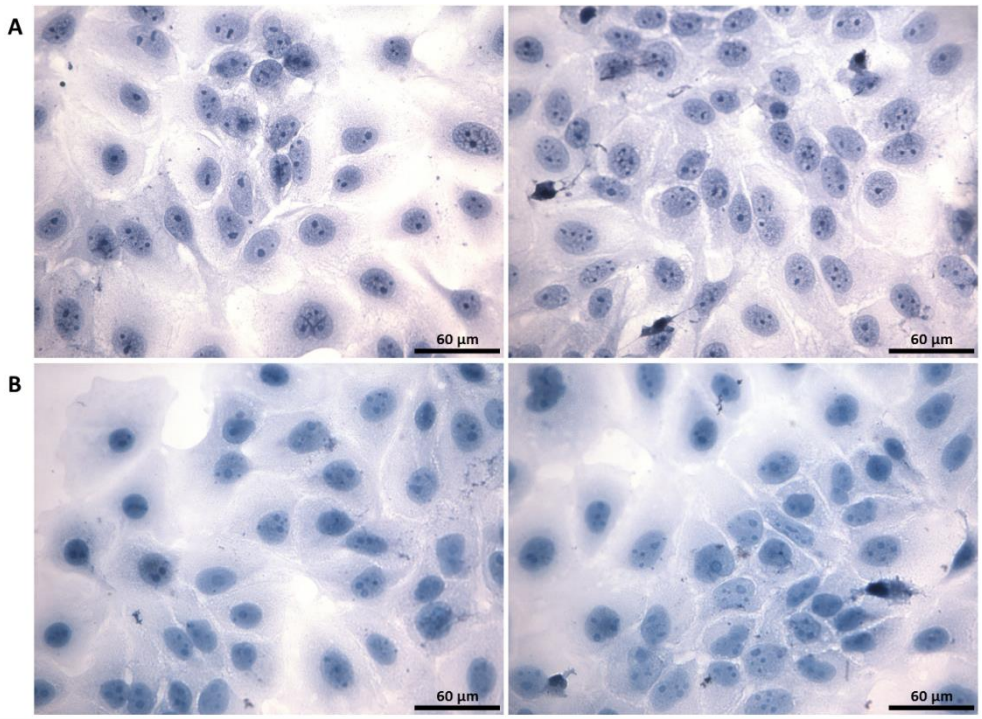


Figure 4.5. ICC staining of UMSCC-47 cells using a (A) mouse matched IgG1 isotype antibody and (B) mouse matched IgG2b isotype antibody as negative control.
Blue staining indicates the haematoxylin stained nuclei counterstain (x400 magnification).

The mean percentage of cells undergoing apoptosis detected using cleaved CK18 over ten x400 fields of view was calculated and showed that treatment with 2.5µM and 5µM etoposide resulted in a slight but non-significant increase in the percentage of cells expressing cleaved CK18 compared with cells that were cultured with DMEM medium only (Figure 4.6). However, following treatment of cells with 10µM and 20µM etoposide, a significant increase in the number of cells having cleaved cytokeratin compared to the control was observed, with 20µM inducing the greatest amount of apoptosis ($p<0.05$).

The mean percentage of DNA-DSBs detected by γH2AX expression over ten fields at x400 magnification showed that the addition of etoposide to the oropharyngeal cells significantly stimulated the induction of a greater number of DNA-DSBs (up to 50% more) over medium only, however the effect did not appear to be dependent on the concentration of etoposide. The positive expression of Bcl-2 on control (no etoposide treatment) and the 20µM etoposide treated cells achieved similar level (7.4% and 7.9% respectively). Compared with the control, the 2.5µM, 5µM and 10µM etoposide resulted lower expression level with the 10µM etoposide treated cells achieved significantly lower expression.

In overall, the addition of etoposide into culture medium of oropharyngeal cells showed increases on the apoptosis level (detected by M30) and DNA-DSBs level (measured by γH2AX). When apoptosis level was increased (M30), the level of anti-apoptotic event is expected to reduce. It was only demonstrated on 10μM of etoposide treatment in which the expression of Bcl-2 was significantly lower than control level while M30 level increased significantly compared with non-treated level.

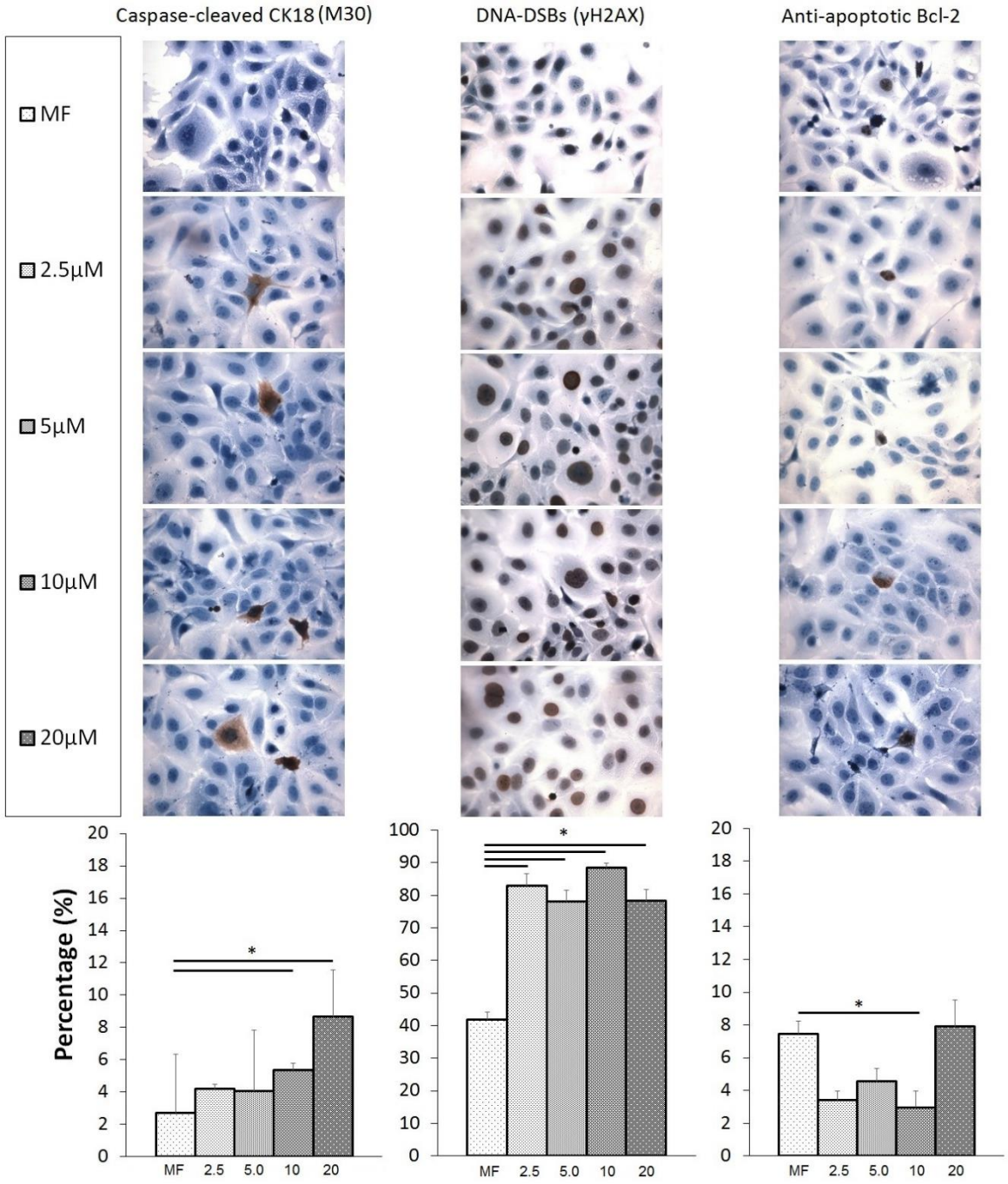


Figure 4.6. ICC staining of γH2AX, caspase-cleaved cytokeratin using the M30 antibody and anti-apoptotic Bcl-2 on UMSCC-47 oropharyngeal cells treated with no etoposide and with increasing concentrations of etoposide (n=6 on each marker).

The representative images of the staining are shown at the top while the bar graph showing the mean percentage of apoptotic cells from ten x400 magnification fields. Mean+SEM. *p<0.05; Student paired t-test.

4.3. Optimisation of the irradiation procedure on tumours maintained in microfluidics

4.3.1 Determination of microfluidics termination time for post-irradiation analysis

The optimal time for analysis of morphology, cell death and detection of DNA-DSBs post-irradiation was evaluated. Seven tissue pieces from a patient with laryngeal supraglottic tumour (TR84) were maintained in parallel microfluidic device and subjected to on-chip irradiation. Following 24-hour culture in microfluidic devices, four tissues from TR84 were respectively subjected to 5Gy, 10Gy, 15Gy or 20Gy irradiation and were snap-frozen at 6 hours post-irradiation. Another three tissues were maintained in microfluidics for same period of time but with no irradiation treatment. The snap-frozen tissues were then serially sectioned for IHC staining of M30, CK and γH2AX. The expression level of these markers at 6-hour post-irradiation was compared with that analysed at 24-hour post-irradiation on the same tumour tissue (laryngeal supraglottic tumour; TR54) to determine the optimal time in evaluating the tumour response following irradiation. The 6-hour post-irradiation was carried out once only due to the limited availability of the LINAC machine in a morning as well as the busy treatment schedules of the machine for NHS patients.

A supraglottic laryngeal tumour (TR84) was maintained in microfluidic device and irradiated with 5, 10, 15 and 20Gy before being embedded in OCT 6 and 24-hour post-irradiation. The CK18-LI for each dose was compared between the 6- and 24-hour post-irradiation times (Figure 4.7). No significant differences in the CK18-LI was observed between 6-hour and 24-hour post-irradiation analysis in tissues subjected to the same microfluidic culture (MF; 0Gy) and irradiation with 5, 10 and 15Gy. The CK18-LI of the 20Gy irradiated tissues showed a greater difference between the two time points with the tissue maintained for 24-hour post-irradiation achieving the highest CK18-LI (31.5+7.0%), which is about 14% more than that of the 6-hour post-irradiation analysis (17.4%). The amount of cleaved-CK18 was detected more at 24 hours than that at 6 hours after 20Gy irradiation.

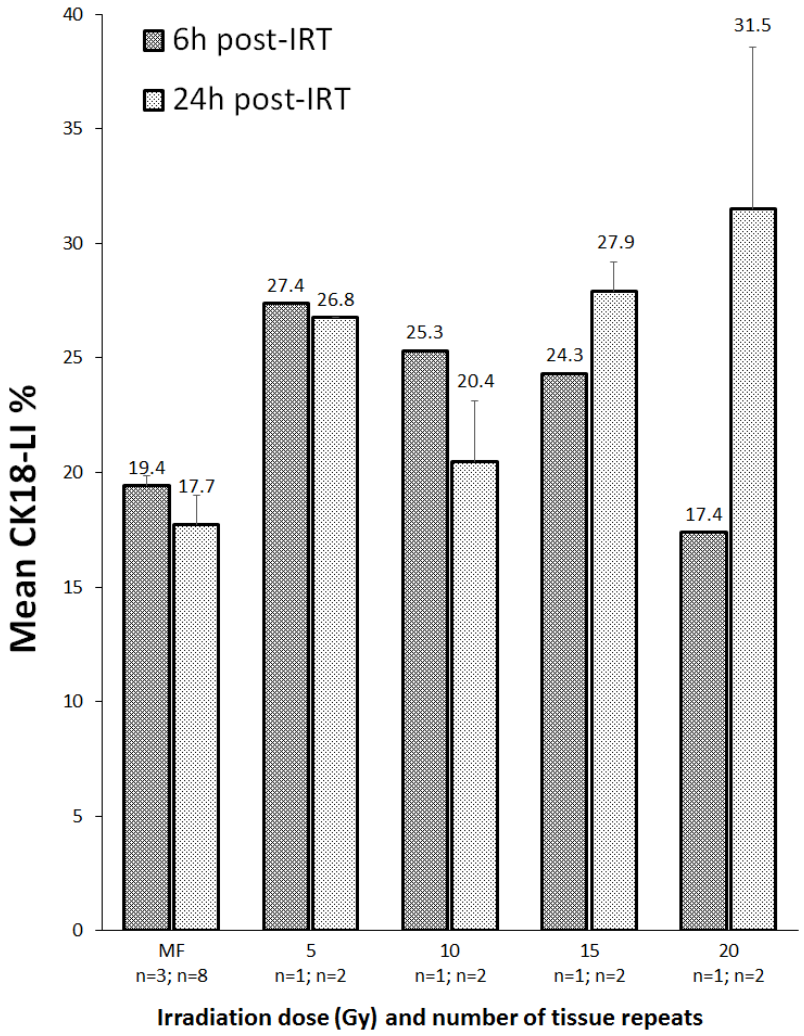


Figure 4.7. Mean CK18-LI of a laryngeal supraglottic tumour (TR84) following microfluidic culture without irradiation (MF) and with irradiation at increasing single doses.
Analysis carried out on tiled x100 magnification field. The mean CK18-LI between the two post-irradiation freezing times (6 and 24 hour) on the same treatment were compared. Mean+SEM. The corresponding numbers of tissue biopsies subjected to each treatment are shown below the x-axis in parentheses.

Various studies showed that the residual expression level of γH2AX after anti-cancer treatment correlates with the fraction of cells that lost clonogenic ability, suggesting that the residual γH2AX becomes a useful indicator to study the cell response/sensitivity to different DNA damaging agents (Banath, MacPhail, and Olive, 2004; Olive and Banáth, 2009; Menegakis *et al*., 2011). For example, the retention of γH2AX foci at 24 hours following cisplatin treatment was correlated with the fraction of cells that lost clonogenic potential by Olive and Banáth (2009) whilst the radiation sensitivity was shown to be useful indicator of the radiation sensitivity as the γH2AX level was shown to be retained up to 30% of the initial signal at 24 hours after irradiation on the most radiosensitive cervical cancer cell lines (C33A; Banath, MacPhail, and Olive, 2004).

Consequently, in the current study, the γH2AX expression was also evaluated at 6-hour and 24-hour post-irradiation on the tissues obtained from the same patient (Figure 4.8). For the non-irradiated tissue maintained in the microfluidic device, the percentage measured at 24 hours was approximately 10% nearly double the percentage measured at 6 hours. The same increase, at 24 hours compared to 6 hours, was seen in γH2AX staining following 5Gy irradiation and the difference increased to almost 4 times as much staining in the 24-hour sample following 10Gy irradiation. Similar percentages of γH2AX positive cells were observed between the two analysis time points following 15Gy and 20Gy irradiation. In overall, it shows that the residual γH2AX at 24-hour post-irradiation has higher percentage compared with that at 6-hour post-treatment. Therefore, microfluidic flow termination and tissue snap-freezing were carried out at 24-hour post-irradiation.

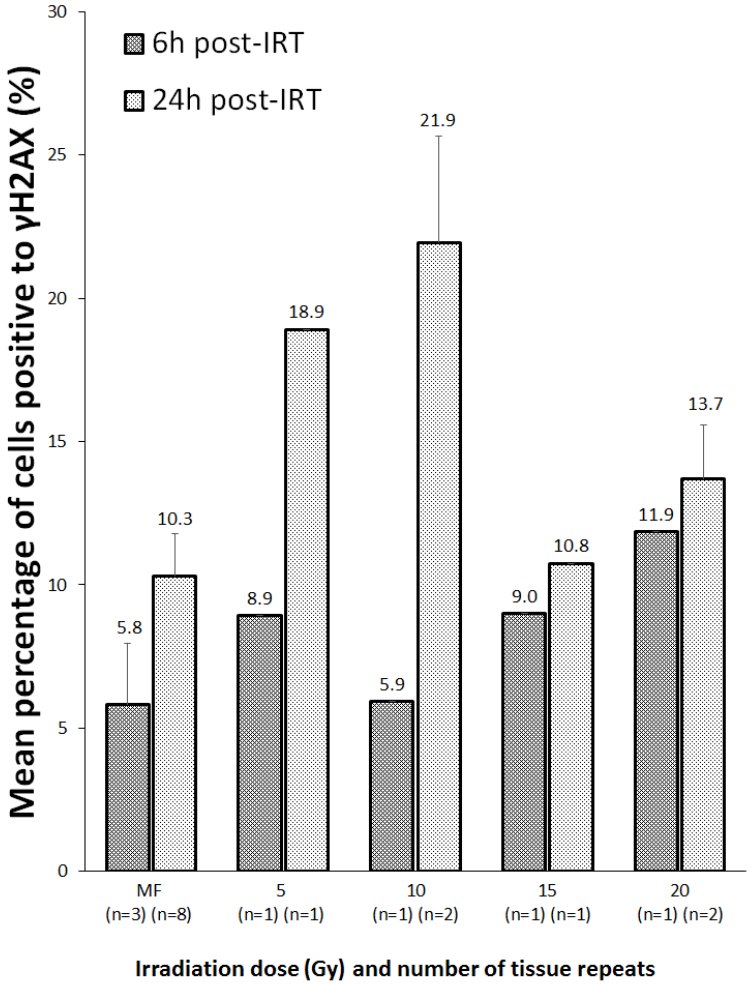


Figure 4.8. Mean percentage of cells positive for γH2AX expression in a laryngeal supraglottic tumour (TR84) following microfluidic culture without irradiation (MF) and with irradiation at increasing single doses.

Analysis carried out on tiled x100 magnification field. The mean percentage between the two post-irradiation freezing times (6 and 24 hour) on the same treatment were compared. Mean+SEM. The corresponding numbers of tissue biopsies subjected to each treatment are shown below the x-axis in parentheses.

4.3.2 The effects of transport of the tumour tissue for irradiation

Irradiation involved the transportation of the entire microfluidics system, including syringe pump, to the Radiation Physics Department and experiments were performed to assess the effect this had on the tissue integrity so as not to mask any tumour response to irradiation. Two tumour biopsies obtained from a floor of mouth oral cavity tumour (TR92) were subjected to parallel microfluidics which were carried out at the same time with the fractionated irradiation experiments (5 fractions of irradiation on oral cavity floor of mouth tissue; section 2.5) and the effluent medium was collected every two hours. One of the tissues was maintained in the microfluidic device with no irradiation and transported to the Radiation Physics Department along with the tissue which was subjected to five fractions of irradiation treatment. The device was placed in the 37ºC incubator throughout the transport and the tissue was maintained for 75 hours in the devices. Another tissue was maintained in the incubator in laboratory throughout the microfluidic perfusion for same period of time. The LDH cytotoxicity assay was carried out to measure LDH release throughout the culture.

Non-irradiated tissue maintained in the microfluidic device in the laboratory with no transportation demonstrated low LDH release following the initial high LDH release thought to be due to handling set up (Figure 4.9). The same LDH release pattern was observed on an independent piece of tissue, from the same sample, which was transported between the sites but not irradiated.

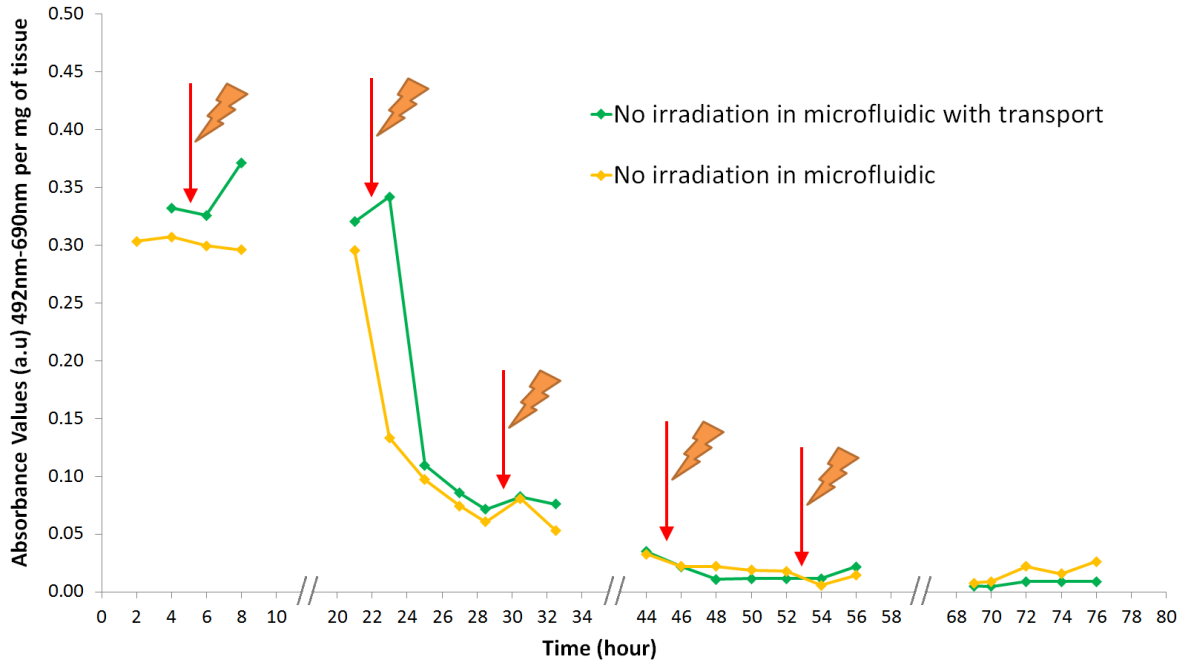


Figure 4.9. Absorbance values of formazan dye indicating the level of LDH release from a floor of mouth oral cavity tumour (TR92) in two parallel microfluidic systems.
One tissue was subjected to microfluidic culture without irradiation and the system was transported to the Radiation Department (green). Another tissue was cultured in microfluidic device without irradiation and remained in laboratory (yellow).

4.4. The effect of microfluidic culture with and without irradiation on tissue morphology and integrity- H&E staining

Following microfluidic and on-chip irradiation experiments, the HNSCC tissue embedding, snap-freezing, cryo-sectioning and H&E staining were carried out according to section 2.7 and 2.8. Under the microscope, the tiled images of x100 magnification fields on each individual tissue and x400 magnification fields were captured and generated. The morphological appearance of the HNSCC tissues [two oral cavity floor of mouth primary tumours (TR89 and TR92), one laryngeal supraglottic tumour (TR84), one lymph node metastasised from an unknown primary tumour (TR73) and one lymph node metastasised from a laryngeal tumour (TR80)] following microfluidic culture with and without irradiation at different doses was evaluated. The H&E staining was also compared with the IHC staining of CK on serial sections of tumour tissues for comparison and the representative staining images are shown in Figure 4.10 and Figure 4.11.

The H&E staining of oral cavity (TR89) primary tumours, which were subjected to parallel microfluidics and single dose irradiations (0Gy, 5Gy, 10Gy, 15Gy and 20Gy) consisted of cells arranged in a circular pattern which corresponded with the tumour

area identified with CK IHC stained serial section (Figure 4.10). The tumour area consisted of more nuclei compared with the non-tumour area. The circular pattern of tumour cells was not observed in all tissues including one of the non-irradiated and 20Gy-irradiated tissues. One of the non-irradiated tissues showed less nuclei compared with the other non-irradiated tissue even though they were subjected to same culture time and no irradiation. The single dose irradiations had no apparent effects on the morphological appearance of the oral cavity tumour tissue compared with the non-irradiated control even with increasing intensity of dose.

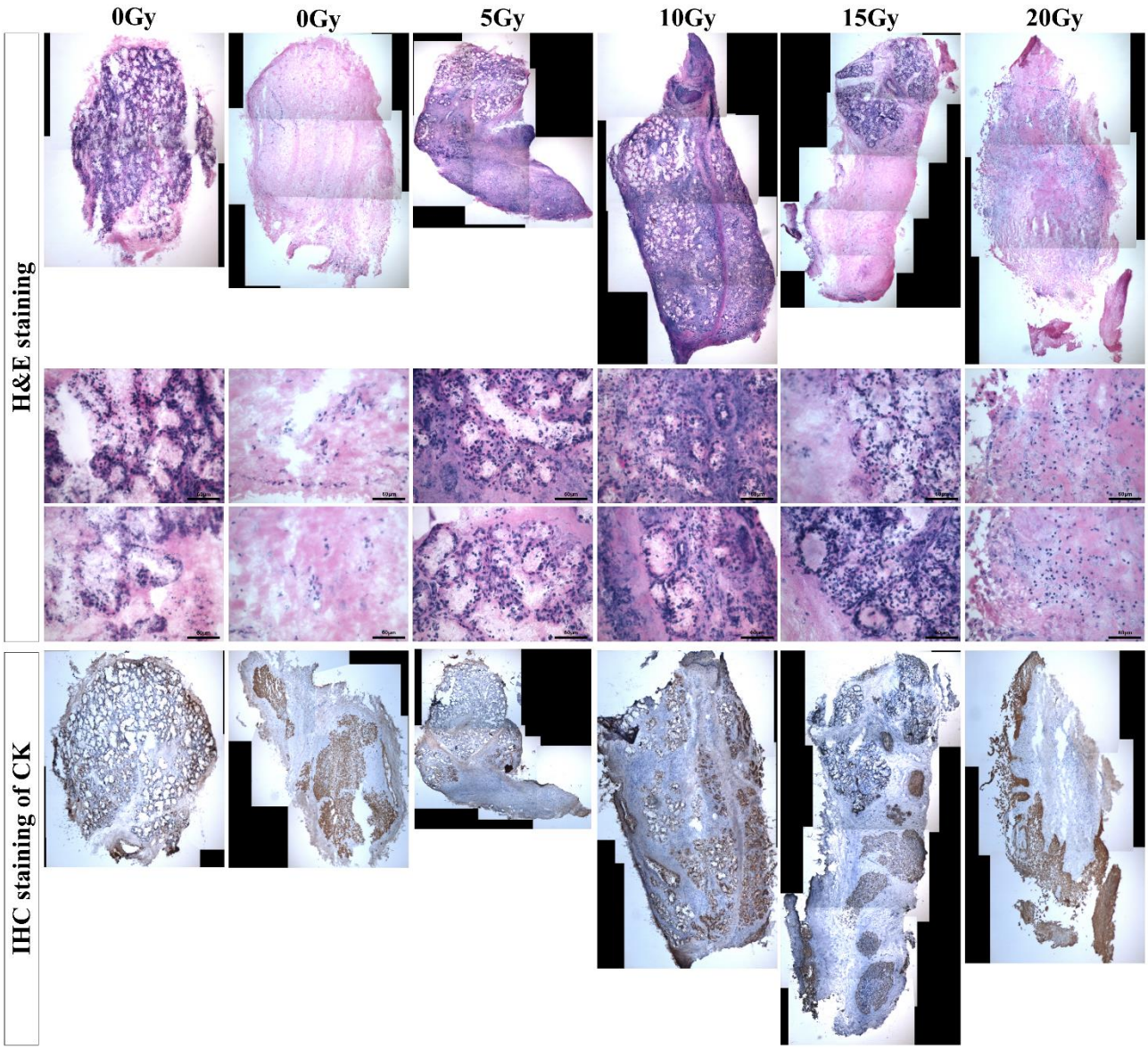


Figure 4.10. Representative staining on frozen tissue sections of an oral cavity floor of mouth (TR89) which was subjected to different treatments (n=2 on each treatment group).
The top row indicates the tiled images of the H&E stained-sections at x100 magnification fields while the middle row images are the H&E stained sections at x400 magnification. The bottom row depicts the tiled images of the IHC staining of CK at x100 magnification fields on serial sections of the same tissue.

In the five TR73 neck node tissues cultured in the microfluidic device with and without irradiation, clusters of nuclei were found distributed throughout the tissue with areas of pink running in between (Figure 4.11). These cell clusters constitute the areas of invading tumour within the tissue sample observed following CK IHC on serial sections. In contrast, a very low number of nuclei was observed in the non-tumour area (CK- area). The four single-dose irradiations showed no observable effects on the tissues based on the morphological staining. The tumour cells were found intact with clear circular nuclei even after irradiation with doses up to 20Gy.

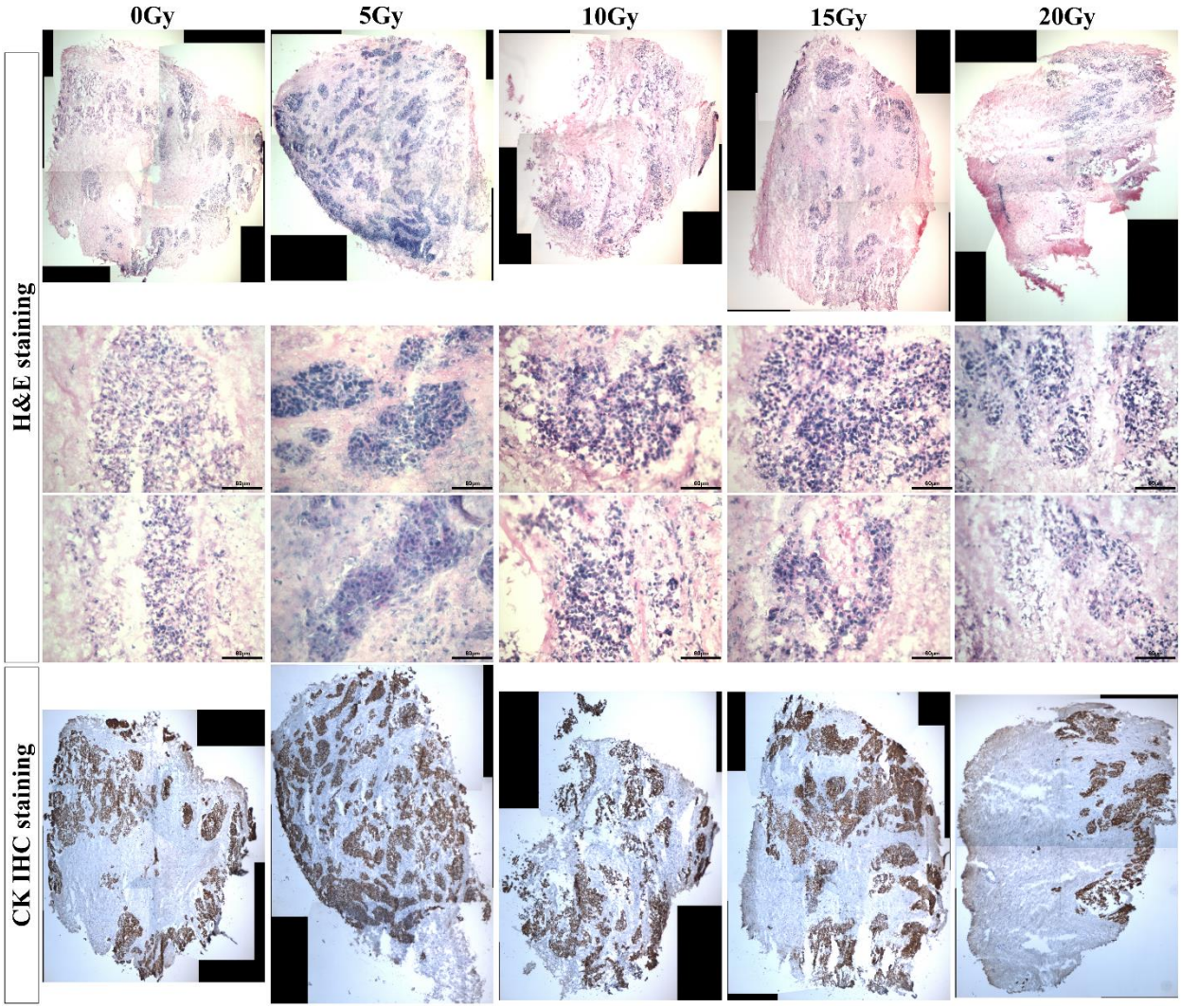


Figure 4.11. Representative staining on frozen tissue sections of lymph node metastasised from an unknown primary tumour (TR73) which was subjected to different treatments (n=2 on each treatment group).

Top row indicates the tiled images of the H&E stained-sections at x100 magnification while the middle row images are the H&E staining images of x400 magnification on the corresponding tissues. The bottom row depicts the tiled images of the IHC staining of CK at x100 magnification fields on serial sections of the same tissue.

4.5. Apoptotic labelling index of HNSCC tissues following microfluidic culture with and without irradiation

In order to measure the apoptotic response of HNSCC to irradiation, IHC staining using the M30 antibody to detect cleaved cytokeratin-18 was used on: (1) tissue without microfluidic culture; (2) microfluidic-cultured tissue wwithout microfluidic device; and (3) microfluidic-cultured tissue with different single-doses of irradiation.

Due to the heterogeneity of the HNSCC tumour tissue and the different distribution of tumour areas across tissues between patients and even between tumour biopsies obtained from the same patient, it was necessary to stain serial sections with a mouse monoclonal anti-human cytokeratin antibody (1.16mg/mL; Clone MNF116, Dako, Cambridgeshire, UK) in order to identify the tumour epithelial cells. This allows the quantification of the apoptotic areas (M30 positive) as a percentage of the total tumour area.

Nine tissues from the thirteen HNSCC patients (six primary tumours and three lymph neck nodes; Table 2.1 and Figure 4.12) subjected to microfluidic culture and single irradiation (0Gy 5Gy, 10Gy, 15Gy and 20Gy) were immunostained for M30 and CK following snap freezing and cryosectioning (Figure 4.12).

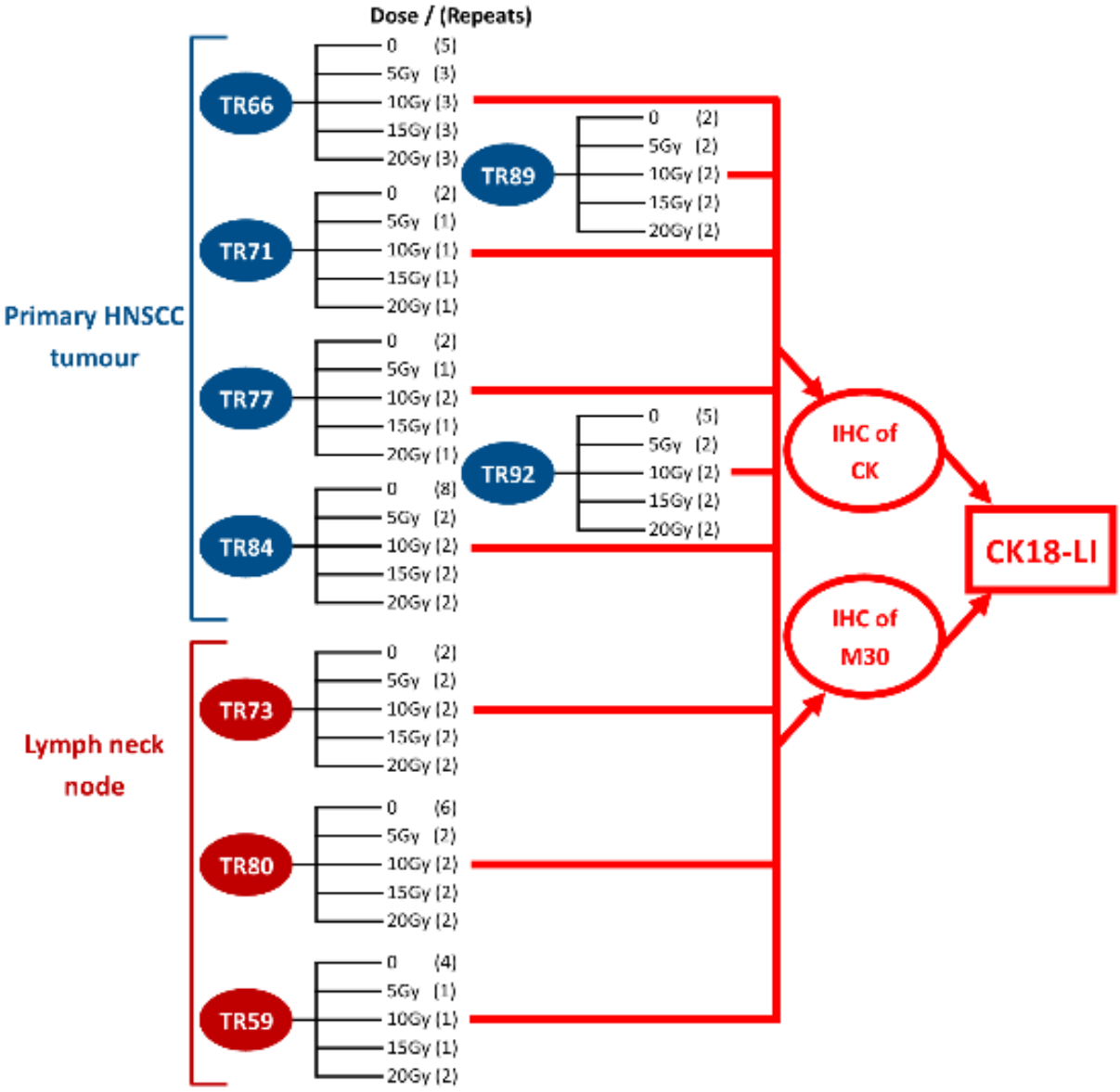


Figure 4.12. Flow chart of the HNSCC tissues used for CK18-LI determination and the number of repeats for each treatment in brackets.
Tumour TR66: paranasal sinus, TR71: oral cavity, TR77: oropharyngeal, TR84: laryngeal, TR89: oral cavity, TR92: oral cavity, TR73: lymph node from unknown primary, TR80: lymph node from laryngeal primary, and TR59: lymph node from oropharyngeal primary.

The stained sections were viewed using a light microscope (Nikon 800) and images were captured at x100 magnification across the tissue section. The images at x100 magnification were then tiled together using Image-Pro Premier software (Figure 4.13). The tiled image of each stained tissue section was used to quantify the apoptotic labelling index by identifying the area of the tissue which was positive for cleaved cytokeratin and expressing this as a percentage of total tumour area identified on a serial section with the anti-cytokeratin antibody again using Image-Pro Premier software. The positive staining on each section was selected and the positive staining area was then shown in red and counted in μm^2 (Figure 4.14).

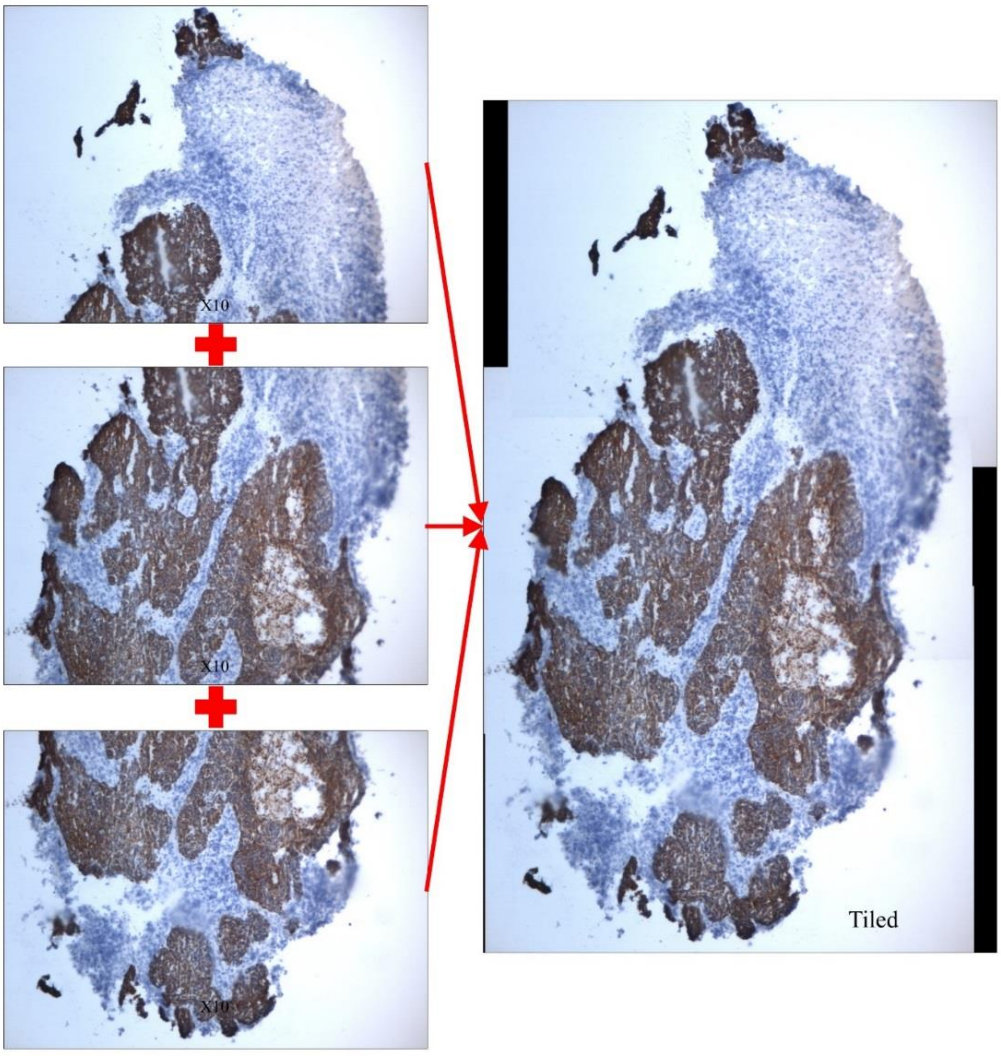


Figure 4.13. Image to show the tiling of x100 magnification fields throughout the entire cytokeratin stained-HNSCC tissue section.

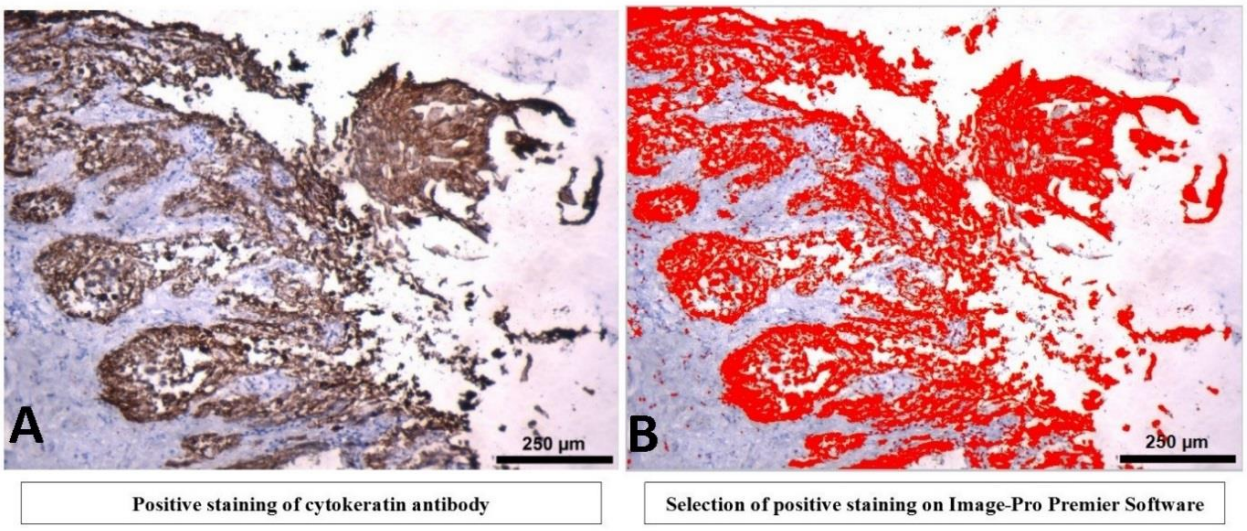


Figure 4.14. Image analysis on IHC staining by using Image-Pro Premier software.
(A) Brown positive staining following IHC for cytokeratin using the monoclonal mouse anti-human cytokeratin antibody on HNSCC frozen tissue section. (B) Automatic selection of the positively stained areas using Image-Pro Premier software generates a red area which is then used to calculate the area of positively stained tissue (μm^2). Blue depicts the haematoxylin counterstained areas.

The apoptotic index was defined as the percentage of apoptotic area (positive M30 staining) over the total area of tumour cells (positive cytokeratin staining) of the tissue section (as shown in the expression below).

$$\text{CK18 labelling index (LI)} = \frac{\text{Area of cleaved CK} - 18 \text{ positive cells in whole tissue section}}{\text{Total area of tumour (CK positive area) in whole tissue section}} \text{X100}$$

The mean CK18-LI of the tissues which were subjected to the same treatment schedule (non-irradiated MF, 5Gy, 10Gy, 15Gy and 20Gy) was calculated, averaged and presented for each individual patient (Figure 4.12). The means CK18-LI of the non-irradiated and irradiated sample on each tumour were statistically compared by One-way ANOVA followed by post-hoc Tukey's Multiple Comparison test (IBM SPSS Statistics 22).

4.5.1 CK18-LI of single-dose irradiated tissues

Positive brown cytoplasmic staining with the M30 antibody to the cleaved CK18 was observed throughout the tumour area across each tissue section. Based on the representative fields of view (Figure 4.15.B), it appeared that the four irradiation doses increased the number of cells having cleaved cytokeratin 18. On the tissue sections which were subjected to IHC staining using the mouse IgG1 matched isotype control for CK antibody and mouse IgG2b matched isotype control for M30 antibody, the staining was found negative and no brown, positive, staining was observed, indicating that there was no non-specific staining of the antibody (Figure 4.15.A).

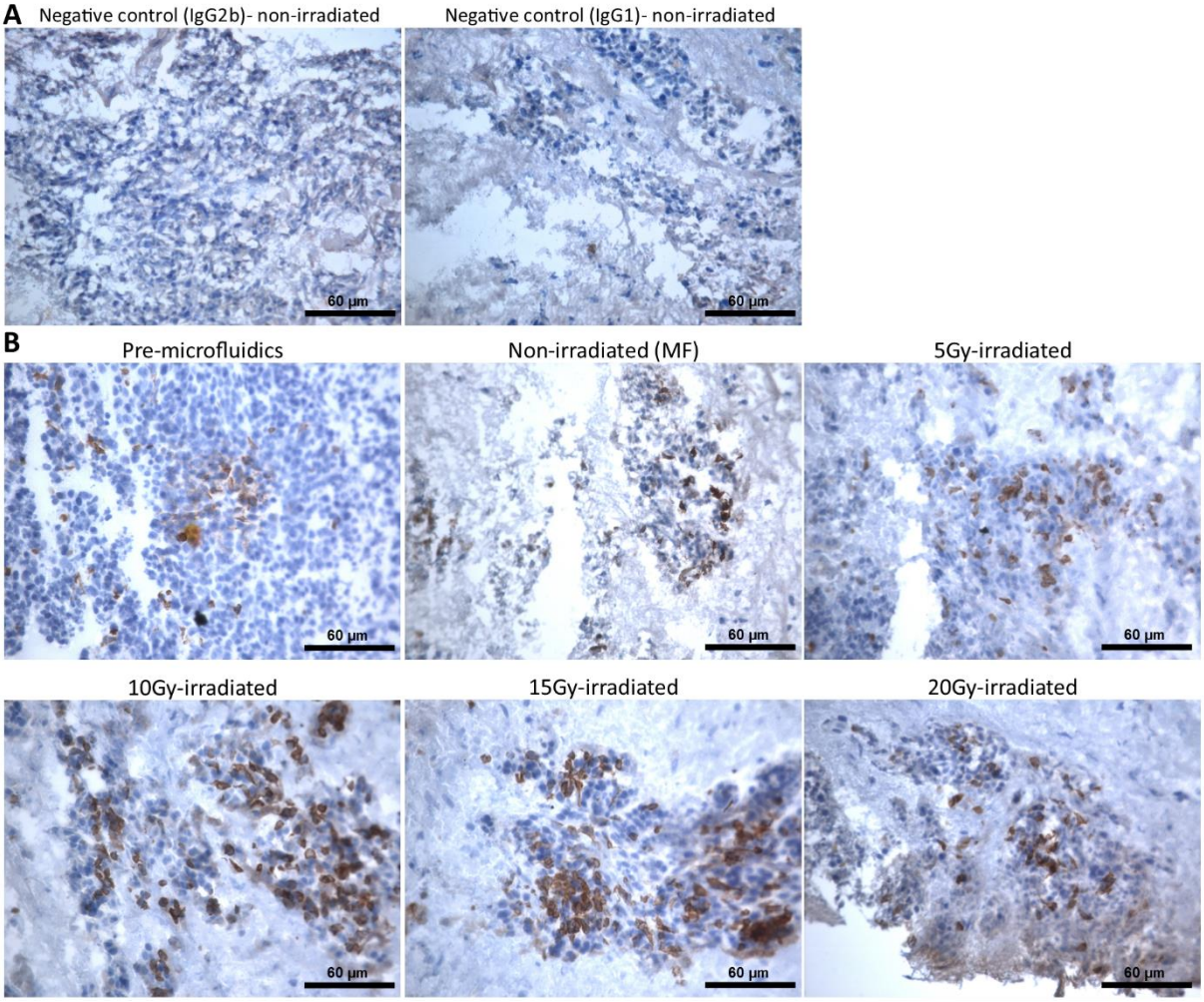


Figure 4.15. Representative photomicrographs of IHC staining on the 9 HNSCC tumours (n=3 on lymph node patients (TR73) and n=5 on patients with primary tumour; x400 magnification).
(A) IHC staining using matched mouse IgG1 isotype negative control for the CK antibody and matched mouse IgG2b isotype negative control for the M30 antibody on non-irradiated metastatic lymph neck nodes (metastasised from unknown primary tumour. (B) Representative images of IHC staining of the metastatic lymph neck nodes with the M30 antibody on pre-microfluidics (tissue without microfluidic culture or irradiation), non-irradiated (tissue cultured in the microfluidic device with no irradiation), 5Gy-irradiated, 10Gy-irradiated, 15Gy-irradiated and 20Gy-irradiated tissues. The positive cytoplasmic brown staining represents the expression of cleaved cytokeratin 18 in the cells and the blue is haematoxylin counterstain.

All of the tissues, except the oral cavity floor of mouth tumour (TR92), showed an increase in the apoptotic index in the MF tissue compared to the Pre-MF control tissue but the difference was not significant (Figure 4.16 A). The Pre-MF tissue derived from the laryngeal TR84 tumour had the highest CK18-LI (12.0%) compared with other Pre-MF tumours (range 1.5-12.0%). The same tissue also displayed the highest CK18-LI (17.7±1.3%) following microfluidic culture without irradiation compared with other MF tumours (range 1.9-17.7%). The mean CK18-LI between the Pre-MF and MF tissues of all nine tumours and nodes were calculated and compared using the independent *t*-test (Figure 4.16 B). Although the MF tissue exhibited a higher CK18-LI than the Pre-MF control, the difference was not significant (p=0.145).

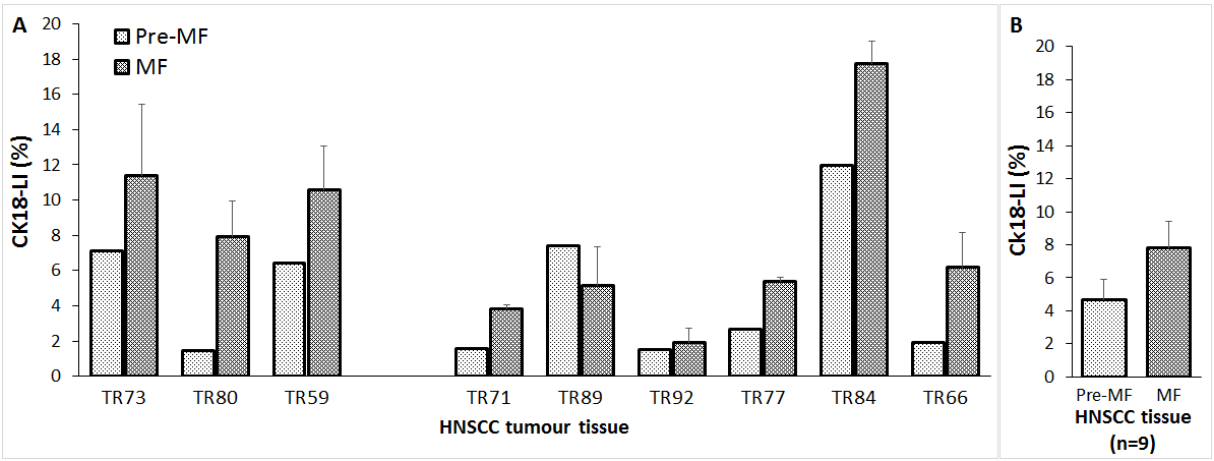


Figure 4.16. CK18-LI of pre-microfluidic (Pre-MF) and microfluidic (MF) control tissues.
(A) CK18-LI of the nine individual HNSCC tumours, compared between tissues without microfluidic culture (Pre-MF) and with microfluidics but without irradiation (MF). Mean labelling index of caspase cleaved cytokeratin+SEM. (B) The combined mean CK18-LI of Pre-MF and MF tissue on all nine HNSCC tumours combined (3 lymph nodes; 6 primary tumours). Mean+SEM.

The effect of increasing doses of irradiation on the same tissues was then determined on the same individual tumour and node tissue. The number of repeats was variable in the same patient and between different HNSCC patients, especially on non-irradiated MF tissues and was dependent on tissue availability and experimental success. On each irradiation experiment, at least one microfluidic device was set up to serve as non-irradiation control. Therefore, more experiments carried out for irradiation resulted in a greater number of repeats for non-irradiation controls.

There was a dose dependent increase in the apoptotic labelling index of the oral cavity TR71 and TR89 following irradiation (Figure 4.17). However, the CK18-LI of TR71 tumour that was irradiated with 20Gy was unable to be evaluated as the tissue biopsies contained no tumour based on the IHC staining of cytokeratin (CK) from the small tissue biopsy that showed no positive CK staining. The CK18-LI for the second floor of mouth oral cavity tumour (TR92) demonstrated a level of apoptosis which remained below 5% even after irradiation, however this was still greater than the non-irradiated MF control for all doses of irradiation. These differences however were not significant.

The oropharyngeal tonsil (TR77) tissue was the only tissue in which irradiation (15Gy) caused a decrease in apoptosis compared to the non-irradiated MF tissue, however in this same tissue all other doses of irradiation resulted in an increase in apoptosis compared to MF control. In particular, the 20Gy-irradiated oropharyngeal tonsil (TR77) tumour achieved an apoptotic labelling index of more than 30% which is much higher than the other irradiation doses and any of the other tumours investigated.

Unfortunately, this result was obtained from a single experiment which although repeated could not be analysed because the repeat sample was destroyed by the irradiation.

The irradiated laryngeal TR84 tumour showed more apoptotic cell death compared with that of other tumours (range 3.8-12.4%) and a general dose-dependent increase was seen following irradiation. The increase in the CK18-LI following 20Gy-irradiation was significantly greater than the non-irradiated control (p<0.05; One-way ANOVA followed by post-hoc Tukey test). The paranasal sinus TR66 tumour tissue demonstrated the same pattern following irradiation as the laryngeal TR84 tumour but at a lower level and none of the increases seen following irradiation were significant.

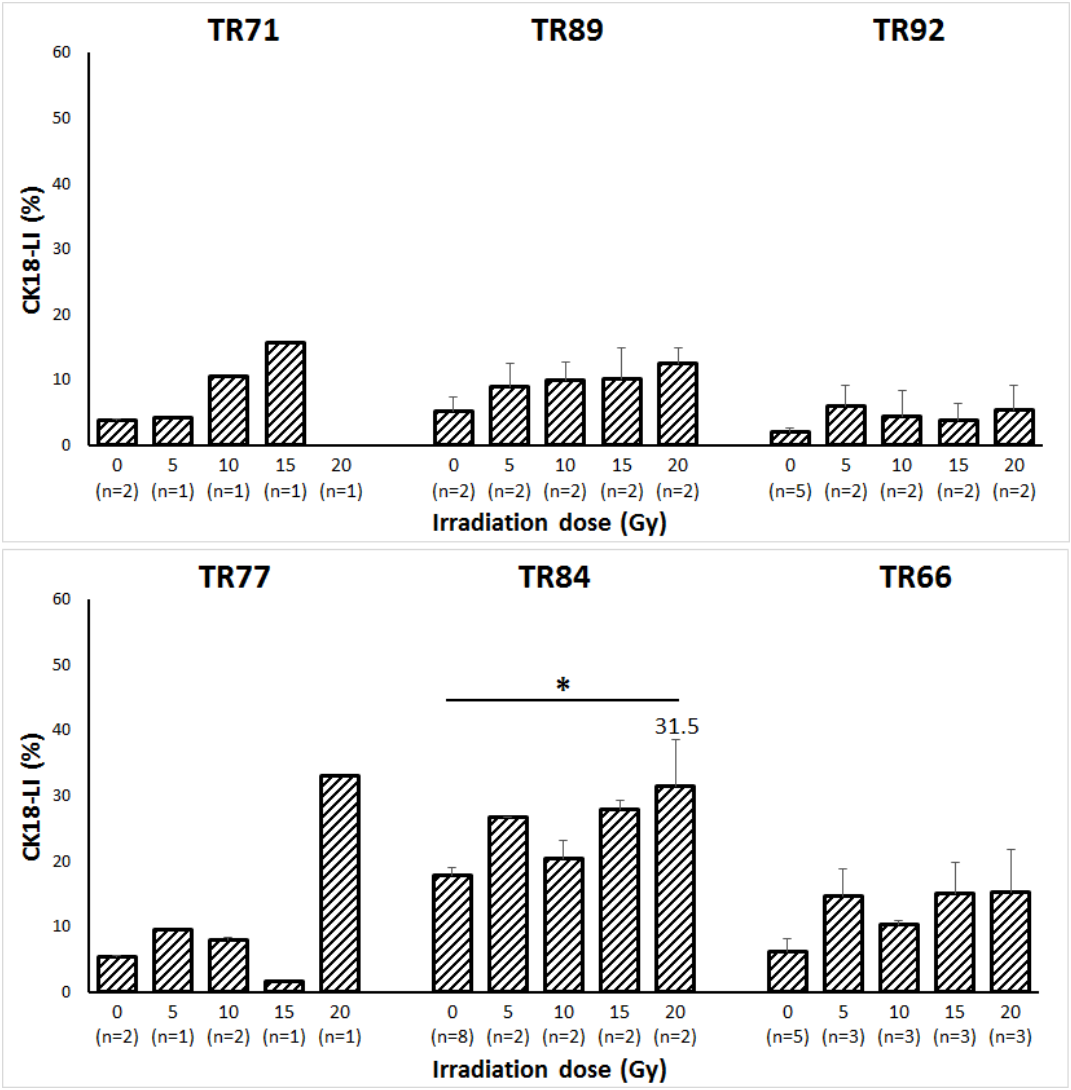


Figure 4.17. Mean CK18-LI of the six primary tumours taken from x100 tiled field (3 oral cavity; 1 oropharyngeal; 1 laryngeal and 1 paranasal sinus) with microfluidics but without irradiation (MF) and irradiation at increasing single doses.
Mean+SEM. The corresponding numbers of tissue biopsies subjected to each treatment are listed below the x-axis in parentheses and these are repeats of the experiment on the same tissue at different times. *indicates significance on One-way ANOVA with post-hoc Tukey test, p<0.05.

The mean CK18-LI of the three individual lymph neck node tissues was also displayed individually to identify any inter patient variability between the nodes metastasised from unknown (TR73), laryngeal (TR80) and oropharyngeal (TR59) primary tumours (Figure 4.18). Both the TR73 and TR80 tumour tissues achieved the highest apoptotic labelling index following 15Gy irradiation compared with those irradiated with 5Gy, 10Gy and 20Gy. Although the 15Gy irradiation induced apparent increases in apoptosis on both tumours, only the 15Gy-irradiated TR80 tumour had significant more apoptosis compared to the non-irradiated MF tissues, 5Gy and 10Gy irradiated tissues ($p<0.05$, One-way ANOVA followed by post-hoc Tukey test). Irradiation of all the four doses on the TR59 lymph node tissue induced higher CK18-LI compared with the non-irradiated control, with the similar levels of apoptosis (~23%) being observed following 5Gy, 10Gy and 20Gy.

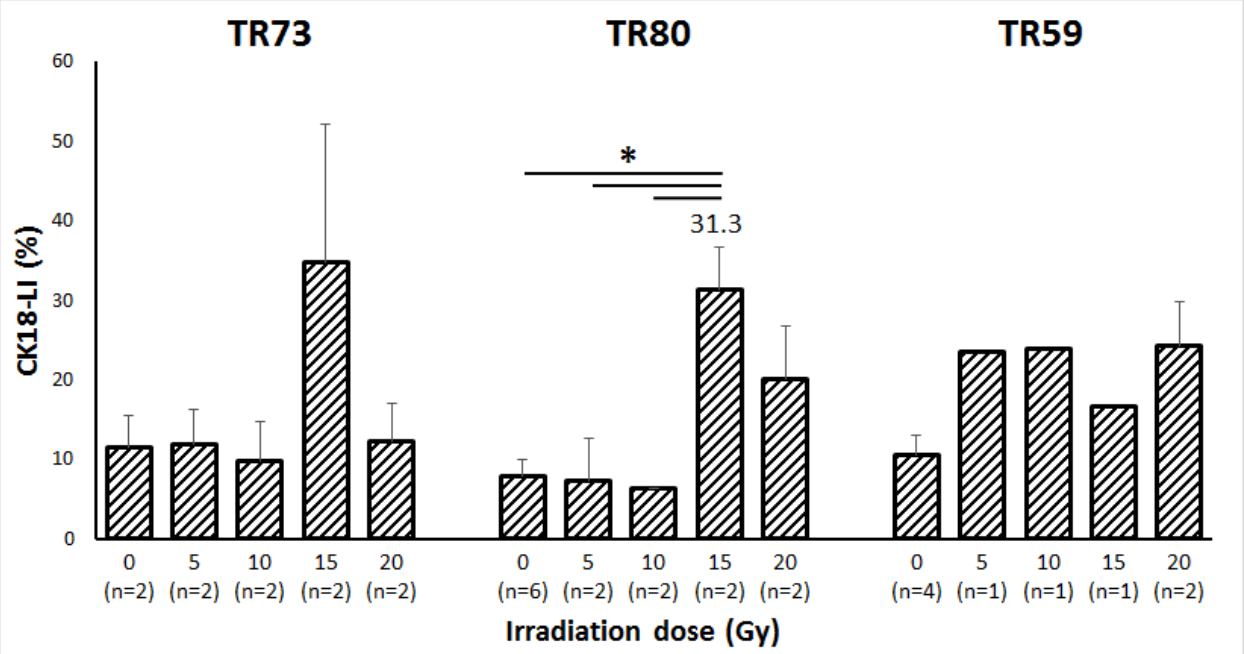


Figure 4.18. Mean CK18-LI of the three metastatic lymph node tissues [metastasised from unknown (TR73), laryngeal (TR80) and oropharyngeal (TR59) primary tumours], with microfluidics but without irradiation (MF) and irradiation at single doses.
Mean+SEM. The corresponding numbers of tissue biopsies subjected to each treatment are listed below the x-axis in parentheses and these are repeats of the experiment on the same tissue at different times. *indicates significance on One-way ANOVA with post-hoc Tukey test ($p<0.05$).

4.5.2 CK18-LI on tissues subjected to fractionated irradiation

The CK18-LI of the three HNSCC tumours subjected to fractionated irradiation treatment (5 x 2Gy and 5 x 4Gy) in the microfluidic device was calculated (Figure 4.19.A). No statistical analysis was performed on the data as there was only one experiment obtained for each fractioned irradiation schedule. The detection level of cleaved cytokeratin was comparable between tumours. A dose-dependent increase in the CK18-LI was observed in lymph node tissue metastasised from a laryngeal tumour (TR80) with the five fractions of 4Gy irradiation inducing the highest CK18-LI (21.5%). Compared with the single-dose irradiation treatment on the corresponding tumour (Figure 4.19.B), the CK18-LI of the 5 x 4Gy treatment induced a similar labelling index to that induced by the 20Gy irradiation (20.0+6.7%).

On the oral cavity TR89 tumour, both the irradiation schedules induced higher CK18-LI than that of the non-irradiated control. The CK18-LI of the tissue exposed to 5x2Gy irradiation was found similar with the level of the single-dose irradiation (5, 10, 15 and 20Gy), achieving approximately 10% of CK18-LI. Similar results were obtained on the oral cavity TR92 tumour between both single-dose and fractionation treatments (Figure 4.19.A and B), with the four single-dose irradiations resulting in approximately a 5% CK18-LI while the 5x2Gy and 5x4Gy irradiations induced a CK18-LI of 5.9% and 7.0% respectively. In general, based on the mean CK18-LI results, little benefits of the fractionated irradiation schedule in inducing more apoptotic cell death was observed compared with the single-dose irradiation.

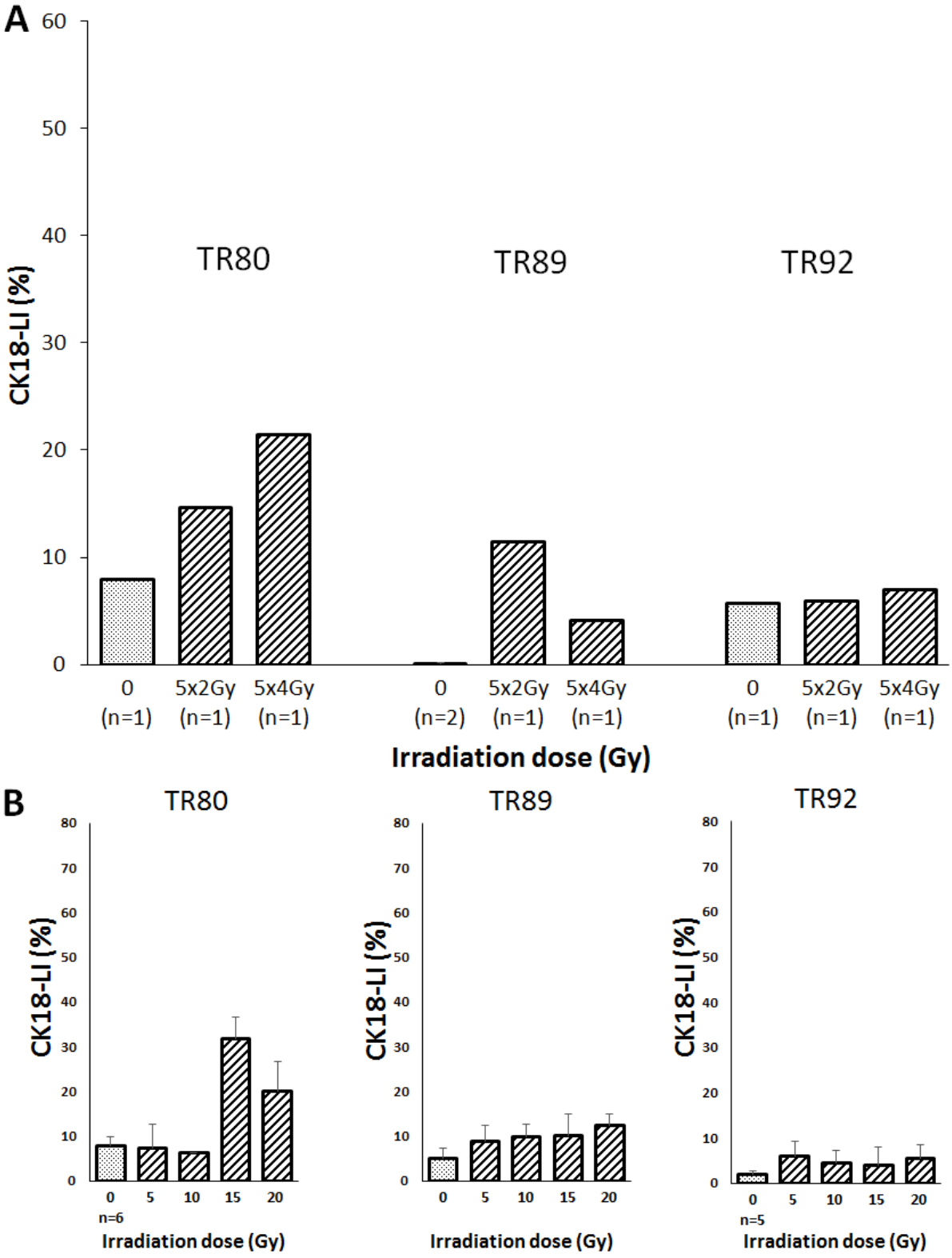


Figure 4.19. Mean percentage of CK18-LI of laryngeal lymph node tumour (TR80), oral cavity floor of mouth I (TR89) and II (TR92) tumours which were subjected to microfluidic culture without irradiation (MF) and different irradiation schedules.

(A) CK18-LI on fractionated irradiation (5x2Gy and 5x4Gy). (B) CK18-LI on single-dose irradiation (results presented previously in 0). Mean+SEM. The number of repeats of the staining on each tissue (n) is shown in parentheses, indicating the number of tissues from the same patient that were subjected to same treatment.

4.6. The effect of irradiation on the release of caspase-cleaved CK18 into the microfluidic effluent

Caspase-cleaved CK18 released from the HNSCC tissues during microfluidic culture with and without irradiation was detected in the effluent medium collected every two hours using the M30 ELISA (section 2.10). Four M30 ELISA assays were conducted on three HNSCC tissues subjected to microfluidics with and without different irradiation doses (Table 4.3). The average absorbance value of each effluent sample at each time point as well as that of the standards was obtained from the duplicate readings and the absorbance value of the medium only was subtracted from each. The absorbance readings of the standards were used to plot a standard curve (Figure 2.13) and the concentrations of the cleaved cytokeratin within each sample was drawn from the graph.

Table 4.3. HNSCC samples used to detect apoptotic response in terms of cleaved cytokeratin release, to irradiation in the microfluidic device.

HNSCC tumour	Microfluidics and treatments
Oral cavity floor of mouth (TR92)	Non-irradiated MF
	10Gy
	20Gy
Oral cavity floor of mouth (TR62)	Non-irradiated MF
	30Gy
Lymph node metastasised from laryngeal tumour (TR80)	Non-irradiated MF
	5x 4Gy

Standard curves (Figure 2.13) were created for each M30 ELISA assay from which the concentration of cleaved-CK18 released from different tumours following irradiation was measured (Figure 4.20). The amount of cleaved CK-18 released from the three tumours investigated remained constant throughout the microfluidic experiments with no increase following irradiation regardless of dose (10, 20 or 30Gy) or schedule (single or fractionated).

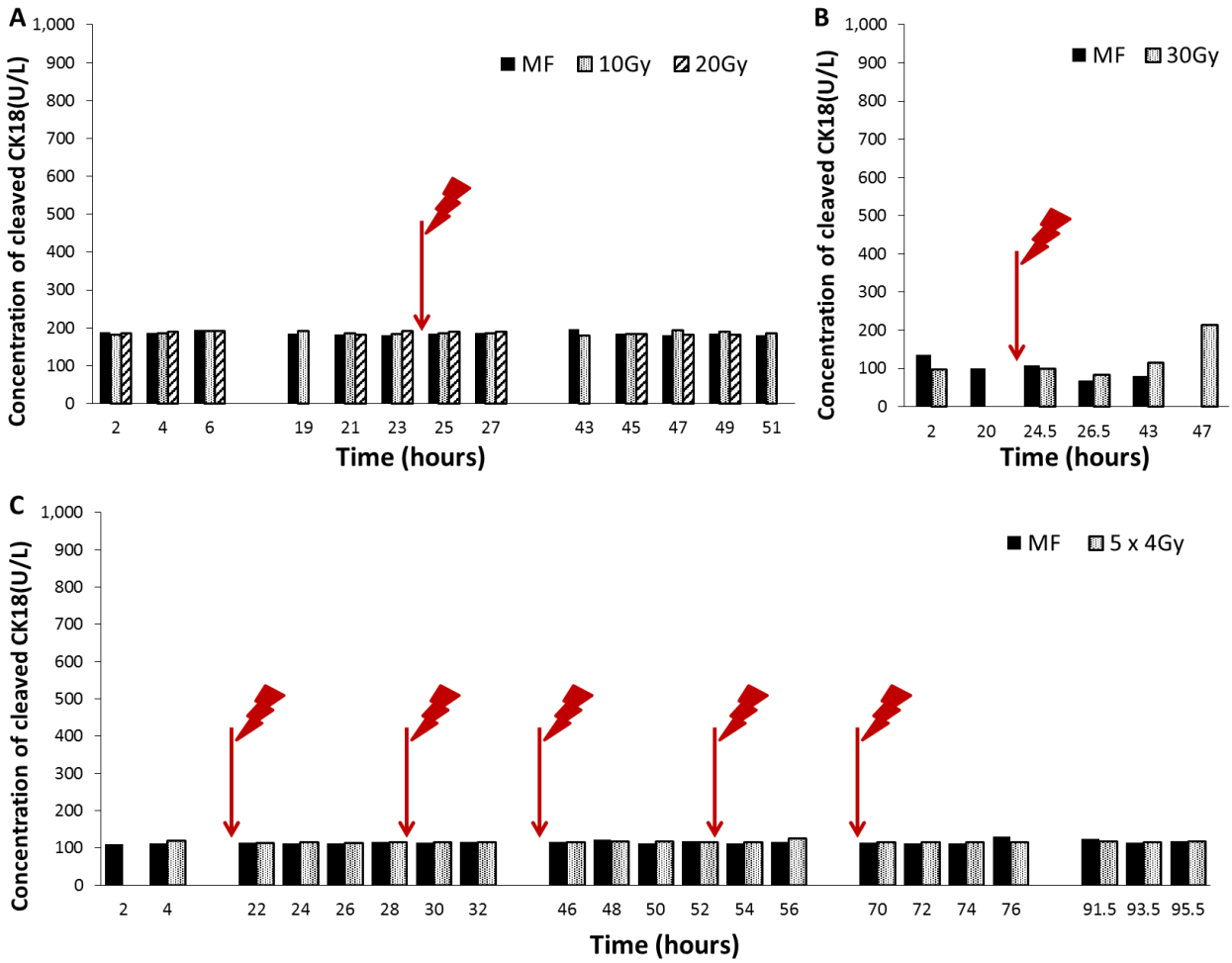


Figure 4.20. The concentration of cleaved-CK18 released from HNSCC tissues subjected to different irradiation schedules.

HNSCC tumours involved (A) oral cavity floor of mouth (TR92), (B) oral cavity floor of mouth (TR62) and (C) a lymph node metastasised from a laryngeal tumour (TR80). Arrows indicate the time of bilateral x-ray irradiation.

4.7. The effect of irradiation on DNA double-strand breaks in HNSCC tissue maintained in the microfluidic device

The expression of γH2AX was assessed, using IHC, in five non-irradiated and irradiated (single-dose irradiation 5, 10, 15 and 20Gy; in total 63 pieces of tissue) HNSCC tissues maintained on the microfluidic device following cryosectioning (Figure 4.21). The amount of antibodies used against these targets during the primary antibody incubation are listed in Table 4.2 and the staining of these markers on the tissue section was viewed using a light microscope (Nikon E800).

The tumour tissues used included a lymph node metastasised from an unknown primary (TR73; n=1), a lymph node metastasised from a laryngeal tumour (TR80; n=1), a laryngeal supraglottic tumour (TR84; n=1) and two oral cavity floor of mouth tumours (TR89 and TR92; n=2; Figure 4.21). These tumours were chosen and subjected to this γH2AX study based on the availability of the number of the repeats in achieving n=2 on each case, excluding the oral cavity (TR71), oropharyngeal (TR77) tumours and the oropharyngeal lymph node (TR59). The paranasal sinus (maxillary sinus; TR66) tumour was not selected because of the limitation of the embedded tissue sections for further IHC staining.

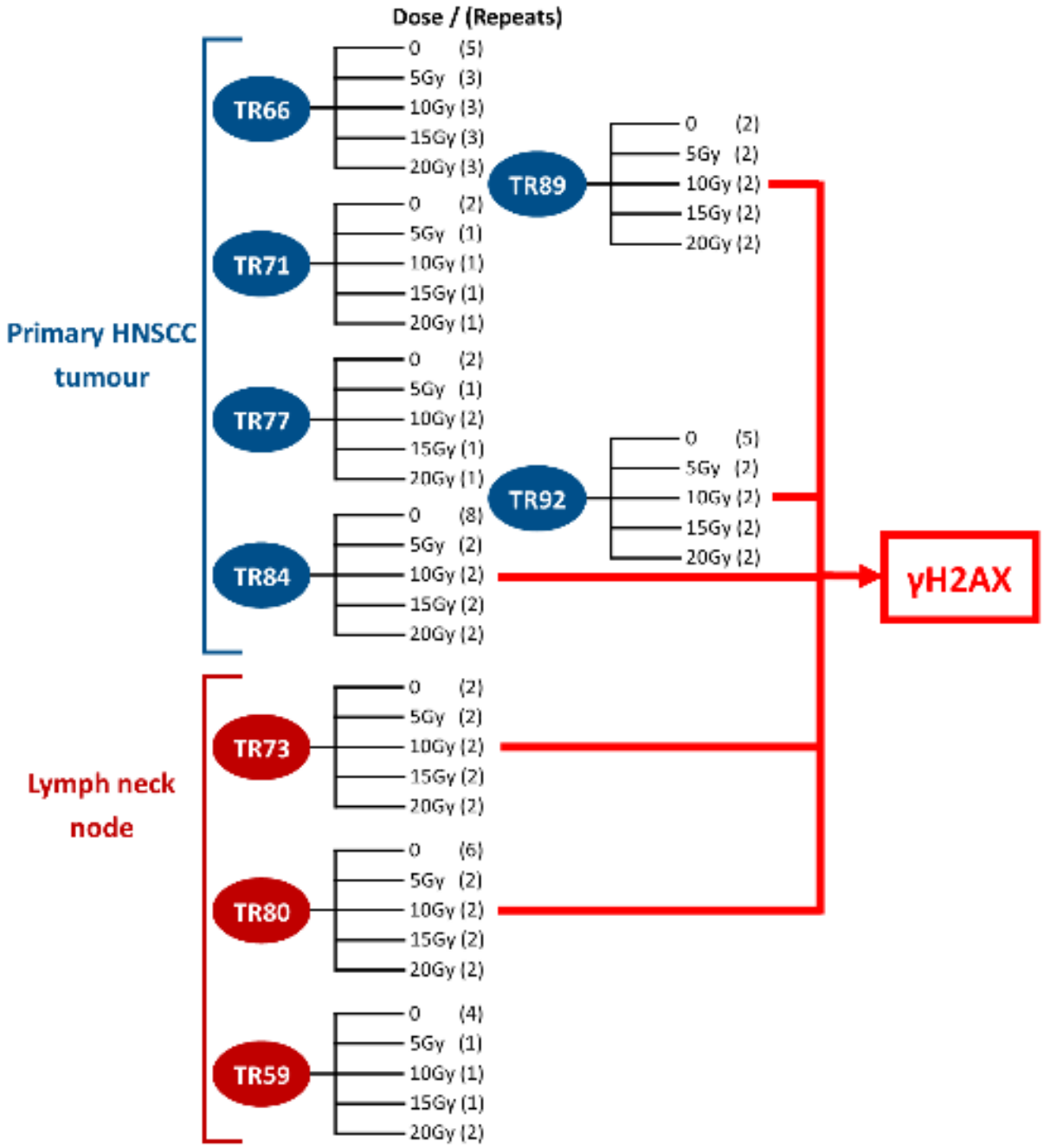


Figure 4.21. A flow chart of the nine HNSCC tumours involved in the current microfluidic irradiation study showing which samples were stained for γH2AX.
Tumour TR66: paranasal sinus, TR71: oral cavity, TR77: oropharyngeal, TR84: laryngeal, TR89: oral cavity, TR92: oral cavity, TR73: lymph node from unknown primary, TR80: lymph node from laryngeal primary, and TR59: lymph node from oropharyngeal primary. The number of repeats for the five treatments (MF 0Gy control, 5Gy, 10Gy, 15Gy and 20Gy) were listed beside each treatment.

Five x400 magnification fields of the tumour area (identified using a serially stained section of cytokeratin) across the tissue sections were photographed and the number of positively stained nuclei and total nuclei on each field were counted manually using the Point or Multi-point function of ImageJ 1.48v (Java 1.6.0_20 64-bit; Figure 4.22). The percentage of cells positive for γH2AX on each of the five tissues (two lymph neck nodes and three primary tumours) was obtained by expressing the number of positive nuclei (brown) as a fraction of the total nuclei (blue and brown) in the five fields. The statistical differences between non-irradiated and irradiated tissues on individual tumour was carried out by One-way ANOVA followed by Tukey's Multiple Comparison test.

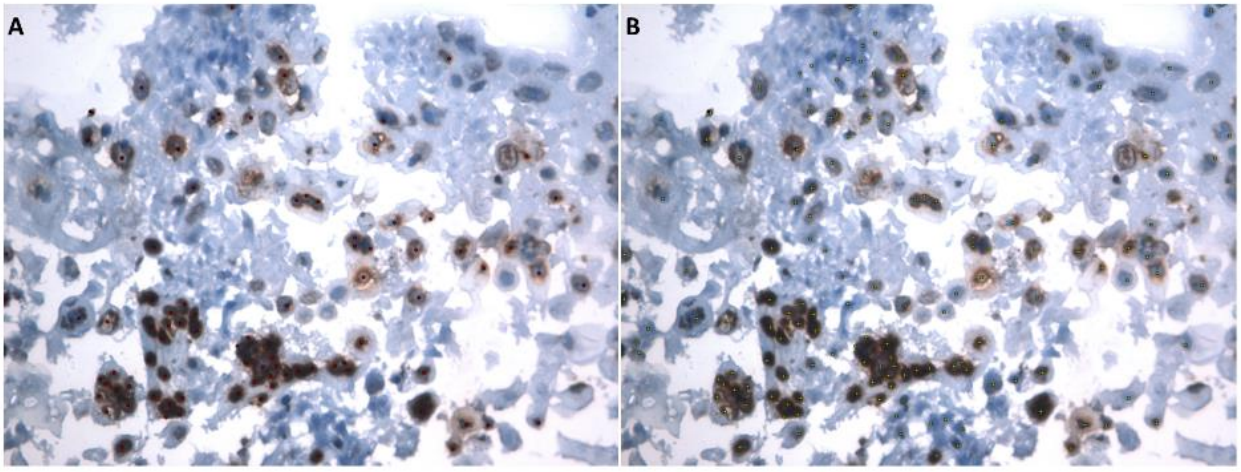


Figure 4.22. Photomicrographs showing the method used to count positive γH2AX staining on all the frozen tissue sections of the five selected HNSCC patients (n=2 for lymph neck node and n=3 for primary tumour).
In total, 74 of tissue samples were analysed. (A) The positive brown stained nuclei were first marked with red dots and (B) all the nuclei on the same field were marked with yellow dots and counted using the Multi-point function of Image-J 1.48v software.

4.7.1 Percentage of γH2AX expression following single-dose irradiation

On the tissue sections which were subjected to IHC staining with the mouse IgG2b matched isotype control, no brown positive staining was observed, indicating that there was no non-specific binding (Figure 4.23 A). Visual analysis of the stained sections indicated that there appeared to be a greater number of brown positive nuclei in the irradiated tissues compared with the non-irradiated MF tissues (Figure 4.23 B).

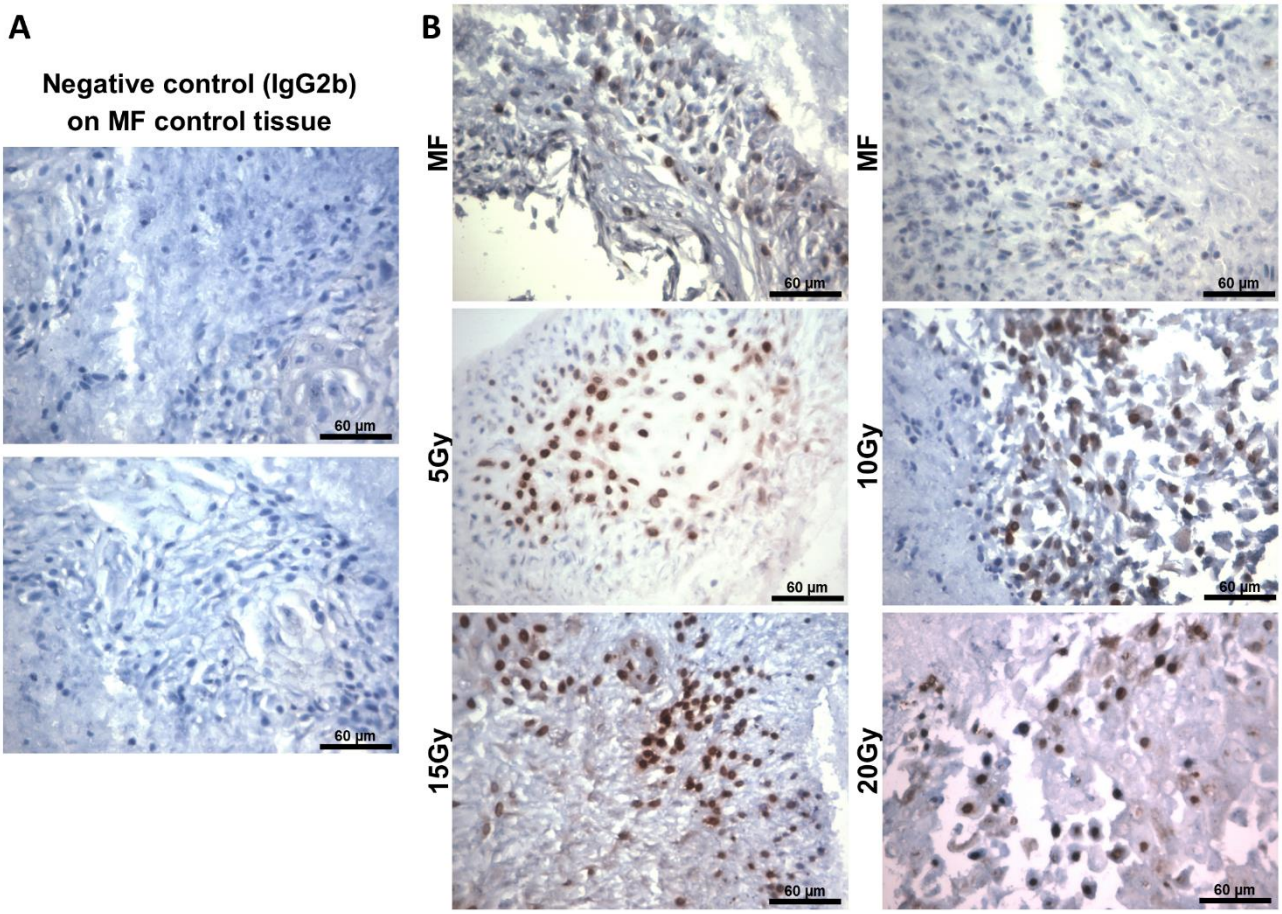


Figure 4.23. Representative IHC staining of γH2AX on an oral cavity floor of mouth tumour II (TR92; n=13).

Brown represents the expression of γH2AX with blue haematoxylin counterstain. (A) Representative IHC staining using matched mouse IgG2b isotype negative control for the γH2AX antibody (x400 magnification) (B) Representative fields at x400 magnification taken based on the areas of tumour (IHC staining of CK; section 4.5).

Once the average percentage was obtained from the five fields, the mean percentage of cells positive for DNA-DSBs on repeated tissues of same treatment was calculated (Figure 4.24 and Figure 4.25). In the HNSCC tissue from the lymph neck node metastasised from an unknown primary (TR73), irradiation induced up to a 50% increase in the percentage of DNA-DSBs compared with the non-irradiated control (Figure 4.24). The greatest increase in DNA-DSBs was seen following 10Gy- and 15Gy-irradiation which caused an increase by 20.2±1.5% and 20.6±2.5% respectively when compared to the non-irradiated control (11.0±0.5%), however, the increase was not statistical significant.

Irradiation of the lymph neck node metastasised from a laryngeal tumour (TR80) resulted in an increase in the percentage of cells expressing γH2AX at all doses of irradiation (Figure 4.24). The highest increase in damage was seen after 15Gy irradiation (41.0±2.5%) which caused a 22% increase over the non-irradiated control. The increasing percentage of DNA-DSBs was dose dependent up to 15Gy but decreased following irradiation with 20Gy (29.8±3.7%), however none of the increases were statistically significant.

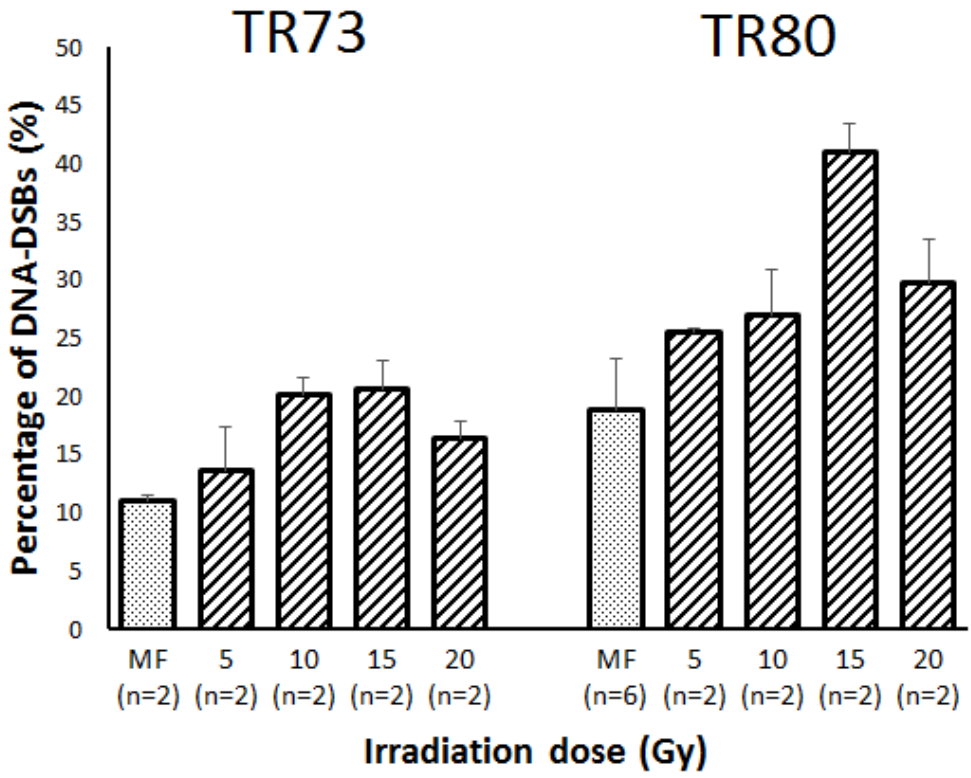


Figure 4.24. Mean percentage of cells positive for DNA-DSBs from five x400 fields of view on two HNSCC lymph neck node tissues following different doses of irradiation.
MF= non-irradiated microfluidic control. Mean+SEM. The number of repeats of the staining on each tissue (n) is shown in parentheses, indicating the number of tissues from the same patient that were subjected to same treatment.

In the oral cavity TR92, there was a dose-dependent increase in the percentage of cells positive for γH2AX, with the 10Gy, 15Gy and 20Gy irradiation induced significantly higher percentage compared with the non-irradiated control (p<0.05; One-way ANOVA followed by post-Hoc Tukey Multiple Comparison test). Among the three tumours, both the TR84 and the TR89 tumours achieved low levels of cells positive for γH2AX (<22%) were observed following all doses of irradiation. The oral cavity TR89 tissues following irradiation have an insignificant higher percentage compared with that of the non-irradiated control tissue.

The 10Gy of irradiation caused higher percentage of cells positive for γH2AX (22.0±3.7%) on the laryngeal TR84 tumour compared with other irradiation doses and with the non-irradiated MF tissue (10.3±1.9%). In fact, both 5Gy and 15Gy resulted in a lower percentage than that of the non-irradiated control tissues.

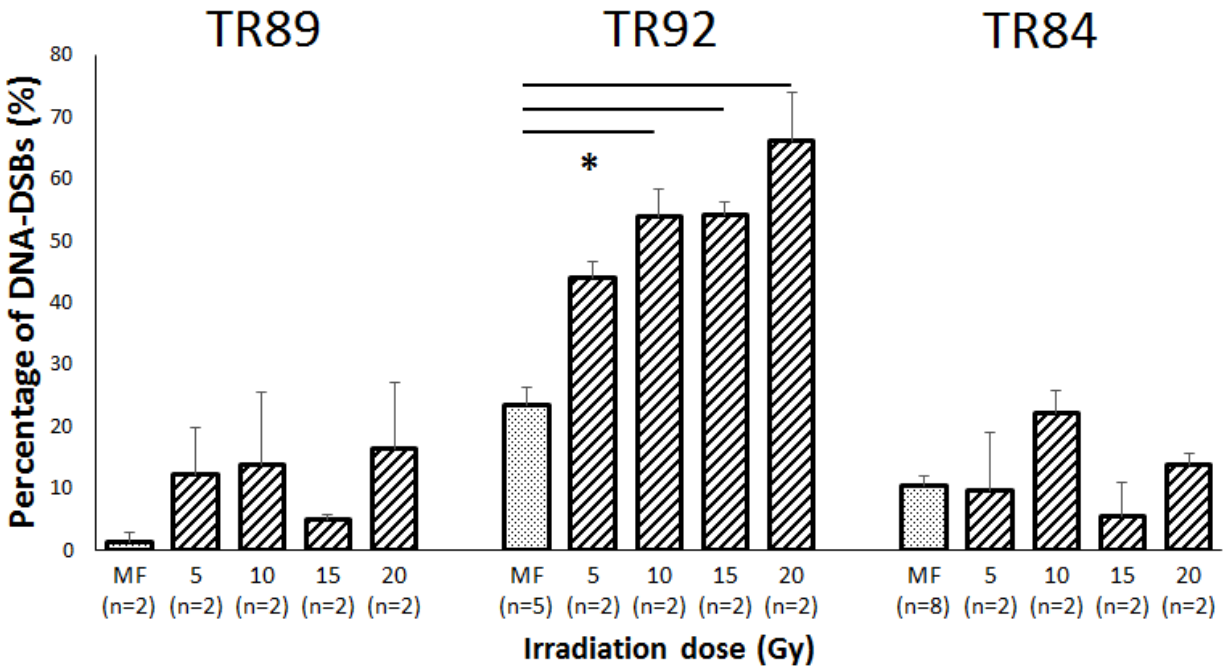


Figure 4.25. Mean percentage of cells positive for γH2AX expression from five x400 fields of view which are positive for DNA-DSBs on three HNSCC primary tumours (oral cavity TR89 and TR92; laryngeal tumour TR84) following different doses of irradiation.
MF= non-irradiated microfluidic control. Mean+SEM. The number of repeats of the staining on each tissue (n) is shown in parentheses, indicating the number of tissues from the same patient that were subjected to same treatment. * Significance using one-way-ANOVA followed by Tukey's Multiple Comparison test between the five treatments, p<0.05.

4.7.2 Percentage of γH2AX expression level following fractioned irradiation

In all three tissues investigated the fractionated irradiation treatments induced a higher percentage of γH2AX positive cells compared with the corresponding non-irradiated tissues maintained in microfluidics for the same period of time, except for the laryngeal node TR80 tissue irradiated with 5 x 4Gy irradiation, which achieved a similar percentage to the control (Figure 4.26.A). Five fractions of 2Gy induced a higher percentage of γH2AX expression compared with the other treatments in both the TR80 and the TR92 tumours. The level in the node reached a similar expression level to that on the same tumour subjected to a 10Gy single-dose irradiation (26.9%; Figure 4.26.B and Figure 4.24).

The oral cavity TR89 tumour showed greatest levels of γH2AX following irradiation with 5 x 4Gy whereas the 5 x 2Gy irradiation induced only marginally more γH2AX than that of the non-irradiated tissue. Both fractionated irradiation schedules resulted in a higher percentage of γH2AX expression, 31.0% and 22.9%, compared with that of the single-dose irradiation on the same tumours, 12.1% after 5Gy, 13.8% after 10Gy, 4.9% after 15Gy and 16.4% after 20Gy irradiation (Figure 4.26.B). The oral cavity TR92 tumour demonstrated the highest percentage of cells positive for γH2AX expression after irradiation compared with the other tumours 65.4% following 5 x 2Gy and 47.1% following 5 x 4Gy irradiation, this was substantially greater than the non-irradiated control (21.4%). Single-dose irradiation on this tumour also reached similar levels of γH2AX expression (ranged from 44% to 66%; Figure 4.26.B) compared with the fractionated doses.

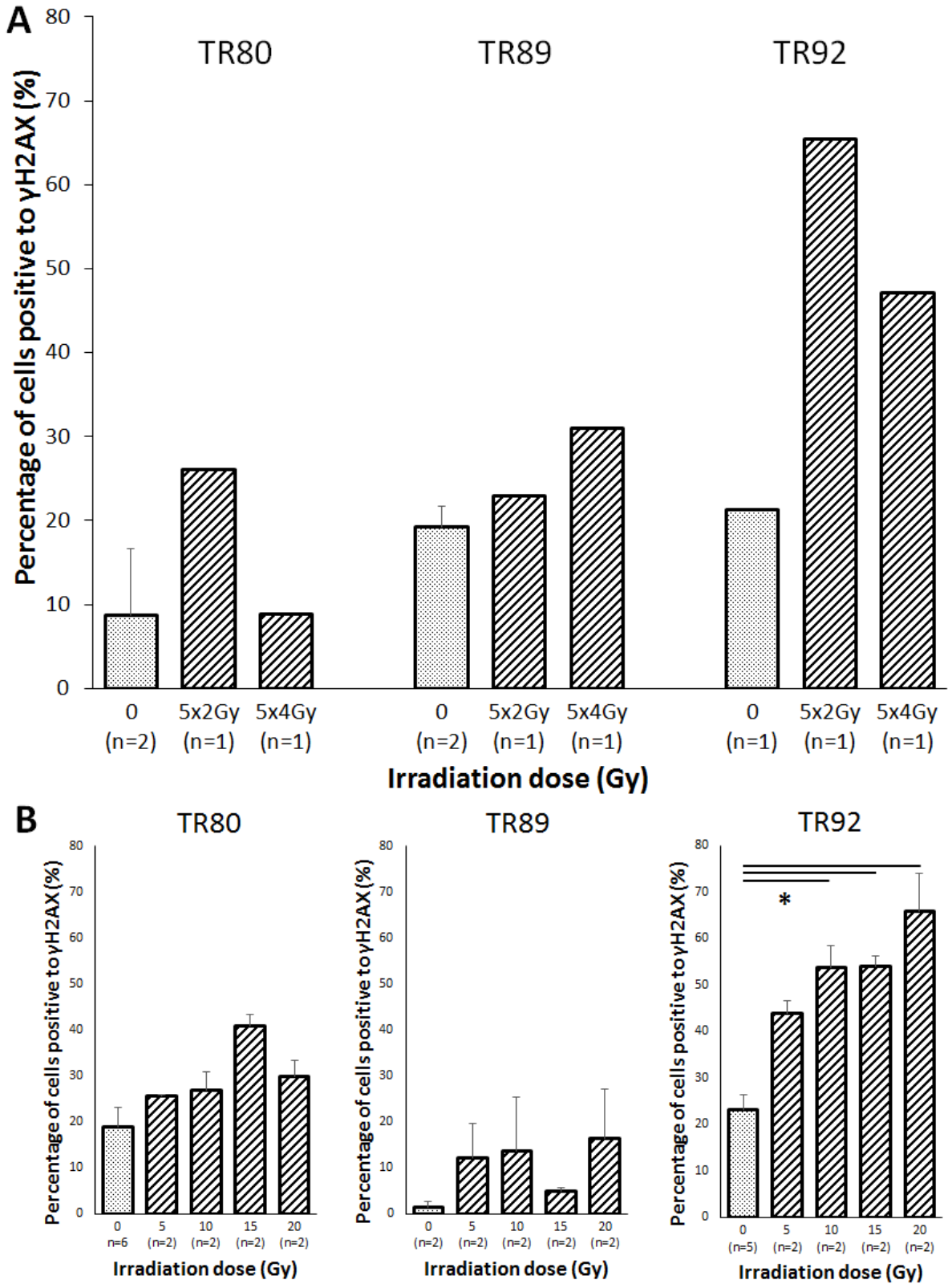


Figure 4.26. Mean percentage of cells positive for γH2AX expression on laryngeal lymph node (TR80) tumour and oral cavity floor of mouth I (TR89) and II (TR92) tumours which were subjected to microfluidic culture and different irradiation schedules.

(A) Mean percentage following fractionated irradiation (5x2Gy and 5x4Gy). (B) Mean percentage following single-dose irradiation (presented previously in 1.1.1). Mean+SEM. The number of repeats of the staining on each tissue (n) is shown in parentheses, indicating the number of tissues from the same patient that were subjected to same treatment.

4.8. Incorporation of FITC-conjugated caspase inhibitor (CaspACE) as a marker of apoptosis following irradiation

A caspase inhibitor (CaspACE FITC-VAD-FMK; Promega, UK) was used to recognise apoptotic cells by irreversibly binding the caspases which are activated following the initiation of apoptosis (section 4.1.4). The bound fluorescent inhibitor can then be detected using fluorescent microscopy. Tissues were maintained in a microfluidic device for 24 hours before irradiation and 10µM of caspase inhibitor (CaspACE™ FITC-VAD-FMK *in situ* marker; Promega, Southampton, UK) was added to the microfluidic system to perfuse the tissues for 2 hours in the dark before tissue was frozen. Three HNSCC patient tissues were analysed: TR84, TR122 and TR54. The tissues were subjected to individual microfluidic culture for approximately 48 hours. Positive control tissues were perfused with medium containing 10µM etoposide to induce apoptosis throughout the microfluidic tissue culture. In this study, the number of tissues used and the corresponding treatments on individual tissue are summarised in Table 4.4.

Table 4.4. Summary of the number of tissues subjected to microfluidic culture and incubation with 10µM caspACE inhibitor (CaspACETM FITC-VAD-FMK in situ marker).

HNSCC tissue	Tumour site	Age; Gender	Treatments	No. of samples
Larynx	Supraglottic (TR84)	68; F	Etoposide	1
			MF Control	1
			20Gy	1
Lymph node	metastasised from oropharyngeal tumours (TR122)	32; M	Etoposide	1
			MF Control	1
	metastasised from oropharyngeal tumours (TR54)	46; M	Etoposide	1
			MF Control	2
			20Gy	3

Etoposide (10µM) was added to additional tissue in the microfluidic device throughout the incubation, serving as a positive control. MF control is the tissue subjected to no irradiation and maintained in microfluidic device. Tumour stage on these tissues was not applicable.

The tissues were taken out from the device and rinsed with PBS before being embedded in OCT, snap-frozen and sectioned (section 2.7). Tissue fixation and fluorescence microscopy were carried out according to the protocol described in section 2.12 and 2.12.1, to evaluate the incorporation of caspACE inhibitor and the cells undergoing apoptosis. The exposure time to view and photograph the DAPI staining was set at 70ms while the exposure time for FITC staining was set at 1.5s.

The fluorescence images were corrected and adjusted on their contrast and brightness by using ZEN fluorescence microscopy software (ZEN 2012; blue edition).

4.8.1 Fluorescence detection of CaspACE markers on HSNCC tissues

During microfluidic culture, a metastatic lymph neck node from a tonsil (TR122) was treated with 10µM of etoposide to induce apoptosis as a positive control for the CaspACE caspase inhibitor marker. Although tissue treated with etoposide showed incorporation of the fluorescence marker into the cytoplasmic area (Figure 4.27; Etoposide+), tissue which was maintained in the microfluidic device but not treated with etoposide also showed green fluorescence indicating the presence of apoptotic cells in non-irradiated control tissue (Figure 4.27; Non-irradiated control). The negative control tissue in which the caspase inhibitor marker was not added showed no FITC green fluorescence, confirming no auto-fluorescence staining (Figure 4.27; Negative control).

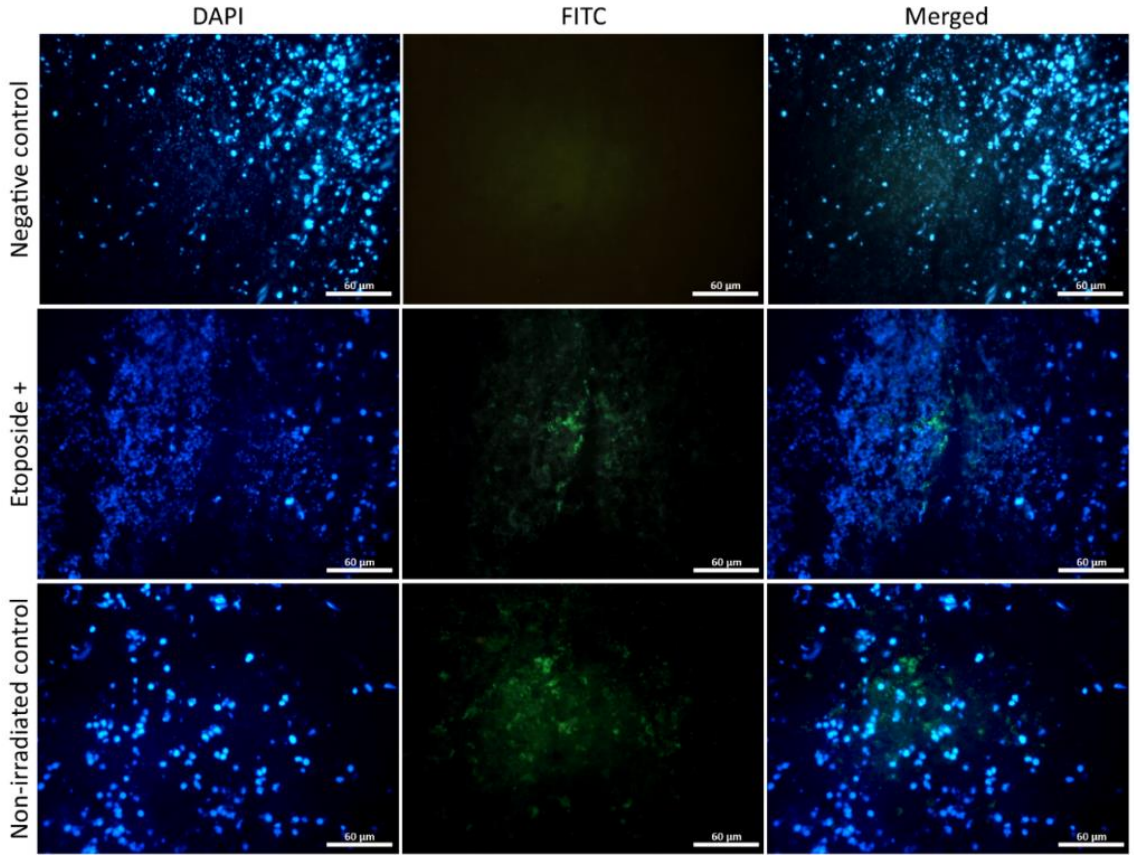


Figure 4.27. Representative fluorescence microscopic images of lymph node tissue metastasised from oropharyngeal tonsil TR122 tumour maintained in a microfluidic device
The tissues were subjected to no caspase inhibitor addition (negative control), etoposide treatment (etoposide +) and no etoposide treatment (non-irradiated microfluidic control (n=3). DAPI blue counterstaining and FITC green fluorescence indicates cells with incorporated CaspACE inhibitor (x400 magnification).

The effect of irradiation on the apoptosis level of two HNSCC tumours (TR54 and TR84) was determined using the CaspACE inhibitor assay. Both of the tumours were cultured in a microfluidic device and subjected to 20Gy single-dose irradiation before addition of the fluorescent caspase inhibitor. On the lymph node TR54 tissue, the incorporation of the marker was detected more by visual assessment on tissues treated with 20Gy irradiation compared with non-irradiated tissues (Figure 4.28; Left column). Although the background green staining was observed on the non-irradiated tissue, the presence of the CaspACE marker was less on this tissue compared with that of the irradiated tissue. Both the tumours (TR54 and TR84) treated with etoposide showed more caspase activity compared to the untreated tissues (Figure 4.28). However, the incorporation level on the laryngeal TR84 tumour was observed similar between the non-irradiated and irradiated tissues (Figure 4.28; Right column).

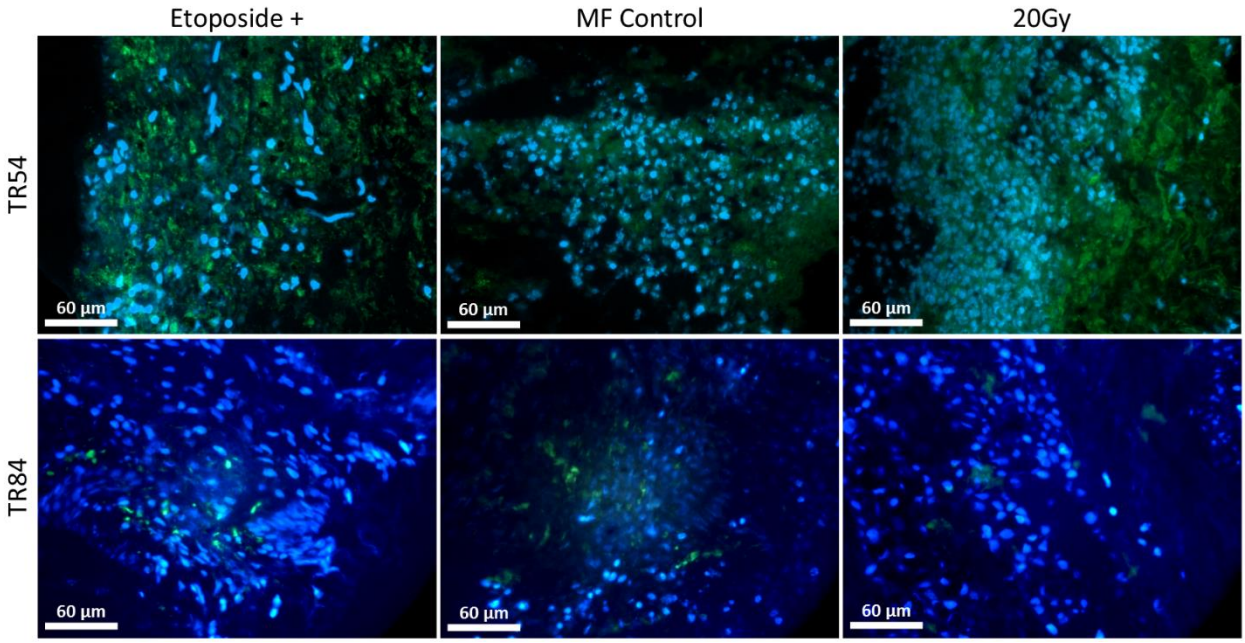


Figure 4.28. Representative fluorescence microscopic images of (Left column) lymph node tissue metastasised from an oropharyngeal tonsil tumour (TR54; n=6) and (Right column) a laryngeal supraglottic tumour (TR84; n=3).
The tissues were maintained in separate microfluidic devices and subjected to etoposide (etoposide +), no irradiation (MF control), and 20Gy irradiation (x400 magnification). DAPI blue counterstain and FITC green fluorescence indicates cells incorporated CaspACE caspase inhibitor.

To further analyse the incorporation of CaspACE markers between the non-irradiated and 20Gy irradiated tissues, the percentage of green positive fluorescence over the blue nuclear DAPI staining was evaluated on each x400 magnification field and the mean percentage on the tissues which subjected to same treatment was calculated (non-irradiated control versus 20Gy-irradiated tissues). The image analysis was carried out by using ZEN 2012 (Carl Zeiss Microscopy GmbH software) and Image-

Pro Premier software, similar with the image analysis implemented on TUNEL assay (Figure 4.30). In total, two non-irradiated tissues and three 20Gy irradiated tissues of the metastatic lymph neck node from an oropharyngeal (TR54) tumour and one non-irradiated tissue and one 20Gy irradiated tissue of the laryngeal supraglottic (TR84) tumour were analysed (Figure 4.29).

On the lymph node TR54 tumour, 20Gy irradiation induced higher incorporation level of the CaspACE fluorescence marker compared with that of the non-irradiated tissues, suggesting that the apoptosis level was increased after irradiation. Different results were observed on laryngeal TR84 tumour in which the 20Gy irradiation induced slightly lower percentage of CaspACE incorporation compared with the control tissue. Since there was only one repeat tissue subjected to CaspACE incorporation on this laryngeal tumour, statistical *t*-test could not be performed. This preliminary data on the CaspACE incorporation suggested the need to subject larger number of HNSCC tumours to microfluidic and CaspACE incorporation experiments, in order to understand the effects of irradiation on the uptake of CaspACE marker and apoptotic level.

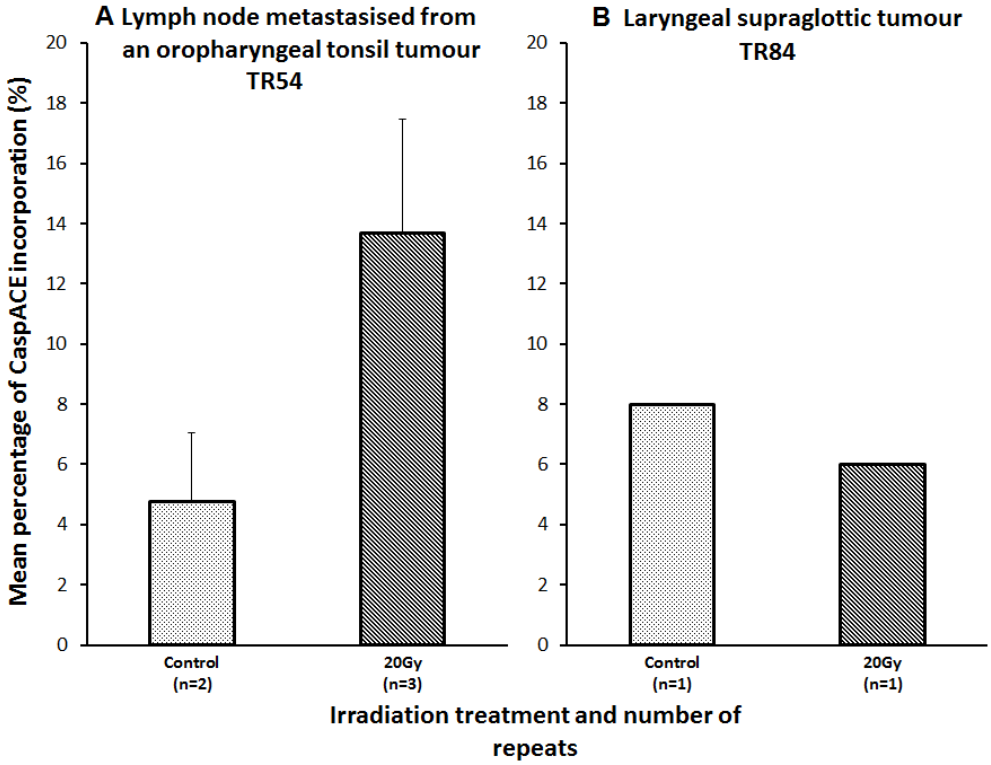


Figure 4.29. Mean percentage of CaspACE incorporation on (A) the lymph node tissues metastasised from an oropharyngeal tonsil (TR54) tumour and (B) laryngeal supraglottic (TR84) tumour which were subjected to microfluidic culture with and without single-dose irradiation. x400 magnification on both DAPI and FITC fields. Mean+SEM.

4.9. The effect of irradiation on DNA fragmentation measured using TUNEL assay

TUNEL was carried out in order to detect the fragmented DNA on the tissue sections following irradiation (section 4.1.5). Five HNSCC patient tumours were cultured in a microfluidic device (no irradiation control; 0Gy) and irradiated (5Gy, 10Gy, 15Gy and 20Gy; section 2.3 and 2.4) prior to snap freezing in OCT and cryo-sectioning. The TdT enzyme was then used to add fluorescent dUTP onto the fragmented ends of the apoptotic cell DNA (section 2.11). The five HNSCC tumours included TR73, TR80, TR89, TR92 and TR84 (Table 2.3).

Two additional slides of tissue sections (pre-microfluidics tissue not subjected to microfluidics and irradiation) were treated with DNase (Roche, UK) which aimed to induce DNA strand breaks in the cells. One of the control slides was then incubated with TdT enzyme and dUTP-FITC conjugate to serve as a positive control, while the other slide was incubated with TUNEL-label solution without TdT enzyme and dUTP conjugate, serving as a negative control.

TUNEL labelling was viewed using a fluorescence microscope in the Department of Biology at The University of Hull. Five x400 fields of view within the tumour areas (identified using serially stained sections of cytokeratin which described in section 4.5 and Figure 4.30.A) were photographed. Exposure times of 70ms and 1000ms were used to photograph the staining of DAPI (blue) and FITC (green), respectively.

To quantify the DNA fragmentation on the sections, ZEN 2012 (Carl Zeiss Microscopy GmbH, Blue Edition, 2011) software was used to adjust the contrast and brightness of the staining (Figure 4.30.B). The areas of DAPI staining (blue nuclei) and FITC (green labelled fragmented DNA) were then measured using the smart count function Image-Pro Premier software (Figure 4.30.C). The percentage of FITC green staining over DAPI blue counterstaining on each x400 magnification field was then calculated and the mean percentage of the five fields of specific treated HNSCC tissue was obtained. The mean percentages of TUNEL expression on non-irradiated HNSCC and irradiated HNSCC were compared using one-way ANOVA followed by post-hoc Tukey Multiple Comparison test.

The mean percentage of cells positive for DNA strand breaks on duplicate tissues (n=2), which were treated with the same irradiation dose in parallel microfluidic

devices, was calculated and the corresponding standard error of mean on the repeats were obtained and presented. The percentage area of cells positive for fragmented DNA was compared between the irradiated and non-irradiated tissues within each tumour sample.

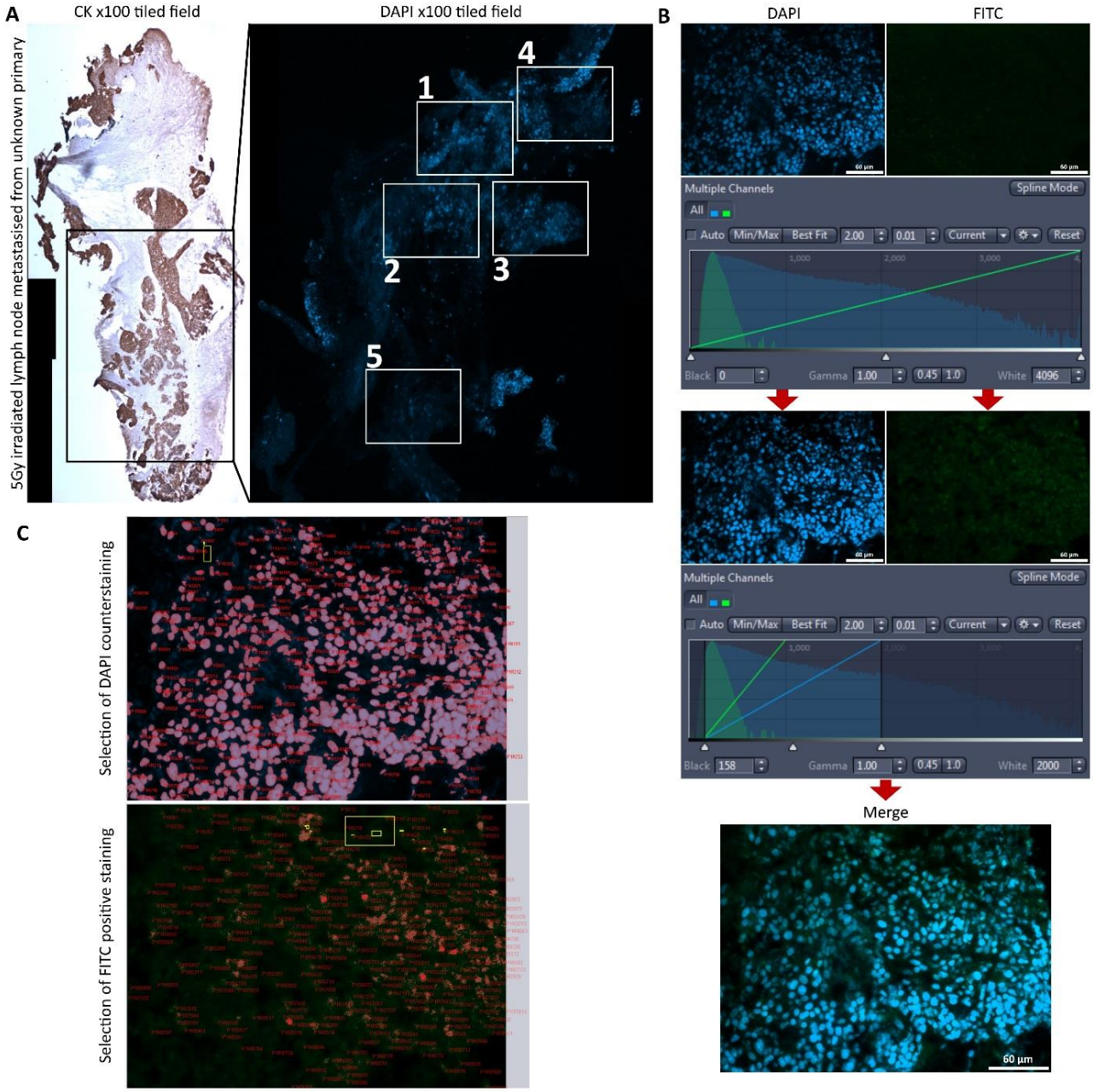


Figure 4.30. Fluorescent image analysis of TUNEL assay on the five HNSCC tumours (n=5). (A) Five x400 magnification fields photographed on TUNEL sections according to tumour area determined by IHC staining of cytokeratin (CK). (B) Example of contrast and brightness adjustment of the DAPI and FITC staining following TUNEL using ZEN 2012 (Carl Zeiss Microscopy GmbH, Blue Edition, 2011). DAPI and FITC channels combined to create merged image. (C) The blue and green fluorescence were respectively selected and counted to give area (μm^2) using Image-Pro Premier software.

4.9.1 Fluorescence detection of DNA fragmentation on HNSCC tissues

DNA fragmentation as a marker of apoptosis in response to irradiation was measured in HNSCC tissue using the TUNEL assay. DNase was used to fragment the DNA to act as a positive control and showed a greater density of green labelled nuclei on serially cut sections of lymph neck node tissue (TR73; without microfluidic culture), compared to the negative control without the TdT enzyme added (Figure 4.31).

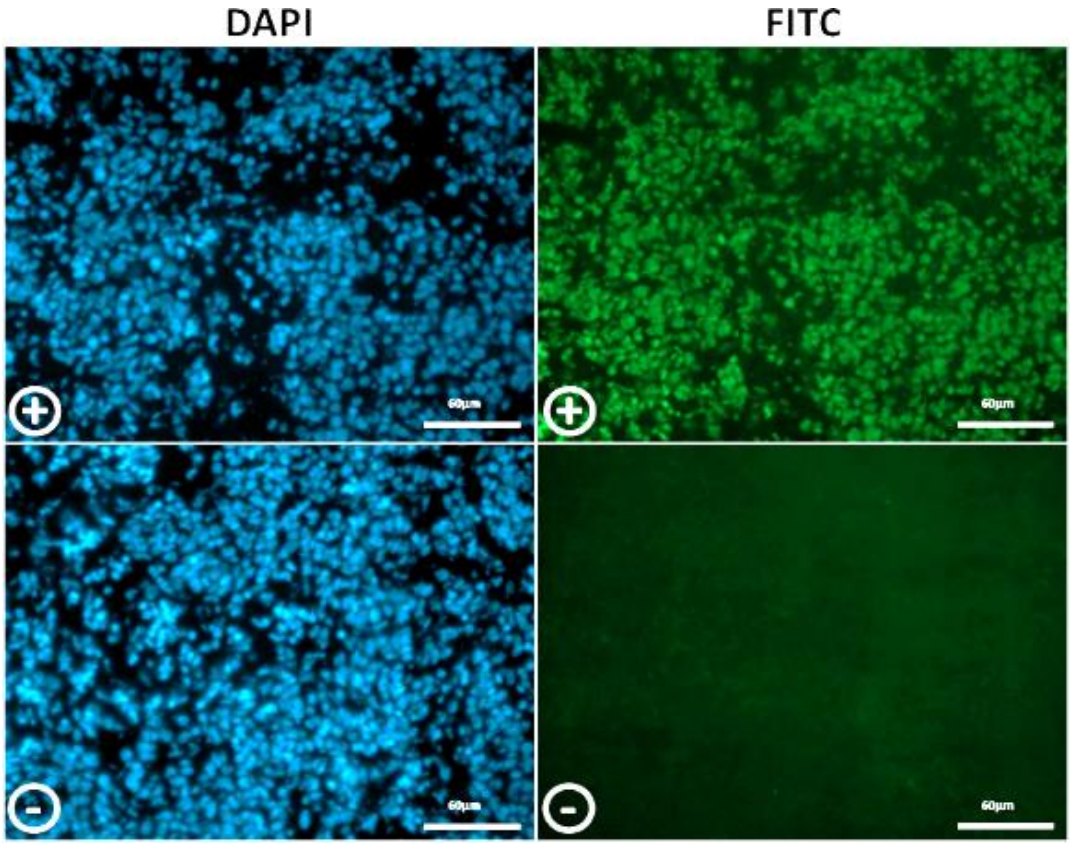


Figure 4.31. Fluorescent images showing the results of the TUNEL assay on two serially sectioned lymph node tissues (TR73) treated with DNAase.
+ indicates the section with the TdT enzyme added to the mixture and – indicates the sections without TdT enzyme. X400 magnification. Blue indicates DAPI counterstained nuclei while the green indicates the presence of incorporated dUTP demonstrating DNA fragmentation

Following irradiation (0, 5, 10, 15 and 20Gy) of a single sample of lymph node TR73 TUNEL was used to assess the levels of apoptosis in the tissue. Fluorescent images of incorporated dUTP into the lymph neck node tissue showed that apoptotic cells were only really evident on the tissues maintained in the microfluidic device and subjected to 15Gy- and 20Gy irradiation (Figure 4.32). It appeared visually that 15Gy- and 20Gy- doses of irradiation induced more apoptosis than the lower doses of irradiation with more positive green nuclei. The non-irradiated tissue sample showed low levels of green FITC staining indicating that the MF control tissue has less cells undergoing DNA fragmentation.

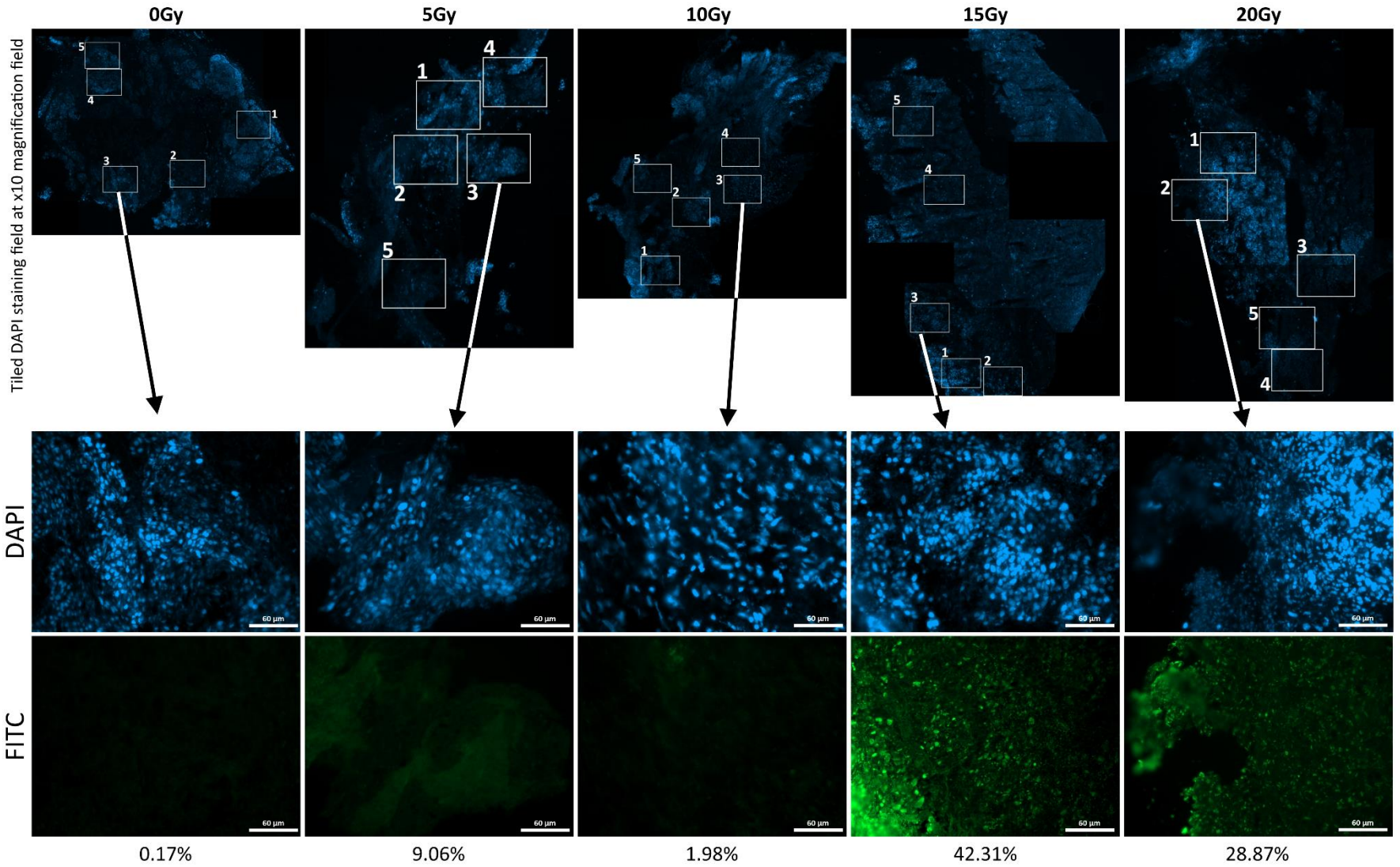


Figure 4.32. Fluorescent images of lymph neck node tissue (TR73) following microfluidic culture with no (0Gy) and with irradiation (5, 10, 15 and 20Gy) and apoptosis analysis using TUNEL.

Five x400 fields of view were photographed in within the tumour area and the staining colour intensity of both the DAPI and FITC were measured using the smart count function in Image-pro Premier. The percentage of cells undergoing DNA fragmentation was determined and is indicated below the photographs.

A dose-dependent increase in the mean percentage of apoptotic cells was clearly observed in the lymph neck node TR73 tissue (Figure 4.33.A). The percentage of cells having DNA fragmentation was significantly higher in the 20Gy-irradiated tissue compared with the corresponding 0Gy control tissues (p=0.047). On the metastatic lymph node TR80 tumour, 15Gy irradiation induced a significantly higher expression level (15.3%) compared with the non-irradiated tissue (2.1%; p=0.038) whereas the other doses of irradiation did not induce any increase in the number of apoptotic cells compared to the non-irradiated control (Figure 4.33.B).

Both 10Gy and 15Gy treatments on oral cavity TR92 tumour induced high mean percentage of cells positive to TUNEL assay on this tumour, 14.1% and 13.7% respectively (Figure 4.33.C). However, the higher level of DNA fragmentation on irradiated samples was not significantly higher than the control tissues. On the laryngeal TR84 tumour, 10Gy irradiation significantly induced a higher percentage of apoptotic cells (35.2%; p=0.01) compared with that of the non-irradiated control (9.1%; Figure 4.33.D). The 5Gy, 15Gy and 20Gy irradiated tissue samples caused a slight but non significant increase in apoptotic cells compared with that of the non-irradiated tissues.

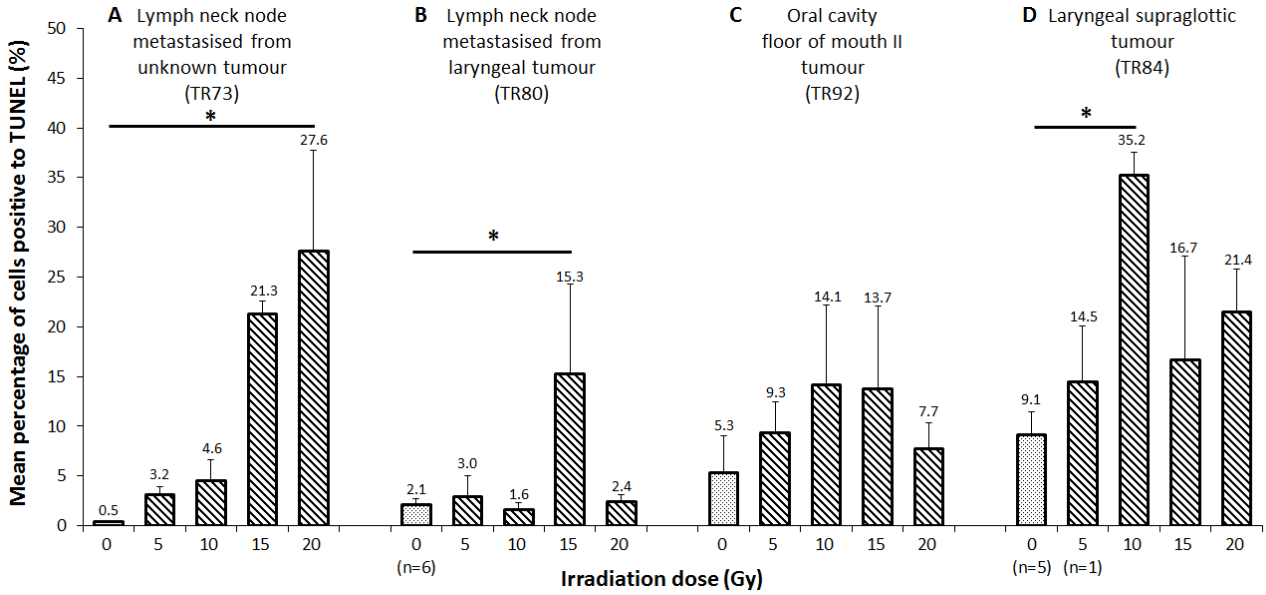


Figure 4.33. Mean percentage of apoptotic cells on the four tumour tissues that subjected to microfluidic culture with and without single-dose irradiation following the TUNEL assay.
x400 magnification on DAPI and FITC fields. Mean+SEM. * Significance using one-way ANOVA followed by Tukey Multiple Comparison test, p<0.05.

4.10. The effect of irradiation on the release of LDH from HNSCC tissue maintained in a microfluidic device with and without irradiation

The LDH cytotoxicity assay was carried out on the effluent medium collected every two hours throughout the microfluidic flow, except overnight time. The cytotoxicity assay was carried out within 7 days of collection of the effluent according to the methods described in section 2.6. The mean absorbance value at each time point was recorded and processed according to Table 2.4. Forty-four LDH assays were carried out following the 44 microfluidics and irradiation experiments (Table 2.1).

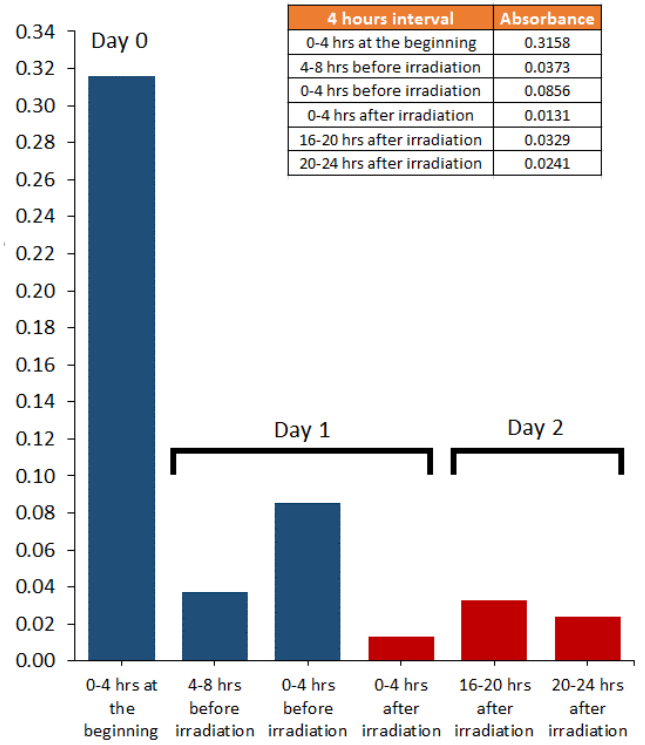
The mean absorbance value of the effluent medium collected at specific time points, (section 2.6), was obtained by deducting the average absorbance of the "medium-only" control from the duplicate samples and then normalized by the weight of the tissue (mg). Due to logistical problems, the collection time of the effluent medium and the time the tissue irradiated were, in some cases, different between experiments running the same tumour samples and same irradiation treatment.

Therefore, the LDH release data was normalised to irradiation time and all the absorbance values were grouped according to a 4-hour interval, giving the mean absorbance value at 4-hour interval before and after irradiation (Figure 4.34). These calculations were carried out on all tissue samples and the 4-hr-interval absorbance values from the tissues of the same patient and subjected to similar treatments (non-irradiation, 5Gy, 10Gy, 15Gy or 20Gy irradiation) were averaged (Figure 4.34):

4 hours at the beginning, 4-8 hours before irradiation, 0-4 hours before irradiation, 0-4 hours after irradiation, 4-8 hours after irradiation, 16-20 hours after irradiation, and 20-24 hours after irradiation.

(Error! Reference source not found.)

Time of collection	irradiation time	4 hours interval	Absorbance Value	4 hours interval	Values at 4hr interval
2	-25	0-4 hrs at the beginning	0.1907	0-4 hrs at the beginning	0.2023
4 (*Time of irradiation 29*)	-23	0-4 hrs at the beginning	0.2139		
20.5	-6.5	4-8 hrs before irradiation	0.0123	4-8 hrs before irradiation	0.0108
22.5	-4.5	4-8 hrs before irradiation	0.0093		
24.5	-2.5	0-4 hrs before irradiation	0.0043	0-4 hrs before irradiation	0.0034
26	-1	0-4 hrs before irradiation	0.0025		
28	1	0-4 hrs after irradiation	0.0072	0-4 hrs after irradiation	0.0081
30	3	0-4 hrs after irradiation	0.0089		
43.5	16.5	16-20 hrs after irradiation	0.0187	16-20 hrs after irradiation	0.0194
45.5	18.5	16-20 hrs after irradiation	0.0202		
47.5	20.5	20-24 hrs after irradiation	0.0134	20-24 hrs after irradiation	0.0136
49.5	22.5	20-24 hrs after irradiation	0.0139		
2	-26	0-4 hrs at the beginning	0.4294	0-4 hrs at the beginning	0.4294
4 (*Time of irradiation 28*)	-24	0-4 hrs at the beginning			
21.5	-6.5	4-8 hrs before irradiation	0.0510	4-8 hrs before irradiation	0.0638
23.5	-4.5	4-8 hrs before irradiation	0.0765		
25.5	-2.5	0-4 hrs before irradiation	0.2008	0-4 hrs before irradiation	0.1678
27	-1	0-4 hrs before irradiation	0.1348		
29	1	0-4 hrs after irradiation	0.0123	0-4 hrs after irradiation	0.0181
31	3	0-4 hrs after irradiation	0.0239		
45.5	17.5	16-20 hrs after irradiation	0.0161	16-20 hrs after irradiation	0.0463
47.5	19.5	16-20 hrs after irradiation	0.0765		
49.5	21.5	20-24 hrs after irradiation	0.0429	20-24 hrs after irradiation	0.0345
51.5	23.5	20-24 hrs after irradiation	0.0261		



4 hours interval	Absorbance
0-4 hrs at the beginning	0.3158
4-8 hrs before irradiation	0.0373
0-4 hrs before irradiation	0.0856
0-4 hrs after irradiation	0.0131
16-20 hrs after irradiation	0.0329
20-24 hrs after irradiation	0.0241

Figure 4.34. Calculation of mean absorbance values at 4-hour interval from two oral cavity floor of mouth tissues which subjected to parallel microfluidics with no irradiation treatment.

The time of irradiation on individual tissue was recorded as time zero and the average absorbance values at 4-hour interval before and after irradiation were calculated that includes 4 hours at the beginning, 4-8 hours before irradiation, 0-4 hours before irradiation, 0-4 hours after irradiation, 4-8 hours after irradiation, 16-20 hours after irradiation, and 20-24 hours after irradiation. The mean values at individual 4-hour-interval time point from these two repeat tissues were obtained and presented, as shown on right. Blue bars indicate the LDH release before irradiation while red bar represents the LDH level after irradiation.

The mean LDH release from seven primary HNSCC tumours (TR66, TR62, TR71, TR89, TR92, TR77, and TR84) and six lymph neck nodes (TR72, TR54, TR59, TR80, TR52 and TR73; Figure 4.35). A high release of LDH at the beginning of the microfluidic flow was observed in all seven primary tumour tissues and it is thought to be as a result of cell damage caused to the surface of the tissue biopsies during tissue handling (Figure 4.35.B). During the next eight hours whilst being maintained on the microfluidic chip, the amount of LDH released from the tissue decreased in all tissues and the absorbance of the tetrazolium product remained low (0.1a.u. to 0.16a.u.). In the subsequent 8-hour period post irradiation, the LDH release reduced further to around 0.02a.u. where it remained for the final 8-hour measurement. The decreases of the LDH release were observed at all different irradiation doses and even in the control tissues subjected to no irradiation, except for the 5Gy irradiation where the LDH released showed a very slight increase in the 8-hour time period immediately following irradiation.

When measuring the LDH release from the metastatic lymph node tissue (Figure 4.35.A), the initial high level of LDH released seen with the primary tumour was also observed (0.2a.u.). It was again reduced to approximately 0.06a.u. during the next 4 hours and to 0.02a.u. in the following 4-hour interval. There was no increment in the LDH release from these node tissues following the four single irradiation doses. The amount of LDH released in the 4 hours immediately post-irradiation in both the non-irradiated and irradiated tissues was similar. Compared between lymph node and primary tumour tissues, the LDH level of the primary tumour after irradiation was found higher than that in lymph node tissues.

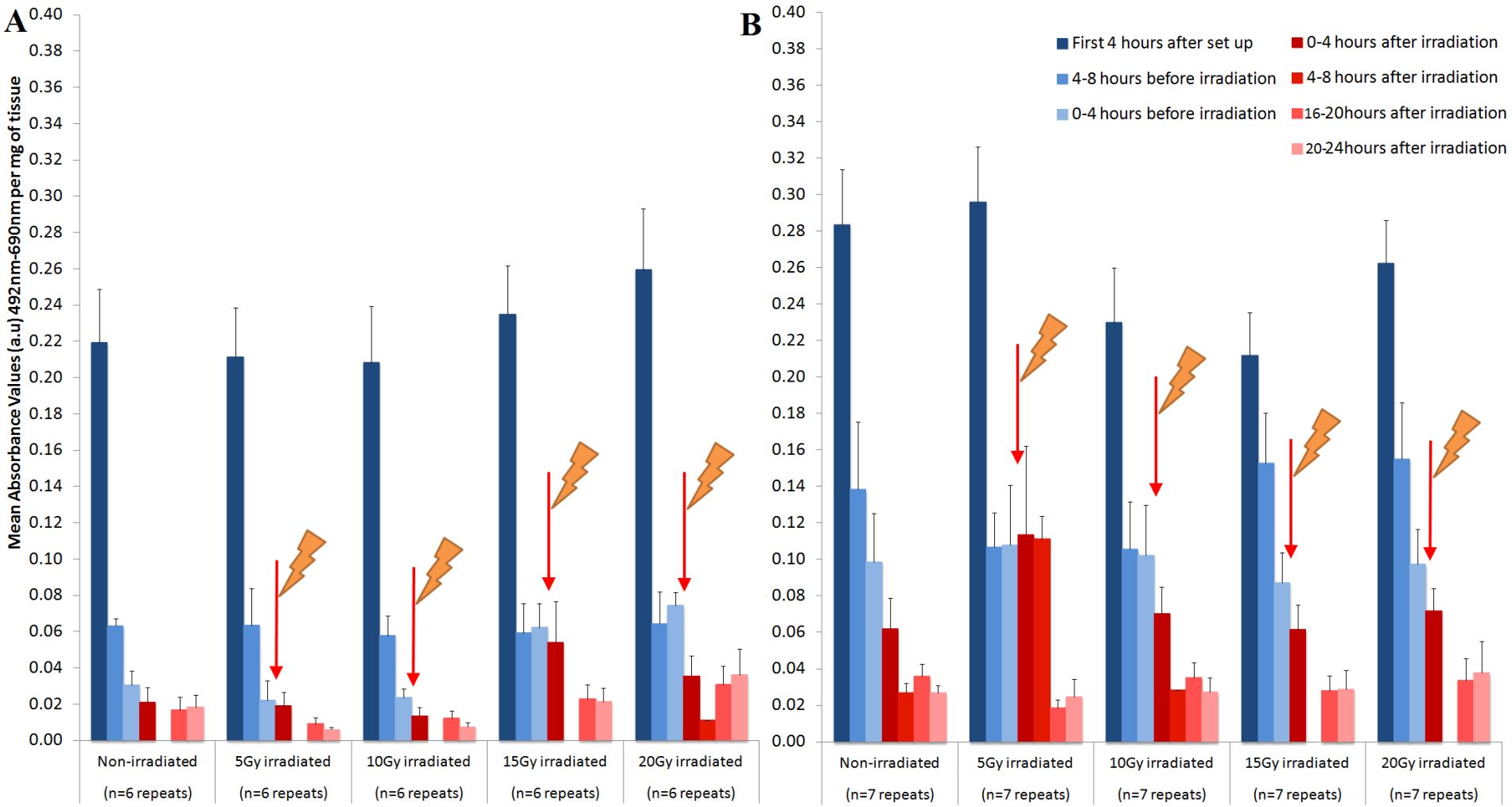


Figure 4.35. Mean absorbance values of the tetrazolium product per mg tissue at 4-hour intervals throughout the tissue culture in microfluidic devices with and without irradiation.

LDH released from (A) HNSCC metastatic lymph neck node tissue (n=6) and (B) HNSCC primary tumour (n=7). Arrows indicate the time of bilateral x-ray irradiation. Mean+SEM.

4.11. The effect of irradiation of apoptotic cell death detection measured using IHC staining of Bcl-2

The primary antibody against Bcl-2 was titrated on lymph node metastasised from an oropharyngeal tonsil tumour (TR54; Table 2.1) and a lymph node metastasised from an oropharyngeal base of tongue tumour (TR120). The lymph node tissues (n=2) were maintained separately in microfluidic devices for 2 and 6 days and serially sectioned for IHC staining of Bcl-2. On both tumours, three different concentrations of anti-Bcl-2 antibodies were tested on three serial sections: 0.05mg/mL, 0.02mg/mL and 0.01mg/mL. The staining intensity of the three antibody concentrations was captured and visually compared. Following the optimisation, IHC staining for Bcl-2 was carried out using 0.01mg/mL of primary antibody (section 2.9). The effects of irradiation on the expression levels of Bcl-2 was investigated on oral cavity floor of mouth tumour and a laryngeal supraglottic tumour. Separate pieces of each tumour were subjected to microfluidic culture with and without four respective single-dose irradiations (5Gy, 10Gy, 15Gy and 20Gy).

4.11.1 IHC staining of Bcl-2 on HNSCC tissues

The tissue stained (matched isotype IgG1 antibody) as negative control showed no brown and negative staining (Figure 4.36.A). The expression of the anti-apoptotic marker Bcl-2 was used as a further marker of response of the HNSCC tissue maintained in the microfluidic device to irradiation. Titration of the antibody on the microfluidic control tissues showed that the higher the concentration of the primary antibody (0.05mg/mL) resulted in more brown staining (Figure 4.36.B). However, it was difficult to distinguish between the positive expression of Bcl-2 and the background staining on the entire section. Higher magnification showed that 0.01mg/mL gave sufficient staining to detect Bcl-2 expression in both the cytoplasm and nucleus (Figure 4.36.C).

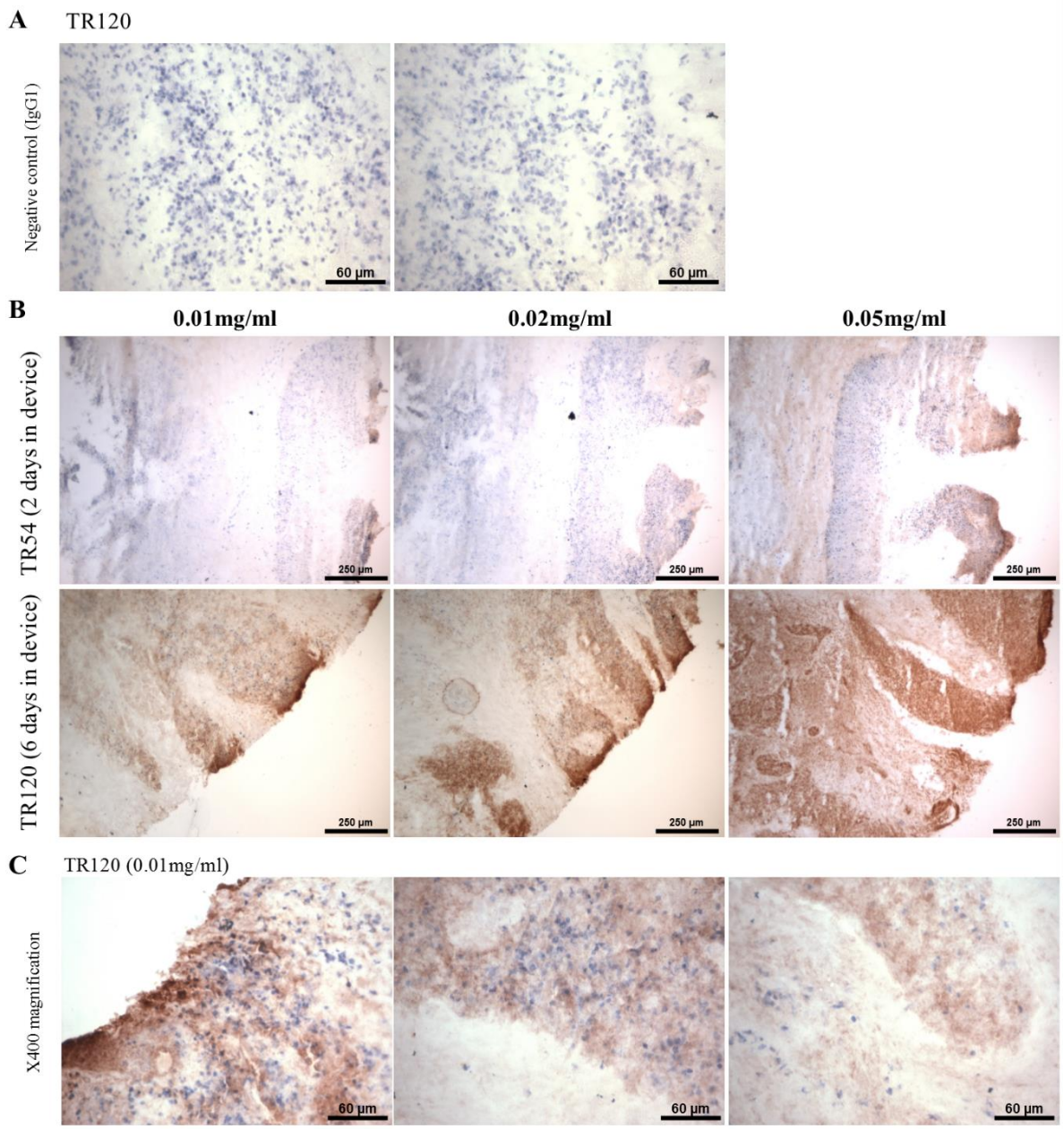


Figure 4.36. IHC staining of Bcl-2 on HNSCC tissues subjected to microfluidic perfusion.
(A) IHC staining using matched mouse IgG1 isotype control antibody for Bcl-2 on TR54 (n=2; x400 magnification). (B) IHC staining images of two lymph node tissues (TR54 and TR120; n=2; x100 magnification) which were subjected to three different concentrations of Bcl-2 antibody (0.01, 0.02 and 0.05mg/mL). The three tissues were cultured in microfluidic control with no irradiation treatment. (C) IHC staining of Bcl-2 (0.01mg/mL) on TR120 at x400 magnification. Brown represents the expression of Bcl-2 with blue haematoxylin counterstain.

In total, two HNSCC tumours were stained by using Bcl-2 antibody, including oral cavity floor of mouth (TR92) and laryngeal supraglottic (TR84) tumours which were subjected to microfluidic culture and irradiation schedules (n=2 on each treatment group; Figure 4.37.A). No expression of Bcl-2 was found on both tumours despite on the irradiation treatments (5Gy, 10Gy, 15Gy and 20Gy) and on changing the length of incubation time with the primary antibody from 1 hour to overnight (Figure 4.37.A and B).

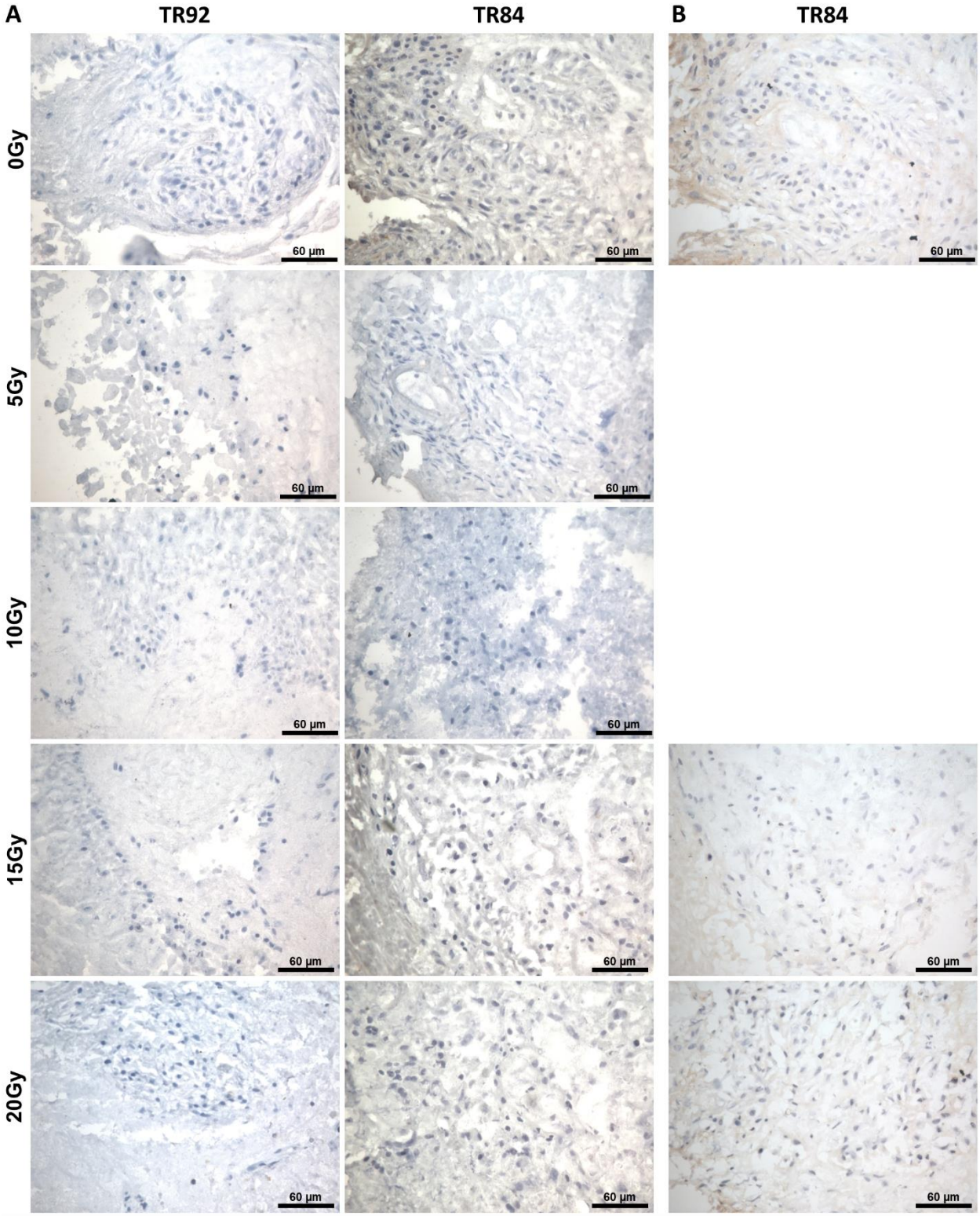


Figure 4.37. IHC staining of Bcl-2 on TR92 and TR84 tissues which were subjected to microfluidics with and without irradiation.

(A) Representative images of IHC staining of Bcl-2 with 1-hour primary antibody incubation (0.01mg/mL) on TR92 and TR84 tumour tissues (n=2 on each treatment group of each tumour x400 magnification). Brown represents the expression of Bcl-2 with blue haematoxylin counterstain. (B) Overnight primary antibody (0.01mg/mL) incubation on TR84 tumour subjected to microfluidics (0Gy), 15Gy and 20Gy irradiation (x400 magnification).

4.12. Discussion

Based on the analysis of cell death markers described in this chapter, the comparison between the non-irradiated and irradiated tissues in microfluidic-based approach showed the potential of microfluidic system in culturing clinical samples as well as studying the HNSCC tumour response to anti-cancer therapies. The validation of the microfluidic device (Chapter 3) for the maintenance of HNSCC tissue allowed the response of the tissue to irradiation to be determined in the current chapter. The experiments carried out by Carr *et al*. (2014) demonstrated the impact of irradiation on different HNSCC tissues maintained in a microfluidic device using IHC staining of caspase cleaved cytokeratin and cytotoxicity LDH assay.

4.12.1 Optimisation of cell death markers staining using ICC on HNSCC cell line

The IHC staining of cleaved cytokeratin (M30), γH2AX and Bcl-2 was optimised on an etoposide-treated oropharyngeal cell line. The results showed a variation in expression level of the three markers, with γH2AX being high (70-80%), Bcl-2 being absent and cleaved cytokeratin being low (4-8%), suggesting the different pathways of apoptosis are occurring in the cells in response to etoposide treatment.

The early steps of apoptosis induction involve the reduction of mitochondrial membrane integrity resulting in the release of cytochrome c, apoptosis-inducing factor (AIF) and endonuclease G (section 1.3.2). The released cytochrome c in turn activates the caspase-dependent pathway that involves the assembly of cytochrome c, procaspase 9 and Apaf-1, leading to the formation of apoptosome on CK18 (Holubec *et al*., 2005). The cytokeratin filaments provide a scaffold where the active caspase-9 can activate caspase-3 and -7, facilitating the cleavage of CK18 (Dinsdale *et al.,* 2004). In addition, the apoptosis could be induced by DEDD (death effector domain containing DNA-binding protein) which manipulates the recruitment of pro-caspase 3 to CK18 in cytoplasm and resulting in the cleavage of CK18 and formation of CK18Asp396 neo-epitope which is detectable by M30 antibody (Lee *et al*., 2002). In contrast, a caspase independent pathway initiated by apoptosis-inducing factor (AIF) with translocation of endonuclease G into the nucleus resulting in subsequent DNA DSB can also occur, inducing the phosphorylation of H2AX (Holubec *et al*., 2005). Therefore, the phosphorylation of H2AX also represents an early chromatin

modification after the initiation of DNA fragmentation (Burma *et al*., 2001; Mah, El-Osta and Karagiannis, 2010).

The effects of etoposide on the reduction of the expression of Bcl-2 in cancer cell lines have been shown in various studies (Gibson *et al*., 1999; Kralovcova *et al*., 2008; Yun *et al*., 2009) and the association between upregulation of Bcl-2 and tumour resistance has also been reported (Tu *et al*., 1996; Sartorius and Krammer, 2002), which were not found in current study. The absence of increased Bcl-2 expression in etoposide-treated oropharyngeal cancer cells observed in the current study suggested that the apoptosis inducer may not induce cell death via Bcl-2-associated mechanisms or that there was a flaw in the methodology which is the more likely the answer since the staining for Bcl-2 on the non-irradiated and irradiated tissues were also negative. This is in contrast to studies which have found Bcl-2 expression in HNSCC tissue sections (Nichols *et al*., 2010) with a positive relationship to chemotherapy resistance (Danial and Korsmeyer, 2004). To improve the application of Bcl-2 detection in this study, the Bcl-2 ICC staining on other HNSCC cell lines can be tested as there was only one cell line used in the study. In addition, the IHC using anti-Bcl-2 antibody from other suppliers can be tried on the tissue sections and the staining using other HNSCC subsites (e.g. oropharyngeal TR54 primary tumour) as well as other tumours could also be established in future in order to validate the methodology.

4.12.2 Tumour heterogeneity of HNSCC tumour tissue

H&E staining of the HNSCC revealed heterogenous tumour cells within the biopsies with tissues from a single patient having different/non-uniform distribution of tumour cells as well as other cell types (fibroblasts and immune cells) distributed across the tissue section. As the sequential tissue sectioning allowed to minimise the variation between sections, the comparison between the IHC staining of CK and the morphological H&E staining on serially cut tissue sections was therefore performed and it showed that the epithelial cancer cells were unevenly distributed across the HNSCC tissue section. Therefore, it is necessary to standardise the quantification of positive expression of the cell death markers to the amount of tumour present. Similar but not identical standardisation on the detection of cleaved CK18 in IHC methods was also established by various studies, for example, the counting of positive cells over the total number of cells (Duan *et al*., 2003; Reis *et al*., 2015) and the scoring of cleaved CK18 expression with the full length un-cleaved CK18 expression (Fareed *et al*.,

2012). In contrast to previous studies which viewed a number of high-power fields (Duan *et al*., 2003; Carr *et al.,* 2014; Reis *et al*., 2015), the current study not only measure the marker expression by taking into account the tumour proportion, the expression across the whole tissue section was also performed via image-tiling, providing a more accurate reflection of expression.

4.12.3 CK18-labelling index as a measure of response to irradiation

A varied response to irradiation in terms of the presence of cleaved cytokeratin 18 was observed between HNSCC tumours from different subsites. For example, the three oral cavity (TR71, TR89 and TR92) tumours which were all at similar (T2 and T3) stages showed minimal response to single-dose irradiation regardless of the dose. The minimal responses detected in the three oral SCC patients (T2/T3) were in contrast with the results of several clinical trials which demonstrated the improved locoregional overall survival and cause-specific survival in patients with T2 oral SCC following post-operative radiotherapy (Shrime *et al*., 2010). However, it has to be kept in mind that the tumour response in the microfluidic irradiation platform was based on a single apoptotic marker and different radiotherapy schedules were used to apply clinically. Therefore, the evaluation of other molecular markers and other clinical-relevant radiotherapy regimens would be advisable.

The same was observed for the paranasal sinus TR66 tumour with low CK18-LI to single-dose irradiation, however, this was an advanced stage tumour (T4N2b) which in general have a much poorer survival rate (Samant *et al*., 2004; Santos *et al*., 2014). It has been reported that reduced apoptosis was detected in advanced gastric carcinoma cells (Soung *et al*., 2005) and in caspase-1-deficient mice with advanced tumours (Hu *et al*., 2010). These agreed and explained the loss of the apoptotic capacity on this advanced stage paranasal sinus tumour and thus the response to irradiation.

In contrast, the laryngeal TR84 tumour demonstrated a positive and significant response to the single-dose irradiation in a dose-dependent manner, however, no tumour stage record was documented. Surprisingly, two of the three metastatic lymph nodes (TR73 and TR80) investigated showed a higher CK18-LI (>30%) following 15Gy irradiation compared with the tissues irradiated with 20Gy. It could presumably due to the degradation and the loss of tissue following high single irradiation dose (20Gy;

Koukourakis, 2012). Whilst on the third lymph node TR59 tumour, 15Gy-irradiation caused less CK18-LI compared with 5Gy, 10Gy and 20Gy irradiation.

The prognostic and predictive value of cleaved CK18 by using IHC staining has also been evaluated by various studies to measure the level of apoptosis in response to chemotherapy or radiotherapy, for example, in patients with rectal cancer (Debucquoy *et al*., 2008a; Debucquoy *et al*., 2008b), with colon cancer (Holubec *et al.,* 2005) and with gastro-oesophageal cancer (Fareed *et al*., 2012). A study has reported the cleaved CK18 detection as a promising predictive biomarker on tumour therapeutic outcome in which caspase-cleaved CK-18 protein expression using immunohistochemistry was evaluated on gastric/gastro-oesophageal cancer patients exposed with and without neoadjuvant chemotherapy (Fareed *et al*., 2012). They revealed that the expression of cleaved CK18 was significantly higher on the patients exposed to chemotherapy compared with those not treated to chemotherapy. The use of cleaved-CK18 marker as a potential useful apoptosis marker was also confirmed previously by Holubec *et al*. (2005) who determined the usefulness and specificity of IHC of cleaved-CK18 in identifying apoptotic index (AI) in freshly resected colon tissues obtained from seven patients (n=7 patients). The AI of the tissues which were stressed *ex vivo* with deoxycholate was evaluated in the study and illustrated that the AI was 82% higher on the stressed tissue than the control tissues (Holubec *et al*., 2005). However, others have failed to demonstrate the prognostic role for cleaved CK18 in rectal cancer (Debucquoy *et al*., 2008a; Debucquoy *et al*., 2008b). The expression levels in the present study has to be cautiously interpreted, even when significant results obtained, because of the small sample size and the well-known tumour heterogeneity. In the current study, the varied responses observed among the nine HNSCC tumours confirmed the inter-tumour variation on the HNSCC tumour response to irradiation and further emphasised the need for individual analysis of tumours to determine the patient specific response. This also demonstrates the potential of this study and prognostic marker to perform individualised tumour response study in larger study cohort and in near future.

4.12.4 Measurement of cell death in response to irradiation using soluble markers

Many researchers have looked at the changes of soluble caspase-cleaved CK18 level following different therapeutic treatment using ELISA-based assay on various different

tumour tissues, including breast (Ueno *et al.,* 2003; Olofsson *et al*., 2007), prostate (Kramer *et al*., 2006), hepatocellular carcinoma (Morris *et al*., 2014), bladder cancer (Benedict *et al*., 2014), colorectal cancer (Ausch *et al*., 2009; Greystoke *et al*., 2012; Koelink *et al*., 2009), gastric cancer (Oyama *et al*., 2013), small cell lung cancer (Dean *et al*., 2011), pancreatic cancer (Dive *et al*., 2010) and HNSCC (Eder-Czembirek *et al*., 2005; Ozturk *et al*., 2009). Together with the M65 ELISA assay, which were developed to measure circulating levels of both full length CK18 and caspase-cleaved CK18 fragments, both assays have been used as important clinical biomarker because the increased levels of circulating CK18 allows prognostic and/or prediction on tumour response to chemotherapy in different solid tumours (Scott *et al*., 2009). Ueno *et al*. (2003) study has also published that the patients with recurrent cancer (n=49 patients who have first recurrence after surgery) had higher serum levels of cleaved CK18 compared with the patients with primary breast cancer and normal control patients.

In the present study, the M30 levels on the effluent medium collected from tumour in microfluidic device were measured. Despite the generation of a standard curve, which proved the ELISA kit was functional, no detectable levels of cleaved cytokeratin could be determined when the tumour was treated with high single-dose irradiation. However, the feasibility and the sensitivity of the ELISA were confirmed by a colleague in the same research group, who performed similar experiments with colorectal tumours and found an increase in released cleaved-CK18 following irradiation (R. Patel, 2016). These results are apparently contradicting to the results obtained for the IHC staining of cleaved CK18 suggesting that caspase-cleaved CK18 is retained by the cells in the HNSCC tissue.

Following the initial high levels of LDH released from the tissue maintained on the chip due to stress during set-up, a minimal detectable level was measured throughout the rest of culture with no discernible increase measured following irradiation regardless of tumour type or irradiation dose, similar to the results for the released cleaved cytokeratin measurements. It has widely been used to determine the cell death in response to chemotherapy or radiotherapy, for example, Temozolomide treatment on glioma cells (Safdie *et al*., 2012), cisplatin treatment on cervical cells (CasKi) and HNSCC (2A3) cells (Harris *et al*., 2013), tunicamycin treatment on hepatoma cells (Fang *et al*., 2014) and radiotherapy treatment on HNSCC tumour (Carr *et al*., 2014). However, there are no other studies except the current study and Carr *et al*. (2014)

which evaluated the LDH release level in response to irradiation. It was suggested that the LDH assay is a sensitive assay for cell death (apoptosis and necrosis) detection, however, the study by Carr *et. al*. (2014) only saw an increase in LDH release from HNSCC tissue following very high doses of irradiation (40Gy) and no release following 20Gy, which was the highest dose in the current study. This suggests that in order to get membrane rupture higher doses of irradiation are required. An increase in LDH release observed following the addition of lysis reagent to the microfluidic device in chapter 3 confirmed that there were still membrane-intact cells within the tissue and they had not all died during the microfluidic set-up stages (Carr *et al*., 2014). Similar with Carr *et al*. (2014) study, the doses of irradiation up to 20Gy do not induce the type of cell death, possibly apoptotic or necrotic cell death (Kroemer *et al*., 2009), which results in a loss of membrane integrity and subsequent release of cellular content.

4.12.5 The detection of DNA-strand breaks by TUNEL in tissues following irradiation in microfluidic device

TUNEL was extensively used to detect DNA fragmentation and later stage of apoptosis (Sundquist *et al*., 2006). The effects of different sensitising methods on the irradiation treatment were analysed using this apoptosis marker (Zou *et al.,* 2008; Ekshyyan *et al*., 2009; Feng *et al.,* 2011; Herzog *et al*., 2013). The cell apoptosis of the sensitised SCCVII cells in response to X-ray irradiation was examined by TUNEL and the cells with inhibited ATM (antisense oligodeoxynucleotides; AS-ODNs) have higher apoptotic rate following irradiation compared with control groups (Zou *et al.,* 2008; Feng *et al.,* 2011), demonstrating that the anti-tumour effect of the different irradiation schedules (with or without sensitizer) was confirmed by the increase level cell death measured by TUNEL assay. This was comparable to the results of the present study which confirmed that the apoptotic rate of the HNSCC tumours increased following irradiation compared to the non-irradiated tissue which had a low level (0.5-9.1%) of DNA-strand breaks. The low non-irradiated level observed here agrees with other studies which showed low apoptosis level in control groups (2-15%; Zou *et al.,* 2008; Ekshyyan *et al*., 2009; Feng *et al.,* 2011; Herzog *et al*., 2013), indicating the ability of microfluidic system to maintain tissue with low cell death level.

The sensitivity and specificity of the TUNEL is controversial as it cannot differentiate apoptosis from necrosis and autolysis which also demonstrate DNA fragmentation (Kumari *et al*., 2008). In the current research, however, it is still useful to detect the

overall cell death in response to irradiation. The DNA-strand break levels varied in a dose independent manner between the four HNSCC patients and between different irradiation doses treated on the same patient's tissues. These agreed with the trend of CK18-LI described previously in this chapter and the facts that the different tissues respond differently to identical conditions (Sundquist *et al*., 2006). On the other hand, the more accurate interpretation could only be made with the greater sample replicates on both non-irradiated and irradiated groups.

4.12.6 Retention level of γH2AX in predicting tumour sensitivity to irradiation

Irradiation-induced DNA-strand breaks can also be determined by monitoring the phosphorylation of the histone protein H2AX (γH2AX) which is not only an indication of DNA damage but also signifies the ability of the cells to repair DNA damage (Olive and Banath, 2009; section 4.1.3). In the absence of irradiation, low levels of phosphorylated H2AX can be detected especially during the cell cycle progression and DNA replication phase (Huang *et al*., 2005). This was demonstrated by the low expression level of γH2AX found on the non-irradiated control tissue maintained in microfluidic device.

In a study by Bourton *et al*. (2011), flow cytometric analysis of γH2AX in patients' blood sample (n=10) showed an increase in relative fluorescence 30-minute post-irradiation, indicating a rapid rise in the radiation-induced DNA-DSB (Figure 4.38). It was followed by a steady drop in the fluorescence due to the repair of the damaged DNA and dephosphorylation of H2AX and, by 24-hour post-irradiation, the level returned to near non-irradiated level. The persistence of γH2AX expression is thought to be a clinical indicator of the tumour sensitivity for radiotherapy and the extended expression of γH2AX measured at 24 hour post-treatment compared with un-treated controls has been repeatedly proved to indicate radiosensitive by various studies in which the γH2AX expression persist long after irradiation exposure in radiosensitive tumour cells (cervical cancer cells C33A in Banath, MacPhail and Olive, 2004; HNSCC SCC-61 cells in Taneja *et al*., 2004; Chinese hamster ovary cell line xrs5 cells in Clingen *et al*., 2008).

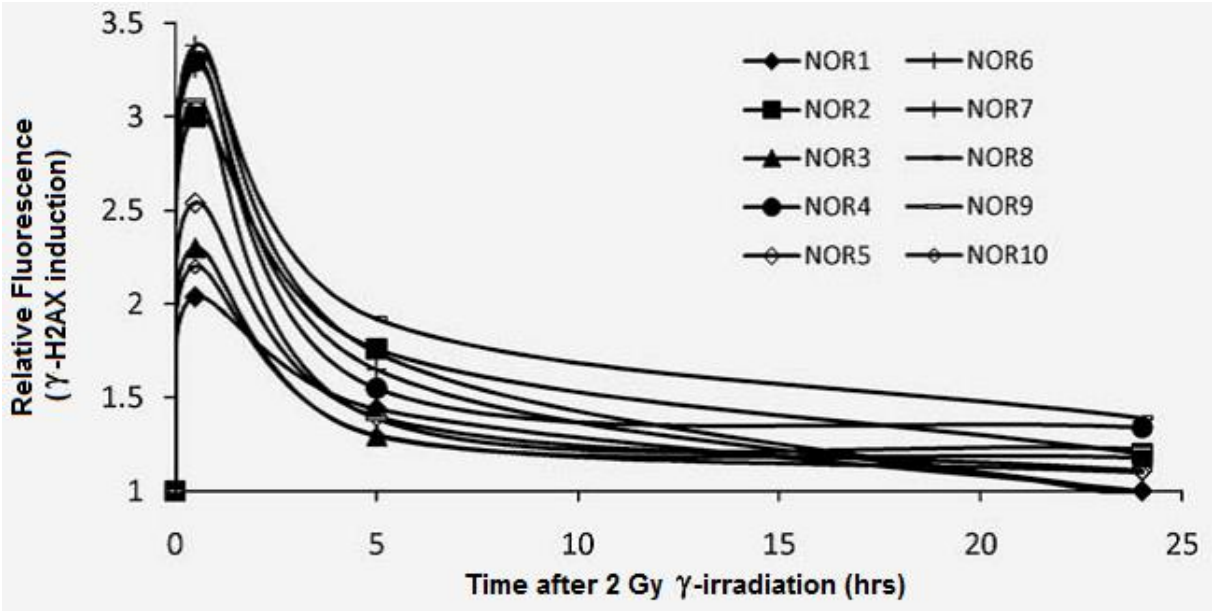


Figure 4.38. Flow cytometric analysis on the γH2AX induction of the cells obtained from patients (n=10) throughout 25 hours following 2Gy irradiation.
(Bourton *et al*., 2011).

Therefore, the level of residual γH2AX in the tumour 24 hours after irradiation treatment in present study implies the suppressed DNA repair, extended DNA repair and radiosensitivity (Banath, MacPhail, and Olive, 2004; Clingen *et al*., 2008; Olive and Banath, 2009; Raju *et al*., 2015). A time-course measurement of γH2AX level at 1, 6 and 24 hours following different irradiation doses on cervical cancer cells has been established by Banath, MacPhail, and Olive. (2004) in which the radiosensitivity determined by the clonogenic-surviving fraction was correlated with the retention level of γH2AX at 24 hours after treatment. The residual γH2AX presented at 24 hours after anti-cancer therapy indicates the cells have defects on DSB repair, leading to the prolonged repair time, resulting the potentially lethal DNA DSBs and more sensitive to irradiation (Kasten-Pisula *et al*., 2009).

The majority of the tumours in the current study had a slight increase in γH2AX following irradiation compared with corresponding control tissues, however, of the five HNSCC tumours, one of the oral cavity tumour (TR92) had a significantly higher expression of γH2AX at 24 hours after irradiation compared with the corresponding non-irradiated samples. One of the lymph node tissues, TR80, had almost double the level of γH2AX compared to the control, indicating the prolonged or deficiency of DNA repair. These results may suggest that these tumours are more sensitive to irradiation. However, the percentage of residual γH2AX was obtained from the mean percentage of five high-power fields from a small sample size. In addition, larger number of

replicate tissues from each individual patient is necessary to confirm this. To meet the aim of this project to produce a device and analytical method which could study a patient's response to radiotherapy prior to treatment, the correlation between the *in vitro* results obtained here and the clinical response of patients to therapies is required (section 5.2.6).

4.12.7 Relationship between single-dose and fractionated irradiation treatments

The application of fractionated irradiation (five fractions of 2Gy and 4Gy) was used to try and replicate the weeklong radiotherapy regimens received by patients in the clinical setting. The CK18-LI in the lymph node tissue TR80 subjected to microfluidics and fractionated irradiation has similar trend to that observed with single dose irradiation, with both fractioned irradiation regimes inducing increases in CK-18 LI in a dose-dependent manner. Although there was an increase in CK18-LI after fractionated irradiation on TR89 tumour, the overall CK18-LI on both oral cavity tumours was remained low, less than 12%, even after treatment.

The level of γH2AX in one of the oral cavity tumours (TR92) investigated was higher following 5 x 2Gy (three-fold higher) and 5 x 4Gy (two-fold higher) compared with their non-irradiated controls. Although the 5 x 4Gy was expected to induce higher CK18-LI than that of 5 x 2Gy, but the γH2AX levels following both fractionated irradiations were in similar trend (47-66% after treatments) with the results following single-dose irradiation (44-66% after treatments). Dose-dependent increase of γH2AX was detected on TR89 tumour while only the 5 x 2Gy induced an obvious rise on the metastatic lymph neck node (TR80).

A few previous studies have determined the HNSCC tumour response to fractionated irradiation, mostly by using *in vivo* human tumour xenografts (Kruser *et al*., 2010; Sattler *et al*., 2010; Yin *et al*., 2010; Tuttle *et al.,* 2012). The groups have used tumour xenografts derived from HNSCC lines to assess the *in vivo* tumour response in mice to fractionated irradiation based on the hypoxia, proliferation and vasculature markers (Kruser *et al*., 2010), the changes on glycolytic metabolism (Sattler *et al*., 2010), the anti-tumour growth effects (EGFR, Raf-1 and phosphorylated Akt; Yin *et al*., 2010) and morphology appearance and proliferation levels (Tuttle *et al.,* 2012). The methodology of these studies involved the fractionated irradiation on the whole body of the mice with tumour xenografts which was different with approach used in the current study

and in a recent microfluidic study by Carr *et al*. (2014) who also maintained small tissue piece (5-10mg) in a microfluidic device and carried out fractionated irradiation targeting the small portion of tumour. Although the fractionated irradiations on the three tumours, in the current study, have generally induced an increase expression on the cell death markers compared with control, however, the fractionated irradiation was expected to trigger higher cell death effects, mainly apoptosis, on the tumours than that observed in single-dose irradiation which was not detected in the current study but in Carr *et al*. (2014) study. The larger effect of fractionated irradiation (5 x 2Gy) on apoptotic index over the single-2Gy irradiation was demonstrated in which the significant difference in the apoptosis level between single 2Gy and 5 x 2Gy was observed (Carr *et al*., 2014). This could be due to the variation on both cell death markers observed among the three HNSCC tumours and more likely because of only one tissue repeat was tested on each dose and each tumour. Therefore, further methodologies by including larger number of tissues (multi-regional tumour sampling) in each irradiation regimen would be useful to draw conclusive results by taking the consideration of intra-tumour heterogeneity.

In conclusion, tumours from different HNSCC patients have displayed a different response to irradiation when they are subjected to the same treatments, which suggests the interpatient variation on the tumour responses and also could be due to the small sampling sizes. The CK18-LI, the positive expression of γH2AX and the level of DNA-strand breaks detected by TUNEL varied between different single-dose treatments on tissues obtained from same patient, demonstrating the different stages of cell death acquired in responding to various radiotherapy modalities. The variation of the cell death expression results across HNSCC patients showed the potential of current microfluidic irradiation platform to determine the radiosensitivity of individual HNSCC patients and emphasise the importance of monitoring each patient individually due to their tumours varied response.

5. Measuring the effects of irradiation on HNSCC tissue maintained in a microfluidic device (II) – Proliferation and metabolism

5.1. Introduction

The proliferation characteristics of a tumour play an important role in determining the tumour response to conventional radiotherapy and the success of cancer therapies (Wilson *et al*., 2006; Rafat *et al*., 2015). Although ionising radiation has the ability to kill tumour cells, some cells possess the ability to adapt to the changes and the damage induced by irradiation leading to radioresistance (Pawlik and Keyomarsi, 2004). For example, rapid proliferation may predispose tumours to worse outcome in radiation due to repopulation through various cell cycle phases during treatment whilst the reduction of proliferation can be attributed to the killing of rapidly proliferating cancer cells (Pawlik and Keyomarsi, 2004; Wilson *et al*., 2006). In general, the detection of a high proliferation rate was considered a bad prognostic marker in cancer treatment and is associated with tumour recurrence (Hass *et al*., 2008; Ermiah *et al*., 2012; Pereira *et al.,* 2012; Bianchini *et al*., 2013). In addition, various studies have also suggested that the differences of cancer stem cell content even on the same histopathological type might contribute to the tumour radioresistance (Hill and Milas, 1989; Baumann, Dubois and Suit, 1990; Baumann, Krause and Hill, 2008). The mechanisms of the cancer stem cells that induced tumour resistance are repopulation during therapy and recovery from radiation-induced damage between fractionated doses (Petersen *et al*., 2001; Petersen *et al*., 2005).

Many studies have assessed the cell cycle phases and proliferation signatures of HNSCC tumour tissues in response to irradiation, as well as in relation to the prognosis of patients with HNSCC tumours (Table 5.1). The detection of the endogenous proliferation marker, Ki-67, has been used to correlate with prognosis of various cancers, including breast cancer (Millar *et al*., 2011, Yang *et al*., 2011; Ermiah *et al*., 2012; Liu *et al*., 2015), head and neck cancer (Raybaud *et al*., 2000; Buffa *et al.,* 2004; Condon *et al*., 2002; Wilson *et al*., 2006; Pereira *et al*., 2008), rectal cancer (Meng *et al*., 2015) and cervical cancer (Cheng *et al*., 2014). Although little is known about the exact function of the Ki-67 protein in cell division, it begins to be expressed in proliferating cells that are entering mid G_1 phase and increases in S and G_2 phase reaching a peak level in M phase of the cell cycle (Braun *et al*., 1988; Tan *et al*., 2005).

At the end of M phase, Ki-67 is immediately catabolized and becomes undetectable in G_0 and early G_1 resting phases (Braun *et al*., 1988; Tan *et al*., 2005). The immunochemical staining of the Ki-67 protein with the monoclonal antibody is a commonly used method that can be applied on either frozen or formalin-fixed and paraffin-embedded tissue sections (Kim *et al*., 2007).

Table 5.1. Proliferation marker studies implemented in determining human tumour response to radiotherapy treatment.

Markers	Tumour types	N	Patients outcome	Research
BrdU	HNSCC	48 (8 recurrence)	High BrdU observed on recurrent tumours	Hass *et al*.,2008
Ki-67	HNSCC	64 (32 recurrence; 32 responsive)	High Ki-67 is indicative of tumour recurrence	Pereira *et al*., 2012
	HNSCC	402	No prognostic role for Ki-67	Wilson *et al*., 2006
	HNSCC (OC and pharyngeal)	56	Tumours with low Ki-67 have a large proportion of cells in G_0 cell cycle phase leading to radioresistance.	Raybaud *et al*., 2000
	HNSCC	402	High Ki-67 observed in patients with worse response to treatment	Buffa *et al*., 2004
	HNSCC	21 (8 RR; 13 RS)	Ki-67 level was similar in both RR and RS groups	Condon *et al*., 2002
	HNSCC	154	Ki-67 not correlated with DFS and OS	Al Gizawy *et al*., 2011

The studies were searched based on the proliferation markers (BrdU and Ki-67) used to study HNSCC tumour response to radiotherapy.
Abbreviation: RR: radioresistance, RS: radiosensitive, DFS: disease free survival, OS: overall survival.

A further well established method to assess cell proliferation is the detection of incorporated 5'-bromo-2'-deoxyuridine (BrdU) in place of thymidine into replicating DNA during the S-phase of proliferating cells. The method for detecting BrdU using IHC staining with anti-BrdU antibodies was first described in 1987 by DeFazio *et al*. and is now widely used to measure cellular proliferation. To date, a few studies have used BrdU incorporation to study the relationship between proliferation in the resected tumour and radioresistance in HNSCC patients (Hass *et al*., 2008; Bertrand *et al*., 2014. It was reported that the recurrent tumours had a higher BrdU labelling index (LI) in comparison with the primary HNSCC, suggesting that the tumour recurrence correlates with increased proliferative characteristics although this was a small-scale study involving only 8 patients (Hass *et al*., 2008). BrdU incorporation has also been used to examine the effects of radiosensitising agents on HNSCC based on the cell

proliferation signatures: liposomal meso-tetrahydroxyphenyl chlorin derivative (Foslipos®) and hypericin on HNSCC cell lines (Besic Gyenge *et al*., 2012), EGFR-inhibitor Cetuximab in HNSCC xenograft models (Stegeman *et al.,* 2013) and isoalantolactone in HNSCC cells (Fan *et al*., 2015).

Other proliferation markers used to measure effects of irradiation in HNSCC tumours include *c-MET* (Akervall *et al*., 2014), cyclin D1 (Ataman *et al*., 2004; Buffa *et al.,* 2004; Rahimi *et al*., 2012; Kothari and Mulherkar, 2012), cyclin-B1 (Hassan *et al*., 2002) and the phosphorylation status of AKT (Freudlsperger *et al*., 2015). These studies reflect the substantial efforts which have been made to evaluate the mechanisms of radioresistance and identify putative biomarkers for radiotherapy response. However, none of the markers have yet been validated for routine clinical use. In the current chapter, the commonly used proliferation markers, Ki-67 protein expression and BrdU/EdU incorporation, were selected and assessed in response to irradiation with the aim of identifying a proliferative biomarker for the study of tumour responses.

In addition to the direct measurement of proliferation, the metabolic activity of the tumours in response to irradiation was also investigated. In the early 1920s, Otto Warburg hypothesized that tumour development is associated with a switch from oxidative to glycolytic energy production which caused aerobic glycolysis even in the presence of oxygen (Warburg, 1925; Blatt *et al*., 2015). The increased glycolytic metabolism was established as a characteristic of tumour cells, in which the overexpression of glycolytic genes and subsequent activation of glycolytic enzymes and membrane transporters have been reported (Kunkel *et al*., 2003; Sattler *et al*., 2010; Ziebart *et al*., 2011). A high glycolytic level was associated with tumour radioresistance, which has been claimed by some studies to predict the tumour response to irradiation *in vivo* in tumour xenografts and in patients' tumour by positron emission tomography (PET) imaging (Sattler *et al*., 2010; Zhong *et al.,* 2013; Zegers *et al*., 2015).

Many markers of metabolism have been used to study tumour prognosis and to predict tumour radioresistance including the increased expression of the glucose transporter-1, GLUT-1 (De Schutter *et al*., 2005; Kunkel *et al*., 2003), high expression of lactate that correlates with tumour recurrence post-irradiation (Blatt *et al*., 2015), [18F] Fluorodeoxyglucose (FDG) PET imaging methods (Allal *et al*., 2002; Wong *et al*., 2002; Zegers *et al*., 2015), and the uptake of 2-[N-(7-nitrobenz-2-oxa-1,3-diazol-4-

yl)amino]-2-deoxyglucose (2-NBDG; Millon *et al*., 2011). The tumour uptake of 2-[^{18}F] fluoro-2-deoxy-D-glucose (FDG) measured by PET has become the most frequently used to study tumour sensitivity to irradiation *in vivo*. The cancer cells which typically have a higher rate of glucose metabolism, also have increased expression of the glucose transporters (GLUT) and hexokinase enzymes (Nitin *et al*., 2009). In FDG PET imaging, the radio-labelled de-oxyglucose is transported into tumour cells by glucose transporters and subsequently phosphorylated by hexokinase enzymes. After phosphorylation, FDG-6-PO_4 formed does not metabolise in the pathway and is trapped within tumour cells, allowing PET imaging (Lowe *et al*., 2000). The use of the radiotracers (FDG or 2-deoxy-D-[^{14}C] glucose) in the study of glucose uptake, however, has several disadvantages for the use in the laboratory such as being manually intensive, expensive with the problems of disposal of radioactive waste and the radioactive clean-up (Nitin *et al*., 2009; Millon *et al*., 2011). In this study, it is interesting to evaluate the metabolism status of HNSCC tumour cells in response to irradiation using the incorporation of 2-[N-(7-nitrobenz-2-oxa-1,3-diazol-4-yl)amino]-2-deoxyglucose (2-NBDG) method.

The 2-NBDG is a fluorescently-labelled deoxyglucose analogue that is used to directly monitor the glucose uptake by living cells and tissues similar to FDG, when 2-NBDG is transported into tumour cells via glucose transporters, it is phosphorylated by hexokinase and entrapped in the cell, allowing optical imaging under the fluorescence microscope. By using optical imaging, wide field images of large areas of tissue labelled with 2-NBDG could be obtained (Nitin *et al*., 2009).

5.2. Materials, methods and corresponding results

The HNSCC tumours subjected to irradiation studies whilst maintained in the microfluidic device have been described in chapter 2, section 2.4. The proliferation status of the five HNSCC tumours used for cell death analysis were studied using the expression of the Ki-67 antigen and nine HNSCC patient tissues were subjected to BrdU incorporation (details of HNSCC tumours involved were summarised in Table 2.1). The incorporation of the EdU and 2-NBDG markers were also tested for respective proliferation and metabolism investigation.

5.2.1 Using BrdU incorporation as a measure of proliferation in response to irradiation

Immunocytochemical (ICC) staining of incorporated BrdU in oropharyngeal cells

The incorporation of BrdU into replicating cells was optimised on oropharyngeal cells (UMSCC-47). Cells (5×10^4) were cultured on each of two square (size) coverslips in a 6-well-plate. Prior to fixation in pre-cooled methanol, the cells were added with medium containing 10µM of BrdU (BD Bioscience, Oxford, UK) for 6 hours. Immunocytochemistry was used to detect cells with incorporated BrdU as described in section 3.2 and 4.2. Mouse monoclonal anti-BrdU antibodies (0.01mg/mL final concentration; AbD Serotec, UK) was used to detect incorporated BrdU and matched isotype control (IgG1; AbD Serotec, UK) at the same concentration was added to one coverslip as a negative control.

Brown nuclear staining was observed in UMSCC-47 cells following 6 hours of BrdU incorporation and ICC to detect the incorporated BrdU. The cells that were added with BrdU showed no brown staining when they were stained with matched isotype IgG1 antibody (Figure 5.1). This showed the negative staining and no non-specific staining by using avidin-biotin-complex secondary antibody and 3, 3 -diaminobenzidine detection methods.

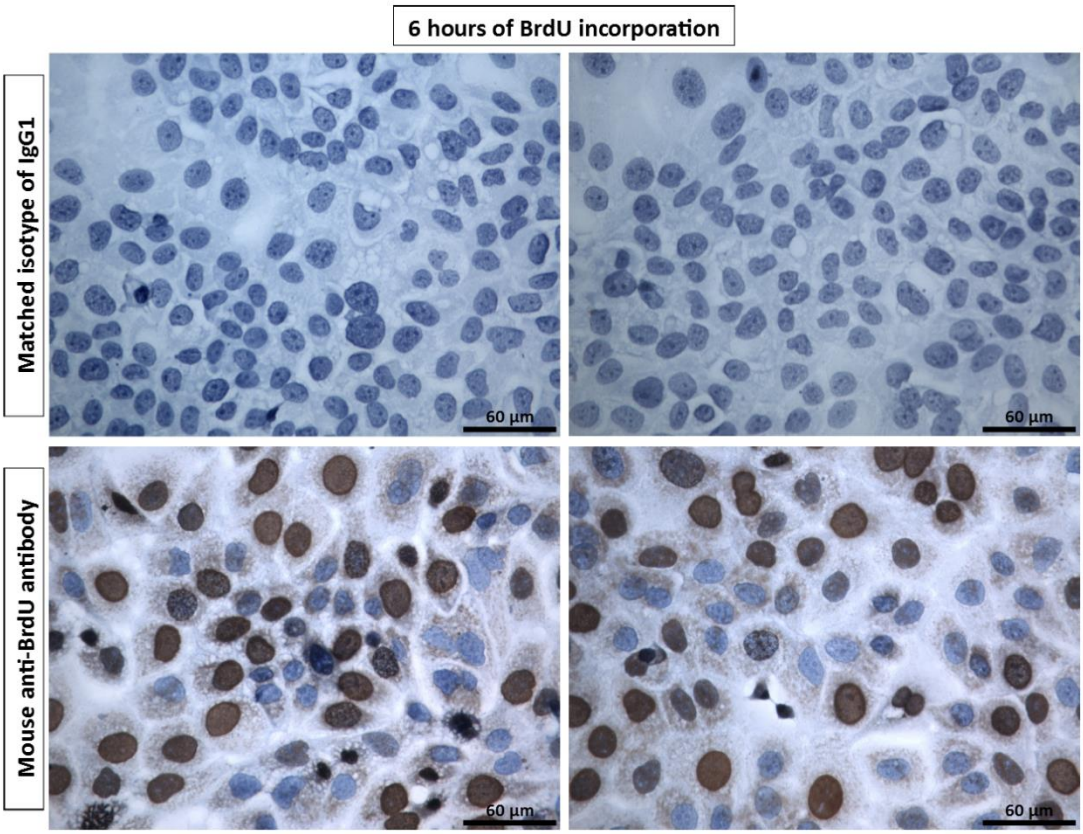


Figure 5.1. Representative ICC staining of oropharyngeal cells (UMSCC-47) following 6 hours of culture with BrdU (10µM) and immunostaining with anti-BrdU antibody (0.01µg/L final concentration, AbD Serotec).
Top panel: matched isotype IgG1 (AbD Serotec) antibody showing blue haematoxylin counterstaining only; bottom panel: BrdU antibody showing brown nuclear staining representing cells with incorporated BrdU. x400 magnification.

IHC staining of incorporated BrdU in HNSCC tissue maintained in microfluidic device

For the tissue studies, all of the HNSCC tissues (indicated in Table 2.1) maintained in the microfluidic device were again perfused with medium containing 10µM of BrdU for 6 hours following irradiation (5, 10, 15 and 20Gy) prior to the termination of the experiment; in a similar manner to the cell lysis. The uptake of BrdU into replicating cells was detected using IHC staining with anti-BrdU antibodies (section 2.9). The matched isotype control (IgG1) was applied on serially cut sections as a negative control. All of the HNSCC tumours (n=9; Table 2.1) were subjected to irradiation and the cells positive for BrdU incorporation were analysed in a similar way to that described for γH2AX (section 4.7). Briefly five fields of x400 magnification were photographed within the tumour areas and the percentage of cells positive for BrdU in each field was determined manually by expressing the number of positive nuclei as a fraction of the total nuclei (the counting was carried out similarly as in Figure 4.22). The mean percentages of BrdU positive cells following different treatments and between different HNSCC patients were statistically compared and analysed using

One-way ANOVA followed by Tukey's post-hoc test. Representative IHC staining of incorporated BrdU on lymph node tissue (TR80), maintained in a microfluidic device and subjected to irradiation is shown in Figure 5.2. Sparse brown nuclear staining indicated positive incorporation of BrdU into nuclei which contained replicating DNA.

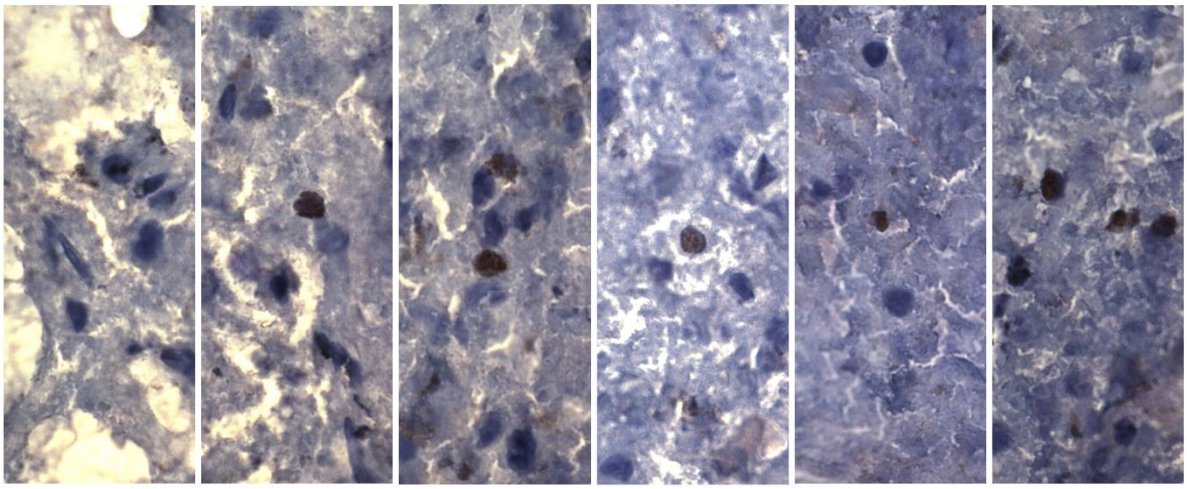


Figure 5.2. Representative IHC staining of BrdU (x400 magnification) on lymph neck node metastasised from a laryngeal tumour subjected to microfluidics and 10Gy irradiation.
Brown nuclear staining represents cells with incorporated BrdU and are undergoing replication blue is the haematoxylin counterstain.

Among the nine HNSCC tumours investigated (Table 2.1), IHC staining of BrdU on the four primary tumours and two lymph node tissues were difficult and unable to be evaluated (Figure 5.3) while the remaining three tumours were successfully analysed (Figure 5.4). The brown nuclear staining was not evident even in the non-irradiated tissues and three of the tumours had a high background staining (Figure 5.3). The tissue integrity of five of the six tissues (TR77, TR66, TR71, TR89 and TR59) was poor with the haematoxylin counterstain showing the presence of very few nuclei. The only tissue which showed good morphology following microfluidic culture was that of the lymph neck node metastasised from an oropharyngeal tonsil (TR54) tumour, however, even though there was a high number of nuclei, no BrdU positive cells were observed.

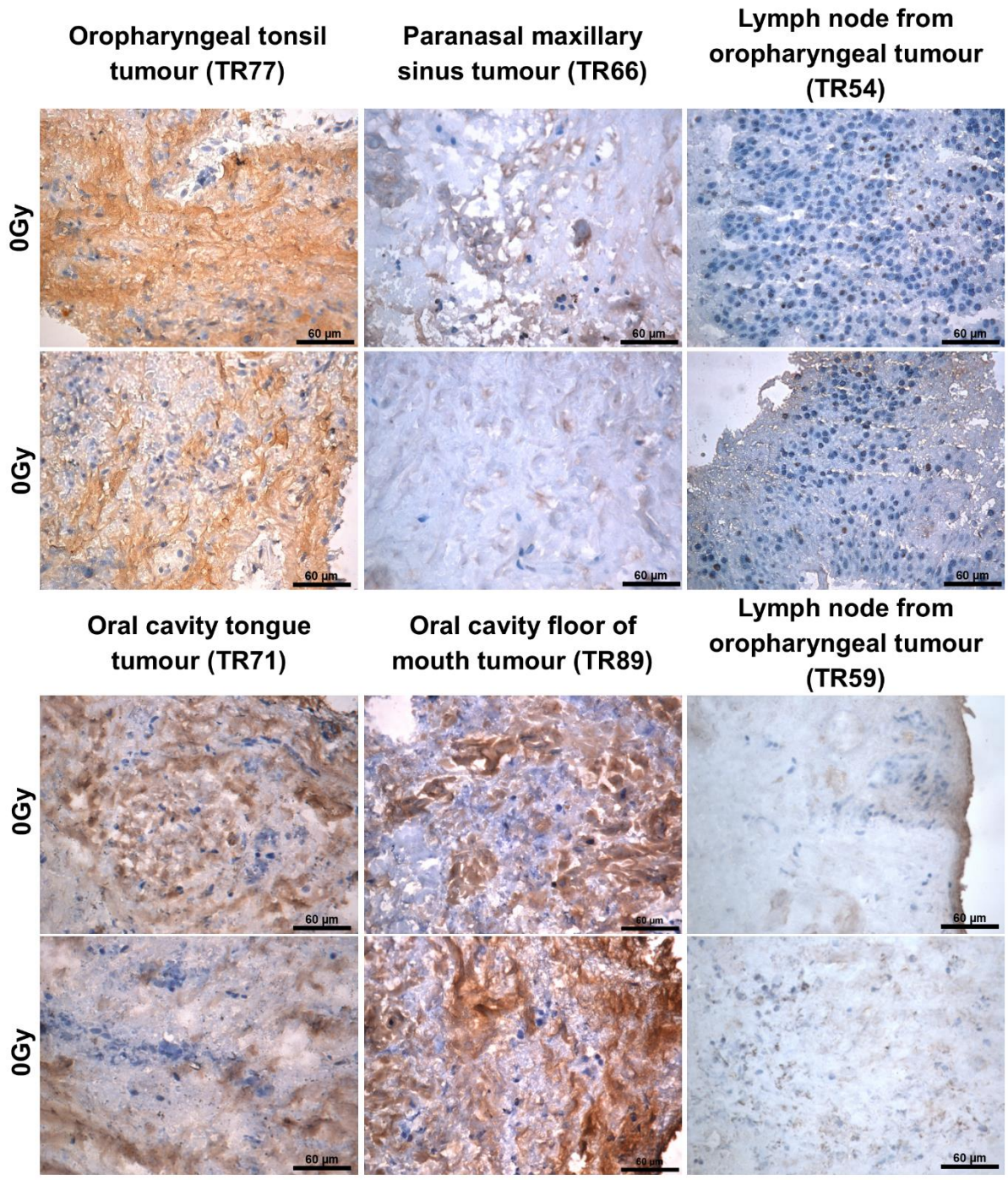


Figure 5.3. Representative staining of BrdU on the microfluidic-cultured tissues of six HNSCC tumours (four primary tumours and two lymph neck node tissues) which were perfused with BrdU for 6 hours.

Non-specific staining with the BrdU antibody was observed on three of the tissues and 5/6 showed deteriorated morphology (x400 magnification).

The mean percentage of cells positive for BrdU incorporation was calculated from the five fields of view for the different treatment groups (0Gy, 5Gy, 10Gy, 15Gy and 20Gy). The IHC staining of BrdU on the three tumours (TR73, TR80 and TR84; Figure 5.4) were successfully quantified to evaluate the effect of irradiation on proliferation.

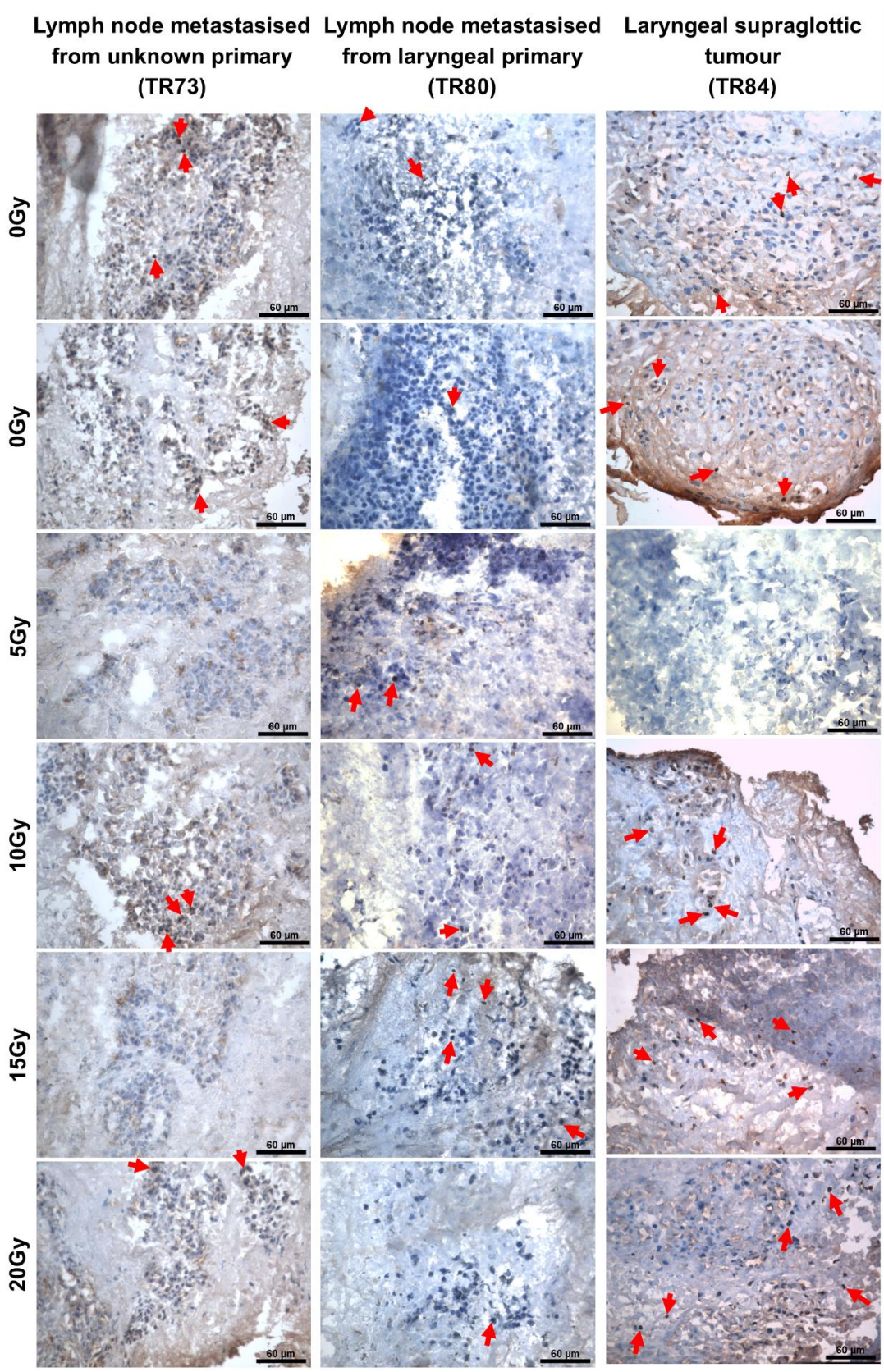


Figure 5.4. Representative IHC staining of BrdU staining (x400 magnification) on two lymph neck nodes (TR73 and TR80) and laryngeal (TR84) tumour which were subjected to microfluidics with different treatments.

The tissues were all perfused with BrdU (10µM) for 6 hours prior to freezing and sectioning. Brown nuclear staining represents cells with incorporated BrdU which are undergoing replication (arrows indicate example of positive staining) and blue is the haematoxylin counterstain.

Both lymph neck node tumours showed a low (<20%) mean percentage of cells positive for BrdU incorporation (Figure 5.5). The percentage of BrdU positive cells was similar in the control and the irradiated tissues in TR73 only a slight (non-significant) dose-dependent reduction of positive BrdU cells was observed in TR80 tumour following irradiation compared to the non-irradiated controls (16.7%). Among the three tumours investigated, the laryngeal TR84 tumour achieved the highest baseline percentage of cells positive to BrdU incorporation (26.8±6.9%). Irradiation of this tumour with 5Gy resulted in a substantial reduction in the percentage of proliferating cells (3.6±3.0%) but displayed more than 22% of cells proliferating on tissues subjected to 10Gy, 15Gy and 20Gy irradiation which was similar to the non-irradiated control.

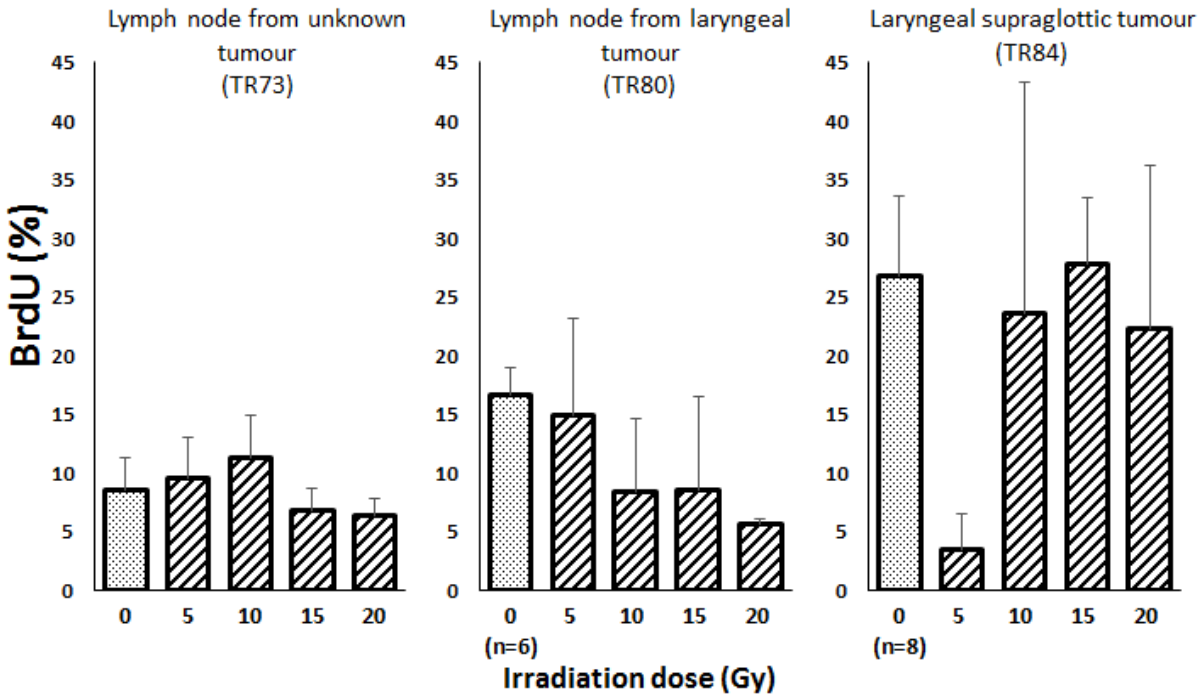


Figure 5.5. Mean percentage of cells positive for BrdU incorporation on two lymph neck nodes (TR73 and TR80) and a laryngeal (TR84) tumour.
Mean+SEM. At least two tissues were subjected to each treatment (n=2) and the number of repeats, if more than two is shown in parentheses.

5.2.2 Using Ki-67 detection as a measure of proliferation in response to irradiation

ICC staining of Ki-67 on oropharyngeal cells

Similar cell culture and ICC staining were carried out (section 2.1 and 4.2). Oropharyngeal cells (UMSCC-47; $5x10^4$) were grown on three coverslips placed in 6-well plates. When the cells reached 70-80% confluence, they were fixed and subjected to immunostaining. The mouse monoclonal anti-human Ki-67 antibody (Clone MIB-1; Dako, Denmark) at final concentration of 0.5mg/µL diluted in TBS was added to two of the coverslips (n=2). The matched isotype antibody (IgG1; AbD Serotec, UK) was added to the third coverslip as a negative control. Following staining, each coverslip was mounted and viewed under the microscope (Figure 5.6 and Figure 5.7).

The effects of etoposide on the expression of Ki-67 was tested on this cell lines which were plated on 6 coverslips and the decrease of Ki-67 expression was expected to be observed (section 4.2). The cell cultures and the etoposide treatments were repeated according to the methods described in section 4.2. The expression level of Ki-67 was viewed and assessed under a microscope. Ten x400 magnification fields were taken for each treatment and the number of proliferating nuclei was expressed as a percentage of the total nuclei within each field. The mean percentage was calculated from the ten fields for each treatment was obtained and the percentage of Ki-67 positive cells was statistically compared between different treatments using the Students paired *t*-test.

On the etoposide treatment of the oropharyngeal cell lines, the expression of the cell death markers obtained from chapter 4 (cleaved CK18, γH2AX and Bcl-2; section 4.2) and the expression of Ki-67 proliferation markers were collated to achieve better understanding on the overall expression patterns across the treatments. The relationship between the four markers on both cell lines was statistical analysed by using Pearson's correlation test in SPSS (IBM, SPSS statistics 22).

The oropharyngeal (UMSCC-47) cells that were stained with anti-Ki-67 antibody showed clear positive brown staining in several nuclei representing cells undergoing replication at G_1, S, G_2 and M phases (Figure 5.6), whereas the IHC staining using the matched IgG1 isotype control at the same concentration was negative.

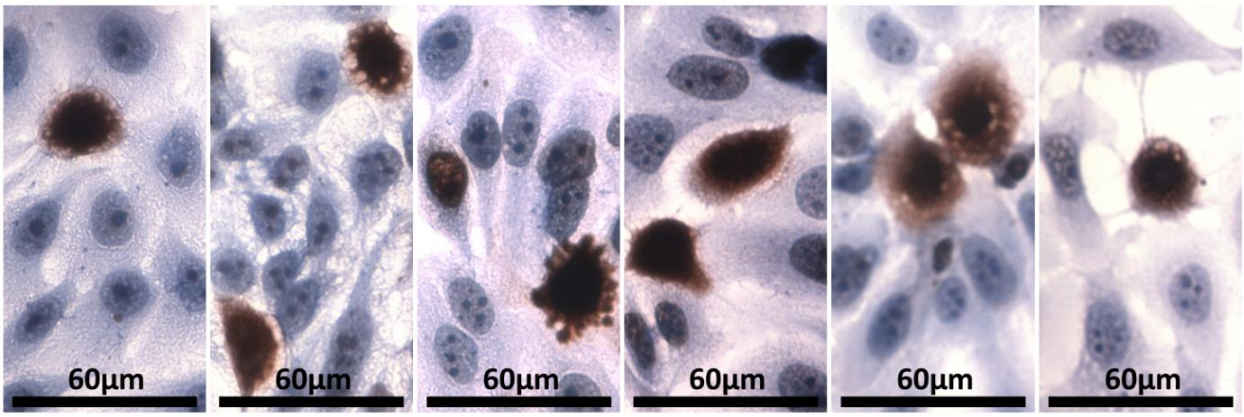


Figure 5.6. Representative ICC staining of oropharyngeal cells (UMSCC-47; x400 magnification fields taken and images were cropped to achieved better view on cells) with the Ki-67 antibody (0.46µg/L final concentration).
Brown cytoplasmic staining represents cells that express Ki-67 and are undergoing replication and blue is the haematoxylin counterstain.

The mean percentage of proliferation from 10 fields of view was calculated for each concentration of etoposide and showed that there was 82.6±2.7% of replicating cells present in UMSCC-47 cells cultured in medium only (Figure 5.7) with a significant decrease in all etoposide treated cells. However, the effect of etoposide was not concentration dependent with 2.5µM and 10µM resulting in the biggest decrease compared to the control.

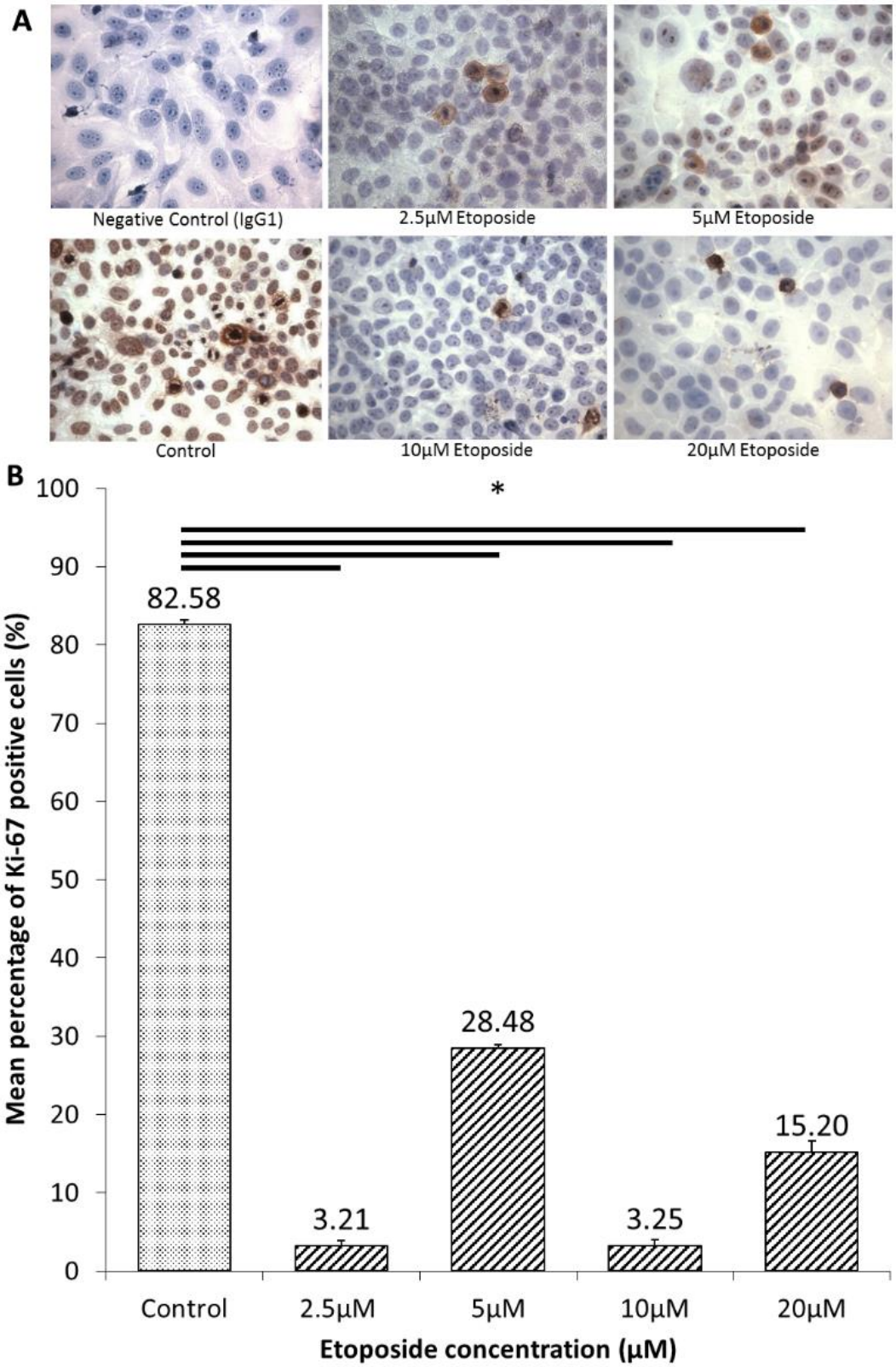


Figure 5.7. ICC staining of Ki-67 on UMSCC-47 oropharyngeal cells treated with no etoposide and with increasing concentrations of etoposide (n=6).

(A) Representative staining of cells using a mouse matched IgG1 isotype antibody at same concentration with the Ki-67 primary antibody (x400 magnification). Blue staining indicates the haematoxylin stained nuclei counterstain. The UMSCC-47 cells subjected to different concentrations of etoposide (non-treated; 2.5µM, 5µM, 10µM and 20µM; x400 magnification). Brown nuclear staining represents Ki-67 positive replicating cells. (B) Bar chart to show the percentage of proliferation of oropharyngeal cells from 10 x400 magnification fields. Mean+SEM. $p<0.05$; Student paired t-test.

Correlation between cell death and proliferation markers on UMSCC-47 cells treated with etoposide

To perform the correlation test on the expression levels on this cell line, the expression data on each marker was subjected to correlation test and summarised in section 9.7/Table 9.3. When etoposide was added, the expression of cell death markers was expected to increase and the proliferation level will reduce. The relationship between the expressions of the cell death markers (caspase-cleaved cytokeratin-18, γH2AX and Bcl-2) was expected to be positive while the relationship between cell death marker and proliferation was predicted to be negative. Based on the correlation results (Figure 5.8), negative relationships were observed expectedly between Ki-67 expression and M30 expression (r=-0.539, n=5, p=0.348) and between Ki-67 expression and γH2AX expression (r= -0.982, n=5, p=0.003), while unexpectedly between Bcl-2 expression and γH2AX expression (r=-0.656, n=5, p=0.229). The relationships between M30 expression and γH2AX expression (r=0.504, n=5, p=0.387) and between M30 expression and Bcl-2 expression (r=0.295, n=5, p=0.629) were positive which was expected. However, a positive correlation was also observed between Ki-67 expression and Bcl-2 expression (r=0.619, n=5, p=0.266).

No significant correlations were detected between the expressions of all the protein markers (Figure 5.8), except between γH2AX and Ki-67 expressions. When the expression levels of cells positive for γH2AX and Ki-67 were compared, a significant negative correlation was observed, indicating that when the number of cells positive for DNA-DSBs increased, the amount of proliferating cells decreased.

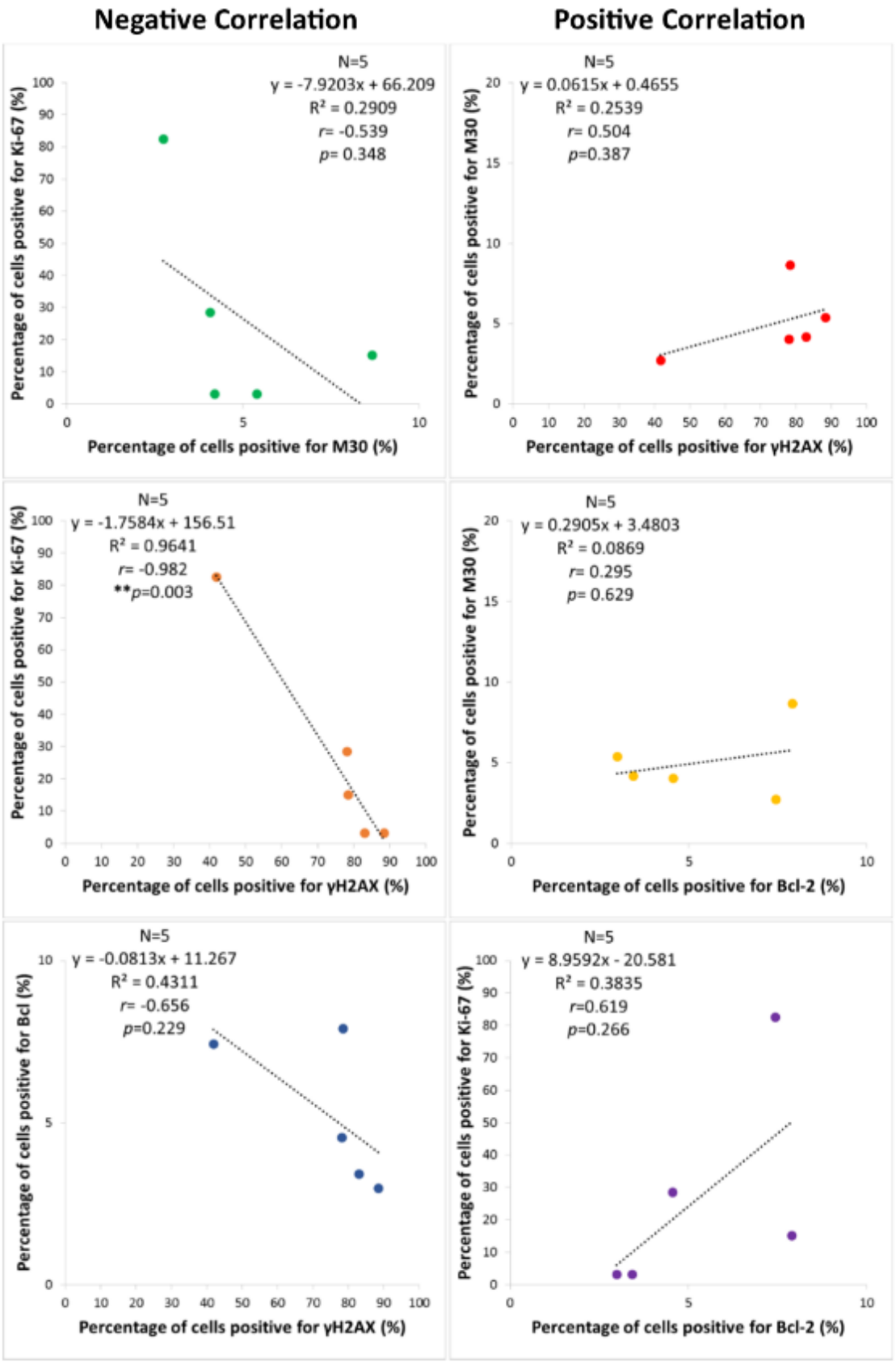


Figure 5.8. Scatterplots represents the relationships for the mean expression levels of M30, γH2AX, Ki-67 and Bcl-2 on the oropharyngeal cells (UMSCC-47) with different concentration of etoposide.

Positive and negative Pearson correlations between the markers expression of cleaved CK18 (M30), γH2AX, Ki67 and Bcl-2 were presented. ** Correlation is significant at the 0.01 level (2-tailed).

The effect of irradiation on Ki-67 expression in HNSCC tissue maintained in the microfluidic device

IHC staining of Ki-67 was carried out (section 2.9) on HNSCC tissues following single dose irradiation and maintenance in the microfluidic device. In total, five different HNSCC tumour tissues were used including TR73, TR80, TR89, TR92 and TR84 (Figure 5.9). Similar with the IHC of γH2AX (section 4.7), these tumours were chosen and subjected to this Ki-67 study based on the availability of the number of the repeats in achieving n=2 on each case. In terms of Ki-67 expression quantification, five fields of x400 magnification of the tumour area across the tissue sections (based on IHC staining of CK) were captured and the number of positively stained nuclei and total nuclei on each field were counted (Figure 5.10) and expressed as a percentage. The percentages were statistically compared between the treatments on each tumour using One-way ANOVA followed by Tukey's post-hoc test. The expression level of Ki-67 was also evaluated on the three HNSCC tumours (TR80, TR89 and TR92) which were subjected to fractionated doses of irradiation whilst being maintained in microfluidic culture (section 2.5 and Table 2.3).

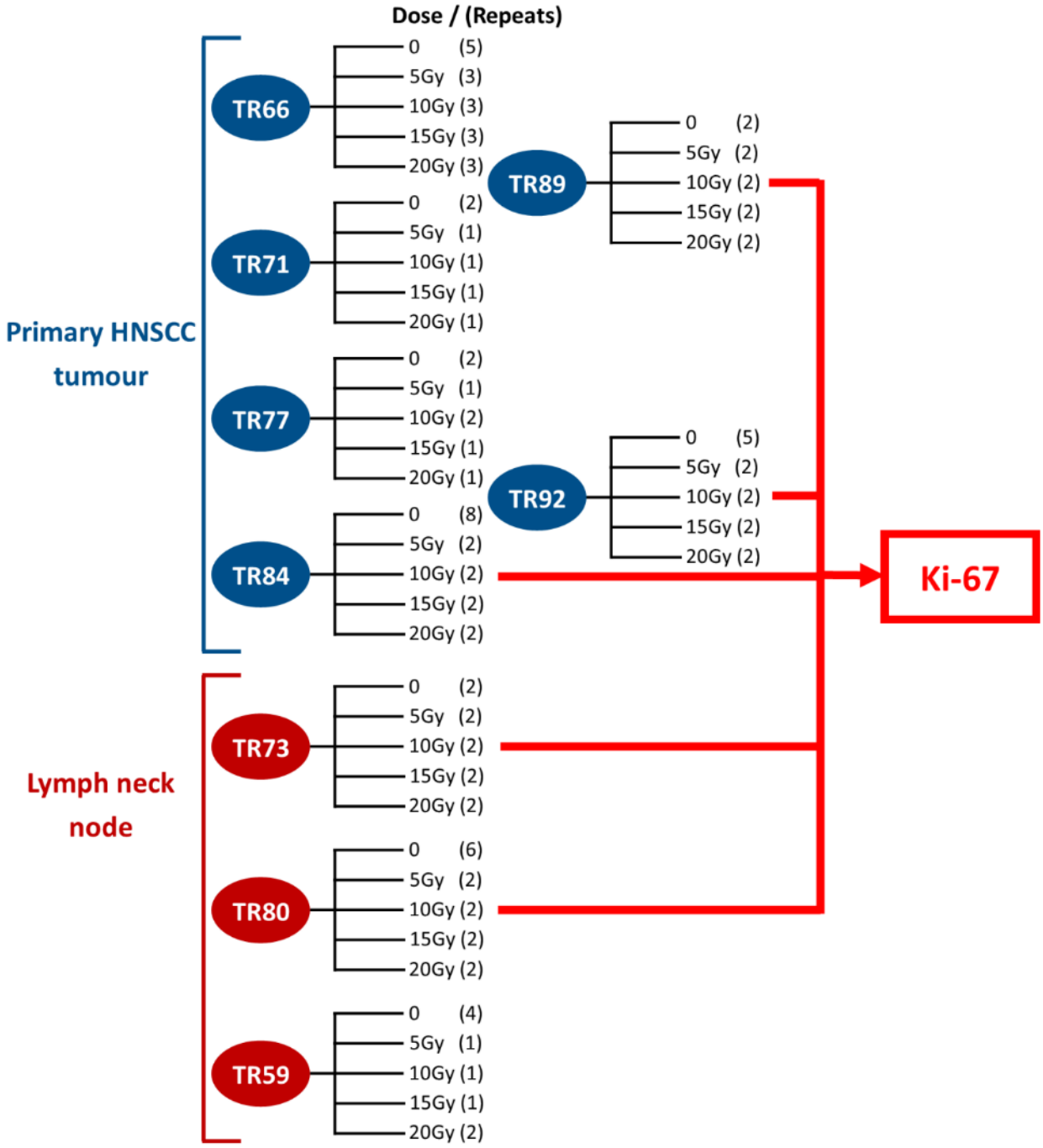


Figure 5.9. A flow chart of the nine HNSCC tumours involved in the current microfluidics and irradiation study and the analysis methods carried out on each one.
Tumour TR66: paranasal sinus, TR71: oral cavity, TR77: oropharyngeal, TR84: laryngeal, TR89: oral cavity, TR92: oral cavity, TR73: lymph node from unknown primary, TR80: lymph node from laryngeal primary, and TR59: lymph node from oropharyngeal primary tumour. The number of repeats for the five treatments (MF, 5Gy, 10Gy, 15Gy and 20Gy) were listed below each treatment. Nine tumour samples were subjected to CK18-labelling index study while the five tumour samples (green bracket) were subjected to IHC staining of Ki-67.

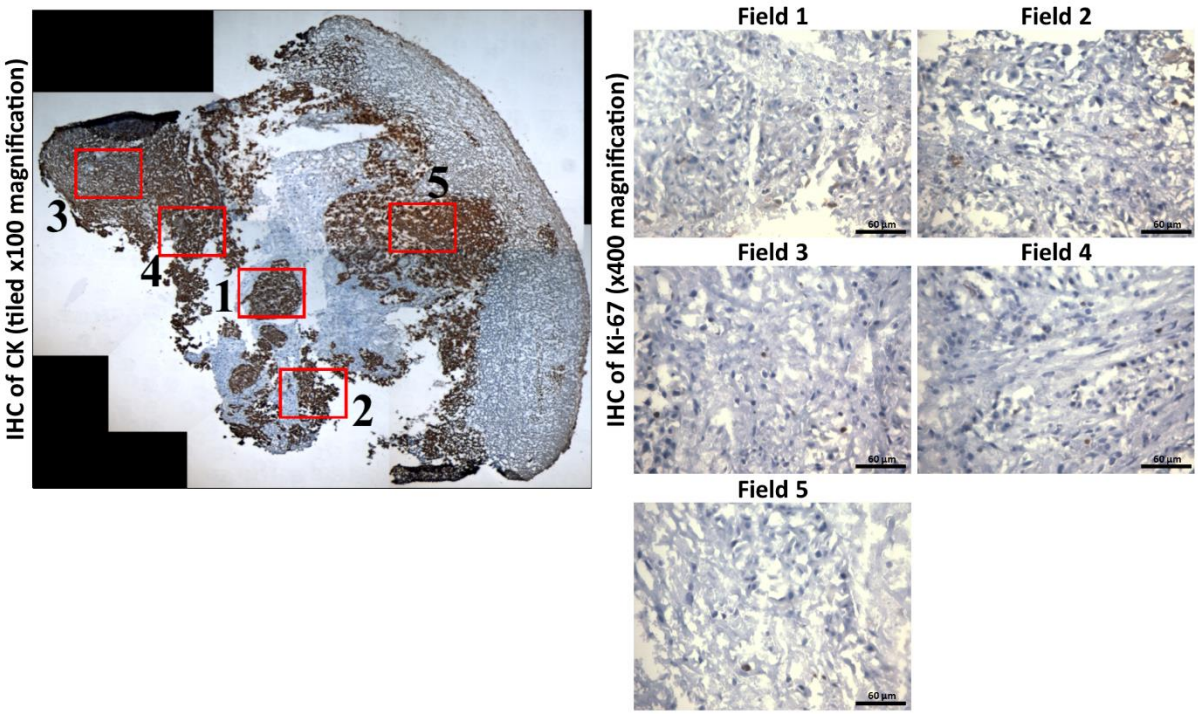


Figure 5.10. Representative IHC staining of cytokeratin (CK; x100 magnification) and Ki-67 (x400 magnification) of serially sectioned laryngeal TR84 tumour subjected to microfluidic culture and on-chip 20Gy irradiation.
In total, 74 of tissue samples were analysed. Five fields of x400 magnification were captured on the tumour area across the tissue section based on the IHC staining of CK.

Based on the representative staining of Ki-67 on the metastatic lymph node TR73 tumour (Figure 5.11), visual analysis of the stained sections clearly showed a greater number of brown positive nuclei on the microfluidics control tissues and on the 5Gy irradiated tissue compared to the tissues subjected to higher doses of irradiation (Figure 5.11.B). Additional tissue sections incubated with the mouse IgG1 matched isotype control showed no brown positive staining (Figure 5.11.A).

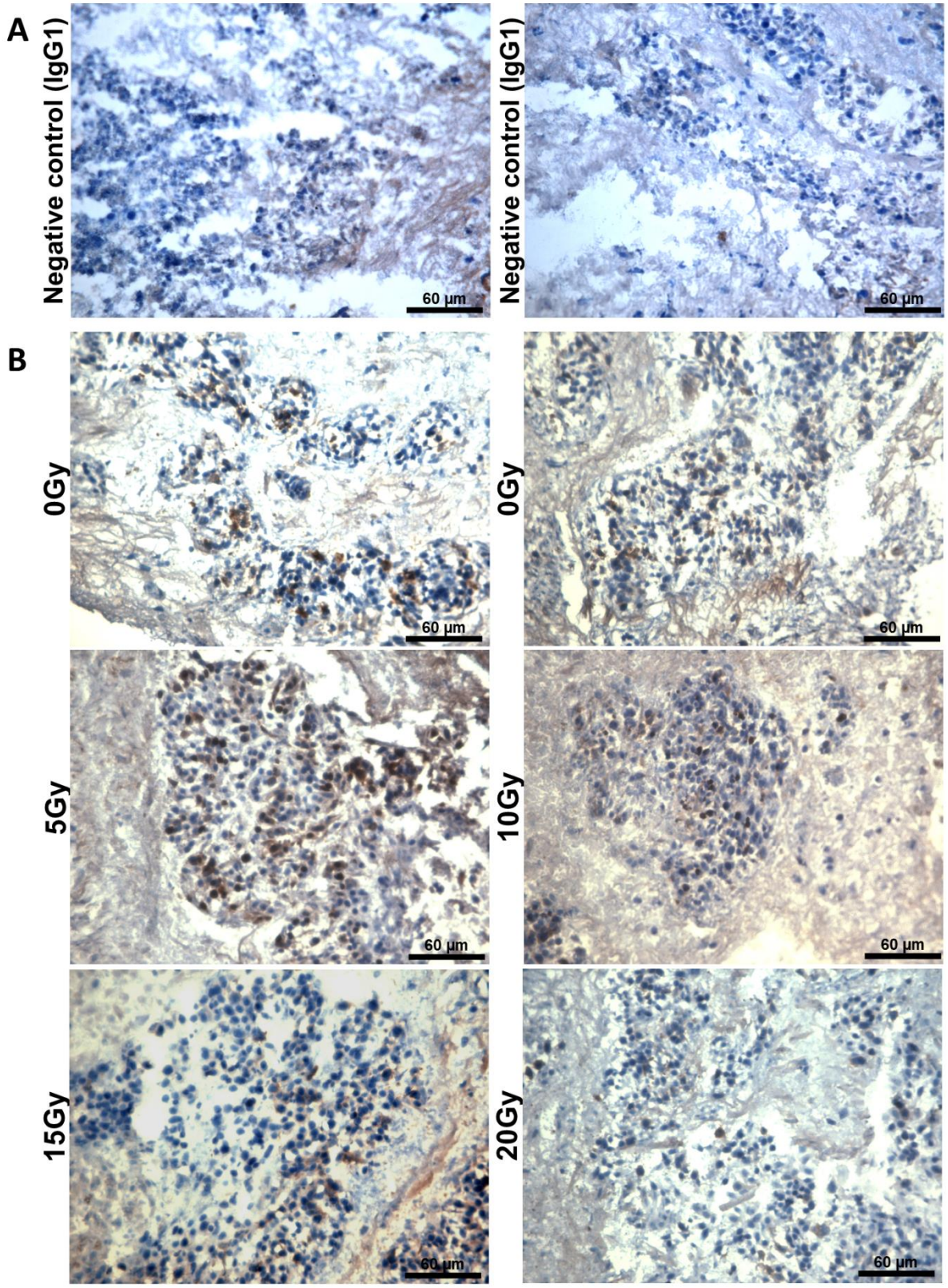


Figure 5.11. Representative IHC staining of Ki-67 on lymph neck node metastasized from an unknown primary tumour (TR73; n=10).

(A) Representative IHC staining of non-irradiated TR73 tissue using a mouse matched IgG1 isotype antibody (x400 magnification). Blue staining indicates the haematoxylin stained nuclei counterstain. (B) Representative IHC staining images of Ki-67 on the TR73 microfluidic-cultured tissues with no irradiation (0Gy), 5Gy, 10Gy, 15Gy and 20Gy irradiation (x400 magnification). Brown nuclei represents the expression of Ki-67 with blue haematoxylin counterstain. The x400 magnification fields were chosen based on the areas of tumour found by IHC staining of a serial section with CK; section 4.5.

The mean percentage of cells positive for Ki-67 expression on each of the five HNSCC tumours subjected to different doses of irradiation was calculated, as described previously (Figure 5.12 and Figure 5.13). In the two lymph neck nodes, the non-irradiated control tissues (0Gy) had a higher percentage of proliferating cells compared with the irradiated samples and there was a dose dependent decrease in the percentage of proliferating cells with increasing irradiation doses, however this was not significant.

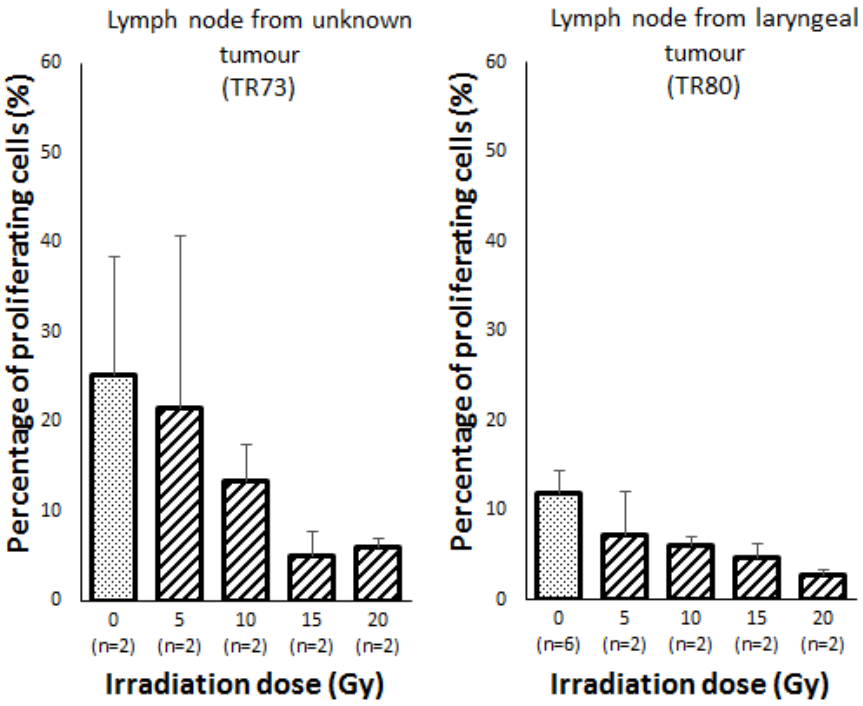


Figure 5.12. Mean percentage of cells positive for Ki-67 expression from five x400 fields of view on two HNSCC lymph node tissues (TR73 and TR80) following different doses of irradiation.
Mean+SEM. The number of repeats of each treatment (n) is shown in parentheses, indicating the number of tissues from the same patient that were subjected to same treatment.

The percentage in the non-irradiated control of TR84 was higher (27.0±5.8%) compared with the control tissues of TR89 and TR92 (4.8±4.8% and 6.6±2.8%; Figure 5.13). The percentage remained low in both oral cavity tumours (<8%), regardless of the irradiation doses applied. In contrast, irradiation of the laryngeal tumour with 5, 10 and 20Gy resulted in a decrease in proliferation compared to the non-irradiated control, but these differences were again not significant. Surprisingly, following 15Gy of irradiation the laryngeal TR84 tumour retained a similar level of proliferating cells to the non-irradiated control, however, this was most likely due to aberrant staining of the sample.

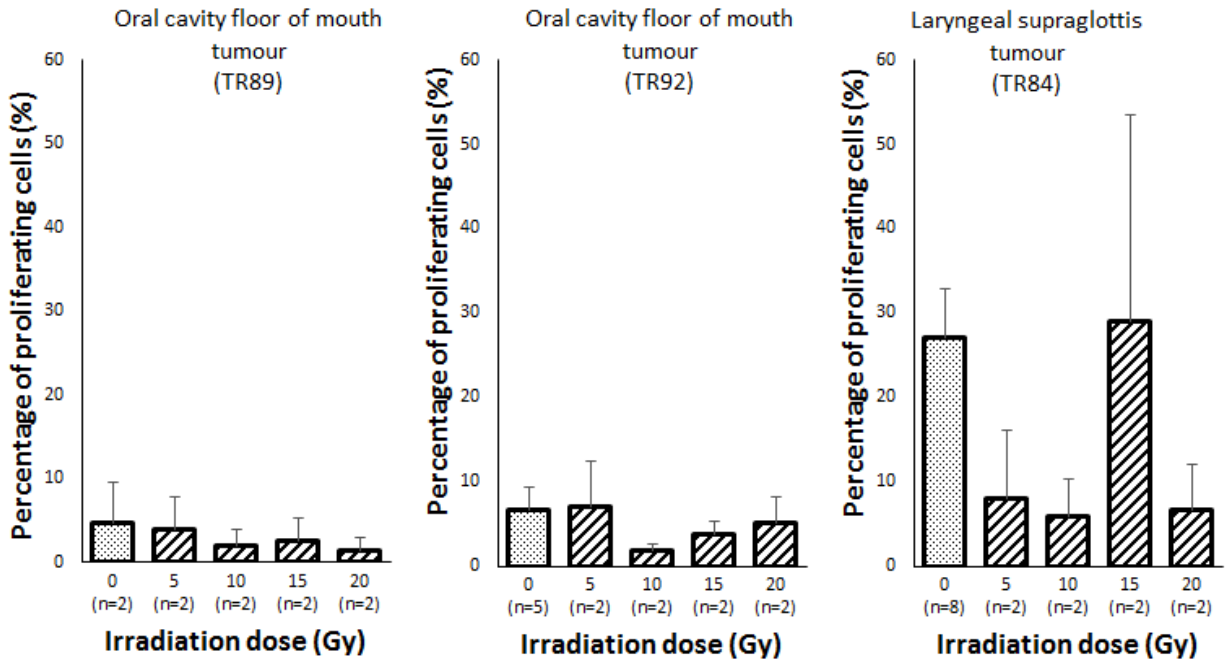


Figure 5.13. Mean percentage of proliferating cells from five x400 fields of view on three primary HNSCC (TR89, TR92 and TR84) tumours following different doses of irradiation.
Mean+SEM. The number of repeats of experiment on each tissue (n) is shown in parentheses, indicating the number of tissues from the same patient that were subjected to the same treatment.

HNSCC tissue [1 lymph node (TR80) and 2 oral cavity tumours(TR89 and TR92)] maintained in a microfluidic device was also subjected to fractionated doses of irradiation to determine if this caused different levels of Ki-67 expression (section 2.5). The percentage of cells positive for Ki-67 expression was low following five fractions of both 2Gy or 4Gy on both oral cavity floor of mouth tumours investigated and was reduced compared to the non-irradiated control (Figure 5.14.A). The percentage of cells positive for Ki-67 in the non-irradiated lymph node TR80 tissue was almost double compared to that of the non-irradiated tissues of the two oral cavity tumours (8.5±2.8% in TR89 and 15.9±5.4% in TR92). Although five doses of 2Gy irradiation caused a decrease in proliferation surprisingly 5 x 4Gy resulted in an increase in proliferation compared to the non-irradiated control. This high proliferation level on the lymph node TR80 tissue was different to that observed on the single-dose irradiation (Figure 5.14.B). Unfortunately, each fractionated irradiation dose for the three individual tissues were carried out once only (n=1) due to the limitation of available tissue.

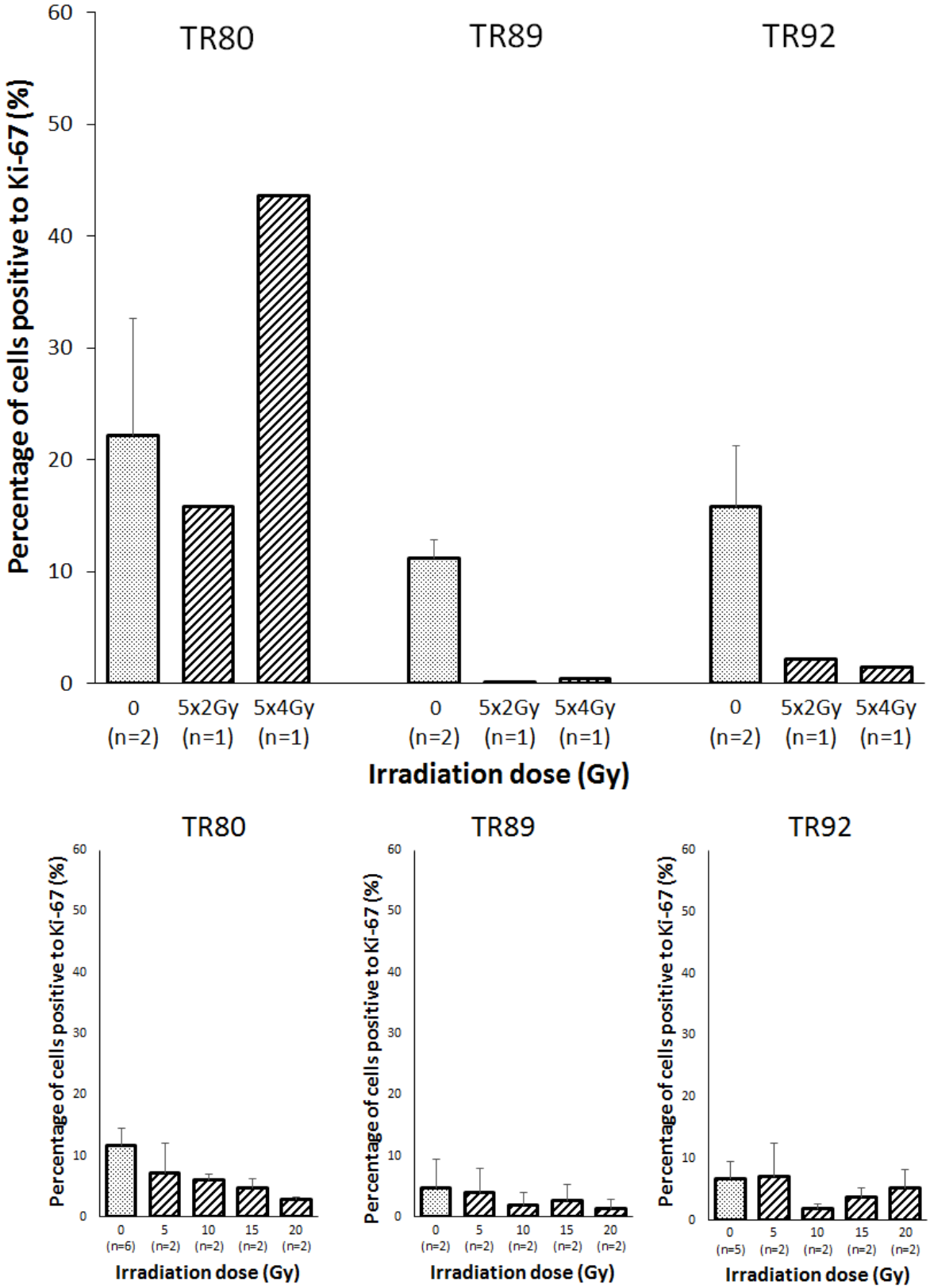


Figure 5.14. Mean percentage of cells positive for Ki-67 expression on TR80, TR89 and TR92 following (A) fractionated irradiation 5x2Gy and 5x4Gy and (B) single-dose irradiation.
Mean+SEM. The number of repeats of experiment (n) is shown in parentheses, indicating the number of tissues from the same patient that were subjected to same treatment.

5.2.3 Using 5-ethynyl-2'-deoxyuridine (EdU) incorporation as a measure of proliferation in response to irradiation

The incorporation of EdU into replicating cells shares the similar mechanism with that of BrdU incorporation. EdU presents in culture medium enters through the cell and into the nucleus where it becomes incorporated into replicating DNA replacing the thymidine nucleoside. In contrast to the IHC staining of BrdU, the detection of EdU does not require acid hydrolysis and instead uses unique Click-iT technology. This uses the “click” reaction involving the ligation of its ethynyl moiety in EdU with a small azide-coupled fluorescent dye that is catalysed by copper (I) catalyst (section 2.12.3 and Figure 2.15; BioSpotlight, 2008).

The incorporation of EdU was first tested on the oropharyngeal cancer cell line (UMSCC-47). Cells (5×10^4 plated on coverslips) were incubated for 1 hour with medium containing 10µM of EdU upon reaching 70% confluence. Bright labelled EdU signal was observed in proliferating cells within the intestinal villi after only one-hour incubation (Thermo Fisher Scientific, 2010) and therefore, one hour EdU incubation was performed on UMSCC-47 cells to confirm the feasibility of the method. Following the markers incubation, the cells were subjected to the detection of EdU-incorporated cells according to procedures described in section 2.12.3.

Three lymph node tissues, two metastasised from an oropharyngeal tumour (TR59 and TR122) and one from a laryngeal tumour (TR80), were maintained for 24 hours in the microfluidic device before medium containing 10µM of EdU was added into the microfluidic system for 6 hours prior to tissue freezing. The frozen tissue was then sectioned and EdU incorporation detected in the same way as for the cell lines (section 2.12 and 2.12.3). Additional pieces of each tumour were maintained in the microfluidic device for the same period of time but without addition of EdU. EdU was visualised and captured using fluorescent microscopy at x400 magnification. The exposure times for both blue (DAPI) and green (Alexa Fluor 488) filters were adjusted to approximately 60ms and 1.5s, respectively.

Green fluorescence was observed in the nuclei of proliferating UMSCC-47 cells (Appendix Figure 9.2). Following EdU addition and subsequent detection, five fields of view were photographed and the percentage of cells proliferating was calculated based on the percentage of positive nuclei (Alexa Fluor 488-stained nucleus) over the total nuclei (DAPI-stained nucleus). The average percentage of proliferating cells over

the five fields was 33.1±3.7%. When the incorporation on tumour tissues were viewed (Appendix Figure 9.3), no green fluorescence was detected on the tissue sections with background green fluorescence. Although there were some green cells appeared on the lymph node tissue metastasised from oropharyngeal tumour II (Appendix Figure 9.3.C), but the positive was not reproducibly evident and quantifiable, thus no further work was undertaken.

5.2.4 Incorporation of 2-NBDG into oropharyngeal cells in cell culture plate and tissues maintained in a microfluidic device

The uptake of 2-NBDG was used to determine the metabolic potential of the cells cultured in the microfluidic device. The uptake of 2-NBDG was firstly optimised on oropharyngeal epithelial cells (UMSCC-47). Different parameters were tested and the corresponding results were summarised below:

(1) Titration of 2-NBDG (0, 0.01 and 0.05mg/mL of 2-NBDG in PBS for 1 hour; (Appendix Figure 9.4): The cells incubated with 2-NBDG at concentration of 0.05mg/mL demonstrated higher level of glucose uptake compared with that of 0.01mg/mL 2-NBDG.

(2) Solvent for 2-NBDG (PBS, low-glucose medium (1g/L of glucose) and glucose-free medium; Appendix Figure 9.6): The glucose-free medium achieved the highest 2-NBDG uptakes compared with those cultured with PBS and low-glucose medium.

(3) Time of 2-NBDG incubation (15, 30 and 60 minutes; Appendix Figure 9.7): Cells incubated for 15 and 30 minutes showed green fluorescence not only in the cytoplasm but also around the cell membrane whereas the cells incubated for 60 minutes appeared to have a more complete uptake of the marker.

(4) Glucose-free incubation prior to 2-NBDG incorporation (Appendix Figure 9.8): The 2-hour pre-starvation step on oropharyngeal cells demonstrated that such cells only had peripheral uptake of the glucose analogue but low uptake of the marker into the cytoplasm.

(5) Different HNSCC cell lines (UMSCC-47 and UMSCC-81b; Appendix Figure 9.9): Under the same conditions the UMSCC-47 cells appeared to take up more of the analogue compared to the UMSCC-81b.

Following the optimisation tests carried out on cells, the uptake of 2-NBDG was then investigated on head and neck tumour tissues in static plate culture. Four pieces (5-

10mg) of a frozen oropharyngeal tumour (TR104) were cultured in separate wells of a 96-well-plate with 0.05mg/mL of 2-NBDG in glucose-free medium, respectively, for 15, 30, 45 and 60 minutes following an equilibrium period of 24 hours in standard high glucose DMEM. The perfusion of the oropharyngeal TR104 tissues with 2-NBDG for 45 and 60 minutes showed more green fluorescence compared with lower perfusion time of 15 and 30 minutes (Appendix Figure 9.10).

Perfusion of 2-NBDG for 60 minutes was then applied on four pieces of lymph neck node metastasised from an oropharyngeal tumour (TR122) tissues in microfluidic flow system. They were subjected to parallel microfluidic culture for 24 hours; two of them were perfused with medium containing 0.05mg/mL 2-NBDG while another two were served as a control with no addition of 2-NBDG. Based on the results (Appendix Figure 9.11), there were no apparent incorporation of green fluorescence in the tissues following 60 minutes of 2-NBDG exposure in microfluidics when the experimental set-up was repeated. As shown in the representative images, there was only few cells have incorporated the fluorescent markers.

5.2.5 Correlation between CK18-LI, TUNEL assay results, expression levels of γH2AX and Ki-67 on the five HNSCC tumours

For the purpose of correlation of the different markers used in the current project, the five tumours [two lymph nodes (TR73 and TR80); three primary tumours (2 oral cavity TR89 and TR92 tumours and 1 laryngeal TR84 tumour) Table 2.1]. The representative photomicrographs of all the staining on tissues of TR73 was summarized in Figure 5.15 while the method summary of the quantifications on each marker is presented in Figure 5.16. Briefly, the labelling index of caspase-3-cleaved CK18 on each tumour tissue was calculated and expressed, on the tiled x100 magnification field, by the percentage of apoptotic area (positive M30 staining) over the total area of tumour cells (positive CK staining; Figure 5.16.A). To evaluate the mean percentage of cells positive to DNA-DSBs (γH2AX) and the proliferating cells (Ki-67), five fields of x400 magnification field on each treatment were taken on the tumour area across the section and the percentage of positive stained nuclei over total nuclei on each field were obtained (Figure 5.16.B). On TUNEL DNA-strand breaks quantification, on the five x400 magnification fields, the percentage of FITC positive staining over the DAPI counterstaining was calculated to express the percentage of cells positive to TUNEL assay (Figure 5.16.B). The mean expression data of the four markers on each

individual tissue of the five primary tumours were subjected to Pearson's correlation test (section 9.10/Table 9.4). This statistical test enables the evaluation on the relationship between these expression markers on each patient.

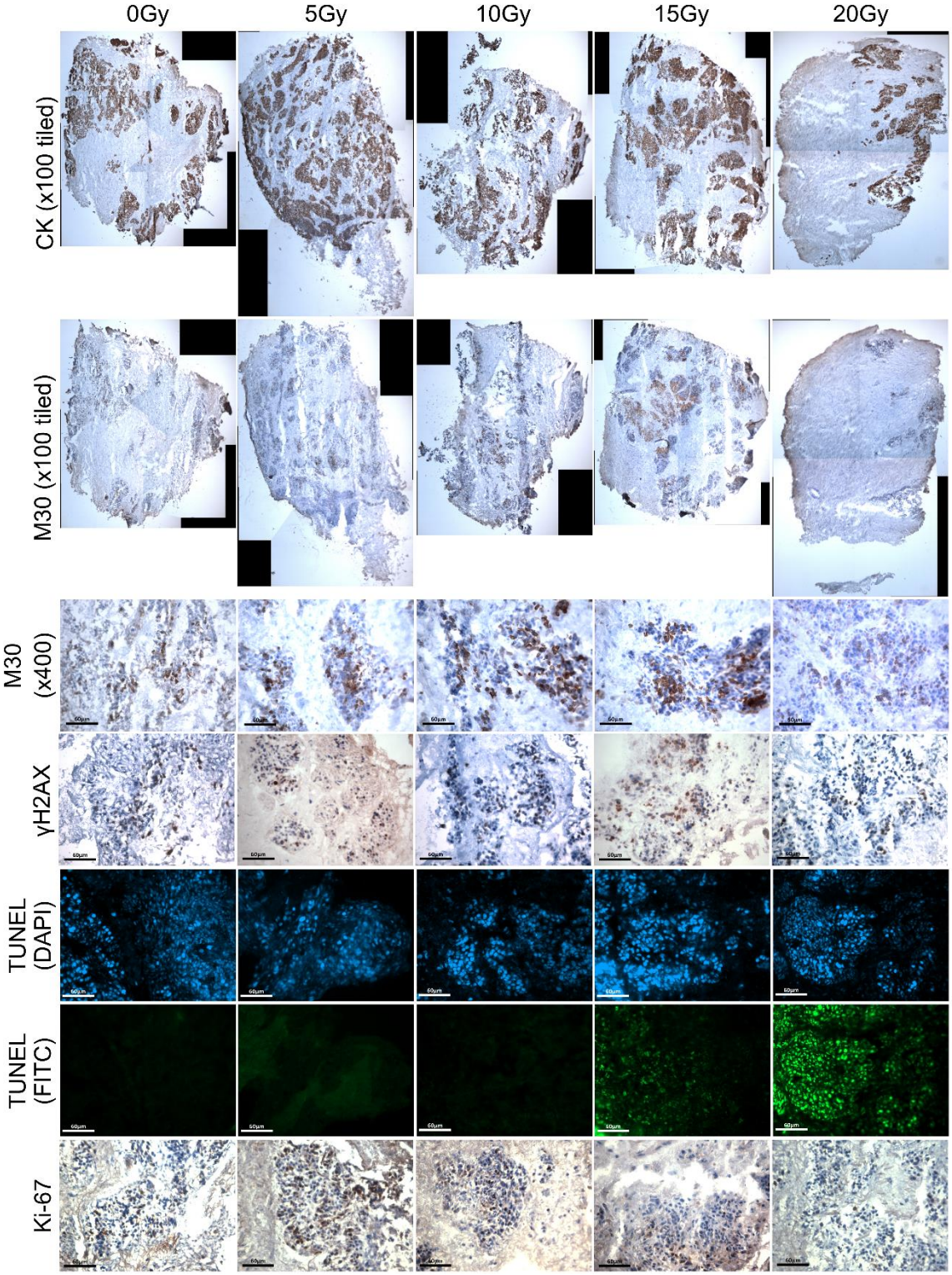


Figure 5.15. Representative photomicrographs of staining of CK, m30, γH2AX, TUNEL assay, Ki-67 and BrdU on serial sections of TR73 (n=10; n=2 on each treatment case).
The tissues were subjected to microfluidic culture (0Gy) and exposure to independent four single-dose irradiations. Tiled x100 magnification on CK and M30 staining (first two rows) and x400 magnification on M30, γH2AX, TUNEL, and Ki-67.

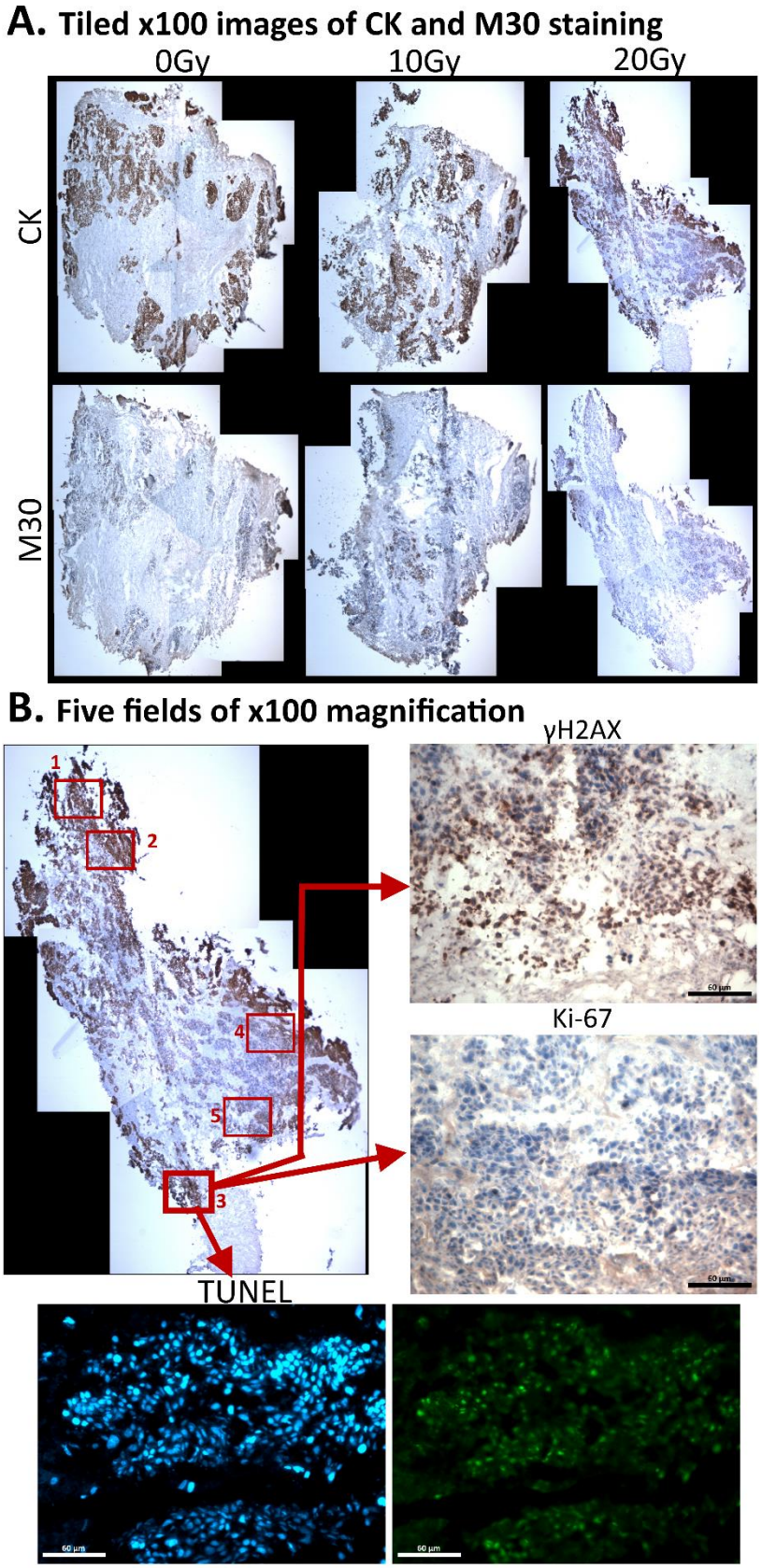


Figure 5.16. Evaluation of percentage of cleaved CK18, γH2AX, Ki-67 expressions and TUNEL assay.

(A) IHC staining of cytokeratin (CK) and cleaved-cytokeratin 18 (M30) on serially sectioned TR73 tissues treated with different doses of irradiation (x100 magnification, tiled). (B) Representative image of TR73 following 20Gy irradiation showing cytokeratin staining and the five fields of view selected, the same areas were visualised following the TUNEL assay and IHC staining of γH2AX and Ki-67.

Following all the staining on the tissue sections using different markers, described in Chapter 4 and 5, it is beneficial to look at the relationship between the markers on each individual HNSCC tumour and all tissues of the five HNSCC tumours were subjected to the CK18-LI, γH2AX, and Ki-67 studies. The overview of all mean expression data across the five HNSCC tumours was presented (Figure 5.17). Four out of five of the tumours were subjected to TUNEL assay as one of the oral cavity tumour (floor of mouth tumour; TR89) could not due to the shortage of the frozen tissue (Table 2.1).

On both lymph neck node tissues (TR73 and TR80), positive correlations were observed between CK18-LI and γH2AX, CK18-LI and TUNEL, as well as γH2AX and TUNEL whereas the expression of Ki-67 reduced with increasing CK18-LI, γH2AX expression and TUNEL which were all expected (Figure 5.18). However, of these, significant correlations were only seen in TR80 (CK18-LI-γH2AX, r=0.747, p=0.02, CK18-LI-Ki-67, r=-0.533, p=0.049, CK18-LI-TUNEL, r=0.712, p=0.004, and Ki-67-γH2AX, r=-0.722, p=0.004). Some of the relationships between the four markers were observed on the three primary tumours, yet some correlations were detected weak and not significant (Data shown in appendix: section 9.11/Figure 9.12). Unexpected relationships between markers were also observed: positive between Ki-67-γH2AX in oral cavity TR89 tumour, positive between Ki-67-TUNEL in oral cavity TR92 tumour, positive between CK18-LI-Ki-67 in TR92 tumour, negative between CK18-LI-γH2AX in both TR89 and TR84 tumours.

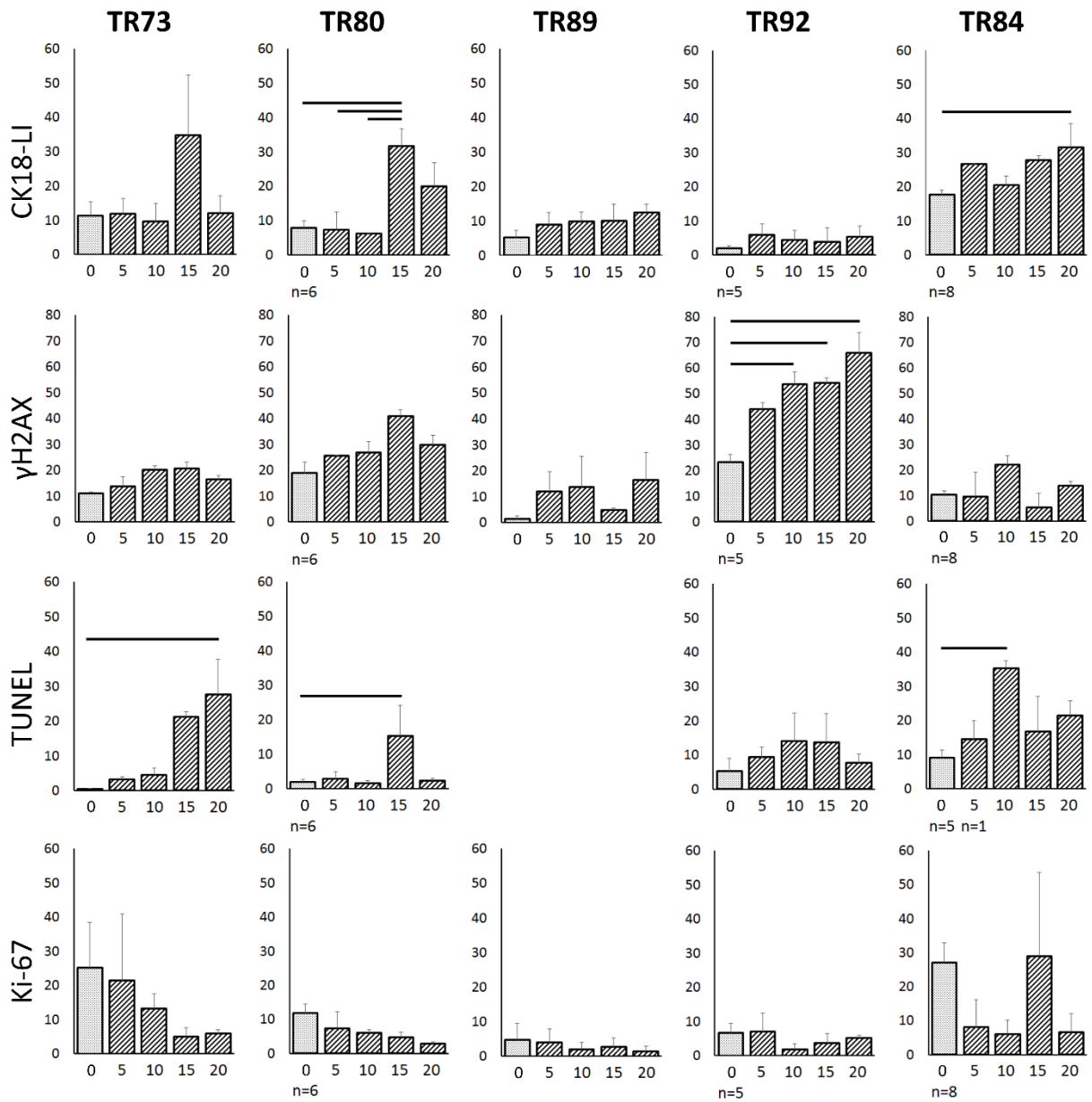


Figure 5.17. Tumour response of five HNSCC tumours with increasing doses of irradiation in terms of the expression of the caspase-cleaved CK18 (early apoptosis marker; CK18-LI), DNA double-strand breaks (γH2AX), DNA fragmentation assay (TUNEL), and proliferation (Ki-67). Mean+SEM. Lines indicate the significant results between treated sample and the non-irradiated control (0Gy) based on One-way ANOVA with post-hoc Tukey test ($p<0.05$). The blank graphs on TUNEL assay and BrdU proliferation study on the oral cavity tumours were due to the insufficient tissue.

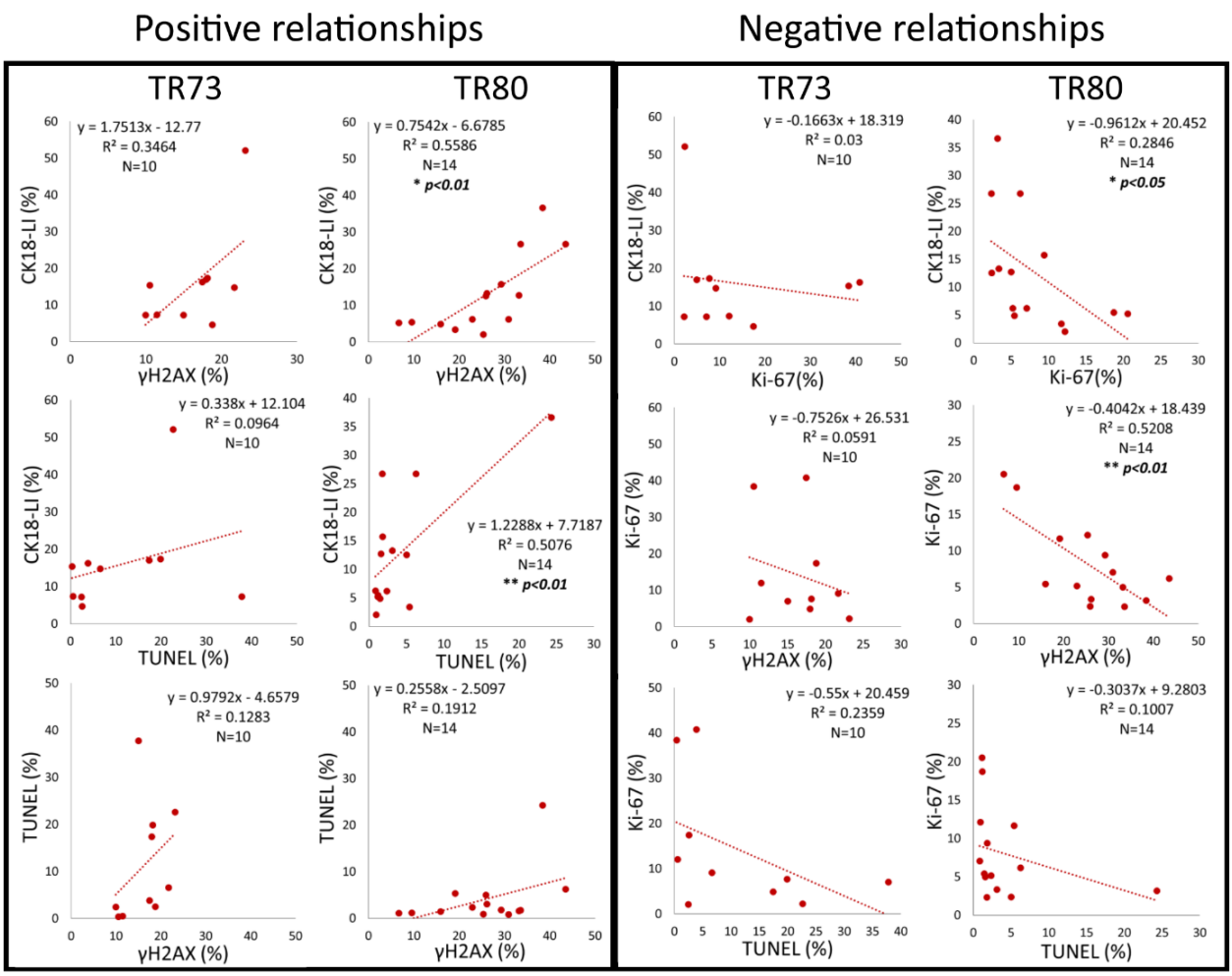


Figure 5.18. Scatter plots exemplifying the positive and negative relationships between markers on TR73 and TR80.

The correlation tests include CK18-LI vs γH2AX, CK18-LI vs TUNEL, TUNEL vs γH2AX, CK18-LI vs Ki-67, Ki-67 vs γH2AX and Ki-67 vs TUNEL. * p<0.05 and ** p<0.01 indicate significant results on Pearson correlation between the markers.

5.2.6 Comparison between *in vitro* results and clinical patients' outcome

In order to determine fully whether the microfluidic culture of HNSCC tissue and its subsequent irradiation can predict whether a tumour is radioresistant/responsive, the data obtained in the current study had to be correlated with the patients' *in vivo* response to irradiation. The clinical details of the patients including the treatments the patient received, the date of treatment and the post-treatment survival were obtained and summarised in Table 2.2Following microfluidic and on-chip irradiation experiments, five tumour samples were subjected to the expression analysis based on the cleaved-CK18 (section 4.5), phorphorylated H2AX (section 4.7), TUNEL (section 4.9) and Ki-67 (section 5.2.2). The expression results were further described in the corresponding chapters. The corresponding treatment outcomes of these five tumour samples (two lymph nodes and three primary tumours) were recruited from NHS ENT secretaries and Lorenzo system with the assistants of few ENT doctors (Table 2.2).

Table 2.2. Based on the corresponding patient clinical records (at 18.02.2016), three of the five patients involved in current study are still alive with no evidence of loco-regional recurrence while no available clinical data was obtained on TR80. The patient with oral cavity tumour (TR89), unfortunately, has passed away because of alcoholic liver disease instead of head and neck cancer; hence death due to other causes. The main problem, appeared in current study, was the fact that in order to get a large enough piece of tissue to study with various doses, the resected tissue samples have to be used and these patients may not be subjected to radiotherapy, for example the two patients with oral cavity tumour (TR89 and TR92) underwent surgical treatment only but not radiotherapy. In addition, the standard radiotherapy regimen received on the HNSCC patients which was 66-70Gy (delivered in fractions for at least 6.5-7 weeks) and some of the patients were treated by chemo-radiotherapy which were different with the *in vitro* treatment (single-dose or fractionated radiotherapy) administered on the tissue sample that maitnained in microfluidic device. Although the treatment the patients received was not equivalent with the irradiation implemented in this study, the clinical therapeutic outcome can still be used as a clinical reference and as an initial step for radioresistance prediction research under microfluidic-based approach. For example, on the patient with laryngeal supraglottic tumour (TR84) who was treated by radiotherapy, positive response in terms of increased cell death (both

CK18-LI and TUNEL) and reduced proliferation (Ki-67 expression) was obtained following *in vitro* irradiation in microfluidic device which agreed with the *in vivo* positive clinical treatment outcome with no loco-regional recurrence diagnosed. Same results were noticed with positive tumour response in this project and on the patient with lymph neck node metastasised from an unknown primary tumour (TR73).

5.3. Discussion

5.3.1 Marker expression in UMSCC-47 cells in response to irradiation

Preliminary experiments to monitor response to DNA damage were performed using oropharyngeal cells (UMSCC-47) treated with four different concentrations of etoposide for 24 hours before being subjected to IHC staining for M30, γH2AX, Bcl-2 and Ki-67 (Chapter 4 and 5). Etoposide is a topoisomerase II inhibitor and causes DNA-DSBs (Doi, 2011). The accumulation of cells in S-phase and G_2/M arrest occurs and apoptosis is induced before entering G_2 and M phase, respectively (Figure 5.19). It was hypothesised that low proliferation, increased DNA damage and a high level of apoptosis would be observed on the cells following etoposide treatment.

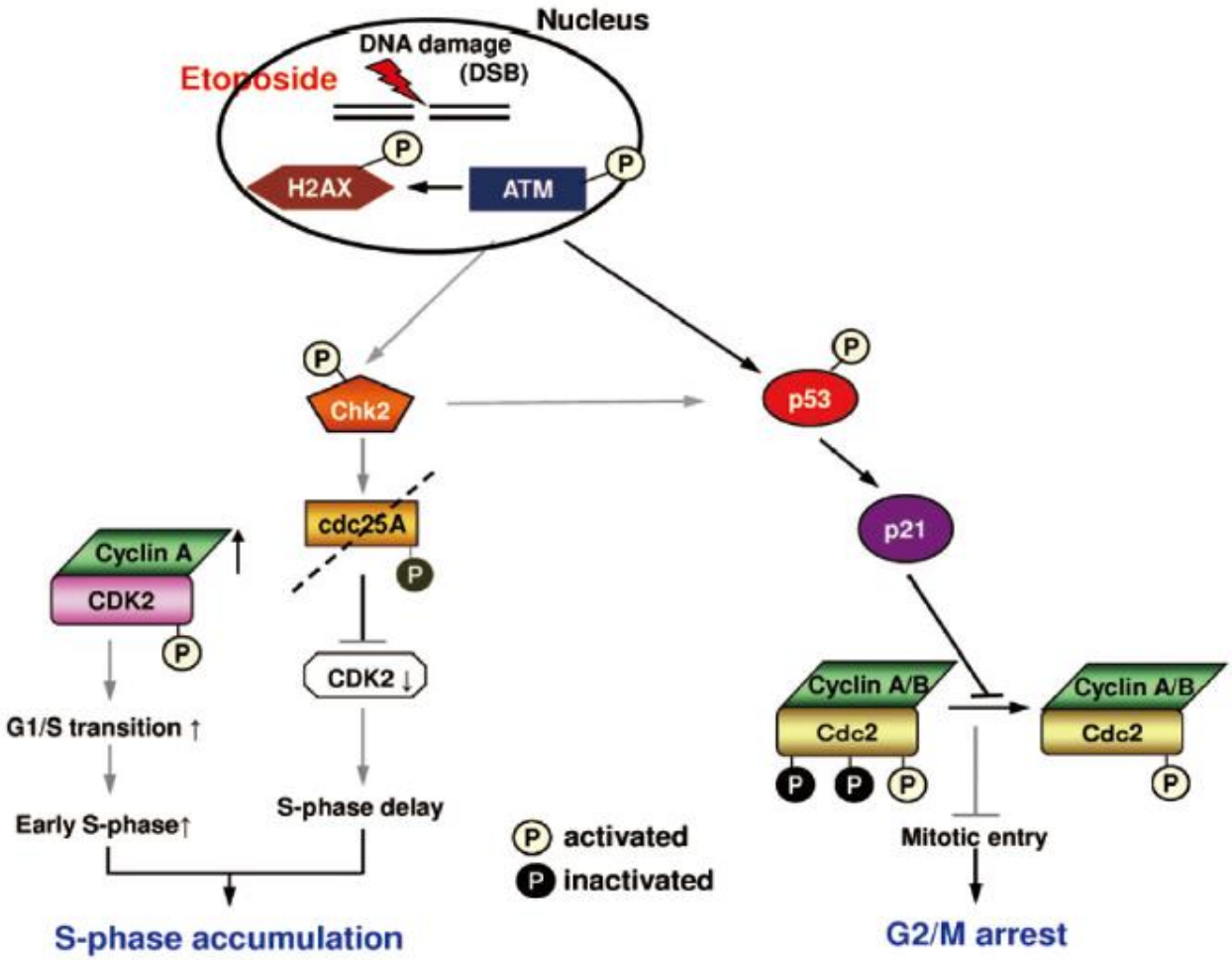


Figure 5.19. Mechanisms of etoposide in inducing cell cycle alterations.
(Extracted from Doi, 2011).
In the ATM- *p*53 pathway, an increase of *p*21 inactivates the cyclin A/B-cdc2 complex and trigger G_2/M arrest by preventing mitotic entry. Increased cyclin A evokes G_1/S transition and cdc25A degradation inactivates Cdk2 which then inhibits S-phase progression. Both events cause S-phase accumulation.
Abbreviation: H2AX: H2AX a histone family member, ATM: ataxia telangiectasia mutated, Chk2: checkpoint kinase 2, CDK2: cyclin-dependent kinase 2, cdc25A: cell division cycle 25 homolog A, cdc2: cell division cycle protein 2 homolog.

The percentage of UMSCC-47 cells positive for the expression of γH2AX was significantly increased by almost double, in etoposide-treated cells compared with control cells. In contrast, the levels of caspase-cleaved CK18 and Bcl-2 were elevated slightly following etoposide treatment. As expected, the UMSCC-47 cells had a significantly lower percentage of cells positive for Ki-67 expression compared with the control untreated cells. This is in agreement with Fujikawa-Yamamoto *et al*. (2012) who reported reduced proliferation in response to similar concentrations of etoposide, in which the doubling time of the hexaploid H1 cells was suppressed and the DNA histograms showed that G_2/M accumulation was increased measured by flow cytometry.

When the correlation between the cell death/DNA damage response and proliferation markers was performed, most of the relationships were not significant, except for that between Ki-67 and γH2AX in which negative correlation was observed. These data suggest that the DNA-strand breaks/DNA damage repair and cellular proliferation go hand in hand on oropharyngeal cells in response to etoposide drug treatment with the cells becoming quiescent, however, the arrest may not lead to apoptosis through the caspase-cleaved CK18 (M30) and anti-apoptotic Bcl-2 pathways. The negative correlation between Ki-67 and γH2AX appears to be dependent on the DNA damage inducing agent since Panopoulos *et al*. (2014) found no such correlation following the treatment of human foreskin fibroblasts with dihydroxycytochalasin (inhibitor of actin assembly which blocks the cell cleavage). In summary, this HNSCC cell culture and etoposide study provided an analytical platform that could then be used to evaluate the expression levels of different markers on serially sectioned tissue, from different treated samples.

5.3.2 BrdU incorporation for measuring proliferation

Among the nine HNSCC tumours evaluated for BrdU incorporation in this study only, three had sufficient quality of staining to be successfully quantified, due to a low number of nuclei and high background staining in both irradiated and control tissues. On the two metastatic lymph nodes (TR73 and TR80), at 24 hours post-irradiation, the percentage of cells positive for BrdU incorporation was lower (<20%) than the non-irradiated tissue (8.5-16.7%). In comparison, the laryngeal TR84 tissue only showed a decrease in BrdU incorporation following 5Gy of irradiation (<5%) compared to the control (about 25%). The poor staining profiles obtained for six of the nine tumours

regardless of the HNSCC subsites and treatments suggested that the interpatient variation may play a part, with different tumours having varied behaviours and tissue susceptibility in the microfluidic device. In order to obviate the need for IHC staining of the incorporated thymidine analogue and hopefully reduce the background staining, BrdU was replaced with a different thymidine analogue EdU. EdU is a fluorescein conjugated molecule and therefore, no IHC staining is required and it also removes the need for harsh DNA denaturation to expose the integrated BrdU which may damage tissue structure and potentially destroy cellular epitopes (Zeng *et al*., 2010).

The use of EdU pulse labelling to study proliferation has been successfully reported on HNSCC cells (Zhang *et al*., 2012; Leelahavanichkul *et al*., 2014), adult central nervous system of mice *ex vivo* (Zeng *et al*., 2010), mouse small intestines *in vivo* (Salic and Mitchison, 2008), chick embryo (Warren, Puskarczyk and Chapman, 2009) and adult murine salivary glands *ex vivo* (Chibly *et al*., 2014). However, this is the first study to use the incorporation of EdU as a measure of proliferation in HNSCC tissue. However, although the EdU was well under the size of size exclusion which was determined in chapter 3 (252.23 g/mol) and the positive incorporation was observed in the oropharyngeal cell line, no positive incorporation was detected in microfluidic-cultured tissue. This could probably be due to the tissue handling processes following microfluidic culture, including tissue snap-frozen, cryo-sectioning and the EdU incorporation protocol, which might affect the fluorescence imaging.

5.3.3 Endogenous Ki-67 antigen expression as a marker of proliferation in response to irradiation

Despite the undeniable usefulness of BrdU incorporation as a method for detecting proliferation *in vitro*, it has limitations and weaknesses for the analysis of proliferation in tissue maintained in the microfluidic device primarily the uncertainty of BrdU diffusion through the tissue (Kee *et al*., 2002). The detection of Ki-67 expression, an antigen expressed in G_1, S, G_2 and M phases was used as an alternative method for detecting proliferation changes in response to irradiation and was reported to have a good correlation with BrdU incorporation (Goodson *et al*., 1998). IHC of Ki-67 was carried out on serial sections of five HNSCC tumour tissues, subjected to treatment with and without irradiation, and the percentage of cells positive for Ki-67 expression within each tumour area was obtained.

Due to the short half-life of the Ki-67 antigen (<2hours) and the fact it is only expressed during G_1, S, G_2 and M phases and not the G_0 phase, allows the accurate detection of proliferation occurring post-irradiation because the tissue is maintained for a 24-hour period following treatment (Lopez *et al*., 1991; Bruno and Darzynkiewicz, 1992; Aoyagi *et al*., 1995). The expression of Ki-67 in the two lymph neck nodes (TR73 and TR80) was reduced following irradiation (<20%) compared to the control, in a dose-dependent manner suggesting the irradiation was preventing the proliferation of the tumour cells within the biopsy. Similar results were seen for the laryngeal TR84 tumour, however, the proliferation was higher to start off with, suggesting the primary tumours and the metastasised tumours may proliferate at different rates depending on the stage of the tumour. The fact that 15Gy irradiation appeared to have little effect in the TR84 tumour, indicates that the tumour heterogeneity may have influenced the results despite the tissue being from the same tumour and that in future experiments at least duplicates need to be established for each condition. In contrast, no effect of irradiation on proliferation was observed in the two oral cavity tumours (TR89 and TR92), again suggesting the difference in sensitivity between tumours. However, the expression levels were studied based on minimally two replicate tissues from microfluidic-irradiation system. Therefore, the analysis on greater number of multiple tissues from an individual patient is of importance in future.

The conventional fractionated radiotherapy aims to allow the recovery of normal tissues from radiation damage as well as allowing the repopulation of surviving normal cells (Muriel, 2002; Pawlik and Keyomarsi, 2004; Pajonk *et al*., 2010). However, the repopulation also occurred on tumour cells, which increase the number of tumour cells that must be eradicated, and the tumour-cell repopulation may accelerate during the course of conventional radiotherapy that could limit the effectiveness of the radiation therapy. Accelerated fractionation radiotherapy which reduces the overall treatment time, therefore, provides less chances for the repopulation of the tumours cells between sessions and has been reported to improve the survival and locoregional control in HNSCC patients (Withers, 1988; Kim and Tannock, 2005; Bourhis *et al*., 2006; Marcu and Bezak, 2009). It was predicted that fractionated doses of irradiation carried out in current study (accelerated by delivering two fractions a day and five fractions administered within 3 days) would be reducing the proliferation level of the HNSCC tumours, which proved to be true for both oral cavity tumours (TR89 and

TR92) which had lower Ki-67 levels compared to untreated controls. However, on the contrary, the lymph node tumour (TR80) had a slight dose-dependent reduction in Ki-67 expression with single-dose irradiation, but had a nearly two-fold rise in expression after 5 x 4Gy irradiation compared with the control. It could be speculated therefore that this tumour may be resistant to the five fractions of 4Gy irradiation as the increased proliferation rate has been reported to link with increased biological aggressiveness and risk of recurrence (Buffa *et al*., 2004; Rao *et al*., 2009; Pereira *et al*., 2012). However, no conclusive deduction could be drawn here as the values of Ki-67 expression on these fractionation-irradiated tissues were obtained from one repeat tissue.

The use of Ki-67 marker in assessing the proliferation on HNSCC cell or tissue response to irradiation has broadly been studied, but no recent study has combined microfluidic platform in determining the HNSCC tumour response to irradiation. Due to the novelty of the microfluidic device being able to maintain tissue whilst it is irradiated, this is the first study to measure the response of human tissue in response to irradiation. Yet, many researches have determined the proliferation labelling index prior to radiotherapy treatment and used the expression profiles to predict the responsiveness to the treatment. However, the results are conflicting. For example no direct correlation between Ki-67 expression in the pre-treatment biopsies and HNSCC tumour recurrence following radiotherapy was detected by some studies (Condon *et al*., 2002; Wilson *et al*., 2006; Al Gizawy *et al*., 2011) and while some studies showed that HNSCC pre-treatment biopsies with high Ki-67 have a less favourable outcome in terms of survival and time to recurrence (Buffa *et al*., 2004; Pereira *et al*., 2012), other studies have proposed the opposite (Raybaud *et al*., 2000; Couture *et al*., 2002).

The inconsistency of the results could be due to the heterogeneity of the tumour populations studied, where groups contained tumours of different histological type, patients who had already received different types of therapy (either surgery alone, radiotherapy alone or a combination), and the lack of standardisation of methods to measure cell proliferation as the analysis methods of Ki-67 expression were different between studies (Pich, Chiusa and Navone, 2004). The area of the tissue, which is quantified for proliferation, could also contribute to the inconsistent results observed by others as the Ki-67 labelling index was found varied on different histological grades of epithelium (Birajdar *et al*., 2014). For example, the expression of Ki-67 in Birajdar

et al. (2014) study was restricted to normal oral epithelium but detected positive on oral SCC and oral epithelial dysplasia. Due to the heterogeneity of the malignancy, the expression of Ki-67 across the tumour tissue is varied (Pich, Chiusa and Navone, 2004) and the reliability of the measurement depends on whether the markers are evaluated solely at the invasive tumour front which are the most proliferative or in randomly selected fields across the tissue (Tisell *et al*., 2003; Andersen *et al*., 2013; Ravikumar *et al*., 2013). In the current study, therefore, the expression of Ki-67 and BrdU, as well as the cell death markers: γH2AX and TUNEL assay, were quantified on the tumour area identified using cytokeratin staining of serial tissue sections. In addition, the inclusion of more tissue samples from corresponding tumour in the assessment of each protein expression would be beneficial to minimise the variation due to intra-tumour heterogeneity.

5.3.4 The multifaceted responses of HNSCC tissue to irradiation in the microfluidic device

Since radioresistance is multifactorial and complicated, the use of more than one independent marker to predict the radioresistance on HNSCC is necessary (Raybaud *et al*., 2000). Few studies used panel of biomarkers to study the biological response of tumours to irradiation (Table 5.2; Wildeman *et al*., 2009; Millar *et al*., 2009 and 2011; Akervall *et al*., 2014). However, in these studies, the identification of prognostic markers was performed using pre-treated tissues obtained from patients who were involved in the randomised clinical trials or who were later diagnosed having local recurrence.

Table 5.2. Studies using panel of biomarkers to study prognostic profiles on different tumours.

Tumour	Results	Reference
HNSCC	VEGF, Bcl-2, CLAUDIN-4, YAP-1 and cMET increased on group of incomplete tumour response. YAP-1 and Bcl-2 associated with poor RFS and YAP-1, VEGF and CLAUDIN-4 associated with poor CSS.	Akervall *et al*., 2014
Breast cancer	The prognosis of ER+ breast cancers can reliably discriminate by using Ki-67 and *p*53 together to ER, PR and HER2 in routine pathology immunohistochemistry.	Millar *et al*., 2011
HNSCC	In laryngeal carcinoma, CA9 hypoxia marker and COX-2 overexpression provide a stronger contribution to an increased risk of local recurrence after radiotherapy compared with the well-known candidate markers *p*53, Bcl-2, and cyclin D1.	Wildeman *et al*., 2009

These studies were searched based on the different markers used to study tumour response to radiotherapy.
Abbreviation: VEGF: vascular endothelial growth factor; YAP-1: Yes-associated protein; RFS: recurrence free survival; CSS: cause specific survival; ER: estrogen receptor; PR: progesterone receptor; DMFS: distant metastasis-free survival; BCSS: breast cancer-specific survival; CA9: carbonic anhydrase 9.

In the current study, consequently, the combined use of both proliferation and cell death markers is beneficial to understand the overall response of the individual tumour to irradiation. Overall, CK18-LI appears to be the best indicator of response to irradiation giving an expression level over the entire tissue section taking into account the proportion of tissue, which is represented by the tumour. The advantages and comparisons of early apoptotic quantification using IHC staining of M30 over the TUNEL assay were described by Kadyrov *et al*. (2001), and includes the limited reproducibility and low specificity of apoptosis detection using TUNEL. In current study, the CK18-LI and the percentage of cells positive to TUNEL assay were found different on each HNSCC tumour subjected to same irradiation treatment. However, the quantification methods on both analyses were different as the CK18-LI was assessed over entire tiled tissue section while TUNEL quantification was performed only on five high-power fields. In addition, the TUNEL assay detects all DNA strand breaks not only induced by irradiation, but also presented on cells in the process of DNA repair and gene transcription (Elmore, 2007). Therefore, the TUNEL assay quantification is necessary to be paired with another cell death assay, which has been demonstrated in current study.

It was hypothesised that following irradiation in tumours which were responsive to the gamma rays, there would be an increase in cell death and DNA repair mechanisms with a concurrent decrease in the proliferative capacity of the tumour cells. The relationships between CK18-LI, γH2AX, TUNEL, and Ki-67 levels on each tissue were evaluated and in some instances such as the irradiation of lymph node tissue metastasised from an unknown tumour (TR73), as expected there was a dose-dependent increase of fragmented DNA (TUNEL) and rise of CK18-LI with an accompanied reduction in Ki-67 expression. The elevation on cell death and the reduction in proliferation levels following almost all single-dose irradiation was also noticed on the TR84 and TR80 where a significant rise of cell death was detected (CK18-LI at 20Gy and TUNEL at 10Gy on TR84; CK18-LI and TUNEL at 15Gy on TR80) with simultaneous decrease in proliferation levels following irradiation. This confirmed the effects of irradiation in causing quiescence of tumour cells. Therefore, the tumours are predicted to be responsive to single-dose irradiation. In contrast, an oral cavity tumour (TR92) demonstrated opposing results in which no changes of CK18-LI, Ki-67 and fragmented DNA (TUNEL) levels were detected but a significant

rise of the retained γH2AX level was observed following irradiation. It is thought that the cells were undergoing the strand breaks repair and triggered cell cycle arrest but not through apoptotic pathway (Nijnik *et al*., 2007).

Nijnik *et al*. (2007) study used γH2AX foci analysis to examine the repair defect and residual repair capacity on mouse embryonic fibroblasts and on the cells with ligase IV defective characteristic, the foci were remained following 1Gy irradiation that represented the failure of DSBs repair. They have concluded that the reduced proliferation capacity is due to the failure in repairing DSBs, which possibly could explain the results obtained in this thesis where the reduced proliferation levels on some tumours could be because of the damage repair defects distinguished by the high γH2AX expression (Nijnik *et al*., 2007; Woodbine *et al*., 2011). Yet, different explanation was observed in Matthaios *et al*. (2012) study in which no significant association was observed between the γH2AX and the Ki-67 expressions across the 96 patients with non-small cell lung cancer (Matthaios *et al*., 2012). They claimed that the high γH2AX expression levels might indicate a more aggressive and highly proliferating tumour phenotype accumulating massive DNA defects. In a study carried out by Staszewski, Nikolova and Kaina (2008), the γH2AX level was significantly reduced in proliferation-compromised cells (low BrdU-labelled cells detected), illustrating that the γH2AX foci formation was replication dependent.

Since γH2AX foci formation also exist in apoptotic cells (Wang *et al*., 2011), it is crucial to determine whether the γH2AX signal induced in specific cells is due to DNA damage or apoptotic pathway. It has been shown that the phosphorylation of H2AX is not limited to DNA damage repair but might also be involved in the regulation of apoptosis (Lu *et al*., 2006). A recent study proposed by Ding *et al*., 2016 has examined the co-localization between the γH2AX and TUNEL staining in human peripheral blood lymphocytes post irradiation and demonstrated that the percentage of TUNEL-positive cells was similar to the percentage of γH2AX-positive cells following the same irradiation dose treatment. The γH2AX and TUNEL immunofluorescent staining on the same lymphocyte cell was accomplished which allowed the co-localised markers identification in studying the relationship of the two markers. Unfortunately, the identification has not been and could not be accomplished in current study, as the different tissue sections were used for γH2AX IHC and TUNEL immunofluorescent staining. Even though the serially cut tissue sections were used, however, the location

of the cells across serial sections changed which caused the staining identification of specific cells difficult.

It is well documented that not all patients respond in the same way to standard radiotherapy (Yaromina, Krause and Baumann, 2012). The development of personalised radiotherapy schedules backed up by evidence from individual experiments on a patient's own tumour is of high priority to further improve the tumour response analysis. The results of the current study have demonstrated that the microfluidic system can provide a platform for carrying out a range of different radiation treatments on individual patient tumours to understand the tumour. Yet, the application of more analytical methods and the development of screening assays in the current study would be beneficial to assist the tumour response study.

5.3.5 Comparison of the microfluidic *in vitro* results and patients' outcome

To achieve the aim of the current study, the *in vitro* results obtained in microfluidic-based approach were related with the patients' clinical outcomes. Over the five HNSCC tumours, one of them (TR84) was allowed to perform the comparison between microfluidic *in vitro* experiment and the clinical patient outcome, as this patient received solely radiotherapy while others received surgery or chemo-radiotherapy. This indicated the limitation of the current study in achieving the direct comparison particularly on the treatments/radiotherapy doses delivered between current project and clinical setting. To fully replicate the clinical radiotherapy setting in microfluidic-based approach, it becomes the major challenge in current project especially to maintain the tissue in microfluidic system under pseudo *in vivo* condition for up to 5-6 weeks which usually take up to 5 weeks to perform fractionated radiotherapy. The combination of chemotherapy, immunotherapy and radiotherapy could also be considered to treat HNSCC tumour samples in microfluidic device. The experiments in the current thesis demonstrate the potential for using microfluidic technology to maintain and investigate the responses of HNSCC tissue to treatment *ex vivo*, however, as there were limited numbers of multi-regional tissue pieces available, it is not possible to make conclusive statements comparing *in vivo* data with the clinical patient outcome. Therefore, the key parameters that need to be carefully considered for future studies include (i) the use of the freshly dissected tumour, (ii) to increase the number of replicates for a single-irradiation dose to assess tumour heterogeneity and

(iii) using tumour samples from the same HNSCC subsite and stage to reduce confounding variables.

In conclusion, out of the nine HNSCC tumours included in current microfluidic and irradiation study, only three tumours were successfully subjected to the quantification on BrdU-positive cells while the remaining six tumour tissues have given high background staining and no BrdU incorporation. This chapter demonstrated the superiority of using endogenous Ki-67 expression over BrdU-pulse labelling in measuring the post-irradiation proliferation level in HNSCC tissue. The quantification of Ki-67-positive cells was successfully carried out on the five HNSCC tumours to evaluate the proliferation levels between different irradiation treatments. The reduced proliferation and elevated cell death following irradiation treatment in microfluidic device suggested that the current microfluidic technology is able to assess the preclinical tumour response. Both cell death and proliferation analytical results suggested that the HNSCC patients respond differently to irradiation even in tumours from patients with the same HNSCC subsites, highlighting the need for personalised assessment of response. The microfluidic technique allows several tissues from each patient to be maintained on parallel microfluidic devices where different irradiation regimens can be delivered. It is essential that the inclusion of more tissue samples would be beneficial to draw a precise and accurate conclusion and the use of the patient samples who received radiotherapy only in current study would be favourable to evaluate and appreciate the effectiveness and mechanisms of irradiation to eliminate squamous cell carcinoma on patients.

6. Identification of changes in gene expression in response to on-chip irradiation

6.1. Introduction

HNSCC develops by progressing through a series of genetic alterations (Figure 1.2) which include the loss of heterozygosity and alterations of various oncogenes and/or tumour-suppressor genes (e.g. *p*16, *p*53 or Rb; section 1.1.1; Melle *et al*., 2003; Haddad and Shin 2008; Pai and Westra, 2009). In the last decade, although the molecular development of HNSCC has been investigated in detail, a better and more effective diagnosis or therapy has yet to be elucidated. The high morbidity rate of HNSCC, high tumour relapse and the failure of radiotherapy treatment on HNSCC could be due to the various alterations and mechanisms described in section 1.3.6 (Leethanakul *et al*., 2000). The lack of suitable markers for early tumour diagnosis and the non-responsiveness of tumour to anti-cancer therapy may also be an important contributing factor and the identification of predictive biomarkers is needed to realise the full potential of advances in radiotherapy (Leethanakul *et al*., 2000; CRUK, 2015). The non-responsiveness of the tumour is affected by the genetic variations acquired within the heterogeneity of the HNSCC tumours. Therefore, many researchers have been focussing on the genetic variations and the tumour progression by implementing genomic methods in parallel (Goldsworthy *et al*., 1999; Melle *et al*., 2003; Zhang *et al*., 2013; Martin *et al*., 2014; Mroz *et al*., 2015). The degree of intra-tumour genetic heterogeneity within a single tumour has been established and reported by Zhang *et al*. (2013) who performed whole-genome sequencing on three separate regions of an oropharyngeal SCC and two separate regions of cervical lymph nodes. Somatic point mutations and small somatic insertions and deletions were detected in at least one sample and the genomic characteristics of a single biopsy may not represent the entire mutational landscape of the HNSCC tumour due to the intra-tumour heterogeneity. The heterogeneity in gene expression within a tumour has widely been studied and the cancer hallmark genes, for example cyclins (Kronblad *et al*., 2003; Warenius *et al*., 2008), Ki-67 (Knutsvik *et al*., 2014), Bcl-2 (Barrans *et al*., 1995; Tsuchiya *et al*., 2015), RAS (Andreeff *et al*., 1986; Konishi *et al*., 1995) and EGFR (Bai *et al*., 2013; Francis *et al*., 2014) were frequently observed to be differentially expressed within a single tumour. The intra-tumour genetic heterogeneity on patients with HNSCC was also observed in various studies (Betts *et al*., 2013; Mroz *et al*., 2015).

Additionally, normal epithelial cell lining consists of only one or at most a few rows of cells whereas in a carcinoma, the epithelial cells are irregularly extended into the normal tissue forming a tumour mass (Figure 6.1; Melle *et al*., 2003). The impact of ionising radiation on tumour cells were further compounded by the irregular distribution and heterogeneity characteristics of the tumour across the biopsy (Leethanakul *et al*., 2000; Mikulowska-Mennis *et al*., 2002; Zhang *et al*., 2013). In addition, a tissue biopsy consists of a heterogeneous population of extracellular material and the measurement of such materials can result in misleading molecular data (Mikulowska-mennis *et al*., 2002). The analysis of gene expression by harvesting bulk tissue or manually microdissecting the tissue, therefore, might not be the most representative to determine response to treatment.

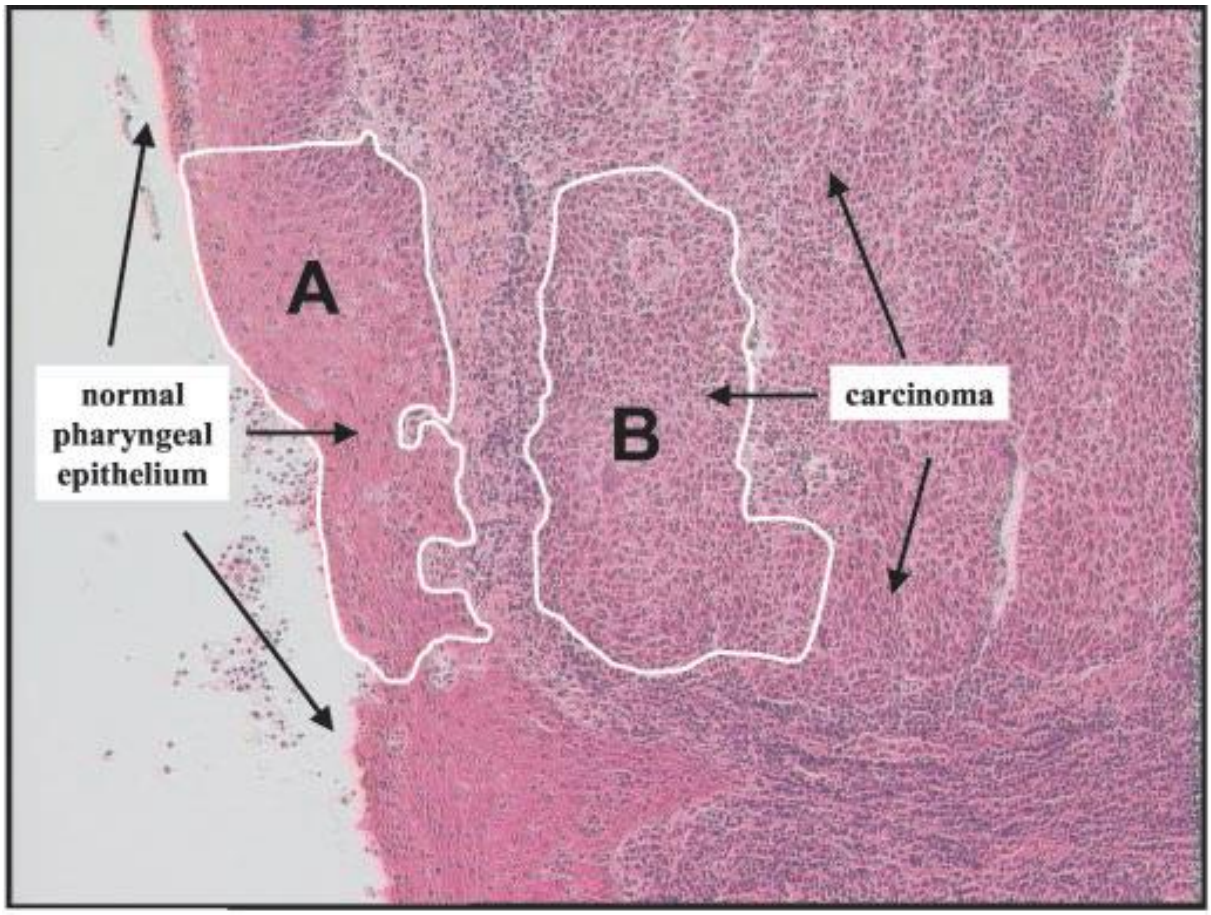


Figure 6.1. H&E staining of a head and neck tumour tissue section.
The course of the laser cuts during microdissection was demonstrated in white lines around (A) normal pharyngeal epithelium and (B) carcinoma (Melle *et al*., 2003).

A method used to try and ensure that only tumour is being analysed for changes in expression is laser microdissection, where the cancer epithelial cells are isolated from other surrounding tissue elements (Curran *et al*., 2000; Mikulowska-Mennis *et al*., 2002; Melle *et al*., 2003; Morrogh *et al*., 2007).

6.1.1. Laser Capture Microdissection (LCM)

LCM is a technique which allows the selective isolation of individual cells or groups of cells from histological samples (Morrogh *et al*., 2007). It is a powerful method in isolating and obtaining specified cells from complex tissue for downstream analysis of their RNA, DNA or protein content (Curran *et al*., 2000; Mikulowska-Mennis *et al*., 2002). The principle of LCM is simple in which a tissue section, usually mounted on membrane glass slides and stained with haematoxylin and eosin for identification of areas of interest (Datta *et al*., 2015), is placed on the stage of the specially designed microscope and the area of interest is selected, a pulsed laser is then used to cut around the particular area (Micke *et al*., 2005). The physical mechanism for such laser beam mechanism is known as photofragmentation which transforms the biological material into atoms and which can be propelled at supersonic velocities. The laser energy is then used to 'catapult' the cells detaching from the tissue section and allow the collection of cells leaving the adjacent cells, nucleic acids and proteins fully intact (Frost *et al*., 2001; Micke *et al*., 2005).

The technique can be implemented to collect thousands of cells within a few minutes, with speed, precision and versatility on frozen tissue sections or formalin fixed, paraffin embedded sections, and it causes no apparent alteration to the morphology of the selected cells which can be directly visualised following microdissection (Fend and Raffeld, 1999; Curran *et al*., 2000; Cummings *et al*., 2011; Datta *et al*., 2015). As this method is a 'no touch' technique, the morphology of the captured cells and the residual tissue is well preserved. In addition, the isolated cells are catapulted in to a collection cap and the risk of tissue loss is minimised, this is in contrast with some microdissection techniques that require the removal of the targeted cells with the help of a needle tip or a microcapillary (Datta *et al*., 2015). Due to the speed of acquisition and the minimal destruction of tissue morphology, multiple areas can be collected sequentially from the same slide, for example both neoplastic and adjacent normal cells can be collected with subsequent, simultaneous, evaluation of gene expression of multiple genes (van't Veer, Paik and Hayes, 2005).

The limitations of using LCM include the potential of the tissue to dry out due to the lack of mounting medium and coverslip leading to degradation in tissue morphology (Datta *et al*., 2015). Another problem that sometimes occurs in LCM is the failure to catapult the laser-cut cells from the slide due to the lack of adherence of the cells to

the membrane (Datta *et al*., 2015). The insufficient adherence is possibly because of the incomplete tissue dehydration or too low laser setting in achieving complete section cut.

The mode of preparation of the tissue sections prior to LCM is critical for getting reliable downstream molecular analyses and in producing meaningful results (Curran *et al*., 2000). For example, the effects of crosslinking fixatives (e.g. aldehydes) and the precipitative fixatives (e.g. ethanol and acetone) on subsequent RNA extraction and amplification from the microdissected tissues all have to be taken into concern. In addition, the quality of the amplification products from frozen tissue is greater than that from paraffin embedded tissue with the amplification of the DNA from formalin fixed tissue being restricted to below 268 base-pair whereas the DNA from frozen tissue samples was amplified up to 1327 base-pair (Maitra *et al*., 1999). However, despite these drawbacks, high speed, good precision, ease of use and efficient handling make LCM an ideal tool for the rapid collection of large amounts of tissue or the pooling of larger numbers of single cells.

6.1.2. Gene expression in response to irradiation

Quantitative real time PCR was used in the current study in order to measure quantitatively the expression of genes on dissected HNSCC samples which were subjected to no microfluidics (pre-MF), microfluidic only control (MF) and microfluidic culture with on-chip irradiation (5Gy, 10Gy, 15Gy, and 20Gy). Based on previous gene expression studies which have looked at radiation response markers to measure effects of radiotherapy on HNSCC tumour, six genes were selected (Table 2.6 and Table 4.1). All these markers were selected carefully based on numerous literature reviews on HNSCC responses against ionising radiation. The genes studied included those involved in DNA repair mechanisms, apoptotic cell death, and cell cycle checkpoints. The expression of ATM, BAX, CDKN1A, ERCC1, XRCC1 and H2AFX genes between pre-MF, microfluidic control and irradiated tissues was measured and analysed.

Ataxia telangiectasia mutated (ATM)

The protein encoded by the ATM gene is an important cell cycle checkpoint kinase which phosphorylates a number of targets and regulates a wide variety of downstream proteins, such as tumour suppressor proteins *p*53 and BRCA1 (Gatei *et al*., 2000), checkpoint kinase Chk2 (Bartek and Lukas, 2003), checkpoint proteins Rad17 and

Rad9, and DNA repair protein NBS1 (Zou *et al*., 2008). It is a member of the PI3/PI4-kinase family and plays an important role in the phosphorylation of H2AX as part of the DNA damage response (Kitagawa and Kastan, 2005; Shiloh *et al*., 2013). It also has a role in cell cycle arrest, apoptosis and senescence (Liang *et al*., 2009).

ATM is present in an inactive dimer form in unstressed cells each monomer of which is made up of two active sites: a kinase domain and a focal adhesion targeting (FAT) domain (Figure 6.2; Kitagawa and Kastan, 2005; Elias *et al*., 2014). Both monomers are bound via a region surrounding Serine 1981, located within the FAT domain. The FAT domain is a region of about 500 amino acids which is conserved among members of the PI3K family of proteins (Bosotti *et al*., 2000; Kitagawa and Kastan, 2005). The kinase domain is blocked by its binding to the internal serine at position 1982 residue (Ser-1982) and when a cell is exposed to stress agents such as ionising radiation or cytotoxic drugs, ATM undergoes rapid intermolecular autophosphorylation on Ser-1981 causing the dissociation of the ATM homodimer (Kitagawa and Kastan, 2005). This intermolecular autophosphorylation event does not directly regulate the activity of the kinase, but in disrupting the ATM oligomers, the accessibility of substrates to the ATM kinase domain is increased leading to activation of the ATM kinase activity (Bakkenist and Kastan, 2003).

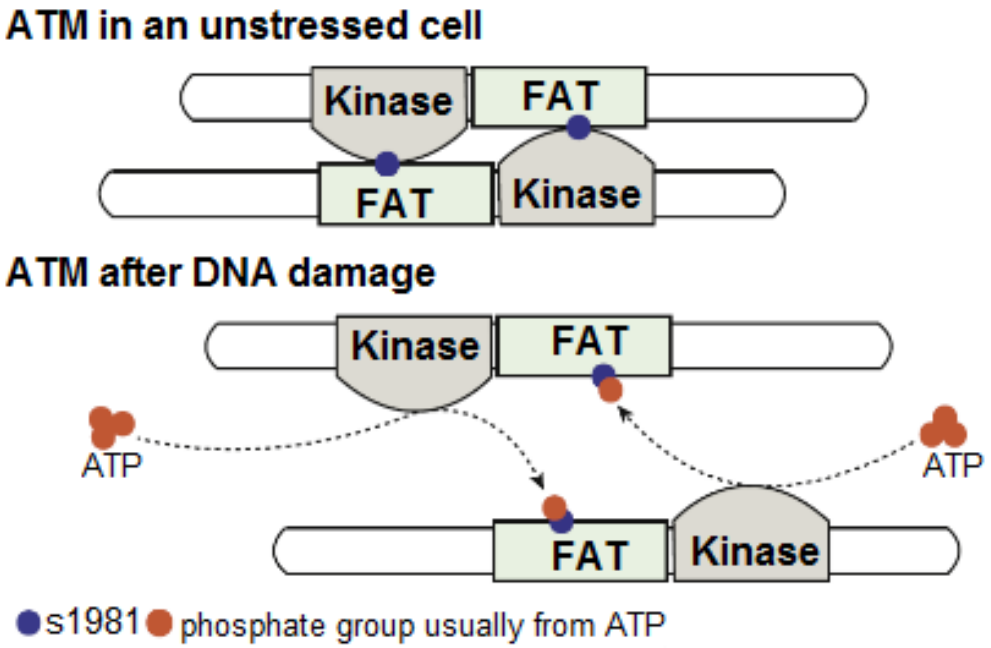


Figure 6.2. Homodimer form of ATM in unstressed cells (top) and the activation of ATM following DNA damage (Bottom).
Auto-phosphorylation of ATM at Ser-1981 occurs rapidly following exposure of cells to stress agents, causing dimer dissociation and ATM activation (Elias *et al*., 2014).
Abbreviation: ATM: ataxia telangiectasia mutated, FAT: focal adhesion targeting, ATP: adenosine triphosphate, s1981: serine 1981.

Bakkenist and Kastan (2003) showed that the ATM activation is not dependent on the direct binding of ATM to the DNA-DSBs site, but is based on the DNA damage that rapidly causes the changes in the chromatin structure. The alteration of the higher-order chromatin structure in turn induces a conformational change in ATM that leads to the autophosphorylation event on ATM (Bakkenist and Kastan, 2003). The active monomers are then free to migrate to and phosphorylate substrates of downstream signalling pathways such as Nbs1 and *p*53 which both in turn stimulate cell-cycle arrests (Bakkenist and Kastan, 2003; Shiloh *et al*., 2013). For example, phosphorylated *p*53 participates in G_1 checkpoints while Nbs1 is involved in S-phase checkpoints, blocking the cell cycle (Wu *et al*., 2000; Maya *et al*., 2001; Bakkenist and Kastan, 2003; Elias *et al*., 2014).

The expression level of ATM has been widely studied in relation to prognosis following different therapeutic treatments. For example, downregulation of ATM gene expression has been reported to contribute to poor outcome in laryngeal and pharyngeal cancers (Lee *et al*., 2011). The poor prognosis caused by loss of ATM has also been observed in pancreatic (Kim *et al*., 2014), colorectal (Beggs *et al*., 2012) and breast cancer (Ye *et al*., 2007; Bueno *et al*., 2014).

Apoptotic regulator BAX (Bcl-2-associated X protein)

The mitochondrial pathway of apoptosis is regulated by the Bcl-2 protein family and the protein members are subdivided into anti- or pro-apoptotic regulators. Bcl-2-associated X (BAX) protein is a 21kDa protein, predominantly located in cytoplasm that serves as an apoptotic activator (Wolter *et al*., 1997; Goping *et al*., 1998; Westphal *et al*., 2011). During apoptosis, BAX translocates from the cytosol to the mitochondrial membrane and interacts with mitochondrial voltage-dependent anion channels (VDAC; Goping *et al*., 1998; Pawlowski and Kraft, 2000; Suen *et al*., 2008). These interactions cause the loss of the mitochondrial membrane potential and induces the release of cytochrome c and the following apoptotic cell death.

The associations between BAX expression, apoptotic cell death and patient prognosis, therefore, are of interest in many studies investigating biological rationale of radiotherapy resistance. For example, in pre-treated 102 patients with oral squamous cell carcinoma Bose *et al*., (2012) showed that 85.7% had high expression of BAX which was associated with significantly improved 5-year disease-specific-survival following radiotherapy, in agreement with previous studies on the same tumour type

(Xie *et al*., 2000) which demonstrated that patients with high BAX expression had a better prognosis and better disease-specific-survival following radiotherapy. In addition, upregulation of the BAX gene has also been shown to offer greater therapeutic efficacy to various chemotherapeutic agents, measured by body weight, tumour volume and tumour regression in nude mice bearing HNSCC xenografts (Guo *et al*., 2000).

Cyclin dependent kinase inhibitor 1A (CDKN1A; p21)

CDKN1A is a gene encoding the cyclin dependent kinase inhibitor *p*21 and is dysregulated (downregulated or overexpressed) in most human cancers as its expression can act as a tumour suppressor or oncogene (Abbas and Dutta, 2009). *p*21 belongs to the Cip and Kip family of cyclin-dependent kinase (CDK) inhibitors. Serving as a negative regulator of the cell cycle, *p*21-mediated growth inhibition depends on two non-overlapping structural domains: the carboxyl-terminal proliferating cell nuclear antigen (PCNA)-binding domain and the amino-terminal CDK-cyclin inhibitory domain. *p*21 binds and inhibits the kinase activity of CDK-cyclin complexes, leading to the cell growth arrest (Besson *et al*., 2008; Abbas and Dutta, 2009). In addition, as a result of binding to PCNA through the carboxyl-terminal domain, *p*21 inhibits replication by blocking activity of PCNA to stimulate polymerases (e.g. DNA polymerase- δ) that are needed for DNA synthesis (Gartel and Tyner, 2002; Moldovan, Pfander and Jentsch, 2007; Abbas and Dutta, 2009).

However, contrary to the tumour suppressor role *p*21 has also been shown to play a role in suppressing apoptosis. The anti-apoptotic function of *p*21 stems from its ability to inhibit the release of cytochrome c from mitochondria and to inhibit the proteins involved in the induction of apoptosis, such as caspase 3, 8, 9, and 10 (section 1.3.2), stress-activated protein kinases (SAPKs) and apoptosis signal-regulating kinase 1 (ASK1; Asada *et al*., 1999; Xu and El-Deiry, 2000; Gartel and Tyner, 2002; Abbas and Dutta, 2009). It also mediates the upregulation of the genes encoding factors involved in anti-apoptotic activities, such as galectin-3, prosaposin, superoxide dismutase 2 (SOD2) and related RAS protein (R-Ras; Chang *et al*., 2000). All of the physiological responses induced by *p*21 are interconnected (Abbas and Dutta, 2009). The cell cycle arrest triggered by *p*21 promotes DNA damage repair by allowing sufficient time for the damaged DNA to be repaired prior its passage to the daughter cells. The cell cycle

arrest is a major route by which the *p*21 exerts its anti-apoptotic activities and the cellular senescence is regulated by the altered gene expression induced by *p*21.

The expression of *p*21 in relation to cell death has therefore been evaluated by various studies. Significant correlation was observed between overexpression of *p*21 and increased locoregional tumour relapse and poor overall survival in HNSCC tumours treated with surgery or radiotherapy (Fischer *et al*., 2011). In addition, the 2-year survival rate of HNSCC patients with positive *p*21 expression was found to be lower (56.81%) than that of those with negative *p*21 expression (90.90%) in Sadaf *et al.* (2015), indicating that *p*21 has a potential to be a prognostic marker in HNSCC.

Excision repair cross-complementing group 1 (ERCC1)

The ERCC1 gene encodes a protein that functions in the nucleotide excision repair (NER) and DNA inter-strand crosslinks (ICL) repair pathways and is required for the repair of DNA lesions induced by, for example, UV light or cisplatin (Stur *et al*., 2015). This protein forms a heterodimer with the xeroderma pigmentosum group F (XPF) endonuclease (also known as ERCC4), and the heterodimer catalyzes the 5' incision in the process of excising the DNA lesion, which is essential for NER, ICL repair and DSB repair (Figure 6.3; Vaezi *et al*., 2011).

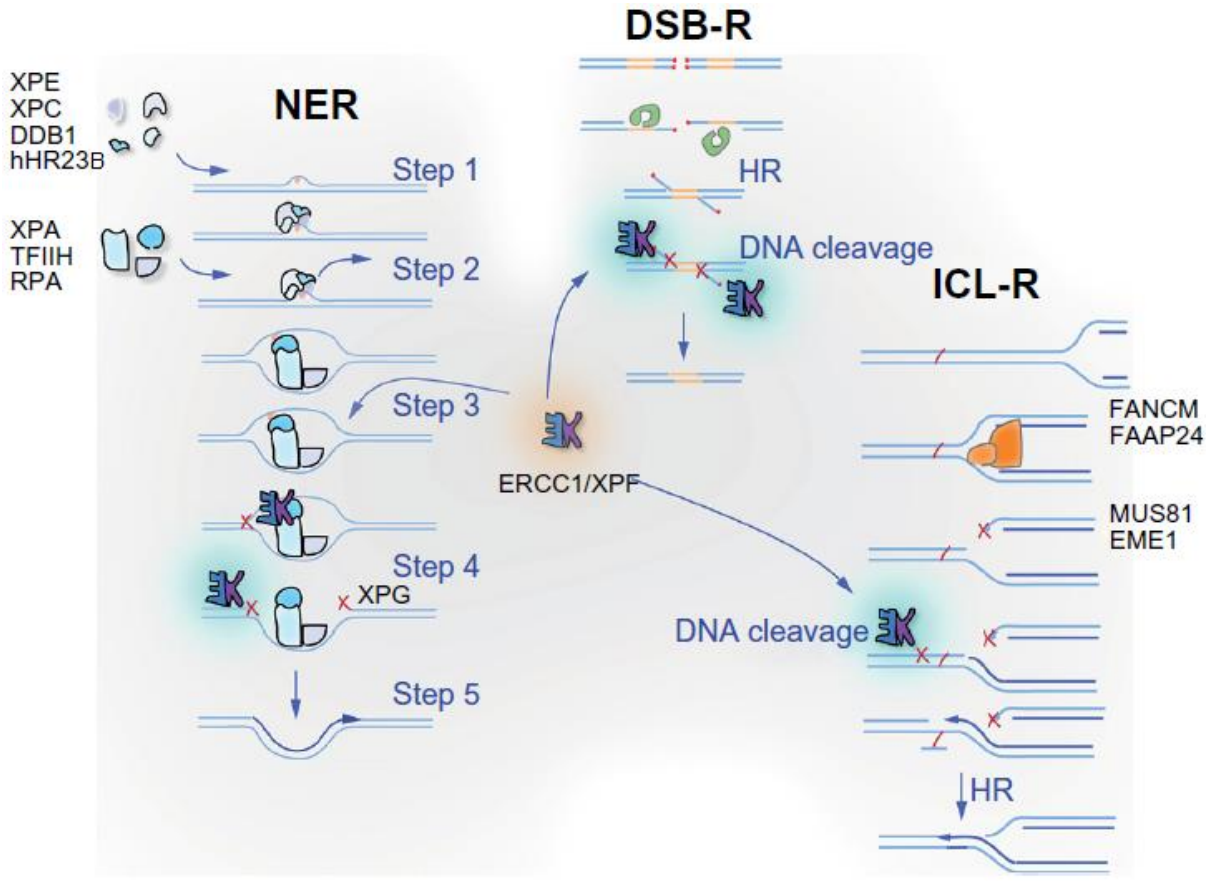


Figure 6.3. The role of ERCC1 and its binding partner XPF in nucleotide excision repair (NER) (shown on the left), double-strand breaks (shown in the middle) and ICL repair (represented on the right).

The ERCC1-XPF heterodimer endonuclease cuts one strand of DNA at the double-strand-single-strand junction which is critical for the three repair pathways. In NER, ERCC1-XPF is recruited by XPA and cuts the damaged strand 5' to the lesion (Step 3) while TFIIH recruits XPG as a second endonuclease to cut the 3' of the lesion (Step 4), leaving the damaged base to be removed as part of a single-stranded oligonucleotide and the incision is repaired (Step 5). In DSB repair, two DNA ends are spliced together in which the ERCC1-XPF functions to remove 3' single-stranded flaps at the ends of the breaks to allow the sealing of the spliced ends. ICLs are predominantly repaired during S-phase of the cell cycle when absolute block to replication is induced by ICLs. When the lesion is detected, the replication fork is collapsed and DSBs are created. The DSB cannot be repaired until ERCC1-XPF splices to release it from one strand, allowing bypass of the adduct by a translesion polymerase (Vaezi *et al.*, 2011).

Abbreviation: XPE: xeroderma pigmentosum group E, XPC: xeroderma pigmentosum group C, DDB1: DNA damage-binding protein 1, hHR23B: human Rad23 homolog, XPA: xeroderma pigmentosum group A, TFIIH: transcription factor II Human, RPA: replication protein A, XPG: xeroderma pigmentosum group G, XPF: xeroderma pigmentosum group F, HR: homologous recombination, FANCM: Fanconi anemia complementation group M, FAAP24: Fanconi Anemia Core Complex Associated Protein 24 and EME1: essential Meiotic Structure-Specific Endonuclease 1.

The DNA lesions induced by chemotherapy (for example by cisplatin) or radiotherapy can affect one strand of DNA (intra-strand crosslinks) or both strands (ICL) and are repaired by NER and ICL repair pathways, respectively (Köberle *et al*., 2010; Vaezi *et al*., 2011; Zhang and Walter, 2014). The ERCC1-XPF heterodimer is critical for both NER and the ICL repair pathways as it is the only enzyme required for the removal of the lesions. Therefore, a reduced expression level of ERCC1-XPF has been reported

to mediate increased susceptibility to chemo-radiation and has been found to be associated with improved therapeutic outcome in various tumour types, including non-small cell lung cancers (Vaezi *et al*., 2011), locally advanced nasopharyngeal cancer (Zhang *et al*., 2014), locally advanced cervical squamous cell carcinoma (Bai *et al*., 2012) and locally advanced HNSCC (Jun *et al*., 2008; Ciaparrone *et al*., 2015).

H2AFX (H2A histone family, member X)

H2AFX mRNA consists of 1594 base pairs that encodes a replication-independent histone that is a member of the histone H2A family. The encoded replication-independent histone is important in transcription regulation, DNA repair, DNA replication and chromosomal stability. The distal chromosomal loss of 11q leads to a diminished DNA damage response in HNSCC and cell lines which was measured by the decrease in the size and number of phosphorylated-H2AX foci (Parikh *et al*., 2007). The copy number loss of H2AFX was found to be associated with reduced γH2AX focus formation in response to radiation-induced DSBs, chromosomal instability and reduced sensitivity to ionising radiation (Parikh *et al*., 2007; Sankunny *et al*., 2014). With a similar principle of the expression to γH2AX (section 4.1.3), the expression of H2AFX mRNA offers a reliable and sensitive method to quantify radiation-induced DNA-DSBs (Sankunny *et al*., 2014).

X-ray repair complementing defective repair in Chinese hamster cells 1 (XRCC1)

The protein encoded by the XRCC1 gene is involved in the repair of DNA single-strand breaks (SSBs) and oxidative DNA damage induced by ionizing radiation or alkylating agents (Okano *et al*., 2005; Vaezi *et al*., 2011). XRCC1 does not possess enzymatic activity but acts as a critical scaffold protein for base excision repair (BER) and SSB repair (Figure 6.4; Vaezi *et al*., 2011; Wei *et al*., 2013). It interacts with DNA ligase III, polymerase beta and poly (ADP-ribose) polymerase which participate in BER pathways (Okano *et al*., 2005) whereas in recognising SSBs, XRCC1 interacts closely with Poly (ADP-Ribose) Polymerase 1 (PARP1; Figure 6.4; Reynolds *et al*., 2015). Similar to ERCC1, a reduced expression level of XRCC1 in cancer patients has been shown to be associated with a higher susceptibility to chemoradiation and better survival (Ang *et al*., 2011; Vaezi *et al*., 2011; Wu *et al*., 2014). Cells which lack XRCC1 are proposed to be hypersensitive to ionising radiation, oxidative stress and alkylating agents (Caldecott, 2003; Brem and Hall, 2005).

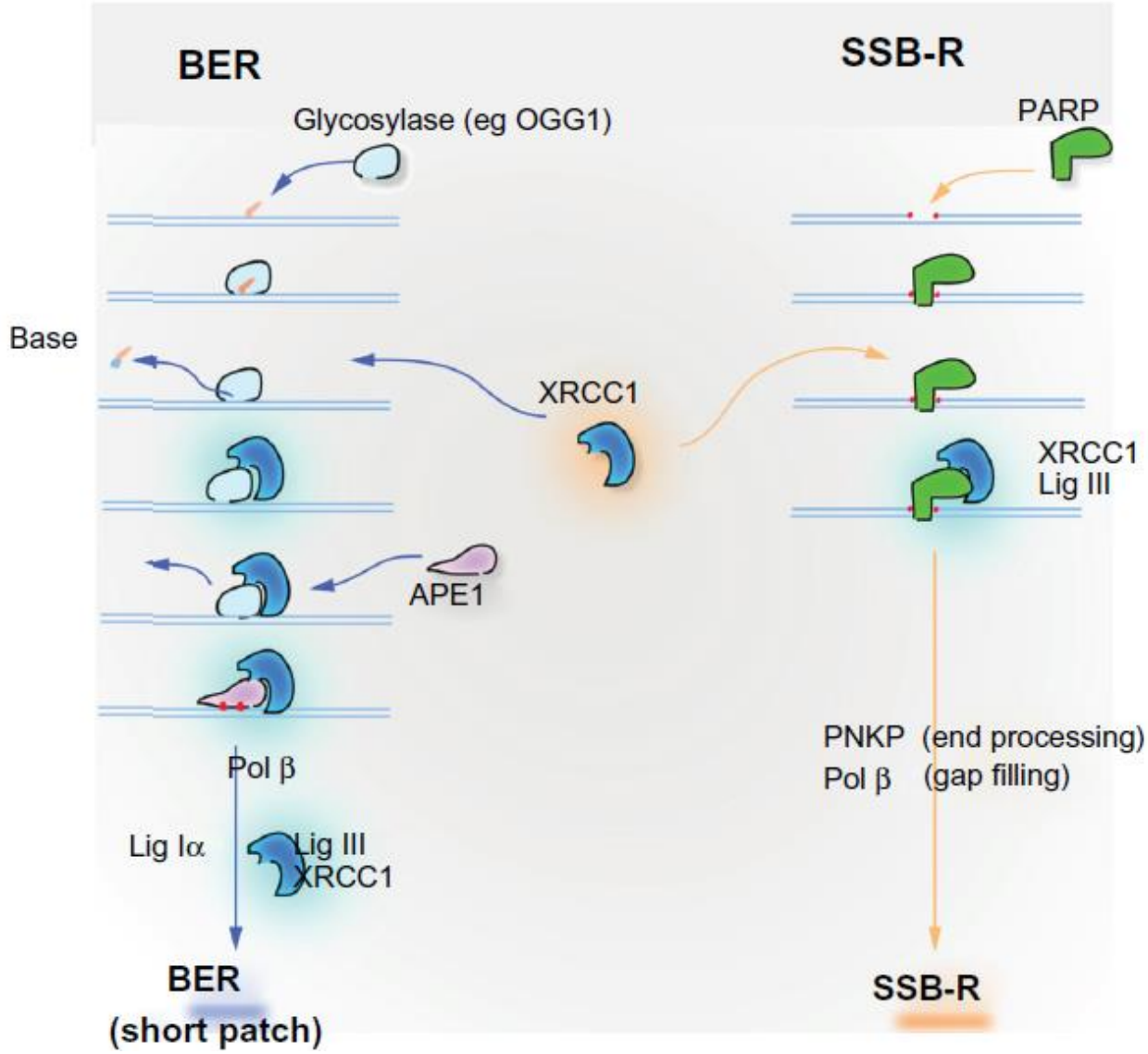


Figure 6.4. Functions of XRCC1 in base excision repair (BER) of small oxidative lesions and a related mechanism for the repair of single-strand breaks (SSB-R), both caused by ionising radiation.

Oxidative damage and alkylation cause modifications of DNA bases that are then repaired by the BER pathway while SSB is mainly induced by irradiation. XRCC1 serves as a scaffold protein which is recruited to the damage site by glycosylase in BER (shown on left) or by PARP1 which binds the newly created SSB (shown on right). XRCC1 forms a complex with LIGIII (the ligase that seals the SSB repair intermediate to complete BER). The SSBs are detected by PARP1 which recruits XRCC1-LIGIII to repair the lesions. PNKP removes the 3′ phosphate groups that block the DNA ligation by LIGIII. Polβ is required to replace the missing nucleotides at the break site (Vaezi *et al*., 2011).

Abbreviation: OGG1: 8-oxoguanine glycosylase, APE1: apurinic/apyrimidinic (AP) endonuclease, Polβ: DNA polymerase β, Lig Iα: ligase Iα, Lig III: ligase III, PARP: poly (ADP-ribose) polymerase, and PNKP: polynucleotide kinase 3'-phosphatase.

In this chapter, by using the powerful technique of LCM to extract genetic material from defined tumour cells, the levels and variation of these six gene expression on HNSCC tissues are aimed to be evaluated in order to study the effects of microfluidic tissue culture as well as the on-chip irradiation treatment on these gene expressions.

6.2. Measuring the effects of section fixation, H&E staining and LCM technique on the RNA level and subsequent PCR products

6.2.1. Material and methods

The effects of section fixation, H&E staining and the LCM technique on the RNA levels were evaluated on a pre-microfluidic tissue of metastatic lymph neck node from an oropharyngeal tonsil tumour (TR54). Tissue was cryosectioned (section 2.7) onto precooled (-20ºC) polyethylene naphthalate (PEN) membrane glass slide (section 2.13.2). RNA was extracted from three differently prepared samples of tissue: firstly, four tissue sections on membrane slide, were fixed in ice-cold 70% ethanol before being scrapped from the slide and directly lysed for RNA extraction (section 2.14; Table 6.1; Sample 1). A further four tissue sections were fixed and H&E stained (section 2.13.1) before being scrapped off from slide and subjected to RNA extraction without being laser-capture microdissected (Table 6.1; Sample 2). Finally, three tissue sections were fixed, H&E-stained and the tumour area (according to serially stained sections of cytokeratin; section 2.13.1) was laser-capture microdissected into 350µL of RLT lysis buffer in a collection tube cap, achieving $45x10^5 \mu m^2$ of tumour area (Table 6.1; Sample 3). The tissue lysates obtained from these 3 samples were all subjected to RNA extraction (section 2.14) and the RNA level was measured using the nanodrop lite spectrophotometer before they were subjected to cDNA synthesis (section 2.15.1).

The expression of GAPDH gene was evaluated using standard PCR reaction as GAPDH is one of the most common housekeeping genes due to its stability and high level expression in most tissues and cells (Barber *et al*., 2005). The expression of GAPDH gene was initially assessed in order to confirm the presence of RNA on frozen pre-MF HNSCC tissue. Each concentration of cDNA was subjected to a PCR reaction for 35 cycles, by mixing the diluted cDNA with BioMix buffer, and forward and reverse primer pairs complementary to GAPDH gene (section 2.15.2). Water was used instead of cDNA as a no template control (Table 6.1; Sample 4). The PCR products and the DNA ladder were then loaded onto agarose gel for electrophoresis to determine and visualise the presence of PCR amplification products (section 2.15.2).

Table 6.1. Samples of TR54 tumour subjected to different procedures of section fixation, H&E staining and LCM process.

Sample No.	RNA input (ng) in 9µL	Number of sections	Fixation	H&E Staining	LCM
1	72.72	4	**+**	**-**	**-**
2	23.76	4	**+**	**+**	**-**
3	10.208	3; 45x10^{5}µm^2	**+**	**+**	**+**
4	No-template negative control (water only)				

LCM: laser capture microdissection.

6.2.2. Standard PCR results on fixed, H&E stained and LCM processed tissue sections

The three samples which were subjected to different processes before RNA extraction showed positive bands between 200bp and 400bp of the DNA ladder band, indicating the presence of the GAPDH amplified gene products (Figure 6.5). No band was observed in the no-amplification control. The positive results of the PCR gene amplification following the tissue section manipulation also suggested that the tissue section fixation using ice-cold 70% ethanol, H&E staining and LCM processes (described in section 2.13.1) could be carried out with the preservation of the RNA level.

A

Lane number	1	2	3	4
RNA Input (ng) in 9µL	72.72	23.76	10.208	Negative control (Water)
Number of sections; Section area	4	4	3; 45x105µm2	
Fixation	+	+	+	
Staining	-	+	+	
LCM	-	-	+	

B

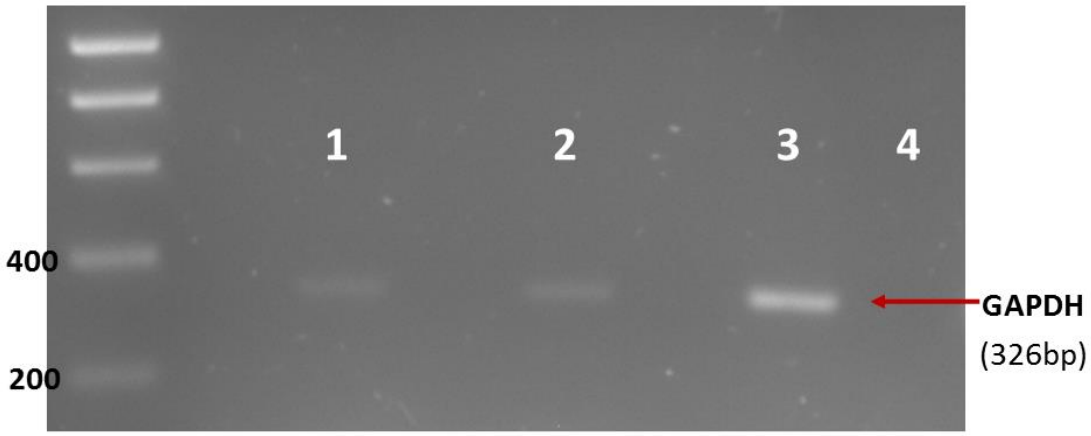


Figure 6.5. Gel electrophoresis results of standard PCR on GAPDH gene on the RNA extracts of three different processes.

(A) A table to show the different methods of section preparation prior to RNA extraction from TR54 (n=1 repeat was done on each of the three procedures). (B) The RNA extracts of the three samples were subjected to qRT-PCR of GAPDH gene and the products (326bp) identified by gel electrophoresis (Lane 1, 2 and 3). Lane 4 was no-amplification control.

6.3. Creation of standard curve of gene expression versus starting RNA/cDNA input using quantitative real-time PCR

6.3.1. Material and methods

The minimum amount of RNA and complementary DNA (cDNA) required for downstream quantitative real-time PCR (qRT-PCR) of β2-microglobulin (B2M) gene was first determined by plotting the standard curve of mean CT value versus RNA/cDNA input. Similar with the GAPDH gene, B2M was used in quantitative real-time RT-PCR as this gene is a commonly used housekeeping genes for normalization and showed constant and stable expression cellular plating density, oxygen partial pressure and hormonal stimulation (Baddela *et al*., 2014).

A pre-microfluidic sample of metastatic lymph neck node tissue (TR54; 10mg) was thawed, vortexed in RLT lysis buffer for 30s and incubated for 30 minutes prior to RNA extraction (section 2.14). Following RNA extraction, 1µL of the RNA was used to measure concentration while the remaining samples was stored immediately at -20ºC. The concentration of RNA from the lymph node tissue as measured by a nanodrop lite spectrophotometer was 320ng/µL with a total of 4160ng in 13µL of extract. By assuming 100% transcription efficiency, 1µL of the extract, containing 320ng of RNA, was reverse transcribed using the iScript advanced cDNA synthesis kit (section 2.15.1) to produce 320ng of cDNA in 20µL. The synthesised cDNA products were stored at -20ºC for PCR and quantitative real-time (qRT-PCR) procedures.

The 320ng of cDNA was diluted to 32ng of cDNA before further serial dilution, in triplicates, from 32ng to 0.5ng in a final volume of 20µL (Figure 6.6). The diluted cDNA was subjected to qRT-PCR analysis against the housekeeping gene B2M using TaqMan Fast Advanced Master Mix and the StepOnePlus system (section 2.15.3). A no reverse transcription (-RT) control was included by serially diluting 320ng RNA (no RT control) insert, to ensure amplification was only from expressed genes and not genomic DNA. The cDNA and RNA samples were added to a microamp fast 96-well reaction plate (Figure 6.6) alongside a no template control (NTC) which contained DEPC-treated sterile water instead of RNA or cDNA. The mean cycle threshold (C_T) of the triplicate samples for each DNA concentration was determined and the standard curve of mean C_T versus the logarithm of cDNA input was plotted.

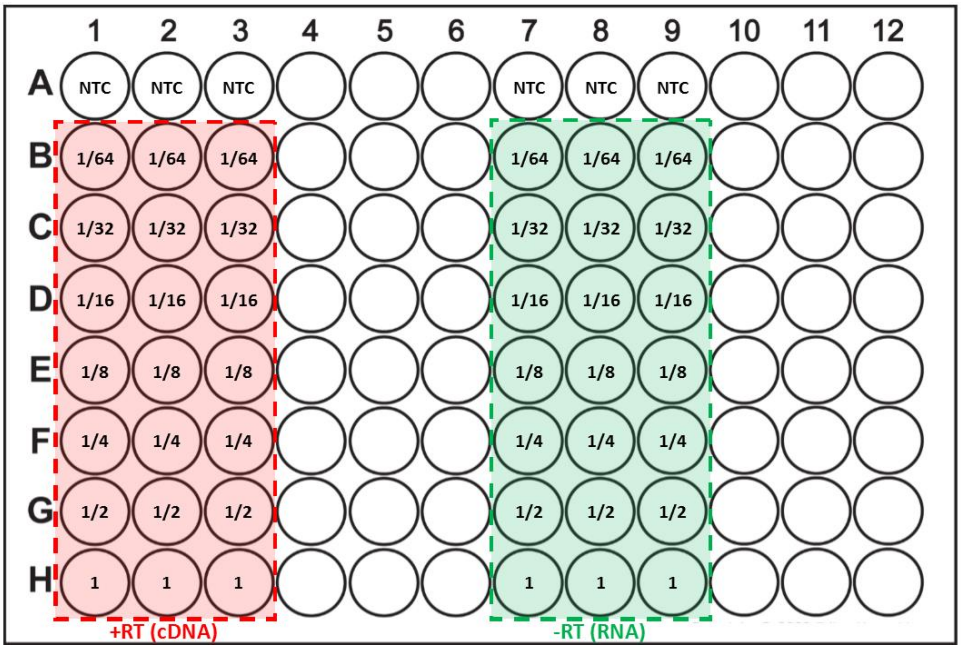


Figure 6.6. Layout of qRT-PCR for detection of the housekeeping gene B2M on a microamp fast 96-well reaction plate using serially diluted cDNA samples (32ng input).
No template control (NTC) wells loaded with sterile water only in the qRT-PCR reaction. +RT represents the samples that were reverse transcribed while the –RT samples were the RNA which was not reverse transcribed.

The ability of the qRT-PCR to amplify picogram amounts of RNA which are obtained from a laser-capture microdissected samples was further evaluated by diluting the cDNA from 2000pg to 1pg. The samples were then subjected to qRT-PCR for B2M (in triplicates) using the procedure described previously and the layout of the 96-well reaction plate as shown in Figure 6.7.

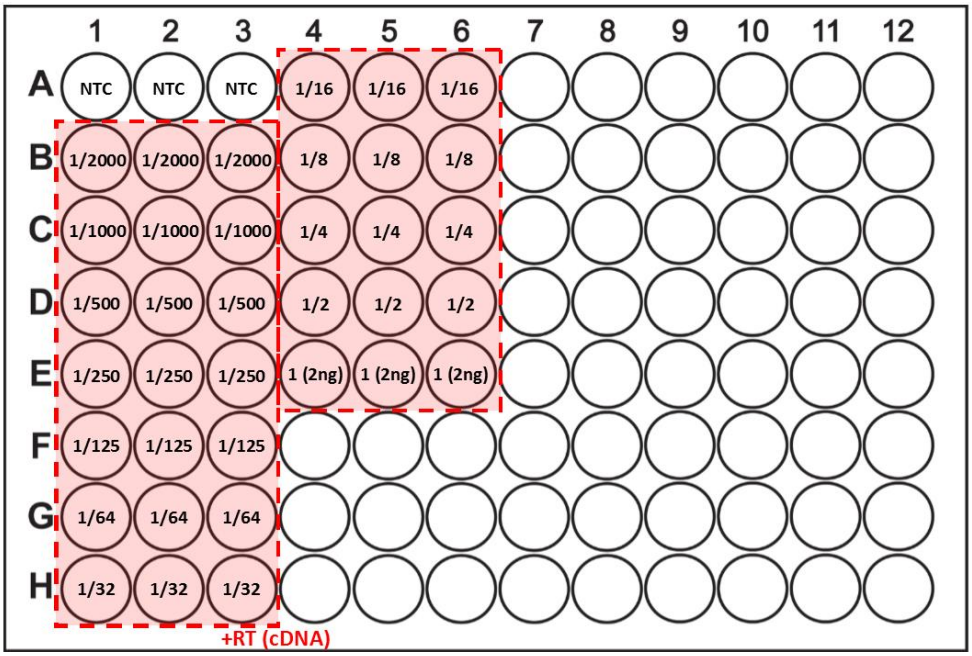
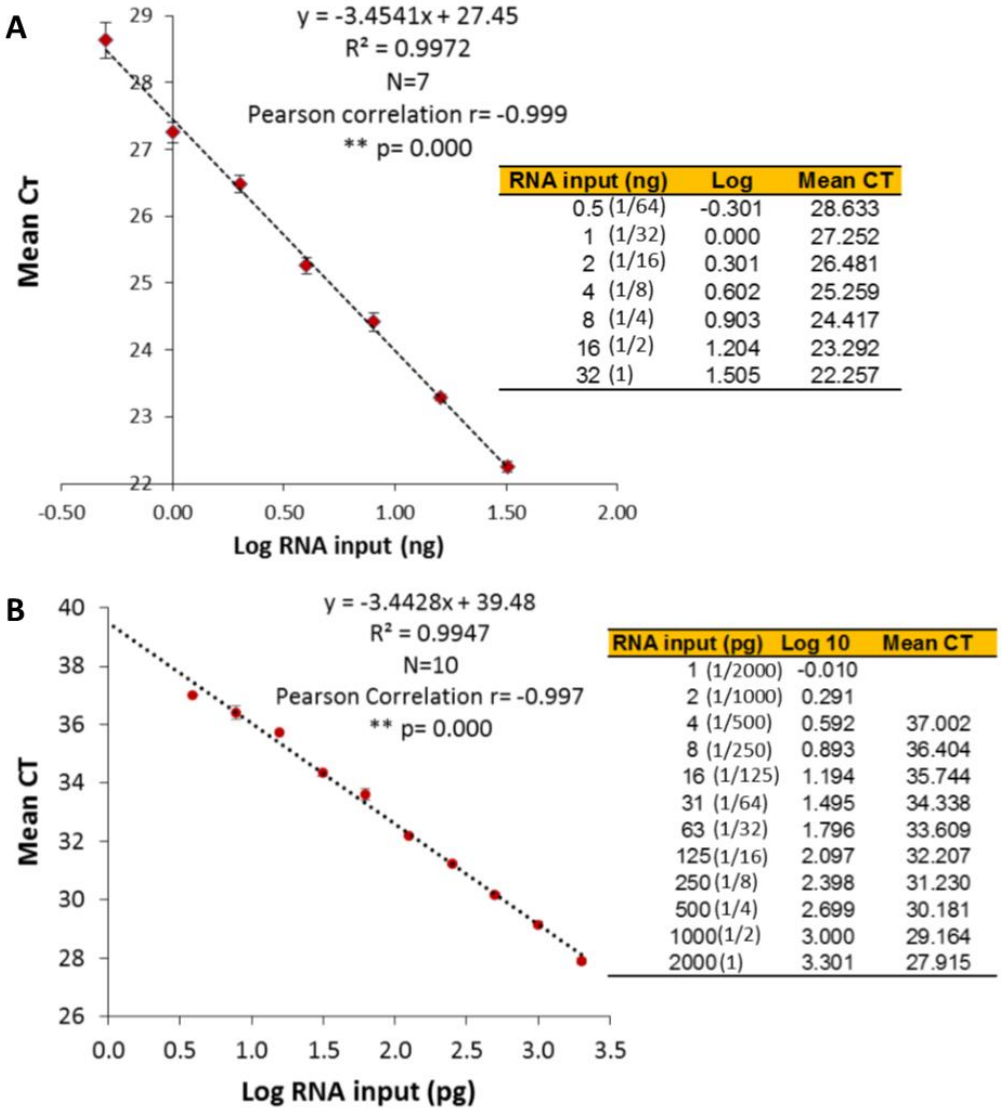


Figure 6.7. Layout of the microamp fast 96-well reaction plate used in the qRT-PCR of the B2M gene using serially diluted cDNA samples (2000pg input).
No template control (NTC) wells loaded with sterile water only in the qRT-PCR reaction. +RT represents the samples that were reverse transcribed.

6.3.2. Quantitative RT-PCR results of B2M gene on serially diluted cDNA insert

A serial dilution (from 32ng) of the cDNA insert was carried out and the resulting cDNA was subjected to B2M gene amplification using qRT-PCR. As expected the mean C_T decreased with increasing amount of cDNA with a significant Pearson's correlation (Figure 6.8. A). Following further dilutions of the cDNA input from 2000pg, it was determined that the minimum amount of cDNA input that could be amplified was 4pg which gave a mean CT of 37 (Figure 6.8. B). The NTC and the –RT control demonstrated no amplification with no increase on the ΔRn confirming that amplification was from the cDNA only (Figure 6.9). qRT-PCR on the HNSCC tissue samples utilised at least 4pg of RNA/cDNA insert in each reaction.



RNA input (ng)	Log	Mean CT
0.5 (1/64)	-0.301	28.633
1 (1/32)	0.000	27.252
2 (1/16)	0.301	26.481
4 (1/8)	0.602	25.259
8 (1/4)	0.903	24.417
16 (1/2)	1.204	23.292
32 (1)	1.505	22.257

RNA input (pg)	Log 10	Mean CT
1 (1/2000)	-0.010	
2 (1/1000)	0.291	
4 (1/500)	0.592	37.002
8 (1/250)	0.893	36.404
16 (1/125)	1.194	35.744
31 (1/64)	1.495	34.338
63 (1/32)	1.796	33.609
125 (1/16)	2.097	32.207
250 (1/8)	2.398	31.230
500 (1/4)	2.699	30.181
1000 (1/2)	3.000	29.164
2000 (1)	3.301	27.915

Figure 6.8. Standard curve of mean CT versus log RNA input on serially diluted RNA samples extracted from the pre-microfluidic metastatic lymph node sample (TR54).
(A) Up to 1/64 dilution of RNA input (32ng) and (B) up to 1/2000 dilution of RNA input (2000pg). ** indicates significant results on Pearson correlation ($p<0.01$). One repeat was performed on each curve.

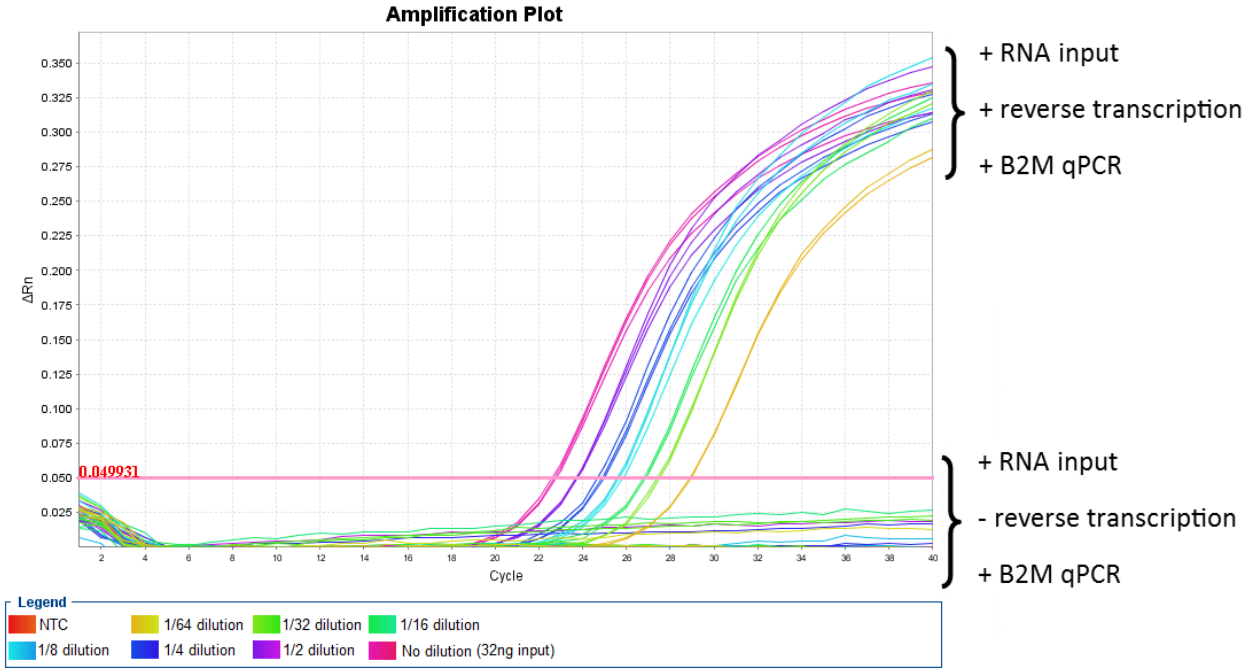


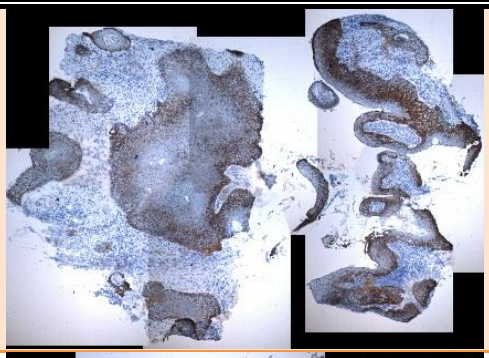
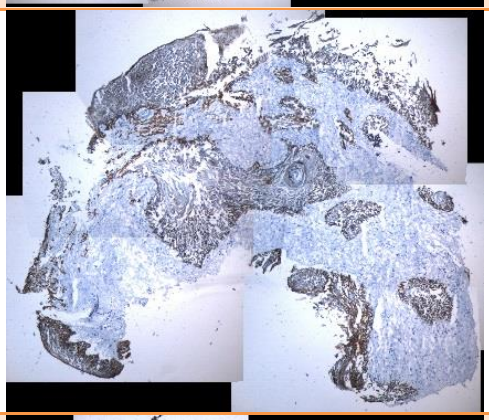
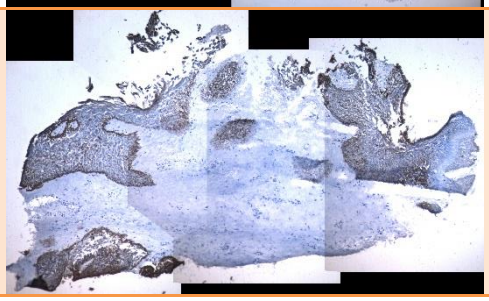
Figure 6.9. Representative of amplification plot of B2M gene expression ΔRn between positive samples (serially diluted sample of 32ng input) and negative control samples that were not reverse transcribed.

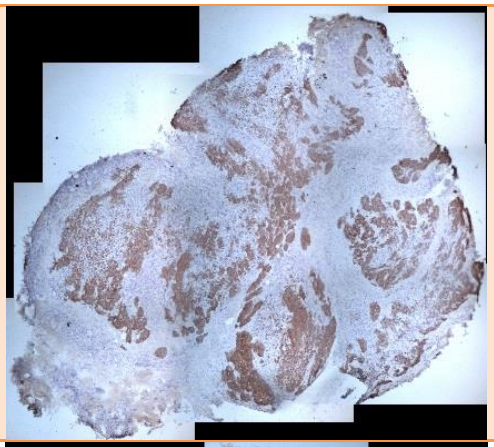
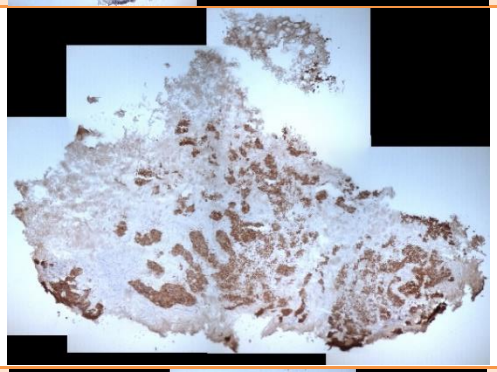
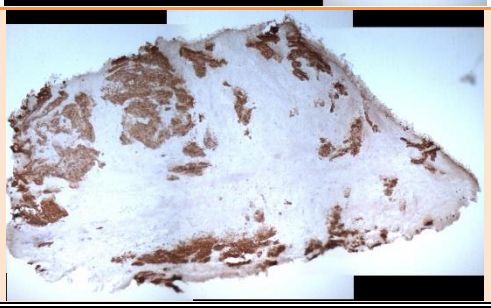
6.4. Quantitative RT-PCR of ATM, BAX, CDKN1A, ERCC1, H2AFX and XRCC1 genes

6.4.1. Material and methods

An oral cavity floor of mouth tumour (TR92) tissue and a metastatic lymph node tissue from a laryngeal tumour (TR80) were included in this qRT-PCR gene expression study. Both primary tumour and lymph node tissue were selected based on the availability of the corresponding tissues which were subjected to non-irradiation and single-dose irradiation as more than 10 tissue sections of each tissue were required for LCM and qPCR works. Both the pre-microfluidic (Pre-MF) tissue and microfluidic tissue, which was maintained in the device without irradiation, from the two tumours was sectioned, fixed, H&E stained and the tumour area was microdissected (section 2.13.1). The malignant epithelial cells were carefully selected with the guidance of IHC staining of CK, which reduces the chance of selecting non-cancerous cells (section 2.13.1), however, the heterogeneity of the tumour tissue itself cannot be avoided. To circumvent this, several areas of tumour across the section were captured and combined in the same tube for downstream RNA extraction in these initial experiments. The total area of the tissue sections captured using LCM was recorded (Figure 6.2). The RNA was extracted from the tissue lysate and reverse transcribed (section 2.14 and 2.15) before ATM, BAX, CDKN1A, ERCC1, H2AFX, and XRCC1 were amplified using specific primers in a qRT-PCR (section 2.14.3). The amount of cDNA from the oral cavity tumour subjected to the qRT-PCR was 0.35ng/20µL whereas the amount of cDNA from the TR80 was 0.745ng/20µL. In overall, there were two qRT-PCR plates/experiments carried out for gene expression experiment: one consists of four tissue samples of the oral cavity tumour (pre-MF, 0Gy, 15Gy and 20Gy irradiated tissues and another plate consists of three tissues of lymph node tumour (pre-MF, 0Gy and 15Gy irradiated tissues). The amplification of the six genes on each sample was analysed in triplicates. A non-template control (DEPC-treated sterile water) was included for each of the six genes. The mean C_T of the triplicates was obtained and the standard error of mean (SEM) was calculated.

Table 6.2. The HNSCC tissues that were subjected to LCM and qRT-PCR for ATM, BAX, CDKN1A, ERCC1, H2AFX and XRCC1 genes.

HNSCC tumour	Treatments	IHC staining of CK on serial section	Total tissue area harvested in LCM
Oral cavity floor of mouth tumour (TR92)	Pre-MF		$6.73x10^6 \mu m^2$
	0Gy		$1.58x10^7 \mu m^2$
	15Gy		$2.85x10^7 \mu m^2$
	20Gy		$3.62x10^7 \mu m^2$

Lymph neck node metastasised from laryngeal tumour (TR80)	Pre-MF		$1.05x10^7 \mu m^2$
	0Gy		$2.10x10^7 \mu m^2$
	15Gy		$1.69x10^7 \mu m^2$

The total area of the tissue section accumulated and harvested in the LCM process was recorded. Brown area indicates the positive CK IHC staining, representing the tumour cells which were microdissected in LCM.

6.4.2. Quantitative RT-PCR results of six genes related to radiation response on HNSCC tumours

The amount of total RNA obtained and the total area of microdissected tissue sections taken from TR92 and TR80 were measured and summarised in Figure 6.10. Interestingly, the 15Gy- and 20Gy-irradiated TR92 tissues yielded less RNA, (11 and 7ng respectively), compared with the corresponding pre-MF and tissue maintained in the microfluidic device without irradiation (0Gy) even though the starting area of tissue was greater. The pre-MF tissues produced the most RNA from both HNSCC samples compared with the corresponding tissues subjected to microfluidic culture (0Gy) and irradiation treatments, again despite having the smallest starting tissue area.

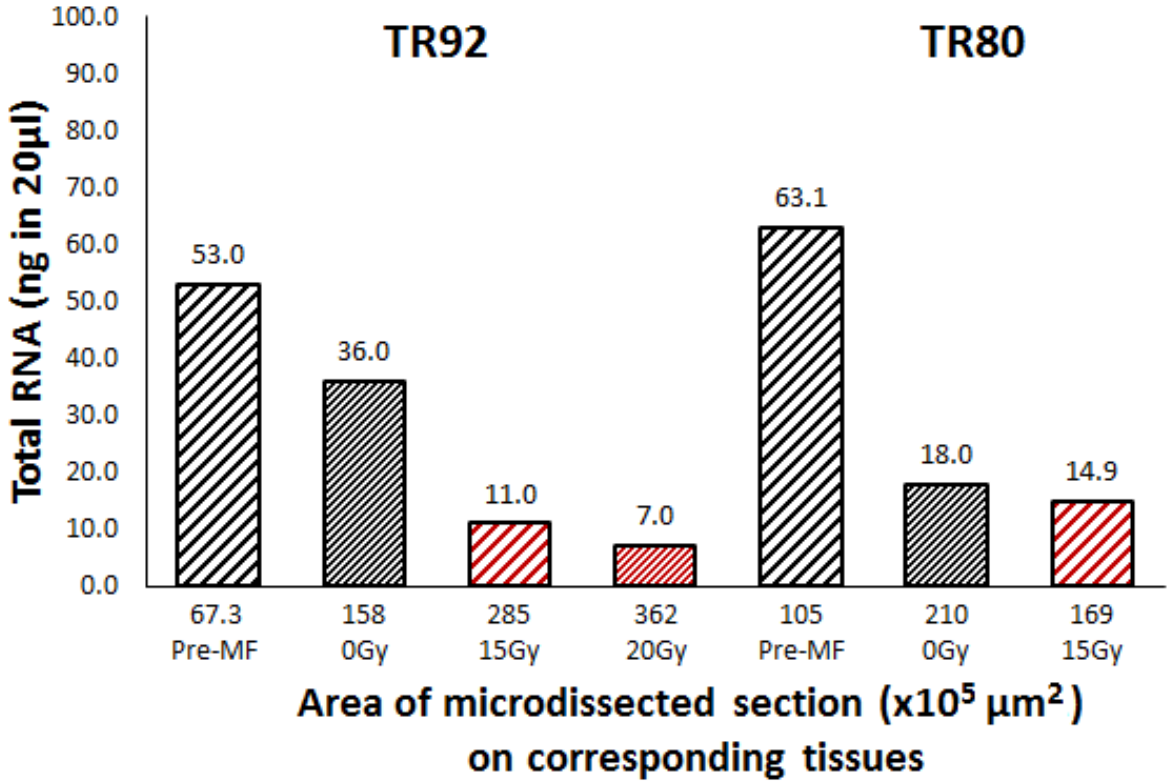


Figure 6.10. The amount of total RNA (ng) obtained from TR92 and TR80 subjected to different treatments.
The area of starting microdissected tissue sections (x10^5 µm^2) on the corresponding tissues which were subjected to different on-chip treatment is shown on the x-axis.

In order to assess the feasibility of using LCM to harvest tumour cells from HNSCC tissues, the expression of 7 genes (reference gene B2M, ATM, BAX, CDKN1A, ERCC1, H2AFX, and XRCC1 genes) was evaluated on the pre-microfluidic tissues, microfluidic-cultured tissues (0Gy) and the microfluidic-cultured tissues treated with irradiation using qRT-PCR. The 15Gy and 20Gy irradiated tissues of TR92 and 15Gy irradiated lymph node (TR80) were selected and analysed based on the expression

results observed in Chapter 4 and 5 (Ki-67, γH2AX, CK18-LI and TUNEL markers) which showed significant effects following the corresponding irradiation on-chip treatment. However, not all of the genes were expressed (no amplification) and the expression of the genes was detected inconsistent on both tumours (result was presented in appendix section 9.12/Figure 9.13).

6.5. Discussion

The previous chapters described the heterogeneous features of HNSCC tumour and the inter-tumour variation of the tissue response to irradiation. The aim of this chapter was to evaluate whether LCM and qRT-PCR could be used to identify changes in gene expression in tumour cells in response to irradiation under microfluidic-based approach.

6.5.1. Sensitivity of TaqMan gene expression assay on serially diluted cDNA input

The serial dilution of the RNA/cDNA demonstrated that amounts as small as 4pg in 20µL total volume (0.2pg/µL) could be amplified by both standard and qRT-PCR, representing the sensitivity of the reverse transcription and the TaqMan qRT-PCR. In a product bulletin published in Thermo Fisher Scientific Product Bulletin (2014), the concentration of cDNA, as low as 2pg in 20µL total volume (0.1pg/µL), was able to be amplified with 34.34 C_T value on the B2M TaqMan® Gene Expression Assay using TaqMan® fast advanced master mix (Thermo Fisher Scientific, 2014). Although the high sensitive TaqMan® Gene Expression Assay was not presented in the current study in which the cDNA concentration of 2pg in 20µL was not amplified, however, the current results were still in agreement with the range of cDNA input allowance (1pg to 100ng) suggested by the manufacturer (TaqMan ® Fast Advanced Master Mix Protocol; AB Applied Biosystems). This showed the minimum extracted value of RNA which could be used in the qRT-PCR experiments in the author's hands. However, these extractions were obtained from the entire HNSCC tissue section containing various different cell types. The aim was to identify changes in gene expression in the tumour epithelial cells. In order to do this, the capability of extraction of RNA from laser-capture microdissected tissue had to be evaluated.

6.5.2. The presence of RNA on fixed, H&E stained and LCM processed tissue sections

LCM involves various upstream procedures including tissue collection, cryosectioning and staining. Various studies have been established to compared different tissue handling and sample preparation methodologies for LCM (Cummings *et al*., 2011; Liu *et al*, 2013; Kolijn and van Leenders, 2016). To handle snap-frozen tissue, a similar protocol was carried out in current study and the study published by Erickson *et al.* (2009) and Liu *et al.* (2013) in which the frozen tissues were kept at -80ºC until cryostat sectioning without thawing the tissues. Additionally, the morphological staining on tissue was carried out one by one for each LCM sample which agreed with the described optimal procedure (Erickson *et al.*, 2009; Liu *et al.*, 2013).

The majority of these steps prior to RNA extraction are routinely carried out at room temperature leading to a deleterious effect on the RNA due to the action of RNases (Yee *et al*., 2014). RNases are found in all cell types and organisms as well as in all standard laboratory settings including in the reagents used, the local environment and human contact. Yee *et al*. (2014) used rat renal proximal tubular cells to optimise H&E staining procedures for the production of quality RNA. The optimisation involved the shortening of the staining procedure from 26-minutes to 5-minutes in order to minimise the RNA degradation. The RNA integrity, which was measured as RNA integrity number (RIN) by using Agilent 2100 Bioanalyzer 7.0, was evaluated in the optimisation and the shortened H&E protocol was found adequate for the identification of rat renal cells in which the shortened protocol produced merely 1 RIN less than that of the tissue subjected to no staining (Yee *et al*., 2014). In terms of the optimal morphological staining prior LCM, although fast/shorten H&E staining is the most popular staining method for LCM on tissue specimens (Erickson *et al*., 2009; Liu *et al*, 2013; Yee *et al*., 2014), the use of an alcohol-based cresyl violet stain has also been shown suitable for the isolation of high quality RNA with minimal RNA degradation (Cummings *et al*., 2011; Kolijn and van Leenders, 2016).

In the current study, a 5-minute H&E staining protocol was enlisted and the amount of RNA measured from the H&E-stained sample was 23.8ng which was approximately three times lower than that of the unstained samples (72.7ng). This suggested that the short staining procedure still incurred a loss amount of RNA, agreeing with the reduction of RNA integrity observed in Yee *et al*. (2014). Even though the RNA level

was reduced by the H&E staining and the RNA integrity was not measured in current study, the RNA extracted from the H&E stained sample was still able to be reversed transcribed and be amplified (GAPDH gene) using standard PCR. Further, the use of LCM carried out following tissue fixation and H&E staining reduced the RNA level further to 10.2ng. Surprisingly however, the band produced corresponding to the GAPDH gene, following electrophoresis, was the brightest compared with the samples which had not undergone LCM. However, the three different protocols were performed only once without additional repeats on the same tissue. Therefore, additional repeats are beneficial in order to fully determine the effects of individual tissue processing step on the amount of RNA presented for the downstream gene expression assay. In addition, to evaluate the effects of each handling step on the RNA quality, the RNA integrity of the microdissected samples can be measured by using sensitive Agilent Bioanalyzer in future which is able measure picograms of RNA material (Kolijn and van Leenders, 2016).

The number of cells needed and the area of sections harvested during LCM for successful gene expression by PCR have been reported by various studies which used different human tissues (Wang *et al*., 2009; Morrison, Bailey and Kulesa, 2012; Braakman *et al*., 2011). The expression of approximately 300 genes using qRT-PCR has been described from as few as 10 cells harvested by LCM in chick embryo tissue (Morrison, Bailey and Kulesa, 2012) while in the LCM of breast cancer tissues, a total area of about 500,000μm^2 on the breast tissue was collected by repeating the microdissection (Braakman *et al*., 2011). It is therefore crucial to have a protocol specifically optimised for HNSCC in determining the relationship between amount of microdissected tissue area and the amount of RNA extracted by the end. As a result, the amount of tissue section microdissected from all the LCM procedures was recorded for comparison with the corresponding measured total RNA level.

When B2M gene expression was evaluated using qRT-PCR, the RNA of the tissues with an area within the range 50-360 x 10^5 μm^2 was quantifiable and could be amplified. It was expected that when the total area of catapulted tissue sections was increased, the total RNA obtained would increase, however the opposite was observed where the RNA level decreased with increasing amount of tissue being microdissected. This could be explained by the fact that although all the LCM procedure was carried out as short as within 1 hour, however, each sample was

subjected to different time lengths of the LCM in order to achieve larger tissue area of microdissection, possibly resulting in different amounts of RNA loss. In addition, the morphology of different tissues and the heterogeneous variability of tumour on each HNSCC tissue could contribute to the variation of time taken for LCM (longer time was used to harvest heavily scattered tumour cells across section), the total tissue area that could be microdissected and ultimately resulting in different amounts of RNA. This indeed emphasised the need of standardisation on the RNA and cDNA insert prior to PCR in order to achieve direct comparison between samples.

6.5.3. LCM and gene expression study on HNSCC tumour response to irradiation under microfluidic-based approach

The combination of LCM and subsequent mRNA expression analysis using quantitative RT-PCR has been used successfully to investigate HNSCC molecular pathogenesis and to identify tissue-specific biomarkers (Leethanakul *et al*., 2000; Malhotra *et al*., 2004; Facchinetti *et al*., 2010; Knauer *et al*., 2013). The analysis of the BIRC5 survivin mutation has been studied by Knauer *et al*. (2013) who used a laser beam to mark the HNSCC tumour cells that showed a prominent nuclear staining for survivin which were then catapulted into a vessel using a laser pulse. The results showed that the inactivation of the nuclear export signal on survivin correlated with an increased chemotherapy response seen in HNSCC cancer patients. The expression of other genes, such as methylation variable positions (MVPs; Lechner *et al*., 2013) and sphingosine kinase-1 (sphk1; Facchinetti *et al*., 2010), have also been studied using real-time PCR performed on LCM HNSCC samples. In Malhotra *et al*. (2004) study, the thickness of 8µm of frozen HNSCC tumour tissue sections were subjected to H&E staining prior to LCM and in the LCM process, they microdissected approximately 2000-3000 tumour cells (approximately 250,000 to 375,000µm^3) from the frozen section and the expression of vascular endothelial growth factor (VEGF) was assessed using real-time reverse transcriptase PCR (TaqMan). The authors showed that the microdissection of this amount of tumour cells was able to obtain sufficient amount of RNA for downstream gene expression reaction. In the Malhotra study, however, the microdissected tissue area was far smaller than that used in the current study which used relatively large areas of tissue; 50-360 x 10^5 µm^2. This may indicate that the RNA in the HNSCC tissues was affected or destroyed to certain extent possibly by all the processes involved prior to RNA extraction. In contrast to the current study, all of these studies have used frozen/fixed tissue biopsies directly after surgery

(Leethanakul *et al*., 2000; Malhotra *et al*., 2004; Facchinetti *et al*., 2010; Knauer *et al*., 2012) whereas the current study maintained tissue samples in the microfluidic device before being frozen, sectioned, fixed, stained and subjected to LCM. The low level of RNA obtained, therefore, could possibly due to the long exposure of the tissue to RNase-unprotected environment throughout the process of tissue freeze-thawing, slicing and handling in laminar flow cabinet for microfluidic set-up, microfluidics perfusion flow, ionising radiation, embedding and snap-freezing, tissue cryo-sectioning, H&E staining and LCM. To improve the technique, the entire tissue handling procedures, which started at the point tumour samples resected from the patients until the time the RNA extracted, should be ensured and subjected to RNase-free environment to preserve RNA.

The aim of the current study was to determine feasibility of this methodology to identify changes in expression of six radiation response genes (ATM, BAX, CDKN1A, ERCC1, H2AFX and XRCC1) following irradiation treatment on the tissue maintained in microfluidic device. The use of a housekeeping gene is needed to normalise mRNA expression levels between different treated samples (Silver *et al*., 2006). Unfortunately, the expression level of the B2M control genes used in this chapter varied among the two tissues. Therefore, the selection of housekeeping genes is critical for the gene expression studies. Although various studies have suggested that the use of B2M gene as a suitable housekeeping gene (Honorato *et al*., 2008; Lallemant *et al*., 2009), but contrary results was obtained by several studies in which the B2M gene was shown unsuitable for internal reference gene (Silver *et al*., 2006; Nihon-Yanagi *et al*., 2013).

The results indicated that the expression of the B2M gene expression was not positive gene on all the tissues of both the oral cavity tumour and lymph node tumour (TR92 and TR80), agreeing with Silver *et al* (2006) study which showed large deviation and variation of B2M ΔCt values across 31 reticulocyte samples. The lack of B2M meant that the normalisation of mRNA level could not be performed in this project and as a results the up- or downregulation of the six genes between non-irradiated and irradiated HNSCC tissues could not be determined to study the tumour response to irradiation in lymph node tumour. Other more suitable and stable housekeeping genes should be tested and evaluated in future for further gene expression studies, e.g. beta-

actin 2 (Casadei *et al*., 2011), GAPDH (Silver *et al*., 2006) and TATA-box binding protein (Lessa *et al*., 2013; Baddela *et al*., 2014).

The method of multi-region tumour sampling, carried out in Jamal-Hanjani *et al*. (2015) study, has been implemented in the current microfluidic experiments, aiming to minimise the influences of heterogeneity. However, it is practically challenging to set up large numbers of devices for multi-regional tumour samples in parallel, given that one device only can accommodate one tissue. The time restraints on the current project only allowed for a single tissue to be cultured, irradiated, sectioned, stained, laser capture microdissected and RNA extracted before qRT-PCR. If more time had been available, a greater number of repeats for each treatment group would have been analysed to allow average values to have been calculated. Since the time between the end of tissue culture in microfluidic device to the RNA extraction post-LCM could be up to 6 hours (depends on the number of sections and amount of tumour cells per section), there is high tendency for the RNA to be degraded by RNases (Yee *et al*., 2014). Therefore, tissue manipulation prior to LCM requires optimisation in order to maximise the RNA integrity within the HNSCC tissue. The low levels of LDH measured throughout microfluidic maintenance of the tissue (section 4.10), inferring cell survival, suggest that it is more likely to be procedural issues leading to RNA loss rather than cell death. However, RNA extraction from the whole lump of tissue immediately post-microfluidic culture could have helped with this verification.

6.5.4. Future work of LCM and qRT-PCR for genomic study

The LCM technique appears to be an effective tool to isolate specific cells from a mixed and heterogeneous population under microscopic visualisation, allowing efficient and accurate results with downstream genomic applications such as qRT-PCR, Sanger sequencing and next-generation sequencing (NGS; Lovendorf *et al*., 2015). It is well known that tumour samples are diverse repertoires of cells with heterogeneity at the morphological and genetic level and consist of non-uniform microenvironment compartments which impose significant obstacles for effective tumour control and clinical development of molecularly targeted agents (Jamal-Hanjani *et al*., 2015; Zardavas *et al*., 2015).

Many approaches have been used in order to overcome the issue of heterogeneity, such as multiregional tumour sampling, serial tumour sampling, pooling of biopsies from a single tumour and detection of circulating cell-free DNA (Jamal-Hanjani *et al*.,

2015; Joung *et al*., 2016). The multi-regional analysis using advanced sequencing technologies, for example NGS, has the potential to reduce the variability due to biopsies taken from a single region (Joung *et al*., 2016). For example, a study carried out by Jamal-Hanjani *et al*. (2015) demonstrated multiregional tumour sampling on four patients with non-small-cell-lung-cancer (NSCLC) and subjected the samples (n=11) to multi-regional whole-exome sequencing (WES) followed by ion AmpliSeq deep-sequencing validation. Both inter- and intra-tumour heterogeneity were detected in which the identified somatic mutations were different across the three regions tested. The single-nucleotide variants detected in each region were then selected for sequencing using multiplexed PCR and NGS (mPCR-NGS) where PCR primers were designed to amplify the genomic DNA and sequence the PCR products. Both WES and mPCR-NGS methods could be utilised in the future following microfluidic maintenance, on-chip irradiation and laser capture microdissection to allow more extensive exploration of the mutational landscape of HNSCC.

In conclusion, TaqMan ® fast advance gene expression analysis used in the current study allowed the sensitive detection of small amounts of RNA/cDNA input. Following the tissue processing protocols and multiple LCM processes on a single tissue, the amount of extracted RNA was sufficient for qRT-PCR reactions that includes B2M housekeeping gene and the six genes with triplicates on each gene. Additional optimisation and comparison works on different tissue processing and LCM procedures are required to maximise the preservation of precious RNA obtained from the microfluidic-cultured and irradiated tissue. Further validation of B2M housekeeping gene or determination of other suitable housekeeping genes for qRT-PCR analyse is urgently needed which could be used to represent the preservation of RNA integrity in the tissue following different treatment in microfluidics and to achieve complete gene expression comparison. More optimisation works and tissue repeats on the LCM technique and the gene expression analysis using HNSCC tissues subjected to microfluidic culture and irradiation treatment are urgently required, in order to accomplish the gene expression comparison between the control and treated samples. This chapter provides a promising avenue in the current research in exploring additional analytical methods on the HNSCC tissues that were subjected to microfluidics and irradiation treatments.

7. Final discussion and conclusion

7.1. Advantages of microfluidic platform for human tissue maintenance and on-chip irradiation

An in-house designed microfluidic device for maintaining HNSCC tumour tissue for on-chip irradiation experiments was optimised and used to assess tumour response to irradiation based on cell death, proliferation and metabolism. It has been demonstrated that the microfluidic device is a powerful technique for HNSCC tissue maintenance, keeping architecture and cell proliferation for up to 6 days based on the LDH cytotoxicity assay, incorporation of proliferative markers and morphology staining. Different irradiation regimens were assessed within the 6 day-period. In addition, the perfusion of fluorescent markers throughout the tissue cultured in the microfluidic device was demonstrated using dextran (4kDa) further clarifying the efficacy of the chip for tissue maintenance and nutrient diffusion.

Radiotherapy remains the standard treatment for HNSCC patients and the central issue of resistance to ionising radiation remains a major barrier in the treatment of head and neck cancer despite the improvements in radiotherapy modality and emergence of new therapies. Still, much remains unknown about the biological mechanisms of malignant cells that confer resistance to ionising radiation. Consequently, many previous studies have assessed the biological responses against radiotherapy on cancerous cells by performing irradiation treatment *in vitro* on cultured cells (Carney, Mitchell and Kinsella, 1983; Randall *et al*., 2010; Matthew *et al*., 2011; Smit *et al*., 2013), cell-line xenograft models (Sørensen *et al*., 2014; Stein *et al*., 2015), patient-derived xenograft techniques (Stebbing *et al*., 2014) as well as microfluidic flow systems (Garty *et al*., 2011; Pješčić *et al*., 2011; Wan and Yeow, 2011; Buonanno *et al*., 2013; Torisawa *et al*., 2014; Carr *et al*., 2014).

The various methodologies for studying radiobiology study have different limitations. The monolayer of cells grown *in vitro* using the conventional cell-plate method and the tumour in xenograft that developed from immortalised cell lines may not be the representative of the original *in vivo* tumours in terms of architectural and cellular complexity (Richmond and Su, 2008; Stein *et al*., 2015). This limitation could be overcome in microfluidic technique which mimic the *in vivo* tumour heterogeneity and tissue microenvironment in the device. The patient-derived xenograft method, also, offers the benefit of more closely replicating human *in vivo* tumour microenvironment

over the previous two cell-line methods in which a tumour biopsy resected from a patient was injected into immunocompromised xenograft mice and subjected to various therapeutic treatments (Jimeno *et al*., 2009; Garrido-Laguna *et al*., 2011; Kimple *et al*., 2013; Stebbing *et al*., 2014).

A personalised patient-derived xenograft model was successfully developed in a study reported by Stebbing *et al*. (2014) for therapeutic decision-making for patients with sarcoma cancer. Fragments of resected tumours from 29 patients were inserted into immunodeficient mice to form tumours from the malignant cells and the associated stroma. The tumour responses to different drugs were then evaluated based on the percentage tumour growth inhibition and correlated with patient outcome. Out of 29 patients, 16 successful xenografts were generated and 13 of these patients showed correlation between laboratory results and clinical outcome of six of the patients had direct clinical benefit from the patient-derived therapy. The Stebbing *et al*. (2014) study has effectively demonstrated the ability of patient-derived xenografts to determine the most efficient therapy for a particular patient. The direct correlation between the laboratory results and the patient clinical outcome performed by Stebbing *et al*. (2014) is something which needs to be conducted for the microfluidic work described in the current study. To do this, biopsies would need to be taken from patients prior to treatment, which would then subject to the same treatment as the patients receive in the clinic, and the real-time tumour responses could then be tested and monitored throughout the on-chip treatment.

Microfluidic model in current study allows the investigation of tumour response to irradiation treatments under pseudo *in vivo* microenvironment which was different with that of the patient-derived mouse model. In xenograft mouse model, tumour cells are never free from the host cell contamination (Yang *et al*., 2000; Kahn, Tofilon and Camphausen, 2012) which could be avoided in present microfluidic flow system. The tumours grown in mouse are not entirely human tumours and do not predict what will happen in the human tumour with regard to the therapeutic response (Richmond and Su, 2008). For example, it has been shown previously that 47% of the mean percentage of contaminating mouse DNA was detected over 93 xenografts with human pancreatic cancer when the human and mouse DNA samples were quantified (Yang *et al*., 2000; Lin *et al*., 2010). Therefore, the microenvironment in xenograft mouse model does not simulate that of the *in vivo* conditions and the use of the

patient's tumour in current microfluidic device, in contrast, appears to more closely mimic the conditions in original patient than that in cell-line/patient-derived xenograft method. The ability to run parallel samples with the same treatment protocols is fundamental to ensure all parts of the tumour are responding in the same way to the treatment supplied if this methodology is to be transferred into the clinical setting. This becomes one of the major advantages of the current microfluidic-irradiation model over other xenograft models in which the development of multiple xenograft models for single regimen testing are much difficult compared with current microfluidic system as the development of xenograft tumours is difficulty and time-consuming (Kahn, Tofilon and Camphausen, 2012).

In microfluidic system, many different treatment schedules could be administered and tested, such as different chemotherapy drugs treatment (Siyan *et al*., 2009; Meng *et al*., 2011; Hattersley *et al*., 2012; An, Kim and Kim, 2014; Liu *et al*., 2015) and concurrent chemo-radiotherapy, and many different solid tumours could also be applied and investigated. As was previously described in Table 1.9, various studies have used microfluidic technology in assessing the impacts of ionizing radiation on biological samples including lymphocytes (Garty *et al*., 2011), isolated DNA (Pješčić *et al*., 2011), *Escherichia coli* (Wan and Yeow, 2011), *Caenorhabditis elegans* (Buonanno *et al*., 2013), bone marrow (Torisawa *et al*., 2014) as well as HNSCC tissue (Carr *et al*., 2014). Carr and colleagues were the first to investigate radiation-induced effects on human HNSCC tissues maintained in a microfluidic device. The current project, was an extension of the Carr *et al.* study, using an increased number of different markers of cell death and proliferation to better understand the fundamental mechanisms of actions, as well as to investigate changes in gene expression following treatment. Unlike the Carr *et al*. (2014) study, the cell death, morphology and proliferation of tissue cultured in a microfluidic device was compared with that of traditional static culture, and the dynamic environment was found to provide superior tissue architecture with a lower level of LDH release. Importantly, the variation of tumour responses observed with different HNSCC tumour samples subjected to the same irradiation doses in the current study suggested that this microfluidic irradiation experimentation offers a potential platform to monitor and predict a patient's response to radiotherapy in an individualised manner. If the radiation-induced effects on the tumours could be demonstrated and observed in future with a larger cohort of tumours

and these give good correlation with clinical patient outcome following radiotherapy, the ultimate goal of the prediction of HNSCC radiosensitivity could be accomplished. Furthermore, the microfluidic-based approach and the downstream analyses provide a platform to potentially divide the spectrum of HNSCC patients and individualise the patients from those who (1) may respond to conventional radiotherapy treatment alone, (2) are totally resistant to radiotherapy, or (3) could respond better to combination of a combination platinum/cetuximab/chemotherapy drug in addition to radiotherapy. This would bring multiple benefits firstly to the patients in terms of treatment effectiveness, reduced toxicity and secondarily to the NHS in terms of cost reduction for radiotherapy and improved patient care.

7.2. Limitations of current study

Throughout the entire project, frozen HNSCC tissues were utilized in order to maximise the number of devices and tissues that could be irradiated in at any one time. Now the procedure is optimised, a reduced number of treatment regimens should be selected for the study so that freshly resected tissue samples can be used in future. The use of fresh resected tissue from surgery is advisable as this reduces potential handling artefacts in order to mimic the *in vivo* tumour condition most closely.

The effects of irradiation were evaluated at 6-hour and 24-hour time points using CK18-LI and γH2AX markers. It is possible that by focusing on only two time-points, potentially important biomarker changes occurring earlier or later may have been overlooked. For example, a time-course induction of γH2AX foci formation following alkylating agent methyl methanesulfonate treatment on ovary cells has been studied previously in Staszewski *et al*. (2008) study which revealed the increased DNA damage repair within the first 8 hours and declined to control level at 24 hours after treatment. Another time-course study of DDR pathways has also been carried out over an extended period of up to 21-day post-irradiation by using xenograft models (Li *et al*., 2011). Li and colleagues revealed that the exposure of ionizing radiation caused rapid activation of DSBs (detected by using γ-H2AX/MDC1-Luc2 reporter genes) within 30 minutes of exposure and dropped at 24 hours (Li *et al*., 2011). Surprisingly, the activities of the genes increased again after 24 hours, peaking around day 5 and reducing back to background levels after day 12. Therefore, a set of time-course experiments need to be designed to determine the time course of tumour response upon ionising radiation. In addition, the advantage of using xenograft model is the

ability to investigate tumour response over extended period of time following irradiation which was lacked and not performed in the current study. Therefore, the maintenance the tissue within microfluidic device for extended periods is worth of further investigation.

It must be noted that the small piece of tissue used in the microfluidic system ($3mm^3$) is only representative of the area of tumour from which it was derived, which in case of the larger tumours can reach >4cm in size. Heterogeneity is known to exist across head and neck tumours, as demonstrated by Mroz *et al*. 2015, which is highly likely to contribute to tumour development, metastasis and treatment resistance as these different quasi-strain can respond differently to treatment (Zhang *et al*., 2013; Hiley *et al*., 2014; McGranahan *et al*., 2015; Sun and Yu, 2015; Zardavas *et al*., 2015; Ledgerwood *et al*., 2016). The tumour heterogeneity has been reported on HNSCC patients' samples by Ledgerwood *et al*. (2016). The differences in mutational heterogeneity on 57 genes were reported across different subsites of HNSCC. Of the total 102 somatic single nucleotide variations (SNVs) detected, none of the SNVs were shared between patients. Only 33.3% of SNVs were distinct between samples from the same patient with oral tongue tumours, whereas the intra-tumoural variation was higher in laryngeal and floor of mouth tumours with 69.2% of SNVs being distinct. A strong association between high intra-tumoural genetic heterogeneity and poorer overall survival in HNSCC was reported by Smeets *et al*. (2009), Stransky *et al*. (2011) and Mroz *et al*. (2015). In the study by Mroz and colleagues, the tumour heterogeneity was quantitatively calculated using mutant-allele tumour heterogeneity (MATH). For each 10% increase in MATH value, there was an 8.8% increment of hazard of death, and decreased overall survival. In addition, many studies have reported that many "cancer hallmark" genes are expressed differently within a single tumour, such as cyclins, Bcl-2, Ki-67 and EGFR, (Barrans *et al*., 1995; Kronblad *et al*., 2003; Warenius *et al*., 2008; Bai *et al*., 2013; Francis *et al*., 2014; Knutsvik *et al*., 2014; Tsuchiya *et al*., 2015). This emphasises the need for multiple sampling across the tissue to give a more accurate reflection of the tumour response to treatment.

In terms of the 'off-chip' analytical methods implemented, further improvement is required, for example, on the measurement of soluble markers in outlet effluent medium. The collection of effluent throughout microfluidic flow allows the real-time assessment of soluble factors released from the tumour and although the two cell

death markers investigated in the current study showed no response to irradiation, changes in LDH release were observed in response to tissue manipulation. However, there are numerous other factors which could be investigated as a functional response to treatment, e.g. interleukin 6 (De Schutter *et al*., 2005; Duffy *et al*., 2008; Meyer *et al*., 2010), matrix metallopeptidase 9 (MMP9; El Houda Aqueznay *et al*., 2007), vascular endothelial growth factor (VEGF; Brieger *et al*., 2007; Halamka *et al*., 2011; Khademi *et al*., 2014), and CD44 (Franzmann *et al*., 2007; Trapasso and Allegra, 2012) which have all been shown previously to be involved in resistance of radiation-induced effects in various tumour.

Furthermore, as discussed previously in section 6.5, the LCM and qRT-PCR experiments which aimed to evaluate the changes of gene expression following irradiation were restricted due to the lack of efficient protocol of tissue handling and LCM in harvesting maximum level of RNA and the varied expression results of beta 2 microglobulin (B2M) housekeeping gene across different tumours. Further validation on B2M housekeeping gene expression or the test of other suitable housekeeping genes are therefore required. The number of LCM experiments and the corresponding times required are collectively large to microdissect the tumour cells and extract sufficient amount of RNA for the downstream qRT-PCR reactions which indicate the urgent need of suitable protocol of tissue handling prior LCM. The entire tissue handling procedures which started at the point tumour samples resected from the patients until the time the RNA extracted have to be ensured free from RNase contamination. The RNase protection step, unfortunately, was not performed on the tissue samples prior to embedding and snap-frozen, which can explain the reason of the inconsistent and inadequate gene expression results observed in Chapter 6.

The low RNA levels obtained from tissue sections during the LCM procedure has been discussed (section 6.5.3), and is thought to be most likely due to the loss of RNA during the tissue extraction. However, it must be noted that there is a possibility that the culture of the tissue on the microfluidic device has led to a reduction in cell viability/functionality. Although, various methods looking at the cell death and proliferation have been utilised to try and confirm that the cells are alive, there is a likelihood that the cells, although not dead may be on the verge of death or senescent and no longer functioning as they would have been before. Previously viability/functional studies looking at urea, albumin, 4-[3-[4-Iodophenyl]-2–4 (4-

nitrophenyl)-2H-5-tetrazolio-1, 3-benzene disulfonate (WST-1) and LDH release from microfluidic cultured rat liver tissue has confirmed the functional state of the tissue (Hattersley *et al*., 2008; Hattersley, 2010; Hattersley *et al*., 2012; Carr, 2013). Moreover, the recent studies utilising thyroid tumour tissue in the microfluidic device have demonstrated continued thyroglobulin production throughout the culture period (conference posters presentation: Mulla *et al*., 2016; Yapa *et al*., 2016). Unfortunately head and neck tumour tissue does not functionally secrete an easily measurable marker, which depicts continued function, however in the future measures of ATP production throughout the culture period would provide better evidence for the metabolic state of the tissue maintained on the device (Hassan, Dong and Wang, 2013; Wu *et al*., 2014).

7.3. Future perspective

In addition to the limitations and the corresponding improvements described above, the use of microfluidic system to investigate the effects of concurrent chemo-radiotherapy, chemotherapy or radiotherapy could also be examined in personalised manner in order to accomplish clinical correlation in future. In order to take full advantage of the tissue-based microfluidic platforms, it will be necessary to extend the culture times of the tissue within the microfluidic device, and to do this further developments of the chip design need to be considered. A study proposed by Komeya *et al*. (2015) used a microfluidic device to culture testis tissue in which a porous membrane separated the tissue from the culture medium and the tissue cultures in the microfluidic device and in conventional agarose gel method were compared. Komeya and colleagues successfully cultured testis tissue for up to 6 months (180 days), with the presence of functional production of sperm and testosterone as well as responses to luteinizing hormone (Komeya *et al*., 2015). This construction, with the porous membrane, imitates the *in vivo* relationship between microvascular flow and the surrounding tissue allowing the exchange of nutrients and waste as well as secretory molecules between the interstitial spaces of the tissue and the microfluidic flow via the porous membrane and provided a functional advantage in terms of spermatogenesis over tissue directly exposed to medium (Figure 7.1). However, the microfluidic device was developed by Komeya and colleagues specifically for the culture of testis tissue. Therefore, the design of the microfluidic device with porous membrane in replicating

the microvascvular system *in vivo* is worth to be tested on other tumour types, such as the HNSCC tissue used in the current study.

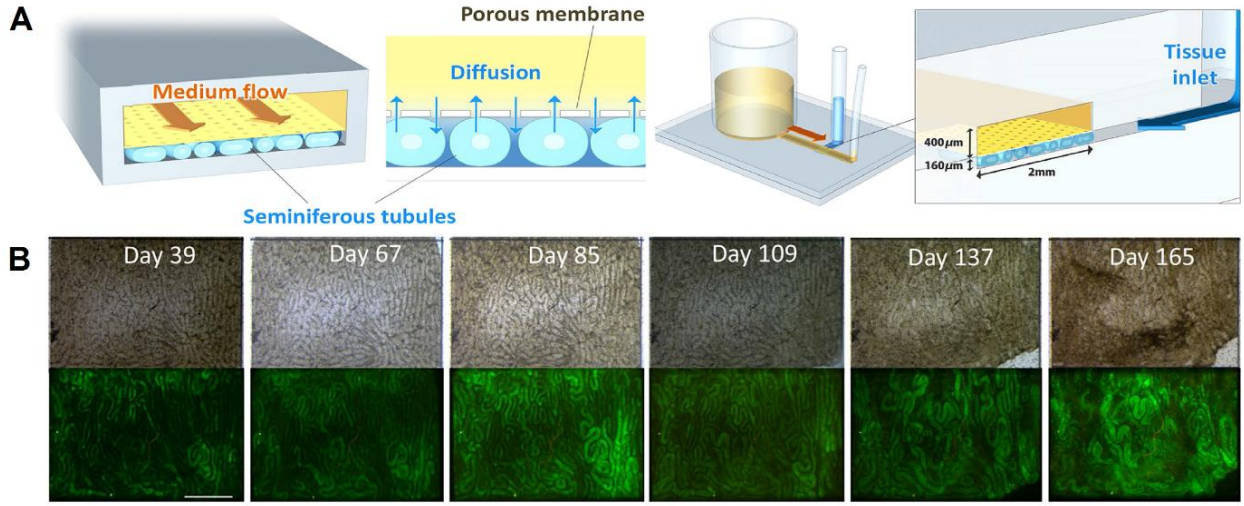


Figure 7.1. Long-term culture of testis tissue developed by Komeya *et al*. (2015).
(A) Schematic 3D image of the microfluidic device showing the porous membrane separating culture medium flow (0.05μl/min) and the testis tissue. (B) Green fluorescence protein expression of tissues cultured in microfluidic device up to 165 days, showing spermatogenesis in the device over the 6-month incubation. Scale bars: 500 μm

The longevity and the *in vivo*-like conditions of the testis tissue maintenance in Komeya's study may be due to the porous membrane preventing the medium flow from directly washing away the molecules secreted from the tissue inside the chamber allowing them to diffuse from the tissue to the medium side of the membrane (Komeya *et al*., 2015). With these results in mind, it might be worth considering the insertion of a porous membrane into the Hull microfluidic device in future in order to half-separate the tissue from the "vascular flow". By doing this, the exchange between the culture medium and the fluid in tissue chamber occurs principally by molecular diffusion which conceptually reproduces the *in vivo* relationship between blood plasma and the tissue interstitial fluid in the body (Figure 7.1.A). The application of porous membrane in microfluidic device has also been implemented in various studies to study renal epithelial structures (Frohlich *et al*., 2013), human intestinal model (Chi *et al*., 2015), blood- and lymphatic vessel permeability (Sato *et al*., 2015) and the alveolar-capillary interface of lung organ (Huh *et al*., 2013). A new tissue-on-a-chip has been designed and developed in-house by Dr. Dmitriy Kuvshinov and Ruth Bower where there is integration of sintered discs and membrane of nylon mesh on the tissue section which theoretically maintained the secreted materials inside the tissue chamber for a longer period than if open to diffuse away freely. These molecules secreted from the tissue itself inside the tissue chamber are mimicking the *in vivo* interstitial fluid that made up

of exudate from capillary plasma and secretions from tissue and are predicted to play crucial role in maintaining tissue function. Thus, this design could potentially be applied in the current study in future and the next step modification does require further optimisation by more precisely setting parameters for the new design, such as the medium flow speed, culture medium constituents, pore size and porosity of the nylon mesh membrane, in order to revolutionize the culture method and better comprehend "organs-on-chips" technology.

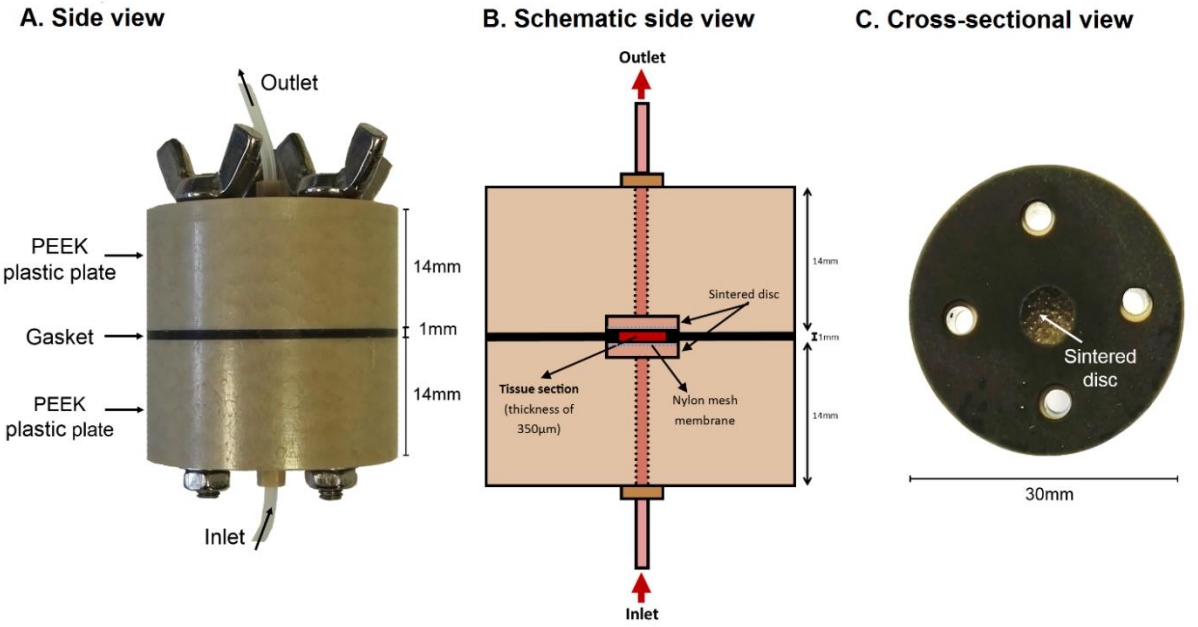


Figure 7.2. Design diagram of a new microfluidic device developed in-house.
The new microfluidic device was designed and developed in-house by Dr. Dmitriy Kuvshinov, Ruth Bower and staffs in Chemistry Department. (A) Side view and (B) schematic side view of the new microfluidic device that consists of two polyether ether ketone (PEEK) plastic plates screwed together to maintain tissue section (350µm of thickness) at the centre of the device. (C) Two sintered discs were sandwiched on the tissue section which serve as a porous membrane to improve the medium supplement across the section.

The identification of predictive markers of radioresistance in HNSCC tissue as well as other tumour types is of great importance for patients and clinicians to enable radiation treatments to be applied on an individual patient basis, avoiding the disappointment of a non-response which would lead to the necessity of further treatment schedules. This will allow the determination of whether this methodology can accurately predict whether a tumour is likely to be radio-resistant prior to application of the treatment. It is, unlikely, that the methods implemented in this thesis will offer a direct clinical approach for routine investigation without further modification due to the skill and time required to carry out a single experiment as well as the associated cost implications. The modification of the microfluidic flow system for better cultural condition, the application of different therapeutic modalities and the following analyses on proteins

and genes expression would be the next steps for improvement in order to achieve the ultimate aim of the study to predict patient radiosensitivity. However, current study undoubtedly does provide an potential starting point from which to build a more robust microfluidic culture and analysis system for the future, in conjuction with the close clinical correlation between patient's outcome and laboratory results, and to finally develop point-of-care system for efficient and individualised tumour screening prior to anti-cancer therapies.

7.4. Final conclusions

The current study has demonstrated that microfluidic culture is a potential platform for maintaining HNSCC tumour tissue morphology and cellular proliferation for up to 6 days, allowing different irradiation regimes to be applied and tested within the period. The differences of the expression profiles between patients using the same irradiation treatment and between different irradiation schedules detected within a single patient sample suggested the inter- and intra-tumour variation of the tumour response to radiotherapy, showing the significance of the tumour screening on an individual patient basis. The preliminary observation of the gene expression analysis on six radiation response genes using LCM and qRT-PCR techniques has created an exciting avenue to explore and to understand the effects of irradiation at the genomic level. In conclusion, with modification this microfluidic technique has the potential to provide the definitive tool in personalised medicine, capable of predicting the response of an individual's tumour to radiotherapy prior to the anti-cancer therapies and has equal applicability to all solid tumours and multiple types of treatment.

8. References

ABBAS, T. & DUTTA, A. 2009. p21 in cancer: intricate networks and multiple activities. *Nat Rev Cancer,* 9**,** 400-14.

ABBOTTS, R. & MADHUSUDAN, S. 2010. Human AP endonuclease 1 (APE1): from mechanistic insights to druggable target in cancer. *Cancer Treat Rev,* 36**,** 425-35.

AbD SEROTEC. 2016. *Streptavidin-Biotin Immunostaining of Frozen Tissue Sections.* Available online: https://www.abdserotec.com/static/2015/ihc-protocols/ihc2-streptavidin-biotin-protocols.pdf [Accessed on January 2016].

ABDULLAH, L. N. & CHOW, E. K. 2013. Mechanisms of chemoresistance in cancer stem cells. *Clin Transl Med,* 2**,** 3.

ADAMS, J. M. & CORY, S. 2007. The Bcl-2 apoptotic switch in cancer development and therapy. *Oncogene,* 26**,** 1324-37.

ADDAE-MENSAH. K. A., WANG. Z., PARSA. H., CHIN. S. Y., LAKSANASOPIN. T. & SIA. S. K. 2010. Fundamentals of microfluidic devices. In Kumar, C. S. (ed) *Microfluidic devices in nanothechnology: Fundamental concepts.* New Jersey: John Wiley & Sons, INC., Publication.

AEBERSOLD, D. M., BURRI, P., BEER, K. T., LAISSUE, J., DJONOV, V., GREINER, R. H. & SEMENZA, G. L. 2001. Expression of hypoxia-inducible factor-1alpha: a novel predictive and prognostic parameter in the radiotherapy of oropharyngeal cancer. *Cancer Res,* 61**,** 2911-6.

AGARWAL, J. P., NEMADE, B., MURTHY, V., GHOSH-LASKAR, S., BUDRUKKAR, A., GUPTA, T., D'CRUZ, A., PAI, P., CHATURVEDI, P. & DINSHAW, K. 2008. Hypofractionated, palliative radiotherapy for advanced head and neck cancer. *Radiother Oncol,* 89**,** 51-6.

AHMED, K. M., FAN, M., NANTAJIT, D., CAO, N. & LI, J. J. 2008. Cyclin D1 in low-dose radiation-induced adaptive resistance. *Oncogene,* 27**,** 6738-48.

AI, L., VO, Q. N., ZUO, C., LI, L., LING, W., SUEN, J. Y., HANNA, E., BROWN, K. D. & FAN, C. Y. 2004. Ataxia-telangiectasia-mutated (ATM) gene in head and neck squamous cell carcinoma: promoter hypermethylation with clinical correlation in 100 cases. *Cancer Epidemiol Biomarkers Prev,* 13**,** 150-6.

AKERVALL, J., NANDALUR, S., ZHANG, J., QIAN, C. N., GOLDSTEIN, N., GYLLERUP, P., GARDINGER, Y., ALM, J., LORENC, K., NILSSON, K., RESAU, J., WILSON, G. & TEH, B. 2014. A novel panel of biomarkers predicts radioresistance in patients with squamous cell carcinoma of the head and neck. *Eur J Cancer,* 50**,** 570-81.

AKHURST, R. J. & HATA, A. 2012. Targeting the TGFβ signalling pathway in disease. *Nat Rev Drug Discov,* 11 (10): 790-811.

AL GIZAWY, S.M., ESSA, H.H., REFAIY, A.M., ELOSAILY, G.M. & AHMED, H.E., 2011. Prognostic value of expression of survivin And Ki-67 in head and neck squamous cell carcinoma treated by chemoradiotherapy. *Life Sci J*, *8*, pp.724-733.

ALBERTS. B., JOHNSON. A., LEWIS. J., RAFF. M., ROBERTS. K. & WALTER. P. (ed) 2002. *Molecular biology of the cell. 4th edition*. New York: Garland Science.

ALLAL, A. S., DULGUEROV, P., ALLAOUA, M., HAENGGELI, C. A., EL GHAZI, E. A., LEHMANN, W. & SLOSMAN, D. O. 2002. Standardized uptake value of 2-[F-18] fluoro-2-deoxy-D-glucose in predicting outcome in head and neck carcinomas treated by radiotherapy with or without chemotherapy. *Journal of Clinical Oncology,* 20**,** 1398-1404.

AMERICAN JOINT COMMITTEE ON CANCER (AJCC). 2016. *Cancer Staging References.* Available online: https://cancerstaging.org/references-tools/Pages/What-is-Cancer-Staging.aspx. [Accessed on March 2013].

AN, D., KIM, K. & KIM, J. 2014. Microfluidic System Based High Throughput Drug Screening System for Curcumin/TRAIL Combinational Chemotherapy in Human Prostate Cancer PC3 Cells. *Biomol Ther (Seoul),* 22**,** 355-62.

ANDERSEN, K. J., KNUDSEN, A. R., KANNERUP, A. S., SASANUMA, H., NYENGAARD, J. R., HAMILTON-DUTOIT, S., ERLANDSEN, E. J., JORGENSEN, B. & MORTENSEN, F. V. 2013. The natural history of liver regeneration in rats: description of an animal model for liver regeneration studies. *Int J Surg,* 11**,** 903-8.

ANDREEFF, M., SLATER, D. E., BRESSLER, J. & FURTH, M. E. 1986. Cellular ras oncogene expression and cell cycle measured by flow cytometry in hematopoietic cell lines. *Blood,* 67**,** 676-81.

ANDREWS, E., SEAMAN, W. T. & WEBSTER-CYRIAQUE, J. 2009. Oropharyngeal carcinoma in non-smokers and non-drinkers: a role for HPV. *Oral Oncol,* 45**,** 486-91.

ANG, M. K., PATEL, M. R., YIN, X. Y., SUNDARAM, S., FRITCHIE, K., ZHAO, N., LIU, Y., FREEMERMAN, A. J., WILKERSON, M. D., WALTER, V., WEISSLER, M. C., SHOCKLEY, W. W., COUCH, M. E., ZANATION, A. M., HACKMAN, T., CHERA, B. S., HARRIS, S. L., MILLER, C. R., THORNE, L. B., HAYWARD, M. C., FUNKHOUSER, W. K., OLSHAN, A. F., SHORES, C. G., MAKOWSKI, L. & HAYES, D.

N. 2011. High XRCC1 protein expression is associated with poorer survival in patients with head and neck squamous cell carcinoma. *Clin Cancer Res,* 17**,** 6542-52.
AOYAGI, M., YAMAMOTO, M., WAKIMOTO, H., AZUMA, H., HIRAKAWA, K. & YAMAMOTO, K. 1995. Immunohistochemical detection of Ki-67 in replicative smooth muscle cells of rabbit carotid arteries after balloon denudation. *Stroke,* 26**,** 2328-31; discussion 2331-2.
ARGIRIS, A., KARAMOUZIS, M. V., RABEN, D. & FERRIS, R. L. 2008. Head and neck cancer. *Lancet,* 371**,** 1695-709.
ARMENTA, J. M., DAWOUD, A. A. & LAZAR, I. M. 2009. Microfluidic chips for protein differential expression profiling. *Electrophoresis,* 30**,** 1145-56.
ASADA, M., YAMADA, T., ICHIJO, H., DELIA, D., MIYAZONO, K., FUKUMURO, K. & MIZUTANI, S. 1999. Apoptosis inhibitory activity of cytoplasmic p21(Cip1/WAF1) in monocytic differentiation. *EMBO J,* 18**,** 1223-34.
ATAMAN, O. U., BENTZEN, S. M., WILSON, G. D., DALEY, F. M., RICHMAN, P. I., SAUNDERS, M. I. & DISCHE, S. 2004. Molecular biomarkers and site of first recurrence after radiotherapy for head and neck cancer. *Eur J Cancer,* 40**,** 2734-41.
AUDUS, K. L. & RAUB, T. J. (ed) 1993. *Biological Barriers to Protein Delivery*. New York: Springer Science
AUSCH, C., BUXHOFER-AUSCH, V., OLSZEWSKI, U., SCHIESSEL, R., OGRIS, E., HINTERBERGER, W. & HAMILTON, G. 2009. Circulating cytokeratin 18 fragment m65-a potential marker of malignancy in colorectal cancer patients. *J Gastrointest Surg,* 13**,** 2020-6.
BADDELA, V. S., BAUFELD, A., YENUGANTI, V. R., VANSELOW, J. & SINGH, D. 2014. Suitable housekeeping genes for normalization of transcript abundance analysis by real-time RT-PCR in cultured bovine granulosa cells during hypoxia and differential cell plating density. *Reprod Biol Endocrinol,* 12**,** 118.
BAEZ, A. & SHILOACH, J. 2014. Effect of elevated oxygen concentration on bacteria, yeasts, and cells propagated for production of biological compounds. *Microb Cell Fact,* 13**,** 181.
BAI, H., WANG, Z., WANG, Y., ZHUO, M., ZHOU, Q., DUAN, J., YANG, L., WU, M., AN, T., ZHAO, J. & WANG, J. 2013. Detection and clinical significance of intratumoral EGFR mutational heterogeneity in Chinese patients with advanced non-small cell lung cancer. *PLoS One,* 8**,** e54170.
BAKIU, E., TELHAJ, E., KOZMA, E., RUCI, F. & MALKAJ, P. 2013. Comparison of 3D CRT and IMRT Tratment Plans. *Acta Inform Med,* 21**,** 211-2.
BAKKENIST, C. J. & KASTAN, M. B. 2003. DNA damage activates ATM through intermolecular autophosphorylation and dimer dissociation. *Nature,* 421**,** 499-506.
BANATH, J. P., MACPHAIL, S. H. & OLIVE, P. L. 2004. Radiation sensitivity, H2AX phosphorylation, and kinetics of repair of DNA strand breaks in irradiated cervical cancer cell lines. *Cancer Res,* 64**,** 7144-9.
BARANSKI, J. D., CHATURVEDI, R. R., STEVENS, K. R., EYCKMANS, J., CARVALHO, B., SOLORZANO, R. D., YANG, M. T., MILLER, J. S., BHATIA, S. N. & CHEN, C. S. 2013. Geometric control of vascular networks to enhance engineered tissue integration and function. *Proc Natl Acad Sci U S A,* 110**,** 7586-91.
BARBER, R. D., HARMER, D. W., COLEMAN, R. A. & CLARK, B. J. 2005. GAPDH as a housekeeping gene: analysis of GAPDH mRNA expression in a panel of 72 human tissues. *Physiol Genomics,* 21**,** 389-95.
BARKER, H. E., PAGET, J. T., KHAN, A. A. & HARRINGTON, K. J. 2015. The tumour microenvironment after radiotherapy: mechanisms of resistance and recurrence. *Nat Rev Cancer,* 15**,** 409-25.
BARRANS, S., RANDERSON, J., EVANS, P., BLYTHE, D., SHIACH, C., CHILD, J. A., MORGAN, G. & JACK, A. S. 1995. Heterogeneity in cell proliferation and expression of p53 and bcl-2 during the indolent phase of germinal centre cell lymphoma: an explanation for clinical variability. *Br J Haematol,* 90**,** 830-6.
BARTEK, J. & LUKAS, J. 2003. Chk1 and Chk2 kinases in checkpoint control and cancer. *Cancer Cell,* 3**,** 421-9.
BARTKOVA, J., HOREJSI, Z., KOED, K., KRAMER, A., TORT, F., ZIEGER, K., GULDBERG, P., SEHESTED, M., NESLAND, J. M., LUKAS, C., ORNTOFT, T., LUKAS, J. & BARTEK, J. 2005. DNA damage response as a candidate anti-cancer barrier in early human tumorigenesis. *Nature,* 434**,** 864-70.
BASKAR, R., LEE, K. A., YEO, R. & YEOH, K. W. 2012. Cancer and radiation therapy: current advances and future directions. *Int J Med Sci,* 9**,** 193-9.
BAUJAT, B., BOURHIS, J., BLANCHARD, P., OVERGAARD, J., ANG, K. K., SAUNDERS, M., LE MAITRE, A., BERNIER, J., HORIOT, J. C., MAILLARD, E., PAJAK, T. F., POULSEN, M. G., BOURREDJEM, A., O'SULLIVAN, B., DOBROWSKY, W., ANDRZEJ, H., SKLADOWSKI, K., HAY, J. H., PINTO, L. H., FU, K. K., FALLAI, C., SYLVESTER, R., PIGNON, J. P. & GROUP, M. C. 2010. Hyperfractionated or accelerated radiotherapy for head and neck cancer. *Cochrane Database Syst Rev***,** CD002026.
BAUMANN, M., DUBOIS, W. & SUIT, H. D. 1990. Response of human squamous cell carcinoma xenografts of different sizes to irradiation: relationship of clonogenic cells, cellular radiation sensitivity *in vivo*, and tumor rescuing units. *Radiat Res,* 123**,** 325-30.
BAUMANN, M., KRAUSE, M. & HILL, R. 2008. Exploring the role of cancer stem cells in radioresistance. *Nat Rev Cancer,* 8**,** 545-54.

BEGG, A. C. 2012. Predicting recurrence after radiotherapy in head and neck cancer. *Semin Radiat Oncol,* 22**,** 108-18.
BEGGS, A. D., DOMINGO, E., MCGREGOR, M., PRESZ, M., JOHNSTONE, E., MIDGLEY, R., KERR, D., OUKRIF, D., NOVELLI, M., ABULAFI, M., HODGSON, S. V., FADHIL, W., ILYAS, M. & TOMLINSON, I. P. 2012. Loss of expression of the double strand break repair protein ATM is associated with worse prognosis in colorectal cancer and loss of Ku70 expression is associated with CIN. *Oncotarget,* 3**,** 1348-55.
BENADA, J. & MACUREK, L. 2015. Targeting the Checkpoint to Kill Cancer Cells. *Biomolecules,* 5**,** 1912-37.
BENEDICT, W. F., FISHER, M., ZHANG, X. Q., YANG, Z., MUNSELL, M. F. & DINNEY, C. N. 2014. Use of monitoring levels of soluble forms of cytokeratin 18 in the urine of patients with superficial bladder cancer following intravesical Ad-IFNalpha/Syn3 treatment in a phase I study. *Cancer Gene Ther,* 21**,** 91-4.
BERNIER, J. & COOPER, J. S. 2005. Chemoradiation after surgery for high-risk head and neck cancer patients: how strong is the evidence? *Oncologist,* 10**,** 215-24.
BERTRAND, G., MAALOUF, M., BOIVIN, A., BATTISTON-MONTAGNE, P., BEUVE, M., LEVY, A., JALADE, P., FOURNIER, C., ARDAIL, D., MAGNE, N., ALPHONSE, G. & RODRIGUEZ-LAFRASSE, C. 2014. Targeting head and neck cancer stem cells to overcome resistance to photon and carbon ion radiation. *Stem Cell Rev,* 10**,** 114-26.
BESIC GYENGE, E., FORNY, P., LUSCHER, D., LAASS, A., WALT, H. & MAAKE, C. 2012. Effects of hypericin and a chlorin based photosensitizer alone or in combination in squamous cell carcinoma cells in the dark. *Photodiagnosis Photodyn Ther,* 9**,** 321-31.
BESSON, A., DOWDY, S. F. & ROBERTS, J. M. 2008. CDK inhibitors: cell cycle regulators and beyond. *Dev Cell,* 14**,** 159-69.
BETTS, G. N., EUSTACE, A., PATIAR, S., VALENTINE, H. R., IRLAM, J., RAMACHANDRAN, A., MERVE, A., HOMER, J. J., MOLLER-LEVET, C., BUFFA, F. M., HALL, G., MILLER, C. J., HARRIS, A. L. & WEST, C. M. 2013. Prospective technical validation and assessment of intra-tumour heterogeneity of a low density array hypoxia gene profile in head and neck squamous cell carcinoma. *Eur J Cancer,* 49**,** 156-65.
BHOSLE, S. M., PANDEY, B. N., HUILGOL, N. G. & MISHRA, K. P. 2002. Membrane oxidative damage and apoptosis in cervical carcinoma cells of patients after radiation therapy. *Methods Cell Sci,* 24**,** 65-8.
BIANCHINI, G., PUSZTAI, L., KARN, T., IWAMOTO, T., RODY, A., KELLY, C., MULLER, V., SCHMIDT, S., QI, Y., HOLTRICH, U., BECKER, S., SANTARPIA, L., FASOLO, A., DEL CONTE, G., ZAMBETTI, M., SOTIRIOU, C., HAIBE-KAINS, B., SYMMANS, W. F. & GIANNI, L. 2013. Proliferation and estrogen signaling can distinguish patients at risk for early versus late relapse among estrogen receptor positive breast cancers. *Breast Cancer Res,* 15**,** R86.
BILYY, R. & STOIKA, R. 2007. Search for novel cell surface markers of apoptotic cells. *Autoimmunity,* 40**,** 249-53.
BIOSPOTLIGHT, 2008. *Click here to EDU-cate proliferating cells* [Online]. Available: http://www.biotechniques.com/multimedia/archive/00003/BTN_A_000112858_O_3742a.pdf [Accessed on October 2015].
BIRAJDAR, S. S., RADHIKA, M., PAREMALA, K., SUDHAKARA, M., SOUMYA, M. & GADIVAN, M. 2014. Expression of Ki-67 in normal oral epithelium, leukoplakic oral epithelium and oral squamous cell carcinoma. *J Oral Maxillofac Pathol,* 18**,** 169-76.
BLATT, S., VOELXEN, N., SAGHEB, K., PABST, A. M., WALENTA, S., SCHROEDER, T., MUELLER-KLIESER, W. & ZIEBART, T. 2016. Lactate as a predictive marker for tumor recurrence in patients with head and neck squamous cell carcinoma (HNSCC) post radiation: a prospective study over 15 years. *Clin Oral Investig*.
BLOMBERG. J. 2008. *Regulation of apoptosis during treatment and resistance development in tumour cells.* Available online: http://umu.diva-portal.org/smash/get/diva2:142199/FULLTEXT01.pdf. PhD thesis. Umeå University.
BOSE, P., KLIMOWICZ, A. C., KORNAGA, E., PETRILLO, S. K., MATTHEWS, T. W., CHANDARANA, S., MAGLIOCCO, A. M., BROCKTON, N. T. & DORT, J. C. 2012. Bax expression measured by AQUAnalysis is an independent prognostic marker in oral squamous cell carcinoma. *BMC Cancer,* 12**,** 332.
BOSOTTI, R., ISACCHI, A. & SONNHAMMER, E. L. 2000. FAT: a novel domain in PIK-related kinases. *Trends Biochem Sci,* 25**,** 225-7.
BOUQUET, F., PAI, A., PILONES, K. A., DEMARIA, S., HANN, B., AKHURST,R. J., BABB, J. S., LONNING, S. M., DEWYNGAERT, J. K., FORMENTI S.C. & BARCELLOS-HOFF, M. H. 2011. TGFβ1 inhibition increases the radiosensitivity of breast cancer cells *in vitro* and promotes tumor control by radiation *in vivo*. *Clin Cancer Res,* 17 (21): 6754-6765.
BOURHIS, J., LAPEYRE, M., TORTOCHAUX, J., RIVES, M., AGHILI, M., BOURDIN, S., LESAUNIER, F., BENASSI, T., LEMANSKI, C., GEOFFROIS, L., LUSINCHI, A., VERRELLE, P., BARDET, E., JULIERON, M., WIBAULT, P., LUBOINSKI, M. & BENHAMOU, E. 2006. Phase III randomized trial of very accelerated radiation therapy compared with conventional radiation therapy in squamous cell head and neck cancer: a GORTEC trial. *J Clin Oncol,* 24**,** 2873-8.

BOURHIS, J., OVERGAARD, J., AUDRY, H., ANG, K. K., SAUNDERS, M., BERNIER, J., HORIOT, J. C., LE MAITRE, A., PAJAK, T. F., POULSEN, M. G., O'SULLIVAN, B., DOBROWSKY, W., HLINIAK, A., SKLADOWSKI, K., HAY, J. H., PINTO, L. H., FALLAI, C., FU, K. K., SYLVESTER, R., PIGNON, J. P., META-ANALYSIS OF RADIOTHERAPY IN CARCINOMAS OF, H. & NECK COLLABORATIVE, G. 2006. Hyperfractionated or accelerated radiotherapy in head and neck cancer: a meta-analysis. *Lancet,* 368**,** 843-54.

BOURTON, E. C., PLOWMAN, P. N., SMITH, D., ARLETT, C. F. & PARRIS, C. N. 2011. Prolonged expression of the gamma-H2AX DNA repair biomarker correlates with excess acute and chronic toxicity from radiotherapy treatment. *Int J Cancer,* 129**,** 2928-34.

BOYLE, J. O., HAKIM, J., KOCH, W., VAN DER RIET, P., HRUBAN, R. H., ROA, R. A., CORREO, R., EBY, Y. J., RUPPERT, J. M. & SIDRANSKY, D. 1993. The incidence of p53 mutations increases with progression of head and neck cancer. *Cancer Res,* 53**,** 4477-80.

BRAAKMAN, R. B., LUIDER, T. M., MARTENS, J. W., FOEKENS, J. A. & UMAR, A. 2011. Laser capture microdissection applications in breast cancer proteomics. *Methods Mol Biol,* 755**,** 143-54.

BRAUN, N., PAPADOPOULOS, T. & MULLER-HERMELINK, H. K. 1988. Cell cycle dependent distribution of the proliferation-associated Ki-67 antigen in human embryonic lung cells. *Virchows Arch B Cell Pathol Incl Mol Pathol,* 56**,** 25-33.

BREM, R. & HALL, J. 2005. XRCC1 is required for DNA single-strand break repair in human cells. *Nucleic Acids Res,* 33**,** 2512-20.

BRENGUES, M., PAAP, B., BITTNER, M., AMUNDSON, S., SELIGMANN, B., KORN, R., LENIGK, R. & ZENHAUSERN, F. 2010. Biodosimetry on small blood volume using gene expression assay. *Health Phys,* 98**,** 179-85.

BRESLAUER, D. N., LEE, P. J. & LEE, L. P. 2006. Microfluidics-based systems biology. *Mol Biosyst,* 2**,** 97-112.

BRIEGER, J., KATTWINKEL, J., BERRES, M., GOSEPATH, J. & MANN, W. J. 2007. Impact of vascular endothelial growth factor release on radiation resistance. *Oncol Rep,* 18**,** 1597-601.

BRITISH ASSOCIATION OF OTORHINOLARYNGOLOGY. 2011. *Head and Neck Cancer: Multidisciplinary Management Guidelines 4th edition*. Available online: http://bahno.org.uk/wp-content/uploads/2014/03/Multidisciplinary-Management-Guidelines-for-Head-and-Neck-Cancer.pdf. [Accessed on March 2013].

BROCKSTEIN, B., HARAF, D. J., RADEMAKER, A. W., KIES, M. S., STENSON, K. M., ROSEN, F., MITTAL, B. B., PELZER, H., FUNG, B. B., WITT, M. E., WENIG, B., PORTUGAL, L., WEICHSELBAUM, R. W. & VOKES, E. E. 2004. Patterns of failure, prognostic factors and survival in locoregionally advanced head and neck cancer treated with concomitant chemoradiotherapy: a 9-year, 337-patient, multi-institutional experience. *Ann Oncol,* 15**,** 1179-86.

BRUNO, S. & DARZYNKIEWICZ, Z. 1992. Cell cycle dependent expression and stability of the nuclear protein detected by Ki-67 antibody in HL-60 cells. *Cell Prolif,* 25**,** 31-40.

BUCCI, B., MISITI, S., CANNIZZARO, A., MARCHESE, R., RAZA, G. H., MICELI, R., STIGLIANO, A., AMENDOLA, D., MONTI, O., BIANCOLELLA, M., AMATI, F., NOVELLI, G., VECCHIONE, A., BRUNETTI, E. & DE PAULA, U. 2006. Fractionated ionizing radiation exposure induces apoptosis through caspase-3 activation and reactive oxygen species generation. *Anticancer Res,* 26**,** 4549-57.

BUENO, R. C., CANEVARI, R. A., VILLACIS, R. A., DOMINGUES, M. A., CALDEIRA, J. R., ROCHA, R. M., DRIGO, S. A. & ROGATTO, S. R. 2014. ATM down-regulation is associated with poor prognosis in sporadic breast carcinomas. *Ann Oncol,* 25**,** 69-75.

BUFFA, F. M., BENTZEN, S. M., DALEY, F. M., DISCHE, S., SAUNDERS, M. I., RICHMAN, P. I. & WILSON, G. D. 2004. Molecular marker profiles predict locoregional control of head and neck squamous cell carcinoma in a randomized trial of continuous hyperfractionated accelerated radiotherapy. *Clin Cancer Res,* 10**,** 3745-54.

BUONANNO, M., GARTY, G., GRAD, M., GENDREL, M., HOBERT, O. & BRENNER, D. J. 2013. Microbeam irradiation of C-elegans nematode in microfluidic channels. *Radiation and Environmental Biophysics,* 52**,** 531-537.

BURMA, S., CHEN, B. P., MURPHY, M., KURIMASA, A. & CHEN, D. J. 2001. ATM phosphorylates histone H2AX in response to DNA double-strand breaks. *J Biol Chem,* 276**,** 42462-7.

CALDECOTT, K. W. 2003. XRCC1 and DNA strand break repair. *DNA Repair (Amst),* 2**,** 955-69.

CALIFANO, J., VAN DER RIET, P., WESTRA, W., NAWROZ, H., CLAYMAN, G., PIANTADOSI, S., CORIO, R., LEE, D., GREENBERG, B., KOCH, W. & SIDRANSKY, D. 1996. Genetic progression model for head and neck cancer: implications for field cancerization. *Cancer Res,* 56**,** 2488-92.

CARL ZEISS MicroImaging GmbH, 2008. *Membrane slide*. Available online: https://www.micro-shop.zeiss.com/index.php?s=21518024678eb4b&l=en&p=uk&f=a&i=40000000470080000&o=&h=32&n=0&sl=415190-9041-000&c=3&id=0#415190-9041-000 [Accessed August 2015]

CARNEY, D. N., MITCHELL, J. B. & KINSELLA, T. J. 1983. *In vitro* radiation and chemotherapy sensitivity of established cell lines of human small cell lung cancer and its large cell morphological variants. *Cancer Res,* 43**,** 2806-11.
CARR, S. 2013. Assessing the effects of radiotherapy on head and neck squamous cell carcinoma using microfluidic techniques. PhD thesis. The University of Hull.
CARR, S. D., GREEN, V. L., STAFFORD, N. D. & GREENMAN, J. 2014. Analysis of radiation-induced cell death in head and neck squamous cell carcinoma and rat liver maintained in microfluidic devices. *Otolaryngol Head Neck Surg,* 150**,** 73-80.
CARTMELL, S. H., PORTER, B. D., GARCIA, A. J. & GULDBERG, R. E. 2003. Effects of medium perfusion rate on cell-seeded three-dimensional bone constructs *in vitro*. *Tissue Eng,* 9**,** 1197-203.
CASADEI, R., PELLERI, M. C., VITALE, L., FACCHIN, F., LENZI, L., CANAIDER, S., STRIPPOLI, P. & FRABETTI, F. 2011. Identification of housekeeping genes suitable for gene expression analysis in the zebrafish. *Gene Expr Patterns,* 11**,** 271-6.
CASSELL, A. & GRANDIS, J. R. 2011. Investigational EGFR-targeted therapies in HNSCC. *Expert Opin Investing Drugs,* 19 (6): 709-722.
CAULIN, C., SALVESEN, G. S. & OSHIMA, R. G. 1997. Caspase cleavage of keratin 18 and reorganization of intermediate filaments during epithelial cell apoptosis. *J Cell Biol,* 138**,** 1379-94.
CAYMAN CHEMICAL (2015). *Product information: 2-NBDG*. Available online: https://www.caymanchem.com/pdfs/11046.pdf [Accessed on June 2015].
CHANG, B. D., WATANABE, K., BROUDE, E. V., FANG, J., POOLE, J. C., KALINICHENKO, T. V. & RONINSON, I. B. 2000. Effects of p21Waf1/Cip1/Sdi1 on cellular gene expression: implications for carcinogenesis, senescence, and age-related diseases. *Proc Natl Acad Sci U S A,* 97**,** 4291-6.
CHAPMAN, J. R., TAYLOR, M. R. & BOULTON, S. J. 2012. Playing the end game: DNA double-strand break repair pathway choice. *Mol Cell,* 47**,** 497-510.
CHEAH, L. T., DOU, Y. H., SEYMOUR, A. M., DYER, C. E., HASWELL, S. J., WADHAWAN, J. D. & GREENMAN, J. 2010. Microfluidic perfusion system for maintaining viable heart tissue with real-time electrochemical monitoring of reactive oxygen species. *Lab Chip,* 10**,** 2720-6.
CHEAH, L. T., FRITSCH, I., HASWELL, S. J. & GREENMAN, J. 2012. Evaluation of heart tissue viability under redox-magnetohydrodynamics conditions: toward fine-tuning flow in biological microfluidics applications. *Biotechnol Bioeng,* 109**,** 1827-34.
CHENG, S., WANG, Z., WANG, L. & ZHANG, M. 2014. [Ki-67 expression in stage III cervical squamous cell carcinoma and its correlation with sensitivity to chemoradiotherapy]. *Zhonghua Zhong Liu Za Zhi,* 36**,** 667-70.
CHI, M., YI, B., OH, S., PARK, D. J., SUNG, J. H. & PARK, S. 2015. A microfluidic cell culture device (muFCCD) to culture epithelial cells with physiological and morphological properties that mimic those of the human intestine. *Biomed Microdevices,* 17**,** 9966.
CHIBLY, A. M., QUERIN, L., HARRIS, Z. & LIMESAND, K. H. 2014. Label-retaining cells in the adult murine salivary glands possess characteristics of adult progenitor cells. *PLoS One,* 9**,** e107893.
CHO, S., KANG, D. K., SIM, S., GEIER, F., KIM, J. Y., NIU, X., EDEL, J. B., CHANG, S. I., WOOTTON, R. C., ELVIRA, K. S. & DEMELLO, A. J. 2013. Droplet-based microfluidic platform for high-throughput, multi-parameter screening of photosensitizer activity. *Anal Chem,* 85**,** 8866-72.
CHUNG, B. G., PARK, J. W., HU, J. S., HUANG, C., MONUKI, E. S. & JEON, N. L. 2007. A hybrid microfluidic-vacuum device for direct interfacing with conventional cell culture methods. *BMC Biotechnol,* 7**,** 60.
CIAPARRONE, M., CASPIANI, O., BICCIOLO, G., SIGNORELLI, D., SIMONELLI, I., DE CAMPORA, L., MAZZARELLA, G., MECOZZI, A., PIANELLI, C., CAMAIONI, A., CATALANO, P., PASQUALETTI, P., FABIANO, A., RADICI, M., MARMIROLI, L. & CORSI, D. C. 2015. Predictive Role of ERCC1 Expression in Head and Neck Squamous Cell Carcinoma Patients Treated with Surgery and Adjuvant Cisplatin-Based Chemoradiation. *Oncology,* 89**,** 227-34.
CLINGEN, P. H., WU, J. Y., MILLER, J., MISTRY, N., CHIN, F., WYNNE, P., PRISE, K. M. & HARTLEY, J. A. 2008. Histone H2AX phosphorylation as a molecular pharmacological marker for DNA interstrand crosslink cancer chemotherapy. *Biochem Pharmacol,* 76**,** 19-27.
COGLIANO, V. J., BAAN, R., STRAIF, K., GROSSE, Y., LAUBY-SECRETAN, B., EL GHISSASSI, F., BOUVARD, V., BENBRAHIM-TALLAA, L., GUHA, N., FREEMAN, C., GALICHET, L. & WILD, C. P. 2011. Preventable exposures associated with human cancers. *J Natl Cancer Inst,* 103**,** 1827-39.
COGNETTI, D. M., WEBER, R. S. & LAI, S. Y. 2008. Head and neck cancer: an evolving treatment paradigm. *Cancer,* 113**,** 1911-32.
COLLINS, K., JACKS, T. & PAVLETICH, N. P. 1997. The cell cycle and cancer. *Proc Natl Acad Sci U S A,* 94**,** 2776-8.
CONDON, L. T., ASHMAN, J. N., ELL, S. R., STAFFORD, N. D., GREENMAN, J. & CAWKWELL, L. 2002. Overexpression of Bcl-2 in squamous cell carcinoma of the larynx: a marker of radioresistance. *Int J Cancer,* 100**,** 472-5.

CONNELL, P. P., JAYATHILAKA, K., HARAF, D. J., WEICHSELBAUM, R. R., VOKES, E. E. & LINGEN, M. W. 2006. Pilot study examining tumor expression of RAD51 and clinical outcomes in human head cancers. *Int J Oncol,* 28**,** 1113-9.

CONNOLLY, E. C., SAUNIER, E. F., QUIGLEY, D., LUU, M. T., DE SAPIO, A., HANN, B., YINGLING, J. M., & AKHURST, R. J. 2011. Outgrowth of drug-resistant carcinomas expressing markers of tumor aggression after long-term TβRI/II kinase inhibition with LY2109761. *Cancer Res,* 71 (6): 2339-49.

COOPER, G. M. 2000. *The development and causes of cancer.* Sunderland: Sinauer Associates.

COUTURE, C., RAYBAUD-DIOGENE, H., TETU, B., BAIRATI, I., MURRY, D., ALLARD, J. & FORTIN, A. 2002. p53 and Ki-67 as markers of radioresistance in head and neck carcinoma. *Cancer,* 94**,** 713-22.

CRANE, J., MITTAR, D., SONI, D. & MCLNTYRE. 2011. Cell cycle analysis using the BD BrdU FITC assay on the BD FACSVerse ™ system. *BD Biosciences Application Note*.

CRUK, 2015. Cancer Strategy 2012-20: Cancer Research UK response to the cancer taskforce. Available online: https://www.cancerresearchuk.org/sites/default/files/cr-uk_response_to_cancer_taskforce_strategy_feb2015_final.pdf. [Accessed on December 2016].

CRUK. 2016 a. *Cancer incidence for common cancers.* Available online: http://www.cancerresearchuk.org/health-professional/cancer-statistics/incidence/common-cancers-compared#heading-Zero. [Accessed on May 2016].

CRUK. 2016 b. *Cancer mortality for common cancers.* Available online: http://www.cancerresearchuk.org/health-professional/cancer-statistics/mortality/common-cancers-compared#heading-Zero. [Accessed on May 2016].

CRUK. 2016 c. *Laryngeal (larynx) cancer incidence statistics*. Available online: http://www.cancerresearchuk.org/health-professional/cancer-statistics/statistics-by-cancer-type/laryngeal-cancer/incidence#heading-Zero. [Accessed on June 2016].

CRUK. 2016 d. *Laryngeal (larynx) cancer mortality statistics.* Available online: http://www.cancerresearchuk.org/health-professional/laryngeal-larynx-cancer-mortality-statistics#heading-Zero. [Accessed on June 2016].

CRUK. 2016 e. Oral cancer diagnosis and treatment statistics. Available online: http://www.cancerresearchuk.org/health-professional/cancer-statistics/statistics-by-cancer-type/oral-cancer/diagnosis-and-treatment#heading-One. [Accessed on April 2016]

CULLEN, D. K., VUKASINOVIC, J., GLEZER, A. & LAPLACA, M. C. 2007. Microfluidic engineered high cell density three-dimensional neural cultures. *J Neural Eng,* 4**,** 159-72.

CUMMINGS, J., HODGKINSON, C., ODEDRA, R., SINI, P., HEATON, S. P., MUNDT, K. E., WARD, T. H., WILKINSON, R. W., GROWCOTT, J., HUGHES, A. & DIVE, C. 2008. Preclinical evaluation of M30 and M65 ELISAs as biomarkers of drug induced tumor cell death and antitumor activity. *Mol Cancer Ther,* 7**,** 455-63.

CUMMINGS, J., RANSON, M., LACASSE, E., GANGANAGARI, J. R., ST-JEAN, M., JAYSON, G., DURKIN, J. & DIVE, C. 2006. Method validation and preliminary qualification of pharmacodynamic biomarkers employed to evaluate the clinical efficacy of an antisense compound (AEG35156) targeted to the X-linked inhibitor of apoptosis protein XIAP. *Br J Cancer,* 95**,** 42-8.

CUMMINGS, M., MCGINLEY, C. V., WILKINSON, N., FIELD, S. L., DUFFY, S. R. & ORSI, N. M. 2011. A robust RNA integrity-preserving staining protocol for laser capture microdissection of endometrial cancer tissue. *Anal Biochem,* 416**,** 123-5.

CURRAN, S., MCKAY, J. A., MCLEOD, H. L. & MURRAY, G. I. 2000. Laser capture microscopy. *Mol Pathol,* 53**,** 64-8.

CURTIN, N. J. 2012. DNA repair dysregulation from cancer driver to therapeutic target. *Nat Rev Cancer,* 12**,** 801-17.

DANIAL, N. N. & KORSMEYER, S. J. 2004. Cell death: critical control points. *Cell,* 116**,** 205-19.

DAS, S., THOMAS, S., PAL, S. K., ISIAH, R. & JOHN, S. 2013. Hypofractionated Palliative Radiotherapy in Locally Advanced Inoperable Head and Neck Cancer: CMC Vellore Experience. *Indian J Palliat Care,* 19**,** 93-8.

DATTA, S., MALHOTRA, L., DICKERSON, R., CHAFFEE, S., SEN, C. K. & ROY, S. 2015. Laser capture microdissection: Big data from small samples. *Histol Histopathol,* 30**,** 1255-69.

DAYYANI, F., ETZEL, C. J., LIU, M., HO, C. H., LIPPMAN, S. M. & TSAO, A. S. 2010. Meta-analysis of the impact of human papillomavirus (HPV) on cancer risk and overall survival in head and neck squamous cell carcinomas (HNSCC). *Head Neck Oncol,* 2**,** 15.

DE BRUIN, E. C. & MEDEMA, J. P. 2008. Apoptosis and non-apoptotic deaths in cancer development and treatment response. *Cancer Treat Rev,* 34**,** 737-49.

DE SCHUTTER, H., LANDUYT, W., VERBEKEN, E., GOETHALS, L., HERMANS, R. & NUYTS, S. 2005. The prognostic value of the hypoxia markers CA IX and GLUT 1 and the cytokines VEGF and IL 6 in head and neck squamous cell carcinoma treated by radiotherapy +/- chemotherapy. *BMC Cancer,* 5**,** 42.

DEBEFVE, E., MITHIEUX, F., PERENTES, J. Y., WANG, Y., CHENG, C., SCHAEFER, S. C., RUFFIEUX, C., BALLINI, J. P., GONZALEZ, M., VAN DEN BERGH, H., RIS, H. B., LEHR, H. A. & KRUEGER, T. 2011. Leukocyte-endothelial cell interaction is necessary for photodynamic therapy induced vascular permeabilization. *Lasers Surg Med,* 43**,** 696-704.

DEBUCQUOY, A., GOETHALS, L., LIBBRECHT, L., PERNEEL, C., GEBOES, K., ECTORS, N., MCBRIDE, W. H. & HAUSTERMANS, K. 2009. Molecular and clinico-pathological markers in rectal cancer: a tissue micro-array study. *Int J Colorectal Dis,* 24**,** 129-38.

DEBUCQUOY, A., LIBBRECHT, L., ROOBROUCK, V., GOETHALS, L., MCBRIDE, W. & HAUSTERMANS, K. 2008. Morphological features and molecular markers in rectal cancer from 95 patients included in the European Organisation for Research and Treatment of Cancer 22921 trial: prognostic value and effects of preoperative radio (chemo) therapy. *Eur J Cancer,* 44**,** 791-7.

DENNOG, C., GEDIK, C., WOOD, S. & SPEIT, G. 1999. Analysis of oxidative DNA damage and HPRT mutations in humans after hyperbaric oxygen treatment. *Mutat Res,* 431**,** 351-9.

DESAI, N., ABDELHAFEZ, F., DRAZBA, J., GOLDFARB, J. & FALCONE, T. 2010. A simple and efficient method for preparation of isolated ovarian follicles for transmission electron microscopy. *J Assist Reprod Genet,* 27**,** 97-101.

DEWEY, W. C., LING, C. C. & MEYN, R. E. 1995. Radiation-induced apoptosis: relevance to radiotherapy. *Int J Radiat Oncol Biol Phys,* 33**,** 781-96.

DIEFFENBACH, C. W., LOWE, T. M. & DVEKSLER, G. S. 1993. General concepts for PCR primer design. *PCR Methods Appl,* 3**,** S30-7.

DINSDALE, D., LEE, J. C., DEWSON, G., COHEN, G. M. & PETER, M. E. 2004. Intermediate filaments control the intracellular distribution of caspases during apoptosis. *Am J Pathol,* 164**,** 395-407.

DINSHAW, K. A., AGARWAL, J. P., GHOSH-LASKAR, S., GUPTA, T. & SHRIVASTAVA, S. K. 2006. Radical radiotherapy in head and neck squamous cell carcinoma: an analysis of prognostic and therapeutic factors. *Clin Oncol (R Coll Radiol),* 18**,** 383-9.

DISCHE, S., SAUNDERS, M., BARRETT, A., HARVEY, A., GIBSON, D. & PARMAR, M. 1997. A randomised multicentre trial of CHART versus conventional radiotherapy in head and neck cancer. *Radiother Oncol,* 44**,** 123-36.

DIVE, C., SMITH, R. A., GARNER, E., WARD, T., GEORGE-SMITH, S. S., CAMPBELL, F., GREENHALF, W., GHANEH, P. & NEOPTOLEMOS, J. P. 2010. Considerations for the use of plasma cytokeratin 18 as a biomarker in pancreatic cancer. *Br J Cancer,* 102**,** 577-82.

DUAN, W. R., GARNER, D. S., WILLIAMS, S. D., FUNCKES-SHIPPY, C. L., SPATH, I. S. & BLOMME, E. A. 2003. Comparison of immunohistochemistry for activated caspase-3 and cleaved cytokeratin 18 with the TUNEL method for quantification of apoptosis in histological sections of PC-3 subcutaneous xenografts. *J Pathol,* 199**,** 221-8.

DUBBEN, H. H., THAMES, H. D. & BECK-BORNHOLDT, H. P. 1998. Tumor volume: a basic and specific response predictor in radiotherapy. *Radiother Oncol,* 47**,** 167-74.

DUFFY, S. A., TAYLOR, J. M., TERRELL, J. E., ISLAM, M., LI, Y., FOWLER, K. E., WOLF, G. T. & TEKNOS, T. N. 2008. Interleukin-6 predicts recurrence and survival among head and neck cancer patients. *Cancer,* 113**,** 750-7.

DURST, M., GISSMANN, L., IKENBERG, H. & ZUR HAUSEN, H. 1983. A papillomavirus DNA from a cervical carcinoma and its prevalence in cancer biopsy samples from different geographic regions. *Proc Natl Acad Sci U S A,* 80**,** 3812-5.

DZIKIEWICZ-KRAWCZYK, A. 2008. The importance of making ends meet: mutations in genes and altered expression of proteins of the MRN complex and cancer. *Mutat Res,* 659**,** 262-73.

EDER-CZEMBIREK, C., CZEMBIREK, C., EROVIC, B. M., SELZER, E., TURHANI, D., VORMITTAG, L. & THURNHER, D. 2005. Combination of betulinic acid with cisplatin--different cytotoxic effects in two head and neck cancer cell lines. *Oncol Rep,* 14**,** 667-71.

EKSHYYAN, O., RONG, Y., RONG, X., PATTANI, K. M., ABREO, F., CALDITO, G., CHANG, J. K., AMPIL, F., GLASS, J. & NATHAN, C. O. 2009. Comparison of radiosensitizing effects of the mammalian target of rapamycin inhibitor CCI-779 to cisplatin in experimental models of head and neck squamous cell carcinoma. *Mol Cancer Ther,* 8**,** 2255-65.

EL HOUDA AGUEZNAY, N., BADOUAL, C., HANS, S., GEY, A., VINGERT, B., PEYRARD, S., QUINTIN-COLONNA, F., RAVEL, P., BRUNEVAL, P., RONCELIN, S., LELONGT, B., BERTOGLIO, J., FRIDMAN, W. H., BRASNU, D. & TARTOUR, E. 2007. Soluble interleukin-2 receptor and metalloproteinase-9 expression in head and neck cancer: prognostic value and analysis of their relationships. *Clin Exp Immunol,* 150**,** 114-23.

EL-ALI, J., SORGER, P. K. & JENSEN, K. F. 2006. Cells on chips. *Nature,* 442**,** 403-11.

EL-ENSAHSY, H. A., ABDEEN, A., ABDEEN, S., ELSAYED, E. A., DEMELLAWY, M. E. & SHEREEF, A. A. E. 2009. Serum concentration effects on the kinetics and metabolism of HeLa-S3 cell growth and cell

adaptability for successful proliferation in serum free medium. *World Applied Sciences Journal*, 6(5), 608-615.
ELIAS, J., DIMITRIO, L., CLAIRAMBAULT, J. & NATALINI, R. 2014. The p53 protein and its molecular network: modelling a missing link between DNA damage and cell fate. *Biochim Biophys Acta,* 1844**,** 232-47.
ELMORE, S. 2007. Apoptosis: a review of programmed cell death. *Toxicol Pathol,* 35**,** 495-516.
ERICKSON, H. S., ALBERT, P. S., GILLESPIE, J. W., RODRIGUEZ-CANALES, J., MARSTON LINEHAN, W., PINTO, P. A., CHUAQUI, R. F. & EMMERT-BUCK, M. R. 2009. Quantitative RT-PCR gene expression analysis of laser microdissected tissue samples. *Nat Protoc,* 4**,** 902-22.
ERIKSSON, D. & STIGBRAND, T. 2010. Radiation-induced cell death mechanisms. *Tumour Biol,* 31**,** 363-72.
ERMIAH, E., BUHMEIDA, A., ABDALLA, F., KHALED, B. R., SALEM, N., PYRHONEN, S. & COLLAN, Y. 2012. Prognostic value of proliferation markers: immunohistochemical ki-67 expression and cytometric s-phase fraction of women with breast cancer in libya. *J Cancer,* 3**,** 421-31.
ESPINA, V., WULFKUHLE, J. D., CALVERT, V. S., VANMETER, A., ZHOU, W., COUKOS, G., GEHO, D. H., PETRICOIN, E. F., 3RD & LIOTTA, L. A. 2006. Laser-capture microdissection. *Nat Protoc,* 1**,** 586-603.
FACCHINETTI, M. M., GANDINI, N. A., FERMENTO, M. E., STERIN-SPEZIALE, N. B., JI, Y., PATEL, V., GUTKIND, J. S., RIVADULLA, M. G. & CURINO, A. C. 2010. The expression of sphingosine kinase-1 in head and neck carcinoma. *Cells Tissues Organs,* 192**,** 314-24.
FAN, S., MULLER, S., CHEN, Z. G., PAN, L., TIGHIOUART, M., SHIN, D. M., KHURI, F. R. & SUN, S. Y. 2013. Prognostic impact of Fas-associated death domain, a key component in death receptor signaling, is dependent on the presence of lymph node metastasis in head and neck squamous cell carcinoma. *Cancer Biol Ther,* 14**,** 365-9.
FAN, Y., WENG, Z., GAO, H., HU, J., WANG, H., LI, L. & LIU, H. 2015. Isoalantolactone Enhances the Radiosensitivity of UMSCC-10A Cells via Specific Inhibition of Erk1/2 Phosphorylation. *PLoS One,* 10**,** e0145790.
FANG, L., GONG, J., WANG, Y., LIU, R., LI, Z., WANG, Z., ZHANG, Y., ZHANG, C., SONG, C., YANG, A., TING, J. P., JIN, B. & CHEN, L. 2014. MICA/B expression is inhibited by unfolded protein response and associated with poor prognosis in human hepatocellular carcinoma. *J Exp Clin Cancer Res,* 33**,** 76.
FAREED, K. R., SOOMRO, I. N., HAMEED, K., ARORA, A., LOBO, D. N., PARSONS, S. L. & MADHUSUDAN, S. 2012. Caspase-cleaved cytokeratin-18 and tumour regression in gastro-oesophageal adenocarcinomas treated with neoadjuvant chemotherapy. *World J Gastroenterol,* 18**,** 1915-20.
FARSHADPOUR, F., HORDIJK, G. J., KOOLE, R. & SLOOTWEG, P. J. 2007. Non-smoking and non-drinking patients with head and neck squamous cell carcinoma: a distinct population. *Oral Dis,* 13**,** 239-43.
FARSHADPOUR, F., KRANENBORG, H., CALKOEN, E. V., HORDIJK, G. J., KOOLE, R., SLOOTWEG, P. J. & TERHAARD, C. H. 2011. Survival analysis of head and neck squamous cell carcinoma: influence of smoking and drinking. *Head Neck,* 33**,** 817-23.
FEND, F. & RAFFELD, M. 2000. Laser capture microdissection in pathology. *J Clin Pathol,* 53**,** 666-72.
FENG, J., ZOU, J., LI, L., ZHAO, Y. & LIU, S. 2011. Antisense oligodeoxynucleotides targeting ATM strengthen apoptosis of laryngeal squamous cell carcinoma grown in nude mice. *J Exp Clin Cancer Res,* 30**,** 43.
FERLAY, J., SOERJOMATARAM, I., DIKSHIT, R., ESER, S., MATHERS, C., REBELO, M., PARKIN, D. M., FORMAN, D. & BRAY, F. 2015. Cancer incidence and mortality worldwide: sources, methods and major patterns in GLOBOCAN 2012. *Int J Cancer,* 136**,** E359-86.
FERNANDEZ-CAPETILLO, O., ALLIS, C. D. & NUSSENZWEIG, A. 2004. Phosphorylation of histone H2B at DNA double-strand breaks. *J Exp Med,* 199**,** 1671-7.
FISCHER, C. A., JUNG, M., ZLOBEC, I., GREEN, E., STORCK, C., TORNILLO, L., LUGLI, A., WOLFENSBERGER, M. & TERRACCIANO, L. M. 2011. Co-overexpression of p21 and Ki-67 in head and neck squamous cell carcinoma relative to a significantly poor prognosis. *Head Neck,* 33**,** 267-73.
FLANDERS, W. D. & ROTHMAN, K. J. 1982. Interaction of alcohol and tobacco in laryngeal cancer. *Am J Epidemiol,* 115**,** 371-9.
FRANCIS, J. M., ZHANG, C. Z., MAIRE, C. L., JUNG, J., MANZO, V. E., ADALSTEINSSON, V. A., HOMER, H., HAIDAR, S., BLUMENSTIEL, B., PEDAMALLU, C. S., LIGON, A. H., LOVE, J. C., MEYERSON, M. & LIGON, K. L. 2014. EGFR variant heterogeneity in glioblastoma resolved through single-nucleus sequencing. *Cancer Discov,* 4**,** 956-71.
FRANZMANN, E. J., REATEGUI, E. P., PEDROSO, F., PERNAS, F. G., KARAKULLUKCU, B. M., CARRAWAY, K. L., HAMILTON, K., SINGAL, R. & GOODWIN, W. J. 2007. Soluble CD44 is a potential marker for the early detection of head and neck cancer. *Cancer Epidemiol Biomarkers Prev,* 16**,** 1348-55.
FREUDLSPERGER, C., HORN, D., WEISSFUSS, S., WEICHERT, W., WEBER, K. J., SAURE, D., SHARMA, S., DYCKHOFF, G., GRABE, N., PLINKERT, P., HOFFMANN, J., FREIER, K. & HESS, J. 2015. Phosphorylation of AKT(Ser473) serves as an independent prognostic marker for radiosensitivity in advanced head and neck squamous cell carcinoma. *Int J Cancer,* 136**,** 2775-85.

FROHLICH, E. M., ALONSO, J. L., BORENSTEIN, J. T., ZHANG, X., ARNAOUT, M. A. & CHAREST, J. L. 2013. Topographically-patterned porous membranes in a microfluidic device as an *in vitro* model of renal reabsorptive barriers. *Lab Chip,* 13**,** 2311-9.

FROST, A. R., ELTOUM, I. E. & SIEGAL, G. P. 2001. Laser capture microdissection. *Curr Protoc Mol Biol,* Chapter 25**,** Unit 25A 1.

FUJIKAWA-YAMAMOTO, K., OTA, T., MIYAGOSHI, M. & YAMAGISHI, H. 2012. Effects of etoposide on the proliferation of hexaploid H1 (ES) cells. *Hum Cell,* 25**,** 45-50.

FUKAI, Y., FUKUCHI, M., MASUDA, N., OSAWA, H., KATO, H., NAKAJIMA, T. & KUWANO, H. 2003. Reduced expression of transforming growth factor-beta receptors is an unfavorable prognostic factor in human esophageal squamous cell carcinoma. *Int J Cancer,* 104**,** 161-6.

FUKUMURA, D. & JAIN, R. K. 2007. Tumor microenvironment abnormalities: causes, consequences, and strategies to normalize. *J Cell Biochem,* 101**,** 937-49.

GABRIELLI, B., BROOKS, K. & PAVEY, S. 2012. Defective cell cycle checkpoints as targets for anti-cancer therapies. *Front Pharmacol,* 3**,** 9.

GALBIATTI, A. L., PADOVANI-JUNIOR, J. A., MANIGLIA, J. V., RODRIGUES, C. D., PAVARINO, E. C. & GOLONI-BERTOLLO, E. M. 2013. Head and neck cancer: causes, prevention and treatment. *Braz J Otorhinolaryngol,* 79**,** 239-47.

GALLO, O., BODDI, V., CALZOLARI, A., SIMONETTI, L., TROVATI, M. & BIANCHI, S. 1996b. bcl-2 protein expression correlates with recurrence and survival in early stage head and neck cancer treated by radiotherapy. *Clin Cancer Res,* 2**,** 261-7.

GALLO, O., CHIARELLI, I., BIANCHI, S., CALZOLARI, A., SIMONETTI, L. & PORFIRIO, B. 1996a. Loss of p53 gene mutation after irradiation is associated with increased aggressiveness in recurring head and neck cancer. *Clin Cancer Res,* 2**,** 1577-82.

GALLO, O., CHIARELLI, I., BODDI, V., BOCCIOLINI, C., BRUSCHINI, L. & PORFIRIO, B. 1999. Cumulative prognostic value of p53 mutations and bcl-2 protein expression in head-and-neck cancer treated by radiotherapy. *Int J Cancer,* 84**,** 573-9.

GANDINI, S., BOTTERI, E., IODICE, S., BONIOL, M., LOWENFELS, A. B., MAISONNEUVE, P. & BOYLE, P. 2008. Tobacco smoking and cancer: a meta-analysis. *Int J Cancer,* 122**,** 155-64.

GARRIDO-LAGUNA, I., USON, M., RAJESHKUMAR, N. V., TAN, A. C., DE OLIVEIRA, E., KARIKARI, C., VILLAROEL, M. C., SALOMON, A., TAYLOR, G., SHARMA, R., HRUBAN, R. H., MAITRA, A., LAHERU, D., RUBIO-VIQUEIRA, B., JIMENO, A. & HIDALGO, M. 2011. Tumor engraftment in nude mice and enrichment in stroma- related gene pathways predict poor survival and resistance to gemcitabine in patients with pancreatic cancer. *Clin Cancer Res,* 17**,** 5793-800.

GARTEL, A. L. & TYNER, A. L. 2002. The role of the cyclin-dependent kinase inhibitor p21 in apoptosis. *Mol Cancer Ther,* 1**,** 639-49.

GARTY, G., GRAD, M., JONES, B. K., XU, Y., XU, J., RANDERS-PEHRSON, G., ATTINGER, D. & BRENNER, D. J. 2011. Design of a Novel Flow-and-Shoot Microbeam. *Radiation Protection Dosimetry,* 143**,** 344-348.

GASPARRI, F., MARIANI, M., SOLA, F. & GALVANI, A. 2004. Quantification of the proliferation index of human dermal fibroblast cultures with the ArrayScan high-content screening reader. *J Biomol Screen,* 9**,** 232-43.

GATEI, M., SCOTT, S. P., FILIPPOVITCH, I., SORONIKA, N., LAVIN, M. F., WEBER, B. & KHANNA, K. K. 2000. Role for ATM in DNA damage-induced phosphorylation of BRCA1. *Cancer Res,* 60**,** 3299-304.

GAZDA, M. J. & COIA, L. R. 2007. Principles of radiation therapy. In Pazdur, R., Coia, L. R., Hoskins, W. K. & Wagman, L. D. (ed) *Cancer managemenr: A multidisciplinary approach*. SCP Oncology Group, Chapter 2.

GIBSON, L. F., FORTNEY, J., MAGRO, G., ERICSON, S. G., LYNCH, J. P. & LANDRETH, K. S. 1999. Regulation of BAX and BCL-2 expression in breast cancer cells by chemotherapy. *Breast Cancer Res Treat,* 55**,** 107-17.

GILLESPIE, M. B., RUBINCHIK, S., HOEL, B. & SUTKOWSKI, N. 2009. Human papillomavirus and oropharyngeal cancer: what you need to know in 2009. *Curr Treat Options Oncol,* 10**,** 296-307.

GILLISON, M. L. 2016. Nivolumab improved survival for patients with head and neck squamous cell carcinoma. Available online: http://www.aacr.org/Newsroom/Pages/News-Release-Detail.aspx?ItemID=882#.V_IMN0wrKUk. [Accessed August 2016].

GILLISON, M. L., D'SOUZA, G., WESTRA, W., SUGAR, E., XIAO, W., BEGUM, S. & VISCIDI, R. 2008. Distinct risk factor profiles for human papillomavirus type 16-positive and human papillomavirus type 16-negative head and neck cancers. *J Natl Cancer Inst,* 100**,** 407-20.

GIOTAKIS, J., GOMATOS, I. P., ALEVIZOS, L., GEORGIOU, A. N., LEANDROS, E., KONSTADOULAKIS, M. M. & MANOLOPOULOS, L. 2010. Bax, cytochrome c, and caspase-8 staining in parotid cancer patients: markers of susceptibility in radiotherapy? *Otolaryngol Head Neck Surg,* 142**,** 605-11.

GOEL, H. L., SAYEED, A., BREEN, M., ZARIF, M. J., GARLICK, D. S., LEAV, I., DAVIS, R. J., FITZGERALD, T. J., MORRIONE, A., HSIEH, C. C., LIU, Q., DICKER, A. P., ALTIERI, D. C. & LANGUINO, L. R. 2013. beta1 integrins mediate resistance to ionizing radiation *in vivo* by inhibiting c-Jun amino terminal kinase 1. *J Cell Physiol,* 228**,** 1601-9.

GOKHALE, S.V., TAYAL, R.K., JAYARAMAN, V.K. & KULKARNI, B.D., 2005. Microchannel reactors: applications and use in process development.*International Journal of Chemical Reactor Engineering*, *3*(1).
GOLDSWORTHY, S. M., STOCKTON, P. S., TREMPUS, C. S., FOLEY, J. F. & MARONPOT, R. R. 1999. Effects of fixation on RNA extraction and amplification from laser capture microdissected tissue. *Mol Carcinog,* 25**,** 86-91.
GOODSON, W. H., 3RD, MOORE, D. H., 2ND, LJUNG, B. M., CHEW, K., FLORENDO, C., MAYALL, B., SMITH, H. S. & WALDMAN, F. M. 1998. The functional relationship between *in vivo* bromodeoxyuridine labeling index and Ki-67 proliferation index in human breast cancer. *Breast Cancer Res Treat,* 49**,** 155-64.
GOPING, I. S., GROSS, A., LAVOIE, J. N., NGUYEN, M., JEMMERSON, R., ROTH, K., KORSMEYER, S. J. & SHORE, G. C. 1998. Regulated targeting of BAX to mitochondria. *J Cell Biol,* 143**,** 207-15.
GRDINA, D. J., MURLEY, J. S., MILLER, R. C., MAUCERI, H. J., SUTTON, H. G., LI, J. J., WOLOSCHAK, G. E. & WEICHSELBAUM, R. R. 2013. A survivin-associated adaptive response in radiation therapy. *Cancer Res,* 73**,** 4418-28.
GREGOIRE, V., LEFEBVRE, J. L., LICITRA, L., FELIP, E. & GROUP, E.-E.-E. G. W. 2010. Squamous cell carcinoma of the head and neck: EHNS-ESMO-ESTRO Clinical Practice Guidelines for diagnosis, treatment and follow-up. *Ann Oncol,* 21 Suppl 5**,** v184-6.
GREGORY, E. M., GOSCIN, S. A. & FRIDOVICH, I. 1974. Superoxide dismutase and oxygen toxicity in a eukaryote. *J Bacteriol,* 117**,** 456-60.
GREYSTOKE, A., DEAN, E., SAUNDERS, M. P., CUMMINGS, J., HUGHES, A., RANSON, M., DIVE, C. & RENEHAN, A. G. 2012. Multi-level evidence that circulating CK18 is a biomarker of tumour burden in colorectal cancer. *Br J Cancer,* 107**,** 1518-24.
GROSBERG, A., ALFORD, P. W., MCCAIN, M. L. & PARKER, K. K. 2011. Ensembles of engineered cardiac tissues for physiological and pharmacological study: heart on a chip. *Lab Chip,* 11**,** 4165-73.
GROUNDS, M. 2010. *Quantification of histopathology in Haemotoxylin and Eosin stained muscle sections*. Available online: http://www.treat-nmd.eu/downloads/file/sops/dmd/MDX/DMD_M.1.2.007.pdf [Accessed on February 2016].
GUO, B., CAO, S., TOTH, K., AZRAK, R. G. & RUSTUM, Y. M. 2000. Overexpression of Bax enhances antitumor activity of chemotherapeutic agents in human head and neck squamous cell carcinoma. *Clin Cancer Res,* 6**,** 718-24.
HADDAD, R. I. & SHIN, D. M. 2008. Recent advances in head and neck cancer. *N Engl J Med,* 359**,** 1143-54.
HALAMKA, M., CVEK, J., KUBES, J., ZAVADOVA, E., KOMINEK, P., HORACEK, J., DUSEK, L. & FELTL, D. 2011. Plasma levels of vascular endothelial growth factor during and after radiotherapy in combination with celecoxib in patients with advanced head and neck cancer. *Oral Oncol,* 47**,** 763-7.
HALLDORSSON, S., LUCUMI, E., GOMEZ-SJOBERG, R. & FLEMING, R. M. 2015. Advantages and challenges of microfluidic cell culture in polydimethylsiloxane devices. *Biosens Bioelectron,* 63**,** 218-31.
HALLOW, D. M., SEEGER, R. A., KAMAEV, P. P., PRADO, G. R., LAPLACA, M. C. & PRAUSNITZ, M. R. 2008. Shear-induced intracellular loading of cells with molecules by controlled microfluidics. *Biotechnol Bioeng,* 99**,** 846-54.
HANSEN, A. R. & SIU, L. L. 2013. Epidermal growth factor receptor targeting in head and neck cancer: have we been just skimming the surface? *J Clin Oncol,* 31**,** 1381-3.
HARRIS, M., WANG, X. G., JIANG, Z., PHAETON, R., KOBA, W., GOLDBERG, G. L., CASADEVALL, A. & DADACHOVA, E. 2013. Combined treatment of the experimental human papilloma virus-16-positive cervical and head and neck cancers with cisplatin and radioimmunotherapy targeting viral E6 oncoprotein. *Br J Cancer,* 108**,** 859-65.
HASHIBE, M. & STURGIS, E. M. 2013. Epidemiology of oral-cavity and oropharyngeal carcinomas: controlling a tobacco epidemic while a human papillomavirus epidemic emerges. *Otolaryngol Clin North Am,* 46**,** 507-20.
HASHIBE, M., BRENNAN, P., BENHAMOU, S., CASTELLSAGUE, X., CHEN, C., CURADO, M. P., DAL MASO, L., DAUDT, A. W., FABIANOVA, E., FERNANDEZ, L., WUNSCH-FILHO, V., FRANCESCHI, S., HAYES, R. B., HERRERO, R., KOIFMAN, S., LA VECCHIA, C., LAZARUS, P., LEVI, F., MATES, D., MATOS, E., MENEZES, A., MUSCAT, J., ELUF-NETO, J., OLSHAN, A. F., RUDNAI, P., SCHWARTZ, S. M., SMITH, E., STURGIS, E. M., SZESZENIA-DABROWSKA, N., TALAMINI, R., WEI, Q., WINN, D. M., ZARIDZE, D., ZATONSKI, W., ZHANG, Z. F., BERTHILLER, J. & BOFFETTA, P. 2007. Alcohol drinking in never users of tobacco, cigarette smoking in never drinkers, and the risk of head and neck cancer: pooled analysis in the International Head and Neck Cancer Epidemiology Consortium. *J Natl Cancer Inst,* 99**,** 777-89.
HASS, H. G., SCHMIDT, A., NEHLS, O. & KAISER, S. 2008. DNA ploidy, proliferative capacity and intratumoral heterogeneity in primary and recurrent head and neck squamous cell carcinomas (HNSCC) - Potential implications for clinical management and treatment decisions. *Oral Oncology,* 44**,** 78-85.

HASSAN, K. A., ANG, K. K., EL-NAGGAR, A. K., STORY, M. D., LEE, J. I., LIU, D., HONG, W. K. & MAO, L. 2002. Cyclin B1 overexpression and resistance to radiotherapy in head and neck squamous cell carcinoma. *Cancer Res,* 62**,** 6414-7.
HATTERSLEY, S. M. 2010. Development of microfluidic devices to maintain and interrogate tissue biopsies-biomedical applications. PhD thesis. The University of Hull.
HATTERSLEY, S. M., DYER, C. E., GREENMAN, J. & HASWELL, S. J. 2008. Development of a microfluidic device for the maintenance and interrogation of viable tissue biopsies. *Lab Chip,* 8**,** 1842-6.
HATTERSLEY, S. M., GREENMAN, J. & HASWELL, S. J. 2011. Study of ethanol induced toxicity in liver explants using microfluidic devices. *Biomed Microdevices,* 13**,** 1005-14.
HATTERSLEY, S. M., SYLVESTER, D. C., DYER, C. E., STAFFORD, N. D., HASWELL, S. J. & GREENMAN, J. 2012. A microfluidic system for testing the responses of head and neck squamous cell carcinoma tissue biopsies to treatment with chemotherapy drugs. *Ann Biomed Eng,* 40**,** 1277-88.
HAYASHI, H., OKAMOTO, I., KIMURA, H., SAKAI, K., NISHIMURA, Y., NISHIO, K. & NAKAGAWA, K. 2012. Clinical outcomes of thoracic radiotherapy for locally advanced NSCLC with EGFR mutations or EML4-ALK rearrangement. *Anticancer Res,* 32**,** 4533-7.
HAYES, M., LAN, C., YAN, J., XIE, Y., GRAY, T., AMIRKHAN, R. H. & DOWELL, J. E. 2011. ERCC1 expression and outcomes in head and neck cancer treated with concurrent cisplatin and radiation. *Anticancer Res,* 31**,** 4135-9.
HE, B., TAN, L. & REGNIER, F. 1999. Microfabricated filters for microfluidic analytical systems. *Anal Chem,* 71**,** 1464-8.
HEAD AND NECK NSSG, 2014. *Head and Neck Network Group: Head and Neck Cancer Treatment Guidelines version number: 4.0*. UK: NHS.
HECHT, S. S. 2008. Progress and challenges in selected areas of tobacco carcinogenesis. *Chem Res Toxicol,* 21**,** 160-71.
HERR, A. E., HATCH, A. V., GIANNOBILE, W. V., THROCKMORTON, D. J., TRAN, H. M., BRENNAN, J. S. & SINGH, A. K. 2007. Integrated microfluidic platform for oral diagnostics. *Ann N Y Acad Sci,* 1098**,** 362-74.
HERZOG, A., BIAN, Y., VANDER BROEK, R., HALL, B., COUPAR, J., CHENG, H., SOWERS, A. L., COOK, J. D., MITCHELL, J. B., CHEN, Z., KULKARNI, A. B. & VAN WAES, C. 2013. PI3K/mTOR inhibitor PF-04691502 antitumor activity is enhanced with induction of wild-type TP53 in human xenograft and murine knockout models of head and neck cancer. *Clin Cancer Res,* 19**,** 3808-19.
HILEY, C., DE BRUIN, E. C., MCGRANAHAN, N. & SWANTON, C. 2014. Deciphering intratumor heterogeneity and temporal acquisition of driver events to refine precision medicine. *Genome Biol,* 15**,** 453.
HILL, R. P. & MILAS, L. 1989. The proportion of stem cells in murine tumors. *Int J Radiat Oncol Biol Phys,* 16**,** 513-8.
HOCKENBERY, D., NUNEZ, G., MILLIMAN, C., SCHREIBER, R. D. & KORSMEYER, S. J. 1990. Bcl-2 is an inner mitochondrial membrane protein that blocks programmed cell death. *Nature,* 348**,** 334-6.
HOFF, C. M., HANSEN, H. S., OVERGAARD, M., GRAU, C., JOHANSEN, J., BENTZEN, J. & OVERGAARD, J. 2011. The importance of haemoglobin level and effect of transfusion in HNSCC patients treated with radiotherapy--results from the randomized DAHANCA 5 study. *Radiother Oncol,* 98**,** 28-33.
HOLLIDAY, E. B. & FRANK, S. J. 2014. Proton radiation therapy for head and neck cancer: a review of the clinical experience to date. *Int J Radiat Oncol Biol Phys,* 89**,** 292-302.
HOLUBEC, H., PAYNE, C. M., BERNSTEIN, H., DVORAKOVA, K., BERNSTEIN, C., WALTMIRE, C. N., WARNEKE, J. A. & GAREWAL, H. 2005. Assessment of apoptosis by immunohistochemical markers compared to cellular morphology in *ex vivo*-stressed colonic mucosa. *J Histochem Cytochem,* 53**,** 229-35.
HONG, D. J. & GHOSH, R. N. 2008. High content screening assay for monitoring cell proliferative activity by multiplexed measurements of DNA content, BrdU and Ki67. *Thermo Scientific Cellomics*.
HONORATO, B., ALCALDE, J., MARTINEZ-MONGE, R., ZABALEGUI, N. & GARCIA-FONCILLAS, J. 2008. TAK1 mRNA expression in the tumor tissue of locally advanced head and neck cancer patients. *Gene Regul Syst Bio,* 2**,** 63-70.
HORN, D., HESS, J., FREIER, K., HOFFMANN, J. & FREUDLSPERGER, C. 2015. Targeting EGFR-PI3K-AKT-mTOR signaling enhances radiosensitivity in head and neck squamous cell carcinoma. *Expert Opin Ther Targets,* 19**,** 795-805.
HOROBIN, R. W. 2010. How do dyes impart color to different components of the tissues? In KUMAR, G. L. and KIERNAN, J. A. (2nd ed) *Education guide: Special stains and H&E*. California: Dako North America, 159-166.
HOSOYA, N. & MIYAGAWA, K. 2014. Targeting DNA damage response in cancer therapy. *Cancer Sci,* 105**,** 370-88.
HU, B., ELINAV, E., HUBER, S., BOOTH, C. J., STROWIG, T., JIN, C., EISENBARTH, S. C. & FLAVELL, R. A. 2010. Inflammation-induced tumorigenesis in the colon is regulated by caspase-1 and NLRC4. *Proc Natl Acad Sci U S A,* 107**,** 21635-40.

HUANG, X., HALICKA, H. D., TRAGANOS, F., TANAKA, T., KUROSE, A. & DARZYNKIEWICZ, Z. 2005. Cytometric assessment of DNA damage in relation to cell cycle phase and apoptosis. *Cell Prolif,* 38**,** 223-43.

HUDDER, A., NATHANSON, L. & DEUTSCHER, M. P. 2003. Organization of mammalian cytoplasm. *Mol Cell Biol,* 23**,** 9318-26.

HUH, D., KIM, H. J., FRASER, J. P., SHEA, D. E., KHAN, M., BAHINSKI, A., HAMILTON, G. A. & INGBER, D. E. 2013. Microfabrication of human organs-on-chips. *Nat Protoc,* 8**,** 2135-57.

HUH, D., MATTHEWS, B. D., MAMMOTO, A., MONTOYA-ZAVALA, M., HSIN, H. Y. & INGBER, D. E. 2010. Reconstituting organ-level lung functions on a chip. *Science,* 328**,** 1662-8.

IARC. 2015. List of Classifications by cancer sites with sufficient or limited evidencen in humans, Volumes 1 to 113. Available online: https://monographs.iarc.fr/ENG/Classification/Table4.pdf. [Accessed on February 2015].

IKARI, A., TAKIGUCHI, A., ATOMI, K., SATO, T. & SUGATANI, J. 2011. Decrease in claudin-2 expression enhances cell migration in renal epithelial Madin-Darby canine kidney cells. *J Cell Physiol,* 226**,** 1471-8.

ITZHAKI. J. 2012. *DNA damage recognition: keeping the right players on board*. Available online: http://www.bioch.ox.ac.uk/aspsite/index.asp?pageid=892. [Accessed on August 2014].

JACKSON, S. P. & BARTEK, J. 2009. The DNA-damage response in human biology and disease. *Nature,* 461**,** 1071-8.

JANG, K. J. & SUH, K. Y. 2010. A multi-layer microfluidic device for efficient culture and analysis of renal tubular cells. *Lab Chip,* 10**,** 36-42.

JAVID, S. & MOHAMMADI, M. 2012. Boundary shear stress in a trapezoidal channel. *International Journal of Engineering-Transactions A: Basics*, 25(4), 323.

JEON, J. S., ZERVANTONAKIS, I. K., CHUNG, S., KAMM, R. D. & CHAREST, J. L. 2013. *In vitro* model of tumor cell extravasation. *PLoS One,* 8**,** e56910.

JIMENO, A., FELDMANN, G., SUAREZ-GAUTHIER, A., RASHEED, Z., SOLOMON, A., ZOU, G. M., RUBIO-VIQUEIRA, B., GARCIA-GARCIA, E., LOPEZ-RIOS, F., MATSUI, W., MAITRA, A. & HIDALGO, M. 2009. A direct pancreatic cancer xenograft model as a platform for cancer stem cell therapeutic development. *Mol Cancer Ther,* 8**,** 310-4.

JIN, Z. & EL-DEIRY, W. S. 2005. Overview of cell death signaling pathways. *Cancer Biol Ther,* 4**,** 139-63.

JUN, H. J., AHN, M. J., KIM, H. S., YI, S. Y., HAN, J., LEE, S. K., AHN, Y. C., JEONG, H. S., SON, Y. I., BAEK, J. H. & PARK, K. 2008. ERCC1 expression as a predictive marker of squamous cell carcinoma of the head and neck treated with cisplatin-based concurrent chemoradiation. *Br J Cancer,* 99**,** 167-72.

KADYROV, M., KAUFMANN, P. & HUPPERTZ, B. 2001. Expression of a cytokeratin 18 neo-epitope is a specific marker for trophoblast apoptosis in human placenta. *Placenta,* 22**,** 44-8.

KAHN, J., TOFILON, P. J. & CAMPHAUSEN, K. 2012. Preclinical models in radiation oncology. *Radiat Oncol,* 7**,** 223.

KAMIJO, T., YOKOSE, T., HASEBE, T., YONOU, H., SASAKI, S., HAYASHI, R., EBIHARA, S., MIYAHARA, H., HOSOI, H. & OCHIAI, A. 2000. Potential role of microvessel density in predicting radiosensitivity of T1 and T2 stage laryngeal squamous cell carcinoma treated with radiotherapy. *Clin Cancer Res,* 6**,** 3159-65.

KANG, M. A., SO, E. Y., SIMONS, A. L., SPITZ, D. R. & OUCHI, T. 2012. DNA damage induces reactive oxygen species generation through the H2AX-Nox1/Rac1 pathway. *Cell Death Dis,* 3**,** e249.

KASTEN-PISULA, U., MENEGAKIS, A., BRAMMER, I., BORGMANN, K., MANSOUR, W. Y., DEGENHARDT, S., KRAUSE, M., SCHREIBER, A., DAHM-DAPHI, J., PETERSEN, C., DIKOMEY, E. & BAUMANN, M. 2009. The extreme radiosensitivity of the squamous cell carcinoma SKX is due to a defect in double-strand break repair. *Radiother Oncol,* 90**,** 257-64.

KASTNER, E., KAUR, R., LOWRY, D., MOGHADDAM, B., WILKINSON, A. & PERRIE, Y. 2014. High-throughput manufacturing of size-tuned liposomes by a new microfluidics method using enhanced statistical tools for characterization. *Int J Pharm,* 477**,** 361-8.

KEE, N., SIVALINGAM, S., BOONSTRA, R. & WOJTOWICZ, J. M. 2002. The utility of Ki-67 and BrdU as proliferative markers of adult neurogenesis. *J Neurosci Methods,* 115**,** 97-105.

KELLY, K. J., SANDOVAL, R. M., DUNN, K. W., MOLITORIS, B. A. & DAGHER, P. C. 2003. A novel method to determine specificity and sensitivity of the TUNEL reaction in the quantitation of apoptosis. *Am J Physiol Cell Physiol,* 284**,** C1309-18.

KELLY, P. N. & STRASSER, A. 2011. The role of Bcl-2 and its pro-survival relatives in tumourigenesis and cancer therapy. *Cell Death Differ,* 18**,** 1414-24.

KERKAR, S. P. & RESTIFO, N. P. 2012. Cellular constituents of immune escape within the tumor microenvironment. *Cancer Res,* 72**,** 3125-30.

KHADEMHOSSEINI, A., LANGER, R., BORENSTEIN, J. & VACANTI, J. P. 2006. Microscale technologies for tissue engineering and biology. *Proc Natl Acad Sci U S A,* 103**,** 2480-7.

KHADEMI, B., SOLEIMANPOUR, M., GHADERI, A. & MOHAMMADIANPANAH, M. 2014. Prognostic and predictive value of serum vascular endothelial growth factor (VEGF) in squamous cell carcinoma of the head and neck. *Oral Maxillofac Surg,* 18**,** 187-96.

KHAN, Z., KHAN, N., TIWARI, R. P., PATRO, I. K., PRASAD, G. B. & BISEN, P. S. 2010. Down-regulation of survivin by oxaliplatin diminishes radioresistance of head and neck squamous carcinoma cells. *Radiother Oncol,* 96**,** 267-73.

KIM, B. M., HONG, Y., LEE, S., LIU, P., LIM, J. H., LEE, Y. H., LEE, T. H., CHANG, K. T. & HONG, Y. 2015. Therapeutic Implications for Overcoming Radiation Resistance in Cancer Therapy. *Int J Mol Sci,* 16**,** 26880-913.

KIM, H. A., KOO, B. K., CHO, J. H., KIM, Y. Y., SEONG, J., CHANG, H. J., OH, Y. M., STANGE, D. E., PARK, J. G., HWANG, D. & KONG, Y. Y. 2012. Notch1 counteracts WNT/beta-catenin signaling through chromatin modification in colorectal cancer. *J Clin Invest,* 122**,** 3248-59.

KIM, H., SAKA, B., KNIGHT, S., BORGES, M., CHILDS, E., KLEIN, A., WOLFGANG, C., HERMAN, J., ADSAY, V. N., HRUBAN, R. H. & GOGGINS, M. 2014. Having pancreatic cancer with tumoral loss of ATM and normal TP53 protein expression is associated with a poorer prognosis. *Clin Cancer Res,* 20**,** 1865-72.

KIM, J. J. & TANNOCK, I. F. 2005. Repopulation of cancer cells during therapy: an important cause of treatment failure. *Nat Rev Cancer,* 5**,** 516-25.

KIM, L., TOH, Y. C., VOLDMAN, J. & YU, H. 2007. A practical guide to microfluidic perfusion culture of adherent mammalian cells. *Lab Chip,* 7**,** 681-94.

KIM, S. J., KIM, B. S., CHOI, C. W., CHOI, J., KIM, I., LEE, Y. H. & KIM, J. S. 2007. Ki-67 expression is predictive of prognosis in patients with stage I/II extranodal NK/T-cell lymphoma, nasal type. *Ann Oncol,* 18**,** 1382-7.

KIMPLE, R. J., HARARI, P. M., TORRES, A. D., YANG, R. Z., SORIANO, B. J., YU, M., ARMSTRONG, E. A., BLITZER, G. C., SMITH, M. A., LORENZ, L. D., LEE, D., YANG, D. T., MCCULLOCH, T. M., HARTIG, G. K. & LAMBERT, P. F. 2013. Development and characterization of HPV-positive and HPV-negative head and neck squamous cell carcinoma tumorgrafts. *Clin Cancer Res,* 19**,** 855-64.

KING, K. L. & CIDLOWSKI, J. A. 1998. Cell cycle regulation and apoptosis. *Annu Rev Physiol,* 60**,** 601-17.

KITAGAWA, R. & KASTAN, M. B. 2005. The ATM-dependent DNA damage signaling pathway. *Cold Spring Harb Symp Quant Biol,* 70**,** 99-109.

KLEIN, H. L. 2008. The consequences of Rad51 overexpression for normal and tumor cells. *DNA Repair (Amst),* 7**,** 686-93.

KNAUER, S. K., UNRUHE, B., KARCZEWSKI, S., HECHT, R., FETZ, V., BIER, C., FRIEDL, S., WOLLENBERG, B., PRIES, R., HABTEMICHAEL, N., HEINRICH, U. R. & STAUBER, R. H. 2013. Functional characterization of novel mutations affecting survivin (BIRC5)-mediated therapy resistance in head and neck cancer patients. *Hum Mutat,* 34**,** 395-404.

KNUTSVIK, G., STEFANSSON, I. M., AZIZ, S., ARNES, J., EIDE, J., COLLETT, K. & AKSLEN, L. A. 2014. Evaluation of Ki67 expression across distinct categories of breast cancer specimens: a population-based study of matched surgical specimens, core needle biopsies and tissue microarrays. *PLoS One,* 9**,** e112121.

KOBERLE, B., DITZ, C., KAUSCH, I., WOLLENBERG, B., FERRIS, R. L. & ALBERS, A. E. 2010. Metastases of squamous cell carcinoma of the head and neck show increased levels of nucleotide excision repair protein XPF *in vivo* that correlate with increased chemoresistance *ex vivo*. *Int J Oncol,* 36**,** 1277-84.

KOCAOEMER, A., KERN, S., KLUTER, H. & BIEBACK, K. 2007. Human AB serum and thrombin-activated platelet-rich plasma are suitable alternatives to fetal calf serum for the expansion of mesenchymal stem cells from adipose tissue. *Stem Cells,* 25**,** 1270-8.

KOELINK, P. J., LAMERS, C. B., HOMMES, D. W. & VERSPAGET, H. W. 2009. Circulating cell death products predict clinical outcome of colorectal cancer patients. *BMC Cancer,* 9**,** 88.

KOLIJN, K. & VAN LEENDERS, G. J. 2016. Comparison of RNA extraction kits and histological stains for laser capture microdissected prostate tissue. *BMC Res Notes,* 9**,** 17.

KOMEYA, M., KIMURA, H., NAKAMURA, H., YOKONISHI, T., SATO, T., KOJIMA, K., HAYASHI, K., KATAGIRI, K., YAMANAKA, H., SANJO, H., YAO, M., KAMIMURA, S., INOUE, K., OGONUKI, N., OGURA, A., FUJII, T. & OGAWA, T. 2016. Long-term *ex vivo* maintenance of testis tissues producing fertile sperm in a microfluidic device. *Sci Rep,* 6**,** 21472.

KONISHI, N., HIASA, Y., MATSUDA, H., TAO, M., TSUZUKI, T., HAYASHI, I., KITAHORI, Y., SHIRAISHI, T., YATANI, R., SHIMAZAKI, J. *& ET AL*. 1995. Intratumor cellular heterogeneity and alterations in ras oncogene and p53 tumor suppressor gene in human prostate carcinoma. *Am J Pathol,* 147**,** 1112-22.

KOSLABOVA, E., HAMSIKOVA, E., SALAKOVA, M., KLOZAR, J., FOLTYNOVA, E., SALKOVA, E., ROTNAGLOVA, E., LUDVIKOVA, V. & TACHEZY, R. 2013. Markers of HPV infection and survival in patients with head and neck tumors. *Int J Cancer,* 133**,** 1832-9.

KOTHARI, V. & MULHERKAR, R. 2012. Inhibition of cyclin D1 by shRNA is associated with enhanced sensitivity to conventional therapies for head and neck squamous cell carcinoma. *Anticancer Res,* 32**,** 121-8.

KOUKOURAKIS, M. I. 2012. Radiation damage and radioprotectants: new concepts in the era of molecular medicine. *Br J Radiol,* 85**,** 313-30.
KOUKOURAKIS, M. I., GIATROMANOLAKI, A., FOUNTZILAS, G., SIVRIDIS, E., GATTER, K. C. & HARRIS, A. L. 2000. Angiogenesis, thymidine phosphorylase, and resistance of squamous cell head and neck cancer to cytotoxic and radiation therapy. *Clin Cancer Res,* 6**,** 381-9.
KOUKOURAKIS, M. I., GIATROMANOLAKI, A., KAKOLYRIS, S., SIVRIDIS, E., GEORGOULIAS, V., FUNTZILAS, G., HICKSON, I. D., GATTER, K. C. & HARRIS, A. L. 2001. Nuclear expression of human apurinic/apyrimidinic endonuclease (HAP1/Ref-1) in head-and-neck cancer is associated with resistance to chemoradiotherapy and poor outcome. *Int J Radiat Oncol Biol Phys,* 50**,** 27-36.
KOUKOURAKIS, M. I., GIATROMANOLAKI, A., SIVRIDIS, E., SIMOPOULOS, K., PASTOREK, J., WYKOFF, C. C., GATTER, K. C. & HARRIS, A. L. 2001. Hypoxia-regulated carbonic anhydrase-9 (CA9) relates to poor vascularization and resistance of squamous cell head and neck cancer to chemoradiotherapy. *Clin Cancer Res,* 7**,** 3399-403.
KRALOVCOVA, D., PEJCHALOVA, M., RUDOLF, E. & CERVINKA, M. 2008. Quantitative analysis of expression level of BCL2 and BAX genes in Hep-2 and HL-60 cells after treatment with etoposide. *Acta Medica (Hradec Kralove),* 51**,** 191-5.
KRAMER, G., ERDAL, H., MERTENS, H. J., NAP, M., MAUERMANN, J., STEINER, G., MARBERGER, M., BIVEN, K., SHOSHAN, M. C. & LINDER, S. 2004. Differentiation between cell death modes using measurements of different soluble forms of extracellular cytokeratin 18. *Cancer Res,* 64**,** 1751-6.
KRAUSE, C. E., OTIENO, B. A., BISHOP, G. W., PHADKE, G., CHOQUETTE, L., LALLA, R. V., PETERSON, D. E. & RUSLING, J. F. 2015. Ultrasensitive microfluidic array for serum pro-inflammatory cytokines and C-reactive protein to assess oral mucositis risk in cancer patients. *Anal Bioanal Chem,* 407**,** 7239-43.
KREIMER, A. R., CLIFFORD, G. M., BOYLE, P. & FRANCESCHI, S. 2005. Human papillomavirus types in head and neck squamous cell carcinomas worldwide: a systematic review. *Cancer Epidemiol Biomarkers Prev,* 14**,** 467-75.
KROEMER, G., EL-DEIRY, W. S., GOLSTEIN, P., PETER, M. E., VAUX, D., VANDENABEELE, P., ZHIVOTOVSKY, B., BLAGOSKLONNY, M. V., MALORNI, W., KNIGHT, R. A., PIACENTINI, M., NAGATA, S., MELINO, G. & NOMENCLATURE COMMITTEE ON CELL, D. 2005. Classification of cell death: recommendations of the Nomenclature Committee on Cell Death. *Cell Death Differ,* 12 Suppl 2**,** 1463-7.
KRONBLAD, A., HELCZYNSKA, K., NIELSEN, N. H., PAHLMAN, E., EMDIN, S., PAHLMAN, S. & LANDBERG, G. 2003. Regional cyclin D1 overexpression or hypoxia correlate inversely with heterogeneous oestrogen receptor-alpha expression in human breast cancer. *In vivo,* 17**,** 311-8.
KRUSER, T. J., WHEELER, D. L., ARMSTRONG, E. A., IIDA, M., KOZAK, K. R., VAN DER KOGEL, A. J., BUSSINK, J., COXON, A., POLVERINO, A. & HARARI, P. M. 2010. Augmentation of radiation response by motesanib, a multikinase inhibitor that targets vascular endothelial growth factor receptors. *Clin Cancer Res,* 16**,** 3639-47.
KUBIAK, J. Z., WEBER, M., DE PENNART, H., WINSTON, N. J. & MARO, B. 1993. The metaphase II arrest in mouse oocytes is controlled through microtubule-dependent destruction of cyclin B in the presence of CSF. *EMBO J,* 12**,** 3773-8.
KUMAR, B., CORDELL, K. G., LEE, J. S., WORDEN, F. P., PRINCE, M. E., TRAN, H. H., WOLF, G. T., URBA, S. G., CHEPEHA, D. B., TEKNOS, T. N., EISBRUCH, A., TSIEN, C. I., TAYLOR, J. M., D'SILVA, N. J., YANG, K., KURNIT, D. M., BAUER, J. A., BRADFORD, C. R. & CAREY, T. E. 2008. EGFR, p16, HPV Titer, Bcl-xL and p53, sex, and smoking as indicators of response to therapy and survival in oropharyngeal cancer. *J Clin Oncol,* 26**,** 3128-37.
KUMARI, S., RASTOGI, R.P., SINGH, K.L., SINGH, S.P. & SINHA, R.P., 2008. DNA damage: detection strategies. *Excli Journal*, 7, pp.44-62.
KUNAS, K. T. & PAPOUTSAKIS, E. T. 1989. Increasing serum concentrations decrease cell death and allow growth of hybridoma cells at higher agitation rates. *Biotechnology Letters*, 11, 525-530.
KUNKEL, M., REICHERT, T. E., BENZ, P., LEHR, H. A., JEONG, J. H., WIEAND, S., BARTENSTEIN, P., WAGNER, W. & WHITESIDE, T. L. 2003. Overexpression of Glut-1 and increased glucose metabolism in tumors are associated with a poor prognosis in patients with oral squamous cell carcinoma. *Cancer,* 97**,** 1015-24.
KUWAHARA, D., TSUTSUMI, K., OYAKE, D., OHTA, T., NISHIKAWA, H. & KOIZUKA, I. 2003. Inhibition of caspase-9 activity and Apaf-1 expression in cisplatin-resistant head and neck squamous cell carcinoma cells. *Auris Nasus Larynx,* 30 Suppl**,** S85-8.
KYRYLKOVA, K., KYRYACHENKO, S., LEID, M. & KIOUSSI, C. 2012. Detection of apoptosis by TUNEL assay. *Methods Mol Biol,* 887**,** 41-7.
LACOMBE, J., PHILLIPS, S. L. & ZENHAUSERN, F. 2016. Microfluidics as a new tool in radiation biology. *Cancer Lett,* 371**,** 292-300.
LALLEMANT, B., EVRARD, A., COMBESCURE, C., CHAPUIS, H., CHAMBON, G., RAYNAL, C., REYNAUD, C., SABRA, O., JOUBERT, D., HOLLANDE, F., LALLEMANT, J. G., LUMBROSO, S. & BROUILLET, J. P.

2009. Reference gene selection for head and neck squamous cell carcinoma gene expression studies. *BMC Mol Biol,* 10**,** 78.
LAMARCHE, B. J., ORAZIO, N. I. & WEITZMAN, M. D. 2010. The MRN complex in double-strand break repair and telomere maintenance. *FEBS Lett,* 584**,** 3682-95.
LAMONT, E. B. & VOKES, E. E. 2001. Chemotherapy in the management of squamous-cell carcinoma of the head and neck. *Lancet Oncol,* 2**,** 261-9.
LAUBER, K., ERNST, A., ORTH, M., HERRMANN, M. & BELKA, C. 2012. Dying cell clearance and its impact on the outcome of tumor radiotherapy. *Front Oncol,* 2**,** 116.
LECHNER, M., FENTON, T., WEST, J., WILSON, G., FEBER, A., HENDERSON, S., THIRLWELL, C., DIBRA, H. K., JAY, A., BUTCHER, L., CHAKRAVARTHY, A. R., GRATRIX, F., PATEL, N., VAZ, F., O'FLYNN, P., KALAVREZOS, N., TESCHENDORFF, A. E., BOSHOFF, C. & BECK, S. 2013. Identification and functional validation of HPV-mediated hypermethylation in head and neck squamous cell carcinoma. *Genome Med,* 5**,** 15.
LEE, H., KIM, S., CHUNG, M., KIM, J. H. & JEON, N. L. 2014. A bioengineered array of 3D microvessels for vascular permeability assay. *Microvasc Res,* 91**,** 90-8.
LEE, J. C., SCHICKLING, O., STEGH, A. H., OSHIMA, R. G., DINSDALE, D., COHEN, G. M. & PETER, M. E. 2002. DEDD regulates degradation of intermediate filaments during apoptosis. *J Cell Biol,* 158**,** 1051-66.
LEE, K. W., TSAI, Y. S., CHIANG, F. Y., HUANG, J. L., HO, K. Y., YANG, Y. H., KUO, W. R., CHEN, M. K. & LIN, C. S. 2011. Lower ataxia telangiectasia mutated (ATM) mRNA expression is correlated with poor outcome of laryngeal and pharyngeal cancer patients. *Ann Oncol,* 22**,** 1088-93.
LEE, P. J., HUNG, P. J. & LEE, L. P. 2007. An artificial liver sinusoid with a microfluidic endothelial-like barrier for primary hepatocyte culture. *Biotechnol Bioeng,* 97**,** 1340-6.
LEE, W. G., KIM, Y. G., CHUNG, B. G., DEMIRCI, U. & KHADEMHOSSEINI, A. 2010. Nano/Microfluidics for diagnosis of infectious diseases in developing countries. *Adv Drug Deliv Rev,* 62**,** 449-57.
LEELAHAVANICHKUL, K., AMORNPHIMOLTHAM, P., MOLINOLO, A. A., BASILE, J. R., KOONTONGKAEW, S. & GUTKIND, J. S. 2014. A role for p38 MAPK in head and neck cancer cell growth and tumor-induced angiogenesis and lymphangiogenesis. *Mol Oncol,* 8**,** 105-18.
LEEMANS, C. R., BRAAKHUIS, B. J. & BRAKENHOFF, R. H. 2011. The molecular biology of head and neck cancer. *Nat Rev Cancer,* 11**,** 9-22.
LEERS, M. P., KOLGEN, W., BJORKLUND, V., BERGMAN, T., TRIBBICK, G., PERSSON, B., BJORKLUND, P., RAMAEKERS, F. C., BJORKLUND, B., NAP, M., JORNVALL, H. & SCHUTTE, B. 1999. Immunocytochemical detection and mapping of a cytokeratin 18 neo-epitope exposed during early apoptosis. *J Pathol,* 187**,** 567-72.
LEETHANAKUL, C., PATEL, V., GILLESPIE, J., SHILLITOE, E., KELLMAN, R. M., ENSLEY, J. F., LIMWONGSE, V., EMMERT-BUCK, M. R., KRIZMAN, D. B. & GUTKIND, J. S. 2000. Gene expression profiles in squamous cell carcinomas of the oral cavity: use of laser capture microdissection for the construction and analysis of stage-specific cDNA libraries. *Oral Oncol,* 36**,** 474-83.
LESSA, R. C., CAMPOS, A. H., FREITAS, C. E., SILVA, F. R., KOWALSKI, L. P., CARVALHO, A. L. & VETTORE, A. L. 2013. Identification of upregulated genes in oral squamous cell carcinomas. *Head Neck,* 35**,** 1475-81.
LEVKOFF, L. H., MARSHALL, G. P., 2ND, ROSS, H. H., CALDEIRA, M., REYNOLDS, B. A., CAKIROGLU, M., MARIANI, C. L., STREIT, W. J. & LAYWELL, E. D. 2008. Bromodeoxyuridine inhibits cancer cell proliferation *in vitro* and *in vivo*. *Neoplasia,* 10**,** 804-16.
LI, C., EGLOFF, A. M., SEN, M., GRANDIS, J. R. & JOHNSON, D. E. 2014. Caspase-8 mutations in head and neck cancer confer resistance to death receptor-mediated apoptosis and enhance migration, invasion, and tumor growth. *Mol Oncol,* 8**,** 1220-30.
LI, L. Y., LUO, X. & WANG, X. 2001. Endonuclease G is an apoptotic DNase when released from mitochondria. *Nature,* 412**,** 95-9.
LI, W., LI, F., HUANG, Q., SHEN, J., WOLF, F., HE, Y., LIU, X., HU, Y. A., BEDFORD, J. S. & LI, C. Y. 2011. Quantitative, noninvasive imaging of radiation-induced DNA double-strand breaks *in vivo*. *Cancer Res,* 71**,** 4130-7.
LI, X. J., VALADEZ, A. V., ZUO, P. & NIE, Z. 2012. Microfluidic 3D cell culture: potential application for tissue-based bioassays. *Bioanalysis,* 4**,** 1509-25.
LIANG, Y., LIN, S. Y., BRUNICARDI, F. C., GOSS, J. & LI, K. 2009. DNA damage response pathways in tumor suppression and cancer treatment. *World J Surg,* 33**,** 661-6.
LIEBER, M. R., GU, J., LU, H., SHIMAZAKI, N. & TSAI, A. G. 2010. Nonhomologous DNA end joining (NHEJ) and chromosomal translocations in humans. *Subcell Biochem,* 50**,** 279-96.
LIN, F. Y., GAO, Y., LI, D. & SHERMAN, P. M. 2010. Development of microfluidic-based heterogeneous immunoassays. *Front Biosci (Schol Ed),* 2**,** 73-84.

LIN, L. & LIN, J.M., 2015. Development of cell metabolite analysis on microfluidic platform. *Journal of Pharmaceutical Analysis*, 5(6), pp.337-347.
LIN, M. T., TSENG, L. H., KAMIYAMA, H., KAMIYAMA, M., LIM, P., HIDALGO, M., WHEELAN, S. & ESHLEMAN, J. 2010. Quantifying the relative amount of mouse and human DNA in cancer xenografts using species-specific variation in gene length. *Biotechniques,* 48**,** 211-8.
LIU, D., ZHANG, H., MAKILA, E., FAN, J., HERRANZ-BLANCO, B., WANG, C. F., ROSA, R., RIBEIRO, A. J., SALONEN, J., HIRVONEN, J. & SANTOS, H. A. 2015. Microfluidic assisted one-step fabrication of porous silicon@acetalated dextran nanocomposites for precisely controlled combination chemotherapy. *Biomaterials,* 39**,** 249-59.
LIU, H., MCDOWELL, T. L., HANSON, N. E., TANG, X., FUJIMOTO, J. & RODRIGUEZ-CANALES, J. 2014. Laser capture microdissection for the investigative pathologist. *Vet Pathol,* 51**,** 257-69.
LIU, Q., WANG, X. Z., MU, D. B., LI, T. Y., LIU, Y. S. & YU, Z. Y. 2015. Correlation analysis of hormone receptors and the expressions of HER-2 and Ki-67 in breast cancer. *Eur J Gynaecol Oncol,* 36**,** 78-83.
LIU, W., WANG, J. C. & WANG, J. 2015. Controllable organization and high throughput production of recoverable 3D tumors using pneumatic microfluidics. *Lab Chip,* 15**,** 1195-204.
LIU, Y. & KULESZ-MARTIN, M. 2001. p53 protein at the hub of cellular DNA damage response pathways through sequence-specific and non-sequence-specific DNA binding. *Carcinogenesis,* 22**,** 851-60.
LIU, Z., LEE, Y., JANG, J., LI, Y., HAN, X., YOKOI, K., FERRARI, M., ZHOU, L. & QIN, L. 2015. Microfluidic cytometric analysis of cancer cell transportability and invasiveness. *Sci Rep,* 5**,** 14272.
LO, J. F., SINKALA, E. & EDDINGTON, D. T. 2010. Oxygen gradients for open well cellular cultures via microfluidic substrates. *Lab Chip,* 10**,** 2394-401.
LOO, D. T. 2002. TUNEL assay. An overview of techniques. *Methods Mol Biol,* 203**,** 21-30.
LOPEZ, F., BELLOC, F., LACOMBE, F., DUMAIN, P., REIFFERS, J., BERNARD, P. & BOISSEAU, M. R. 1991. Modalities of synthesis of Ki67 antigen during the stimulation of lymphocytes. *Cytometry,* 12**,** 42-9.
LOPEZ-CONTRERAS, A. J. & FERNANDEZ-CAPETILLO, O. 2010. The ATR barrier to replication-born DNA damage. *DNA Repair (Amst),* 9**,** 1249-55.
LOWE, V. J., BOYD, J. H., DUNPHY, F. R., KIM, H., DUNLEAVY, T., COLLINS, B. T., MARTIN, D., STACK, B. C., JR., HOLLENBEAK, C. & FLETCHER, J. W. 2000. Surveillance for recurrent head and neck cancer using positron emission tomography. *J Clin Oncol,* 18**,** 651-8.
LU, C., ZHU, F., CHO, Y. Y., TANG, F., ZYKOVA, T., MA, W. Y., BODE, A. M. & DONG, Z. 2006. Cell apoptosis: requirement of H2AX in DNA ladder formation, but not for the activation of caspase-3. Mol Cell, 23, 121-32.
LU, Q. L., HANBY, A. M., NASSER HAJIBAGHERI, M. A., GSCHMEISSNER, S. E., LU, P. J., TAYLOR-PAPADIMITRIOU, J., KRAJEWSKI, S., REED, J. C. & WRIGHT, N. A. 1994. Bcl-2 protein localizes to the chromosomes of mitotic nuclei and is correlated with the cell cycle in cultured epithelial cell lines. *J Cell Sci,* 107 (Pt 2)**,** 363-71.
LU, S. L., HERRINGTON, H., REH, D., WEBER, S., BORNSTEIN, S., WANG, D., LI, A. G., TANG, C. F., SIDDIQUI, Y., NORD, J., ANDERSEN, P., CORLESS, C. L. & WANG, X. J. 2006. Loss of transforming growth factor-beta type II receptor promotes metastatic head-and-neck squamous cell carcinoma. *Genes Dev,* 20**,** 1331-42.
LUBIN, J. H., PURDUE, M., KELSEY, K., ZHANG, Z. F., WINN, D., WEI, Q., TALAMINI, R., SZESZENIA-DABROWSKA, N., STURGIS, E. M., SMITH, E., SHANGINA, O., SCHWARTZ, S. M., RUDNAI, P., NETO, J. E., MUSCAT, J., MORGENSTERN, H., MENEZES, A., MATOS, E., MATES, I. N., LISSOWSKA, J., LEVI, F., LAZARUS, P., LA VECCHIA, C., KOIFMAN, S., HERRERO, R., FRANCESCHI, S., WUNSCH-FILHO, V., FERNANDEZ, L., FABIANOVA, E., DAUDT, A. W., MASO, L. D., CURADO, M. P., CHEN, C., CASTELLSAGUE, X., BRENNAN, P., BOFFETTA, P., HASHIBE, M. & HAYES, R. B. 2009. Total exposure and exposure rate effects for alcohol and smoking and risk of head and neck cancer: a pooled analysis of case-control studies. *Am J Epidemiol,* 170**,** 937-47.
MA, H., XU, H. & QIN, J. 2013. Biomimetic tumor microenvironment on a microfluidic platform. *Biomicrofluidics,* 7**,** 11501.
MAH, L. J., EL-OSTA, A. & KARAGIANNIS, T. C. 2010. gammaH2AX: a sensitive molecular marker of DNA damage and repair. *Leukemia,* 24**,** 679-86.
MAIER, H., BORN, I. A. & MALL, G. 1988. Effect of chronic ethanol and nicotine consumption on the function and morphology of the salivary glands. *Klin Wochenschr,* 66 Suppl 11**,** 140-50.
MAIER, H., DIETZ, A., GEWELKE, U., HELLER, W. D. & WEIDAUER, H. 1992. Tobacco and alcohol and the risk of head and neck cancer. *Clin Investig,* 70**,** 320-7.
MAITRA, A., WISTUBA, II, VIRMANI, A. K., SAKAGUCHI, M., PARK, I., STUCKY, A., MILCHGRUB, S., GIBBONS, D., MINNA, J. D. & GAZDAR, A. F. 1999. Enrichment of epithelial cells for molecular studies. *Nat Med,* 5**,** 459-63.

MALHOTRA, P. S., MALEKFZALI, A., BONNER, R. F., JUHN, S., VAN WAES, C. & CHEN, Z. 2004. Assessment of gene expression in head and neck carcinoma using laser capture microdissection and real-time reverse transcription polymerase chain reaction. *Laryngoscope,* 114**,** 2123-8.

MARCU, L. G. & BEZAK, E. 2009. Radiobiological modeling of interplay between accelerated repopulation and altered fractionation schedules in head and neck cancer. *J Med Phys,* 34**,** 206-11.

MARRON, M., BOFFETTA, P., ZHANG, Z. F., ZARIDZE, D., WUNSCH-FILHO, V., WINN, D. M., WEI, Q., TALAMINI, R., SZESZENIA-DABROWSKA, N., STURGIS, E. M., SMITH, E., SCHWARTZ, S. M., RUDNAI, P., PURDUE, M. P., OLSHAN, A. F., ELUF-NETO, J., MUSCAT, J., MORGENSTERN, H., MENEZES, A., MCCLEAN, M., MATOS, E., MATES, I. N., LISSOWSKA, J., LEVI, F., LAZARUS, P., LA VECCHIA, C., KOIFMAN, S., KELSEY, K., HERRERO, R., HAYES, R. B., FRANCESCHI, S., FERNANDEZ, L., FABIANOVA, E., DAUDT, A. W., DAL MASO, L., CURADO, M. P., CADONI, G., CHEN, C., CASTELLSAGUE, X., BOCCIA, S., BENHAMOU, S., FERRO, G., BERTHILLER, J., BRENNAN, P., MOLLER, H. & HASHIBE, M. 2010. Cessation of alcohol drinking, tobacco smoking and the reversal of head and neck cancer risk. *Int J Epidemiol,* 39**,** 182-96.

MARSANO, A., CONFICCONI, C., LEMME, M., OCCHETTA, P., GAUDIELLO, E., VOTTA, E., CERINO, G., REDAELLI, A. & RASPONI, M. 2016. Beating heart on a chip: a novel microfluidic platform to generate functional 3D cardiac microtissues. *Lab Chip,* 16**,** 599-610.

MARSIT, C. J., LIU, M., NELSON, H. H., POSNER, M., SUZUKI, M. & KELSEY, K. T. 2004. Inactivation of the Fanconi anemia/BRCA pathway in lung and oral cancers: implications for treatment and survival. *Oncogene,* 23**,** 1000-4.

MARTIN, D., ABBA, M. C., MOLINOLO, A. A., VITALE-CROSS, L., WANG, Z., ZAIDA, M., DELIC, N. C., SAMUELS, Y., LYONS, J. G. & GUTKIND, J. S. 2014. The head and neck cancer cell oncogenome: a platform for the development of precision molecular therapies. *Oncotarget,* 5**,** 8906-23.

MATTHAIOS, D., FOUKAS, P. G., KEFALA, M., HOUNTIS, P., TRYPSIANIS, G., PANAYIOTIDES, I. G., CHATZAKI, E., PANTELIDAKI, E., BOUROS, D., KARAKITSOS, P. & KAKOLYRIS, S. 2012. Gamma-H2AX expression detected by immunohistochemistry correlates with prognosis in early operable non-small cell lung cancer. Onco Targets Ther, 5, 309-14.

MATTHEWS, Q., JIRASEK, A., LUM, J. J. & BROLO, A. G. 2011. Biochemical signatures of *in vitro* radiation response in human lung, breast and prostate tumour cells observed with Raman spectroscopy. *Phys Med Biol,* 56**,** 6839-55.

MAYA, R., BALASS, M., KIM, S. T., SHKEDY, D., LEAL, J. F., SHIFMAN, O., MOAS, M., BUSCHMANN, T., RONAI, Z., SHILOH, Y., KASTAN, M. B., KATZIR, E. & OREN, M. 2001. ATM-dependent phosphorylation of Mdm2 on serine 395: role in p53 activation by DNA damage. *Genes Dev,* 15**,** 1067-77.

MCGINLEY, J. N., KNOTT, K. K. & THOMPSON, H. J. 2000. Effect of fixation and epitope retrieval on BrdU indices in mammary carcinomas. *J Histochem Cytochem,* 48**,** 355-62.

MCGRANAHAN, N. & SWANTON, C. 2015. Biological and therapeutic impact of intratumor heterogeneity in cancer evolution. *Cancer Cell,* 27**,** 15-26.

MCILWAIN, D. R., BERGER, T. & MAK, T. W. 2013. Caspase functions in cell death and disease. *Cold Spring Harb Perspect Biol,* 5**,** a008656.

MCKEAN-COWDIN, R., FEIGELSON, H. S., ROSS, R. K., PIKE, M. C. & HENDERSON, B. E. 2000. Declining cancer rates in the 1990s. *J Clin Oncol,* 18**,** 2258-68.

MEHANNA, H., WEST, C. M., NUTTING, C. & PALERI, V. 2010. Head and neck cancer--Part 2: Treatment and prognostic factors. *BMJ,* 341**,** c4690.

MEHLING, M. & TAY, S. 2014. Microfluidic cell culture. *Curr Opin Biotechnol,* 25**,** 95-102.

MEIRING, T., PROZESKY, L., DU PREEZ, E. R. & VERWOERD, D. J. 2011. The diagnosis and prevalence of persistent infection with bovine viral diarrhoea virus in South African feedlot cattle. *Onderstepoort J Vet Res,* 78**,** 323.

MELLE, C., ERNST, G., SCHIMMEL, B., BLEUL, A., KOSCIELNY, S., WIESNER, A., BOGUMIL, R., MOLLER, U., OSTERLOH, D., HALBHUBER, K. J. & VON EGGELING, F. 2003. Biomarker discovery and identification in laser microdissected head and neck squamous cell carcinoma with ProteinChip technology, two-dimensional gel electrophoresis, tandem mass spectrometry, and immunohistochemistry. *Mol Cell Proteomics,* 2**,** 443-52.

MENEGAKIS, A., EICHELER, W., YAROMINA, A., THAMES, H. D., KRAUSE, M. & BAUMANN, M. 2011. Residual DNA double strand breaks in perfused but not in unperfused areas determine different radiosensitivity of tumours. *Radiother Oncol,* 100**,** 137-44.

MENG, Q., HE, Z., ZHANG, L., ZHAO, L., LI, E., ZHANG, Q., ZHANG, X., YANG, D., ZOU, L., GAO, Z. & WANG, Q. 2011. Development of a double-layer microfluidic chip with flow medium for chemotherapy resistance analysis of lung cancer. *Electrophoresis,* 32**,** 3446-53.

MENG, W. J., PATHAK, S., DING, Z. Y., ZHANG, H., ADELL, G., HOLMLUND, B., LI, Y., ZHOU, Z. G. & SUN, X. F. 2015. Special AT-rich sequence binding protein 1 expression correlates with response to preoperative radiotherapy and clinical outcome in rectal cancer. *Cancer Biol Ther,* 16**,** 1738-45.

MERCK MILLIPORE. 2016. *Histological staining solutions*. Available online: http://www.merckmillipore.com/GB/en/products/ivd-oem-materials-reagents/microscopy/histology/histological-staining-solutions/AReb.qB.xBAAAAFAjehkiQpx,nav [Accessed on September 2016].

MERKEL, T. C., BONDAR, V. I., NAGAI, K., FREEMAN, B. D. & PINNAU, I. 2000. Gas sorption, diffusion, and permeation in poly(dimethylsiloxane). *Journal of Polymer Science Part B-Polymer Physics*, 38, 415-434.

MEYER, F., SAMSON, E., DOUVILLE, P., DUCHESNE, T., LIU, G. & BAIRATI, I. 2010. Serum prognostic markers in head and neck cancer. *Clin Cancer Res,* 16**,** 1008-15.

MEYVANTSSON, I. & BEEBE, D. J. 2008. Cell culture models in microfluidic systems. *Annu Rev Anal Chem (Palo Alto Calif),* 1**,** 423-49.

MICKE, P., OSTMAN, A., LUNDEBERG, J. & PONTEN, F. 2005. Laser-assisted cell microdissection using the PALM system. *Methods Mol Biol,* 293**,** 151-66.

MIKULOWSKA-MENNIS, A., TAYLOR, T. B., VISHNU, P., MICHIE, S. A., RAJA, R., HORNER, N. & KUNITAKE, S. T. 2002. High-quality RNA from cells isolated by laser capture microdissection. *Biotechniques,* 33**,** 176-9.

MILLAR, E. K., GRAHAM, P. H., MCNEIL, C. M., BROWNE, L., O'TOOLE, S. A., BOULGHOURJIAN, A., KEARSLEY, J. H., PAPADATOS, G., DELANEY, G., FOX, C., NASSER, E., CAPP, A. & SUTHERLAND, R. L. 2011. Prediction of outcome of early ER+ breast cancer is improved using a biomarker panel, which includes Ki-67 and p53. *Br J Cancer,* 105**,** 272-80.

Millipore. 2010. BrdU assay (Mouse primary antibody) for high content screening. [Online] Available from: http://www.millipore.com/userguides.nsf/a73664f9f981af8c852569b9005b4eee/f390b84b52f15dea852575ca00807405/$FILE/HCS201MAN.pdf. [Accessed: 13 June 2013]

MILLON, S. R., OSTRANDER, J. H., BROWN, J. Q., RAHEJA, A., SEEWALDT, V. L. & RAMANUJAM, N. 2011. Uptake of 2-NBDG as a method to monitor therapy response in breast cancer cell lines. *Breast Cancer Res Treat,* 126**,** 55-62.

MISHRA, K. P. 2004. Cell membrane oxidative damage induced by gamma-radiation and apoptotic sensitivity. *J Environ Pathol Toxicol Oncol,* 23**,** 61-6.

MOESER, A. J., BORST, L. B., OVERMAN, B. L. & PITTMAN, J. S. 2012. Defects in small intestinal epithelial barrier function and morphology associated with peri-weaning failure to thrive syndrome (PFTS) in swine. *Res Vet Sci,* 93**,** 975-82.

MOLDOVAN, G. L., PFANDER, B. & JENTSCH, S. 2007. PCNA, the maestro of the replication fork. *Cell,* 129**,** 665-79.

MORRIS, K. L., TUGWOOD, J. D., KHOJA, L., LANCASHIRE, M., SLOANE, R., BURT, D., SHENJERE, P., ZHOU, C., HODGSON, C., OHTOMO, T., KATOH, A., ISHIGURO, T., VALLE, J. W. & DIVE, C. 2014. Circulating biomarkers in hepatocellular carcinoma. *Cancer Chemother Pharmacol,* 74**,** 323-32.

MORRISON, J. A., BAILEY, C. M. & KULESA, P. M. 2012. Gene profiling in the avian embryo using laser capture microdissection and RT-qPCR. *Cold Spring Harb Protoc,* 2012.

MORROGH, M., OLVERA, N., BOGOMOLNIY, F., BORGEN, P. I. & KING, T. A. 2007. Tissue preparation for laser capture microdissection and RNA extraction from fresh frozen breast tissue. *Biotechniques,* 43**,** 41-2, 44, 46 passim.

MROZ, E. A., TWARD, A. D., HAMMON, R. J., REN, Y. & ROCCO, J. W. 2015. Intra-tumor genetic heterogeneity and mortality in head and neck cancer: analysis of data from the Cancer Genome Atlas. *PLoS Med,* 12**,** e1001786.

MULLA, O., CHEAH, R., YAPA, S., GREENMAN, J., KARSAI, L., GREEN, V. & ENGLAND, J. 2016. The use of a microfluidic device to investigate thyroid tissue response to treatment. (Abstract and poster presentation) Joint Meeting of the German Association of Endocrine Surgeons (CAEK) and the British Association of Endocrine and Thyroid Surgeons (BAETS; October 2016, Berlin, Germany).

MURIEL, V. P. 2002. The biological basis of fractionation in radiotherapy. *Revista de Oncología*. Volume 4, Issue 3, pp 161-166.

NAIDU, M. U., RAMANA, G. V., RANI, P. U., MOHAN, I. K., SUMAN, A. & ROY, P. 2004. Chemotherapy-induced and/or radiation therapy-induced oral mucositis--complicating the treatment of cancer. *Neoplasia,* 6**,** 423-31.

NATIONAL CANCER INSTITUTE, 2013. *FDA Approval for Cetuximab.* Available online: https://www.cancer.gov/about-cancer/treatment/drugs/fda-cetuximab. [Accessed September 2016].

National Cancer Institute. 2013. *Head and neck cancers*. Available online: http://www.cancer.gov/types/head-and-neck/head-neck-fact-sheet [Accessed on January 2013].

NEEVES, K. B., ONASOGA, A. A. & WUFSUS, A. R. 2013. The use of microfluidics in hemostasis: clinical diagnostics and biomimetic models of vascular injury. *Curr Opin Hematol,* 20**,** 417-23.

NGE, P. N., ROGERS, C. I. & WOOLLEY, A. T. 2013. Advances in microfluidic materials, functions, integration, and applications. *Chem Rev,* 113**,** 2550-83.

NICHOLS, A. C., FINKELSTEIN, D. M., FAQUIN, W. C., WESTRA, W. H., MROZ, E. A., KNEUERTZ, P., BEGUM, S., MICHAUD, W. A., BUSSE, P. M., CLARK, J. R. & ROCCO, J. W. 2010. Bcl2 and human papilloma virus 16 as predictors of outcome following concurrent chemoradiation for advanced oropharyngeal cancer. *Clin Cancer Res,* 16**,** 2138-46.

NIHON-YANAGI, Y., TERAI, K., MURANO, T., KAWAI, T., KIMURA, S. & OKAZUMI, S. 2013. beta-2 microglobulin is unsuitable as an internal reference gene for the analysis of gene expression in human colorectal cancer. *Biomed Rep,* 1**,** 193-196.

NIJNIK, A., WOODBINE, L., MARCHETTI, C., DAWSON, S., LAMBE, T., LIU, C., RODRIGUES, N. P., CROCKFORD, T. L., CABUY, E., VINDIGNI, A., ENVER, T., BELL, J. I., SLIJEPCEVIC, P., GOODNOW, C. C., JEGGO, P. A. & CORNALL, R. J. 2007. DNA repair is limiting for haematopoietic stem cells during ageing. Nature, 447, 686-90.

NITIN, N., CARLSON, A. L., MULDOON, T., EL-NAGGAR, A. K., GILLENWATER, A. & RICHARDS-KORTUM, R. 2009. Molecular imaging of glucose uptake in oral neoplasia following topical application of fluorescently labeled deoxy-glucose. *Int J Cancer,* 124**,** 2634-42.

NIX, P., LIND, M., GREENMAN, J., STAFFORD, N. & CAWKWELL, L. 2004. Expression of Cox-2 protein in radioresistant laryngeal cancer. *Ann Oncol,* 15**,** 797-801.

NOBLITT, S. D., LEWIS, G. S., LIU, Y., HERING, S. V., COLLETT, J. L., JR. & HENRY, C. S. 2009. Interfacing microchip electrophoresis to a growth tube particle collector for semicontinuous monitoring of aerosol composition. *Anal Chem,* 81**,** 10029-37.

OFFICE FOR NATIONAL STATISTICS. 2013. Cancer survival in England: patients diagnosed 2007–2011, followed up to 2012. London: Office for National Statistics.

OKANO, S., LAN, L., TOMKINSON, A. E. & YASUI, A. 2005. Translocation of XRCC1 and DNA ligase IIIalpha from centrosomes to chromosomes in response to DNA damage in mitotic human cells. *Nucleic Acids Res,* 33**,** 422-9.

OLIVE, P. L. & BANATH, J. P. 2009. Kinetics of H2AX phosphorylation after exposure to cisplatin. *Cytometry B Clin Cytom,* 76**,** 79-90.

OLOFSSON, M. H., UENO, T., PAN, Y., XU, R., CAI, F., VAN DER KUIP, H., MUERDTER, T. E., SONNENBERG, M., AULITZKY, W. E., SCHWARZ, S., ANDERSSON, E., SHOSHAN, M. C., HAVELKA, A. M., TOI, M. & LINDER, S. 2007. Cytokeratin-18 is a useful serum biomarker for early determination of response of breast carcinomas to chemotherapy. *Clin Cancer Res,* 13**,** 3198-206.

ONUL, A., COLVARD, M. D., PARADISE, W. A., ELSETH, K. M., VESPER, B. J., GOUVAS, E., DELIU, Z., GARCIA, K. D., PESTLE, W. J. & RADOSEVICH, J. A. 2012. Application of immunohistochemical staining to detect antigen destruction as a measure of tissue damage. *J Histochem Cytochem,* 60**,** 683-93.

OSTAFE, R., PRODANOVIC, R., LLOYD UNG, W., WEITZ, D. A. & FISCHER, R. 2014. A high-throughput cellulase screening system based on droplet microfluidics. *Biomicrofluidics,* 8**,** 041102.

OVERGAARD, J., ERIKSEN, J. G., NORDSMARK, M., ALSNER, J., HORSMAN, M. R., DANISH, H. & NECK CANCER STUDY, G. 2005. Plasma osteopontin, hypoxia, and response to the hypoxia sensitiser nimorazole in radiotherapy of head and neck cancer: results from the DAHANCA 5 randomised double-blind placebo-controlled trial. *Lancet Oncol,* 6**,** 757-64.

OXFORD CANCER INTELLIGENCE UNIT. 2010. *Profiles of Head and Neck Cancers in England: Incidence, Mortality and Survival*. Available online: http://webcache.googleusercontent.com/search?q=cache:elzP9Ae0unAJ:www.ncin.org.uk/view%3Frid%3D69+&cd=1&hl=en&ct=clnk&gl=uk [Accessed on December 2015].

OYAMA, K., FUSHIDA, S., KINOSHITA, J., OKAMOTO, K., MAKINO, I., NAKAMURA, K., HAYASHI, H., INOKUCHI, M., NAKAGAWARA, H., TAJIMA, H., FUJITA, H., TAKAMURA, H., NINOMIYA, I., KITAGAWA, H., FUJIMURA, T. & OHTA, T. 2013. Serum cytokeratin 18 as a biomarker for gastric cancer. *Clin Exp Med,* 13**,** 289-95.

OZTURK, B., COSKUN, U., SANCAK, B., YAMAN, E., BUYUKBERBER, S. & BENEKLI, M. 2009. Elevated serum levels of M30 and M65 in patients with locally advanced head and neck tumors. *Int Immunopharmacol,* 9**,** 645-8.

OZTURK, S. S. & PALSSON, B. O. 1991. Examination of serum and bovine serum albumin as shear protective agents in agitated cultures of hybridoma cells. *J Biotechnol,* 18**,** 13-28.

PAI, S. I. & WESTRA, W. H. 2009. Molecular pathology of head and neck cancer: implications for diagnosis, prognosis, and treatment. *Annu Rev Pathol,* 4**,** 49-70.

PAJONK, F., VLASHI, E. & MCBRIDE, W. H. 2010. Radiation resistance of cancer stem cells: the 4 R's of radiobiology revisited. *Stem Cells,* 28**,** 639-48.

PANOPOULOS, A., PACIOS-BRAS, C., CHOI, J., YENJERLA, M., SUSSMAN, M. A., FOTEDAR, R. & MARGOLIS, R. L. 2014. Failure of cell cleavage induces senescence in tetraploid primary cells. *Mol Biol Cell,* 25**,** 3105-18.

PAPAGEORGIS, P. & STYLIANOPOULOS, T. 2015. Role of TGFβ in regulation of the tumor microenvironment and drug delivery (review). *Int J Oncol*, 46 (3): 933-943.

PARIKH, R. A., WHITE, J. S., HUANG, X., SCHOPPY, D. W., BAYSAL, B. E., BASKARAN, R., BAKKENIST, C. J., SAUNDERS, W. S., HSU, L. C., ROMKES, M. & GOLLIN, S. M. 2007. Loss of distal 11q is associated with DNA repair deficiency and reduced sensitivity to ionizing radiation in head and neck squamous cell carcinoma. *Genes Chromosomes Cancer,* 46**,** 761-75.

PARK, J., BYUN, A., KIM, D. H., SHIN, S. S., KIM, J. H. & KIM, J. W. 2014. Microfluidic fabrication and permeation behaviors of uniform zwitterionic hydrogel microparticles and shells. *J Colloid Interface Sci,* 426**,** 162-9.

PARKIN, D. M. 2011. 3. Cancers attributable to consumption of alcohol in the UK in 2010. *Br J Cancer,* 105 Suppl 2**,** S14-8.

PATEL, R. 2016. *An observational pilot study to assess the potential of a microfluidic tissue culture model to predict rectal cancer response to neo-adjuvant therapy.* M.D. thesis.

PAULOSKI, B. R. 2008. Rehabilitation of dysphagia following head and neck cancer. *Phys Med Rehabil Clin N Am,* 19**,** 889-928, x.

PAULOVICH, A. G., TOCZYSKI, D. P. & HARTWELL, L. H. 1997. When checkpoints fail. *Cell,* 88**,** 315-21.

PAWLIK, T. M. & KEYOMARSI, K. 2004. Role of cell cycle in mediating sensitivity to radiotherapy. *Int J Radiat Oncol Biol Phys,* 59**,** 928-42.

PAWLOWSKI, J. & KRAFT, A. S. 2000. Bax-induced apoptotic cell death. *Proc Natl Acad Sci U S A,* 97**,** 529-31.

PAYNE, S. & Miles, d. 2008. Mechanisms of anticancer drugs. In GLEESON. M. (ed) *Scott-Brown's Otorhinolaryngology: Head and Neck Surgery 7Ed*. CRC Press. 34-46.

PEREIRA, C. S., OLIVEIRA, M. V., FRAGA, C. A., BARROS, L. O., DOMINGOS, P. L., ROY, A., DE-PAULA, A. M. & GUIMARAES, A. L. 2012. Impact of the epithelial dysplasia grading and Ki67 proliferation index in the adjacent non-malignant mucosa on recurrence and survival in head and neck squamous cell carcinoma. *Pathol Res Pract,* 208**,** 651-6.

PERRI, F., PACELLI, R., DELLA VITTORIA SCARPATI, G., CELLA, L., GIULIANO, M., CAPONIGRO, F. & PEPE, S. 2015. Radioresistance in head and neck squamous cell carcinoma: Biological bases and therapeutic implications. *Head Neck,* 37**,** 763-70.

PETERSEN, C., ZIPS, D., KRAUSE, M., SCHONE, K., EICHELER, W., HOINKIS, C., THAMES, H. D. & BAUMANN, M. 2001. Repopulation of FaDu human squamous cell carcinoma during fractionated radiotherapy correlates with reoxygenation. *Int J Radiat Oncol Biol Phys,* 51**,** 483-93.

PETERSEN, C., ZIPS, D., KRAUSE, M., VOLKEL, W., THAMES, H. D. & BAUMANN, M. 2005. Recovery from sublethal damage during fractionated irradiation of human FaDu SCC. *Radiother Oncol,* 74**,** 331-6.

PEVIVA. 2011. *The PEVIVA Cell Death Product Line*. Available online: http://vincibiochem.it/M30Apoptosense.htm#M30_CytoDeath™_ELISA [Accessed on November 3].

PHILCHENKOV, A. 2004. Caspases: potential targets for regulating cell death. *J Cell Mol Med,* 8**,** 432-44.

PICH, A., CHIUSA, L. & NAVONE, R. 2004. Prognostic relevance of cell proliferation in head and neck tumors. *Ann Oncol,* 15**,** 1319-29.

PJESCIC, I., TRANTER, C. A., HAYWOOD, J. C., PAIDIPALLI, M., GANVEER, A., HAYWOOD, S. E., THAM, J. & CREWS, N. D. 2011. Real-time damage monitoring of irradiated DNA. *Integrative Biology,* 3**,** 937-947.

PLATANIOTIS, G. A., THEOFANOPOULOU, M. E., KALOGERA-FOUNTZILA, A., HARITANTI, A., CIULEANOU, E., GHILEZAN, N., ZAMBOGLOU, N., DIMITRIADIS, A., SOFRONIADIS, I. & FOUNTZILAS, G. 2004. Prognostic impact of tumor volumetry in patients with locally advanced head-and-neck carcinoma (non-nasopharyngeal) treated by radiotherapy alone or combined radiochemotherapy in a randomized trial. *Int J Radiat Oncol Biol Phys,* 59**,** 1018-26.

PODHORECKA, M., SKLADANOWSKI, A. & BOZKO, P. 2010. H2AX Phosphorylation: Its Role in DNA Damage Response and Cancer Therapy. *J Nucleic Acids,* 2010.

POPE, I. A., BARBER, P. R., HORN, S., AINSBURY, E., ROTHKAMM, K. & VOJNOVIC, B. 2011. A portable microfluidic fluorescence spectrometer device for gamma-H2AX-based biological dosimetry. *Radiation Measurements,* 46**,** 907-911.

POPE, J. A. 1999. *Medical Physics: Imaging*. Heinemann Advanced Science.

PRABHAKARPANDIAN, B., SHEN, M. C., NICHOLS, J. B., MILLS, I. R., SIDORYK-WEGRZYNOWICZ, M., ASCHNER, M. & PANT, K. 2013. SyM-BBB: a microfluidic Blood Brain Barrier model. *Lab Chip,* 13**,** 1093-101.

PROMEGA. 2013. *Certificate of analysis: CaspACE TM FITC-VAD-FMK in situ marker.* Available online: https://www.promega.co.uk/~/media/files/resources/protocols/product%20information%20sheets/g/caspace%20fitc-vad-fmk%20in%20situ%20marker%20protocol.pdf [Accessed on July 2015]

PYTYNIA, K. B., GRANT, J. R., ETZEL, C. J., ROBERTS, D. B., WEI, Q. & STURGIS, E. M. 2004. Matched-pair analysis of survival of never smokers and ever smokers with squamous cell carcinoma of the head and neck. *J Clin Oncol,* 22**,** 3981-8.

QIAGEN. 2014. *RNeasy ® Micro Handbook.* Available online: https://www.qiagen.com/resources/download.aspx?id=682963a5-737a-46d2-bc9f-fa137b379ab5&lang=en. [Accessed on May 2015].
R&D SYSTEMS A BIOTECHNE BRAND, 2015. *TUNEL assays*. Available online: https://www.rndsystems.com/products/tunel-assays [Accessed on October 2014].
RAFAT, M., ALI, R. & GRAVES, E. E. 2015. Imaging radiation response in tumor and normal tissue. *Am J Nucl Med Mol Imaging,* 5**,** 317-32.
RAGIN, C. C., MODUGNO, F. & GOLLIN, S. M. 2007. The epidemiology and risk factors of head and neck cancer: a focus on human papillomavirus. *J Dent Res,* 86**,** 104-14.
RAHIMI, A. S., WILSON, D. D., SAYLOR, D. K., STELOW, E. B., THOMAS, C. Y., REIBEL, J. F., LEVINE, P. A., SHONKA, D. C., JAMESON, M. J. & READ, P. W. 2012. p16, Cyclin D1, and HIF-1alpha Predict Outcomes of Patients with Oropharyngeal Squamous Cell Carcinoma Treated with Definitive Intensity-Modulated Radiation Therapy. *Int J Otolaryngol,* 2012**,** 685951.
RAMOS, M., BENAVENTE, S. & GIRALT, J. 2010. Management of squamous cell carcinoma of the head and neck: updated European treatment recommendations. *Expert Rev Anticancer Ther,* 10**,** 339-44.
RANDALL, L. M., MONK, B. J., MOON, J., PARKER, R., AL-GHAZI, M., WILCZYNSKI, S., FRUEHAUF, J. P., MARKMAN, M. & BURGER, R. A. 2010. Prospective evaluation of an *in vitro* radiation resistance assay in locally advanced cancer of the uterine cervix: a Southwest Oncology Group Study. *Gynecol Oncol,* 119**,** 417-21.
RAO, S., SADIYA, N., DORAISWAMI, S. & PRATHIBA, D. 2009. Characterization of morphologically benign biologically aggressive meningiomas. *Neurol India,* 57**,** 744-8.
RAVIKUMAR, G. & CRASTA, J. A. 2013. Vascular endothelial growth factor expression in ovarian serous carcinomas and its effect on tumor proliferation. *South Asian J Cancer,* 2**,** 87-90.
RAYBAUD, H., FORTIN, A., BAIRATI, I., MORENCY, R., MONTEIL, R. A. & TETU, B. 2000. Nuclear DNA content, an adjunct to p53 and Ki-67 as a marker of resistance to radiation therapy in oral cavity and pharyngeal squamous cell carcinoma. *Int J Oral Maxillofac Surg,* 29**,** 36-41.
REIS, H., WOHLSCHLAGER, J., HAGEMANN, S., WENZEL, P., BECHMANN, L. P., SUTTORP, A. C., SCHLATTJAN, M. J., HERZER, K., CANBAY, A. & BABA, H. A. 2015. (Cleaved) CK18 serum and tissue expression levels differentiate acute HCV reinfection from acute rejection in liver allografts. *Liver Int,* 35**,** 905-13.
RETTIG, E., KIESS, A. P. & FAKHRY, C. 2015. The role of sexual behavior in head and neck cancer: implications for prevention and therapy. *Expert Rev Anticancer Ther,* 15**,** 35-49.
REYNOLDS, P., COOPER, S., LOMAX, M. & O'NEILL, P. 2015. Disruption of PARP1 function inhibits base excision repair of a sub-set of DNA lesions. *Nucleic Acids Res,* 43**,** 4028-38.
RICHMOND, A. & SU, Y. 2008. Mouse xenograft models vs GEM models for human cancer therapeutics. *Dis Model Mech,* 1**,** 78-82.
RIEDL, S. J. & SHI, Y. 2004. Molecular mechanisms of caspase regulation during apoptosis. *Nat Rev Mol Cell Biol,* 5**,** 897-907.
ROBERG, K., JONSSON, A. C., GRENMAN, R. & NORBERG-SPAAK, L. 2007. Radiotherapy response in oral squamous carcinoma cell lines: evaluation of apoptotic proteins as prognostic factors. *Head Neck,* 29**,** 325-34.
ROBERTSON, G., BUSHELL, T. J. & ZAGNONI, M. 2014. Chemically induced synaptic activity between mixed primary hippocampal co-cultures in a microfluidic system. *Integr Biol (Camb),* 6**,** 636-44.
ROCHE DIAGNOSTICS GmbH. 2011. *Cytotoxicity Detection Kit Plus (LDH) Version 5.0.* Available online: https://cssportal.roche.com/LFR_PublicDocs/ras/04744926001_en_05.pdf. [Accessed June 2013].
ROLSTON, R., SASATOMI, E., HUNT, J., SWALSKY, P. A. & FINKELSTEIN, S. D. 2001. Distinguishing *de novo* second cancer formation from tumor recurrence: mutational fingerprinting by microdissection genotyping. *J Mol Diagn,* 3**,** 129-32.
RONDEAU, S., VACHER, S., DE KONING, L., BRIAUX, A., SCHNITZLER, A., CHEMLALI, W., CALLENS, C., LIDEREAU, R. & BIECHE, I. 2015. ATM has a major role in the double-strand break repair pathway dysregulation in sporadic breast carcinomas and is an independent prognostic marker at both mRNA and protein levels. *Br J Cancer,* 112**,** 1059-66.
ROSSER, C. J., GAAR, M. & PORVASNIK, S. 2009. Molecular fingerprinting of radiation resistant tumors: can we apprehend and rehabilitate the suspects? *BMC Cancer,* 9**,** 225.
ROTEM, A., RAM, O., SHORESH, N., SPERLING, R. A., SCHNALL-LEVIN, M., ZHANG, H., BASU, A., BERNSTEIN, B. E. & WEITZ, D. A. 2015. High-Throughput Single-Cell Labeling (Hi-SCL) for RNA-Seq Using Drop-Based Microfluidics. *PLoS One,* 10**,** e0116328.
ROTHENBERG, S. M. & ELLISEN, L. W. 2012. The molecular pathogenesis of head and neck squamous cell carcinoma. *J Clin Invest,* 122**,** 1951-7.

ROZ, L., WU, C. L., PORTER, S., SCULLY, C., SPEIGHT, P., READ, A., SLOAN, P. & THAKKER, N. 1996. Allelic imbalance on chromosome 3p in oral dysplastic lesions: an early event in oral carcinogenesis. *Cancer Res,* 56**,** 1228-31.
RUECKERT, R. R. & MUELLER, G. C. 1960. Effect of oxygen tension on HeLa cell growth. *Cancer Res,* 20**,** 944-9.
RUKSTALIS, D. B. 2002. Treatment options after failure of radiation therapy-a review. *Rev Urol,* 4 Suppl 2**,** S12-7.
RUTZKY, L. P., TAYLOR, W. G. & PUMPER, R. W. 1971. In-Vitro Stimulation of Rat Liver Cells by Homologous Partial Hepatectomy Serum. *In vitro-Journal of the Tissue Culture Association,* 7**,** 1-&.
SAAD, M. A., KUO, S. Z., RAHIMY, E., ZOU, A. E., KORRAPATI, A., RAHIMY, M., KIM, E., ZHENG, H., YU, M. A., WANG-RODRIGUEZ, J. & ONGKEKO, W. M. 2015. Alcohol-dysregulated miR-30a and miR-934 in head and neck squamous cell carcinoma. *Mol Cancer,* 14**,** 181.
SADAF, S., LOYA, A., MUSHTAQ, S., AKHTER, N., HUSSAIN, R. & JAMSHED, A. 2015. Correlation of p21 expression in head and neck squamous cell carcinoma with clinicopathologic and prognostic parameters. *Journal of Cancer & Allied Specialties*, 1(2).
SAFDIE, F., BRANDHORST, S., WEI, M., WANG, W., LEE, C., HWANG, S., CONTI, P. S., CHEN, T. C. & LONGO, V. D. 2012. Fasting enhances the response of glioma to chemo- and radiotherapy. *PLoS One,* 7**,** e44603.
SAITO, T., WU, C. C., SHIKU, H., YASUKAWA, T., YOKOO, M., ITO-SASAKI, T., ABE, H., HOSHI, H. & MATSUE, T. 2006. Oxygen consumption of cell suspension in a poly (dimethylsiloxane) (PDMS) microchannel estimated by scanning electrochemical microscopy. *Analyst,* 131**,** 1006-11.
SAKAI, H., NODA, A., SHIRAI, N., IIDAKA, T., YANAI, T., MASEGI, T., SHIRAI, N., IIDAKA, T., YANAI, T. & MASEGI, T. 2002. Proliferative activity of canine mast cell tumours evaluated by bromodeoxyuridine incorporation and Ki-67 expression. *J Comp Pathol,* 127**,** 233-8.
SALIC, A. & MITCHISON, T. J. 2008. A chemical method for fast and sensitive detection of DNA synthesis *in vivo*. *Proc Natl Acad Sci U S A,* 105**,** 2415-20.
SAMANT, S., ROBBINS, K. T., VANG, M., WAN, J. & ROBERTSON, J. 2004. Intra-arterial cisplatin and concomitant radiation therapy followed by surgery for advanced paranasal sinus cancer. *Arch Otolaryngol Head Neck Surg,* 130**,** 948-55.
SAMUEL, T., WEBER, H. O. & FUNK, J. O. 2002. Linking DNA damage to cell cycle checkpoints. *Cell Cycle,* 1**,** 162-8.
SAN FILIPPO, J., SUNG, P. & KLEIN, H. 2008. Mechanism of eukaryotic homologous recombination. *Annu Rev Biochem,* 77**,** 229-57.
SANKUNNY, M., PARIKH, R. A., LEWIS, D. W., GOODING, W. E., SAUNDERS, W. S. & GOLLIN, S. M. 2014. Targeted inhibition of ATR or CHEK1 reverses radioresistance in oral squamous cell carcinoma cells with distal chromosome arm 11q loss. *Genes Chromosomes Cancer,* 53**,** 129-43.
SANTOS, M. R., SERVATO, J. P., CARDOSO, S. V., DE FARIA, P. R., EISENBERG, A. L., DIAS, F. L. & LOYOLA, A. M. 2014. Squamous cell carcinoma at maxillary sinus: clinicopathologic data in a single Brazilian institution with review of literature. *Int J Clin Exp Pathol,* 7**,** 8823-32.
SAPKOTA, A., GAJALAKSHMI, V., JETLY, D. H., ROYCHOWDHURY, S., DIKSHIT, R. P., BRENNAN, P., HASHIBE, M. & BOFFETTA, P. 2007. Smokeless tobacco and increased risk of hypopharyngeal and laryngeal cancers: a multicentric case-control study from India. *Int J Cancer,* 121**,** 1793-8.
SARTORIUS, U. A. & KRAMMER, P. H. 2002. Upregulation of Bcl-2 is involved in the mediation of chemotherapy resistance in human small cell lung cancer cell lines. *Int J Cancer,* 97**,** 584-92.
SATO, M., SASAKI, N., ATO, M., HIRAKAWA, S., SATO, K. & SATO, K. 2015. Microcirculation-on-a-Chip: A Microfluidic Platform for Assaying Blood- and Lymphatic-Vessel Permeability. *PLoS One,* 10**,** e0137301.
SATTLER, U. G., MEYER, S. S., QUENNET, V., HOERNER, C., KNOERZER, H., FABIAN, C., YAROMINA, A., ZIPS, D., WALENTA, S., BAUMANN, M. & MUELLER-KLIESER, W. 2010. Glycolytic metabolism and tumour response to fractionated irradiation. *Radiother Oncol,* 94**,** 102-9.
SCAIFE, L., HODGKINSON, V. C., DREW, P. J., LIND, M. J. & CAWKWELL, L. 2011. Differential proteomics in the search for biomarkers of radiotherapy resistance. *Expert Rev Proteomics,* 8**,** 535-52.
SCHIFF, B. A. 2016. *Overview of Head and Neck Tumors.* Available online: https://www.msdmanuals.com/en-gb/professional/ear,-nose,-and-throat-disorders/tumors-of-the-head-and-neck/overview-of-head-and-neck-tumors. [Accessed on May 2016].
SCHUTTE, B., HENFLING, M., KOLGEN, W., BOUMAN, M., MEEX, S., LEERS, M. P., NAP, M., BJORKLUND, V., BJORKLUND, P., BJORKLUND, B., LANE, E. B., OMARY, M. B., JORNVALL, H. & RAMAEKERS, F. C. 2004. Keratin 8/18 breakdown and reorganization during apoptosis. *Exp Cell Res,* 297**,** 11-26.
SCOTT, L. C., EVANS, T. R., CASSIDY, J., HARDEN, S., PAUL, J., ULLAH, R., O'BRIEN, V. & BROWN, R. 2009. Cytokeratin 18 in plasma of patients with gastrointestinal adenocarcinoma as a biomarker of tumour response. *Br J Cancer,* 101**,** 410-7.

SCOTTISH INTERCOLLEGIATE GUIDELINES NETWORK (SIGN), 2006. Diagnosis and management of head and neck cancer: A national clinical guideline. Edinburgh.
SCULLY, R. & XIE, A. 2013. Double strand break repair functions of histone H2AX. *Mutat Res,* 750**,** 5-14.
SEDELNIKOVA, O. A., ROGAKOU, E. P., PANYUTIN, I. G. & BONNER, W. M. 2002. Quantitative detection of (125)IdU-induced DNA double-strand breaks with gamma-H2AX antibody. *Radiat Res,* 158**,** 486-92.
SHACKELFORD, R. E., KAUFMANN, W. K. & PAULES, R. S. 1999. Cell cycle control, checkpoint mechanisms, and genotoxic stress. *Environ Health Perspect,* 107 Suppl 1**,** 5-24.
SHARP LABORATORIES OF EUROPE. 2014. *Health and medical devices.* Available online: http://www.sle.sharp.co.uk/sharp/apps/sle-web/research/health_medical/index.html. [Accessed on June 2015].
SHAW, R. J. & DHANDA, J. 2011. Hyperbaric oxygen in the management of late radiation injury to the head and neck. Part I: treatment. *Br J Oral Maxillofac Surg,* 49**,** 2-8.
SHEAHAN, P. 2014. Management of advanced laryngeal cancer. *Rambam Maimonides Med J,* 5**,** e0015.
SHILOH, Y. & ZIV, Y. 2013. The ATM protein kinase: regulating the cellular response to genotoxic stress, and more. *Nat Rev Mol Cell Biol,* 14**,** 197-210.
SHILOH, Y. 2001. ATM and ATR: networking cellular responses to DNA damage. *Curr Opin Genet Dev,* 11**,** 71-7.
SHINTU, L., BAUDOIN, R., NAVRATIL, V., PROT, J. M., PONTOIZEAU, C., DEFERNEZ, M., BLAISE, B. J., DOMANGE, C., PERY, A. R., TOULHOAT, P., LEGALLAIS, C., BROCHOT, C., LECLERC, E. & DUMAS, M. E. 2012. Metabolomics-on-a-chip and predictive systems toxicology in microfluidic bioartificial organs. *Anal Chem,* 84**,** 1840-8.
SIEGEL, R. L., MILLER, K. D. & JEMAL, A. 2015. Cancer statistics, 2015. *CA Cancer J Clin,* 65**,** 5-29.
SILVA, P., HOMER, J. J., SLEVIN, N. J., MUSGROVE, B. T., SLOAN, P., PRICE, P. & WEST, C. M. 2007. Clinical and biological factors affecting response to radiotherapy in patients with head and neck cancer: a review. *Clin Otolaryngol,* 32**,** 337-45.
SILVER, N., BEST, S., JIANG, J. & THEIN, S. L. 2006. Selection of housekeeping genes for gene expression studies in human reticulocytes using real-time PCR. *BMC Mol Biol,* 7**,** 33.
SIONOV. R. V., HAYON. I. L. & HAUPT, Y. 2000. The regulation of p53 growth suppression. (ed) *Madame Curie Bioscience Database*. Austin Texas: Landes Bioscience, 2000-2013
SIYAN, W., FENG, Y., LICHUAN, Z., JIARUI, W., YINGYAN, W., LI, J., BINGCHENG, L. & QI, W. 2009. Application of microfluidic gradient chip in the analysis of lung cancer chemotherapy resistance. *J Pharm Biomed Anal,* 49**,** 806-10.
SMIT, J. K., FABER, H., NIEMANTSVERDRIET, M., BAANSTRA, M., BUSSINK, J., HOLLEMA, H., VAN OS, R. P., PLUKKER, J. T. & COPPES, R. P. 2013. Prediction of response to radiotherapy in the treatment of esophageal cancer using stem cell markers. *Radiother Oncol,* 107**,** 434-41.
SMITH, J., THO, L. M., XU, N. & GILLESPIE, D. A. 2010. The ATM-Chk2 and ATR-Chk1 pathways in DNA damage signaling and cancer. *Adv Cancer Res,* 108**,** 73-112.
SOK, J. C., COPPELLI, F. M., THOMAS, S. M., LANGO, M. N., XI, S., HUNT, J. L., FREILINO, M. L., GRANER, M. W., WIKSTRAND, C. J., BIGNER, D. D., GOODING, W. E., FURNARI, F. B. & GRANDIS, J. R. 2006. Mutant epidermal growth factor receptor (EGFRvIII) contributes to head and neck cancer growth and resistance to EGFR targeting. *Clin Cancer Res,* 12**,** 5064-73.
SOMANI, N., GOYAL, S., PASRICHA, R., KHUTETA, N., AGARWAL, P., GARG, A. K. & SINGHAL, H. 2011. Sequential therapy (triple drug-based induction chemotherapy followed by concurrent chemoradiotherapy) in locally advanced inoperable head and neck cancer patients - Single institute experience. *Indian J Med Paediatr Oncol,* 32**,** 86-91.
SOMOGYI, A., ROSTA, A., LANG, I. & WERLING, K. 1996. Treatment of drug-induced bone marrow suppression with recombinant human granulocyte/monocyte colony stimulating factor. *Adverse Drug React Toxicol Rev,* 15**,** 119-24.
SORENSEN, B. S., BUSK, M., HORSMAN, M. R., ALSNER, J., OVERGAARD, J., KYLE, A. H. & MINCHINTON, A. I. 2014. Effect of radiation on cell proliferation and tumor hypoxia in HPV-positive head and neck cancer *in vivo* models. *Anticancer Res,* 34**,** 6297-304.
SOUNG, Y. H., LEE, J. W., KIM, S. Y., JANG, J., PARK, Y. G., PARK, W. S., NAM, S. W., LEE, J. Y., YOO, N. J. & LEE, S. H. 2005. CASPASE-8 gene is inactivated by somatic mutations in gastric carcinomas. *Cancer Res,* 65**,** 815-21.
SQUARIZE, C. H., CASTILHO, R. M., ABRAHAO, A. C., MOLINOLO, A., LINGEN, M. W. & GUTKIND, J. S. 2013. PTEN deficiency contributes to the development and progression of head and neck cancer. *Neoplasia,* 15**,** 461-71.
STASZEWSKI, O., NIKOLOVA, T. & KAINA, B. 2008. Kinetics of gamma-H2AX focus formation upon treatment of cells with UV light and alkylating agents. Environ Mol Mutagen, 49, 734-40.
STEBBING, J., PAZ, K., SCHWARTZ, G. K., WEXLER, L. H., MAKI, R., POLLOCK, R. E., MORRIS, R., COHEN, R., SHANKAR, A., BLACKMAN, G., HARDING, V., VASQUEZ, D., KRELL, J., ZACHAROULIS,

S., CIZNADIJA, D., KATZ, A. & SIDRANSKY, D. 2014. Patient-derived xenografts for individualized care in advanced sarcoma. *Cancer,* 120**,** 2006-15.
STEGEMAN, H., KAANDERS, J. H., VAN DER KOGEL, A. J., IIDA, M., WHEELER, D. L., SPAN, P. N. & BUSSINK, J. 2013. Predictive value of hypoxia, proliferation and tyrosine kinase receptors for EGFR-inhibition and radiotherapy sensitivity in head and neck cancer models. *Radiother Oncol,* 106**,** 383-9.
STEIN, A. P., SWICK, A. D., SMITH, M. A., BLITZER, G. C., YANG, R. Z., SAHA, S., HARARI, P. M., LAMBERT, P. F., LIU, C. Z. & KIMPLE, R. J. 2015. Xenograft assessment of predictive biomarkers for standard head and neck cancer therapies. *Cancer Med,* 4**,** 699-712.
STROOCK, A. D. & FISCHBACH, C. 2010. Microfluidic culture models of tumor angiogenesis. *Tissue Eng Part A,* 16**,** 2143-6.
STUR, E., AGOSTINI, L. P., GARCIA, F. M., PETERLE, G. T., MAIA, L. L., MENDES, S. O., ANDERS, Q. S., REIS, R. S., SANTOS, J. A., VENTORIM, D. P., CARVALHO, M. B., TAJARA, E. H., SANTOS, M., PAULA, F., SILVA-CONFORTI, A. M. A. & LOURO, I. D. 2015. Prognostic significance of head and neck squamous cell carcinoma repair gene polymorphism. *Genetics and Molecular Research,* 14**,** 12446-12454.
SUEN, D. F., NORRIS, K. L. & YOULE, R. J. 2008. Mitochondrial dynamics and apoptosis. *Genes Dev,* 22**,** 1577-90.
SUN, P., LIU, Y., SHA, J., ZHANG, Z., TU, Q., CHEN, P. & WANG, J. 2011. High-throughput microfluidic system for long-term bacterial colony monitoring and antibiotic testing in zero-flow environments. *Biosens Bioelectron,* 26**,** 1993-9.
SUN, Q., ZHENG, X., ZHANG, L. & YU, J. 2011. Smac modulates chemosensitivity in head and neck cancer cells through the mitochondrial apoptotic pathway. *Clin Cancer Res,* 17**,** 2361-72.
SUN, X. X. & YU, Q. 2015. Intra-tumor heterogeneity of cancer cells and its implications for cancer treatment. *Acta Pharmacol Sin,* 36**,** 1219-27.
SUNDQUIST, T.E.R.R.I., MORAVEC, R., NILES, A.N.D.R.E.W., O'BRIEN, M.A.R.T.H.A. & RISS, T., 2006. Timing your apoptosis assays. *Cell Notes*, 16, pp.18-21.
SUNG, J. H. & SHULER, M. L. 2009. A micro cell culture analog (microCCA) with 3-D hydrogel culture of multiple cell lines to assess metabolism-dependent cytotoxicity of anti-cancer drugs. *Lab Chip,* 9**,** 1385-94.
TAKAYAMA, S., OSTUNI, E., LEDUC, P., NARUSE, K., INGBER, D. E. & WHITESIDES, G. M. 2003. Selective chemical treatment of cellular microdomains using multiple laminar streams. *Chem Biol,* 10**,** 123-30.
TAKENAKA, T., YOSHINO, I., KOUSO, H., OHBA, T., YOHENA, T., OSOEGAWA, A., SHOJI, F. & MAEHARA, Y. 2007. Combined evaluation of Rad51 and ERCC1 expressions for sensitivity to platinum agents in non-small cell lung cancer. *Int J Cancer,* 121**,** 895-900.
TAN, P. H., BAY, B. H., YIP, G., SELVARAJAN, S., TAN, P., WU, J., LEE, C. H. & LI, K. B. 2005. Immunohistochemical detection of Ki67 in breast cancer correlates with transcriptional regulation of genes related to apoptosis and cell death. *Mod Pathol,* 18**,** 374-81.
TANAKA, S., TAK, Y. S. & ARAKI, H. 2007. The role of CDK in the initiation step of DNA replication in eukaryotes. *Cell Div,* 2**,** 16.
TANEJA, N., DAVIS, M., CHOY, J. S., BECKETT, M. A., SINGH, R., KRON, S. J. & WEICHSELBAUM, R. R. 2004. Histone H2AX phosphorylation as a predictor of radiosensitivity and target for radiotherapy. *J Biol Chem,* 279**,** 2273-80.
TANIGUCHI, T. & D'ANDREA, A. D. 2006. Molecular pathogenesis of Fanconi anemia: recent progress. *Blood,* 107**,** 4223-33.
TANWEER, F., GREEN, V. L., STAFFORD, N. D. & GREENMAN, J. 2013. Application of microfluidic systems in management of head and neck squamous cell carcinoma. *Head Neck,* 35**,** 756-63.
TARN, M. D. 2008. Standard operating procedures for the fabrication of glass microchips. University of Hull.
TEMAM, S., PAPE, E., JANOT, F., WIBAULT, P., JULIERON, M., LUSINCHI, A., MAMELLE, G., MARANDAS, P., LUBOINSKI, B. & BOURHIS, J. 2005. Salvage surgery after failure of very accelerated radiotherapy in advanced head-and-neck squamous cell carcinoma. *Int J Radiat Oncol Biol Phys,* 62**,** 1078-83.
THE ROYAL AUSTRALIAN AND NEW ZEALAND COLLEGE OF RADIOLOGISTS, 2015. Position paper on image guided radiation therapy (IGRT) 2015. Australia.
THE ROYAL COLLEGE OF RADIOLOGISTS, 2006. *Radiotherapy Dose-Fractionation.* Available online: https://www.rcr.ac.uk/publication/radiotherapy-dose-fractionation. [Accessed on December 2012].
THERMO FISHER SCIENTIFIC. 2010 Taking the Pulse of Cell Proliferation- Single-Pulse and Dual-Pulse Click-iT® EdU Assays. *BioProbes 63–Cell Biology by Invitrogen.* Issues 62-63
THERMO FISHER SCIENTIFIC. 2014. *TaqMan® Fast Advanced Master Mix: Performance superior to standard master mixes in less than half the time.* Available online: https://tools.thermofisher.com/content/sfs/brochures/cms_084549.pdf. [Accessed on May 2016]
THERMO SCIENTIFIC. 2008. *260/280 and 260/230 ratios*. Available online: http://www.nanodrop.com/Library/T009-NanoDrop%201000-&-NanoDrop%208000-Nucleic-Acid-Purity-Ratios.pdf [Accessed on August 2015].

THERMO SCIENTIFIC. 2015. *Thermo Scientific Shandon ® Sequenza Immunostaining Center: Organized, reliable method for immunostaining.* Available online: http://cellab.se/pdfbroschyr/inkubation/Sequenza%20Immunostaining%20Center.pdf [Accessed on November 2015].

THERMOFISHER SCIENTIFIC, 2015. *MicroAmp® Fast Optical 96-Well Reaction Plate with Barcode, 0.1mL*. Available online: www.thermofisher.com/order/catalog/product/4346906 [Accessed on March 2016]

THURLOW, J. K., PENA MURILLO, C. L., HUNTER, K. D., BUFFA, F. M., PATIAR, S., BETTS, G., WEST, C. M., HARRIS, A. L., PARKINSON, E. K., HARRISON, P. R., OZANNE, B. W., PARTRIDGE, M. & KALNA, G. 2010. Spectral clustering of microarray data elucidates the roles of microenvironment remodeling and immune responses in survival of head and neck squamous cell carcinoma. *J Clin Oncol,* 28**,** 2881-8.

TILLES, A. W., BASKARAN, H., ROY, P., YARMUSH, M. L. & TONER, M. 2001. Effects of oxygenation and flow on the viability and function of rat hepatocytes cocultured in a microchannel flat-plate bioreactor. *Biotechnol Bioeng,* 73**,** 379-89.

TISELL, L. E., ODEN, A., MUTH, A., ALTIPARMAK, G., MOLNE, J., AHLMAN, H. & NILSSON, O. 2003. The Ki67 index a prognostic marker in medullary thyroid carcinoma. *Br J Cancer,* 89**,** 2093-7.

TONER, M. & O'REGAN, E. M. 2009. Head and neck squamous cell carcinoma in the young: a spectrum or a distinct group? Part 2. *Head Neck Pathol,* 3**,** 249-51.

TORISAWA, Y. S., SPINA, C. S., MAMMOTO, T., MAMMOTO, A., WEAVER, J. C., TAT, T., COLLINS, J. J. & INGBER, D. E. 2014. Bone marrow-on-a-chip replicates hematopoietic niche physiology *in vitro*. *Nature Methods,* 11**,** 663-+.

TRAPASSO, S. & ALLEGRA, E. 2012. Role of CD44 as a marker of cancer stem cells in head and neck cancer. *Biologics,* 6**,** 379-83.

TSUCHIYA, M., NAKAJIMA, Y., WAKU, T., HIYOSHI, H., MORISHITA, T., FURUMAI, R., HAYASHI, Y., KISHIMOTO, H., KIMURA, K. & YANAGISAWA, J. 2015. CHIP buffers heterogeneous Bcl-2 expression levels to prevent augmentation of anticancer drug-resistant cell population. *Oncogene,* 34**,** 4656-63.

TU, Y., XU, F. H., LIU, J., VESCIO, R., BERENSON, J., FADY, C. & LICHTENSTEIN, A. 1996. Upregulated expression of BCL-2 in multiple myeloma cells induced by exposure to doxorubicin, etoposide, and hydrogen peroxide. *Blood,* 88**,** 1805-12.

TURATI, F., GARAVELLO, W., TRAMACERE, I., PELUCCHI, C., GALEONE, C., BAGNARDI, V., CORRAO, G., ISLAMI, F., FEDIRKO, V., BOFFETTA, P., LA VECCHIA, C. & NEGRI, E. 2013. A meta-analysis of alcohol drinking and oral and pharyngeal cancers: results from subgroup analyses. *Alcohol Alcohol,* 48**,** 107-18.

TUTTLE, S., HERTAN, L., DAURIO, N., PORTER, S., KAUSHICK, C., LI, D., MYAMOTO, S., LIN, A., O'MALLEY, B. W. & KOUMENIS, C. 2012. The chemopreventive and clinically used agent curcumin sensitizes HPV (-) but not HPV (+) HNSCC to ionizing radiation, *in vitro* and in a mouse orthotopic model. *Cancer Biol Ther,* 13**,** 575-84.

UENO, T., TOI, M., BIVEN, K., BANDO, H., OGAWA, T. & LINDER, S. 2003. Measurement of an apoptotic product in the sera of breast cancer patients. *Eur J Cancer,* 39**,** 769-74.

ULUKAYA, E., KARAAGAC, E., ARI, F., ORAL, A. Y., ADIM, S. B., TOKULLUGIL, A. H. & EVRENSEL, T. 2011. Chemotherapy increases caspase-cleaved cytokeratin 18 in the serum of breast cancer patients. *Radiol Oncol,* 45**,** 116-22.

UNGER, F. T., WITTE, I. & DAVID, K. A. 2015. Prediction of individual response to anticancer therapy: historical and future perspectives. *Cell Mol Life Sci,* 72**,** 729-57.

VAEZI, A., FELDMAN, C. H. & NIEDERNHOFER, L. J. 2011. ERCC1 and XRCC1 as biomarkers for lung and head and neck cancer. *Pharmgenomics Pers Med,* 4**,** 47-63.

VALDIGLESIAS, V., GIUNTA, S., FENECH, M., NERI, M. & BONASSI, S. 2013. gammaH2AX as a marker of DNA double strand breaks and genomic instability in human population studies. *Mutat Res,* 753**,** 24-40.

VALENCIA, P. M., FAROKHZAD, O. C., KARNIK, R. & LANGER, R. 2012. Microfluidic technologies for accelerating the clinical translation of nanoparticles. *Nat Nanotechnol,* 7**,** 623-9.

VAN DER MEER, A. D. & VAN DEN BERG, A. 2012. Organs-on-chips: breaking the *in vitro* impasse. *Integr Biol (Camb),* 4**,** 461-70.

VAN DER SCHROEFF, M. P. & BAATENBURG DE JONG, R. J. 2009. Staging and prognosis in head and neck cancer. *Oral Oncol,* 45**,** 356-60.

VAN HOUTEN, V. M., SNIJDERS, P. J., VAN DEN BREKEL, M. W., KUMMER, J. A., MEIJER, C. J., VAN LEEUWEN, B., DENKERS, F., SMEELE, L. E., SNOW, G. B. & BRAKENHOFF, R. H. 2001. Biological evidence that human papillomaviruses are etiologically involved in a subgroup of head and neck squamous cell carcinomas. *Int J Cancer,* 93**,** 232-5.

VAN MIDWOUD, P. M., GROOTHUIS, G. M., MEREMA, M. T. & VERPOORTE, E. 2010. Microfluidic biochip for the perifusion of precision-cut rat liver slices for metabolism and toxicology studies. *Biotechnol Bioeng,* 105**,** 184-94.

VAN'T VEER, L. J., PAIK, S. & HAYES, D. F. 2005. Gene expression profiling of breast cancer: a new tumor marker. *J Clin Oncol,* 23**,** 1631-5.
VEGA-AVILA, E. & PUGSLEY, M. K. 2011. An overview of colorimetric assay methods used to assess survival or proliferation of mammalian cells. *Proc West Pharmacol Soc,* 54**,** 10-4.
VERMEULEN, K., VAN BOCKSTAELE, D. R. & BERNEMAN, Z. N. 2003. The cell cycle: a review of regulation, deregulation and therapeutic targets in cancer. *Cell Prolif,* 36**,** 131-49.
VERMORKEN, J. B. & SPECENIER, P. 2010. Optimal treatment for recurrent/metastatic head and neck cancer. *Ann Oncol,* 21 Suppl 7**,** vii252-61.
WALBOOMERS, J. M., JACOBS, M. V., MANOS, M. M., BOSCH, F. X., KUMMER, J. A., SHAH, K. V., SNIJDERS, P. J., PETO, J., MEIJER, C. J. & MUNOZ, N. 1999. Human papillomavirus is a necessary cause of invasive cervical cancer worldwide. *J Pathol,* 189**,** 12-9.
WALDEN, M. J. & AYGUN, N. 2013. Head and neck cancer. *Semin Roentgenol,* 48**,** 75-86.
WALKER, G. M., ZERINGUE, H. C. & BEEBE, D. J. 2004. Microenvironment design considerations for cellular scale studies. *Lab Chip,* 4**,** 91-7.
WAN, W. J. & YEOW, J. T. W. 2011. Study of a novel cell lysis method with titanium dioxide for Lab-on-a-Chip devices. *Biomedical Microdevices,* 13**,** 527-532.
WANG, H., WANG, M., WANG, H., BOCKER, W. & ILIAKIS, G. 2005. Complex H2AX phosphorylation patterns by multiple kinases including ATM and DNA-PK in human cells exposed to ionizing radiation and treated with kinase inhibitors. *J Cell Physiol,* 202**,** 492-502.
WANG, W. Z., OESCHGER, F. M., LEE, S. & MOLNAR, Z. 2009. High quality RNA from multiple brain regions simultaneously acquired by laser capture microdissection. *BMC Mol Biol,* 10**,** 69.
WANG, X., ZENG, L., WANG, J., CHAU, J. F., LAI, K. P., JIA, D., POONEPALLI, A., HANDE, M. P., LIU, H., HE, G., HE, L. & LI, B. 2011. A positive role for c-Abl in Atm and Atr activation in DNA damage response. Cell Death Differ, 18, 5-15.
WARBURG, O. 1925. Iron, the Oxygen-Carrier of Respiration-Ferment. *Science,* 61**,** 575-82.
WARENIUS, H. M., SEABRA, L., KYRITSI, L., WHITE, R., DORMER, R., ANANDAPPA, S., THOMAS, C. & HOWARTH, A. 2008. Theranostic proteomic profiling of cyclins, cyclin dependent kinases and Ras in human cancer cell lines is dependent on p53 mutational status. *Int J Oncol,* 32**,** 895-907.
WARREN, M., PUSKARCZYK, K. & CHAPMAN, S. C. 2009. Chick embryo proliferation studies using EdU labeling. *Dev Dyn,* 238**,** 944-9.
WEBSTER, A., GREENMAN, J. & HASWELL, S. J. 2011. Development of microfluidic devices for biomedical and clinical application. *Journal of Chemical Technology and Biotechnology,* 86**,** 10-17.
WEI, L., NAKAJIMA, S., HSIEH, C. L., KANNO, S., MASUTANI, M., LEVINE, A. S., YASUI, A. & LAN, L. 2013. Damage response of XRCC1 at sites of DNA single strand breaks is regulated by phosphorylation and ubiquitylation after degradation of poly(ADP-ribose). *J Cell Sci,* 126**,** 4414-23.
WERNER-WASIK, M., SWANN, R. S., BRADLEY, J., GRAHAM, M., EMAMI, B., PURDY, J. & SAUSE, W. 2008. Increasing tumor volume is predictive of poor overall and progression-free survival: secondary analysis of the Radiation Therapy Oncology Group 93-11 phase I-II radiation dose-escalation study in patients with inoperable non-small-cell lung cancer. *Int J Radiat Oncol Biol Phys,* 70**,** 385-90.
WESTPHAL, D., DEWSON, G., CZABOTAR, P. E. & KLUCK, R. M. 2011. Molecular biology of Bax and Bak activation and action. *Biochim Biophys Acta,* 1813**,** 521-31.
WHITE, A. K., VANINSBERGHE, M., PETRIV, O. I., HAMIDI, M., SIKORSKI, D., MARRA, M. A., PIRET, J., APARICIO, S. & HANSEN, C. L. 2011. High-throughput microfluidic single-cell RT-qPCR. *Proc Natl Acad Sci U S A,* 108**,** 13999-4004.
WHITESIDES, G. M. 2006. The origins and the future of microfluidics. *Nature,* 442**,** 368-73.
WILDEMAN, M. A., GIBCUS, J. H., HAUPTMANN, M., BEGG, A. C., VAN VELTHUYSEN, M. L., HOEBERS, F. J., MASTIK, M. F., SCHUURING, E., VAN DER WAL, J. E. & VAN DEN BREKEL, M. W. 2009. Radiotherapy in laryngeal carcinoma: can a panel of 13 markers predict response? *Laryngoscope,* 119**,** 316-22.
WILLERS, H., AZZOLI, C. G., SANTIVASI, W. L. & XIA, F. 2013. Basic mechanisms of therapeutic resistance to radiation and chemotherapy in lung cancer. *Cancer J,* 19**,** 200-7.
WILSON, G. D., SAUNDERS, M. I., DISCHE, S., DALEY, F. M., BUFFA, F. M., RICHMAN, P. I. & BENTZEN, S. M. 2006. Pre-treatment proliferation and the outcome of conventional and accelerated radiotherapy. *European Journal of Cancer,* 42**,** 363-371.
WITHERS, H. R., TAYLOR, J. M. & MACIEJEWSKI, B. 1988. The hazard of accelerated tumor clonogen repopulation during radiotherapy. *Acta Oncol,* 27**,** 131-46.
WOLTER, K. G., HSU, Y. T., SMITH, C. L., NECHUSHTAN, A., XI, X. G. & YOULE, R. J. 1997. Movement of Bax from the cytosol to mitochondria during apoptosis. *J Cell Biol,* 139**,** 1281-92.
WONG, C., ANDERSON, D. J., LEE, E. F., FAIRLIE, W. D. & LUDLAM, M. J. 2012. Direct visualization of Bcl-2 family protein interactions using live cell fluorescent protein redistribution assays. *Cell Death Dis,* 3**,** e288.

WONG, K. H., CHAN, J. M., KAMM, R. D. & TIEN, J. 2012. Microfluidic models of vascular functions. *Annu Rev Biomed Eng,* 14**,** 205-30.
WONG, R. J., LIN, D. T., SCHODER, H., PATEL, S. G., GONEN, M., WOLDEN, S., PFISTER, D. G., SHAH, J. P., LARSON, S. M. & KRAUS, D. H. 2002. Diagnostic and prognostic value of [(18)F]fluorodeoxyglucose positron emission tomography for recurrent head and neck squamous cell carcinoma. *J Clin Oncol,* 20**,** 4199-208.
WOODBINE, L., BRUNTON, H., GOODARZI, A. A., SHIBATA, A. & JEGGO, P. A. 2011. Endogenously induced DNA double strand breaks arise in heterochromatic DNA regions and require ataxia telangiectasia mutated and Artemis for their repair. Nucleic Acids Res, 39, 6986-97.
WU, G. Q., LIU, N. N., XUE, X. L., CAI, L. T., ZHANG, C., QU, Q. R. & YAN, X. J. 2014. Multiplex real-time PCR for RRM1, XRCC1, TUBB3 and TS mRNA for prediction of response of non-small cell lung cancer to chemoradiotherapy. *Asian Pac J Cancer Prev,* 15**,** 4153-8.
WU, G., LEE, W. H. & CHEN, P. L. 2000. NBS1 and TRF1 colocalize at promyelocytic leukemia bodies during late S/G2 phases in immortalized telomerase-negative cells. Implication of NBS1 in alternative lengthening of telomeres. *J Biol Chem,* 275**,** 30618-22.
WU, K. L. H., HUNG, C.Y., CHAN, J. Y. H., & WU, C. W. 2014. An increase in adenosine-5'-triphosphate (ATP) content in rostral ventrolateral medulla is engaged in the high fructose diet-induced hypertension. *J Biomed Sci,* 21(1), 8.
WYNDER, E. L., BROSS, I. J. & FELDMAN, R. M. 1957. A study of the etiological factors in cancer of the mouth. *Cancer,* 10**,** 1300-23.
XIE, X., CLAUSEN, O. P., DE ANGELIS, P. & BOYSEN, M. 1999. The prognostic value of spontaneous apoptosis, Bax, Bcl-2, and p53 in oral squamous cell carcinoma of the tongue. *Cancer,* 86**,** 913-20.
XU, S. Q. & EL-DEIRY, W. S. 2000. p21(WAF1/CIP1) inhibits initiator caspase cleavage by TRAIL death receptor DR4. *Biochem Biophys Res Commun,* 269**,** 179-90.
YANG, J., LIU, A., DOUGHERTY, C., CHEN, X., GUZMAN, R. & NANDI, S. 2000. Beware of contaminating mouse cells in human xenografts from nude mice. *Anticancer Res,* 20**,** 1635-9.
YANG, J., LIU, X., BHALLA, K., KIM, C. N., IBRADO, A. M., CAI, J., PENG, T. I., JONES, D. P. & WANG, X. 1997. Prevention of apoptosis by Bcl-2: release of cytochrome c from mitochondria blocked. *Science,* 275**,** 1129-32.
YANG, L., LIU, Y., SUN, C., YANG, X., YANG, Z., RAN, J., ZHANG, Q., ZHANG, H., WANG, X. & WANG, X. 2015. Inhibition of DNA-PKcs enhances radiosensitivity and increases the levels of ATM and ATR in NSCLC cells exposed to carbon ion irradiation. *Oncol Lett,* 10**,** 2856-2864.
YANG, M. H., CHIANG, W. C., CHOU, T. Y., CHANG, S. Y., CHEN, P. M., TENG, S. C. & WU, K. J. 2006. Increased NBS1 expression is a marker of aggressive head and neck cancer and overexpression of NBS1 contributes to transformation. *Clin Cancer Res,* 12**,** 507-15.
YANG, X. Q., WANG, F. B., CHEN, C., PENG, C. W., ZHANG, J. F. & LI, Y. 2011. High Ki-67 expression is a poor prognostic indicator of 5-year recurrence free survival in patients with invasive breast cancer. *Asian Pac J Cancer Prev,* 12**,** 3101-5.
YAO, M., EPSTEIN, J. B., MODI, B. J., PYTYNIA, K. B., MUNDT, A. J. & FELDMAN, L. E. 2007. Current surgical treatment of squamous cell carcinoma of the head and neck. *Oral Oncol,* 43**,** 213-23.
YAPA, S., CHEAH, R., MULLA, O., GREENMAN, J., KARSAI, L., GREEN, V. & ENGLAND, J. 2016. To investigate the viability of thyroid tumour tissue maintained in a microfluidic system. (Abstract and poster presentation) International Federation of Head and Neck Oncologic Societies (September 2016, Delhi, India).
YAROMINA, A., KRAUSE, M. & BAUMANN, M. 2012. Individualization of cancer treatment from radiotherapy perspective. *Mol Oncol,* 6**,** 211-21.
YAROMINA, A., KRAUSE, M., THAMES, H., ROSNER, A., KRAUSE, M., HESSEL, F., GRENMAN, R., ZIPS, D. & BAUMANN, M. 2007. Pre-treatment number of clonogenic cells and their radiosensitivity are major determinants of local tumour control after fractionated irradiation. *Radiother Oncol,* 83**,** 304-10.
YE, C., CAI, Q., DAI, Q., SHU, X. O., SHIN, A., GAO, Y. T. & ZHENG, W. 2007. Expression patterns of the ATM gene in mammary tissues and their associations with breast cancer survival. *Cancer,* 109**,** 1729-35.
YEE, J. Y., LIMENTA, L. M., ROGERS, K., ROGERS, S. M., TAY, V. S. & LEE, E. J. 2014. Ensuring good quality RNA for quantitative real-time PCR isolated from renal proximal tubular cells using laser capture microdissection. *BMC Res Notes,* 7**,** 62.
YIN, X., ZHANG, H., LUNDGREN, K., WILSON, L., BURROWS, F. & SHORES, C. G. 2010. BIIB021, a novel Hsp90 inhibitor, sensitizes head and neck squamous cell carcinoma to radiotherapy. *Int J Cancer,* 126**,** 1216-25.
YING-YAN, W., TAO, W., XIN, L., HONG-WEI, G., BING-CHENG, L. & QI, W. 2008. The analysis of chemotherapy resistance in human lung cancer cell line with microchip-based system. *Biomed Microdevices,* 10**,** 429-35.

YUM, K., HONG, S. G., HEALY, K. E. & LEE, L. P. 2014. Physiologically relevant organs on chips. *Biotechnol J,* 9**,** 16-27.
YUN, S. I., YOON, H. Y. & CHUNG, Y. S. 2009. Glycogen synthase kinase-3beta regulates etoposide-induced apoptosis via Bcl-2 mediated caspase-3 activation in C3H10T1/2 cells. *Apoptosis,* 14**,** 771-7.
ZACKRISSON, B., MERCKE, C., STRANDER, H., WENNERBERG, J. & CAVALLIN-STAHL, E. 2003. A systematic overview of radiation therapy effects in head and neck cancer. *Acta Oncol,* 42**,** 443-61.
ZEGERS, C. M., VAN ELMPT, W., HOEBERS, F. J., TROOST, E. G., OLLERS, M. C., MOTTAGHY, F. M. & LAMBIN, P. 2015. Imaging of tumour hypoxia and metabolism in patients with head and neck squamous cell carcinoma. *Acta Oncol,* 54**,** 1378-84.
ZENG, C., PAN, F., JONES, L. A., LIM, M. M., GRIFFIN, E. A., SHELINE, Y. I., MINTUN, M. A., HOLTZMAN, D. M. & MACH, R. H. 2010. Evaluation of 5-ethynyl-2'-deoxyuridine staining as a sensitive and reliable method for studying cell proliferation in the adult nervous system. *Brain Res,* 1319**,** 21-32.
ZERP, S. F., STOTER, T. R., HOEBERS, F. J., VAN DEN BREKEL, M. W., DUBBELMAN, R., KUIPERS, G. K., LAFLEUR, M. V., SLOTMAN, B. J. & VERHEIJ, M. 2015. Targeting anti-apoptotic Bcl-2 by AT-101 to increase radiation efficacy: data from *in vitro* and clinical pharmacokinetic studies in head and neck cancer. *Radiat Oncol,* 10**,** 158.
ZHANG, J. & WALTER, J. C. 2014. Mechanism and regulation of incisions during DNA interstrand cross-link repair. *DNA Repair (Amst),* 19**,** 135-42.
ZHANG, J., SUN, Q., ZHANG, Z., GE, S., HAN, Z. G. & CHEN, W. T. 2013. Loss of microRNA-143/145 disturbs cellular growth and apoptosis of human epithelial cancers by impairing the MDM2-p53 feedback loop. *Oncogene,* 32**,** 61-9.
ZHANG, S. Y., LU, Z. M., LUO, X. N., CHEN, L. S., GE, P. J., SONG, X. H., CHEN, S. H. & WU, Y. L. 2013. Retrospective analysis of prognostic factors in 205 patients with laryngeal squamous cell carcinoma who underwent surgical treatment. *PLoS One,* 8**,** e60157.
ZHANG, X. C., XU, C., MITCHELL, R. M., ZHANG, B., ZHAO, D., LI, Y., HUANG, X., FAN, W., WANG, H., LERMA, L. A., UPTON, M. P., HAY, A., MENDEZ, E. & ZHAO, L. P. 2013. Tumor evolution and intratumor heterogeneity of an oropharyngeal squamous cell carcinoma revealed by whole-genome sequencing. *Neoplasia,* 15**,** 1371-8.
ZHANG, Z. X., JIANG, C. Q. & HU, L. K. 2014. Low expression of excision repair cross-complementation group-1 protein predicts better outcome in patients with locally advanced nasopharyngeal cancer treated with concurrent chemoradiotherapy. *Tumori,* 100**,** 328-332.
ZHENG, W., WANG, Z., ZHANG, W. & JIANG, X. 2010. A simple PDMS-based microfluidic channel design that removes bubbles for long-term on-chip culture of mammalian cells. *Lab Chip,* 10**,** 2906-10.
ZHENG, Y., CHEN, J., CRAVEN, M., CHOI, N. W., TOTORICA, S., DIAZ-SANTANA, A., KERMANI, P., HEMPSTEAD, B., FISCHBACH-TESCHL, C., LOPEZ, J. A. & STROOCK, A. D. 2012. *In vitro* microvessels for the study of angiogenesis and thrombosis. *Proc Natl Acad Sci U S A,* 109**,** 9342-7.
ZHONG, J., RAJARAM, N., BRIZEL, D. M., FREES, A. E., RAMANUJAM, N., BATINIC-HABERLE, I. & DEWHIRST, M. W. 2013. Radiation induces aerobic glycolysis through reactive oxygen species. *Radiother Oncol,* 106**,** 390-6.
ZIEBART, T., WALENTA, S., KUNKEL, M., REICHERT, T. E., WAGNER, W. & MUELLER-KLIESER, W. 2011. Metabolic and proteomic differentials in head and neck squamous cell carcinomas and normal gingival tissue. *J Cancer Res Clin Oncol,* 137**,** 193-9.
ZOU, J., QIAO, X., YE, H., YANG, Y., ZHENG, X., ZHAO, H. & LIU, S. 2008. Antisense inhibition of ATM gene enhances the radiosensitivity of head and neck squamous cell carcinoma in mice. *J Exp Clin Cancer Res,* 27**,** 56.
ANTOINE, E. E., VLACHOS, P. P. & RYLANDER, M. N. 2015. Tunable collagen I hydrogels for engineered physiological tissue micro-environments. *PLoS One,* 10**,** e0122500.
ARRIO-DUPONT, M., CRIBIER, S., FOUCAULT, G., DEVAUX, P. F. & D'ALBIS, A. 1996. Diffusion of fluorescently labeled macromolecules in cultured muscle cells. *Biophys J,* 70**,** 2327-32.
ASTOLFI, M., PEANT, B., LATEEF, M. A., ROUSSET, N., KENDALL-DUPONT, J., CARMONA, E., MONET, F., SAAD, F., PROVENCHER, D., MES-MASSON, A. M. & GERVAIS, T. 2016. Micro-dissected tumor tissues on chip: an *ex vivo* method for drug testing and personalized therapy. *Lab Chip,* 16**,** 312-25.
BACABAC, R. G., SMIT, T. H., COWIN, S. C., VAN LOON, J. J., NIEUWSTADT, F. T., HEETHAAR, R. & KLEIN-NULEND, J. 2005. Dynamic shear stress in parallel-plate flow chambers. *J Biomech,* 38**,** 159-67.
BONNER, J. A., HARARI, P. M., GIRALT, J., AZARNIA, N., SHIN, D. M., COHEN, R. B., JONES, C. U., SUR, R., RABEN, D., JASSEM, J., OVE, R., KIES, M. S., BASELGA, J., YOUSSOUFIAN, H., AMELLAL, N., ROWINSKY, E. K. & ANG, K. K. 2006. Radiotherapy plus cetuximab for squamous-cell carcinoma of the head and neck. *N Engl J Med,* 354**,** 567-78.
CALAIS, P. J. & TURNER, J. H. 2012. Outpatient 131I-rituximab radioimmunotherapy for non-Hodgkin lymphoma: a study in safety. *Clin Nucl Med,* 37**,** 732-7.

ECONOMOPOULOU, P., PERISANIDIS, C., GIOTAKIS, E. I. & PSYRRI, A. 2016. The emerging role of immunotherapy in head and neck squamous cell carcinoma (HNSCC): anti-tumor immunity and clinical applications. *Ann Transl Med,* 4**,** 173.
FLUCKEY, J. D., PLOUG, T. & GALBO, H. 1999. Mechanisms associated with hypoxia- and contraction-mediated glucose transport in muscle are fibre-dependent. *Acta Physiol Scand,* 167**,** 83-7.
FUEREDER, T. 2016. Immunotherapy for head and neck squamous cell carcinoma. *Memo,* 9**,** 66-69.
GANTENBEIN-RITTER, B., POTIER, E., ZEITER, S., VAN DER WERF, M., SPRECHER, C. M. & ITO, K. 2008. Accuracy of three techniques to determine cell viability in 3D tissues or scaffolds. *Tissue Eng Part C Methods,* 14**,** 353-8.
HANSEN, A. R. & SIU, L. L. 2013. Epidermal growth factor receptor targeting in head and neck cancer: have we been just skimming the surface? *J Clin Oncol,* 31**,** 1381-3.
HASSAN, W., DONG, Y. & WANG, W. 2013. Encapsulation and 3D culture of human adipose-derived stem cells in an in-situ crosslinked hybrid hydrogel composed of PEG-based hyperbranched copolymer and hyaluronic acid. *Stem Cell Res Ther,* 4**,** 32.
JAMAL-HANJANI, M., WILSON, G. A., HORSWELL, S., MITTER, R., SAKARYA, O., CONSTANTIN, T., SALARI, R., KIRKIZLAR, E., SIGURJONSSON, S., PELHAM, R., KAREHT, S., ZIMMERMANN, B. & SWANTON, C. 2016. Detection of ubiquitous and heterogeneous mutations in cell-free DNA from patients with early-stage non-small-cell lung cancer. *Ann Oncol,* 27**,** 862-7.
JOUNG, J. G., BAE, J. S., KIM, S. C., JUNG, H., PARK, W. Y. & SONG, S. Y. 2016. Genomic Characterization and Comparison of Multi-Regional and Pooled Tumor Biopsy Specimens. *PLoS One,* 11**,** e0152574.
LOVENDORF, M. B., MITSUI, H., ZIBERT, J. R., ROPKE, M. A., HAFNER, M., DYRING-ANDERSEN, B., BONEFELD, C. M., KRUEGER, J. G. & SKOV, L. 2015. Laser capture microdissection followed by next-generation sequencing identifies disease-related microRNAs in psoriatic skin that reflect systemic microRNA changes in psoriasis. *Exp Dermatol,* 24**,** 187-93.
MCCREEDY, T. & WILSON, N. G. 2001. Microfabricated reactors for on-chip heterogeneous catalysis. *Analyst,* 126**,** 21-3.
MCKEOWN, S. R. 2014. Defining normoxia, physoxia and hypoxia in tumours-implications for treatment response. *Br J Radiol,* 87**,** 20130676.
PAKOLA, S. J. & GRUNWALD, J. E. 1993. Effects of oxygen and carbon dioxide on human retinal circulation. *Invest Ophthalmol Vis Sci,* 34**,** 2866-70.
ROBERT, F., EZEKIEL, M. P., SPENCER, S. A., MEREDITH, R. F., BONNER, J. A., KHAZAELI, M. B., SALEH, M. N., CAREY, D., LOBUGLIO, A. F., WHEELER, R. H., COOPER, M. R. & WAKSAL, H. W. 2001. Phase I study of anti--epidermal growth factor receptor antibody cetuximab in combination with radiation therapy in patients with advanced head and neck cancer. *J Clin Oncol,* 19**,** 3234-43.
STUBBS, M., ROBINSON, S. P., RODRIGUES, L. M., PARKINS, C. S., COLLINGRIDGE, D. R. & GRIFFITHS, J. R. 1998. The effects of host carbogen (95% oxygen/5% carbon dioxide) breathing on metabolic characteristics of Morris hepatoma 9618a. *Br J Cancer,* 78**,** 1449-56.
VERMORKEN, J. B., MESIA, R., RIVERA, F., REMENAR, E., KAWECKI, A., ROTTEY, S., ERFAN, J., ZABOLOTNYY, D., KIENZER, H. R., CUPISSOL, D., PEYRADE, F., BENASSO, M., VYNNYCHENKO, I., DE RAUCOURT, D., BOKEMEYER, C., SCHUELER, A., AMELLAL, N. & HITT, R. 2008. Platinum-based chemotherapy plus cetuximab in head and neck cancer. *N Engl J Med,* 359**,** 1116-27.
WANG, C., LU, H. & SCHWARTZ, M. A. 2012. A novel *in vitro* flow system for changing flow direction on endothelial cells. *J Biomech,* 45**,** 1212-8.
WU, K. L., HUNG, C. Y., CHAN, J. Y. & WU, C. W. 2014. An increase in adenosine-5'-triphosphate (ATP) content in rostral ventrolateral medulla is engaged in the high fructose diet-induced hypertension. *J Biomed Sci,* 21**,** 8.
YOKOTA, T. 2014. Is biomarker research advancing in the era of personalized medicine for head and neck cancer? *Int J Clin Oncol,* 19**,** 211-9.
ZARDAVAS, D., IRRTHUM, A., SWANTON, C. & PICCART, M. 2015. Clinical management of breast cancer heterogeneity. *Nat Rev Clin Oncol,* 12**,** 381-94.

9. Appendix

9.1. Patient demographics of HNSCC samples included in current research group

Table 9.1. Patient demographics of HNSCC tumour samples (n=71) which were consented in accordance with Local Research Ethics Committee (LREC-10/H1304/6) and NHS Trust R&D approval (R0987).

TR number	HNSCC	site	Tumour stage	Gender; age	Sample date	No. of tubes	Treatment	Note
52	LN	OC (FOM)	T1/T2N2c	59; M	30.10.12	11		Used in current study
53	LN	PS	NA	59; F	30.10.12	3	Surgery and RT	
54	LN	OP (tonsil)	NA	46; M	06.11.12	16	Surgery	Used in current study
55	PT	L (glottis)	T1N0	NA; M	20.11.12	NIL	Surgery	No Samples
56	PT	L	T4N0	76; M	27.11.12	NIL	Surgery	
57	LN	Parotid	N2b	74; M	18.12.12	11	Surgery	
58	LN	OP (tonsil)	T3N2c	79; M	08.01.13	11	Surgery and CRT	
59	LN	OP (tonsil)	T4N2b	68; M	22.01.13	10	Surgery and CRT	Used in current study
60	LN	OP (tonsil)	T1N2b	66; M	22.01.13	5	Surgery and CRT	
61	LN	OP (tonsil)	T2N2b	43; M	29.01.13	6	Surgery and CRT	
62	PT	OC (FOM)	T4N0M0	59; M	07.02.13	7	Surgery	Used in current study
63	PT	OC (buccal mucosa)	T1N0M0	58; M	14.02.13	3	Surgery	
64	PT	L (vocal cord)	T1aN0	73; M	19.02.12	NIL	Surgery	No Samples
65	PT	OC (lateral tongue)	T2N0M0	84; F	21.02.13	3	Surgery	
66	PT	PS (maxillary sinus)	T4N2b	82; F	25.02.13	8	Surgery	Used in current study
67	PT	OC (soft palate)	T1N0	59; F	28.02.13	3	Surgery	
68	LN	L (piriform fossa)	T4N2c	NA; M	05.03.13	8	Surgery	
69	PT	OC (tongue)	T2N0M0	48; M	07.03.13	4	Surgery	
70	LN	Unknown	N1M0	55; M	19.03.13	5	Surgery and RT	
71	PT	OC (tongue)	T2N2bM0	61; M	21.03.13	5	Surgery	Used in current study
72	PT	OP (BOT)	NA	NA	26.03.13	8	RT and CRT	Used in current study
73	LN	Unknown	N2aM0	61; M	09.04.13	7	Surgery and CRT	Used in current study
74	LN	OP (BOT)	T2N2b	64; M	23.04.13	6		Previously treated
75	LN	Unknown	T0N3	62; M	30.04.13	9		
76	LN	NC (sinus)	T2N1M0	50; M	30.04.13	6	Surgery	
77	PT	OP (tonsil)	T2N2a	64; M	14.05.13	7	Surgery and RT	Used in current study
78	PT	OC (soft palate)	NA	57; M	21.05.13	3		
79	PT	OC (FOM)	T2N2a	62; M	30.05.13	3	Surgery	
80	LN	L (supraglottis)	T4N2bM0	58; M	10.06.13	9	Surgery and CRT	Used in current study

81	PT	OC (tongue)	T2N1M0	56; F	13.06.13	1	Surgery	
82	PT	OP (tonsil)	T1N2a	60; M	25.06.13	3		
83	PT	OC (tongue)	T2N0M0	53; F	27.06.13	1	Surgery	
84	PT	L (supraglottis)	T2N0M0	68; F	02.07.13	8	Surgery and RT	Used in current study
85	PT	OP (BOT)	T1N2a	60; M	02.07.13	10	Surgery and CRT	
86	PT	L (supraglottis)	NA	49; M	23.07.13	3		
87	PT	OP (tonsil)	NA	59; F	23.07.13	6		
88	LN	Unknown	N2b	60; M	30.07.13	10	Surgery and CRT	
89	PT	OC (FOM)	T3N0M0	49; M	15.08.13	5	Surgery	Used in current study
90	PT	L (vocal cord)	T1/T2N0	57; M	20.08.13	NIL	Surgery	No Samples
91	PT	OP (tonsil)	NA	66; F	27.08.13	4		
92	PT	OC (FOM)	T2N0	64; M	29.08.13	8	Surgery	Used in current study
93	PT	OP (tonsil)	T1/T2N0M0	51; M	03.09.13	8	Surgery and CRT	
94	PT	L (vocal cord)	T1aN0M0	80; M	10.09.13	NIL	Surgery	No Samples
95	PT	L (aryepiglottis)	NA	76; M	17.09.13	2		
96	NA	L (piriform fossa)	NA	47; M	17.09.13	NIL		No Samples
97	LN	Unknown	T0N2b	76; M	24.09.13	10	Surgery and CRT	
98	LN	Unknown	NA	86; M	24.09.13	NIL		No Samples
99	LN	OP (tonsil)	NA	71; M	24.09.13	21	Surgery and CRT	
100	PT	L (glottis)	T1N0	63; F	24.09.13	NIL	Surgery	No Samples
101	PT	PS (sinonasal)	NA	72; M	01.10.13	11	Surgery	
102	PT	L (glottis)	T1N0	73; M	01.10.13	NIL	Surgery	No Samples
103		Lymphoma	NA	35; M	01.10.13	NIL		
104	PT	OP (tonsil)	T3N2	88; F	08.10.13	3	Surgery	
105	PT	OP (tonsil)	NA	51; M	15.10.13	7	Surgery	
106	PT	L	T4N0	71; M	15.10.13	NIL	Surgery	No Samples
107	NA	NA	T3N1	88; F	29.10.13	NIL	Surgery	
108	NA	NA	NA	62; F	15.10.13	NIL	Surgery	
109	NA	NA	T2N0M0	68; F	10.12.13	NIL	Surgery	
110	PT	L	T1bN0	62; M	17.12.13	NIL	Surgery	
111	LN	Unknown	N1	53; M	17.12.13	5	Surgery	
112	LN	Unknown	NA	54; M	07.01.14	NIL		No Samples
113	PT	OP (tonsil)	T3N1	70; F	14.01.14	12		
114	PT	OP (tonsil)	T2N1	47; M	04.02.14	2	Surgery	
115	PT	OC (tongue)	TxN0	55; M	04.02.14	NIL	Surgery	No Samples
116	PT	OP (tonsil)	TxNx	54; M	25.02.14	4	Surgery	
117	NA	NA	NA	47; F	25.02.14	1		

118	PT	L	T4N0	79; F	25.02.14	NIL	Surgery	No Samples
119	PT	L	T1N0	84; M	11.03.14	NIL	Surgery	
120	PT	OP (BOT)	T2N2a	62; F	11.03.14	8	Surgery	
121	PT	L	T4N2	78; M	25.03.14	9	Surgery	
122	LN	OP (tonsil)	NA	32; M	08.04.14	18	Surgery	Used in current study

The tumour tissues were recruited during 30.10.2012-08.04.2014. NIL labels indicate that there are no tissue sample was recruited following informed consent but the blood samples were recruited for other research project in current research group. NA samples indicate no additional information could be recruited.
Abbreviation: PT: primary tumour; LN: lymph node; OP: oropharyngeal; L: laryngeal; OC: oral cavity; PS: paranasal sinus; NA: not applicable; RT: radiotherapy; CRT: chemo-radiotherapy.

9.2. Representative H&E staining on pre-MF tissues

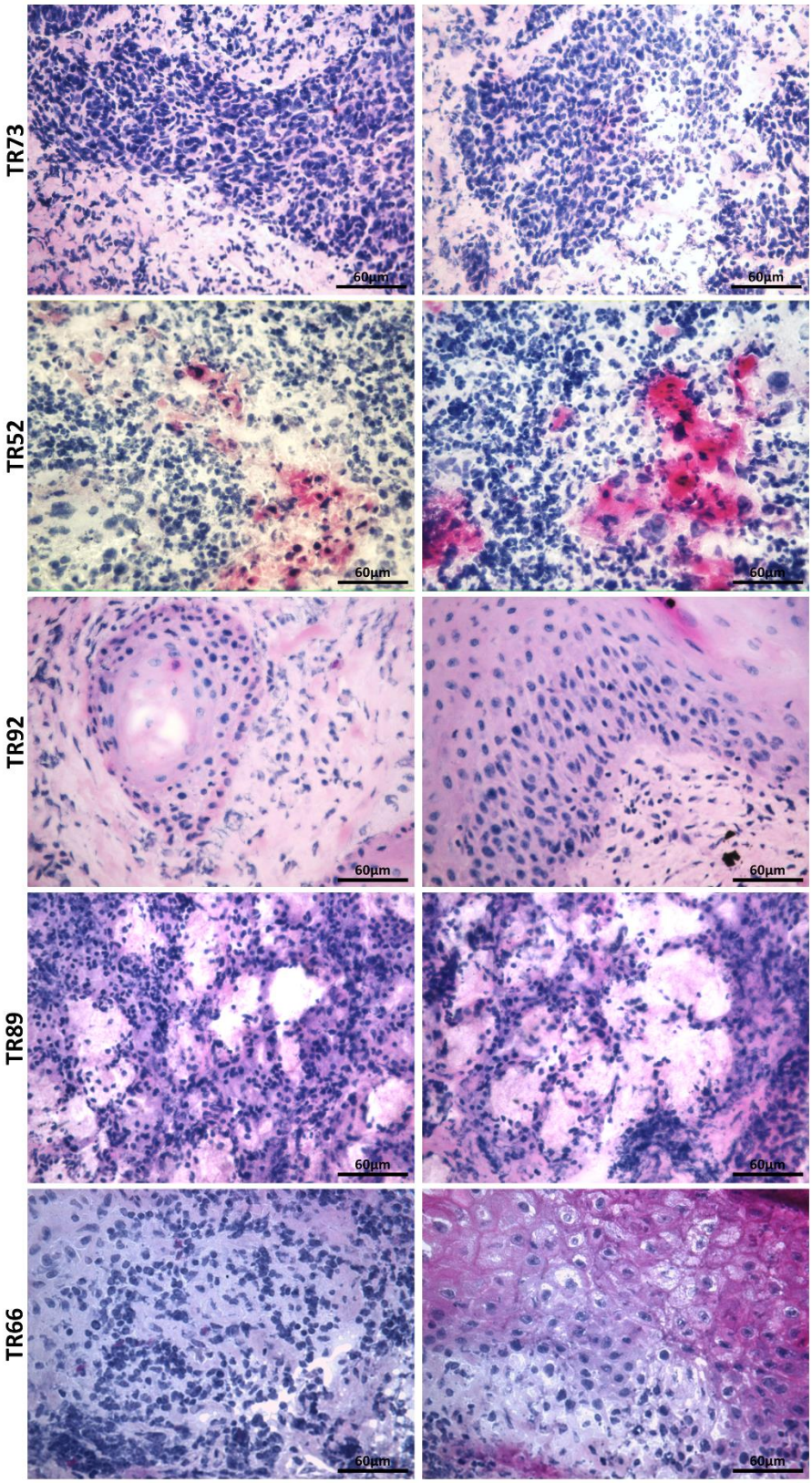


Figure 9.1. Representative staining on frozen tissue sections of 5 HNSCC pre-MF tissues which was not subjected to microfluidic system and on-chip irradiation.
Images are the H&E stained sections at x400 magnification.

9.3. Tris buffered saline (TBS)

1L of dH_2O containing 121g (1M) of Tris (Trizma T1503; Sigma-Aldrich) and 170g (3M) of NaCl (S3014; Sigma-Aldrich) was prepared. The pH was adjusted to 7.6 by adding about 80mL of concentrated HCl and measured by using pH meter. The stock solution (20x concentrated stock solution) was stored at room temperature and was added into distilled-water in 50 times dilution before use.

9.4. TAE buffer

Into 600 mL of double-distilled water, 242g of Tris Base (121.1g of MW), 57.1mL of glacial acetic acid and 100mL of 0.5M ethylenediaminetetraacetic acid (EDTA) were added to make up to final volume of 1 litre. The stock solution (50x concentrated) was stored at room temperature and final working concentration (1x) was prepared in distilled water before use which contained 0.04M of Tris, 0.001M of EDTA and acetic acid.

9.5. Borate buffer

To make 100mL of borate buffer, 55mL of Boric acid (0.2M) and 45mL of sodium tetraborate (0.05M) were mixed and the pH of the buffer was adjusted to 8.4. The buffer was stored at room temperature.

9.6. Mean absorbance values (LDH) of 13 rat liver tissues perfused with medium at different flow rates

Table 9.2. Mean LDH absorbance values of 13 rat liver tissues perfused with different flow rates. Mean values of every 24 hours throughout the 4 days in the device were obtained and the standard deviation of the mean was calculated.

Flow rates	Microfluidic time	Number of repeat				Mean LDH absorbance	Standard Deviation
2µL/min	Day 0	0.391	0.295	0.327	0.318	0.333	0.041
	Day 1	0.202	0.132	0.139	0.187	0.165	0.035
	Day 2	0.054	0.039		0.020	0.038	0.017
	Day 3	0.021	0.000		0.000	0.007	0.012
	Day 4	0.052	0.004	0.030	0.066	0.038	0.027
5µL/min	Day 0	0.256	0.373	0.313		0.314	0.059
	Day 1	0.026	0.004	0.099		0.043	0.050
	Day 2	0.000		0.024		0.012	0.017
	Day 3	0.001		0.009		0.005	0.006
	Day 4	0.000	0.002	0.013		0.005	0.007
7µL/min	Day 0	0.363	0.311			0.337	0.037
	Day 1	0.159	0.200			0.179	0.029
	Day 2	0.052	0.043			0.047	0.007
	Day 3	0.000	0.000			0.000	0.000
	Day 4	0.019	0.000			0.009	0.013
10µL/min	Day 0	0.193	0.284			0.238	0.064
	Day 1	0.215	0.064			0.140	0.106
	Day 2	0.025	0.010			0.018	0.011
	Day 3	0.070	0.005			0.037	0.046
	Day 4	0.008	0.000			0.004	0.005
12µL/min	Day 0	0.294				0.294	
	Day 1	0.034				0.034	
	Day 2	0.004				0.004	
	Day 3	0.028				0.028	
	Day 4	0.001				0.001	
15µL/min	Day 0	0.338				0.338	
	Day 1	0.046				0.046	
	Day 2	0.002				0.002	
	Day 3	0.006				0.006	
	Day 4	0.001				0.001	

9.7. Expression data of γH2AX, caspase-cleaved CK18, Ki-67 and Bcl-2 on two HNSCC cell lines

Table 9.3. Summary of expression data on two cell lines (UMSCC-47 and UMSCC-11) which were subjected to different treatment.

Dependent Variable	Treatment	UMSCC-47		UMSCC-11	
		Mean	SEM	Mean	SEM
γH2AX (DNA-DSBs)	Control	41.8	2.4	41.2	10.5
	2.5μM	82.9	3.6	72.3	11.1
	5μM	78.0	3.5		
	10μM	88.4	1.5		
	20μM	78.4	3.4	67.5	7.1
M30 (Caspase-cleaved CK18)	Control	2.7	0.6	0.8	0.4
	2.5μM	4.2	0.7	3.7	0.5
	5μM	4.1	0.5		
	10μM	5.4	0.8		
	20μM	8.7	1.4	2.6	0.3
Ki-67 (Proliferation)	Control	82.6	3.6	64.6	1.9
	2.5μM	3.2	0.3	39.5	8.8
	5μM	28.5	3.8		
	10μM	3.2	0.4		
	20μM	15.2	2.9	25.4	8.0
Bcl-2 (Anti-apoptosis marker)	Control	7.4	0.8	-	-
	2.5μM	3.4	0.6	-	-
	5μM	4.6	0.8		
	10μM	3.0	1.0		
	20μM	7.9	1.6	-	-

The expression data includes the mean percentage of cells positive to γH2AX, caspase-cleaved CK18, Ki-67 and Bcl-2.

9.8. Results of EdU incorporation into HNSCC cells and tissues

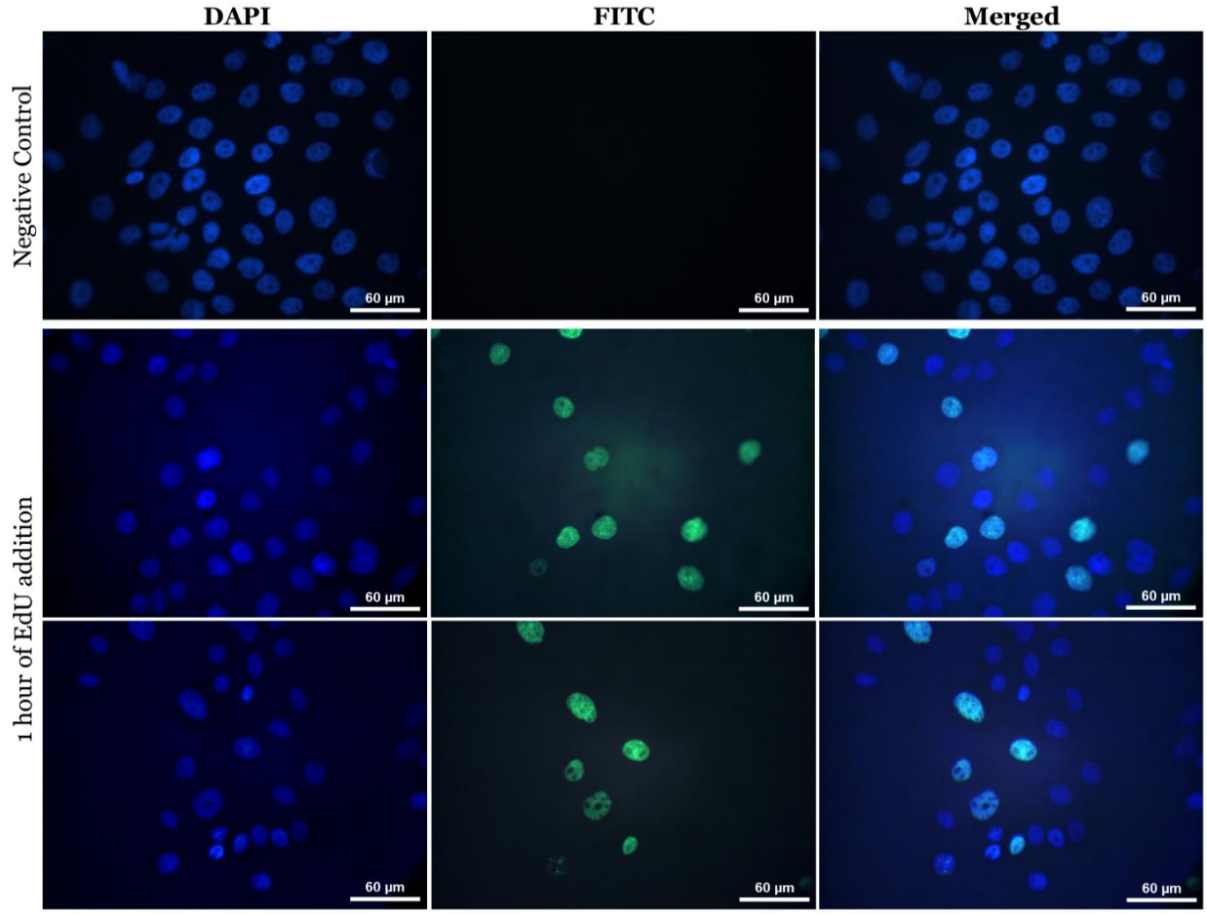


Figure 9.2. Representative fluorescent microscopy images (x400 magnification) of an oropharyngeal epithelial cell line (UMSCC-47) following 1-hour exposure to EdU and subsequent detection using Click-iT technology.
Medium with no EdU addition acted as a negative control. Cells were counter-stained with DAPI to identify the nuclei. Blue indicates DAPI counterstain for nuclei and green indicates the presence of incorporated.

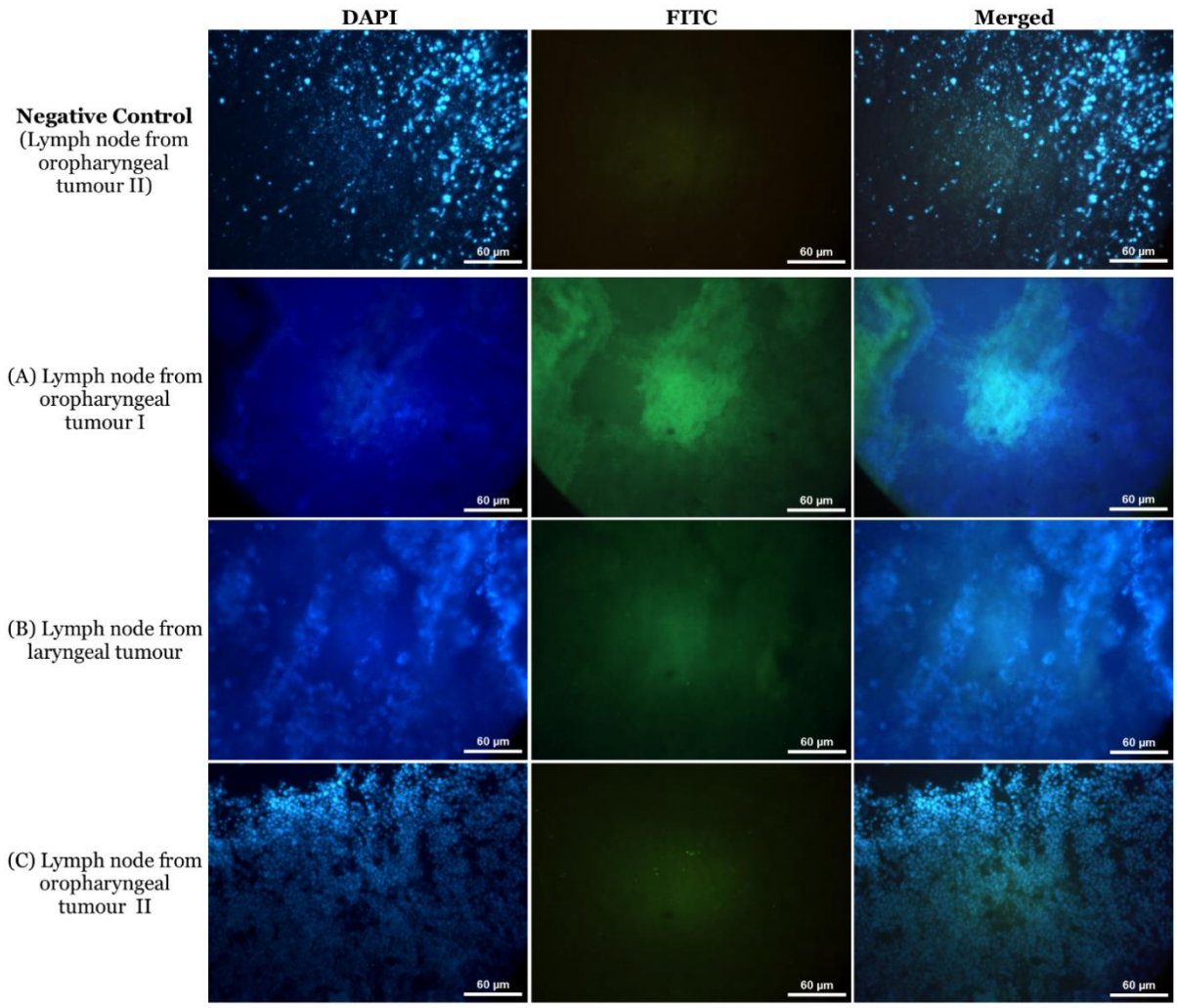


Figure 9.3. Representative fluorescent microscopy (x400 magnification) of EdU on three lymph node tissues

Metastastic lymph node from (A) an oropharyngeal tumour I, (B) a laryngeal tumour and (C) an oropharyngeal tumour II following 6-hour exposure to EdU (Green) in microfluidic culture. Tissue with no EdU addition acted as a negative control. Cells were counter-stained with DAPI to identify the nuclei (blue).

9.9. Results of 2-NBDG incorporation into HNSCC cells and tissues

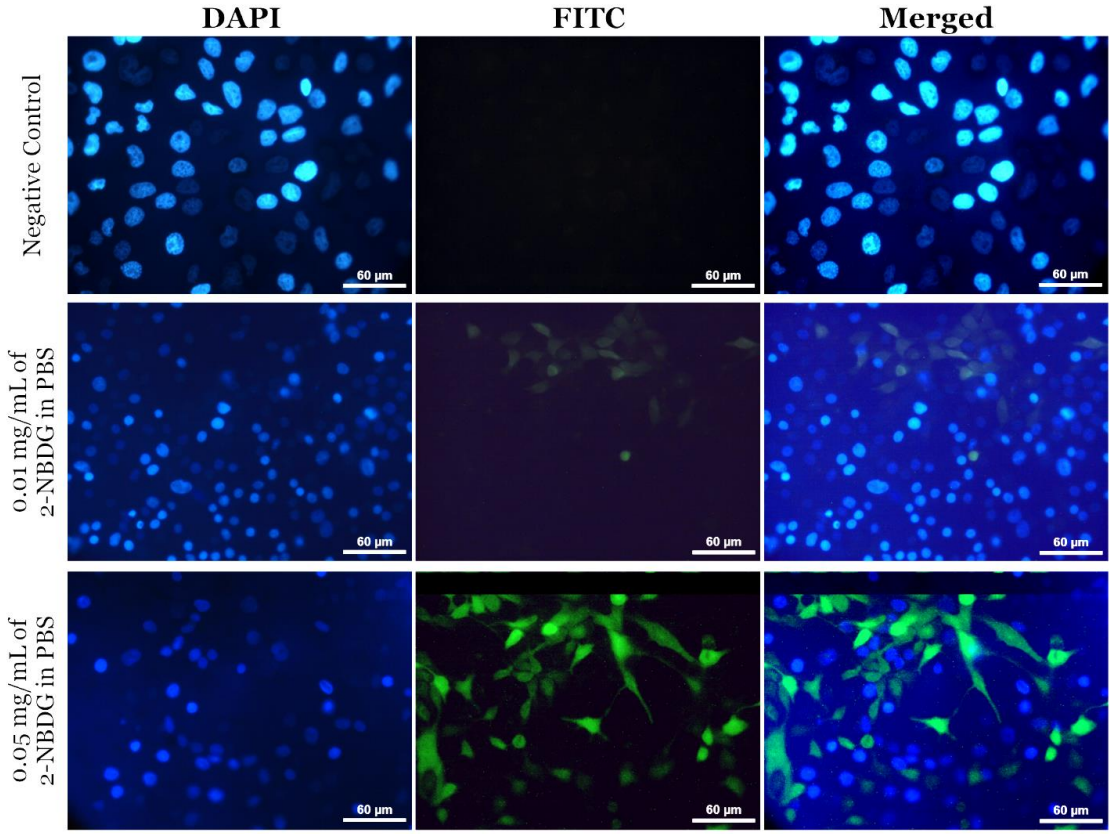


Figure 9.4. Representative fluorescent microscopic images (x400 magnification) of an oropharyngeal cell line (UMSCC-47) following 1-hour exposure to PBS containing no 2-NBDG (negative control), 0.01mg/mL and 0.05mg/mL of 2-NBDG.
Cells were counter-stained with DAPI to identify the nuclei (blue). Green represents positive uptake of 2-NBDG, images to the right are composite images of both DAPI and green fluorescence (2-NBDG).

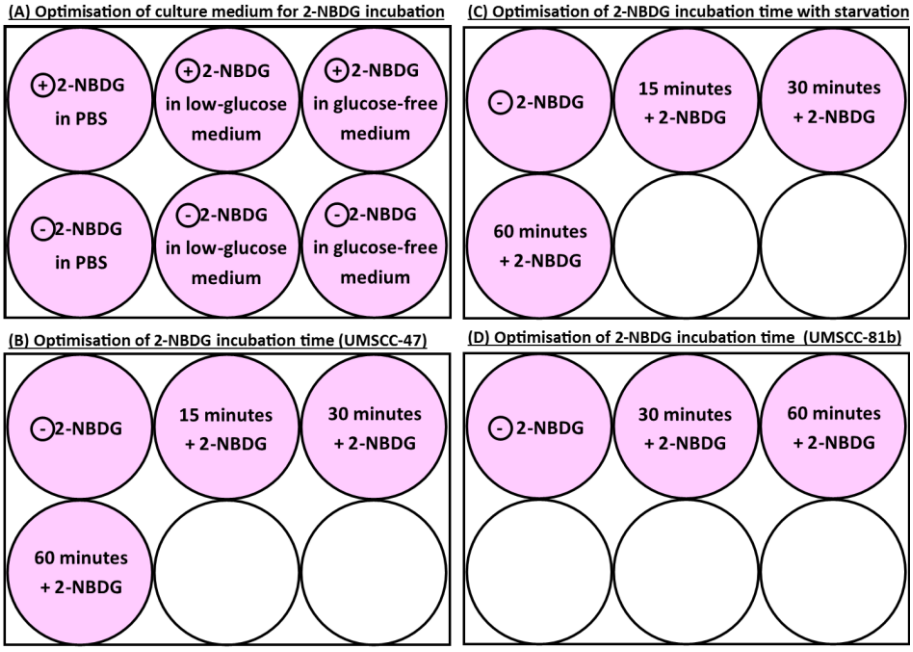


Figure 9.5. Layout of 6 well plates prepared with UMSCC cells on sterile coverslips for the analysis of uptake of the glucose analogue 2-NBDG.
(A) Different medium comparison on UMSCC-47 cells. (B) and (C) Optimisation of incubation time with and without starvation on UMSCC-47 cells. (D) Comparison of 30- and 60-minute incubation time on UMSCC-81b cells.

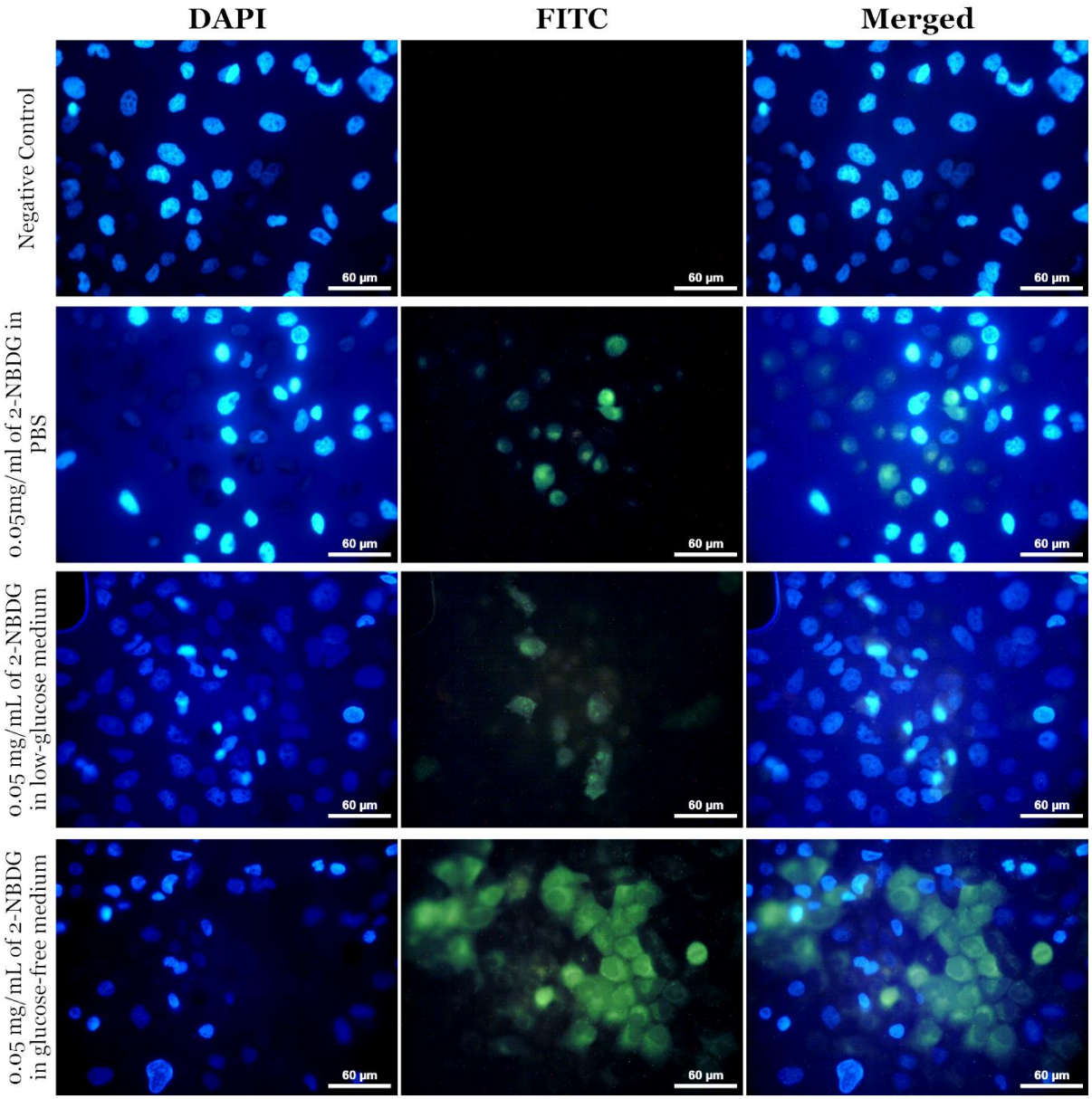


Figure 9.6. Representative fluorescent microscopic images (x400 magnification) of an oropharyngeal epithelial cell line (UMSCC-47) following 1-hour exposure to medium only (negative control), 0.05mg/mL of 2-NBDG in: PBS, low-glucose medium and glucose-free medium.

Cells were counter-stained with DAPI to identify the nuclei (blue). Green represents fluorescent stains for positive uptake of 2-NBDG.

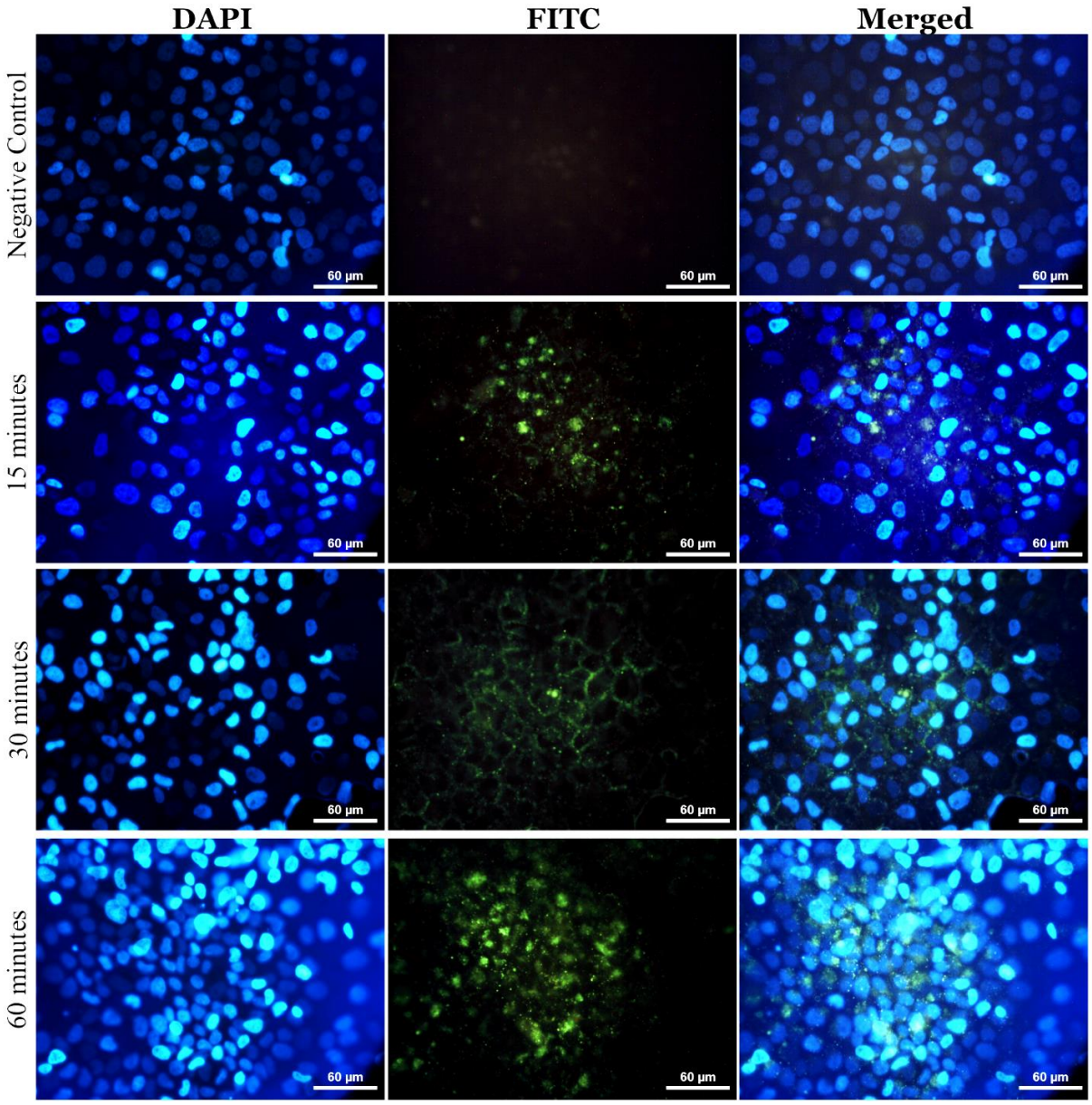


Figure 9.7. Representative fluorescent microscopic images (x400 magnification) of oropharyngeal cells (UMSCC-47) following 15, 30 and 60 minutes of exposure to glucose-free medium containing 0.05mg/mL of 2-NBDG and medium only (negative control).
Cells were counter-stained with DAPI to identify the nuclei (blue). Green represents fluorescent stains for positive uptake of 2-NBDG.

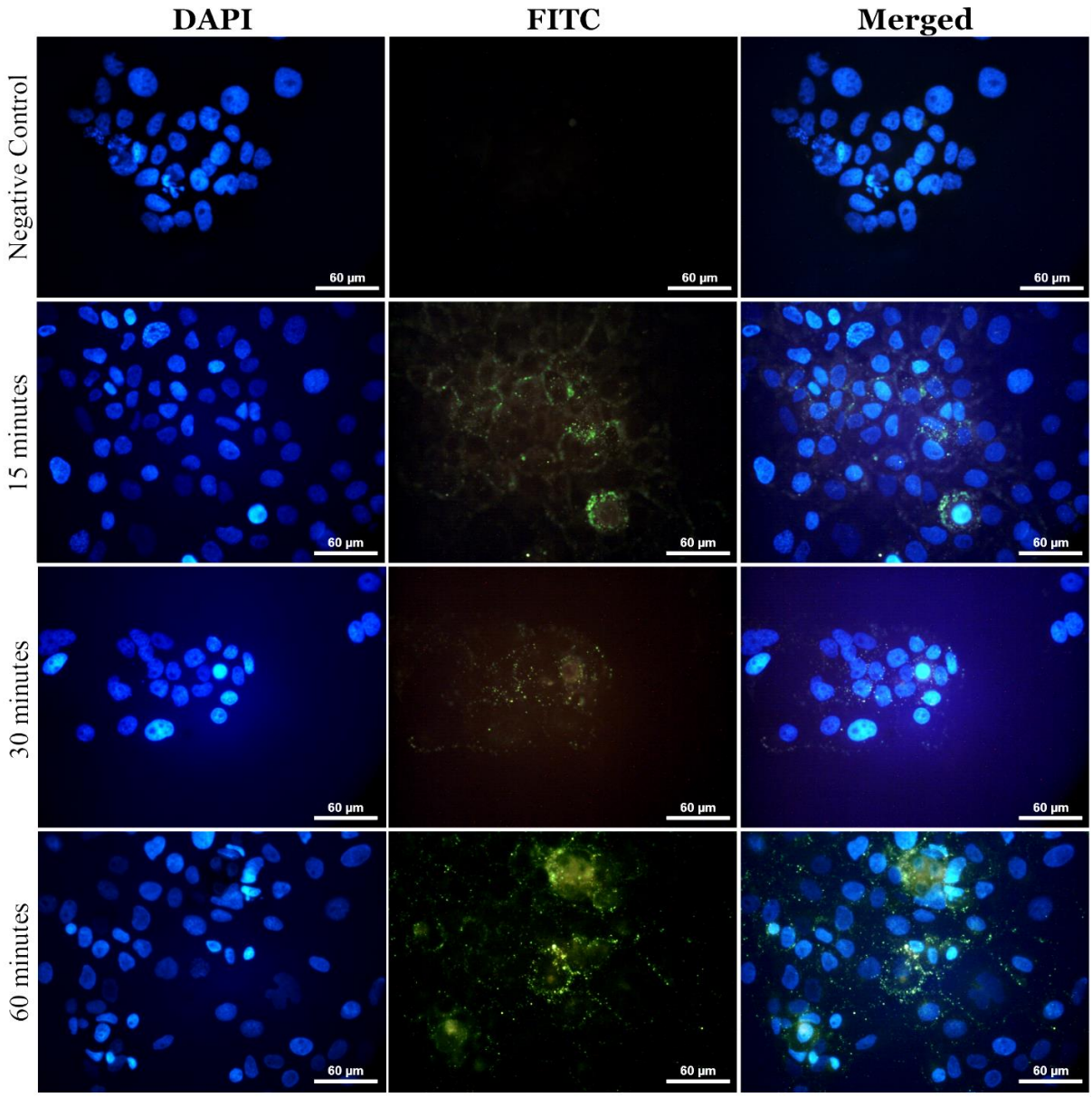


Figure 9.8. Representative fluorescent microscopic images (x400 magnification) of oropharyngeal cells (UMSCC-47) which were starved with glucose-free medium for 2 hours and followed by the exposure to medium only (negative control) and medium containing 0.05mg/mL of 2-NBDG for 15, 30 and 60 minutes.

Cells were counter-stained with DAPI to identify the nuclei (blue). Green represents fluorescent stains for positive uptake of 2-NBDG.

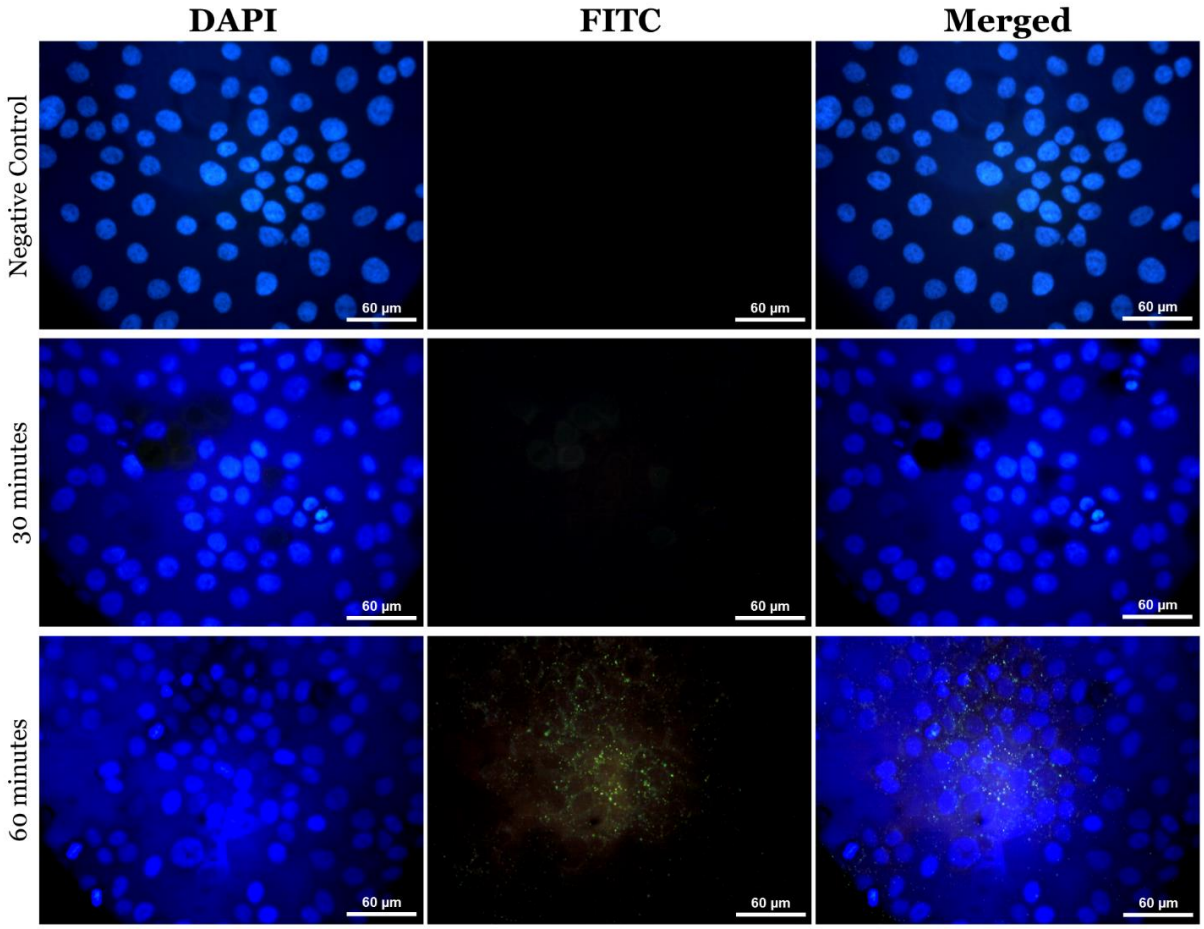


Figure 9.9. Representative fluorescent microscopic images (x400 magnification) of second oropharyngeal epithelial cell line (UMSCC-81b) which exposed to medium only (negative control) and medium containing 0.05mg/mL of 2-NBDG for 30 and 60 minutes.
Cells were counter-stained with DAPI to identify the nuclei (blue). Green represents fluorescent stains for positive uptake of 2-NBDG.

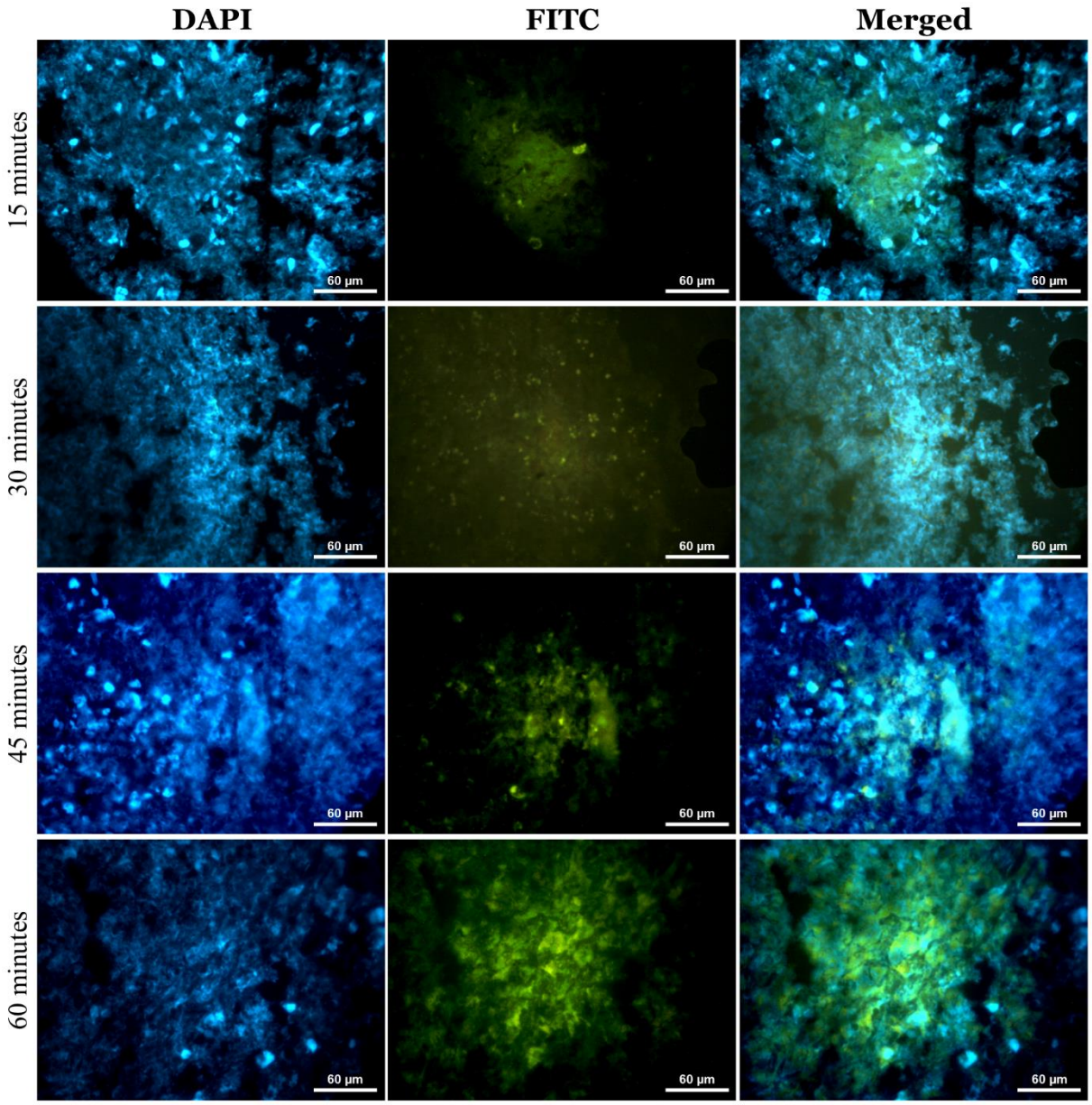


Figure 9.10. Representative fluorescent microscopic images (x400 magnification) of the uptake of 2-NBDG on primary oral cavity SCC (tonsil) tumours following 15, 30, 45, and 60 minutes of incubation with 0.05mg/mL of 2-NBDG.

Tissue sections were counter-stained with DAPI to identify the nuclei (blue). Green represents fluorescent stains for positive uptake of 2-NBDG.

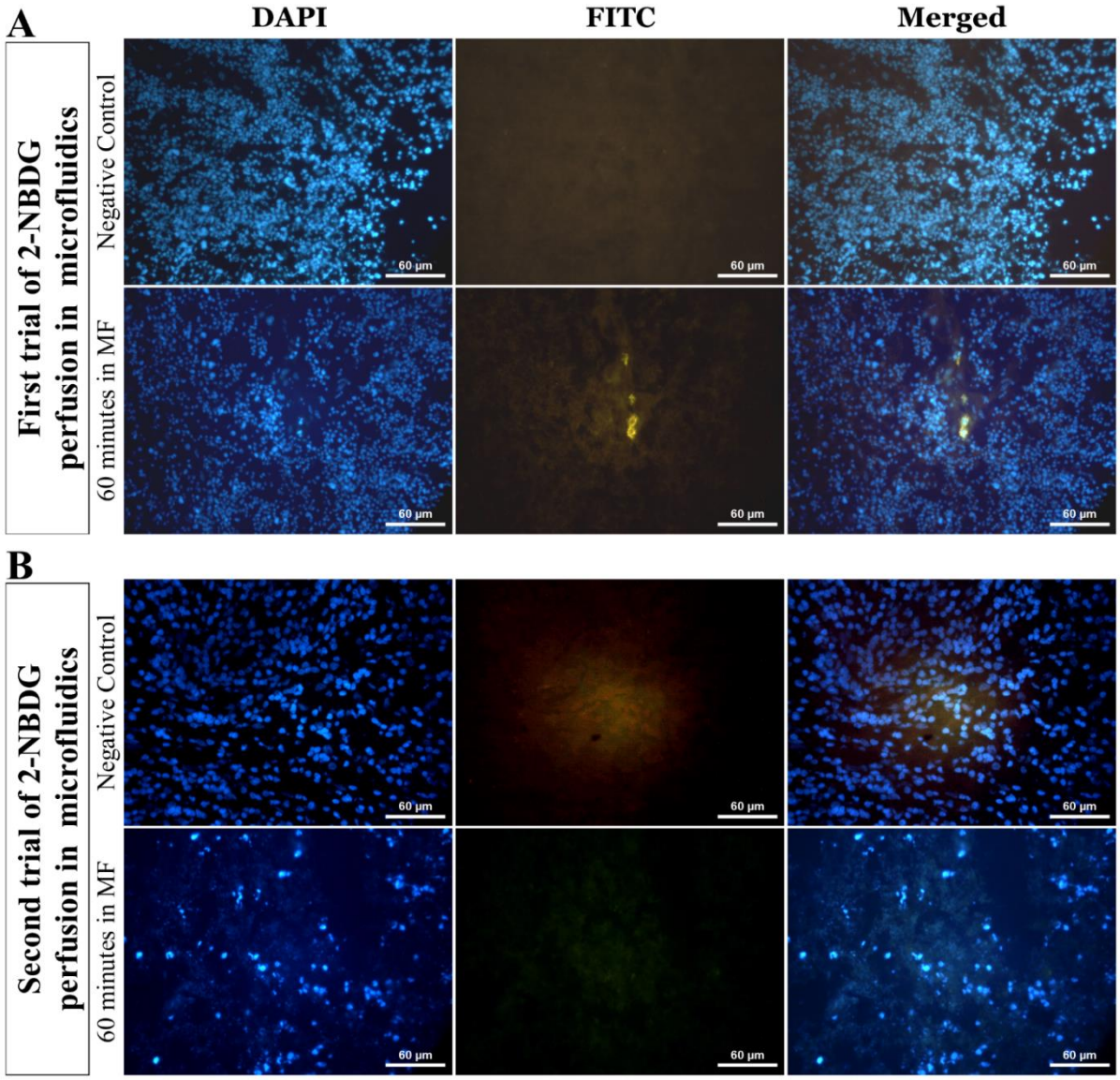


Figure 9.11. Representative fluorescent microscopic images (x400 magnification) of the uptake of 2-NBDG on metastatic lymph neck node from oropharyngeal tumour following 60 minutes of incubation with medium only (negative control) and medium containing 0.05mg/mL of 2-NBDG in two independent sets of microfluidics (A&B).

The 0.05mg/mL of 2-NBDG was prepared in glucose-free medium and in dark. Tissue sections were counter-stained with DAPI to identify the nuclei (blue). Green represents fluorescent stains for positive uptake of 2-NBDG. MF: microfluidic device.

9.10. Results data of CK18-LI, γH2AX, Ki-67 and TUNEL assay of five HNSCC tumours

Table 9.4. Summary of CK18-LI, mean percentage of cells positive to γH2AX, Ki-67 and TUNEL assay on all individual tissues of the five primary tumours.

		CK18LI	γH2AX	Ki-67	TUNEL
Lymph node (unknown)	MF	7.38	11.46	12.04	0.53
	MF	15.41	10.50	38.44	0.38
	5Gy	7.26	9.96	2.12	2.44
	5Gy	16.30	17.45	40.82	3.87
	10Gy	14.77	21.69	9.13	6.59
	10Gy	4.67	18.77	17.45	2.54
	15Gy	52.17	23.15	2.25	22.63
	15Gy	17.36	18.14	7.70	19.89
	20Gy	7.27	14.98	7.03	37.78
	20Gy	17.01	17.95	4.88	17.40
Lymph node (laryngeal)	MF	3.42	19.12	11.69	5.37
	MF	4.89	15.92	5.43	1.45
	MF	12.73	33.17	5.00	1.58
	MF	15.74	29.23	9.41	1.81
	MF	5.25	6.66	20.53	1.13
	MF	5.47	9.50	18.71	1.17
	5Gy	12.57	25.88	2.40	4.99
	5Gy	2.05	25.31	12.16	0.94
	10Gy	6.23	22.92	5.18	2.34
	10Gy	6.24	30.91	7.06	0.84
	15Gy	36.64	38.40	3.18	24.29
	15Gy	26.77	43.46	6.19	6.23
	20Gy	13.32	26.09	3.35	3.09
	20Gy	26.77	33.50	2.33	1.76
Oral cavity floor of mouth I	MF	7.34	0.00	9.54	-
	MF	3.00	2.72	0.00	-
	5Gy	5.29	19.70	7.89	-
	5Gy	12.41	4.49	0.00	-
	10Gy	7.26	25.43	4.00	-
	10Gy	12.62	2.07	0.00	-
	15Gy	5.30	5.62	5.32	-
	15Gy	14.92	4.21	0.00	-
	20Gy	9.93	27.03	2.93	-
	20Gy	14.92	5.75	0.00	-
Oral cavity floor of mouth II	MF	0.96	33.82	6.73	0.95
	MF	4.69	17.34	14.16	19.53
	MF	1.96	21.99	0.00	0.00
	MF	0.13	25.45	11.26	5.66
	MF	1.96	17.73	1.02	0.46
	5Gy	9.15	41.44	12.51	4.43
	5Gy	2.71	46.60	1.77	14.22
	10Gy	8.42	55.87	3.42	26.87
	10Gy	0.29	51.65	0.34	1.36
	15Gy	6.46	67.65	6.50	26.87
	15Gy	1.28	40.66	0.87	0.58
	20Gy	9.08	71.79	4.39	3.58
	20Gy	1.64	60.18	5.95	11.81
Laryngeal supraglottic tumour	MF	13.69	10.05	21.91	-
	MF	21.93	12.47	46.60	-
	MF	17.69	8.20	24.74	2.57
	MF	13.96	8.16	17.80	2.92
	MF	17.05	18.21	10.35	12.14
	MF	19.33	3.66	5.39	10.43
	MF	14.66	11.28	42.38	15.57
	MF	23.44	10.52	46.87	
	5Gy	26.75	18.92	0.00	8.98
	5Gy	26.75	0.00	16.16	20.03
	10Gy	23.10	18.26	1.70	32.90
	10Gy	17.79	25.64	10.23	37.51
	15Gy	29.20	0.00	53.51	6.36
	15Gy	26.57	10.75	4.52	27.07
	20Gy	38.56	15.57	11.99	17.09
	20Gy	24.49	11.81	1.22	25.78

The data was subjected to statistical Pearson's correlation test.

9.11. Pearson's correlation between tested markers on primary tumours

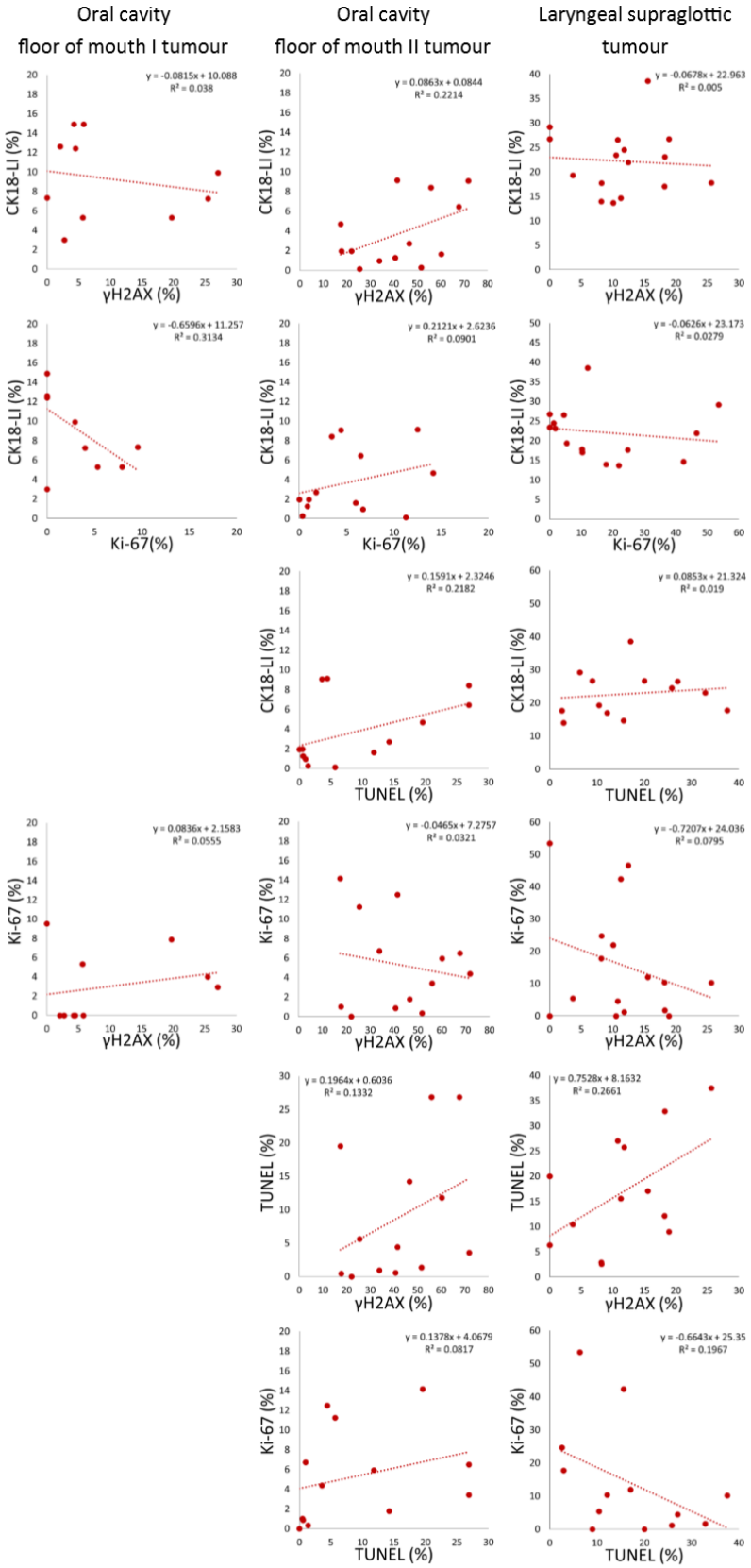


Figure 9.12. Scatter plots exemplifying the Pearson's correlation between markers on the three primary tumour (oral cavity I and II and laryngeal).
The correlation tests include CK18-LI vs γH2AX, CK18-LI vs Ki-67, CK18-LI vs TUNEL, Ki-67 vs γH2AX, TUNEL vs γH2AX, and Ki-67 vs TUNEL.

9.12. Quantitative RT-PCR results of six genes related to radiation response on HNSCC tumours

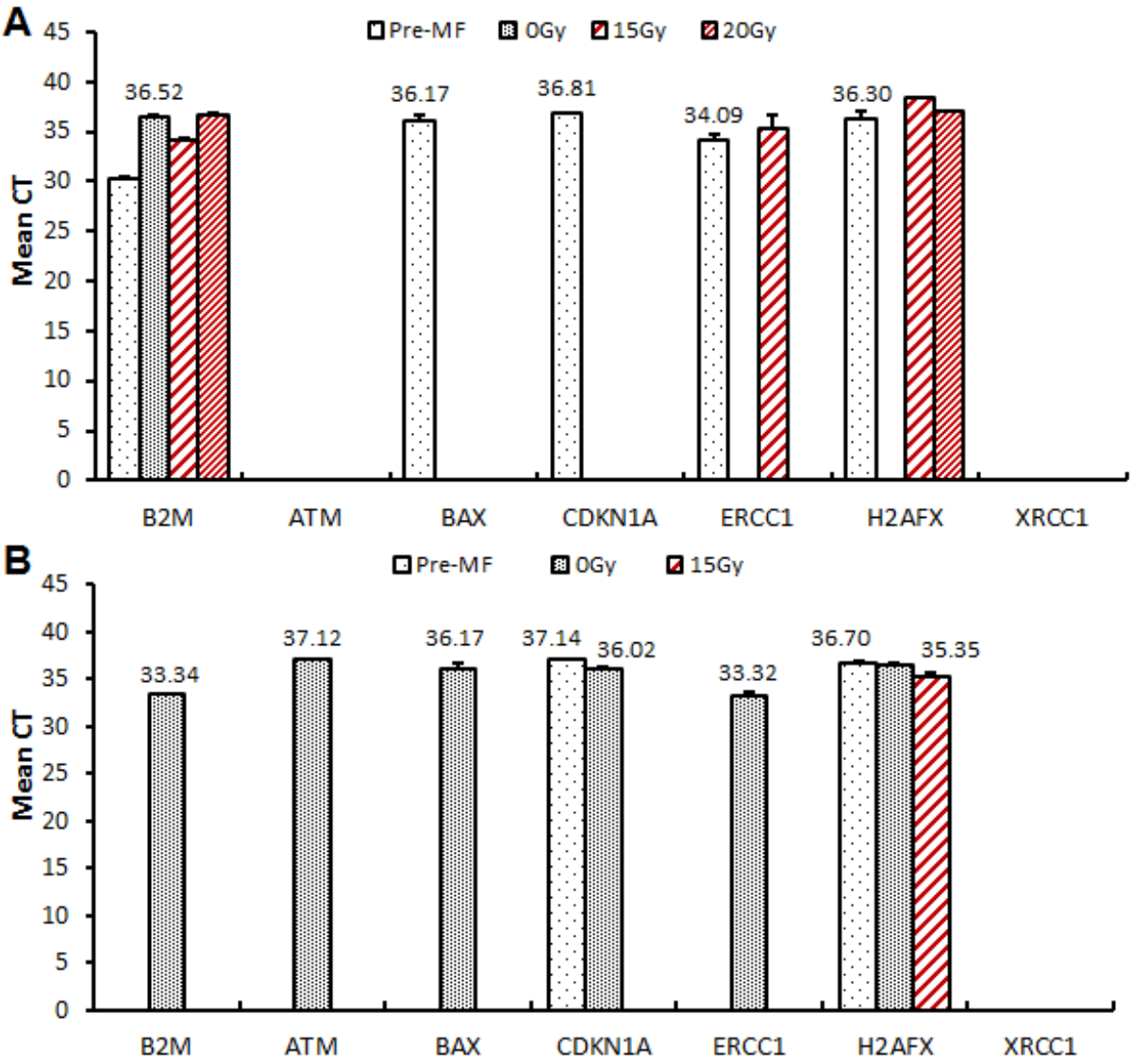


Figure 9.13. Quantitative RT-PCR analysis of the reference B2M gene and the six irradiation response genes on (A) TR92 and (B) TR80.
The pre-MF, 0Gy, 15Gy and 20Gy irradiated tissues of TR92 tumour and the pre-MF, 0Gy and 15Gy irradiated tissues of TR80 were involved in q-RT-PCR. There was n=1 carried out on each sample. The mean CT for each gene was obtained from triplicate wells.